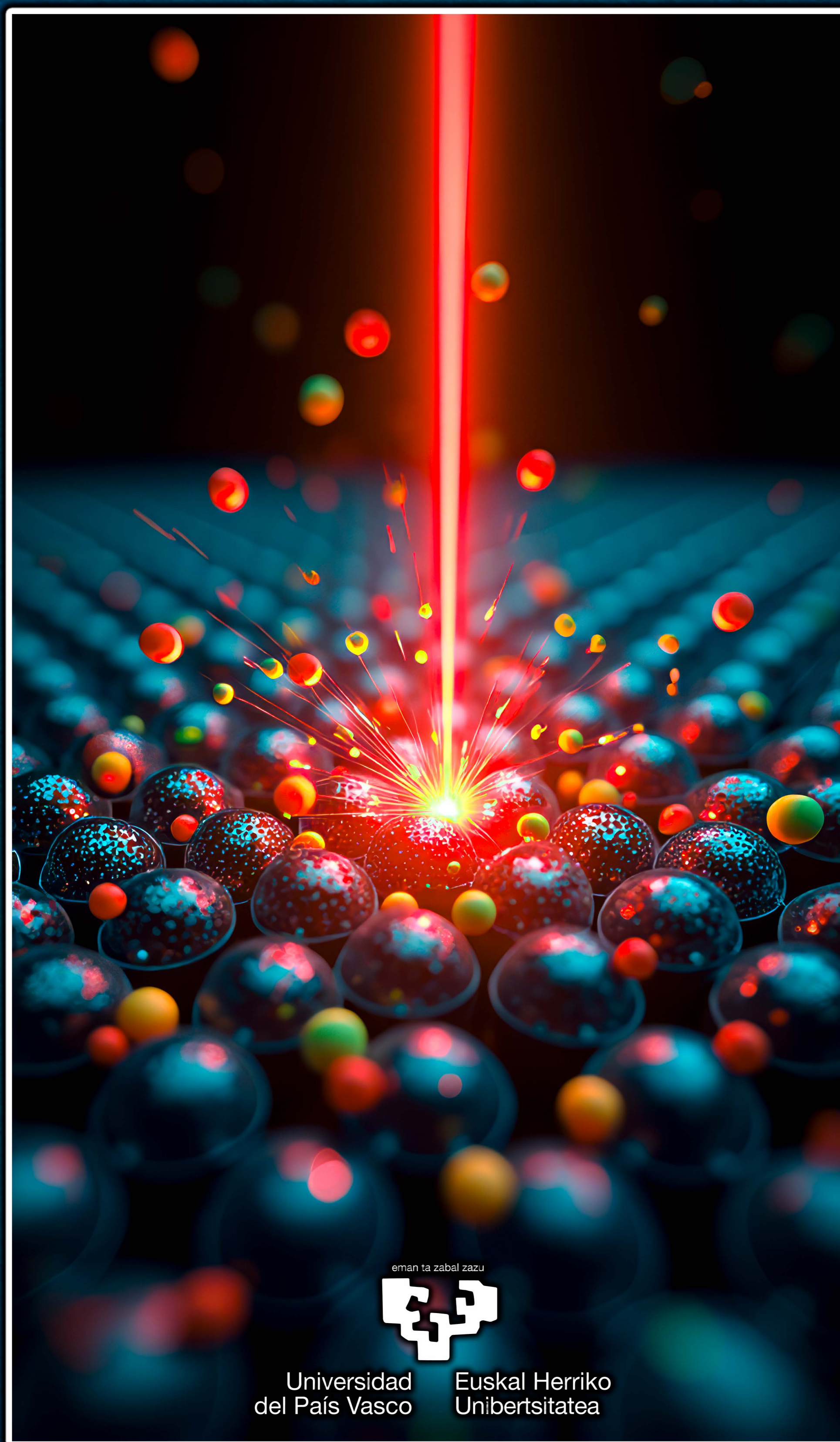


Theoretical description of femtosecond laser-induced desorption dynamics using ab initio and machine learning methods: pure CO and mixed CO+O adlayers on Pd(111)



**Alfredo Serrano Jiménez**

Supervised by

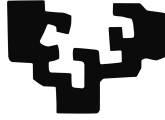
Dr. Maite Alducin Ochoa & Prof. Joseba Iñaki Juaristi Oñden

2024





eman ta zabal zazu



Universidad del País Vasco Euskal Herriko Unibertsitatea

---

**Theoretical description of femtosecond laser-induced desorption dynamics using ab initio and machine learning methods: pure CO and mixed CO+O adlayers on Pd(111)**

---

**Alfredo Serrano Jiménez**

**Supervisors / Zuzendariak / Directores:**

Dr. Maite Alducin Ochoa

Prof. Joseba Iñaki Juaristi Oliden

**Manuscript submitted for the degree of Doctor (PhD)  
in Physics of Nanostructures and Advanced Materials**

*Material Aurreratuak eta Nanoegituren Fisika Doktorea  
titulua lortzeko aurkeztutako eskuizkribu*

Manuscrito presentado para la obtención del título de Doctor  
en Física de Nanoestructuras y Materiales Avanzados

**2024**

## **Supervisors**

**Dr. Maite Alducin Ochoa**

Centro de Física de Materiales CFM/MPC (CSIC-UPV/EHU)

**Prof. Joseba Iñaki Juaristi Oliden**

Departamento de Polímeros y Materiales Avanzados: Física, Química y Tecnología; Facultad de Química (UPV/EHU)

Centro de Física de Materiales CFM/MPC (CSIC-UPV/EHU)

## **Financial Support**

**Centro de Física de Materiales CFM/MPC (CSIC-UPV/EHU)**

**Donostia International Physics Center (DIPC)**

**Universidad del País Vasco/Euskal Herriko Unibertsitatea (UPV/EHU)**

**Departamento de Educación (Gobierno Vasco)**

**Ministerio de Ciencia, Innovación y Universidades (Gobierno de España)**

# Contents

---

<b>Contents</b>	<b>iii</b>
<b>Abstract</b>	<b>vii</b>
<b>Resumen</b>	<b>xv</b>
<b>Acknowledgments</b>	<b>xxv</b>
<b>Eskerrak</b>	<b>xxix</b>
<b>Agradecimientos</b>	<b>xxxiii</b>
<b>List of Publications</b>	<b>xxxvii</b>
<b>List of Acronyms</b>	<b>xxxix</b>
<b>1 Introduction</b>	<b>1</b>
<b>I Theoretical background</b>	<b>11</b>
<b>2 Theory of molecule-surface interactions</b>	<b>13</b>
2.1 Adiabatic approximation . . . . .	13
2.2 Born-Oppenheimer approximation . . . . .	18
2.3 Density functional theory . . . . .	23
2.3.1 Hohenberg-Kohn theorem . . . . .	27
2.3.2 Kohn-Sham equations . . . . .	31
2.3.3 Exchange-correlation functionals . . . . .	37
2.3.3.1 Local density approximation (LDA) . . . . .	40
2.3.3.2 Generalized gradient approximation (GGA) . . . . .	44
2.3.3.3 Meta-generalized gradient approximation (mGGA) . . . . .	45
2.3.3.4 Hybrid functionals . . . . .	47
2.3.3.5 Van der Waals functionals . . . . .	48

<b>3</b>	<b>Femtosecond laser-induced photodesorption</b>	<b>53</b>
3.1	Photoinduced desorption mechanisms . . . . .	53
3.2	Photoinduced desorption on metallic surfaces . . . . .	61
3.2.1	Substrate excitation: the two-temperature model . . . . .	62
3.2.2	Dynamics on adsorbates . . . . .	68
3.2.2.1	Classical approach for dynamics . . . . .	68
3.2.2.2	Adsorbate dynamics and the local density friction approximation . . . . .	70
3.2.2.3	Contribution of phononic excitations . . . . .	73
3.2.2.4	Calculation of adiabatic forces: ab initio molecular dynamics with electronic friction . . . . .	76
3.2.2.5	PES-mediated molecular dynamics with electronic friction . . . . .	79
<b>4</b>	<b>Machine learning and surface science</b>	<b>81</b>
4.1	Neural networks: general features and training process . . . . .	81
4.2	Methods for constructing neural network potential energy surfaces . . . . .	88
4.3	Embedded atom neural network (EANN) approach . . . . .	102
<b>II</b>	<b>Research results</b>	<b>109</b>
<b>5</b>	<b>0.75 ML CO/Pd(111) potential energy surface</b>	<b>111</b>
5.1	Description of the system in the reference ( $T_e, T_l$ ) – AIMDEF simulations . . . . .	112
5.2	Construction of a 0.75 ML CO/Pd(111) EANN PES: computational details . . . . .	113
5.2.1	Input data selection . . . . .	113
5.2.2	EANN parameter optimization . . . . .	116
5.2.3	PES quality assessment: static approach . . . . .	122
5.3	Determination of friction: numerical fit . . . . .	129
5.4	( $T_e, T_l$ ) – MDEF on 0.75 ML CO/Pd(111): dynamical quality tests . . . . .	134
5.5	Conclusions . . . . .	146
<b>6</b>	<b>Isotopic effect search on 0.75 ML CO/Pd(111)</b>	<b>149</b>
6.1	Theoretical background . . . . .	150
6.2	MDEF results for both CO isotopologues . . . . .	152
6.3	Conclusions . . . . .	157

<b>7</b>	<b>Multicoverage studies on CO/Pd(111) with MDEF</b>	<b>159</b>
7.1	Preliminary studies on multicoverage PESs . . . . .	160
7.2	Multicoverage EANN PES training and quality assessment . . . . .	164
7.3	Coverage dependence of the desorption of CO from Pd(111) induced by a single femtosecond laser pulse . . . . .	177
7.4	Simulations of two-pulse correlation experiments of CO desorption from Pd(111) at different coverages . . . . .	195
7.5	Conclusions . . . . .	203
<b>8</b>	<b>Photoinduced desorption on O+2CO/Pd(111) studied with (T<sub>e</sub>,T<sub>l</sub>)-AIMDEF</b>	<b>207</b>
8.1	The O+2CO/Pd(111) system: computational settings . . . . .	207
8.1.1	Relaxation . . . . .	207
8.1.2	Thermalization . . . . .	208
8.2	(T <sub>e</sub> , T <sub>l</sub> ) – AIMDEF and T <sub>e</sub> – AIMDEF on O+2CO/Pd(111) . . . . .	212
8.2.1	Insights into adsorbate dynamics . . . . .	213
8.2.2	CO desorption and oxidation probabilities on O+2CO/Pd(111)	218
8.2.2.1	Reaction probabilities by sites . . . . .	221
8.3	Conclusions . . . . .	223
<b>9</b>	<b>Conclusions &amp; Outlook</b>	<b>227</b>
	<b>List of Figures</b>	<b>249</b>
	<b>List of Tables</b>	<b>254</b>
	<b>Bibliography</b>	<b>255</b>



# Abstract

---

The present Thesis is devoted mainly to study and understand from a theoretical perspective the femtosecond laser-induced desorption of CO from Pd(111) with different coverages as well as the photodesorption and photooxidation of CO from Pd(111) when covered with 0.25 ML of oxygen and 0.50 ML of carbon monoxide (0.25 ML O+0.50 ML CO/Pd(111)).

**Chapter 1** introduces the research involved in this Thesis. Palladium (Pd) is a transition metal with well known catalytic properties, notably in facilitating hydrogenation, dehydrogenation, and oxidation reactions. Therefore, it is employed in a number of applications involving heterogeneous catalysis, such as in car exhaust systems, fuel cell technologies, or in the production of chemicals for agrochemical or pharmacological use, among others. It is also used for gas-sensing technologies. As a result, it becomes crucial to understand how Pd behaves dynamically in various contexts, this being linked with the current growing relevance of this metal species in heterogeneous catalysis and in chemical industry. Adsorption and desorption of gas-phase atoms and molecules are among the main chemical processes of interest Pd participates at. In addition, one of the molecules most commonly involved in the reactions catalyzed by Pd is carbon monoxide (CO). On this basis, we aim to conduct a theoretical study of the femtosecond laser-induced desorption of CO adsorbed on Pd(111) [CO/Pd(111)], in first instance, as well as the photodesorption and photooxidation of CO on a Pd(111) surface covered with 0.25 monolayers (ML) of atomic oxygen (O) and 0.50 ML of CO [O+2CO/Pd(111)]. Studying both systems across various initial conditions, for instance, CO coverage and absorbed laser fluence, we aim to unravel the underlying mechanisms of the laser-induced chemical processes.

As concluded in previous experimental works, CO/Pd(111) exhibits intricate structural properties that vary with coverage, and has more than 15 stable ways adsorbed CO can arrange on Pd(111). Hence, such a complex adsorbate-substrate system requires sophisticated theoretical models to accurately capture adsorption sites, energy coupling, and reaction dynamics. We pursue to simulate the desorption dynamics under femtosecond laser excitation using *ab initio* molecular dynamics with electronic friction and thermostats [( $T_e, T_l$ )-AIMDEF], which effectively incorporates both the laser-induced electronic and phononic excitations, while the adiabatic forces are calculated on-the-fly from the first principles density functional

theory (DFT). However, its high computational demand for calculating the DFT adiabatic forces limits this kind of simulations to short time scales and small statistical ensembles. To overcome these limitations, we train neural network-based potential energy surfaces (NN PESs) using AIMDEF data and employ those NN PESs to perform the equivalently accurate molecular dynamics simulations,  $(T_e, T_i)$ -MDEF. This alternative method dramatically enhances computational efficiency, thereby enabling extended simulations over longer time scales, the use of larger data sets, and the study of the laser-induced dynamics under more diverse initial conditions.

During our research we pursue to investigate several key aspects that were unsolved in experiments performed on CO/Pd(111). We want to unravel the relative role of surface electrons and phonons in the photoinduced processes. Also, we want to investigate whether there exists any isotope effect or not, this being linked to which mechanism –electronic or phononic– dominates photodesorption. Along with this, we are interested in simulating two-pulse correlation (2PC) experiments to further clarify the interplay between electronic and phononic excitations. Another goal is to examine how CO desorption probability changes with initial CO coverage and laser fluence, as well as how CO behaves after excitation, e.g., regarding its motion parallel and perpendicular to the surface plane. As a further step, we want to extend our approach to mixed O and CO adlayers on Pd(111), address some of the mentioned questions on CO/Pd(111) and also investigate how the presence of oxygen influences interadsorbate energy transfer and alters the desorption dynamics. Our findings should offer a comprehensive understanding of CO desorption mechanisms from Pd(111) surfaces under femtosecond laser excitation, and the integration of AIMDEF model with NN PESs should open the way to similar studies of complex surface reactions on other systems with greater computational feasibility. Ultimately, the methodologies developed and insights gained during this work can have broader implications, potentially benefiting the design of more efficient catalytic systems and advancing theoretical models in surface chemistry.

**Chapter 2** provides a comprehensive theoretical background for understanding molecule-surface interactions and how these can be efficiently modeled computationally in complex multiatomic systems. The chapter begins by introducing the adiabatic theorem and the Born-Oppenheimer approximation to show how electronic and nuclear degrees of freedom of a multiatomic system can be uncoupled to simplify their theoretical characterization.

Next, the Kohn-Sham DFT is introduced as a fundamental tool for calculating the electronic PESs of multiatomic systems and hence for simulating molecular dynamics on surfaces. The chapter ends with an overview of commonly used exchange-correlation functionals.

**Chapter 3** focuses on the dynamics of metal surfaces with adsorbed molecules

when excited by a femtosecond laser pulse. Such excitation can induce a number of processes in the adsorbates, including desorption, dissociation, recombination, rotation, vibration, and diffusion on the surface. The primary goal is to understand and describe femtochemical phenomena on adsorbate-decorated surfaces, in particular, desorption. We begin by describing photoinduced desorption mechanisms, starting with some insights about the development of femtochemistry and the experimental techniques that have enabled access to ultrafast time scales. The chapter distinguishes between direct and indirect photoinduced desorption, introducing key concepts such as desorption induced by electronic transitions (DIET) and desorption induced by multiple electronic transitions (DIMET). These mechanisms are accessed depending on the incident laser fluence and involve a different amount of electronic excitations, and particularly within DIMET multiple excitations can enhance desorption probabilities through rapid adsorbate excitation processes like “multiple-level ladder climbing”. As a first approach to modeling photoinduced desorption, two simple two-state models, the Menzel-Gomer-Redhead (MGR) and Antoniewicz ones, are briefly explained. Although these models provide some foundational understanding, they fall short in explaining complex experimental observations, particularly for metal surfaces where indirect excitation routes and nonadiabatic effects play significant roles. This remarks the need for more profound theoretical frameworks to accurately describe the intricate dynamics of photoinduced processes on metal surfaces.

For metal substrates, we consider the two-temperature model (2TM) to describe the substrate excitation process. The 2TM accounts for the nonequilibrium dynamics of the electronic and lattice temperatures following laser irradiation. Electrons absorb the laser energy, leading to a rapid increase in electronic temperature and subsequent energy transfer to the lattice through electron-phonon coupling. Afterwards, we examine the dynamics of adsorbates, focusing on nonadiabatic effects. The chapter introduces molecular dynamics with electronic friction (MDEF) as a method to model the energy transfer processes between excited electrons and adsorbate nuclei, which are obviously not captured by the Born-Oppenheimer approximation. The local density friction approximation (LDFA) is employed to calculate position-dependent friction coefficients for each adsorbate by considering the metal as a homogeneous free electron gas at each point of the surface. The contribution of phononic excitations is also incorporated by coupling the lattice to a thermostat, specifically using the Nosé-Hoover thermostat to ensure that the lattice follows the time-dependent temperature predicted by 2TM. This allows for the inclusion of both electronic and phononic energy inputs in the adsorbate dynamics. The calculation of adiabatic forces is discussed, comparing AIMDEF and PES-mediated MDEF. While AIMDEF provides high accuracy by calculating forces

on-the-fly using DFT, PES-mediated MDEF significantly reduces computational costs by utilizing a precalculated PES.

**Chapter 4** addresses the computational challenges in accurately simulating photoinduced chemical processes on gas-decorated metal surfaces. While AIMDEF provides a powerful and accurate framework for such simulations, its computational expense limits its applicability to time intervals of a few picoseconds and to small statistical ensembles of a few hundreds of trajectories. To overcome these limitations, the development of NN PESs as an efficient alternative to AIMDEF is explored. Neural networks offer a way to approximate the complex PES of the adsorbate-substrate system, significantly reducing the computational costs, while maintaining high accuracy. The chapter begins with an introduction to neural networks, detailing their general features and the training process. It covers the architecture of feed-forward NNs, the role of neurons and activation functions, and the methods used to optimize the network weights during training. Key concepts such as cost functions, overfitting, and early stopping are defined, and their importance to ensure the robustness of the NN models is remarked.

Subsequently, the chapter focuses on methods for constructing NN-based PESs. It highlights the limitations of early feed-forward NN approaches, which lacked of transferability and symmetry preservation. The introduction of high-dimensional neural network potentials (HDNNPs) by Behler and Parrinello marks a breakthrough in this respect, solving these limitations through the use of atom-centered symmetry functions (ACSFs) that ensure invariance under translations, rotations, and permutations of atoms. ACSFs are then explained, including radial and angular symmetry functions, and the challenges associated with selecting appropriate parameters to accurately represent atomic environments are discussed. The evolution of HDNNPs towards more sophisticated versions is also briefly addressed.

The focus then shifts to the embedded atom neural network (EANN) approach, which is inspired by the embedded atom method (EAM) applied to metallic systems. EANN utilizes Gaussian-type orbitals (GTOs) to construct embedded atomic densities that inherently preserve the required symmetries. This approach extends the applicability of EAM by allowing for more accurate modeling of both metallic and non-metallic systems. In this respect, we discuss the mathematical formulation of EANN, including the calculation of embedded densities and the training process that incorporates both energies and forces from AIMDEF data.

**Chapter 5** handles the study of femtosecond laser-induced desorption of CO from the Pd(111) surface with a specific coverage of 0.75 ML, using a PES generated by the EANN method (EANN PES). The data used to train the PES were obtained from previous AIMDEF simulations of the same process, whose relevant details are described in the beginning of the chapter. This characterization includes the system

configuration, computational parameters, and simulated experimental conditions. It is emphasized that modeling laser-induced reactions requires considering multiple adsorbates, variations in adlayer coverage, and significant fluctuations in surface temperature, which increases the complexity of the configurational space.

Subsequently, the process of constructing the EANN PES for the CO/Pd(111) system at 0.75 ML is detailed. A representative set of input data is selected for training, categorizing trajectories according to the number of desorption events observed. Specific EANN parameters, such as the NN architecture and GTO parameters within EANN model are optimized, seeking a balance between accuracy and computational efficiency. It is determined that an architecture with two hidden layers of 60 nodes each (60-60) provides the best performance in terms of accuracy and computation time. The quality of the trained PES is then evaluated using a static approach, comparing the energies and forces predicted by the PES with reference AIMDEF values on an independent set of configurations not used in training. It is noted how initial maximum errors in atomic forces are reduced after identifying and adding to the training set those configurations that contribute significantly to the errors prior to PES retraining. This refinement also leads to lower root mean square error (RMSE) values in energies and atomic forces. To include electronic friction forces in the simulations, a numerical fitting method is developed to model the surface electronic density required to calculate friction coefficients within LDFA. A density generator function (DGF) based on a sum of exponential functions is proposed, with parameters adjusted to reproduce the electronic density values obtained in AIMDEF simulations.

Molecular dynamics simulations with electronic friction and thermostats, hence including interactions with both hot electrons and phonons  $[(T_e, T_l) - \text{MDEF}]$ , are then performed using the optimized PES and the proposed DGF. Two data sets are generated, one of 100 trajectories with the same initial conditions used for AIMDEF calculations, and the other one of 2000 trajectories. Both reproduce with high precision the CO desorption data reported in the original AIMDEF simulations, such as desorption probabilities and energy distributions of the desorbed molecules. Additionally, the statistical improvement allowed by the computational efficiency of MDEF enables more detailed analysis of the dynamic processes involved. As a preliminary example, a study of the rovibrational states of desorbed CO molecules in the initial dynamics stage is performed on the larger MDEF dynamics ensemble using a quasiclassical approach. Most of these desorbed molecules are found to be in the vibrational ground state and low rotational states, providing valuable information on how CO is excited during the desorption process. We also highlight how usage of EANN PESs significantly reduces computational times compared

to AIMDEF simulations –from several days to mere seconds per trajectory, under equal conditions– without sacrificing accuracy.

**Chapter 6** presents our study on the photoinduced desorption dynamics from Pd(111) of two CO isotopologues,  $^{12}\text{C}^{16}\text{O}$  and  $^{13}\text{C}^{18}\text{O}$ , with a coverage of 0.75 ML under high laser fluence conditions. Using our 0.75 ML CO/Pd(111) PES, we perform extensive MDEF to explore potential isotope effects in the desorption process. Two types of simulation are performed: one set of  $(T_e, T_1)$  – MDEF, and another that includes only phonon interactions ( $T_1$  – MDEF). For each kind of calculation, an ensemble of 2000 trajectories is generated. Our results reveal minor differences in desorption probabilities between isotopologues at early times (up to 4 ps) in the  $(T_e, T_1)$  – MDEF simulations, attributable to interactions with hot electrons. However, these differences become negligible over extended simulation times up to 50 ps, as both isotopologues show similar desorption probabilities and rates, indicating that phonon-mediated mechanisms dominate the desorption process at longer time scales. The desorption rates further support this finding, showing nearly identical patterns for both isotopologues in each simulation type, with  $(T_e, T_1)$  – MDEF rates peaking earlier and sharper due to the influence of hot electrons in the initial stages. Notably, an analysis of the vibrational states of desorbed CO shows minimal vibrational excitation, primarily induced by interactions with hot electrons. While a slight isotope effect is observed in the high-energy tail of desorbed molecules, this favoring vibrational excitation of the lighter isotopologue, such an effect is limited to about 1% of the total desorption yield. Consequently, our study finds no significant isotope effect on the CO/Pd(111) photodesorption dynamics and points to a phonon-dominated dynamics.

**Chapter 7** investigates the femtosecond laser-induced desorption of CO/Pd(111) surface under different conditions than those considered in AIMDEF. To begin with, the transferability of our 0.75 ML PES towards a 0.33 ML coverage and that of a 0.33 ML towards a 0.75 ML adlayer is examined. We find that incorporating data from both coverages to train an EANN PES is convenient to solve the energy mismatches between coverages and to gain accuracy in their analysis. Subsequently, a multicoverage EANN PES is developed with AIMDEF data at both 0.33 and 0.75 ML adlayers, both coming from  $(T_e, T_1)$  – AIMDEF and from dynamics that only allow electron interactions with adsorbates ( $T_e$  – AIMDEF). This multicoverage PES demonstrates high accuracy and transferability, allowing successful simulation of CO desorption even at intermediate coverages not included in the training, such as 0.60 ML.

Afterwards, around 100 000 MDEF trajectories are calculated under different absorbed laser fluence and coverage conditions, for  $T_e$  – MDEF (only electron excitation on adsorbates allowed) and  $(T_e, T_1)$  – MDEF situations. Our simulations

show that the probability of CO desorption increases with coverage and that there is a superlinear relationship between desorption probability and absorbed laser fluence, hence consistent with the DIMET regime. Moreover, we find that both hot electrons and phonons contribute to the desorption process, with the phonon mechanism dominating at higher fluences and longer time scales. Additionally, it is also noted that CO molecules can desorb directly or after being temporarily trapped in the physisorption region, with the latter phenomenon appearing to be more pronounced at higher coverages. We also find that CO moves along the full surface plane after becoming excited and that those desorbing molecules do not take any preferred polar angle to desorb.

In addition, two-pulse correlation (2PC) experiments are also simulated for both 0.33 and 0.75 ML adlayers to further analyze the desorption mechanisms and the relative roles of electrons and phonons. The simulations qualitatively reproduce the experimental observations, suggesting that desorption is a synergistic process driven by both subsystems. However, some discrepancies are found with the experimental data, especially at low coverage and negative time delays, indicating the need for further investigations. Despite this, our study overall demonstrates the effectiveness of machine-learning-based PESs for simulating complex laser-induced desorption processes on metallic surfaces. The developed MDEF methodology provides a deeper understanding of the CO desorption dynamics on Pd(111) and lays the groundwork for future studies in other complex systems and under various experimental conditions.

**Chapter 8** describes the femtosecond laser-induced desorption and potential oxidation of CO in the O+2CO/Pd(111) system. Using DFT calculations with the VASP code, we first determine the most energetically favorable arrangement of CO and O adsorbates on the Pd(111) surface. Our relaxation studies show that the minimum energy configuration for the unperturbed system corresponds to O atoms adsorbed at fcc sites and CO molecules at top and hcp sites. We then thermalize the system at an initial temperature of 90 K to prepare for photodesorption dynamics. We then perform AIMDEF simulations under various conditions, including two different laser fluences and different types of simulations ( $T_e$  – AIMDEF and  $(T_e, T_1)$  – AIMDEF).

We observe that CO molecules and O atoms, when excited, gain significant mobility along the  $z$  axis, which is perpendicular to the surface, and the  $xy$  plane parallel to the surface, the mobility being enhanced when both electron and phonon excitations are considered. In this respect, O atoms occasionally dive below the top-most Pd layer and CO desorbs either directly or after remaining transiently trapped, as seen for CO/Pd(111). Our simulations also reveal that both CO desorption and recombinative oxidation to form CO<sub>2</sub> can occur, especially when both electronic

and phononic excitations are considered, this further implying the existence of a cooperative effect of both channels in adsorbate excitation. Although recombinative oxidation happens less frequently than desorption, especially at higher fluence, it is almost as frequent as desorption for lower fluence. Nonetheless, the statistics of the  $(T_e, T_i)$  – AIMDEF simulations are at the moment too limited and it is not possible to extract reliable conclusions in this respect. Furthermore, we have examined the desorption and reaction probabilities for each adsorption site. Interestingly, most of the desorbed CO, including the single CO<sub>2</sub> desorption occurring at each fluence, are molecules that were initially adsorbed at top sites, which are characterized by a higher desorption energy than those adsorbed on hcp sites. The additional analysis of the adsorbate kinetic energies evidences that the latter molecules initially gain slightly more energy than those at top. Altogether, these results showing more desorption from top sites remark that the laser-induced dynamics in this system cannot be interpreted in terms of the energetics under equilibrium conditions.

To end with, the main conclusions of this Thesis, along with additional remarks on future research, are presented in **Chapter 9**.

# Resumen

---

Esta Tesis se centra principalmente en el estudio y la comprensión, desde una perspectiva teórica, de la desorción inducida por láser de femtosegundo del CO adsorbido sobre una superficie de Pd(111) con diferentes recubrimientos. Asimismo, se aborda la fotodesorción y la fotooxidación de CO en Pd(111) cuando la superficie está cubierta con 0,25 monocapas (ML) de oxígeno y 0,50 ML de monóxido de carbono (0,25 ML O + 0,50 ML CO/Pd(111)).

El **Capítulo 1** presenta la investigación desarrollada en esta Tesis. El paladio (Pd) es un metal de transición con conocidas propiedades catalíticas, especialmente para reacciones de hidrogenación, deshidrogenación y oxidación. Por ello, se emplea en muchas aplicaciones relacionadas con la catálisis heterogénea, como en sistemas de escape de automóviles, tecnologías de pilas de combustible o producción de compuestos para la industria agroquímica o farmacéutica, entre otras. También se utiliza en sensores de detección de gases. Por estas razones, resulta crucial entender la dinámica del Pd en diferentes contextos, dada la relevancia creciente de este metal en la catálisis heterogénea y en la industria química. Entre los procesos químicos más relevantes en los que participa el Pd se encuentran la adsorción y desorción de átomos y moléculas en fase gaseosa. Además, una de las moléculas más comunes en las reacciones catalizadas por Pd es el monóxido de carbono (CO). Partiendo de esta base, queremos llevar a cabo un estudio teórico de la desorción inducida por láser de femtosegundo del CO adsorbido en Pd(111) [CO/Pd(111)], y también de la fotodesorción y fotooxidación de CO en la superficie Pd(111) cubierta con 0,25 ML de oxígeno atómico (O) y 0,50 ML de CO [O+2CO/Pd(111)]. Mediante el estudio de ambos sistemas bajo diversas condiciones iniciales —por ejemplo, bajo diferentes coberturas de CO y fluencias del láser— pretendemos desentrañar los mecanismos subyacentes a estos procesos químicos inducidos por láser.

Tal y como han concluido diferentes trabajos experimentales previos, el CO/Pd(111) exhibe complejas propiedades estructurales que varían con el recubrimiento, presentando más de 15 configuraciones estables de CO adsorbido en Pd(111). Por ello, un sistema adsorbato-sustrato tan complejo requiere de modelos teóricos sofisticados para determinar con exactitud los sitios de adsorción, el acoplamiento energético y la dinámica de reacción. Nosotros buscamos simular la dinámica de desorción bajo excitación de láser de femtosegundo empleando dinámica molecular ab initio con fricción electrónica y termostatos [( $T_e, T_l$ )-AIMDEF], la cual incorpora

de forma efectiva las excitaciones, tanto electrónicas como fonónicas, inducidas por el láser, mientras que las fuerzas adiabáticas se calculan sobre la marcha a partir de primeros principios mediante la teoría del funcional de la densidad (DFT). Sin embargo, el alto coste computacional asociado al cálculo de fuerzas adiabáticas con DFT limita este tipo de simulaciones a escalas temporales cortas y a pequeños conjuntos estadísticos. Para superar estas limitaciones, entrenamos superficies de energía potencial basadas en redes neuronales (NN PESs) usando datos de AIMDEF y empleamos estas NN PESs para realizar simulaciones de dinámica molecular con fricción electrónica y termostatos  $[(T_e, T_l)\text{-MDEF}]$ , equivalentes en precisión pero mucho más eficientes computacionalmente. Este método alternativo permite extender las simulaciones a escalas temporales más largas, usar conjuntos de datos más amplios y estudiar la dinámica inducida por láser bajo condiciones iniciales más diversas.

Durante nuestra investigación pretendemos abordar varios aspectos clave que quedaron sin resolver en experimentos anteriormente realizados en CO/Pd(111). Queremos desentrañar el papel relativo de los electrones y fonones de la superficie en los procesos fotoinducidos. También nos interesa averiguar si existe o no un efecto isotópico, lo cual está relacionado con qué mecanismo —electrónico o fonónico— domina en la fotodesorción. Además, nos proponemos simular experimentos de correlación de dos pulsos láser (2PC) para avanzar en la clarificación de la interacción entre excitaciones electrónicas y fonónicas. Otro objetivo es examinar cómo varía la probabilidad de desorción de CO con el recubrimiento inicial de CO y la fluencia del láser, así como el comportamiento del CO tras la excitación, por ejemplo, en cuanto a su movimiento paralelo y perpendicular a la superficie. Como paso adicional, extenderemos nuestro enfoque a mezclas de O y CO adsorbidas en Pd(111), abordando algunas de las cuestiones mencionadas en CO/Pd(111) e investigando cómo la presencia de oxígeno influye en la transferencia de energía entre adsorbatos y altera la dinámica de desorción. Nuestros hallazgos deberían proporcionar una comprensión detallada de los mecanismos de desorción de CO desde superficies de Pd(111) bajo la excitación con láser de femtosegundo, y la integración del modelo AIMDEF con NN PESs debería allanar el camino a estudios similares de reacciones superficiales complejas en otros sistemas con una mayor viabilidad computacional. En última instancia, las metodologías desarrolladas y los conocimientos adquiridos a lo largo de este trabajo pueden tener implicaciones más amplias, beneficiando el diseño de sistemas catalíticos más eficientes y llevando a mejorar los modelos teóricos en química de superficies.

El **Capítulo 2** ofrece una base teórica completa para entender las interacciones molécula-superficie y cómo se pueden modelar computacionalmente de manera eficiente en sistemas multiatómicos complejos. El capítulo comienza introduciendo

el teorema adiabático y la aproximación de Born-Oppenheimer para mostrar cómo los grados de libertad electrónicos y nucleares de un sistema multiatómico pueden desacoplarse y, así, simplificar su caracterización teórica.

A continuación, se presenta el método de Kohn-Sham como una herramienta fundamental para calcular las superficies de energía potencial electrónicas (PES) de sistemas multiatómicos en DFT y, por ende, para simular la dinámica molecular en superficies. El capítulo finaliza con una visión general de varios de los funcionales de intercambio y correlación más utilizados.

El **Capítulo 3** se centra en la dinámica de superficies metálicas con moléculas adsorbidas cuando son excitadas por un pulso láser de femtosegundo. Dicha excitación puede inducir diversos procesos en los adsorbatos, incluyendo desorción, disociación, recombinación, rotación, vibración y difusión sobre la superficie. El objetivo principal es entender y describir fenómenos femtoquímicos en superficies decoradas con adsorbatos, en particular la desorción. Comenzamos describiendo los mecanismos de fotodesorción, partiendo de algunos apuntes sobre el desarrollo de la femtoquímica y las técnicas experimentales que han permitido acceder a escalas de tiempo ultrarrápidas. Este capítulo distingue entre desorción fotoinducida directa e indirecta, introduciendo conceptos clave como la desorción inducida por una transición electrónica (DIET) y la desorción inducida por múltiples transiciones electrónicas (DIMET). Estos mecanismos dependen de la fluencia del láser incidente e involucran diferentes niveles de excitación electrónica; en particular, en el caso de DIMET, múltiples excitaciones pueden incrementar las probabilidades de desorción mediante procesos de ascenso por la "escalera de niveles múltiples". Como primer acercamiento a la caracterización teórica de la fotodesorción, se describen brevemente dos modelos simples de dos estados: los de Menzel-Gomer-Redhead (MGR) y Antoniewicz. Aunque estos modelos brindan una comprensión inicial, no logran explicar observaciones experimentales más complejas, sobre todo en superficies metálicas, donde las rutas de excitación indirectas y los efectos no adiabáticos desempeñan un papel significativo. Esto resalta la necesidad de marcos teóricos más profundos para describir con precisión la dinámica intrincada de los procesos fotoinducidos en superficies metálicas.

Para sustratos metálicos, se considera el modelo de dos temperaturas (2TM) para describir el proceso de excitación del sustrato. El 2TM tiene en cuenta la dinámica de no equilibrio de las temperaturas electrónica y de la red cristalina tras la irradiación láser. Los electrones absorben la energía del láser, aumentando rápidamente su temperatura y transfiriendo energía a la red a través del acoplamiento electrón-fonón. Más adelante, se examina la dinámica de los adsorbatos, centrándose en los efectos no adiabáticos. En este capítulo se introduce la dinámica molecular con fricción electrónica (MDEF) para modelar los procesos de transferencia de energía

entre electrones excitados y núcleos de los adsorbatos, los cuales no son capturados por la aproximación de Born-Oppenheimer. La aproximación local de fricción electrónica (LDFA) se emplea para calcular coeficientes de fricción dependientes de la posición de cada adsorbato, considerando el metal como un gas de electrones libres homogéneo en cada punto de la superficie. La contribución de excitaciones fonónicas se incorpora acoplando la red a un termostato, específicamente un termostato de Nosé-Hoover, para asegurar que la red siga la temperatura dependiente del tiempo predicha por el 2TM. Esto permite incluir tanto las aportaciones electrónicas como fonónicas en la dinámica del adsorbato. Se discute el cálculo de las fuerzas adiabáticas, comparando AIMDEF y la MDEF mediada por PES. Si bien AIMDEF provee gran exactitud al calcular fuerzas con DFT en tiempo real, la MDEF mediada por PES reduce significativamente los costes computacionales al utilizar una PES previamente calculada.

El **Capítulo 4** aborda los desafíos computacionales en la simulación precisa de procesos químicos fotoinducidos en superficies metálicas decoradas con gases. Aunque AIMDEF ofrece un marco sólido y preciso para dichas simulaciones, su alto coste computacional limita su aplicabilidad a intervalos de tiempo de pocos picosegundos y a pequeños conjuntos estadísticos de cientos de trayectorias. Para superar estas limitaciones, se explora el desarrollo de PES basadas en redes neuronales (NN PESs) como una alternativa eficiente a AIMDEF. Las redes neuronales ofrecen un medio para aproximar la compleja PES del sistema adsorbato-sustrato, reduciendo enormemente los costes computacionales y manteniendo, al mismo tiempo, una alta precisión. El capítulo comienza con una introducción a las redes neuronales, detallando sus características generales y el proceso de entrenamiento. Se describen la arquitectura de redes de alimentación directa (feed-forward), el papel de las neuronas y las funciones de activación, y los métodos para optimizar los pesos de la red durante el entrenamiento. Se definen conceptos clave como las funciones de coste, el sobreajuste (overfitting) y el criterio de parada temprana (early stopping), destacando su importancia para asegurar la robustez de los modelos de NN.

Posteriormente, el capítulo se centra en los métodos para construir PES basadas en NN. Se señalan las limitaciones de los primeros enfoques de redes feed-forward, que carecían de transferibilidad y preservación de simetrías. La introducción de los potenciales de redes neuronales de alta dimensión (HDNNP) por Behler y Parrinello supuso un gran avance, al resolver estas limitaciones mediante el uso de funciones de simetría centradas en átomos (ACSFs) que garantizan invariancia bajo traslaciones, rotaciones y permutaciones de átomos. Se explican las ACSFs, incluyendo las funciones de simetría radiales y angulares, y se discuten los desafíos en la selección de parámetros apropiados para representar con precisión los entornos atómicos.

También se comenta brevemente la evolución de los HDNNP hacia versiones más sofisticadas.

A continuación, la atención se centra en el enfoque de redes neuronales de átomos incrustados (EANN), inspirado en el método del átomo incrustado (EAM) aplicado a sistemas metálicos. El modelo EANN utiliza orbitales de tipo gaussiano (GTO) para construir densidades atómicas incrustadas que preservan de forma inherente las simetrías requeridas. Este enfoque extiende la aplicabilidad del EAM, permitiendo un modelado más preciso tanto de sistemas metálicos como no metálicos. En este sentido, se discute la formulación matemática de EANN, incluida la construcción de densidades incrustadas y el proceso de entrenamiento que incorpora tanto energías como fuerzas derivadas de datos AIMDEF.

El **Capítulo 5** se dedica al estudio concreto de la desorción inducida por láser de femtosegundo de CO adsorbido en una superficie de Pd(111) con una cobertura específica de 0.75 ML, utilizando una PES generada mediante el método EANN (EANN PES). Los datos utilizados para entrenar la PES se obtuvieron de simulaciones AIMDEF previas del mismo proceso y sobre el mismo sistema gas-superficie, cuyos detalles relevantes se describen al inicio del capítulo. Esta caracterización incluye la configuración del sistema, los parámetros computacionales y las condiciones experimentales simuladas. Se enfatiza que modelar reacciones inducidas por láser requiere considerar múltiples adsorbatos, variaciones en la cantidad de recubrimiento sobre la superficie y fluctuaciones significativas en la temperatura de la superficie, aumentando la complejidad del espacio de configuraciones atómicas.

Posteriormente, se detalla el proceso de construcción de la EANN PES para el sistema CO/Pd(111) a 0.75 ML. Se selecciona un conjunto representativo de datos de entrada para el entrenamiento, clasificando las trayectorias según el número de eventos de desorción observados. Se optimizan parámetros específicos de EANN, como la arquitectura de la red neuronal y los parámetros presentes en los GTOs dentro del modelo EANN, buscando un equilibrio entre exactitud y eficiencia computacional. Se determina que una arquitectura con dos capas ocultas de 60 nodos cada una (60-60) proporciona el mejor rendimiento en términos de precisión y tiempo de cálculo. La calidad de la PES entrenada se evalúa, en primera instancia, usando un enfoque estático, comparando las energías y fuerzas predichas por la PES con resultados previos calculados con AIMDEF en un conjunto independiente de configuraciones no utilizado en el entrenamiento. Se observa cómo los errores máximos iniciales en las fuerzas atómicas se reducen tras identificar y añadir al conjunto de entrenamiento aquellas configuraciones que contribuyen significativamente a los errores antes de reentrenar la PES. Esta refinación también conduce a una menor raíz del error cuadrático medio (RMSE) en energías y fuerzas atómicas. Para incluir las fuerzas de fricción electrónica en las simulaciones, se desarrolla un

método de ajuste numérico para modelar la densidad electrónica de la superficie necesaria para calcular los coeficientes de fricción en el marco de la aproximación LDFA. Se propone una función generadora de densidad (DGF) basada en una suma de funciones exponenciales, con parámetros ajustados para reproducir los valores de densidad electrónica obtenidos en las simulaciones AIMDEF.

A continuación, se llevan a cabo simulaciones de dinámica molecular con fricción electrónica y termostatos  $[(T_e, T_l) - \text{MDEF}]$ , incluyendo interacciones tanto con electrones calientes como con fonones, empleando la PES optimizada y la DGF propuesta. Se generan dos conjuntos de datos, uno de 100 trayectorias con las mismas configuraciones iniciales usadas en las simulaciones AIMDEF y otro de 2000 trayectorias. Ambos reproducen con gran precisión los datos de desorción de CO proporcionados en las simulaciones AIMDEF originales, tales como las probabilidades de desorción y las distribuciones de energía de las moléculas desorbidas. Además, la mejora estadística lograda por la eficiencia computacional de MDEF permite un análisis más detallado de los procesos dinámicos involucrados. Como ejemplo preliminar, se estudian los estados rovibracionales de las moléculas de CO desorbidas en la etapa inicial de la dinámica utilizando una aproximación semi-clásica. Se determina que la mayoría de estas moléculas desorbidas se encuentran en el estado vibracional fundamental y en niveles rotacionales bajos, proporcionando información valiosa sobre cómo se excita el CO durante el proceso de desorción. También se destaca cómo el uso de EANN PESs reduce significativamente los tiempos de cálculo en comparación con las simulaciones AIMDEF —de varios días a apenas segundos por trayectoria, bajo condiciones equivalentes— sin sacrificar exactitud computacional.

El **Capítulo 6** presenta el estudio de la dinámica de fotodesorción de dos isotopólogos de CO,  $^{12}\text{C}^{16}\text{O}$  y  $^{13}\text{C}^{18}\text{O}$ , con una cobertura de 0.75 ML bajo condiciones de alta fluencia láser. Empleando nuestra PES para CO/Pd(111) con un recubrimiento igual a 0.75 ML, realizamos MDEF extensiva para explorar posibles efectos isotópicos en el proceso de desorción. Se llevan a cabo dos tipos de simulaciones: un conjunto de  $(T_e, T_l) - \text{MDEF}$  y otro que sólo incluye interacciones fonónicas  $(T_l - \text{MDEF})$ . Para cada tipo de cálculo se generan 2000 trayectorias. Nuestros resultados muestran pequeñas diferencias en las probabilidades de desorción entre los isotopólogos en tiempos cortos (hasta 4 ps) en las simulaciones  $(T_e, T_l) - \text{MDEF}$ , atribuibles a las interacciones con electrones calientes. Sin embargo, estas diferencias se vuelven insignificantes al extender las simulaciones hasta 50 ps, ya que ambos isotopólogos presentan probabilidades y tasas de desorción similares, indicando que los mecanismos mediados por fonones dominan la desorción a escalas temporales más largas. Las tasas de desorción también respaldan este hallazgo, mostrando patrones casi idénticos para ambos isotopólogos en cada tipo de simulación, con picos más tem-

pranos y marcados en  $(T_e, T_1)$  – MDEF debido a la influencia inicial de los electrones calientes. Además, el análisis de los estados vibracionales de las moléculas de CO desorbidas revela una excitación vibracional mínima, inducida principalmente por interacciones con electrones calientes. Aunque se observa un ligero efecto isotópico en la cola de alta energía de las moléculas desorbidas, favoreciendo la excitación vibracional del isotópulo más ligero, este efecto se limita a alrededor del 1% de total de moléculas desorbidas. En consecuencia, nuestro estudio no encuentra un efecto isotópico significativo en la fotodesorción de CO/Pd(111) y apunta a una dominación de los fonones en la dinámica analizada.

El **Capítulo 7** investiga la desorción inducida por láser de femtosegundo de CO/Pd(111) bajo condiciones diferentes a las consideradas en AIMDEF. En primer lugar, se examina la transferibilidad de nuestra PES a 0.75 ML hacia un recubrimiento de 0.33 ML y viceversa. Según nuestros resultados, incorporar datos de ambos recubrimientos para entrenar una EANN PES resulta conveniente para solventar las diferencias de energía entre recubrimientos y mejorar la precisión del análisis. A continuación, se desarrolla una PES EANN para varios recubrimientos, con datos AIMDEF tanto a 0.33 como a 0.75 ML anteriormente obtenidos a partir de  $(T_e, T_1)$  – AIMDEF y de simulaciones que solo permiten interacción electrónica con adsorbatos ( $T_e$  – AIMDEF). Esta PES multirrecubrimiento demuestra gran exactitud y transferibilidad, permitiendo simular con éxito la desorción de CO incluso a recubrimientos intermedios no incorporados en el entrenamiento, como el de 0.60 ML.

Posteriormente, se calculan alrededor de 100 000 trayectorias MDEF bajo diferentes condiciones de fluencia láser absorbida y cobertura, para situaciones  $T_e$  – MDEF (solo excitación electrónica en adsorbatos) y  $(T_e, T_1)$  – MDEF. Nuestras simulaciones muestran que la probabilidad de desorción de CO aumenta con el recubrimiento y que existe una relación superlineal entre la probabilidad de desorción y la fluencia láser absorbida, compatible con el régimen DIMET. Además, encontramos que tanto los electrones calientes como los fonones contribuyen al proceso de desorción, dominando el mecanismo fonónico a mayores fluencias y escalas de tiempo más largas. Asimismo, observamos que las moléculas de CO pueden desorber directamente o después de quedar temporalmente atrapadas en la región de fisorción, fenómeno más marcado a mayores coberturas. También se verifica que el CO se mueve a lo largo de todo el plano superficial tras ser excitado, y que las moléculas desorbidas no presentan un ángulo polar preferente para desorberse.

Además, se simulan experimentos de correlación a dos pulsos (2PC) para adláyeres de 0.33 y 0.75 ML con el fin de estudiar con más detalle los mecanismos de desorción y el papel relativo de electrones y fonones en estos procesos. Las simula-

ciones reproducen cualitativamente las observaciones experimentales, sugiriendo que la desorción es un proceso sinérgico impulsado por ambos subsistemas. Sin embargo, se hallan algunas discrepancias con los datos experimentales, especialmente a bajos recubrimientos y retardos temporales negativos entre el pulso de bombeo y el de medición, lo que indica la necesidad de llevar a cabo investigaciones adicionales. A pesar de ello, nuestro estudio demuestra la eficacia de las PES basadas en aprendizaje automático para simular complejos procesos de desorción inducida por láser en superficies metálicas. La metodología MDEF desarrollada proporciona una comprensión más profunda de la dinámica de desorción del CO en Pd(111) y sienta las bases para futuros estudios en otros sistemas complejos y bajo diversas condiciones experimentales.

El **Capítulo 8** describe la desorción inducida por láser de femtosegundo y la posible oxidación de CO en el sistema  $O+2CO/Pd(111)$ . Mediante cálculos DFT con el código VASP, primero determinamos la disposición más favorable energéticamente de los adsorbatos CO y O sobre la superficie Pd(111). Nuestros cálculos de relajación energética muestran que la configuración de energía mínima para el sistema sin perturbar corresponde a los átomos de O en sitios tipo fcc y a las moléculas de CO en sitios top y hcp. Posteriormente, se termaliza el sistema a una temperatura inicial de 90 K para prepararlo para las dinámicas de fotodesorción. A continuación, se llevan a cabo simulaciones AIMDEF bajo diversas condiciones, incluyendo dos fluencias láser diferentes y distintos tipos de simulaciones ( $T_e$  – AIMDEF y  $(T_e, T_l)$  – AIMDEF).

Observamos que las moléculas de CO y los átomos de O, al ser excitados, adquieren una movilidad significativa tanto en el eje  $z$ , perpendicular a la superficie, como en el plano  $xy$  paralelo a la misma, siendo esta movilidad mayor cuando se consideran excitaciones electrónicas y fonónicas. En este sentido, los átomos de O ocasionalmente se sumergen por debajo de la capa superficial de Pd, mientras que el CO se desorbe ya sea directamente o tras permanecer atrapado transitoriamente, como se observó para el CO/Pd(111). Nuestras simulaciones también revelan que tanto la desorción de CO como la oxidación recombinativa para formar  $CO_2$  pueden ocurrir, especialmente cuando se consideran excitaciones electrónicas y fonónicas, lo que implica la existencia de un efecto cooperativo de ambos canales en la excitación de las especies adsorbidas. Aunque la oxidación recombinativa ocurre con menor frecuencia que la desorción, especialmente a mayor fluencia, se acerca a ser casi tan frecuente como la desorción a menor fluencia. Sin embargo, la estadística de las simulaciones  $(T_e, T_l)$  – AIMDEF es por el momento demasiado limitada y no es posible extraer conclusiones sólidas al respecto. Asimismo, hemos examinado las probabilidades de desorción y reacción para cada sitio de adsorción. Llama la atención que la mayor parte del CO desorbido, incluyendo la única desorción de  $CO_2$  que se observa en cada fluencia, corresponde a moléculas que inicialmente

estaban en sitios top, caracterizadas por una mayor energía de desorción que las adsorbidas en sitios hcp. El análisis adicional de las energías cinéticas de los adsorbatos evidencia que las moléculas en hcp adquieren inicialmente un poco más de energía que las de sitios top. En conjunto, estos resultados muestran que la dinámica inducida por láser en este sistema no puede interpretarse únicamente en términos de la transferencia de energía bajo condiciones de equilibrio.

Finalmente, en el **Capítulo 9** se presentan las principales conclusiones de esta Tesis, junto con comentarios adicionales sobre posibles investigaciones futuras.



# Acknowledgments

---

Firstly, I would like to express my deepest gratitude to my Thesis supervisors, Maite Alducin and Joseba Iñaki Juaristi. Thank you for trusting me from the very beginning and opening the doors of your group at the Materials Physics Center (MPC), within the Gas/Solid Interfaces group. Your closeness, dedication, and patience have been fundamental to my development as a scientist over these years. Thank you for teaching me, guiding me, and allowing me to learn so much; your help has been key at every stage of this process. But, above all, I sincerely thank you for your commitment to me and for never leaving me alone. I will always remember you with special affection as my “scientific parents.” My gratitude also extends to Ricardo Díez Muiño for welcoming me with the same warmth into the group.

To my colleagues in the Gas/Solid Interfaces group at MPC: Auguste Tetenoire, Alejandro Rivero, Alberto P. Sánchez Muzas, Raúl Bombín, Oihana Galparsoro, Ivan Žugeč, and Natalia Koval. Thank you for your friendship, kindness, and support throughout these years. You have created an exceptional environment, both in group meetings and in our gatherings outside the MPC. I would also like to thank other researchers with whom I shared good times during their temporary stays at MPC. In particular, I want to highlight three colleagues. To Auguste, who was also my office mate for four years, thank you for your help with VASP and Python when I was starting to use them. To Alejandro, for introducing me to neural network training, whose lessons proved very useful for my subsequent research. And specially to Alberto, whose work in developing the molecular dynamics with electronic friction (MDEF) code and the analysis tools for calculations was essential in obtaining many of the most important results of this Thesis. Thank you for your friendliness, your willingness to help me, and for making our work together an enriching experience. I also extend my gratitude to collaborators from other research groups, whose contribution was fundamental to this work: among others, Yaolong Zhang, Ce Hu, and Bin Jiang, for developing the embedded atom neural network (EANN) model and code; Juraj Ovčar and Ivor Lončarić, for your work on the empirical density generator function used in the MDEF simulations. Likewise, thanks to all the colleagues at MPC and Donostia International Physics Center (DIPC) who have crossed my path over these years and for so many wonderful times. I will always carry you in my heart with great affection.

I also wish to remember those who were key in my first steps as a researcher at the Institute of Fundamental Physics (IFF) in Madrid between 2017 and 2018. To my supervisor, Alberto García Vela, and to Luis Bañares at the Complutense University of Madrid: thank you for trusting me, for giving me the opportunity to begin my research career, and for your teachings, which have been valuable during this stage and will continue to be in the future. My gratitude also goes to my colleagues at the IFF: Raúl Rodríguez, Carlos García, Josu Ortiz de Zárate, Álvaro Castillo, Dani Arismendi, Nissrin Alharzali, Judit Montes de Oca, Raquel Yanes, and Mónica Valentín, among others. Thank you for your friendship, your kindness, and for so many good times inside and outside the institute. I remember you all fondly.

I want to dedicate a few words to all the people who left their mark on my life during the years I studied for my Bachelor's degree in Physics at the University of Zaragoza. Firstly, my gratitude to the professors who left an indelible mark on my education, such as Pedro Antonio Martínez, Luis Mario Floría, José Tornos, Andrés Cruz, José Luis Cortés, José Manuel Carmona, and many others whose impact endures, even if I do not mention them here. Thank you for your effort, for sharing your knowledge, and for inspiring me to keep moving forward. To the many friends I made during that time, such as Gonzalo Alonso, Miguel García Bosque, Patricia Castiella, Mario Abadía, and many more, thank you for the hours we spent together between classes, laughter, and unforgettable moments. In particular, I would like to mention a group of good friends from Zaragoza: Iván Ruiz, Fran López, Javi Inchaurrealde, and Miguel den Holder, among others, with whom I shared unforgettable experiences both during university and in the following years (and more yet to come!). Your friendship has been a gift, and even though distance may separate us, I always carry you with me. Those years were essential not only for my academic training, but also for my personal growth, and I will forever be grateful to every person who accompanied me on that journey. The memories of those days, and of those who made them so special, will always remain in my heart.

Finally, I want to dedicate a few words to my family, my refuge and my greatest support. Thank you to my family in Madrid, whose affection and companionship have been a fundamental pillar in my life, for all the moments shared and for those yet to come. In particular, thanks to my uncle Antonio and aunt Mari Paz, my aunt Joaquina, and my cousins Pablo and Miguel, for welcoming me with open arms and making me feel at home during my research period at the IFF. To my dear grandparents from Caparrosa and Valtierra, José María and Victoria, who were always an example of love and strength. I am sure that wherever they are, they are proud to see me reach this point. Thank you also to my uncle Patxi and my cousins David and Marisa, for their closeness and for being present in my life. Ich möchte mich auch bei Elisabeth für ihre Großzügigkeit und Freundlichkeit gegenüber meiner

Familie und mir herzlich bedanken. Sie war eine außergewöhnliche Person, die einen besonderen Platz in unseren Herzen hat und unser Leben nachhaltig geprägt hat. And, above all, thanks to my closest family: my parents, Alfredo and Beatriz, and my brother, Javier. There are not enough words to express how much you mean to me. Thank you for your unconditional love, your infinite patience, and for being my greatest source of support at every step of this journey. I will never be able to repay everything you have given me, but I hope this achievement reflects how much I value and owe you. If I have come this far, it is thanks to you.

*Porque llegaron las fiestas,  
de esta gloriosa ciudad,  
que son en el mundo entero,  
unas fiestas sin igual.  
¡Riau Riau!*



# Eskerrak

---

Lehenik eta behin, nire esker onik sakonena adierazi nahi diet nire tesi-zuzendariei, Maite Alducin eta Joseba Iñaki Juaristiri. Eskerrik asko hasieratik nigan konfiantza izateagatik eta Materialen Físika Zentroko (CFM) gas eta azal solidoen taldea (Gas/Solid Interfaces) niretzat irekitzeagatik. Zuen gertutasuna, dedikazioa eta pazientzia oinarrizkoak izan dira urte hauetan zehar nire garapen zientifikoan. Eskerrik asko irakasteagatik, gidatzeagatik eta hainbeste ikasteko aukera emateagatik; zuen laguntza fase bakoitzean erabakigarria izan da. Baina, batez ere, bihotzez eskertzen dizuet nirekin hartu duzuen konpromisoa eta inoiz bakarrik ez uztea. Beti gogoratuko zaituztet maitasun bereziz, nire “guraso zientifikoak” bezala. Nire eskerrik beroenak Ricardo Díez Muiñori ere, taldean hurbiltasun berberarekin hartu ninduelako.

CFMko Gas/Solid Interfaces taldeko lankideei: Auguste Tetenoire, Alejandro Rivero, Alberto P. Sánchez Muzas, Raúl Bombín, Oihana Galparsoro, Ivan Žugeč eta Natalia Koval. Eskerrik asko urte hauetan guztietan eman didazuen adiskidetasunagatik, adeitasunagatik eta laguntzagatik. Giro paregabea sortu duzue bai talde-bileretan bai CFMtik kanpoko topaketetan. Era berean, CFMn aldi baterako egon diren beste ikertzaileei ere eskerrak eman nahi dizkiet, elkarrekin bizi izan ditugun une ederrengatik. Bereziki, hiru lankide nabarmendu nahi ditut. Augusteri, lau urtez nire bulegokide izateaz gain, VASP eta Python erabiltzen hasi nintzenezan laguntzeagatik. Alejandrori, sare neuronalak trebatzen irakasteagatik, geroago nire ikerketan oso baliagarriak izan ziren irakaspenak eman zizkidalako. Eta bereziki Albertorentzat, marruskadura elektronikoarekin dinamika molekularra (MDEF) kodea eta kalkuluen analisi tresnak garatzeko egin zuen lanarengatik, tesi honetako emaitza garrantzitsuenetako asko lortzeko oinarrizkoak izan zirelako. Eskerrik asko zure adeitasunagatik, laguntzeko prestutasunagatik eta zurekin lan egitea esperientzia aberasgarria bihurtzeagatik. Era berean, beste ikerketa-talde batzuetako lankideei ere eskerrak, haien ekarpena lan honetarako ezinbestekoa izan delako: besteak beste, Yaolong Zhang, Ce Hu eta Bin Jiang, atomo txertatuen sare neuronal (EANN) eredu eta kodea garatzeagatik; Juraj Ovčar eta Ivor Lončarić, MDEF simulazioetan erabili den dentsitate-sorgailu enpirikoaren funtzioan egindako lanagatik. Halaber, CFM eta Donostia International Physics Centerko (DIPC) lankide guztiei, urte hauetan nire bizitzan igaro zaretenoi, eskerrik asko bizi izan ditugun une zoragarri ugariengatik. Beti gordeko zaituztet bihotzean maitasun handiz.

Nire ibilbide zientifikoaren lehen urratsetan lagungarri izan ziren pertsonak ere gogoratu nahi ditut, Madrilgo Fisika Fundamentaleko Institutuan (IFF) 2017 eta 2018 artean. Nire arduradunari, Alberto García Velari, eta Madrilgo Unibertsitate Konplutentseko Luis Bañaresi: eskerrik asko nigan konfiantza izateagatik, nire ikerketa-karrera hasteko aukera emateagatik eta zuen irakaspenengatik, etapa honetan zein etorkizunean baliagarriak izango direlako. Nire esker onik beroena IFFko lankideei ere: Raúl Rodríguez, Carlos García, Josu Ortiz de Zárate, Álvaro Castillo, Dani Arismendi, Nissrin Alharzali, Judit Montes de Oca, Raquel Yanes eta Mónica Valentín, besteak beste. Eskerrik asko zuen adiskidetasunagatik, adeitasunagatik eta institutuan zein handik kanpo partekatu genituen une atseginengatik. Oroitzapen onez gogoratzen zaituztet.

Zaragozako Unibertsitatean Fisika Gradua ikasi nuen urteetan zehar, nire bizitzan arrastoa utzi zuten pertsona guztiei hitz batzuk eskaini nahi dizkiet. Lehenik eta behin, nire prestakuntzan ezabaezinezko arrastoa utzi zuten irakasleei mila esker, hala nola Pedro Antonio Martínez, Luis Mario Floría, José Tornos, Andrés Cruz, José Luis Cortés, José Manuel Carmona, eta hemen aipatu ez ditudan beste askori ere. Eskerrik asko zuen ahaleginagatik, zuen ezagutza partekatzeagatik eta bide honetan aurrera jarraitzera inspiratzeagatik. Etapa hartan lagun asko egin nituen, besteak beste, Gonzalo Alonso, Miguel García Bosque, Patricia Castiella, Mario Abadía eta askoz gehiago, eskerrik asko eskolen artean, barreen artean eta ahaztezinak diren uneen artean elkarbanatutako orduengatik. Bereziki, Zaragoza inguruko lagun talde zoragarri bat aipatu nahi dut: Iván Ruiz, Fran López, Javi Inchaurre eta Miguel den Holder, besteak beste, unibertsitate garaian zein urteetan aurrera partekatu genituen esperientzia ahaztezinengatik (eta etorkizunean datozkigunak!). Zuen adiskidetasuna opari bat da, eta distantziak bereizi arren, beti nirekin eramango zaituztet. Urte horiek ezinbestekoak izan ziren nire prestakuntza akademikorako ez ezik, nire garapen pertsonalerako ere, eta beti egongo naiz eskertuta bidai horretan nirekin izan zineten pertsona guztiei. Garai haietako oroitzapenek, eta haiek berezi egin zituzten pertsonak, betirako iraungo dute nire bihotzean.

Azkenik, nire familiari hitz batzuk eskaini nahi dizkiot, nire babeslekua eta nire sostengu handiena direlako. Eskerrik asko nire Madrilgo familiari, zuen maitasuna eta laguntasuna nire bizitzan zutabe sendo bat izan direlako, partekatu ditugun une guztiengatik eta etorkizunean elkarrekin biziko ditugunengatik. Bereziki, eskerrik asko osaba Antonio eta izeba Mari Pazi, izeba Joaquina, eta lehengusu Pablo eta Miguel, IFFn nire ikerketa garaian beso zabalik hartu ninduzuelako eta etxean bezala sentiarazi ninduzuelako. Nire Caparrosoko aitona eta Valtierra amona maiteei, José María eta Victoria, beti maitasun eta indarraren eredu izan zineten. Ziur nago nonbaitetik harro daudela ni honaino iritsi izateaz. Eskerrik asko, halaber, osaba Patxiri eta lehengusu David eta Marisari, hurbil egoteagatik eta nire bizitzan

presente egoteagatik. Ich möchte mich auch bei Elisabeth für ihre Großzügigkeit und Freundlichkeit gegenüber meiner Familie und mir herzlich bedanken. Sie war eine außergewöhnliche Person, die einen besonderen Platz in unseren Herzen hat und unser Leben nachhaltig geprägt hat. Eta, batez ere, eskerrik asko nire familia hurbilenari: nire gurasoei, Alfredo eta Beatriz, eta nire anaiari, Javier. Ez dago hitz nahikorik adierazteko zenbat suposatzen duzuen niretzat. Eskerrik asko zuen maitasun baldintzagabearengatik, zuen pazientzia infinituagatik eta ibilbide honetan zehar nire babes iturri handiena izateagatik. Eman didazuen guztiaren ordaina inoiz ezin izango dizuet eman, baina espero dut lorpen honek adieraztea zenbat estimatzen zaituztedan eta zenbat zor dizuedan. Hemen iritsi banaiz, zuei esker da.

*Lolo lololo lololo lolololololo,  
gurea da, bizitza basatia!*



# Agradecimientos

---

En primer lugar, quiero expresar mi más profundo agradecimiento a mis directores de tesis, Maite Alducin y Joseba Iñaki Juaristi. Gracias por confiar en mí desde el primer momento y abrirme las puertas de vuestro grupo en el Centro de Física de Materiales (CFM), dentro del grupo de Gases y Superficies Sólidas (Gas/Solid Interfaces). Vuestra cercanía, dedicación y paciencia han sido fundamentales para mi desarrollo como científico durante estos años. Gracias por enseñarme, guiarme y permitirme aprender tanto; vuestra ayuda ha sido clave en cada etapa de este proceso. Pero, por encima de todo, os agradezco de corazón vuestro compromiso conmigo y el no haberme dejado nunca solo. Siempre os recordaré con especial cariño como mis "padres científicos". Mi agradecimiento también a Ricardo Díez Muiño, por recibirme con la misma cercanía en el grupo.

A mis compañeros del grupo Gas/Solid Interfaces del CFM: Auguste Tetenoire, Alejandro Rivero, Alberto P. Sánchez Muzas, Raúl Bombín, Oihana Galparsoro, Ivan Žugeč y Natalia Koval. Gracias por vuestra amistad, simpatía y apoyo a lo largo de estos años. Habéis creado un ambiente excepcional, tanto en las reuniones de grupo como en nuestras reuniones fuera del CFM. También quiero agradecer a otros investigadores con los que compartí buenos momentos durante sus estancias temporales en el CFM. En particular, quiero destacar a tres compañeros. A Auguste, quien fue también mi compañero de oficina durante cuatro años. Gracias por tu ayuda con VASP y Python cuando comenzaba a usarlos. A Alejandro, por iniciarme en el entrenamiento de redes neuronales, cuyas enseñanzas fueron de gran utilidad para mi investigación posterior. Y, especialmente, a Alberto, cuyo trabajo en el desarrollo del código de dinámica molecular con fricción electrónica (MDEF) y las herramientas de análisis de cálculos fue esencial para obtener buena parte de los resultados más importantes de esta tesis. Gracias por tu simpatía, tu disposición para ayudarme y por hacer de trabajar contigo una experiencia enriquecedora. Mi agradecimiento también a colaboradores de otros grupos de investigación, cuya contribución fue fundamental para este trabajo: entre otros, Yaolong Zhang, Ce Hu y Bin Jiang, por el desarrollo del modelo y el código de redes neuronales de átomos incrustados (EANN); Juraj Ovčar e Ivor Lončarić, por vuestro trabajo en la función generadora de densidad empírica utilizada en las simulaciones MDEF. Asimismo, gracias a todos los compañeros del CFM y del Donostia International

Physics Center (DIPC) que habéis pasado por mi vida durante estos años y por tantos ratos maravillosos. Os llevaré siempre con mucho cariño en mi corazón.

Quiero también recordar a quienes fueron clave en mis primeros pasos como investigador en el Instituto de Física Fundamental (IFF) de Madrid entre 2017 y 2018. A mi supervisor, Alberto García Vela, y a Luis Bañares, de la Universidad Complutense de Madrid: gracias por confiar en mí, por darme la oportunidad de iniciar mi carrera investigadora y por vuestras enseñanzas, que han sido valiosas durante esta etapa y lo seguirán siendo en el futuro. Mi gratitud también a mis compañeros del IFF: Raúl Rodríguez, Carlos García, Josu Ortiz de Zárate, Álvaro Castillo, Dani Arismendi, Nissrin Alharzali, Judit Montes de Oca, Raquel Yanes y Mónica Valentín, entre otros. Gracias por vuestra amistad, vuestra simpatía y por tantos buenos momentos vividos dentro y fuera del instituto. Os recuerdo con mucho cariño.

Quiero dedicar unas palabras a todas las personas que marcaron mi vida durante los años en los que estudié el Grado en Física en la Universidad de Zaragoza. En primer lugar, mi agradecimiento a los profesores que tuve y que dejaron una huella imborrable en mi formación, como Pedro Antonio Martínez, Luis Mario Floría, José Tornos, Andrés Cruz, José Luis Cortés, José Manuel Carmona, y muchos otros cuyo impacto sigue presente, aunque no los mencione aquí. Gracias por vuestro esfuerzo, por compartir vuestro conocimiento y por inspirarme a seguir avanzando en este camino. A muchos amigos que me llevé de esa etapa, como Gonzalo Alonso, Miguel García Bosque, Patricia Castiella, Mario Abadía y tantos más, gracias por las horas compartidas entre clases, risas y momentos inolvidables. En particular, quiero mencionar a un grupo de buenos amigos de Zaragoza, como Iván Ruiz, Fran López, Javi Inchaurrealde y Miguel den Holder, entre otros, con quienes compartí experiencias imborrables tanto durante la universidad como en años posteriores (¡y lo que nos queda!). Vuestra amistad ha sido un regalo y, aunque la distancia pueda separarnos, os llevo siempre conmigo. Aquellos años fueron esenciales no solo para mi formación académica, sino también para mi crecimiento personal, y por ello siempre estaré agradecido a cada una de las personas que me acompañaron en este viaje. Los recuerdos de esos días y de quienes los hicieron tan especiales permanecerán siempre en mi corazón.

Finalmente, quiero dedicar unas palabras a mi familia, mi refugio y mi mayor apoyo. Gracias a mi familia de Madrid, cuyo cariño y compañía han sido un pilar fundamental en mi vida, por todos los momentos compartidos y por los que aún nos quedan por vivir juntos. En especial, gracias a mis tíos Antonio y Mari Paz, a mi tía Joaquina y a mis primos Pablo y Miguel, por acogerme con los brazos abiertos y hacerme sentir como en casa durante mi etapa investigadora en el IFF. A mis queridos yayos de Caparros y Valtierra, José María y Victoria, que siempre fueron

un ejemplo de amor y fortaleza. Estoy seguro de que, desde donde estén, se sienten orgullosos de verme llegar hasta aquí. Gracias también a mi tío Patxi y a mis primos David y Marisa, por su cercanía y por estar presentes en mi vida. Ich möchte mich auch bei Elisabeth für ihre Großzügigkeit und Freundlichkeit gegenüber meiner Familie und mir herzlich bedanken. Sie war eine außergewöhnliche Person, die einen besonderen Platz in unseren Herzen hat und unser Leben nachhaltig geprägt hat. Y, sobre todo, gracias a mi familia más cercana: mis padres, Alfredo y Beatriz, y mi hermano, Javier. No hay palabras suficientes para expresar cuánto significáis para mí. Gracias por vuestro amor incondicional, por vuestra paciencia infinita y por ser mi mayor fuente de apoyo en cada paso de este camino. Nunca podré devolver todo lo que me habéis dado, pero espero que este logro sea un reflejo de cuánto os valoro y de cuánto os debo. Si he llegado hasta aquí, es gracias a vosotros.

*Somos un equipo, valiente y luchador,  
que defiende sus colores con el corazón.  
Los años van pasando, y seguimos aquí,  
porque somos Osasuna... ¡y esto nunca va a morir!*



# List of Publications

---

## Articles in Refereed Journals

- [1] A. Serrano Jiménez, A. P. S. Muzas, Y. Zhang, J. O. Ovčar, B. Jiang, I. Lončarić, J. I. Juaristi, and M. Alducin. **Photoinduced Desorption Dynamics of CO from Pd(111): A Neural Network Approach.** *J. Chem. Theory Comput.* **17**, 8, 4648–4659 (2021). DOI: [10.1021/acs.jctc.1c00347](https://doi.org/10.1021/acs.jctc.1c00347).
- [2] A. P. S. Muzas, A. Serrano Jiménez, J. Ovčar, I. Lončarić, M. Alducin, and J. I. Juaristi. **Absence of isotope effects in the photo-induced desorption of CO from saturated Pd(111) at high laser fluence.** *Chem. Phys.* **558**, 111518 (2022). DOI: [10.1016/j.chemphys.2022.111518](https://doi.org/10.1016/j.chemphys.2022.111518).
- [3] A. P. S. Muzas, A. Serrano Jiménez, Y. Zhang, B. Jiang, J. I. Juaristi, and M. Alducin. **Multicoverage Study of Femtosecond Laser-Induced Desorption of CO from Pd(111).** *J. Phys. Chem. Lett.* **15**, 9, 2587–2594 (2024). DOI: [10.1021/acs.jpcllett.4c00026](https://doi.org/10.1021/acs.jpcllett.4c00026).



# List of Acronyms

---

2PC	two-pulse correlation. 158–160, 177, 179, 187, 195–197, 200, 201, 204, 205, 218, 229, 231, 253
2TM	two-temperature model. 61, 64–68, 73–75, 135, 150, 179, 181, 182, 188, 196, 200–203, 205, 212, 227, 235, 245, 248
3TM	three-temperature model. 66, 68
ACSF	atom-centered symmetry function. 95, 97, 98, 100, 102
AIMDEF	ab initio molecular dynamics with electronic friction. 72, 76–81, 88, 107, 112, 125, 135, 149, 157–160, 164, 167, 169, 177, 181, 188, 197, 207, 211, 218, 221, 223, 225, 227, 231, 252–254
CM	center of mass. 57, 134, 137, 142, 163, 165, 173, 191–193, 204, 212, 214–216, 219, 220, 244–247, 249
DFT	density functional theory. 23, 27, 29, 31, 34, 37–41, 48, 50, 51, 71, 72, 76–78, 87, 88, 94, 103, 112, 128, 162–165, 170–177, 182, 183, 187, 204, 207, 222, 234, 240, 244, 245, 252, 254
DGF	density generator function. 133–135, 139, 147, 149, 181, 228
DIET	desorption induced by one electronic transition. 56, 57, 59
DIMET	desorption induced by multiple electronic transitions. 56, 60, 70, 177, 179, 181, 185, 204, 229
DOF	degree of freedom. 23, 27, 61, 66, 134, 152, 160, 196, 227
EAM	embedded atom model. 102, 104, 107
EANN	embedded atom neural network. 102, 104–108, 111, 113, 115–118, 120–126, 128–130, 134–142, 146, 147, 149–151, 157, 159–161, 163–165, 167, 169–178, 203–205, 228, 229, 231, 239–245, 251, 252

ECDF	empirical cumulative distribution function. 142
EML-LM	extreme machine learning and Levenberg-Marquardt. 115
fcc	face-centered cubic. 112, 114, 129, 130, 135, 136, 138, 139, 160, 162–165, 172–175, 182, 187, 193, 207, 208, 212–214, 217, 221–224, 230, 239–241, 244, 245, 249, 253, 254
FEG	free electron gas. 38, 71, 72
FWHM	full width at half maximum. 67, 113, 150, 179, 181, 195–197, 212, 235, 245
GGA	generalized gradient approximation. 44–47, 50, 51
GLO	generalized Langevin oscillator. 73
GTO	Gaussian-type orbital. 104–106, 116, 118–120, 122, 123, 167, 239, 240, 251
hcp	hexagonal close packed. 112, 114, 129, 131, 135, 136, 138, 139, 162–165, 172–174, 182, 193, 207, 208, 213, 221–223, 225, 230, 239–241, 244, 245
HDNNP	high-dimensional neural network potential. 93–96, 100, 102, 106, 107, 111, 238, 239
HEG	homogeneous electron gas. 40, 42, 44, 71, 103
HK	Hohenberg-Kohn. 27, 29–31, 38, 103
HWHM	half width at half maximum. 196, 200, 201, 205
IAA	independent atom approximation. 73, 129
KS	Kohn-Sham. 31–39, 42, 46, 48, 49, 71, 76, 233
LDA	local density approximation. 40, 42–47, 50, 72
LDFA	local density friction approximation. 71, 73, 77, 111, 112, 129, 132, 133, 181, 212, 240
LEED	low energy electron diffraction. 183, 227
LSDA	local spin density approximation. 43, 72
MAE	mean absolute error. 87
MDEF	molecular dynamics with electronic friction. 72, 73, 75, 79, 80, 135, 149, 150, 158, 159, 177, 179, 181, 187, 203, 204, 225, 227–229

MESMAE	maximum error set mean absolute error. 124–127, 129, 162, 169, 172, 174, 175, 240, 252, 253
mGGA	meta-generalized gradient approximation. 46–48, 51
MGR	Menzel-Gomer-Redhead. 56–61, 234, 235
ML	machine learning. 81, 91, 146
NH	Nosé-Hoover. 74, 75, 181, 182, 208, 212
NN	neural network. 80–84, 86–96, 100, 102, 105–107, 111, 116, 118, 120, 129, 132, 219, 225, 228, 236–239, 251
PAW	projector augmented-wave. 207
PEANN	piecewise embedded atom neural network. 108
PES	potential energy surface. 22, 23, 27, 29, 54, 56–60, 70, 71, 73, 79–82, 86–88, 90–95, 100, 102, 105, 108, 111, 113, 115–118, 120–130, 134–143, 146, 147, 149–151, 157, 159–167, 169–179, 183, 184, 187, 197, 203–205, 219, 225, 227–229, 231, 234, 235, 237, 239–245, 251–253
REANN	recursive embedded atom neural network. 108
RMSE	root mean square error. 87, 121, 122, 124, 125, 127, 129, 130, 147, 162, 166, 167, 169, 172, 174, 175, 240, 252, 253
STM	scanning tunneling microscopy. 227
TDDFT	time-dependent density functional theory. 71
VASP	Vienna Ab initio Simulation Package. 112, 207, 208, 212
vdW-DF	van der Waals density functional. 49–51, 112, 162, 163, 165, 172–175, 177, 204, 207, 222, 244, 245, 252, 254
WIEG	weakly inhomogeneous electron gas. 44



Palladium (Pd) is a transition metal with interesting features. Within the family of platinum-group elements, to which Pd belongs with platinum, rhodium, ruthenium, osmium, and iridium, it is the least dense element, and its melting point is the lower one. This metal does not oxidize at ambient temperatures in contact with air, and at room temperature it can absorb up to 900 times its volume of hydrogen and form palladium hydride ( $\text{PdH}_x$ ) [1, 2]. In addition, Pd facilitates various chemical reactions, for instance, hydrogenation and dehydrogenation [1, 3, 4] or carbon monoxide (CO) and hydrocarbon oxidation [5, 6, 7]. Properties such as these motivate its wide use for a number of applications. Perhaps the most popular are related to gas-solid heterogeneous catalysis, as solid catalysts are involved in the international production of more than 90 % of all chemicals in the industry [4]. Pd is commonly used in motor vehicle catalytic converters, mainly in three-way catalytic converters of car exhaust systems, where some dangerous gases are converted into less life- and environmental-harmful substances [5]. In these catalysts, nitrogen oxides ( $\text{NO}_x$ ) are reduced to  $\text{N}_2$ , while CO and hydrocarbons are oxidized to  $\text{CO}_2$  and  $\text{H}_2\text{O}$ . Recall in particular that CO in the gas phase is colorless, odorless, and tasteless. It is also neurotoxic and highly flammable, so therefore its oxidation as carbon dioxide ( $\text{CO}_2$ ) is crucial for a number of situations, particularly at low temperatures due to the irreversibility of this process [8, 9]. In addition, its ability to absorb large volumes of  $\text{H}_2$  and to catalyze hydrogenation and dehydrogenation processes makes Pd suitable for hydrogen-related technologies such as hydrogen storage, purification, or fuel cells, either alone or as part of metal alloys [2, 10]. Regarding fuel cells, Pd can be of great use to avoid poisoning of the catalyst with gases like CO [11]. Furthermore, Pd-catalyzed reactions play a role in developing agrochemical or pharmacological chemicals, or new materials, to list some other examples [12]. Another interesting use of Pd is for gas sensing technologies, using adsorption to detect and measure the environmental concentration of a given gas, and also profiting from desorption to reset the sensors for new measurements [6, 13, 14, 15]. Examples such as these reveal the growing relevance of Pd for various technological purposes, and hence a proper understanding of Pd dynamics under different contexts is essential.

Among these, we are interested in learning more about adsorption and desorption. In general, in processes such as heterogeneous catalysis, photocatalysis, and

nanochemistry on surfaces, to list some examples, adsorption and desorption of atoms and/or molecules occur very frequently, so their characterization becomes essential [16]. From a chemical perspective, any adsorbed species is able to change the electronic properties or geometric structure of Pd when it is chemisorbed, and hence its catalytic features may be modified as a result. Both chemical processes may also be useful to search active adsorption sites on any surface and to gain broader insights into reaction dynamics of the latter one. Consequently, a comprehensive knowledge of the interplay between any adsorbing and/or desorbing species and a given substrate is of great theoretical and applied interest.

Now let us consider a Pd(111) substrate, with adsorbed CO gas, initially in isolation (Chapters 5 to 7), and later accompanied by O atoms (Chapter 8). CO adsorbed on Pd(111), denoted CO/Pd(111), is a system known for its intricate structural properties. Depending on coverage, from adlayers smaller than 0.33 ML to saturation coverage at 0.75 ML, there are a minimum of 17 ordered structures [17]. CO binding structures in Pd (111) transition from three-fold fcc site adsorption at coverages of 0.33 ML and below, to a mixture of three-fold hollow sites (mainly bridge and near-bridge) at coverages in the range [0.50,0.67] ML, plus top CO adsorption from 0.60 ML on, to another combination of top and three-fold hollow until reaching saturation at 0.75 ML. This consensus was reached after different experimental works involving various techniques, for instance low energy electron diffraction (LEED) [17, 18, 19], infrared reflection-absorption spectroscopy (IRAS) [20, 21, 22], sum frequency generation spectroscopy (SFG) [23], photoelectron diffraction [24], high resolution X-ray spectroscopy [25], and scanning tunneling microscopy (SFM) [26]. This also found support from different computational works [27, 28, 29]. There exists a strong relationship between substrate-adsorbate energy coupling and adlayer –or, more precisely, on the specific adsorption sites– for CO/Pd(111), which has been investigated experimentally with femtosecond laser-induced desorption and two-pulse correlation (2PC) techniques, with subsequent phenomenological proposals to explain it [30] and more elaborated theoretical works supported in computational simulations of femtosecond CO photodesorption [31].

On the basis of the latter two works mentioned in the previous paragraph, the work presented in this Thesis aims to gain a deeper insight on how CO desorbs from Pd under femtosecond laser excitation conditions. Under irradiation of femtosecond pulses in the ultraviolet, visible, and near-infrared ranges, a large fraction of the light is absorbed by a metal surface [16, 32, 33]. When the latter is decorated with adsorbates, these can undergo different chemical reactions, diffusion, and desorption as a result. Photons interact with the metallic target and this leads to the emergence of electron-hole pairs that may populate excited adsorbate-substrate states. These initially nonthermal hot electrons scatter to other electrons, as well as to surface

phonons, resulting in rapid electronic relaxation into a hot Fermi-Dirac distribution and gradual heating of the substrate lattice. These excited electronic states and excited phonons couple to the adsorbate degrees of freedom, leaving kinetically excited adsorbates after relaxation. Interplay of both subsystems can either enhance the reaction rates of some chemical processes undergone by adsorbates or even give rise to new reaction channels [16, 30, 32, 33, 34, 35, 36, 37, 38].

Notably, a key parameter in femtosecond photoexcited adsorbate-substrate reactions is the fluence of the incoming laser. This affects the density of excited substrate electron-hole pairs that adsorbed species can encounter. Particularizing on desorption, two regimes can be distinguished [16, 32]. For fluences below some cutoff that depends on the features of the adsorbate-substrate complex, desorption induced by an electronic transition (DIET) takes place. Here, an adsorbate gains kinetic energy after coupling a photoexcited electron-hole pair and either relaxes back to its ground state rapidly or, if the energy input is larger than the adsorption energy, the adsorbate surpasses its adsorption well and can desorb. On the contrary, if the fluence is higher than a certain threshold, desorption induced by multiple electronic transitions (DIMET) becomes the predominant reaction mechanism. In this case, the adsorbate encounters a larger density of hot electrons than for DIET, so each adsorbed species on the verge of relaxation can experience secondary excitations with a larger probability than in DIET. Hence, adsorbates can undergo several consecutive excitation-deexcitation cycles, preventing them to relax back to their ground states, so they "ladder-climb" the desorption barriers and ultimately overcome them instead. As a result, the reaction output experiences a dramatic increase in the DIMET regime compared to DIET, as it becomes superlinear with fluence instead of linear as for DIET. Furthermore, because of DIMET, the kinetic energy becomes approximately linear with the incoming fluence, and reaction yields may vary for different isotopes of the adsorbed species, i.e., isotope effects may occur depending on the gas-solid system under study. Therefore, theoretical proposals that characterize the DIMET regime well aim to reproduce these properties in accordance with experimental observations, while providing time- and space-resolved insights into the photoinduced dynamics.

From the theoretical side, the DIMET mechanism can be efficiently modeled on the basis of molecular dynamics with electronic friction (MDEF) [39, 40, 41, 42, 43, 44, 45, 46, 47, 48, 49]. Two main ingredients are involved in such approaches. First, the interaction between the laser pulse and the surface is characterized macroscopically according to the two-temperature model [50]. This yields two time-dependent temperatures, one corresponding to the electron bath, excited first after pulse absorption, and the other for the subsequently heated phonons. Addition of an electron-phonon coupling constant ensures the thermal interplay between

electronic and phononic subsystems during dynamics. Secondly, the response of the adsorbates to the excited electrons is described by a Langevin equation of motion. Adsorbates are considered to stay in the ground state potential energy surface (PES), therefore experiencing adiabatic forces handled within the Born-Oppenheimer approximation, while nonadiabatic effects due to hot electrons (i.e., the aforementioned "ladder-climbing") is simulated with stochastic and dissipation forces, both due to electronic friction and proportional to the transient electronic temperature.

However, modeling the adiabatic forces in MDEF simulations was a hard task due to the large computational demand of density functional theory (DFT) calculations. Hence, initially its inclusion in the mentioned simulations of femtosecond laser-induced reactions and in more general gas-surface dynamics studies [51, 52] was tackled with approximate methods. A common option employed in the mentioned works was to generate the ground-state adiabatic PES for the adsorbate-substrate of interest, but, again, the computational cost restricted this possibility to quite simplified systems. Thus, it was possible to tackle six-dimensional PESs for single diatomic adsorbates, but neither energy exchange with the surface nor coverage effects could be treated with this dimensionally restricted PES. A further improvement to incorporate surface temperature effects into six-dimensional gas-surface dynamics consisted of using the generalized Langevin oscillator (GLO) model [53, 54, 55, 56], where all surface atoms are assumed to move synchronously. Examples of its application in photoinduced desorption simulations are the studies of  $O_2/Ag(110)$  [45, 46] and  $CO/Ru(0001)$  [47, 48]. Still, an important downside of GLO is its inability to capture the surface deformations at the atomic level, which can be particularly important at the high surface temperatures reached upon irradiating the surface.

The development of ever more powerful computers during the last decade promoted the use of *ab initio* molecular dynamics (AIMD) in many of the gas-surface dynamics studies. In this type of simulations the adiabatic forces are calculated on-the-fly with DFT along the whole trajectory and it is possible to incorporate naturally surface temperature effects by including all the necessary degrees of freedom in the equations of motion. Nonadiabatic effects due to the coupling of the moving gas-species/adsorbates with the metal electrons were also introduced in the *ab initio* molecular dynamics with electronic friction (AIMDEF) method developed in Refs. [57, 58, 59, 60, 61, 62]. AIMD and AIMDEF are the most advanced and reliable methods to use in gas-surface dynamics when extensive statistical sampling of the initial conditions is not mandatory. In the particular case of femtosecond laser-induced reactions, the effect of the laser-excited electrons, the electron-excited phonons, and also interadsorbate interactions can be successfully described with

$(T_e, T_1)$  – AIMDEF simulations [31] that will be described in more detail in Section 3. Crucial insights into the strong coverage dependence of photoinduced desorption of CO from Pd(111) [31] and into the competition between CO desorption and oxidation on Ru(0001) with different coverages [63, 64, 65] have been obtained thanks to  $(T_e, T_1)$  – AIMDEF simulations. Also the laser-induced recombinative desorption of different isotopologues that was observed in experiments performed in Ru(0001) with varying mixtures of H and D adsorbates [37] was reproduced with simpler  $(T_e, T_1)$  – AIMDEF simulations that only included the effect of the laser-excited electrons [66].

The  $(T_e, T_1)$  – AIMDEF framework provides an improved and reliable theoretical description of complex processes involving adsorbates and substrates, but requires substantial computational resources. Due to this shortcoming,  $(T_e, T_1)$  – AIMDEF simulations are typically able to describe intervals of only a few picoseconds after photoexcitation, and statistical analysis is commonly limited to just a few hundred trajectories in reasonable computational times. As an example, calculation of a single trajectory of femtosecond laser excitation of CO/Pd(111) over a time range of 4.0 ps and with an integration time step of the order of fs takes around 7 days to complete when 24 cores are utilized. This circumstance also notably restricts the amount of statistics one can obtain with  $(T_e, T_1)$  – AIMDEF for a fixed set of initial conditions to the order of hundreds of trajectories. Therefore, alternative methods are required to study photoinduced reactions for a broader range of experimental conditions and dynamical time spans. A powerful way to improve the scope that is realistically reachable by  $(T_e, T_1)$  – AIMDEF capabilities has been provided by machine learning (ML), or more precisely, by neural networks (NNs).

Application of NN schemes for PES production began during the 1990s [67, 68]. Early examples refer to the vibrational spectrum of a polyethylene molecule in both ground and excited states [69] and in the study of CO adsorption on Ni(111) and H<sub>2</sub> recombinative desorption from Si(100) with very simple PESs [70]. The early NN PESs involved functional expressions whose complexity could be reduced simply by setting a different structure for NN, which allowed a straightforward evaluation of energies and atomic forces. Moreover, these models do not require prior knowledge of the chemical nature of the system, e.g., its chemical bonds. Unfortunately, usage of plain atomic coordinates and/or angles as NN input parameters resulted in PESs that were difficult to transfer to system atomic arrangements with different amounts of atoms and atomic positions. A major advancement in this respect was achieved in 2007, with the proposal of training NN PESs using translational, rotational, and atom permutational-invariant descriptors and partitioning the energy of the atomic arrangement as a sum of the contributions of the atomic species present in the system [71]. This made it possible to extend the construction of NN PESs beyond

low amounts of degrees of freedom to systems of arbitrary size. As a result, the generation and use of NN PESs in molecular dynamics simulations have become increasingly popular in recent years, as reflected in the increasing number of recent works available in the literature involving solid-liquid water interfaces [72, 73, 74] and gas-solid interfaces [75, 76, 77, 78, 79, 80, 81, 82, 83, 84, 85, 86]. The work performed in this Thesis demonstrates that it is also possible to develop accurate NN PESs to study the complex dynamics and reactions induced by femtosecond laser pulses. Its impressive accuracy and computational efficiency pave the way to studies that would otherwise have been infeasible with  $(T_e, T_1)$  – AIMDEF in realistic times. The femtosecond laser-induced desorption of CO from Pd(111) surfaces with different coverages that is studied in this Thesis and published in Refs. [87, 88, 89] is a good example. By constructing an accurate multicoverage PES, it has been possible to reproduce and understand many of the experimental findings, such as the strong coverage dependence of the desorption probability for fixed laser fluence and the different fluence dependence of the desorption probabilities that is obtained for each coverage.

Another open question that could not be determined in experiments [30] and we tried to answer along this Thesis was whether CO desorption from Pd(111) was electron- or phonon-dominated and if the dominant mechanism changes with coverage. There are different ways to answer this question. First, we can look for potential isotope effects, as previously mentioned. In fact, its presence signals the predominance of the electron mechanism in the excitation of adsorbates. Notable isotope effects for different systems have been reported in previous experimental works. These include, for instance, the oxidative desorption of O+CO on Ru(0001) [36, 90], the recombinative desorption of H<sub>2</sub> in the H/Ru(0001) system [37], and the recombinative desorption of O<sub>2</sub> in the O/Pd(111) system [91]. In contrast, there are also reports on systems without isotope effect such as the desorption of CO from Ru(0001) [92]. In this Thesis we have developed a NN PES trained on previous  $(T_e, T_1)$  – AIMDEF calculations, which allowed us to determine the absence of isotopic effects in the photoinduced desorption of CO/Pd(111) [88].

Another way to determine which mechanism dominates, electronic or phononic, is provided by two-pulse correlation (2PC). In these experiments, an adsorbate-substrate complex is irradiated with two short laser pulses separated by a certain time interval [93]. The first pulse, known as pump pulse, excites the system and initiates the dynamic processes under study. The second pulse, known as the probe pulse, is used to measure the time-dependent dynamic properties of the system. Depending on the full width at half maximum (FWHM) of the 2PC reaction yield measured at different pump-probe delays, the predominant energy source can be determined in the adsorbed species. If electrons govern this transfer, widths of

$\sim 1$  ps or less are observed, while larger widths are compatible with both electron- and phonon-mediated energy inputs. Experimentally, this technique has been applied to systems such as NO/Pd(111) [34], CO/Ru(0001) [36, 92], H/Ru(0001) and D/Ru(0001) [37], O<sub>2</sub>/Pd(111) [38], and CO/Pd(111) [30], among others. A theoretical study of 2PC experiments based on AIMDEF was computationally unaffordable because it requires to perform statistically meaningful simulations at many different pump-probe delays. Fortunately, as will be shown in this Thesis, these simulations can now be conducted with the help of accurate NN PESs.

A third possibility to determine the contribution of electrons and phonons consists in performing different type of MDEF simulations that include or neglect each of these mechanisms. In particular, one may study the process either when substrate energy transfer to adsorbates mediated by both hot electrons and phonons is enabled or when one of these mechanisms is not operating. Then, the reaction probability under these three different conditions may be explored in order to better understand the role of both electronic and phononic subsystems in adsorbate dynamics. Previous AIMDEF works initiated this analysis exploring the initial picoseconds after laser excitation, finding in particular a cooperation between electrons and phonons in the desorption of CO from Pd(111) [31] and in the desorption of CO and CO<sub>2</sub> from mixed O+CO/Ru(0001) [64]. In this Thesis, the developed multicoverage CO/Pd(111) NN PES has allowed us to extend the previous AIMDEF study until 100 ps after laser pulse arrival on the metal substrate and confirm the dominant role of the phonons [89]. Thus, a promising theoretical methodology to understand the role of hot electrons and phonons of the substrate driving chemical processes on adsorbed species has been opened. Trying this on other systems should be straightforward.

Finally, having as inspiration recent AIMDEF and MDEF studies on O+CO/Ru(0001) [63, 65, 94, 95], one may speculate whether the presence of atomic O together with CO could open the chemical path of photoinduced CO oxidation and desorption in the form CO<sub>2</sub>. In this respect, an initial AIMDEF characterization should shed some light on the aforementioned questions and serve as a preliminary basis for a more in-depth analysis with a suitable NN PES for this adsorbate-substrate complex.

This Thesis focuses on the topics mentioned previously with the following structure. First, the theoretical foundations of this work are introduced in Part I. To begin with, the framework to characterize a multiatomic system in its ground state is introduced in Chapter 2. First, a crucial simplification for solving time-dependent dynamics on such a system, the adiabatic approximation [96], is described. As reasoned in the following Section, this is used in order to uncouple the electronic and nuclear degrees of freedom and determine these dynamics theoretically on the system ground state PES with Born-Oppenheimer approximation [97]. Next, it is

explained from an introductory perspective how DFT is used to obtain the electronic structure. Finally, some of the more popular exchange-correlation functionals in DFT are reviewed, including those more suitable for describing interactions in sparse systems like gas-solid systems, which are the focus in this Thesis.

Chapter 3 is devoted to the basics of femtosecond laser-induced desorption on adsorbate-decorated surfaces. To start with, an overview of photoinduced desorption for a general adsorbate-substrate complex is provided. This includes a description of how adsorbates can be excited directly by the incoming light or indirectly by the substrate, as well as a brief explanation of some simple primitive approaches to explain these chemical processes [98, 99]. The next Section focuses on how femtosecond laser-induced desorption of adsorbed species on metal surfaces can be modeled theoretically. On one hand, the incoming laser effects are modeled using a two-temperature model (2TM) [50] that describes the coupling of electron and phonon subsystems. On the other hand, adsorbate and substrate atom dynamics after photoexcitation are described from a microscopic perspective. Adiabatic forces on atoms are calculated within Born-Oppenheimer approximation on the basis of the adsorbate-substrate ground state PES. Adsorbate motion is governed by Langevin equations, with electronic friction forces and stochastic forces that depend on the electronic temperature  $T_e$ . Moreover, it is explained how excitations driven by the hot surface lattice on the adsorbates were either approximated with the GLO model [45, 46, 47, 49] or directly discarded in first instance, but with different downsides and limitations. These are overcome in more recent approaches that consider some substrate layers coupled to a Nosé-Hoover thermostat, as discussed. Altogether, the cornerstones of ab initio molecular dynamics with electronic friction [31, 51, 52, 57, 58, 59, 60, 61, 62, 66] are explored in some detail.

Then, Chapter 4 discusses how machine learning and neural networks appear as a promising solution to overcome AIMDEF limitations. This chapter starts with a conceptual introduction of what neural networks are, how they are trained, how their accuracy is improved, and what risks one should avoid when training a neural network. Next, an overview of neural network usage for training PESs is presented, briefly explaining what has been the historic development of this very recent field, the challenges encountered and the ways to solve them. Finally, one of the more recent frameworks for neural network PESs training employed along this work, the embedded atom neural network (EANN) model, is described with more detail.

Afterwards, Part II is devoted to the discussion of the research results yielded during this work. To begin with, Chapter 5 details the study of CO desorption from Pd(111) at a 0.75 ML coverage, using data from  $(T_e, T_l)$  – AIMDEF simulations to construct an EANN PES. The chapter outline includes the description of  $(T_e, T_l)$  –

AIMDEF simulations, the selection of the input data and the EANN parameters for the construction of the PES, the numerical fitting for friction coefficients, and the results from molecular dynamics simulations using the precalculated PES. As discussed, these simulations reproduce the 0.75 ML CO/Pd(111) photodesorption results with a remarkable level of accuracy and provide new insights into the early stages of this chemical process.

Using the EANN PES obtained in Chapter 5, Chapter 6 shows a preliminary hint of the  $(T_e, T_1)$  – MDEF capabilities regarding the search of a possible isotopic effect on 0.75 ML CO/Pd(111) photoinduced desorption. First, some theoretical basics required for our analysis are explained. Next, the chapter focuses on the analysis of the simulations performed for the light ( $^{12}\text{C}^{16}\text{O}$ ) and heavy ( $^{13}\text{C}^{18}\text{O}$ ) isotopologues during a maximum time of 50 ps, ten times larger than the time ranges surveyed within AIMDEF. Simulations including both surface electrons and phonons to excite the adsorbates and simulations that only include phonon-mediated energy input allow us to determine the role of electrons and phonons in quantities such as desorption probabilities, desorption rates, and CO vibrational states.

Chapter 7 is devoted to a comprehensive MDEF study of CO/Pd(111) photodesorption under different conditions. First, the performance of previous 0.75 ML CO/Pd(111) PES is checked against both 0.75 ML and 0.33 ML adlayers and compared to the predictions of both coverages yielded by a PES trained with 0.33 ML AIMDEF data. In particular, adsorption wells on both coverages are predicted with each PES. Making use of the lessons taken from this analysis, the next Section details the procedure for constructing a multicoverage PES, including parameter selection, accuracy check, and some preliminary tests on intermediate 0.60 ML adlayer not present in the EANN training data set. Subsequently, after running MDEF under different conditions, it is analyzed how CO photodesorption varies with initial laser fluence for 0.33, 0.60 and 0.75 ML coverages. Also, the experimental strong coverage dependence of the desorption probability for fixed laser fluence is reproduced and explained. The detailed analysis of the trajectories provide meaningful information on diverse dynamical properties, such as diffusion on the surface, existence of dynamics trapping in the physisorption region, as well as the angular and rovibrational state distributions of the reflected molecules.

To conclude the results part, Chapter 8 presents an AIMDEF study of the photoinduced desorption and oxidation of CO in Pd(111) covered with 0.25 ML O + 0.50 ML CO. The first Section contains details on the DFT calculations, including determination of the energetically most favorable adsorption sites for O and CO and thermalization of the system in order to produce a set of initial configurations to perform dynamics on. Subsequently, the results of the  $(T_e, T_1)$  – AIMDEFsimulations performed in the mixed adlayer under two different fluences are discussed and

compared with the results obtained for 0.75 ML CO/Pd(111) with  $(T_e, T_1)$  – AIMDEF simulations also carry on in this chapter. Quantities such as desorption probability, kinetic energy, and adsorbate movement along and over the Pd substrate are determined, and, apart from CO desorption, CO recombinative oxidation is also characterized.

Finally, Chapter 9 wraps up the main findings of this Thesis work and discusses some ideas for future research.

Part I

Theoretical background



## 2.1 Adiabatic approximation

Studying how a quantum system behaves with time is usually a complex task. From an analytic perspective, when the Hamiltonian of a system incorporates a time dependence, its related Schrödinger equation cannot be solved exactly except for very particular situations and systems. Therefore, approximation methods must be considered in order to simplify this problem [100]. One of these strategies can be tackled when a given Hamiltonian changes slowly enough compared to the natural frequencies of the system under consideration. In such conditions, one can use the adiabatic approximation, also called the adiabatic theorem.

The adiabatic theorem was first stated by Born and Fock for the case of systems with discrete, nondegenerate eigenvalues of the Hamiltonian, i.e., for Hamiltonians whose energy spectra ordering remains stable for all times. For this, originally it was assumed that the eigenvalues of the energy must be separated sufficiently between each other to prevent overlapping (gap condition) [96]. Later, Kato proved its validity in the more general case of the existing degeneracy in the energy eigenvalues [101]. Afterwards, it was reformulated for situations with no gap condition, such as quantized radiation fields acting on initially unexcited atoms [102]. Its statement is quite intuitive. For an arbitrary quantum system, let us consider that the corresponding time-evolving Hamiltonian  $\hat{H}(t)$  has a set of instantaneous eigenstates  $\{|n(t)\rangle\} = \{|0(t)\rangle, |1(t)\rangle, |2(t)\rangle \dots\}$ , which are solutions of the Schrödinger equation with eigenvalues  $E_n(t)$  only at the considered time instant  $t$ , i.e., in Dirac notation,

$$\hat{H}(t)|n(t)\rangle = E_n(t)|n(t)\rangle \quad \text{for all } n. \quad (2.1)$$

Now, given an initial state  $|\psi(t=0)\rangle = |n(0)\rangle$ , if the Hamiltonian varies slowly with time,  $d\hat{H}/dt \rightarrow 0$ , then the system evolution is synchronous with  $\hat{H}$ . Therefore, it remains in its equivalent eigenstate for a given time  $t$ ,  $|\psi(t)\rangle \sim |n(t)\rangle$ . In other words, slowly changing conditions allow the system to adapt its configuration state in response to these evolving conditions. The probability density changes for an adiabatic system,  $|\psi(t)|^2 \neq |\psi(0)|^2$ , but the Hamiltonian eigenstate basis at any arbitrary time  $t$  is equivalent (not the same) to the eigenstate basis at  $t=0$ . The slow evolution of the Hamiltonian should not be confused with a perturbative

theory, as in the latter case the zero-order term of the expansion does not depend on time, whereas in the adiabatic approximation the full Hamiltonian preserves its time dependence (in a parametric way).

An adiabatic change of a quantum system has to be distinguished from a diabatic one. In the latter case, the evolution of the system is fast enough to prevent it from adapting to the new situation. The system continues under the former conditions, so that its probability density does not change:  $|\psi(t)|^2 = |\psi(0)|^2$ . However, its final state becomes a linear combination of different eigenstates of  $\hat{H}(t)$ , which is likely not as simple as applying an adiabatic transformation to the system.

In this respect, adiabaticity is related to the transfer of work to a quantum system, in an analogous fashion to the usual thermodynamical definition of an adiabatic process. When only work is plunged into a system, the spacing between consecutive energy levels is altered, although their relative ordering does not change. Furthermore, since no heat transfer is involved, the population of each energy level or eigenstate remains unchanged because no particle of the system is excited. In contrast, when heat is exchanged with the system (diabatic process), energy of the system constituents can vary, and so can do their quantum states as well, while no modification on the difference in energy between adjacent energy eigenstates occurs.

But what is understood as *fast* and *slow* perturbations? An illustrative example to distinguish between these situations is a particle trapped in an infinite potential well, oscillating in a certain mode, *i.e.* eigenstate of the Hamiltonian. Let us assume that one of the walls is free to move. If it moves too fast, the particle state cannot adapt itself to the new well horizontal dimension; its probability density will not change, but the final state will evolve into a more complex expression based on a harmonic expansion with a Fourier series. This is an example of a fast or diabatic process. Conversely, if the wall is displaced slowly enough, the state has enough time to adapt itself to the new conditions. As a result, the probability density will vary, but the particle will remain oscillating in the same mode, thus staying at a time  $t$  in the equivalent eigenstate of  $t = 0$  it was originally. A theoretical analysis of this can be found elsewhere [103].

Let us prove the adiabatic theorem using the variation of constants method [100]. For simplicity, the eigenenergies  $E_k(t)$  are assumed to be nondegenerate for all states  $|k(t)\rangle$ . We start from the time-dependent Schrödinger equation,

$$i\hbar \frac{d}{dt} |\psi(t)\rangle = \hat{H} |\psi(t)\rangle, \quad (2.2)$$

where the state  $|\psi(t)\rangle$  is its exact solution at a given  $t$ . It can be expressed in terms

of the instantaneous eigenstate basis  $\{|k(t)\rangle\}$  as follows,

$$|\psi(t)\rangle = \sum_k c_k(t) e^{-\frac{i}{\hbar} \int_0^t dt' E_k(t')} |k(t)\rangle, \quad (2.3)$$

where the exponential term  $e^{-\frac{i}{\hbar} \int_0^t dt' E_k(t')}$  is the *dynamic phase factor*, and the coefficients  $c_k(t)$  have to be fixed so that  $|\psi(t)\rangle$  satisfies Eq. (2.2). Substituting this state in the time-dependent Schrödinger equation and after some algebra, one gets:

$$\begin{aligned} i\hbar \sum_k e^{-\frac{i}{\hbar} \int_0^t dt' E_k(t')} [\dot{c}_k(t) |k(t)\rangle + c_k(t) |\dot{k}(t)\rangle] + \\ + \sum_k c_k(t) E_k(t) e^{-\frac{i}{\hbar} \int_0^t dt' E_k(t')} |k(t)\rangle = \sum_k c_k(t) e^{-\frac{i}{\hbar} \int_0^t dt' E_k(t')} \hat{H} |k(t)\rangle, \end{aligned} \quad (2.4)$$

where the dot notation stands for the time derivative and  $|\dot{k}\rangle = (d/dt) |k\rangle$ . From Eq. (2.1) it is clear that the last term on the left part cancels with the right one. Now let us project Eq. (2.4) on another arbitrary eigenstate of the Hamiltonian,  $\langle n|$ . Then we get the following expansion:

$$\sum_k \dot{c}_k(t) e^{-\frac{i}{\hbar} \int_0^t dt' E_k(t')} \langle n(t) | k(t)\rangle = - \sum_k c_k(t) e^{-\frac{i}{\hbar} \int_0^t dt' E_k(t')} \langle n(t) | \dot{k}(t)\rangle. \quad (2.5)$$

By the orthonormalization condition for the eigenstate basis,  $\langle n(t) | k(t)\rangle = \delta_{nk} \forall t$ , one arrives to:

$$\dot{c}_n(t) e^{-\frac{i}{\hbar} \int_0^t dt' E_n(t')} = - \sum_k e^{-\frac{i}{\hbar} \int_0^t dt' E_k(t')} c_k(t) \langle n(t) | \dot{k}(t)\rangle, \quad (2.6)$$

and then  $\dot{c}_n(t)$  can be solved as

$$\dot{c}_n(t) = - \sum_{k \neq n} c_k(t) e^{-\frac{i}{\hbar} \int_0^t dt' (E_k(t') - E_n(t'))} \langle n(t) | \dot{k}(t)\rangle - c_n(t) \langle n(t) | \dot{n}(t)\rangle \quad \forall k. \quad (2.7)$$

The off-diagonal matrix elements  $\langle n(t) | \dot{k}(t)\rangle$  are unknown to us in principle. But there is an elegant way of linking them with the Hamiltonian of the system in order to transform them into more manageable terms. Differentiation with respect to time on both sides of Eq. (2.1) for each  $|k(t)\rangle$  brings us to:

$$\dot{\hat{H}}(t) |k(t)\rangle + \hat{H}(t) |\dot{k}(t)\rangle = \dot{E}_k(t) |k(t)\rangle + E_k(t) |\dot{k}(t)\rangle. \quad (2.8)$$

Following this, let us project on  $\langle n(t) | \neq \langle k(t) |$  Eq. (2.8). In the second term of the left side, the hermiticity of the Hamiltonian allows us to make it act on  $\langle n(t) |$ , that is,  $\langle n(t) | \hat{H}(t) = E_n(t) \langle n(t) |$ , while the first term on the right vanishes due to orthonormality. Hence, one gets that,

$$\langle n(t) | \dot{k}(t) \rangle = \frac{\langle n(t) | \dot{\hat{H}}(t) | k(t) \rangle}{E_k(t) - E_n(t)}. \quad (2.9)$$

Once we substitute Eq. (2.9) into Eq. (2.7), we arrive at,

$$\dot{c}_n(t) = - \sum_{k \neq n} c_k(t) e^{-\frac{i}{\hbar} \int_0^t dt' (E_k(t') - E_n(t'))} \frac{\langle n(t) | \dot{\hat{H}}(t) | k(t) \rangle}{E_k(t) - E_n(t)} - c_n(t) \langle n(t) | \dot{n}(t) \rangle. \quad (2.10)$$

Here, the adiabatic approximation is incorporated. A very slow change of the Hamiltonian with time,  $\dot{\hat{H}}(t) \ll 1$ , implies the off-diagonal elements of Eq. (2.10) to be much smaller than the diagonal matrix element of the instantaneous eigenstate basis, i.e.,

$$\frac{1}{\tau} \equiv \frac{\langle n(t) | \dot{\hat{H}}(t) | k(t) \rangle}{E_k(t) - E_n(t)} \ll \langle n(t) | \dot{n}(t) \rangle \sim \omega_n = \frac{E_n}{\hbar}, \quad (2.11)$$

or, equivalently, the time scale  $\tau$  over which  $\hat{H}$  changes becomes much longer than the inverse of the natural frequency  $\omega_n$  of the dynamic phase involved in the time evolution of  $|n(t)\rangle$  [104]. The energy eigenstates can change with time fast enough to adapt to the Hamiltonian evolution, and adiabaticity holds, so  $\dot{c}_n(t)$  becomes only proportional to the diagonal matrix element of the instantaneous eigenstate basis. We recall that this situation corresponds to the one in which no degeneration is assumed in any energy eigenstate [96]; the more general proof by Kato will not be explored in this work [101].

It is interesting to go a little further in deriving the coefficients  $c_n(t)$  after using the adiabatic approximation. Equation (2.10) is simply:

$$\dot{c}_n(t) \approx -c_n(t) \left\langle n(t) \left| \frac{d}{dt} n(t) \right. \right\rangle \Rightarrow c_n(t) \approx c_n(0) e^{-\int_0^t dt' \langle n(t') | \frac{d}{dt'} n(t') \rangle}, \quad (2.12)$$

where the dot notation for the time derivative  $|\dot{n}(t)\rangle$  has been reverted to show the independent variable of the equation. If we take  $c_n(0) = 1$  and use  $-1 = i^2$ , we can reexpress the integral term as  $c_n(t) = e^{i\gamma_n(t)}$ , where we are defining the geometric

or Berry phase  $\gamma_n$  as [105]

$$\gamma_n(t) := i \int_0^t dt' \left\langle n(t') \left| \frac{d}{dt'} n(t') \right. \right\rangle. \quad (2.13)$$

This term is actually a true phase, as it is purely real. This is easily demonstrated by the normalization condition of the  $|n(t)\rangle$  eigenstate,  $\langle n(t)|n(t)\rangle = 1$  and its derivative,  $(d/dt) \langle n(t)|n(t)\rangle = 0$ .

The notion of geometric phase was formulated independently first by Pancharatnam [106] and later by Longuet-Higgins [107] in some particular situations. For a long time, this term did not evoke special interest in the scientific community with regard to the adiabatic approximation and was consequently overlooked [108]. The main reason was that  $|\psi(t)|^2$  is obviously not affected by the phase terms, and hence there is no observable effect due to the phase of the wavefunction. Furthermore, Eq. (2.13) becomes zero if the integral is evaluated along a one-dimensional variable following a closed path, which for the time variable would be the period, and if the system eigenstates are purely real and have no imaginary part. However, this picture changed in the 1980s, as Michael Berry generalized the concept of geometric phase for quantum mechanics and pointed out its importance related to the parameter space of the system [105]. This phase factor becomes very relevant when the quantum state evolves adiabatically following a closed path, and some examples of its manifestation at the quantum scale were previously stated, such as the Aharonov-Bohm effect [109]. A simple macroscopic analogy of this geometric phase appearance is the following. Given a Foucault pendulum at a starting position in the equatorial plane oscillating in the same plane the North Pole is at, let us displace it slowly enough towards that pole, then return it slowly to another location in the Equator, and finally moving back along the equatorial circumference to the starting position. Its oscillation frequency is preserved adiabatically along the displacement path, and it ends the pathway oscillating normally to the Equator. However, its oscillatory plane is no more the same as the original one but ends up having been rotated a given phase angle due to the spheroid geometry of Earth and its rotational movement. In other words, back at the beginning point the pendulum describes a precession movement. This phenomenon, also called parallel transportation, happens in the quantum scale as well, being the geometric phase over a closed path, its measurable manifestation [110, 111].

More information on the Berry phase can be checked in references such as Refs. [105, 108, 112]. Nevertheless, the work of this Thesis does not consider the emergence of a Berry phase, and it is based strictly on both the adiabatic approximation and on another popular approximation in atomic and condensed-

matter physics: the Born-Oppenheimer approximation. Let us now explore the latter.

## 2.2 Born-Oppenheimer approximation

The aforementioned adiabatic approximation is a good starting point to try to characterize the time evolution of a system with multiple degrees of freedom. Molecular and Solid State Physics focus on the study of these kind of systems, with several atoms and/or molecules, being the internal degrees of freedom of the system in the form of dynamical parameters. Except for the hydrogen atom system, the rest of multiatomic systems have no exact solution due to the electrostatic potential terms on the Schrödinger equation. Therefore, one needs to look for approximate solutions for these systems. A classic simplification is offered by the Born-Oppenheimer approximation, proposed by Max Born and Robert Oppenheimer in 1929 [97], which is described in the following lines.

We will stay on the atomic scale without considering subatomic particles. One can approximate a given  $i$ -th atom as being formed by a positive-charged ion as the atomic nucleus, at position  $\mathbf{R}_i$ , and a set of  $n_i$  electrons with positions  $\{\mathbf{r}_j\}$ , where  $j = 1, \dots, n_i$ . Extrapolation to a many-body system of  $N$  atoms and  $n = \sum_{i=1}^N n_i$  electrons implies that the corresponding wave function will depend on a set of atomic and electronic positions or degrees of freedom,  $\{\mathbf{R}_i\}$  and  $\{\mathbf{r}_{i,j}\}$ . On this basis, and assuming that the atomic system evolves with time, its quantum dynamics is determined with the time-dependent Schrödinger equation,

$$i\hbar \frac{\partial}{\partial t} |\psi(\{\mathbf{R}_i(t)\}, \{\mathbf{r}_{i,j}(t)\})\rangle = \hat{H} |\psi(\{\mathbf{R}_i(t)\}, \{\mathbf{r}_{i,j}(t)\})\rangle. \quad (2.14)$$

The Hamiltonian operator for such multiatomic system is obtained as a sum of different kinetic and potential operators,  $\hat{T}$  and  $\hat{V}$ , respectively,

$$\hat{H} = \hat{T}_n + \hat{V}_{n-n} + \hat{T}_e + \hat{V}_{e-e} + \hat{V}_{e-n}. \quad (2.15)$$

Here, subscripts  $n$  and  $e$  specify which operators act on the set of atomic nuclei and/or on the electronic distribution, respectively. More precisely, these five operators have the following expressions:

- Kinetic energy operator for the nuclei distribution:

$$\hat{T}_n = -\hbar^2 \sum_{i=1}^N \frac{\nabla_{\mathbf{R}_i}^2}{2M_i}, \quad (2.16)$$

where  $M_i$  is the mass of  $i$ -th nucleus.

- Repulsive electrostatic potential for the nuclei:

$$\hat{V}_{n-n} = \frac{e^2}{4\pi\epsilon_0} \sum_{\substack{i=1 \\ j>i}}^N \frac{Z_i Z_j}{|\mathbf{R}_i - \mathbf{R}_j|}, \quad (2.17)$$

with  $Z_i$  being the atomic number of nucleus  $i$ .

- Kinetic energy operator for the electrons:

$$\hat{T}_e = -\hbar^2 \sum_{j=1}^n \frac{\nabla_{\mathbf{r}_j}^2}{2m_e}, \quad (2.18)$$

being  $m_e$  the mass of the electron.

- Repulsive electrostatic potential for the electrons:

$$\hat{V}_{e-e} = \frac{e^2}{4\pi\epsilon_0} \sum_{\substack{i,j=1 \\ j>i}}^n \frac{1}{|\mathbf{r}_i - \mathbf{r}_j|}, \quad (2.19)$$

where  $e$  is the electric charge of an electron.

- Attractive electrostatic potential between nuclei and electrons:

$$\hat{V}_{e-n} = -\frac{e^2}{4\pi\epsilon_0} \sum_{i=1}^N \sum_{j=1}^n \frac{Z_i}{|\mathbf{R}_i - \mathbf{r}_j|}. \quad (2.20)$$

which obviously has a different sign than its only-nuclei or only-electronic counterparts.

Notice that no spin contribution to the potential energies is considered here, as they are much smaller than the Coulombian interaction terms. Nevertheless, it plays a role in the symmetric or antisymmetric behavior of the total wavefunction, but spin quantum numbers of each particle have not been written explicitly as part of  $|\psi(\{\mathbf{R}_i(t)\}, \{\mathbf{r}_{i,j}(t)\})\rangle$  for simplicity [113].

Using Hartree atomic units [114], and replacing Eqs. (2.16)–(2.20) in Eq. (2.15),

this latter expression becomes:

$$\hat{H} = -\frac{1}{2} \sum_{i=1}^N \frac{\nabla_{\mathbf{R}_i}^2}{M_i} + \sum_{\substack{i=1 \\ j>i}}^N \frac{Z_i Z_j}{|\mathbf{R}_i - \mathbf{R}_j|} - \frac{1}{2} \sum_{j=1}^n \frac{\nabla_{\mathbf{r}_j}^2}{m_e} + \sum_{\substack{i,j=1 \\ j>i}}^n \frac{1}{|\mathbf{r}_i - \mathbf{r}_j|} - \sum_{i=1}^N \sum_{j=1}^n \frac{Z_i}{|\mathbf{R}_i - \mathbf{r}_j|}. \quad (2.21)$$

For a system with  $n > 1$  electrons and/or with  $N > 1$  nuclei, Eq. (2.14) cannot be solved exactly due to the inverse position dependencies  $1/r$  and  $1/R$  in the electrostatic potential operators  $\hat{V}$  respectively [115]. This implies that the only atomic system with an exact analytic solution is the hydrogen atom ( $n = N = 1$ ). In addition, Eq. (2.21) depends on  $3(N + n)$  degrees of freedom. Consequently, a considerable amount of computational power and capacity is required to solve it numerically and to store the output, even for simple multiatomic systems. As a result, resorting to approximate methods is a need.

Now, the following point is considered. For equal nuclei and electron kinetic energies,  $T_n = T_e$ , and taking into account that the mass of any nucleus is much larger than that of an electron  $M_n \gg m_e$  (at least 1836 times bigger), this implies that the electrons move at much faster velocities than the nuclei,  $|\mathbf{v}_n| \ll |\mathbf{v}_e|$ . Therefore, the time scale for the change in nuclear positions is much longer than that for electrons  $\tau_n \gg \tau_e$ . Recalling the adiabatic approximation we have seen in Section 2.1, we can distinguish between *fast* and *slow* degrees of freedom in the multiatomic system. In a multiatomic system, because of the aforementioned differences in velocities, the electronic distribution is able to adapt to the new instantaneous positions of atomic nuclei, which move very slowly with respect to the electrons. As a result, electrons can remain in their instantaneous eigenstates at each given time  $t$  while nuclei positions change, so the adiabatic approximation is of application here. This grants us the possibility of uncoupling the electronic and nuclei motions in such a way that we can solve the Schrödinger equation for a multiatomic system in an approximate way, this statement being the essence of the Born-Oppenheimer approximation.

Now let us explore formally how the movements of nuclei and electrons can be separated [113]. As a starting point, we are interested in leaving the nuclear kinetic energy operator aside from the remaining terms of  $\hat{H}$  (Eq. (2.21)), i.e.,

$$\hat{H} = \hat{T}_n + \hat{H}_e = -\frac{1}{2} \sum_{i=1}^N \frac{\nabla_{\mathbf{R}_i}^2}{M_i} + \hat{H}_e, \quad (2.22)$$

where we define the electronic Hamiltonian  $\hat{H}_e$  as the operator containing the

kinetic energy of the electron distribution and all potential terms,

$$\hat{H}_e = -\frac{1}{2} \sum_{j=1}^n \frac{\nabla_{\mathbf{r}_e}^2}{m_j} + \sum_{\substack{i=1 \\ j>i}}^N \frac{Z_i Z_j}{|\mathbf{R}_i - \mathbf{R}_j|} + \sum_{\substack{i,j=1 \\ j>i}}^n \frac{1}{|\mathbf{r}_i - \mathbf{r}_j|} - \sum_{i=1}^N \sum_{j=1}^n \frac{Z_i}{|\mathbf{R}_i - \mathbf{r}_j|}. \quad (2.23)$$

Considering the time independent Schrödinger equation (Eq. (2.1)),  $\hat{H}_e$  verifies that:

$$\hat{H}_e |\varphi_k(\{\mathbf{R}_i(t)\}, \{\mathbf{r}_{i,j}(t)\})\rangle = E_{e,k}(\{\mathbf{R}_i(t)\}) |\varphi_k(\{\mathbf{R}_i(t)\}, \{\mathbf{r}_{i,j}(t)\})\rangle, \quad (2.24)$$

where  $|\varphi_k(\{\mathbf{R}_i(t)\}, \{\mathbf{r}_{i,j}(t)\})\rangle$  is a wavefunction describing an electronic state  $k$  with eigenenergy  $E_k(\{\mathbf{R}_i(t)\})$  for a fixed ensemble of nuclei positions at a given time. Each energy depends on the nuclear positions. The set of electronic eigenstates forms a basis for each collection of nuclear positions at a given time, which can be taken as orthonormal, so  $\langle \varphi_k | \varphi_l \rangle = \delta_{kl}$ . By the completeness of the set of  $|\varphi_k\rangle$ , we can expand the total wavefunction in terms of the  $k$  electronic states of the system:

$$|\psi(\{\mathbf{R}_i(t)\}, \{\mathbf{r}_j(t)\})\rangle = \sum_k |\chi_k(\{\mathbf{R}_i(t)\})\rangle |\varphi_k(\{\mathbf{R}_i\}, \{\mathbf{r}_j(t)\})\rangle. \quad (2.25)$$

where we are introducing a basis of nuclear wavefunctions  $\{|\chi_k\rangle\}$  as expansion coefficients of the electronic states. Let us remark that this latter set of wavefunctions only depend on the position vectors of the nuclei distribution, entering as variables. In contrast, for determining electronic states using Eq. (2.24), nuclear positions are taken as constant parameters at each  $t$ . This is consistent with the adiabatic evolution of the electron distribution when nuclei rearrange their positions during infinitesimal time scales.

At this point let us consider the time independent Schrödinger equation, Eq. (2.1) for the full system wavefunction,

$$\hat{H} |\psi(\{\mathbf{R}_i(t)\}, \{\mathbf{r}_j(t)\})\rangle = E_T |\psi(\{\mathbf{R}_i(t)\}, \{\mathbf{r}_j(t)\})\rangle, \quad (2.26)$$

where  $E_T$  is the total energy. Substituting Eqs. (2.22) and (2.25) here, this leads to:

$$\left( \hat{T}_n + \hat{H}_e \right) \sum_k (|\varphi_k\rangle |\chi_k\rangle) = E_T \sum_k (|\varphi_k\rangle |\chi_k\rangle), \quad (2.27)$$

where the dependence of each kind of wavefunction is omitted hereinafter for convenience.

Not let us project Eq. (2.27) over an arbitrary electronic state  $|\varphi\rangle_m$ , so that we

get:

$$\sum_k \langle \varphi_m | (\hat{T}_n + \hat{H}_e) (|\varphi_k\rangle | \chi_k) \rangle = \sum_k \langle \varphi_m | E_T (|\varphi_k\rangle | \chi_k) \rangle, \quad (2.28)$$

and, considering the time independent Schrödinger equation for the electronic distribution (Eq. (2.24)) and by orthonormality of  $\{|\varphi\rangle\}$ , i.e.,  $\langle \varphi_m | \varphi_k \rangle = \delta_{km}$ , one arrives to the following equation:

$$\sum_k \langle \varphi_m | \hat{T}_n (|\varphi_k\rangle | \chi_k) \rangle = (E_T - E_{e,m}) | \chi_m \rangle \quad , \quad m = 0, 1, 2, \dots, \quad (2.29)$$

Now it only remains to evaluate the expected value of the nuclear kinetic energy operator,

$$\begin{aligned} & \sum_k \langle \varphi_m | \hat{T}_n (|\varphi_k\rangle | \chi_k) \rangle = \\ & = - \sum_k \sum_{i=1}^N \frac{\hbar^2}{2M_i} \langle \varphi_m | \nabla_{\mathbf{R}_i}^2 (|\varphi_k\rangle | \chi_k) \rangle = \\ & = - \sum_k \sum_{i=1}^N \frac{\hbar^2}{2M_i} \left( \langle \varphi_m | \nabla_{\mathbf{R}_i}^2 | \varphi_k \rangle | \chi_k \rangle + \langle \varphi_m | \nabla_{\mathbf{R}_i} | \varphi_k \rangle \nabla_{\mathbf{R}_i} | \chi_k \rangle + \right. \\ & \left. + \nabla_{\mathbf{R}_i} | \chi_k \rangle \langle \varphi_m | \nabla_{\mathbf{R}_i} | \varphi_k \rangle + \delta_{mk} \nabla_{\mathbf{R}_i}^2 | \chi_k \rangle \right). \end{aligned} \quad (2.30)$$

At this point, we can invoke the Born-Oppenheimer approximation. As electrons move much faster than nuclei, they remain approximately in the same electronic eigenstates at any  $t + dt$  when the nuclear positions change during any infinitesimal time scale  $dt$ . As a result, variation of electronic states with respect to nuclear coordinates can be safely neglected. Applying this in Eq. (2.30), only the last term of the last row survives. This effectively leads to a set of equations with uncoupled spatial variables  $\mathbf{R}$  and  $\mathbf{r}$ , thus allowing one to solve the dynamics of the atomic or molecular system. Summarizing, we can solve a multiatomic system with the Born-Oppenheimer approximation as follows:

$$\hat{H}_e(\{\mathbf{R}_i\}, \{\mathbf{r}_j(t)\}) |\varphi_k(\{\mathbf{R}_i\}, \{\mathbf{r}_j(t)\})\rangle = E_{e,k}(\{\mathbf{R}_i\}) |\varphi_k(\{\mathbf{R}_i\}, \{\mathbf{r}_j(t)\})\rangle, \quad (2.31)$$

$$[\hat{T}_n(\{\mathbf{R}_i(t)\}) + E_{e,k}(\{\mathbf{R}_i\})] | \chi_k(\{\mathbf{R}_i(t)\}) \rangle = E_T | \chi_k(\{\mathbf{R}_i(t)\}) \rangle. \quad (2.32)$$

The first step in determining the quantum state of the system consists in solving Eq. (2.31) to obtain the electronic state for a fixed nuclear geometry. This yields the energy for the configuration of electrons or electronic potential energy surface

(PES)  $E_{e,k}(\{\mathbf{R}_i\})$  for that spatial arrangement of nuclei. Afterwards, Eq. (2.32) is solved, and the nuclear quantum states are calculated. Then, this process would be repeated for the successive new nuclei arrangements. In the following Section, let us explore how the electronic PES,  $E_{e,k}$ , can be determined theoretically.

## 2.3 Density functional theory

Once we have described the Born-Oppenheimer approximation, the next straightforward task is to calculate the electronic PES. A priori, unveiling this information from the different electronic configurations seems to be a challenge, especially when considering that our many-body wavefunction has  $3 n_e$  degrees of freedom (DOFs) and the subsequent exponentially increasing computational cost in calculation time and required memory, as well as in output data size. But there is a neat, popular framework on doing this in a computationally less demanding way, with first principles (and great results!). This is density functional theory (DFT) and depends on a set of key formulations. Let us introduce its main aspects.

DFT relies on some key functions. Let us consider a many-body system of identical particles; in our case, a gas of  $n_e$  electrons, each of them at one position of the set  $\{\mathbf{r}_i\}$ ,  $i = 1, 2, \dots, n_e$ . The electronic system is described by the wavefunction  $|\varphi(\mathbf{r}_1, \mathbf{r}_2, \dots, \mathbf{r}_{n_e})\rangle$ . One defines the one-body density as the mean number of particles per volume unit  $d\mathbf{r}$ , where the number of particles is  $n_e$  times the probability of finding one of the particles in the differential volume element centered at a given position  $\mathbf{r}$ ,  $p(\mathbf{r}) d\mathbf{r}$ , without caring on the positions of the remaining  $n_e - 1$  electrons, i.e.,

$$n(\mathbf{r}) = \frac{n_e p(\mathbf{r}) d\mathbf{r}}{d\mathbf{r}} = n_e \int d\mathbf{r}_2 \dots d\mathbf{r}_{n_e} |\varphi(\mathbf{r}, \mathbf{r}_2, \dots, \mathbf{r}_{n_e})|^2. \quad (2.33)$$

The total number of particles of the system is, obviously, the integral of the one-body density on the whole space,

$$n_e = \int d\mathbf{r} n(\mathbf{r}). \quad (2.34)$$

In addition to this, we can define a quantity related to having a pair of electrons inside two different volume elements  $d\mathbf{r}$  and  $d\mathbf{r}'$  centered at positions  $\mathbf{r}$  and  $\mathbf{r}'$ , respectively, and regardless of the location of the remaining electrons. This can be called two-body density  $n_2(\mathbf{r}, \mathbf{r}')$  and quantifies the number of pairs of particles in the system inside the generic volume elements  $d\mathbf{r}$  and  $d\mathbf{r}'$ . Its formal definition is

as follows:

$$n_2(\mathbf{r}, \mathbf{r}') = \frac{\binom{n_e}{2} p_2(\mathbf{r}, \mathbf{r}') d\mathbf{r} d\mathbf{r}'}{d\mathbf{r} d\mathbf{r}'} = \frac{n_e (n_e - 1)}{2} \int d\mathbf{r}_3 \dots d\mathbf{r}_{n_e} |\varphi(\mathbf{r}, \mathbf{r}', \mathbf{r}_3, \dots, \mathbf{r}_{n_e})|^2, \quad (2.35)$$

where  $p_2(\mathbf{r}, \mathbf{r}') = \int d\mathbf{r}_3 \dots d\mathbf{r}_{n_e} |\varphi|^2$  is the probability density of finding simultaneously two particles, one inside  $d\mathbf{r}$  and the other one inside  $d\mathbf{r}'$ , no matter the positions of the remaining ones in the system. Notice that, integrating both sides with respect to  $d\mathbf{r}'$ , one can get the relationship between both one- and two-body densities as

$$n(\mathbf{r}) = \frac{2}{n_e - 1} \int d\mathbf{r}' n_2(\mathbf{r}, \mathbf{r}'). \quad (2.36)$$

Eq. (2.35) can be split in two different contributions: one related to each particle moving with no influence of the other ones in the system,  $n_2^I(\mathbf{r}, \mathbf{r}')$ , and the other accounting for the correlations or influence of the neighbor particles on the ones in  $d\mathbf{r}$  and  $d\mathbf{r}'$ ,  $n_2^C(\mathbf{r}, \mathbf{r}')$ , i.e.,

$$n_2(\mathbf{r}, \mathbf{r}') = n_2^I(\mathbf{r}, \mathbf{r}') + n_2^C(\mathbf{r}, \mathbf{r}'), \quad (2.37)$$

where the contribution linked to the ideal particle system with no internal interactions is [116]

$$n_2^I(\mathbf{r}, \mathbf{r}') = \frac{n_e - 1}{2n_e} n(\mathbf{r}) n(\mathbf{r}'), \quad (2.38)$$

and the correlation term  $n_2^C(\mathbf{r}, \mathbf{r}')$  accounts for the inner interactions between particles and the Pauli exclusion principle.

In addition to these definitions, let us define one-body operators as those acting on all the particles individually. For a discrete number of particles,

$$\hat{A} = \sum_{i=1}^{n_e} \hat{A}_i. \quad (2.39)$$

Furthermore, one-body operators are said to be local if their expected values depend on the position of the wavefunction they are acting at, i.e., in the  $\mathbf{r}$  representation,

$$\langle \mathbf{r}_i | \hat{A}_i | \mathbf{r}'_i \rangle = a(\mathbf{r}_i) \delta(\mathbf{r}_i - \mathbf{r}'_i). \quad (2.40)$$

For a system of  $n_e$  particles, it is straightforward to see that

$$\left\langle \varphi \left| \sum_{i=1}^{n_e} \hat{A}_i \right| \varphi \right\rangle = \sum_j \sum_{i=1}^{n_e} \langle \varphi | \mathbf{r}_j \rangle a(\mathbf{r}_i) \delta(\mathbf{r}_j - \mathbf{r}'_j) \langle \mathbf{r}'_j | \varphi \rangle = \sum_j \sum_{i=1}^{n_e} a(\mathbf{r}_i) |\varphi(\mathbf{r}_j)|^2. \quad (2.41)$$

By the indistinguishability of the  $n_e$  particles, Eqs. (2.40) and (2.41) do not depend on which exact particle  $i$  the operator is acting, but simply on its position. With this in mind, and as the position basis  $\{|\mathbf{r}\rangle\}$  is continuous:

$$\langle \varphi | \hat{A} | \varphi \rangle = n_e \int d\mathbf{r}_2 \dots d\mathbf{r}_{n_e} \int d\mathbf{r} a(\mathbf{r}) |\varphi(\mathbf{r}, \mathbf{r}_2, \dots, \mathbf{r}_{n_e})|^2 = \int d\mathbf{r} a(\mathbf{r}) n(\mathbf{r}), \quad (2.42)$$

where Eq. (2.33) has been substituted. Thus, local one-body operators depend on the one-body density function when summing on the whole space.

An analog can be formulated for pairs of particles. So, two-body operators are those acting on pairs of particles, or two-particle quantum states,

$$\hat{B} = \sum_{i=1}^{n_e} \sum_{j>i}^{n_e} \hat{B}_{ij}, \quad (2.43)$$

and the locality condition reads then:

$$\langle \mathbf{r}_i \mathbf{r}_j | \hat{B}_{ij} | \mathbf{r}'_i \mathbf{r}'_j \rangle = b(\mathbf{r}_i, \mathbf{r}_j) \delta(\mathbf{r}_i - \mathbf{r}'_i) \delta(\mathbf{r}_j - \mathbf{r}'_j). \quad (2.44)$$

Reasoning analogously as for 1-particle case, Eq. (2.44) in the continuous limit becomes:

$$\left\langle \varphi \left| \sum_{i=1}^{n_e} \sum_{j>i}^{n_e} \hat{B}_{ij} \right| \varphi \right\rangle = \binom{n_e}{2} \int d\mathbf{r}_3 \dots d\mathbf{r}_{n_e} \int d\mathbf{r} d\mathbf{r}' b(\mathbf{r}, \mathbf{r}') |\varphi(\mathbf{r}, \mathbf{r}', \dots, \mathbf{r}_{n_e})|^2. \quad (2.45)$$

Using Eq. (2.35), we find that the expected value of a given local two-body operator is linked to the two-body density:

$$\langle \varphi | \hat{B} | \varphi \rangle = \int d\mathbf{r} d\mathbf{r}' b(\mathbf{r}, \mathbf{r}') n_2(\mathbf{r}, \mathbf{r}'). \quad (2.46)$$

Eqs. (2.42) and (2.46) have important implications, as one- and two-body operators for systems of many (tending to infinite) particles can be modeled in terms of the particle densities we have defined previously. Hence, any external potential  $\hat{V}(\mathbf{r})$  acting on a particle is a one-body local operator, thus depending on the one-body

density. Moreover, inner interactions affecting pairs of particles at generic positions  $\mathbf{r}$  and  $\mathbf{r}'$ ,  $\hat{W}(\mathbf{r}, \mathbf{r}')$ , are then two-body local operators and, as those, functions of the two-body density.

This situation is a bit more complex for the kinetic energy operator  $\hat{T}$ , which is not a local operator as it depends on spatial derivatives instead of being a raw function of the position. It can be shown that one- and two-body operators in general can be written in terms of creation and annihilation operators in the space representation, which are known as field operators. The creation and annihilation operators are the antisymmetrizers (symmetrizers for bosonic many-body systems) we use to produce an antisymmetric fermion (or symmetric boson) basis of  $n + 1$  or  $n - 1$  particles from a given  $n$ -particle basis. Or, in other words, these operators create or annihilate a particle by putting it in or removing it from one of the single-particle states of a  $n + 1$  or  $n - 1$ -particle wavefunction, after acting on the  $n$ -particle one. multiparticle states and the action of creation and annihilation operators are central points of the second quantization formalism, which we will not move further into as it lies beyond the scope of this work. So then, in general, one particle operators in a general space basis can be written starting from a discrete general basis,  $\hat{O}_1 = \sum_{\alpha=1, \beta=1}^{\infty} \langle \alpha | \hat{o}_1 | \beta \rangle$  as:

$$\hat{O}_1 = \int d\mathbf{r}_1 d\mathbf{r}'_1 \hat{\psi}^\dagger(\mathbf{r}_1) \langle \mathbf{r}_1 | \hat{o}_1 | \mathbf{r}'_1 \rangle \hat{\psi}(\mathbf{r}'_1), \quad (2.47)$$

where  $\hat{\psi}^\dagger$  and  $\hat{\psi}$  correspond to the creation and annihilation spacial field operators, respectively, and  $\hat{o}_1$  is the differential operator that acts on a single particle state of the system. If  $\hat{O}_1$  is diagonal on the space basis, obviously  $\langle \mathbf{r}' | \hat{o}_1 | \mathbf{r} \rangle = o(\mathbf{r}) \delta(\mathbf{r}' - \mathbf{r})$ . For two-body operators  $\hat{O}_2$ , conversely, one finds –being  $\hat{o}_2$  the corresponding two-particle differential operator– that:

$$\hat{O}_2 = \frac{1}{2} \int d\mathbf{r}_1 d\mathbf{r}'_1 d\mathbf{r}_2 d\mathbf{r}'_2 \hat{\psi}^\dagger(\mathbf{r}_1) \hat{\psi}^\dagger(\mathbf{r}'_1) \langle \mathbf{r}_1 \mathbf{r}'_1 | \hat{o}_2 | \mathbf{r}_2 \mathbf{r}'_2 \rangle \hat{\psi}(\mathbf{r}_2) \hat{\psi}(\mathbf{r}'_2). \quad (2.48)$$

This is also valid for local operators if one defines operators linked to the one- and two-body densities. So, using Eqs. (2.47) and (2.48), respectively, with the differential density operators  $\hat{o}_1(\hat{n}(\mathbf{r})) = \delta(\mathbf{r} - \mathbf{r}_1)$  and  $\hat{o}_2(\hat{n}_2(\mathbf{r}, \mathbf{r}')) = \delta(\mathbf{r} - \mathbf{r}_1) \delta(\mathbf{r}' - \mathbf{r}'_1)$ , one can obtain the density operators  $\hat{n}(\mathbf{r}) = \hat{\psi}^\dagger(\mathbf{r}) \hat{\psi}(\mathbf{r})$  and  $\hat{n}_2(\mathbf{r}, \mathbf{r}') = \hat{\psi}^\dagger(\mathbf{r}) \hat{\psi}^\dagger(\mathbf{r}') \hat{\psi}(\mathbf{r}) \hat{\psi}(\mathbf{r}')$ . This allows us to reexpress in the second quantization formalism local operators, in particular the potentials  $\hat{V}$  and  $\hat{W}$ , and thus the full Hamiltonian. Anyway, let us remark that knowledge of the one- and two-body density functions is enough to obtain the potential operators with Eqs. (2.42) and (2.46).

It is relevant to recall that in the above discussion the spin quantum number has been omitted for simplicity.

Recapping, the full multiparticle Hamiltonian for our  $n_e$  electronic system can be expressed, in the space basis and with diagonalized kinetic and potential operators, as:

$$\hat{H} = \hat{T} + \hat{V} + \hat{W} = \int d\mathbf{r} \hat{\psi}^\dagger(\mathbf{r}) \hat{t}(\mathbf{r}) \hat{\psi}(\mathbf{r}) + \int d\mathbf{r} \hat{v}(\mathbf{r}) n(\mathbf{r}) + \int d\mathbf{r} d\mathbf{r}' \hat{w}(\mathbf{r}, \mathbf{r}') n_2(\mathbf{r}, \mathbf{r}'). \quad (2.49)$$

At this point, we have introduced the basic ingredients of DFT. Instead of calculating the quantum operators as usual, in terms of the wavefunction of the system of  $n_e$  electrons, we have seen how to reformulate the operators in terms of one- and two-body density functions. In doing so, we simplify their calculation, as we have to deal with one or two DOFs to determine each operator instead of the 3  $n_e$  ones. However, we have not yet calculated the PES of the electronic subsystem (Eqs. (2.31) and (2.32)) at a given time. As we shall see, the Hohenberg-Kohn (HK) theorem marks the way to go next.

### 2.3.1 Hohenberg-Kohn theorem

Let us rename the wavefunction that describes our  $n_e$ -electron system as  $|\varphi_0\rangle$ . For simplicity, electrons will be assumed to be spin-compensated, i.e., there is the same number of spin-up and spin-down electrons in the system. As we are dealing with a multifermionic system, we know that  $|\varphi_0\rangle$  must be antisymmetric. Its corresponding one-body density function can be calculated using Eq. (2.33), as we have seen before.

As Pierre Hohenberg and Walter Kohn first stated in 1964 [117], there exists a one-to-one correspondence between the external potential  $\hat{V}(\mathbf{r})$  and  $n(\mathbf{r})$ , so knowing the one-body density allows us to determine the potential energy surface related to the system up to an arbitrary constant. In other words,  $\hat{V}$  becomes a functional of the density,  $\hat{V}(\mathbf{r}) = v[n_0](\mathbf{r})$ , thereby giving meaning to the name of this framework as Density Functional Theory. This statement is the HK theorem.

Its proof is done in two ways, as we need to show that there are bijections linking the spaces of external potentials  $\mathcal{V}$  and of ground states  $\psi_0$ , on the one side, and  $\psi_0$  and the space of densities  $\mathcal{N}$ , on the other. We will restrict ourselves to nondegenerate, single ground states, even though this can be proved for the degenerate case, for statistical mixtures of states or excited wavefunctions as well. Let us first show the mappings  $\mathcal{N} \rightarrow \psi_0 \rightarrow \mathcal{V}$  by *reductio ad absurdum*:

1.  $\psi_0 \rightarrow \mathcal{V}$ : let us assume that there are two different potentials  $\hat{V}$  and  $\hat{V}'$  that

come from the same ground state  $|\varphi_0\rangle$ . Then, time independent Schrödinger equation (2.14) tells us that

$$\begin{aligned}\hat{H}|\varphi_0\rangle &= (\hat{T} + \hat{W} + \hat{V})|\varphi_0\rangle = E_0|\varphi_0\rangle, \\ \hat{H}'|\varphi_0\rangle &= (\hat{T} + \hat{W} + \hat{V}')|\varphi_0\rangle = E'_0|\varphi_0\rangle.\end{aligned}\quad (2.50)$$

Fixing the total number of electrons in the system implies that  $\hat{T}$  and  $\hat{W}$  are also fixed and equal in both cases. So, subtracting both equations (2.50):

$$(\hat{V}_0 - \hat{V}'_0)|\varphi_0\rangle = (E_0 - E'_0)|\varphi_0\rangle, \quad (2.51)$$

or, in the position basis representation, as both external potentials are one-body local operators,

$$\left\{ \sum_{i=1}^{n_e} [v_0(\mathbf{r}_i) - v'_0(\mathbf{r}_i)] \right\} |\varphi_0\rangle = (E_0 - E'_0)|\varphi_0\rangle, \quad (2.52)$$

As each of the  $v_0(\mathbf{r}_i)$ ,  $v'_0(\mathbf{r}_i)$  is a constant value, the subtractions  $v_0(\mathbf{r}_i) - v'_0(\mathbf{r}_i)$  are indeed constant, and thus both external potentials are equivalent. So, this means that  $|\varphi_0\rangle$  determines a unique external potential (up to a constant).

2. To show  $\mathcal{N} \rightarrow \psi_0$ , we start by assuming that two ground states  $|\varphi_0\rangle \neq |\varphi'_0\rangle$  can be obtained from the same ground state density  $n_0(\mathbf{r})$ . As  $|\varphi\rangle$  and  $\hat{V}$  have become functionals of the one-body density, a variational principle can be defined for them. In this way, if we consider the ground state energies  $E_0 = \langle \varphi_0 | \hat{H} | \varphi_0 \rangle$  and  $E'_0 = \langle \varphi'_0 | \hat{H}' | \varphi'_0 \rangle$ , as these are the respective minimum energies for  $\hat{H}$  and  $\hat{H}'$  with eigenstates  $|\varphi_0\rangle$  and  $|\varphi'_0\rangle$  the following inequalities actually hold:

$$\begin{aligned}E_0 &< \langle \varphi_0 | \hat{H}' | \varphi_0 \rangle = \langle \varphi_0 | \hat{H} + \hat{V}' - \hat{V} | \varphi_0 \rangle = E_0 + \int d\mathbf{r} (v'(\mathbf{r}) - v(\mathbf{r})) n_0(\mathbf{r}) \\ E'_0 &< \langle \varphi'_0 | \hat{H} | \varphi'_0 \rangle = \langle \varphi'_0 | \hat{H}' + \hat{V} - \hat{V}' | \varphi'_0 \rangle = E'_0 + \int d\mathbf{r} (v(\mathbf{r}) - v'(\mathbf{r})) n_0(\mathbf{r}).\end{aligned}\quad (2.53)$$

By our initial hypothesis, if we add both equations (2.53), the potential terms cancel and we arrive at a contradiction,  $E_0 + E'_0 < E'_0 + E_0$ . In sum, different ground states (that is, ground states with different energies,  $E_0 \neq E'_0$ ) must come from different densities  $n_0(\mathbf{r})$  and  $n'_0(\mathbf{r})$ .

Now it remains to prove the injections  $\mathcal{V} \rightarrow \psi_0 \rightarrow \mathcal{N}$ , which is a trivial task. If we set an external potential  $\hat{V}$ , we can get  $\hat{H}$ , because  $\hat{T}$  and  $\hat{W}$  are determined

simply by knowing how many particles we have and the positions at which they are located. Knowledge of  $\hat{H}$  means that we can solve the time-independent Schrödinger equation (2.14) and obtain  $E_0$  and  $|\varphi_0\rangle$ . Then, Eq. (2.33) gives us  $n_0(\mathbf{r})$ . This completes the proof for the HK theorem. Notice that this holds not only for equivalent potentials  $\hat{V}' = \hat{V} + \text{const}$ , but also we can get the same densities and potentials regardless of the constant phase factor  $\gamma$  it carries, i.e.,  $|\varphi_0\rangle$  and  $|\varphi_0\rangle e^{-i\gamma}$  produce the same results.

This theorem has powerful implications. First, as we can compute the external potential from the one-body density, this implies a reduction of the calculation degrees of freedom from  $3n_e$  –corresponding to  $|\varphi_0\rangle$ – to 3, which implies a simplification in the multielectronic PES calculation within the DFT framework. Moreover, if we find  $n_0(\mathbf{r})$  and thus gain complete knowledge of  $\hat{H}$  (except for a constant), we are able to obtain the system ground state  $|\varphi_0\rangle[n_0]$  and all excited multiparticle states  $|\varphi_j\rangle[n_0]$  and consequently characterize all its properties. Notice that the functional dependence with the one-body density is being made explicit as  $[n_0]$  in the following lines.

The HK theorem also implies the following corollary, also commonly called the second HK theorem in the literature. In the same fashion as for  $\hat{V}[n]$ , the energy of a many-body system –for some external potential– can be also defined as a functional of the one-body density,

$$E_{V_0}[n] = \langle \varphi[n] | \hat{T} + \hat{W} + \hat{V}_0 | \varphi[n] \rangle. \quad (2.54)$$

As this functional dependence is linked to a subjacent variational principle, there exists a global minimum of the energy, which corresponds to the exact ground state density  $n_0$ ,  $E_0 = E_{V_0}[n_0]$ . For densities  $n \neq n_0$ , one obtains  $E_{V_0}[n] > E_0$ . Mathematically stated,

$$E_0 := \min_{n \in \mathcal{N}} E_{V_0}[n]. \quad (2.55)$$

This has an alternative expression. As the one-body density has to fulfill Eq. (2.34), this can be introduced as a constraint of the system through a Lagrange multiplier  $\mu$  when taking the Euler-Lagrange equation on  $E_{V_0}$ ,

$$\frac{\delta}{\delta n(\mathbf{r})} \left\{ E_{V_0}[n] - \mu \left( \int d\mathbf{r}' n(\mathbf{r}') - n_e \right) \right\} = 0, \quad (2.56)$$

where the implicit assumption of a differentiable  $n(\mathbf{r})$  is made. Let us insist on

Eq. (2.56) a bit more. The energy functional can be separated in two terms,

$$E_{V_0}[n] = F[n] + \int d\mathbf{r}' v_0(\mathbf{r}') n(\mathbf{r}'), \quad (2.57)$$

where  $F[n] := T[n] + W[n] = \langle \varphi[n] | \hat{T} + \hat{W} | \varphi[n] \rangle$  is called HK functional, is usually of unknown exact shape and appears for every external potential acting on the system (thereby being regularly referred as to *universal* in the literature). So then, solving Eq. (2.56), we have

$$\frac{\delta F[n]}{\delta n(\mathbf{r})} + v_0(\mathbf{r}) = \mu. \quad (2.58)$$

This result means that the functional derivative of  $F[n]$ , which is an unknown function, differs from the external potential at  $\mathbf{r}$  (a quantity initially fixed by us) in a constant factor  $\mu$ . In addition, it can be shown that this Lagrange multiplier is actually the chemical potential of the multiparticle system [118].

The application of the HK theorem brings to light a particular challenge that merits a brief discussion [119, 120, 121]. The validity of Eq. (2.55) is limited solely to electron densities  $n_0(\mathbf{r})$  that can arise from some external potential in a noninteracting system. Such specific densities are referred to as V-representable, and the potential lack of correspondence between a given density and any  $V$  from which we can derive  $n$  is called the V-representability problem. It is important to note that this scenario also introduces the N-representability problem, consisting of whether a density can be associated with any physically realizable many-body wavefunction. Let us recall the mappings  $\mathcal{N} \leftrightarrow \psi_0 \leftrightarrow \mathcal{V}$ . It is straightforward to realize that the space of every existing  $n$ ,  $\mathcal{N}$ , contains a subset of all N-representable  $n$ 's,  $\mathcal{N}_{\text{N-repr}}$ , which subsequently encompasses a smaller subset of V-representable densities,  $\mathcal{N}_{\text{V-repr}}$ . Otherwise,  $\mathcal{N}_{\text{V-repr}} \subset \mathcal{N}_{\text{N-repr}} \subset \mathcal{N}$ .

Taking advantage of this circumstance, an innovative approach for computing Eq. (2.55) while bypassing the V-representability issue was proposed independently by Mel Levy in 1979 [122] and Elliott H. Lieb in 1983 [123]. This procedure is valid for either nondegenerate or degenerate ground states. They proposed to perform the minimization process of Eq. (2.55) in two stages,

$$E_0 = \min_n \left\{ \min_{\varphi \rightarrow n} \langle \varphi | \hat{T} + \hat{W} + \hat{V}_0 | \varphi \rangle \right\} = \min_n \left\{ F_{\text{LL}}[n] + \int d\mathbf{r}' v_0(\mathbf{r}') n(\mathbf{r}') \right\}, \quad (2.59)$$

with  $F_{\text{LL}}[n] := \min_{\varphi \rightarrow n} \langle \varphi | \hat{T} + \hat{W} | \varphi \rangle$  being the Levy-Lieb redefinition of the HK universal energy functional in terms of the minimizing wavefunction. In doing

so, we first minimize the energy functional with respect to the wavefunctions yielding one particular one-body density (by tuning, e.g., the parameters inside each wavefunction accordingly). After that we minimize among the densities obtained from all of the tried wavefunctions, which are thus  $N$ -representable. Both Eqs.(2.55) and (2.59) bring us to the same ground-state energy value, but the method due to Levy and Lieb (or Levy-Lieb constrained search) does not require  $n$  to be produced from its related  $V_0[n]$ . The main disadvantage of this approach is the difficulty in trying Eq. (2.59) for an infinite number of wavefunctions [124].

At this point a problem is still there. We are able to compute  $V_0[n]$  from the ground-state density. But the total energy  $E_{V_0}[n]$  is still unknown to us, in particular the HK functional part,  $F[n]$ . In addition, we have said nothing about how to formally calculate the ground-state density. In the next subsection, we will see how to perform this task in an approximate way.

### 2.3.2 Kohn-Sham equations

Taking the HK theorem as a basis, we know that the ground state of the system is an unique functional of the density of the system  $n_0$ . The following natural step consists on calculating the full  $E[n_0]$ . For that, one requires the kinetic and inner potential interaction terms,  $T[n_0]$  and  $W[n_0]$ . The main contribution of the latter can be computed with the expression for the Coulomb repulsion term between electronic densities at different points (for a semiclassical many body system we are considering here), also called Hartree energy [121, 125],

$$J[n_0] = \frac{1}{2} \int d\mathbf{r}_1 d\mathbf{r}_2 \frac{n_0(\mathbf{r}_1)n_0(\mathbf{r}_2)}{|\mathbf{r}_1 - \mathbf{r}_2|}, \quad (2.60)$$

and the result of this functional is exact as for the external potential as it depends on the one-body density. In contrast, the kinetic part is more challenging. DFT-precursor frameworks such as the Thomas-Fermi model or the Weiszäcker approximation yield expected values for the kinetic energy that do not satisfy the virial theorem,  $T = -(V_0+W)/2$  and  $E = -T$ . Consequently, some way to accurately evaluate the functional kinetic energy is required for DFT to work properly. This practical difficulty of DFT was overcome thanks to the solution proposed by Kohn and Lu Jeu Sham in 1965 [126].

The basis of the Kohn-Sham (KS) framework is to consider a toy system in which there is no interaction between the electrons. The HK theorem holds regardless of the features of the electron-electron interaction term considered, so that the bijection between the external potential and the density (through the wavefunction)

remains. This system without internal interactions is known as the KS system and their quantities are represented with the subscript  $s$ , so that we have  $\hat{W}_s = 0$ . From this follows that  $F_s[n] = \langle \varphi_s[n] | \hat{T} | \varphi_s[n] \rangle = T_s[n]$ , with  $\varphi_s[n]$  being the ground-state wavefunction for this system. In addition, the energy functional (2.54) adopts the following form:

$$E_{V_s}[n] = T_s[n] + \int d\mathbf{r}' v_s(\mathbf{r}') n_s(\mathbf{r}') \quad (2.61)$$

where  $n_s$  is the KS ground-state density. Now another key assumption enters: we impose the ground-state densities of both systems without and with inner interactions to be the same, so that  $n_s = n_0$ . Furthermore, the Euler-Lagrange equation for this system is as follows:

$$\frac{\delta E_s[n]}{\delta n(\mathbf{r})} = \frac{\delta T_s[n]}{\delta n(\mathbf{r})} + v_s(\mathbf{r}) = \mu. \quad (2.62)$$

As we have a system of  $n_e$  noninteracting fermions, each of their wavefunctions can be expressed in terms of a Slater determinant (which is obviously antisymmetric). The electronic ground-state wavefunction is then written in terms of  $n_e$  single-particle states or orbitals  $|\phi_i\rangle$  as

$$|\varphi(\mathbf{r}_1, \dots, \mathbf{r}_{n_e})\rangle = \frac{1}{\sqrt{n_e!}} \begin{vmatrix} |\phi_1(\mathbf{r}_1)\rangle & \dots & |\phi_{n_e}(\mathbf{r}_1)\rangle \\ \dots & \dots & \dots \\ |\phi_1(\mathbf{r}_{n_e})\rangle & \dots & |\phi_{n_e}(\mathbf{r}_{n_e})\rangle \end{vmatrix}. \quad (2.63)$$

Taking into account that the Hamiltonian of the full system is

$$\hat{H}_s = \hat{T}_s + \hat{V}_s = \sum_{i=1}^{n_e} \left[ -\frac{1}{2} \nabla_i^2 + v_s(\mathbf{r}_i) \right], \quad (2.64)$$

it can be shown (see, e.g., Ref. [127]) that each orbital of the ground-state KS wavefunction fulfills a Schrödinger equation with energy eigenvalue  $\epsilon_i$ ,

$$\left[ -\frac{1}{2} \nabla_i^2 + v_s(\mathbf{r}) \right] |\phi_i(\mathbf{r})\rangle = \epsilon_i |\phi_i(\mathbf{r})\rangle, \quad (2.65)$$

being this expression valid only for nondegenerate states. Notice that we are assuming that the orbital energies follow this ordering:  $\epsilon_1 < \epsilon_2 < \dots < \epsilon_{n_e} < \dots$ . Hence, solving the  $n_e$  one-particle equations, we can determine the orbitals the ground-state KS wavefunction contains. Furthermore, this allows us to obtain complete

knowledge of its associated ground-state density  $n_s(\mathbf{r})$ , as for a wavefunction of the form (2.63) the one-body density adopts a very simple expression

$$n_s(\mathbf{r}) = \sum_{i=1}^{n_e} |\phi_i(\mathbf{r})|^2. \quad (2.66)$$

Now let us see how we can relate the energy components in the KS system and in the real one that we actually want to solve completely. First, the kinetic energy in the KS toy system also adopts a simple expression. Starting from Eq. (2.47), taking a change of basis for the field operators from the spacial to the (discrete) one formed by the one-body orbitals and applying the orthogonality of the Slater determinants, we can arrive at

$$T_s[n] = \sum_{i=1}^{n_e} \left\langle \phi_i[n] \left| -\frac{1}{2} \nabla_i^2 \right| \phi_i[n] \right\rangle. \quad (2.67)$$

For the real many-body system with inner interactions, each single particle is affected by the screening action of the other  $n_e - 1$  ones. This originates a kind of correlated interaction, which also leads to a weakening of the Coulombic repulsive inner interactions. This correlation produces an additional kinetic term  $T_c[n]$  that is missing for the system in the absence of inner interactions, forcing us to add it to the KS kinetic energy (2.67) to match the kinetic part of the real system,  $T_0[n] = T_s[n] + T_c[n]$ .

Next, in terms of internal interactions, they have been set as zero in the KS system. But in fact, only the electrostatic potential term (2.60) has been discarded in this analysis; the real operator  $\hat{W}[n]$  also includes a non-Coulombic exchange-correlation inner potential contribution, which has to be added by hand to the toy system. Thus,  $W[n] = J[n] + U_{xc}[n]$ .

After these comments, let us reexpress the energy functional defined in Eq. (2.54) as:

$$E_{V_0}[n] = T[n] + V_0[n] + W[n] = T_s[n] + V_0[n] + J[n] + E_{xc}[n], \quad (2.68)$$

where we are defining the exchange-correlation energy  $E_{xc}[n]$  as

$$E_{xc}[n] := T_c[n] + U_{xc}[n] = T[n] - T_s[n] + W[n] - J[n]. \quad (2.69)$$

Now if we take the functional derivative of  $E_{V_0}[n]$  with respect to  $n(\mathbf{r})$ :

$$\frac{\delta E_{V_0}[n]}{\delta n(\mathbf{r})} = \frac{\delta T_s[n]}{\delta n(\mathbf{r})} + v_0[n](\mathbf{r}) + \frac{\delta J[n]}{\delta n(\mathbf{r})} + \frac{\delta E_{xc}[n]}{\delta n(\mathbf{r})} = \mu. \quad (2.70)$$

Keeping the number of electrons  $n_e$  (and thus its associated Lagrange multiplier) to be the same for both real and KS systems, this equation is equal to Eq. (2.62) if we take the KS potential to be as follows:

$$v_s[n](\mathbf{r}) = v_0(\mathbf{r}) + \int d\mathbf{r}' \frac{n(\mathbf{r}')}{|\mathbf{r} - \mathbf{r}'|} + v_{xc}(\mathbf{r}). \quad (2.71)$$

As a result, each orbital of the ground-state KS wavefunction obeys a single-particle Schrödinger equation of the form

$$\left[ -\frac{1}{2}\nabla_i^2 + v_s[n](\mathbf{r}) \right] |\phi_i(\mathbf{r})\rangle = \epsilon_i |\phi_i(\mathbf{r})\rangle, \quad (2.72)$$

and the ground-state density of the real system is the same as the KS one for non-interacting electrons,

$$n_0(\mathbf{r}) = n_s(\mathbf{r}) = \sum_{i=1}^{n_e} |\phi_i(\mathbf{r})|^2. \quad (2.73)$$

Eqs. (2.71), (2.72), and (2.73) conform the system KS equations. These are self-consistent, so that one has to solve them iteratively [120]: one starts with a trial density, solves the equations, and obtains new KS orbitals and a new density closer to the ground-state one after each epoch. Only when the difference in energies or densities before the previous and last iterations lies below a cutoff value ( $\Delta\epsilon_c$  and  $\Delta n_c$ , respectively), the iterative part comes to an end. After this convergence of the density to (almost) its ground-state value, one is able to calculate all density-dependent parameters of the many-body system with a remarkable level of accuracy. This self-consistent evaluation procedure of KS equations is summarized in the flowchart of Fig. 2.1.

Regarding the meaning of the KS formalism, calculations of the DFT ground-state energies for different atomic species help us to understand its importance [125]. Let us have in mind Eq. (2.68). In fact,  $T_s[n]$  is equal to a large part of the total kinetic energy and is of the same order of magnitude as the ground-state energy of the atom. Recalling its definition (Eq. (2.67)), the KS kinetic energy is actually an exact quantity. In addition, the Hartree energy is determined exactly in the KS system. Given that the ground-state potential is known, only the exchange-correlation part  $E_{xc}[n]$  remains to be exactly indeterminable in DFT, yet it is very small compared to the total ground-state energy, and becomes comparatively smaller the more complex the atomic species is. We will discuss exchange-correlation approximations in more detail in Section 2.3.3.

Before that, let us progress a bit further. If we substitute Eq. (2.72) on Eq. (2.67),

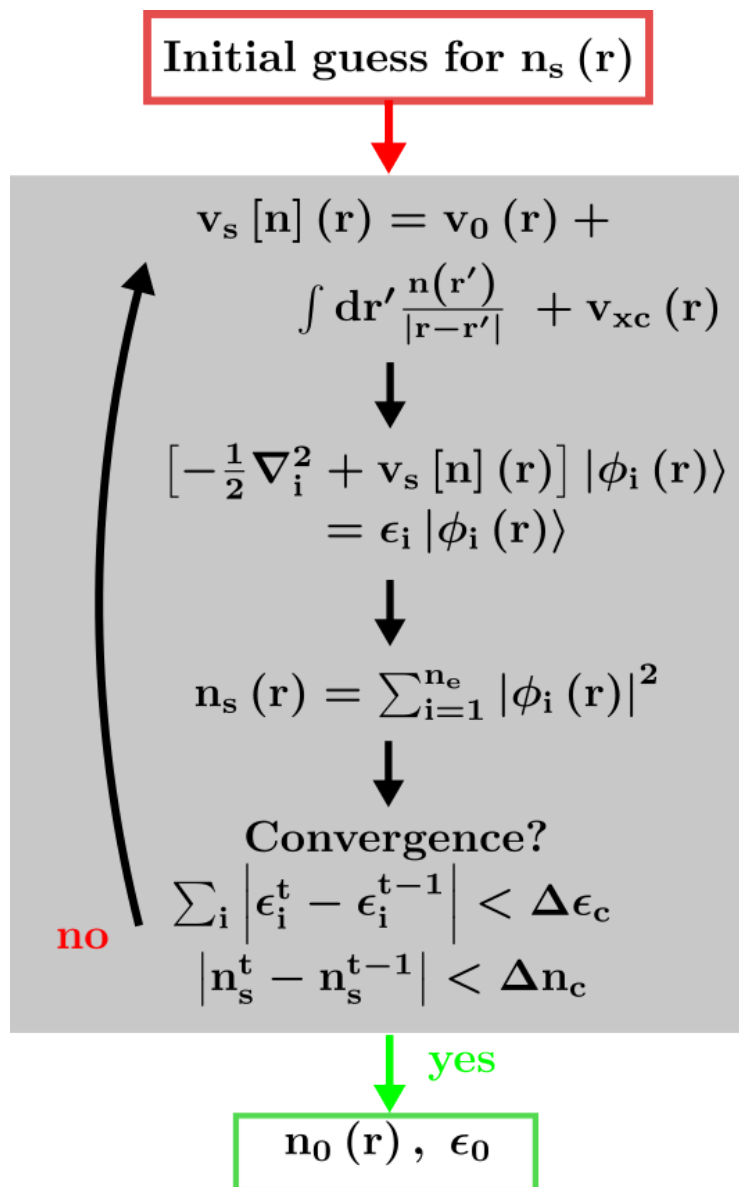


**Figure 2.1:** Flowchart of the self-consistent evaluation of the KS equations for a given system. To begin with, some trial  $n_s(\mathbf{r})$  is guessed. It is then used for evaluating the KS potential (Eq. (2.71)), taking into account some exchange-correlation potential  $v_{xc}(\mathbf{r})$ . For this KS potential, the Schrödinger equations for the ground-state KS wavefunctions are solved (Eq. (2.72)). As a result, one gets a new set of KS orbitals and, consequently, some new electronic density (Eq. (2.73)) and associated total energy. At the end of each iteration  $t$ , either the total energies of the system or the electronic densities are compared with their counterparts at iteration  $t - 1$ . If the differences  $\sum_i |\epsilon_i^t - \epsilon_i^{t-1}| \geq \Delta\epsilon_c$  or  $|n_s^t - n_s^{t-1}| \geq \Delta n_c$ , being  $\Delta\epsilon_c$  and  $\Delta n_c$  some cutoff values for the energy and density, respectively, the iterative process undergoes a new iteration. The cutoffs are chosen to be small enough to ensure that the minimum energy of the system, or equivalently the ground-state density has been reached (recall the variational principle of Eq. (2.55)). Only when the difference in energies or densities lies below its corresponding cutoff, this self-consistent process is finished, yielding approximately the ground-state electronic density  $n_0(\mathbf{r})$  and energy of the system  $\epsilon_0$ .

we can reexpress the kinetic energy in the KS system for  $n_0(\mathbf{r})$  as:

$$T_s[n_0] = \sum_{i=1}^{n_e} \epsilon_i - \int d\mathbf{r} v_s[n_0](\mathbf{r}) n_0(\mathbf{r}). \quad (2.74)$$

Substituting this on Eq. (2.68), we get the following expression for the total energy of the real system for the ground-state density,  $E_{V_0}[n_0]$ :

$$E_{V_0}[n_0] = \sum_{i=1}^{n_e} \epsilon_i + \int d\mathbf{r} (v_0[n_0](\mathbf{r}) - v_s[n_0](\mathbf{r})) n_0(\mathbf{r}) + J[n_0] + E_{xc}[n_0]. \quad (2.75)$$

The one-body potential difference integrand can be worked out using Eq. (2.71), so that we get:

$$E_{V_0}[n_0] = \sum_{i=1}^{n_e} \epsilon_i - J[n_0] - \int d\mathbf{r} (v_{xc}[n_0](\mathbf{r})) n_0(\mathbf{r}) + E_{xc}[n_0]. \quad (2.76)$$

As the ground-state energy in the KS system is obviously

$$E_s[n_0] = \sum_{i=1}^{n_e} \epsilon_i, \quad (2.77)$$

this leads to the following relationship between the total ground-state energies of both systems:

$$E_{V_0}[n_0] = E_s[n_0] - J[n_0] - \int d\mathbf{r} (v_{xc}[n_0](\mathbf{r})) n_0(\mathbf{r}) + E_{xc}[n_0]. \quad (2.78)$$

The latter relationship holds independently of how the correlation part is approximated. Straightforwardly, the smaller  $J[n_0]$  becomes, the closer the noninteracting KS system and the interacting ground state are to each other.

Another comment can be made on the meaning of the KS orbitals and their energies. In principle, they are no more than a mathematical tool to get the ground-state density of the real system and its energy, so that they mean nothing special from a physical perspective. However, there is an actual physical quantity linked to the highest energy among the occupied KS orbitals. This eigenvalue is identified if we check how densities should become when one takes out an electron from the

atomic or molecular system, i.e., exploring the asymptotic limit  $|\mathbf{r}| \rightarrow \infty$  [120]:

$$\begin{aligned} \text{Real system:} \quad n_0(\mathbf{r}) &\xrightarrow[r \rightarrow \infty]{} c e^{-2\sqrt{2I(n_e)} r} \\ \text{Kohn-Sham system:} \quad n_s(\mathbf{r}) &\xrightarrow[r \rightarrow \infty]{} c e^{-2\sqrt{2[-\epsilon_{n_e}(n_e)+v_s(r)]} r} . \end{aligned} \quad (2.79)$$

where  $I(n_e)$  is the ionization energy for a system of  $n_e$  electrons (and nuclei), and  $c$  is a constant that is not so relevant here. If we set the KS potential minimum in the asymptotic limit,  $v_s(r \rightarrow \infty) \rightarrow 0$ , and by the equality of ground-state densities of both systems we imposed before, we obtain that

$$\epsilon_{n_e}(n_e) = -I(n_e) = E_0(n_e) - E_0(n_e - 1), \quad (2.80)$$

where the rightmost equality is simply the usual definition of the ionization energy. From this, we also come to the following relationship:

$$\epsilon_{n_e+1}(n_e + 1) = -I(n_e + 1) = -A(n_e), \quad (2.81)$$

where  $A(n_e)$  is the electronic affinity. Additional conclusions we will not cover here can be extracted by comparing both systems; more information on these can be found elsewhere [120, 128].

Recall that here we have dealt with nondegenerate ground states. The KS method with degeneracy entails some particularities that are covered in the DFT literature [116, 120]. Additionally, we have not considered the spin in our discussion, which would enter into the KS equations as an additional degree of freedom in the potential terms, in the orbital energies and in the ground-state wavefunction and density. This is covered in the literature in references such as Ref. [129].

So far, we have used no approximations on DFT, which makes it an exact theory. However, there is only one point that we must be careful about. In practice, the quality of the determination of the one-body density for the real ground state is clearly influenced by how one has previously tuned the interactive exchange-correlation part of the system  $E_{xc}$ , or more precisely  $v_{xc}(\mathbf{r})$ . This has given rise to several approximations in the literature, a topic that we will cover in the following subsection.

### 2.3.3 Exchange-correlation functionals

The next challenge is to find a good exchange-correlation functional in terms of accuracy of the resulting computed energies. Such functionals encapsulate the exchange and correlation effects of the electronic distribution and play a pivotal

role in accurately determining the electronic properties of atoms, molecules, and solids. In Section 2.3.2, we have mentioned that the exchange-correlation energy is small in magnitude compared to other energy terms that contribute to the ground-state energy (Eq. (2.68)), so one might underscore its importance in DFT. However, exchange correlation plays an important role in determining quantities such as binding energy, since its contribution to the latter reaches up to 100 % when van der Waals interactions are present in the system [125]. Therefore, approximating it accurately enough becomes crucial in DFT. Generally, the total exchange-correlation functional  $E_{xc}[n]$  is split as a sum of an exchange form,  $E_x[n]$ , and a correlation part,  $E_c[n]$ , so  $E_{xc}[n] = E_x[n] + E_c[n]$ . Nevertheless, it is not possible to find an exact  $E_{xc}[n]$ , because this would mean that the many-body Schrödinger equation can be exactly solved. Only exchange and correlation may be exactly determined for the free electron gas (FEG) [130]. Moreover, we do not have classical analogues as to how this functional should be.

Naively, one can try to construct an exchange-correlation functional in such a way that Hartree-Fock total energy  $E^{\text{HF}}$  and electronic density  $n_{\text{HF}}$  are reproduced [120]. It is important to recall that Hartree-Fock theory assumes each single electron of a system to be described by orbitals and to move inside an average potential created by the remaining electrons, i.e., a mean field approximation is involved. Due to this last point, electronic correlations are neglected, so there is no Hartree-Fock correlation functional ( $E_c^{\text{HF}}[n] = 0$ ). Then, if only Hartree-Fock exchange is assumed, the total energy functional in such situation would become:

$$E^{\text{only HF}}[n] = T_s[n] + V_0[n] + J[n] + \tilde{E}_x[n], \quad (2.82)$$

where the condition  $E^{\text{only HF}}[n_{\text{HF}}] = E^{\text{HF}}$  is imposed. According to the HK theorem,  $\tilde{E}_x[n]$  must exist. One can try to determine it by solving Eq. (2.82) in the KS system. However, this leads to KS energies and orbitals that are inconsistent with their Hartree-Fock counterparts. Moreover, such an exact exchange functional is impossible to be obtained exactly in terms of the electronic density or wavefunction, and thus neither a virial relation nor a gradient expansion can be defined. In contrast, an alternative exchange term incorporating ingredients from Hartree-Fock theory can be defined [131, 132],

$$E_x^{\text{exact}}[n] = U_x[n] = W[n] - J[n], \quad (2.83)$$

where, in the KS system,  $W[n] = \langle \varphi[n] | \hat{W} | \varphi[n] \rangle$ , with  $|\varphi[n]\rangle$  as defined in Eq. (2.63). The electron-electron interaction operator corresponds to the usual electrostatic repulsion,  $\hat{W} = \sum_{l>k}^{n_e} (1/|\mathbf{r}_k - \mathbf{r}_l|) = (1/2) \sum_{k \neq l}^{n_e} (1/|\mathbf{r}_k - \mathbf{r}_l|)$ , whereas

if we reexpress  $J[n]$  (Eq. (2.60)) in terms of the KS orbitals, one can see that the terms corresponding to  $k = l$  (i.e., the interaction of an electronic state with itself) are also contained in  $J[n]$ . Thus,  $E_x^{\text{exact}}$  needs to be defined in such a way that this unphysical effect cancels.

Equation (2.83) can be solved exactly in the KS orbital basis, thus leading to an exact, Hartree-Fock-kind contribution to the exchange energy in DFT,

$$\begin{aligned} E_x^{\text{exact}} &= -\frac{1}{2} \sum_{\sigma} \sum_{i=1}^{n_e} \sum_{j=1}^{n_e} \int d\mathbf{r} d\mathbf{r}' \phi_i^*(\mathbf{r}, \sigma) \phi_j^*(\mathbf{r}', \sigma) w(\mathbf{r}, \mathbf{r}') \phi_j(\mathbf{r}, \sigma) \phi_i(\mathbf{r}', \sigma) \\ &= -\frac{1}{2} \sum_{\sigma} \sum_{i=1}^{n_e} \sum_{j=1}^{n_e} \int d\mathbf{r} d\mathbf{r}' \frac{\phi_i^*(\mathbf{r}, \sigma) \phi_j^*(\mathbf{r}', \sigma) \phi_j(\mathbf{r}, \sigma) \phi_i(\mathbf{r}', \sigma)}{|\mathbf{r} - \mathbf{r}'|}, \end{aligned} \quad (2.84)$$

where  $\sigma$  is the spin linked to each KS orbital and its related sum is over orbitals with the same spin. Notice that  $E_x^{\text{exact}}$  as obtained in this way does not depend explicitly on the density, but on the one-particle KS orbital, thus there arises an implicit one-body density dependence for the exact exchange part. The structure of  $E_x^{\text{exact}}$  implies the description of nonlocal interactions, while the explicit presence of KS orbitals poses an additional difficulty in calculating the exact exchange term. We will return to this point in more detail in Section 2.3.3.4.

For now, as mentioned above, the exchange part (2.84) allows to suppress the electronic self-interaction error for the terms  $i = j$ . Its related potential  $v_x = dU_x/dr$  also verifies that  $v_x \xrightarrow{r \rightarrow \infty} -1/r$ , which is the expected behavior. To understand this, let us introduce the so-called hole picture. Recall the two-body density decomposition (Eq. (2.37)) in terms of an independent part  $n_2^I(\mathbf{r}, \mathbf{r}')$  (Eq. (2.38)), accounting for the system behavior with no inner interactions, and an exchange-correlation term that we can define by

$$n_2^C(\mathbf{r}, \mathbf{r}') = n_2^I(\mathbf{r}, \mathbf{r}') h(\mathbf{r}, \mathbf{r}') = \frac{n_e - 1}{2n_e} n(\mathbf{r}) n(\mathbf{r}') h(\mathbf{r}, \mathbf{r}'), \quad (2.85)$$

where we introduce the exchange-correlation hole density  $h(\mathbf{r}, \mathbf{r}')$  accounting for the exchange-correlation interactions in the system. Now, incorporating this definition of  $n_2^C(\mathbf{r}, \mathbf{r}')$ , for a large number of particles  $n_e \rightarrow \infty$ , Eq. (2.37) becomes

$$n_2(\mathbf{r}, \mathbf{r}') = \frac{1}{2} n(\mathbf{r}) n(\mathbf{r}') [1 + h(\mathbf{r}, \mathbf{r}')]. \quad (2.86)$$

Now let us integrate both sides with respect to  $d\mathbf{r}'$ . Using Eq. (2.36) in the process,

we are able to get that

$$\int d\mathbf{r}' n(\mathbf{r}') h(\mathbf{r}, \mathbf{r}') = -1. \quad (2.87)$$

This result makes sense if we think that the presence of a particle at a given point has an effect of "pushing" the remaining  $n_e - 1$  particles slightly farther from the remaining one. In this way, the given particle generates a density perturbation on the neighbors equal to  $-1$ , as the particle needs to generate some room for being inside the system, a "hole" that justifies the hole picture name. Now, remembering that the only inner exchange-correlation potential in a system of two identical particles is due to the exchange interaction, and due to the Coulombic nature of the potential  $U_x$  (i.e., proportional to  $1/r$ ), we see that the asymptotic limit  $v_x \xrightarrow{r \rightarrow \infty} -1/r$  makes complete sense.

At this point, let us insist on the impossibility of finding  $E_{xc}[n]$  exactly, as previously mentioned. Instead, at least part of the exchange and correlation functional needs to be approximated, its quality depending on how close the DFT results are to the experimental measurements in the atomic and molecular systems. In this respect, the more intricate the exchange-correlation functional becomes, the higher the computational cost it turns out to be. The wide inhomogeneity of features present in real systems means that less exact but computationally less demanding approximations may suffice for certain systems to accurately evaluate energies and other quantities, whereas more complex exchange-correlation functionals may be required for others. The available functional approximations can be sorted in a paradigmatic categorization called Jacob's Ladder [133], which is depicted in Fig. 2.2. Let us "climb" this ladder from bottom to top.

### 2.3.3.1 Local density approximation (LDA)

The local density approximation (LDA) model was originally stated by Kohn and Sham in their seminal paper in 1965 [126]. It is based on the features of an homogeneous electron gas (HEG), which is a system of infinite electrons placed uniformly in space and under the action of a background positive charge density such that the net charge of the entire ensemble is zero. The homogeneity of this system implies the energy to be proportional to the volume, i.e., for a volume element  $d\mathbf{r}$ ,

$$dE_{xc}^{\text{HEG}} = n_{\text{HEG}} e_{xc}^{\text{HEG}}(n_{\text{HEG}}) d\mathbf{r}, \quad (2.88)$$

being  $n_{\text{HEG}}$  the constant-valued density for the HEG and  $e_{xc}(n_{\text{HEG}})$  the exchange-correlation energy density per particle for this uniform electron gas, also a constant. Translating this expression into the real (inhomogeneous) system, we have to re-

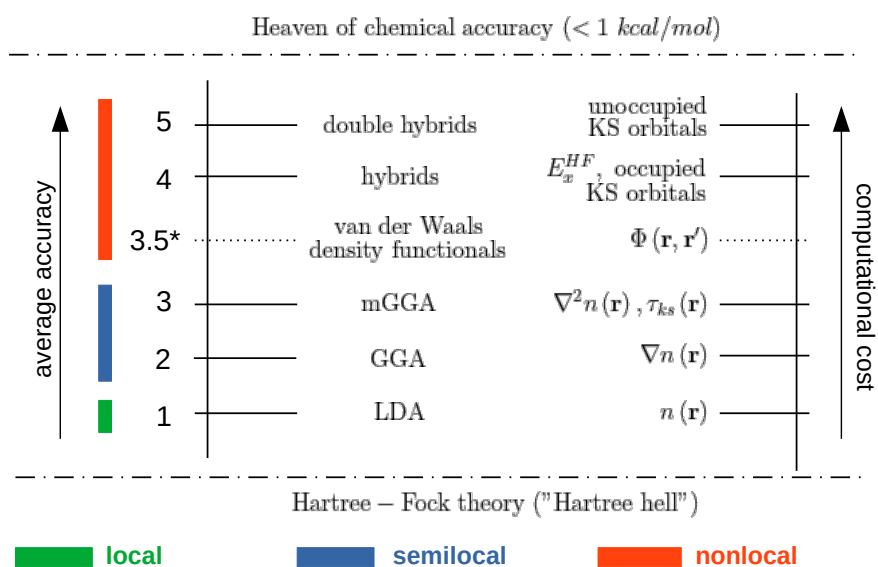


**Figure 2.2:** Jacob's Ladder of exchange-correlation functionals in DFT. The ladder starts from Hartree-Fock approximation floor or "Hartree hell", the least precise way of representing exchange and correlation. The higher the considered approximation is in the ladder, the more precisely quantum chemical properties are predicted, with a larger computational expense in time and resources. The ideal peak of the ladder represents discrepancies between the DFT computed and the actual energy density of the many body system below 1 kcal/mol. Moving towards the higher steps implies going from the local density approximation, showed in green, to semilocal approaches exploring first or second derivatives of the density at some point  $n(\mathbf{r})$  (blue) and afterwards to functionals describing nonlocal or long-range effects, depicted in red. Central columns indicate the name of each family of exchange-correlation functionals (left) and the key functions handled by each family (right). Van der Waals approximations (step 3.5) did not exist before Jacob's Ladder diagram was first published in Ref. [133]; a discussion regarding its placement in the diagram is given in Ref. [134].

place  $n_{\text{HEG}}$  with  $n(\mathbf{r})$  and  $e_{xc}^{\text{HEG}}(n_{\text{HEG}})$  with  $e_{xc}^{\text{HEG}}(n(\mathbf{r}), \mathbf{r})$ . The exchange-correlation energy within LDA approximation is obtained then as:

$$E_{xc}^{\text{LDA}}[n] = \int d\mathbf{r} n(\mathbf{r}) e_{xc}^{\text{HEG}}(n_{\text{HEG}} = n(\mathbf{r})). \quad (2.89)$$

As such, the exchange-correlation of the real, inhomogeneous system at  $\mathbf{r}$  is approximated to the exchange-correlation energy density per particle of an HEG of the same density,  $n_{\text{HEG}} = n(\mathbf{r})$ .

Let us now explore how both the exchange and the correlation parts are calculated in LDA. The exchange energy has a quite simple analytical expression, as KS orbitals (and also Hartree-Fock ones) become plane waves for the HEG. In this manner, starting from Eq. (2.83), we can compute the exchange energy density for the HEG as [116]:

$$e_x^{\text{HEG}} = -\frac{3}{4} \left( \frac{3}{\pi} \right)^{1/3} n_{\text{HEG}}^{1/3}. \quad (2.90)$$

In the real system, we obtain:

$$E_x^{\text{LDA}}[n] = -\frac{3}{4} \left( \frac{3}{\pi} \right)^{1/3} \int d\mathbf{r} n^{4/3}(\mathbf{r}). \quad (2.91)$$

The correlation part depends on the HEG ground-state density. Initially, the correlation model considered was the one proposed by Eugene Wigner for the Hartree-Fock model [135]. Starting with a work in 1980 on zero-temperature hydrogen gas, several one-body densities have been evaluated numerically using quantum Monte Carlo simulations, yielding values of  $E_c$  of an arbitrary degree of precision [136]. However, its exact analytic characterization is not possible and only approximate expressions are feasible in this respect. Only the limits of high and low density are analytically described and its expressions can be found elsewhere [137]. They are written in terms of the Wigner-Seitz parameter or radius  $r_{ws}$ , which is the radius of a sphere whose volume is equal to the volume occupied by a single electron in a region with local electronic density  $n(\mathbf{r})$ ,

$$r_{ws} = \left[ \frac{3}{4\pi n(\mathbf{r})} \right]^{1/3} \approx \frac{1.919}{k_F}, \quad (2.92)$$

with  $k_F(\mathbf{r}) = (3\pi^2 n(\mathbf{r}))^{1/3}$  being the Fermi wavevector.  $r_{ws} \rightarrow \infty$  in the low density limit and  $r_{ws} \rightarrow 0$  in the higher one. Although there were previous proposals for analytical approximations of the correlation part [138, 139], the most widely used

analytical approximation for the correlation part is due to John P. Perdew and Yue Wang [140]. They proposed an approximate correlation energy density in terms of  $r_{ws}$  with 12 parameters fitted in agreement with several quantum Monte Carlo calculations. Anyway, recalling Eq. (2.89), the correlation energy is obviously:

$$E_c^{\text{LDA}}[n] = \int d\mathbf{r} n(\mathbf{r}) e_c^{\text{HEG}}(\mathbf{r}_{ws}). \quad (2.93)$$

LDA works remarkably well in systems with slow density variations, i.e.,  $\nabla n(\mathbf{r}) \rightarrow 0$ , and breaks out with sudden variations of the density, e.g., close to a nucleus. In fact, it gives good results when the following condition linked to the Fermi wavevector holds:

$$\frac{|\nabla n(\mathbf{r})|}{n(\mathbf{r})} \ll k_F. \quad (2.94)$$

LDA performs fairly well for Coulombic systems, e.g., giving total energies of atoms and molecules with an error margin of 1 to 5% compared to experimental data [121]. Moreover, for large absolute values of  $r$  ( $|\mathbf{r}| \rightarrow \infty$ ) the exchange potential decays exponentially,  $v_x \xrightarrow{r \rightarrow \infty} e^{-r}$ , thus diverging from the behavior of the exact Hartree exchange potential,  $v_x^{\text{HF}} \xrightarrow{r \rightarrow \infty} -1/r$ .

There exists also a spin-dependent version of LDA and local spin density approximation (LSDA). For two possible spin orientations  $\sigma_1$  and  $\sigma_2$  in a multielectronic system (and thus two different kind of one-body densities  $n_{\text{HEG}, \sigma_1}^{4/3}$  and  $n_{\text{HEG}, \sigma_2}^{4/3}$ ), the exchange energy density per particle takes the form:

$$e_x^{\text{HEG}}(n_{\sigma_1}, n_{\sigma_2}) = -\frac{3}{4} \left( \frac{3}{\pi} \right)^{1/3} 2^{1/3} \frac{n_{\sigma_1}^{4/3}(\mathbf{r}) + n_{\sigma_2}^{4/3}(\mathbf{r})}{n(\mathbf{r})}, \quad (2.95)$$

and, consequently, the exchange LSDA contribution in the real system is:

$$E_x^{\text{LSDA}}[n] = \int d\mathbf{r} n(\mathbf{r}) e_x^{\text{HEG}}(n_{\sigma_1}, n_{\sigma_2}). \quad (2.96)$$

For the correlation part, analogous considerations as for LDA hold, i.e., this part is determined numerically with quantum Monte Carlo simulations and then analytically fitted to the numerical results. This gave rise to functionals such as PW92 [140] or VWN [138]. An overview of the available fittings can be seen in Ref. [141].

### 2.3.3.2 Generalized gradient approximation (GGA)

The generalized gradient approximation (GGA) consists in incorporating some inhomogeneity in the electron density without discarding one-point density for computing the exchange-correlation part. Its original aim was to improve LDA in nonhomogeneous density conditions. It takes its foundations on the weakly inhomogeneous electron gas (WIEG) [117], a perturbative departure of the HEG described by the Hamiltonian [120],

$$H^{\text{WIEG}} = T^{\text{WIEG}} + W^{\text{WIEG}} + \int d\mathbf{r} n^{\text{WIEG}}(\mathbf{r}) \delta v(\mathbf{r}), \quad (2.97)$$

where  $\delta v(\mathbf{r})$  is a weak external potential originated by a small positive charge density in order to stay close to the charge neutrality of the homogeneous gas. This creates a small nonhomogeneous perturbation on the one-body density of the system.

Returning to the real system, the exchange-correlation energy of the real system is handled as a perturbative expansion in terms of a reduced gradient of the one-body density,

$$s(\mathbf{r}) = \frac{1}{2} \frac{|\nabla n(\mathbf{r})|}{k_F(\mathbf{r})n(\mathbf{r})}, \quad (2.98)$$

which is a dimensionless term also related to the Fermi wavevector. In terms of this factor, the following exchange-correlation expansion can be proposed:

$$E_{xc}^{\text{GEA}}[n] = \int d\mathbf{r} n(\mathbf{r}) e_{xc}^{\text{HEG}} \left( n(\mathbf{r}) + c_{xc}^{(2)}(n(\mathbf{r})) s^2(\mathbf{r}) + \dots \right), \quad (2.99)$$

with  $c_{xc}^{(2)}(n(\mathbf{r}))$  being fitting parameters. Notice that the first term of the expansion is obviously  $E_{xc}^{\text{LDA}}[n]$ . As the integrals of odd powers of  $\nabla n(\mathbf{r})$  are zero, only even powers of  $s(\mathbf{r})$  survive the integration. The first gradient-dependent attempt truncated the expansion at  $s^2$  power and was called the gradient-expansion approximation (GEA). However, some sum rules related to the only-exchange and only-correlation densities of the system were violated with that expansion, leading to a more inaccurate performance of  $E_{xc}^{\text{GEA}}[n]$  than of  $E_{xc}^{\text{LDA}}[n]$ . Therefore, one needs to consider either more terms in the power series of Eq. (2.99), or another kind of dependence of  $E_{xc}$  on  $\nabla n(\mathbf{r})$ . These approaches are designed to also fulfill the referred summation rules GEA violates, and are encompassed under the name

of GGA in the more generic expression,

$$E_{xc}^{\text{GGA}}[n] = \int d\mathbf{r} n(\mathbf{r}) f_{xc}[n(\mathbf{r}), \nabla n(\mathbf{r})], \quad (2.100)$$

being  $f_{xc}[n(\mathbf{r}), \nabla n(\mathbf{r})]$  an appropriately defined exchange-correlation functional of the density and its gradient. The sum conditions mentioned above are soft enough requirements to allow formulation of many different GGA exchange-correlation functionals, which usually rely on parameters (part of them of semi-empirical basis).

In this respect, among the more popular GGA functionals, one can find PBE [142, 143], PW91 [144] or BLYP [145]. But, as mentioned before, there is a remarkable, currently growing variety of GGA functionals. Some lists collecting a number of them can be found elsewhere in the literature [141, 146]. When there exists an improvement of GGA with respect to LDA applied on a given system, the use of density gradients implies some more computational cost than models based solely on density.

Notice that spin-dependent GGA models can be formulated as well; these would adjust to the following generic expression (again for two spin orientations  $\sigma_1, \sigma_2$ ):

$$E_{xc}^{\text{GGA}}[n_{\sigma_1}, n_{\sigma_2}] = \int d\mathbf{r} n(\mathbf{r}) f_{xc}[n_{\sigma_1}(\mathbf{r}), n_{\sigma_2}(\mathbf{r}), \nabla n_{\sigma_1}(\mathbf{r}), \nabla n_{\sigma_2}(\mathbf{r})]. \quad (2.101)$$

With respect to LDA, the exchange and correlation energies for a number of atomic systems are predicted more exactly and very closely between different GGA models [120]. Furthermore, compared to LDA, both exchange and correlation energies become closer to the exact values than LDA and thus more accurate. Additional results related to molecular or metallic systems are accurately computed for different molecular systems [120]. Among the downsides, the addition of gradient terms leads to more complexity in the calculation of GGA exchange and correlation than for LDA (recall Fig. 2.2). In addition, GGA functionals lead to worse computations of parameters such as molecular bond lengths than LDA [121]. The exchange potential continues to decay exponentially as for LDA and unlike the asymptotic limit of Hartree exchange. In addition, although some nonlocality is incorporated with density gradient terms in contrast to LDA, longer-range interactions are not accurately described [120].

### 2.3.3.3 Meta-generalized gradient approximation (mGGA)

In order to further improve the description of exchange and correlation and to overcome the limitations of GGA functionals, further extensions were developed

under the collective name of meta-generalized gradient approximation (mGGA). These functionals incorporate to the exchange-correlation energy the Laplacian of the one-body density,  $\nabla^2 n(\mathbf{r})$ , as well as a quantity proportional to the gradient of the KS orbitals, the KS kinetic energy density (KED), defined as the kinetic energy of the occupied KS orbitals per volume unit [147],

$$\tau(\mathbf{r}) = \frac{1}{2} \sum_{i=1}^{(\text{occ})} |\nabla \phi_i(\mathbf{r})|^2. \quad (2.102)$$

These ingredients are incorporated to the mGGA exchange correlation energy density, so that

$$E_{xc}^{\text{mGGA}}[n] = \int d\mathbf{r} n(\mathbf{r}) f_{xc}[n(\mathbf{r}), \nabla n(\mathbf{r}), \nabla^2 n(\mathbf{r}), \tau(\mathbf{r})], \quad (2.103)$$

or, for its spin-dependent version,

$$E_{xc}^{\text{mGGA}}[n_{\sigma_1}, n_{\sigma_2}] = \int d\mathbf{r} n(\mathbf{r}) \cdot f_{xc}[n_{\sigma_1}(\mathbf{r}), n_{\sigma_2}(\mathbf{r}), \nabla n_{\sigma_1}(\mathbf{r}), \nabla n_{\sigma_2}(\mathbf{r}), \nabla^2 n_{\sigma_1}(\mathbf{r}), \nabla^2 n_{\sigma_2}(\mathbf{r}), \tau(\mathbf{r}, \sigma_1), \tau(\mathbf{r}, \sigma_2)]. \quad (2.104)$$

Again, there are different choices for the exchange-correlation integrand, with PKZB [148] and TPSS [149] the most popular mGGA models. A number of mGGA functionals avoid incorporating  $\nabla^2 n(\mathbf{r})$  terms due to divergences in the vicinity of atomic nuclei. There are references collecting various choices for mGGA forms [141].

These kinds of functionals further improve the already good results computed with GGA, and also make it possible to decrease self-interaction-related errors as well as problematic behaviors of the exchange and correlation local potentials. However, there is a higher computational cost due to the Laplacian evaluation and, especially, to the KED term that explicitly depends on the KS orbitals. As KED does not depend explicitly on density, the local exchange-correlation potential  $v_{xc} = \delta E_{xc}[n(\mathbf{r})]/\delta \mathbf{r}$  cannot be determined directly, in contrast to other explicit density functionals. Moreover, mGGA functionals are frequently used after previously performed self-consistent GGA calculations, and therefore they lead to modest refinements to GGA [120]. Reasons like these explain why they are less commonly used in quantum chemistry than GGA or LDA functionals.

### 2.3.3.4 Hybrid functionals

Previous exchange-correlation approaches were called local or semilocal because they involved the knowledge of the density at some  $\mathbf{r}$  (local) or some of its derivatives –gradient or Laplacian– implying some directionality, but evaluated at the same point (semilocal). However, interactions of a longer range than the semilocal ones require  $E_{xc}[n]$  to incorporate some nonlocal part. As it is an exact functional, it is particularly convenient to consider the Hartree-Fock exchange  $E_x^{\text{HF}}[n]$  we defined at the beginning of Section 2.3.3 in Eq. (2.84). We already mentioned that each electron is affected by a potential because the remaining ones of a given system in the Hartree-Fock framework are nonlocal, thus  $E_x^{\text{HF}}[n]$ . Therefore, an exchange-correlation functional incorporating the Hartree-Fock exchange can handle interactions beyond the semilocal limit.

Now we can take advantage of the Hartree-Fock system, from which we know exactly both the exchange (Eq. (2.84)) and correlation ( $E_c^{\text{HF}}[n] = 0$ ) functionals. In fact, one can mix a fraction of the Hartree-Fock regime with the real system whose  $E_{xc}[n]$  needs to be approximated with methods such as the ones we have seen, LDA, GGA and/or mGGA. Both regimes are mixed for these exchange-correlation forms, which fall under the category of hybrid functionals.

The first hybrid form was proposed by Axel D. Becke in 1993 and combines GGA exchange-correlation with the exact one [150]:

$$E_{xc}^{\text{B93}} = aE_x^{\text{HF}} + (1 - a)E_x^{\text{GGA}} + E_c^{\text{GGA}}, \quad (2.105)$$

with a numeric parameter  $a \in [0, 1]$  adjusted to fit a set of atomization energies. For B93,  $a \approx 1/4$ . There are other hybrid functional proposals, such as the PBE0 [151] and HSE functionals, that combine exact exchange with the GGA type PBE exchange correlation functional [152, 153]. But the most popular approach is a variation of the B3PW91 functional [154], namely the B3LYP form [155],

$$E_{xc}^{\text{B3LYP}} = (1 - a)E_x^{\text{LSDA}} + aE_x^{\text{HF}} + bE_x^{\text{B88}} + (1 - c)E_c^{\text{LSDA}} + cE_c^{\text{LYP}}, \quad (2.106)$$

with  $a = 0.20$ ,  $b = 0.72$  and  $c = 0.81$ . B3LYP adds to the exact Hartree-Fock exchange energy the exchange-correlation contributions of LSDA as well as the two GGA terms contained in the BLYP functional, namely Becke-88 (B88) for the exchange [145] and LYP for the correlation [156].

Thanks to the addition of  $E_x^{\text{HF}}[n]$  to  $E_{xc}[n]$ , quantities such as vibrational frequencies, bond lengths, and atomization energies for a majority of molecular species can be calculated more accurately than with mGGA or simpler functional approaches [157]. Unlike semilocal and local forms, for hybrid functionals, the

exchange local potential for long distances takes the asymptote  $v_x \xrightarrow[r \rightarrow \infty]{} -a/r$ , so the larger  $a$ , the closer the correct asymptotic behavior described in the beginning of Section 2.3.3 approaches [121, 133]. These improvements come at the expense of a higher computational cost due to the evaluation of the KS orbitals required to obtain  $E_x^{\text{HF}}$ . Not only that, but Hartree-Fock limitations are transferred to hybrid functionals, e.g., by sorting energies of spin states in metals incorrectly, or by failing to describe noncovalent interactions [158].

More proposals exist regarding hybrid functionals. Some recent examples consider highly parametrized forms as mixtures of hybrid-like and mGGA terms. These belong to the family of the so-called Minnesota functionals [159]. Climbing to the fifth step in Jacob's Ladder (Fig. 2.2), there is an even more powerful refinement of the hybrid functional approach in which unoccupied KS orbitals are incorporated, with even better results but computationally more expensive than the aforementioned hybrid functionals. However, let us insist once more on the idea that there exists no perfect  $E_{xc}[n]$ , but its quality depends on the system under study in DFT and the compromise between complexity and accuracy reached for each choice of functional.

Unfortunately, the inability of hybrid forms to handle noncovalent interactions is an important obstacle when studying solid surfaces as we do in this work. In particular, van der Waals interactions fall under this category, and its description is paramount for surfaces. A different group of forms, namely van der Waals functionals, can overcome this problem, as we are discussing next.

### 2.3.3.5 Van der Waals functionals

Due to their importance for the systems studied in this Thesis, and before advancing to van der Waals functionals, let us briefly introduce van der Waals interactions. These involve groups of electrically neutral molecular assemblies (i.e., molecules with their electronic subshells filled). Two kinds of forces can arise: between dipoles formed by polar molecules (dipole-dipole interactions) or between nonpolar molecules whose instantaneous electronic distributions form different charge densities on each side of the molecule (London dispersion interactions) [160]. Dispersion interactions are often regarded as the only van der Waals forces, overshadowing polarization interactions between induced dipoles, which are typically weaker [161, 162]. These long-range interactions are responsible for the adsorption of many molecules and other quantum chemical phenomena on surfaces, as well as for the structural cohesion of van der Waals atomic and molecular systems, crystalline solids, nanostructures, and different biomolecules such as DNA.

Van der Waals intermolecular interaction energy is modeled with the following

decomposition,

$$V^{\text{vdW}} = V^{\text{vdW,sh}} + V^{\text{vdW,elec}} + V^{\text{VDW,ind}} + V^{\text{VDW,disp}}, \quad (2.107)$$

being  $V^{\text{VDW,sh}}$  an exponential-decaying, short-ranged electrostatic repulsion term,  $V^{\text{VDW,elec}}$  the interaction between the electronic distributions of the molecules on their ground states, and  $V^{\text{VDW,ind}}$  and  $V^{\text{VDW,disp}}$  the potentials for the aforementioned dipole-dipole and dispersion interactions. These terms can be encompassed in the following multipole expansion [163],

$$V^{\text{vdW}} = - \sum_{i=0}^{\infty} \frac{C_{2i+6}}{|\mathbf{r} - \mathbf{r}'|^{2i+6}}, \quad (2.108)$$

with the  $C_{2i+6}$  coefficients being numerically-adjustable parameters. Equation (2.108) shows how weak van der Waals interactions become compared to electrostatic interactions. Although these interactions last for a short time with respect to single pairs of particles, together they become strong enough to preserve the consistency of systems such as surfaces and biomolecules [164, 165]. In fact, some approaches to define the contribution of nonlocal correlation focus on fixing the  $C_{2i+6}$  coefficients in different ways, also with the aid of reference results of quantum chemical calculations. Among these, we can find proposals like PBE-D2 [166] or TS-vdW [167], which truncate Eq. (2.108) in its first term and thus determine approximate expressions for the coefficient  $C_6$ .

At this point, and unlike semilocal families of forms (recall Fig.2.2), van der Waals functionals are capable of describing long-range forces [168]. Regarding their functional modeling for handling exchange and correlation, some initial proposals based on first principles were developed [169, 170, 171]. Later, a key milestone was achieved with van der Waals density functional (vdW-DF), first introduced by Dion *et al.* [172]. Modeling nonlocal exchange-correlation effects with vdW-DF does not require KS orbitals, thus avoiding the aforementioned theoretical complications their introduction brings. Furthermore, it excels in sparse systems, within which there are areas of high electronic density separated from each other by large empty spaces. In contrast with electronically dense matter, not only strong local forces inside each electron cloud but also nonlocal van der Waals interactions between these electron distributions –weaker, yet collectively significant– play a crucial role [173]. A particular example of a sparse system is a multilayered interface of metallic atoms. Each individual atom layer is tightly bound by electrostatic forces, whereas cohesion between separate layers occurs through van der Waals forces. This vdW-DF exchange-correlation functional in particular and its family of

functionals in general become particularly relevant for us as the vdW-DF exchange-correlation functional is used in the DFT calculations performed during this Thesis.

However, let us return to the vdW-DF form. As van der Waals interactions come from correlating, nonoverlapping distributions of electrons, they affect only the correlation of the many-body system. Hence the way of incorporating them in the exchange-correlation energy combines local exchange (LDA), semilocal correlation (GGA) and a nonlocal correlation part  $E_c^{\text{NL}}$ :

$$E_{xc}^{\text{vdW-DF}} = E_x^{\text{GGA}} + E_c^{\text{LDA}} + E_c^{\text{NL}}. \quad (2.109)$$

In the original vdW-DF formulation by Dion *et al.* [172], the GGA form chosen to evaluate  $E_x^{\text{GGA}}$  is the rev-PBE one [174], which is a variant of the PBE functional [142, 143]. This choice avoids one typical problem present in a number of GGA proposals, namely that they overvalue the exchange contribution to van der Waals binding. This behavior is wrong, according to calculations on some systems, such as the benzene dimer, of exact Hartree-Fock exchange energy  $E_x^{\text{HF}}$  (Eq. (2.84)) [173]. Insisting on this, although the bond lengths are slightly overestimated by rev-PBE, the equilibrium energies are closer to the experimental results than when  $E_x^{\text{HF}}$  is taken as the exchange part. Nevertheless, consideration of other modified exchange forms may improve the accuracy of  $E_{xc}^{\text{vdW-DF}}$ , as has been verified for different sparse systems [175]. On the other hand, the correlation energy  $E_c^{\text{vdW-DF}}$  is decomposed into one local term calculated with LDA and a nonlocal part  $E_c^{\text{NL}}$ . The latter incorporates the van der Waals force description in vdW-DF and is modeled as:

$$E_c^{\text{NL}}[n] = \frac{1}{2} \int d\mathbf{r} d\mathbf{r}' n(\mathbf{r}) \Phi(\mathbf{r}, \mathbf{r}') n(\mathbf{r}'), \quad (2.110)$$

where  $\Phi(\mathbf{r}, \mathbf{r}')$  is a function proportional to the difference  $|\mathbf{r} - \mathbf{r}'|$ . Details on the derivation of an approximate expression for this kernel function involve the adiabatic connection formalism [173] and can be followed in Ref. [172]. This form cannot be used together with the exact Hartree-Fock-based exchange energy, as has been shown elsewhere [176]. Notice also that for short-range interactions LDA and GGA contributions to exchange and correlation become dominant, thus making vdW-DF treatment consistent also in shorter scales.

In the original vdW-DF, the nonlocal correlation energy  $E_c^{\text{NL}}$  is determined with a model dielectric function, and it works as a nonlocal correction to the LDA correlation  $E_c^{\text{LDA}}$ , as  $E_c^{\text{NL}} \ll E_c^{\text{LDA}}$  [172, 173]. Later, a correlation potential incorporating the nonlocal effects was proposed, thus vdW-DF becoming a self-consistent

framework [177],

$$v_c^{\text{NL}}[n](\mathbf{r}) = \frac{\delta E_c^{\text{NL}}[n]}{\delta n(\mathbf{r})}. \quad (2.111)$$

Even though being a more complete approach than original vdW-DF form, in general its self-consistent extension does not give rise to significant changes in a number of quantum chemical quantities due to its rapid decay with growing intermolecular distance as given in Eq. (2.108). Only in some specific applications, incorporation of the self-consistently calculated correlation potential yields relevant improved results, such as the evaluation of Hellmann-Feynman forces [177]. In particular, because of this latter aspect, we use the self-consistent vdW-DF version in our DFT calculations.

In addition to this, other proposals have emerged based on the original vdW-DF approach, aiming to improve its features. This has been pursued by determining the  $E_x^{\text{GGA}}$  exchange with a reparameterized version of PW86, rPW86 [178] (instead of rev-PBE as in vdW-DF) and modifying an internal parameter of the vdW-DF approach, leading to the vdW-DF2 form [179] or incorporating changes to the GGA exchange part such as in rev-vdW-DF2 [180]. A more current vdW-DF generation, called vdW-DF3 [181], adds a new empirical-like degree of freedom to the original vdW-DF model. However, improvement of vdW-DF-based functionals is an ongoing task to this day.

Although becoming reliable when treating van der Waals interactions, computational evaluation of this kind of nonlocal functionals has only a slightly higher cost than GGA approximations [173, 182, 183]. With this in mind, the vdW-DF family of functionals can be placed between mGGA and hybrid functional rungs of Jacob's Ladder (see Fig.2.2) [134], as part of the so-called nonlocal exchange approximations [184, 185]. The balance between accuracy and relative computational cost motivates the use of vdW-DF for ab initio dynamical calculations in this work (Chapters 5-8).



# 3

## Femtosecond laser-induced photodesorption

---

The core of the work developed in this Thesis is the study of the dynamics concerning a metal surface with molecules adsorbed on its top which is excited with a femtosecond laser pulse. Such particular kind of excitation can affect the adsorbates, which can desorb, dissociate, recombine, or just rotate, vibrate, and/or diffuse on the surface. Understanding how to describe the femtochemical phenomena of adsorbate-decorated surfaces is the main goal of this chapter.

### 3.1 Photoinduced desorption mechanisms

Femtochemistry is a relatively recent branch of quantum chemistry. Although some theoretical background formulations appeared in the 1930s [186, 187, 188], experimental tools for accessing smaller time scales had to wait some decades to become available [189]. The first femtochemistry experiments had to wait until the 1980s, once ultrashort laser pulses lasting subpicosecond times could first be produced, as was reported by different groups [190, 191, 192, 193, 194]. The use for the first time of a Ti-sapphire laser in 1991 [195] was crucial for the generalization of femtosecond-scale experiments in a number of laboratories. More recently, even laser pulses on the attosecond time scale were successfully produced [196, 197]. Returning to the femtoscale, in pioneering femtosecond laser experiments the transition states of ICN breakage into I+CN products [198, 199] and later on both NaI and NaBr dissociation [200] were observed for the first time, as well as a transformation process from covalent to ionic bonds. But, above all, studies like these paved the way for extensive research in diverse areas, including gas and liquid systems, biological molecules, and interactions in solutes, solvents, and polymers [189].

Different considerations require experimentally reaching a time resolution of the order of  $10^{-15}$  s (i.e., 1 fs). Elemental processes such as bond formation and rupture occur within the femtosecond time scale. Moreover, vibrations in molecules elapse in time periods on the order of 10 to 100 fs [189]. Additionally, transition states of different reactions exist for times of the order of picoseconds or even shorter (see, e.g., Refs. [201, 202, 203]). Reaching a femtosecond time resolution is crucial in order to follow the movement of atoms and molecules in the angstrom ( $10^{-10}$  m)

space scale in real time, and to monitor their behavior and interactions during chemical reactions [204].

To explore the subpicosecond regime, the most common experimental technique is the usage of femtosecond pump-probe laser pulses, or femtosecond transition state spectroscopy as designed by Ahmed Zewail for the dissociation of gas molecules [204]. A typical pump-probe experiment begins with the target in its ground state being irradiated by a first femtosecond width pulse, the pump, and thus gaining energy and going into an excited state in general [93]. Then, a second pulse or probe is fired on the excited system to monitor it and measure some of its properties. The probe laser wavelength is carefully set and its intensity is generally smaller than the pump pulse one in order to provide to the excited state a minimal energy input, thus not perturbing its pump-driven state one wants to investigate. In a typical experimental set up, both pulses are generated at the same time, with the probe being delayed from the pump by making it follow an optical path of variable length according to the retardation time one wants to fix. Depending on the delay time between both pulses, different stages of the chemical reaction intercourse can be observed. Information on observables such as the atomic and molecular positions, the energy distribution in translational and rovibrational components, the vibration of atoms in a crystalline net and the spin orientation of ferromagnetic atoms can be acquired. Notice that a pump-probe experiment can fail due to reasons such as the pump pulse energy being insufficient to excite the target or the excited system relaxing faster than the probe pulse arrival.

As highlighted earlier in the beginning of this Section, the scope of femtochemical studies extends across various domains of applicability. However, from the beginning, a specific category of systems posed particular challenges to comprehension: surfaces with adsorbed atoms and/or molecules present a highly intricate dynamical interplay [32]. This is motivated by the nonadiabatic coupling between the degrees of freedom of the electrons and nuclei present in the system. At a PES level, this coupling arises as conical intersections between the PESs of different electronic configurations for a given arrangement of the system nuclei and intensifies with a larger number of nuclear degrees of freedom, and the electronic configurations close in energies to each other [205]. Between a metal surface and an atom or molecule, nonadiabaticity can occur in the form of electron transfer from the surface to ionize a free species or from the adsorbate to the substrate [206]. As a result of these nonadiabatic couplings, adsorbates can experience a number of phenomenological phenomena such as rotational and/or vibrational excitation, diffusion, dissociation, recombination, or even desorption. These phenomena play a relevant role in applications such as heterogeneous catalysis, the process of speeding up a chemical reaction by making some reactant or reactants interact with a catalyst in a different

aggregation state. Usually, some atoms or molecules in the gas- or liquid-phase adsorb on a solid surface, diffuse along it, and interact with each other, eventually being able to easily recombine and desorb from the catalyst. Examples of heterogeneous catalytic reactions in real life are the synthesis of chemical compounds such as  $\text{NH}_3$ , the synthesis of fertilizers, oil refining, and the oxidation of CO and other hydrocarbons in car exhaust systems [4]. Surface nanochemistry, electrochemistry, and materials science (for example, the hydrophobic effect [207]) are other examples of practical applications of photoinduced processes in adsorbate-substrate complexes [16, 32].

Let us focus on photoinduced desorption processes that can be triggered by direct and indirect excitation of the adsorbate [16]. In the first case, photons are absorbed by each adsorbate, which has either a permanent dipolar momentum or a surface-induced transient dipolar momentum. If the photons transmit enough energy to each adsorbate, then some of the latter are capable of overcoming the potential barrier and desorb. The energy input does not necessarily need to be too high. Adsorbates weakly bound to the surface can desorb even with environmental black body radiation at ambient temperature as seen for  $\text{H}_2$  and  $\text{D}_2$  in Cu(510) [208] and He on Pt(111) [209]. This type of excitation is influenced by the orientation of light polarization and reaches maximum efficiency when aligned with the direction of the transition dipole moment created by the bond between the adsorbate and the substrate that is to be broken [16]. This behavior was observed, for example, for H/Si(100)-(2 × 1) [210]. In general, photon-stimulated desorption is due to infrared [211] or UV or visible light [212]. In terms of electronic conductivity, while insulating and semiconducting substrates exhibit direct desorption upon UV/visible light irradiation, metallic surfaces typically undergo this process when exposed to infrared radiation [16].

Indirect photoinduced desorption is a process typically observed in metal surfaces as they have a high absorptivity for short-wavelength light (near-infrared, visible, and UV) [16]. It is more complex due to the involvement of surface-driven nonadiabatic mechanisms. First, the incident light is absorbed by the surface electrons creating electron-hole pair excitations that can pump energy directly to the adsorbates and indirectly by excitation of the surface phonons. Because of this indirect mechanism, incident light polarization does not play a relevant role in the indirect photoinduced desorption route, in contrast to the aforementioned direct one [16]. This was verified experimentally, for instance, in NO desorption from Pt(111), as reported elsewhere [213, 214]. In contrast, the laser energy absorbed per unit area –i.e., the absorbed fluence,  $F$ – has a strong influence on the desorption yield  $Y$ .

Whether directly or indirectly, two different regimes of desorption can arise

depending on the nature and amount of excitations on an adsorbate. First, desorption induced by one electronic transition (DIET) occurs for low laser fluences. In DIET, light absorption triggers eventual uncorrelated electronic excitations in the adsorbate-substrate complex, which leads to subsequent stimulation of adsorbates and to their potential desorption. Consequently, this process is characterized by a relatively low desorption probability per absorbed photon and a linear dependence between yield and fluence,  $Y \propto F$ . Second, desorption induced by multiple electronic transitions (DIMET) arises after using intense light sources such as a femtosecond laser [34, 35, 215, 216, 217]. The stream of incoming high-energy photons either hits the adsorbed species directly or is absorbed by the substrate and excites a high density of electrons and phonons to subsequently excite the adsorbate. Either way, this leads to multiple, correlated excitations in the adsorbed species in faster time scales than electronic and vibrational relaxation from the excited state to the ground state. As a result, before an adsorbate fully damps its excited energy after relaxation, it undergoes multiple excitation/deexcitation cycles, each of them pushing it to a higher energy state in the potential well. In this way, the adsorbed species can effectively "climb up" multiple energy states in just one cycle until it eventually surpasses the adsorption energy barrier and desorbs. This mechanism leads to an increase in desorption likelihood compared to DIET for the same adsorbate-substrate complex, reflected in the superlinear enhancement of the yield with fluence,  $Y \propto F^n$ . The exponent  $n > 1$  depends on the system considered and can be of the order of 1 or 10. Additionally, translational and/or rovibrational energy distributions of desorbed species and branching ratios become fluence-dependent quantities. Notice that for a given system, different reaction pathways can open depending on the emergence of DIET or DIMET. Let us mention the CO+O<sub>2</sub>/Pt(111) system as an example. Here, DIET leads to slightly more CO oxidation and desorption as CO<sub>2</sub> than desorption of O<sub>2</sub>, while for DIMET the last reaction channel prevails by a larger factor [218, 219].

Understanding of the fundamental mechanisms of electron-stimulated desorption was originally sustained in some simple two-state theoretical approaches, among which two of them gained the most popularity [220]. The first is the Menzel-Gomer-Redhead (MGR) model [98, 221]. It is inspired by considerations about the ionization and dissociation mechanisms in isolated molecules [222]. Either by direct absorption of a photon or by interaction with an incoming electron, an adsorbate modifies its electronic state and thus undergoes a vertical transition or Franck-Condon process from its ground state to a repulsive excited state (Fig. 3.1). Then, the adsorbed species remains in the excited-state PES for some brief residence time, during which part of the electronic energy due to the excitation transforms into rovibrational and/or translational kinetic energy. As a result, the adsorbate gains nuclear motion

and evolves toward a growing reaction coordinate (often the distance between the adsorbate center of mass (CM) and the substrate). Afterwards, the adsorbed species relaxes to a bonding adsorbate-substrate potential with some excess kinetic energy. Such potential can correspond either to the ground state  $S + A$  or to a state of the form  $\{S^* + A\}$ , where the adsorbate  $A$  is unexcited and the substrate  $S$  has some excitation due to the remaining electronic energy coming from the adsorbate after relaxation. Now, if its kinetic energy gain is larger than the ground-state PES potential barrier, the adsorbate is able to desorb. This occurs if the residence time has surpassed some critical value  $t_c^{\text{rel}}$ . If the adsorbate remains excited for a shorter time, its excess energy upon relaxation is insufficient to overcome the barrier, leading to its recapture by the substrate. If the electronic energy that excites the adsorbate is sufficiently large, or if electron transfer from the adsorbate occurs, the species can not only gain enough kinetic energy to desorb but also become ionized and desorb as an ion. If such situations do not occur, the adsorbate may desorb as a neutral species.

MGR model offered a simple explanation of how adsorbed species can desorb under the action of incoming photons or electrons. However, for some atoms adsorbed on metallic surfaces, it was experimentally seen that after being excited with photons or electrons with energies of 10 eV, lifetimes of the adsorbate excited states were of the order of  $10^{-16}$  s [223, 224]. That is two orders of magnitude shorter than the time required for an average ion of 10 eV to move 1 Å [99]. Following MGR framework, if an adsorbate is excited to an antibonding state with an energy equal or larger than 10 eV, the lifetime of such an excited resonance would be too short to allow for desorption. To overcome this inconsistency, Antoniewicz provided an alternative two-state image for DIET process [99] (see Fig. 3.2). As a starting point, let us consider an incident electron or photon interacting with an adsorbate and exciting by a Franck-Condon transition to a positive ion. As a result, an image charge arises in the surface and an attractive potential between it and the adsorbed species ( $S + A^+$ ) establishes. Hence, the equilibrium position of the adsorbate-substrate complex is shifted towards a smaller adsorbate-substrate distance, so the adsorbate becomes accelerated towards the surface and approaches the minimum of the excited adsorbate-substrate potential. The adsorbed species not only gains kinetic energy when approaching the surface, but also its probability of capturing a substrate electron by resonant tunneling or Auger neutralization and hence becoming neutral increases. RENEUTRALIZATION of this ionic resonance leads to the disappearance of the attractive image potential and the electrostatic repulsion of the adsorbate, which desorbs if the kinetic energy gain surpasses the potential barrier  $E_b$ . Furthermore, the adsorbed species may also desorb in the form of a positive ion if the initial excitation brings the system to an excited

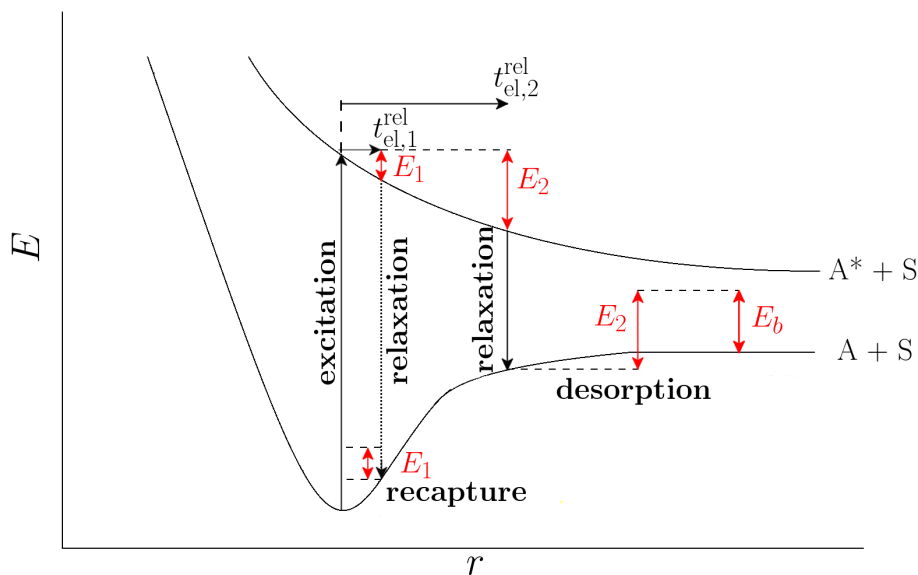


**Figure 3.1:** Representation of the MGR model showing the energy versus the adsorbate-surface distance  $r$ . Starting from the adsorbate-substrate complex in the ground state  $A+S$ , photoexcitation heats the electrons of the surface, and after them colliding the adsorbate the latter is driven through a Franck-Condon excitation into an excited state  $A^*+S$ . There, excited adsorbate remains for some time in the excited PES until relaxing back to the ground state with some kinetic energy gain, leading to it separating some  $r$  from the substrate. Two possible situations can arise depending of if time before quenching falls below or reaches some critical value  $t_c^{rel}$ . For relaxation times as  $t_{el,1}^{rel} < t_c^{rel}$  the adsorbate gains not enough energy to surpass the potential well  $E_b$ , so that with an energy gain  $E_1 < E_b$  it loses the kinetic energy gained after excitation and gets recaptures by the substrate. On the contrary, if it remains longer of, at least, as long as some critical time,  $t_{el,2}^{rel} \geq t_c^{rel}$ , it gains enough kinetic energy to surpass the potential barrier after quenching back to ground state,  $E_2 \geq E_b$ , and becomes able to desorb.

ionic state  $(S + A^+)^*$ . After acceleration toward the surface and reneutralization of the adsorbate, the latter may be reionized as the probability of electron hopping from it to the substrate also increases with decreasing adsorbate-substrate distance. If this positive ion has a kinetic energy greater than the potential barrier of the ionic adsorbate-substrate complex  $S + A^+$ , it may desorb as a non-neutral species. Notice that this theoretical model can be applied to nonmetal substrates, parameters such as the nature of the adsorbate interaction with its surface image charge and reneutralization probabilities obviously varying with respect to metals.

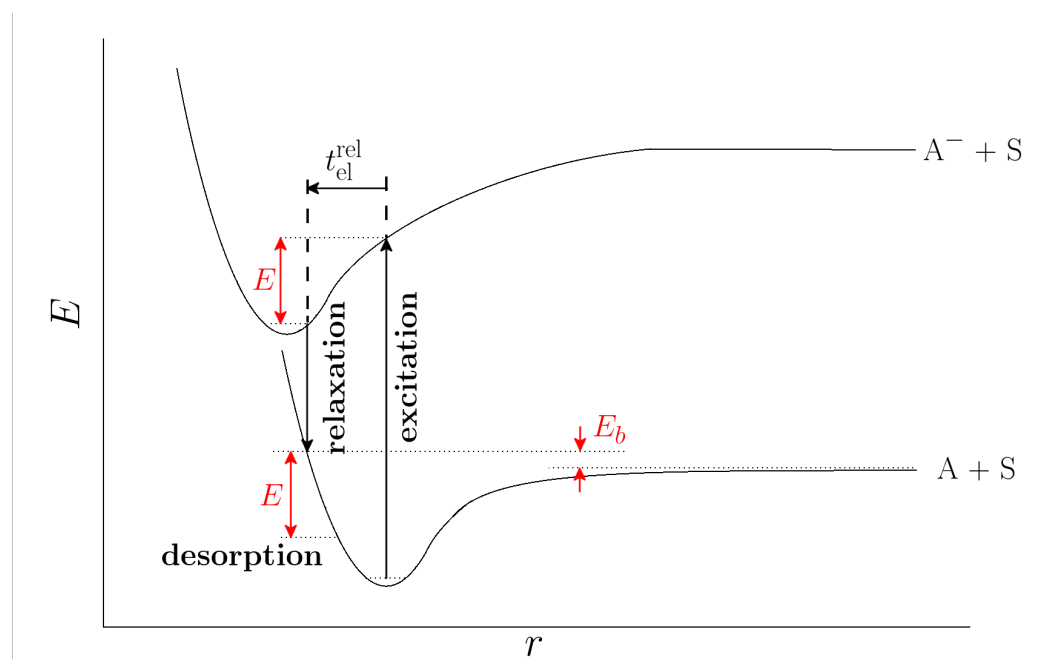


**Figure 3.2:** Surface photodesorption mechanism as described by Antoniewicz. Considering once more the energy dependence of the adsorbate with its distance to the substrate  $r$ , and starting again from the adsorbate-substrate system on ground state as in MGR proposal, some photoexcited surface electrons are captured by the adsorbate orbitals, bringing the adsorbate into a negative ionic state PES  $A^- + S$  through a Franck-Condon process. Anionic atom or molecule then approaches the surface before relaxing back to the ground-state PES after some relaxation time  $t_{el}^{rel}$ . While approaching the surface and quenching back to it, the adsorbate has an energy gain  $E$  which, if it equals or surpasses the energy barrier of the ground PES ( $E \geq E_b$ ), allows the adsorbed species to desorb.

Both MGR and Antoniewicz pictures yield analogous conclusions, basically differing in the nature of the excited-state PES and the energetic reasoning of how desorption originates. For DIET to occur, the average time interval between

two different photon- or electron-induced Franck-Condon transitions  $t_{\text{exc}}$  must be large enough compared to both electronic and vibrational relaxation times, i.e.,  $t_{\text{exc}} \gg t_{\text{el}}^{\text{rel}}, t_{\text{vib}}^{\text{rel}}$  [16]. Moreover, properties of the desorbates such as branching ratios between different reaction channels and translational energies do not depend on the laser fluence in this case [219]. Conceptually, these two-state models are compatible with DIMET as well [35]. In this regime, an adsorbate can undergo more than one Franck-Condon excitation (and hence more than one relaxation to the ground state), preventing it from being recaptured by the surface. As a result, it is easier for it to gain enough kinetic energy to surpass a potential barrier.

Despite their simplicity, MGR and Antoniewicz models have helped to understand how desorption due to electron and photon stimulation works, and can be used to predict some properties of real systems which could be supported or not by later experiments [220]. However, their simplicity involves some limitations. For the MGR picture, there are challenges in rationalizing a number of features about electron-stimulated desorption. This includes describing the sizes of high-energy desorption barriers, differences between neutral and ion desorbates, the charge state of the desorbing species, the smallness of the electron-stimulated desorption cross section compared to its counterparts in the ionization of gas-phase species, the absence of isotope effects for desorbed neutrals, and high kinetic energies of the desorbing particles [225]. Regarding the Antoniewicz approach, the attractive electrostatic interaction with the substrate image charge appears to be much less relevant than proposed, according to experimental results on photon-stimulated desorption of CO, CO<sup>+</sup> and CO<sup>-</sup> from Pt [226]. Moreover, both models fail to explain experimental results, such as the observed large isotope effect on nonthermal UV photodesorption of NH<sub>3</sub> from GaAs(100) surfaces [227]. In addition to this, these approaches miss effects such as multidimensionality of the PESs involved and the potential existence of more than one available excited state [220]. Although they provide a simple basis to describe desorption from a theoretical perspective, aspects such as the previous ones show that these two-state models are clearly insufficient or even unsuccessful in characterizing the properties of different adsorbate-substrate systems. The more complex the latter ones become (e.g., for adsorbates arranged in multiple layers or complex surface geometries), the more evident the problems of these simple models are.

Apart from the aforementioned ones, a notable limitation arises particularly in the context of the MGR and Antoniewicz models, which assume the initial excitation is concentrated around the adsorbed entities. This issue becomes especially relevant in the case of DIMET on metal substrates under the influence of ultrashort laser pulses, where an indirect excitation route may emerge. In this scenario, photon absorption by the surface becomes predominant, energizing its electrons and lattice phonons,

which in turn stimulate the adsorbates. Thus, a more comprehensive theoretical framework is necessary for understanding desorption from metal surfaces, beyond what the MGR or Antoniewicz models offer. This cornerstone of our work will be explored in the next Section.

## 3.2 Photoinduced desorption on metallic surfaces

Adsorbate-decorated metallic surfaces have been attracting growing interest due to two main reasons [32]. First, metals can create a beneficial energy environment for reactions with adsorbed species, leading to, e.g., lower reaction barriers than for free, gas-phase species. Secondly, positioning reactants closely together on a metal surface enhances control over the dynamics of a chemical process, which simplifies their set-up for a number of applications such as heterogeneous catalysis (recall some additional examples mentioned in Section 3.1). Such reasons have led to the growth of a research area that started in the 1990s [228] with experimental work on NO-decorated Pd(111) substrates [34, 215, 217, 229].

Photoinduced chemical processes on metal surfaces cannot be characterized as adiabatic processes, since they are the result of the coupling of the electrons excited by the laser pulse with the nuclear DOFs of the adsorbates [230]. Hence, this coupling of DOFs means a departure from the basic assumption of the Born-Oppenheimer approximation. These nonadiabatic effects have also been theorized to affect processes such as the vibrational relaxation of adsorbed molecules [231]. Furthermore, experimental observations have confirmed that this coupling can occur, leading to changes in the nuclear dynamics and the production of electron-hole pairs and excitations such as phonons and plasmons in the substrate. Examples of these nonadiabatic phenomena reported experimentally are the emission of surface photons, electrons, and ions during the oxidation of alkali metal surfaces [232], the scattering of molecules with highly excited vibrational motion and their related energy dissipation [206] or the desorption of gas molecules from metal substrates such as N<sub>2</sub> (after recombination) from Ru(0001) [233] and CO from Pd(111) [30], among many other examples in the literature.

Let us now focus on femtosecond laser-induced desorption on metal substrates. Starting from the laser excitation, two distinct stages for the energy flow in the system can be identified. First, incoming photons induce electronic excitations in the surface, and second, these excitations couple to the lattice (phonons) and adsorbate DOFs, which also couple among them, altogether leading the adsorbates to desorb. From a theoretical perspective, the two-temperature model (2TM) is commonly used to characterize substrate excitations [50]. Regarding the subsequent coupling

of the latter ones to adsorbed species, several models have been proposed, but we are considering one involving molecular dynamics with electronic friction [39, 40]. Let us explore both frameworks in more detail.

### 3.2.1 Substrate excitation: the two-temperature model

Let us assume that the adsorbate-metal system is initially thermalized at some temperature  $T_0$ . After irradiating the system with a femtosecond laser pulse, the adsorbate-metal system is driven out of its initial thermal equilibrium state, as shown in Fig. 3.3, left panel. Microscopically, metal electrons absorb the incoming photons of energy  $E_{\text{ph}} = h\nu$  and become excited, thus producing a nonthermal distribution of energy states. Therefore, right after the laser beam reaches the metal, its electronic subsystem cannot be characterized by a well defined macroscopic temperature [32, 234, 235]. However, the energy of the hot electrons is redistributed after they scatter with each other and at a later times with the surface lattice and adsorbed species. As a result, the very initial nonthermal distribution relaxes to a Fermi-Dirac one with a certain electronic temperature  $T_e(t)$  and a tail of states with energies above the Fermi one,  $E_F$ , as depicted in Fig. 3.3, right panel. Due to the low heat capacity of the electrons  $C_e$ ,  $T_e(t)$  increases sharply above the initial surface temperature and can reach peak values of several thousand K, even surpassing the melting temperature of the surface species (see, e.g., Refs. [34, 216]). Moreover, as electrons are much lighter and faster than the lattice atoms forming the metallic substrate, the latter ones do not become directly excited in the first instance. This leads to both electronic and lattice subsystems being out of thermal equilibrium after the laser excitation. Hot electrons are considered to thermalize on time scales of the order of  $\sim 100$  fs [32, 236, 237]. This has been observed with pump-probe photoemission experiments [236, 238, 239, 240, 241, 242, 243, 244].

Once the hot electron distribution has thermalized, excited electrons continue scattering with the atomic lattice of the metal. This leads to the coupling of the electronic subsystem and the atomic lattice, and to the subsequent excitation of phonons on the latter one. Hence,  $T_e$  drops and the lattice temperature  $T_l$  rises until both electronic and phononic subsystems thermally equilibrate with a temperature  $T_1 > T_0$ . Due to the larger mass and smaller heat capacity of an atom with respect to an electron, the lattice does not reach maximum temperatures as large as photoexcited electrons,  $T_{l,\text{max}} < T_{e,\text{max}}$ . Depending on the atomic heat capacity and the intensity of the electron-phonon coupling constant  $g$ ,  $T_{l,\text{max}}$  can vary within the scale of  $\sim 100$  to  $\sim 1000$  K. Thermal equilibrium in the metal is reached after a time scale  $\tau_{e-l} \sim 1/g$ . Afterwards, both the electron distribution and the lattice continue to cool until the metal substrate recovers its original temperature  $T_0$ .

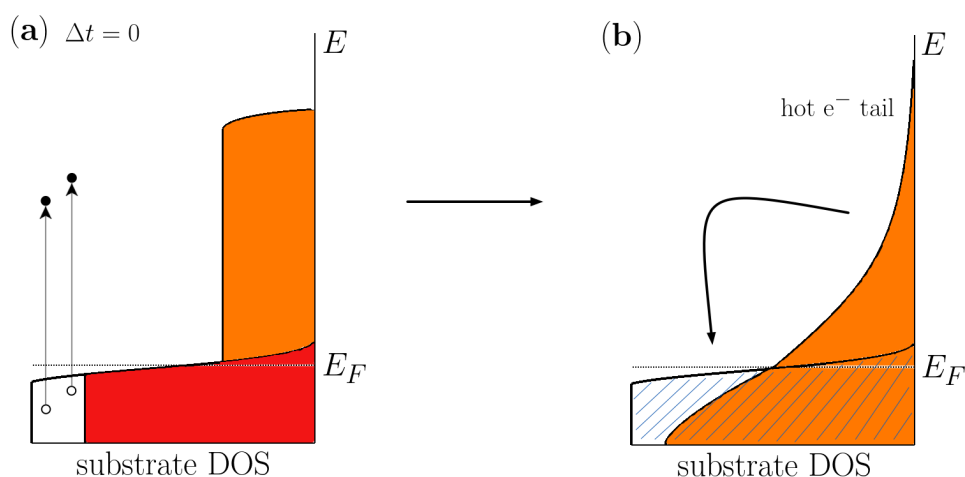


**Figure 3.3:** Electronic density of states for a metal substrate that is excited with a femtosecond laser pulse. (a) Right after the laser pulse reaches the substrate ( $\Delta t = 0$ ), electrons (black dots) are excited from lower energy states below the Fermi level  $E_F$  to higher energy states, creating a nonequilibrium distribution of electrons (orange area) that deviates from the original, Fermi-Dirac one, part of which is shown in red. This hot electron distribution cannot be characterized by an electronic temperature  $T_e$ . (b) Subsequent relaxation process of the electron distribution due to electrons redistributing their energy by scattering with other electrons and the adsorbates, if present. This leads to the distribution thermalizing to a Fermi-Dirac one with a tail of higher energy states above  $E_F$ , depicted in orange, with a well defined  $T_e$ . Meanwhile, the system seeks to return to thermal equilibrium, and the electronic density of states evolves towards regaining the Fermi-Dirac equilibrium distribution (shaded region).

The aforementioned thermodynamics of a metal surface was experimentally observed in different metals such as Au and Cu [245, 246, 247]. Preliminary theoretical work on this framework started in 1957, with the paper of Kaganov *et al.*, but with a more general scope [248]. It was not until 1974 when Anisimov *et al.* first considered the model by Kaganov *et al.* to describe incident laser-triggered diffusion of heat flow between electronic and phononic subsystems during the nonequilibrium stage under the name of 2TM [50]. This model is one of the possible solutions of the Boltzmann transport equation for electrons, namely the parabolic two-step model, as formally proved for the first time some time later by Qiu and Tien [249]. Other possible solutions for describing the heat diffusion between electrons and phonons after subpicosecond laser excitation can be derived from the transport equation as well [249], but their description is beyond the scope of this Thesis. Returning to Anisimov 2TM, thermodynamics of the nonequilibrium surface is encompassed in two equations of state which describe the dynamics of the heat fluxes inside each electronic (Eq. (3.1)) and phononic subsystem (Eq. (3.2)):

$$C_e(T_e) \frac{\partial T_e}{\partial t} = \nabla_z [\kappa_e(T_e) \nabla_z T_e] - g(T_e - T_l) + S(z, t), \quad (3.1)$$

$$C_l(T_l) \frac{\partial T_l}{\partial t} = g(T_e - T_l). \quad (3.2)$$

Let us describe both equations. Positive and negative signs indicate heat flux gains into and losses from the subsystem, respectively.  $C_i$  ( $i \equiv e, l$ ) is the heat capacity of electrons and phonons, respectively. The right-hand side of Eq. (3.1) contains three terms. The first describes the diffusion of heat from the surface to the bulk of the solid and depends on electronic thermal conduction  $\kappa_e$ . The middle term accounts for the electronic energy dissipation in the lattice and is proportional to the electron-phonon coupling constant  $g$  and the temperature difference between the electron and phonon baths.  $S(z, t)$  is the source term, which corresponds to the subpicosecond laser excitation power absorbed by the surface in the time unit. Equation (3.2) is much simpler, as it only contains the photoexcited electron-incoming energy contribution through electron-phonon coupling.

Source term takes the following expression:

$$S(z, t) = \frac{1 - \Gamma_{\text{ref}}}{\delta} I(t) \exp\left(-\frac{z}{\delta}\right), \quad (3.3)$$

where the surface specific parameters  $\Gamma_{\text{ref}}$  and  $\delta$  are the reflectivity coefficient and the optical penetration depth, respectively, whereas  $I(t)$  is the time-dependent incident laser intensity. Here, the dependence of  $\Gamma_{\text{ref}}$  and  $\delta$  on  $T_l$  is discarded [249],

an approximation which breaks down for laser wavelengths shorter than visible ones [250, 251].  $I(t)$  contains laser pulse-specific parameters such as its shape, wavelength, and fluence.

The following assumptions are made when solving Eqs. (3.1) and (3.2). First,  $C_l$  is calculated from a Debye model and for a metal surface of constant volume of Debye temperature  $T_D$ ; this means that  $C_l \propto (T_l/T_D)^3$  for  $0 < T_l \leq 0.1 T_D$  and becoming a parameter,  $C_l = 3Nk_B$  for  $T_l \gg T_D$  (with  $N$  the number of atoms in the surface and  $k_B$  the Boltzmann constant) [252, 253].  $C_e$  is taken to depend linearly on  $T_e$ , with a proportionality constant  $c_e$ , so that  $C_e(T_e) = c_e T_e$  [32]. The diameter of the experimental laser beams is typically of the order of 10–100  $\mu\text{m}$ , which is some orders of magnitude larger than the mean free path or penetration depth of the electron into the surface, and the penetration depth of optical heat  $\delta$  (both of  $\sim 10$ – $100$  nm) [254]. Consequently, the metallic surface is assumed to be uniformly irradiated, thus there exists isotropy in the temperature distribution in each plane orthogonal to the vertical axis  $z$  and no lateral heat diffusion in each of the  $x$  and  $y$  axis of the surface plane [249]. This means that the temperature gradients in  $x$  and  $y$  are neglected and the heat transfer problem becomes spatially one-dimensional on the orthogonal axis  $z$ , therefore appearing only as a partial derivative with respect to  $z$ ,  $\nabla_z \equiv \partial/\partial z$ . Moreover, Eq. (3.2) should actually have an extra right-hand side summand: a phonon thermal diffusion term which incorporates the heat transference by phonon-phonon scattering,  $\nabla_z[\kappa_l(T_l)\nabla_z T_l]$ , proportional to the phonon conductivity  $\kappa_l$ . This contribution is neglected in the original 2TM [50], as hot electron velocities are around  $\sim 10^6$  m/s, near the Fermi velocity value, whereas phonons move at much smaller sound speed,  $\sim 10^3$  m/s, therefore being phonon-phonon diffusion a non-existent process from the point of view of excited electrons. In other words, the phonon-phonon thermal diffusion time scale is much slower than the electronic energy input into the lattice. Electronic heat conductivity depends linearly on the temperatures of each bath, that is,  $\kappa_e(T_e) \simeq \kappa_0(T_e/T_l)$ , where  $\kappa_0$  is the electronic heat conductivity in thermal equilibrium; for this formula, the Sommerfeld expansion up to first order has been taken into account [255, 256]. Examples of the electronic and lattice temperatures calculated with 2TM for a Pd surface irradiated with laser pulses of different fluences are shown in Fig. 3.4.

Using Anisimov's 2TM requires some caution to be taken.  $C_e \propto T_e$  is valid in the temperature range  $0 < T_e \leq 0.1 T_F$ , with  $T_F$  being the Fermi temperature of the metal; for higher temperatures,  $C_e$  approaches the constant value capacity of an ideal electron gas. Moreover, the  $\kappa_e$  formula written in the previous paragraph holds for temperatures  $T_D < T_e \leq 0.1 T_F$ . In order to explore other temperature ranges, more general expressions for  $C_e$  and  $\kappa_e$  are required; a proposal for such an extension takes the mean kinetic energy per electron, the chemical potential

and the electronic density of states as a basis for a quantum model to analytically evaluate these quantities [254]. Indeed, 2TM demands that each of the electronic and phononic distributions of states be in local equilibrium, so that both subsystems have well-defined temperatures. This means that the electron–electron and phonon–phonon scattering times  $\tau_{ee}$  and  $\tau_{ll}$  (or equivalently the electron and phonon relaxation lifetimes) need to be smaller than the electron–phonon scattering time  $\tau_{el}$ , in order to preserve the respective Fermi–Dirac and Bose–Einstein distributions and thus their well-defined temperatures. If this picture fails, energy transfer from hot electrons to lattice would take place before the electron distribution having thermalized. As some experimental works point out, the electron–electron scattering time scale  $\tau_{ee}$  could be comparable to the characteristic time for electron–phonon scattering  $\tau_{el}$  particularly for electrons close to the Fermi level in some systems, which could be a scenario where the Anisimov formulation breaks down [257]. Anyway, this risk could be avoided by using enough high laser fluences, as hinted for Au [239, 240], and could be even more difficult to happen for some metals with a high density of electronic states close to the Fermi level [32], such as Pt, Pd, W and Ru [258]. 2TM also does not cover the effect of nonthermalized electrons on the hot electron distribution. Through resonance of these electrons with certain energy levels of adsorbates, a wavelength dependence of a given photochemical reaction outcome of the adsorbate–substrate system can be introduced. This phenomenon was detected in some systems such as  $O_2 + CO/Pt(111)$  [259, 260],  $O_2/Pt(111)$  [219] and  $D_2 + O/Ru(001)$  [244]. In particular, in the latter referenced system, a lower internal energy density of the Ru(001) substrate is observed compared to the theoretical calculation from Anisimov’s 2TM, motivating a proposal for refining the 2TM to address these types of theoretical inconsistencies. Apart from these considerations, however, this formulation of 2TM with no extra complication has been successfully applied for studying subpicosecond laser excitation of metal substrates with and without adsorbed species in a number of systems, including the ones studied in this Thesis.

As a final comment, the coupling of both surface-linked heat baths to the adsorbate prior to its desorption implies the existence of an additional thermal reservoir within the adsorbate. Therefore, one can define an adsorbate temperature  $T_{ads}(t)$ , and incorporate an additional equation into the macroscopic thermal description, giving rise to a three-temperature model (3TM) [16]. Although our research remains at the 2TM level, a simple proposal of this third equation for a system where electronic coupling to the adsorbate kinetic DOFs dominates over the phononic one is as follows [261]:

$$\frac{\partial T_{ads}}{\partial t} = \eta_e (T_e - T_{ads}), \quad (3.4)$$

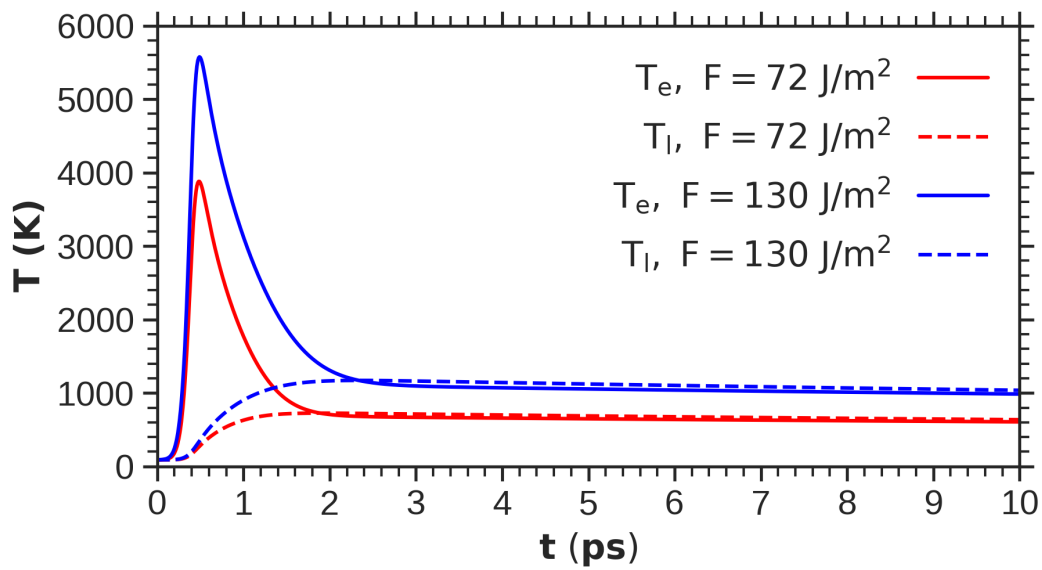


**Figure 3.4:** Time evolution of the electronic temperature  $T_e$  (solid curves) and lattice temperature  $T_l$  (dashed curves) calculated with 2TM for incident femtosecond pulses of sech shape centered at  $t = 0.41 \text{ ps}$ , full width at half maximum (FWHM) equal to  $100 \text{ fs}$ , wavelength  $\lambda = 780 \text{ nm}$ , and surface absorbed fluences,  $F = 72 \text{ J/m}^2$  (red curves) and  $F = 130 \text{ J/m}^2$  (blue curves).

being  $\eta_e$  the coupling constant between the adsorbate and electronic subsystems, also called electronic friction (Section 3.2.2). Analogously, if the lattice contribution to  $T_{ads}(t)$  is to be considered, a lattice-adsorbate coupling  $\eta_l$  would also need to be taken into account. Anyway, as reasoned before, for the present Thesis the macroscopic description given by 2TM is considered, and 3TM models are not further considered. A schema of the photoinduced desorption process in metals can be found in Fig. 3.5.

### 3.2.2 Dynamics on adsorbates

Now that we have seen how the surface reacts macroscopically to the incident femtosecond laser pulse, let us explore how this process affects adsorbates, leading them to desorb, among other chemical processes.

#### 3.2.2.1 Classical approach for dynamics

Before we move on to adsorbate dynamics characterization, it is necessary to clarify one point. As we are dealing with atoms, a straightforward way of thinking is that their dynamics has to be determined only solving time-dependent Schrödinger equation, thus requiring the quantum mechanics approach. Classical mechanics would be ruled out as a valid framework at this scale. However, as we discussed in Section 2.2, no exact quantum solution for any atomic or molecular dynamics is available with the sole exception of the hydrogen atom. Therefore, one would be interested in treating many-body systems with atoms and/or molecules with several degrees of freedom using classical dynamics, so that no quantum effects complicating their dynamical description would need to be taken care of. One can look for some correspondence rules between quantum and classical regimes. A good example of such a rule is provided by a well-known quantum mechanical result, Ehrenfest theorem [262], as it links time derivatives of expectation values of quantum observables to Newton classical equations of motion:

$$\frac{d\langle\mathbf{R}\rangle}{dt} = \frac{1}{m}d\langle\mathbf{P}\rangle, \quad (3.5)$$

$$\frac{d\langle\mathbf{P}\rangle}{dt} = -\langle\nabla V(\mathbf{R})\rangle, \quad (3.6)$$

with  $\mathbf{R}$  and  $\mathbf{P}$  being, respectively, the position and momentum operators of a particle of mass  $m$  in a potential  $V(\mathbf{R})$ . The key point is that, for atomic wavefunctions localized enough at the corresponding atomic nucleus, solving quantum observables as classical quantities is equivalent – up to some negligible error – to solve them



with quantum mechanics, i.e., using time-dependent Schrödinger equation. The heavier the atomic nucleus considered becomes, the more localized the atomic wavefunction will be at its nucleus, and the smaller the associated quantum effects will become. As even for H-decorated surfaces no significant differences between classical and quantum-based characterizations have been found elsewhere [263, 264], this ensures the safeness of treating atomic nuclei such as the ones handled in this Thesis (C, O and Pd) as classical particles from a microscopic perspective. As a result, computational simulations can be used to solve dynamics of these quantum systems treated as classical ones, with some time step one can set according to the computational power available and looking for a certain accuracy requirement.

### 3.2.2.2 Adsorbate dynamics and the local density friction approximation

The question now is how to theoretically characterize the energy processes that involve the adsorbate. If one considers DIMET, one needs to calculate the quantum probability amplitudes of the transition between ground and excited PESs using Fermi Golden Rule-like expressions, as determination of the full excited-state PES of a given system is not feasible. Quantum effects such as state quantization, including zero-point, interference, and tunneling can appear in such treatments. Moreover, exiting adiabaticity means that each electronic configuration-linked PES should be calculated [265]. Aspects like these difficult the way desorption process can be handled theoretically, and more precisely with computational dynamics simulations. Tully and collaborators provided a neat workaround for this using a generalized Langevin model [266, 267, 268] to substitute unwanted degrees of freedom in a classical formalism by stochastic and friction forces, which ended up in the *molecular dynamics with electronic friction* framework [265, 269, 270]. Quantum nonadiabaticity brought by electron-hole excitations can be replaced by a classical molecular dynamics model where energy transfer from excited electron-hole pairs to adsorbates transforms into a random force, while the converse is represented by an electronic friction on the adsorbed nuclei (see Ref. [270] for the full proof). Electron-driven transitions to the excited states for each adsorbate are modeled only on the basis of the ground-state PES, as ladder-climbing processes, so that no knowledge of the excited-state PES is required.

Adsorbed nuclei follow then generalized Langevin equations:

$$M_i \frac{d^2 \mathbf{R}_i}{dt^2} = -\nabla_{\mathbf{R}_i} V(\{\mathbf{R}_m\}) - \eta_e \frac{d\mathbf{R}_i}{dt} + \mathcal{R}_{e,i}(t), \quad (3.7)$$

where each nucleus  $i$  of mass  $M_i$  is located at  $\mathbf{R}_i$ . The first term on the right hand side of Eq. (3.7) is the adiabatic force due to the internal potential  $V(\{\mathbf{R}_m\})$  of the ground

state produced by the  $N_m$  atoms (adsorbates and substrate-constituent) of the system at some time  $t$ . The central right term is the dissipation force, proportional to the electronic friction constant  $\eta_e$  (which becomes a  $d \times d$  tensor for  $d > 1$  degrees of freedom). The rightmost term contains the random force  $\mathcal{R}_{e,i}(t)$ , which is not proportional to the atomic velocities. These stochastic forces, which are related to the friction ones through the fluctuation-dissipation theorem, act in the system as Gaussian white noise, so their average is  $\langle \mathcal{R}_{e,i}(t) \rangle = 0$  and their variance is [270],

$$\text{Var}[\mathcal{R}_{e,i}(t)] = \frac{2k_B T_e \eta_e}{\Delta t}. \quad (3.8)$$

Here  $k_B$  is the Boltzmann constant and  $\Delta t$  is the integration time step.

Let us discuss how  $\eta_e$  can be determined. Here we use the local density friction approximation (LDFA) [51, 52]. This is a simple, computationally low-cost way of evaluating the friction coefficient as a function of atomic position, and at the same time able to accurately describe the main physical features of electronic excitations incorporated into an adiabatic, multidimensional adsorbate-substrate PES. In this respect, suppose that the electronic density at each point of the surface is known, particularly at the position at which each adsorbed atom is located. Then, according to LDFA the friction coefficient at a given position is taken as the one corresponding to a homogeneous FEG of density equal to the local surface density at that point.

How is then friction evaluated in the homogeneous FEG framework? To begin with, the idea is to picture the metal as a homogeneous gas composed by free-moving electrons and a background positive charge density playing the role of atomic nuclei. Let us consider a given positive ion or atomic nucleus (projectile or adsorbate) of charge  $Z$  appearing in such system. It would enter as a perturbation in the FEG, generating an attractive electrostatic potential in its vicinity and an induced screening electronic density  $n(\mathbf{R})$ . These electrons exert a stopping force retarding the ion movement per length unit. To evaluate exactly both time-dependent screening electronic density and stopping force time-dependent density functional theory (TDDFT) is required. However, if the adiabatic limit is taken and the surface considered is metallic, TDDFT calculation of both parameters can be replaced by simply solving the time-independent KS equations, as proved elsewhere [271]. Such static DFT calculation poses an evident simplification to the description of friction inside the HEG produced by metal atoms. Adiabatic scenario would correspond to have enough small relative speed of the ion with respect to the surrounding electrons,  $v_{ion-e}$ , so that the potential it creates in the electron gas changes slowly.

Summarizing, an atomic nucleus moving inside a homogeneous FEG slow enough with respect to the electrons surrounding it experiences a stopping force linearly

proportional to its velocity, and related to the density of the FEG as follows:

$$\mathbf{F}_S(\mathbf{v}_i) = -n_{FEG} k_F \sigma^T(k_F) \mathbf{v}_i, \quad (3.9)$$

where  $k_F$  is the Fermi momentum of the FEG and  $\sigma^T$  is the transport cross section of the nucleus at Fermi level, which contains the perturbative effect of the atom on the FEG.  $\sigma^T$  is computed as an expansion of the quantum scattering phase shift contributions at Fermi level  $\delta_l(k_F)$  to the FEG wavefunction in each order of the orbital angular momentum  $l$ . Its expression is as follows (more details on its derivation can be found in well-known quantum mechanics books such as Refs. [113, 272]):

$$\sigma^T(k_F) = \frac{4\pi}{k_F^2} \sum_{l=0}^{\infty} (l+1)^2 \sin[\delta_l(k_F) - \delta_{l+1}(k_F)]. \quad (3.10)$$

Phase shifts arise due to the scattering potential created by the atomic nucleus inside the FEG that affects the electrons near the nucleus. Such shifts reflect the change in phase on the radial part of each  $l$ -th partial wave due to entering and later exiting the potential region, and do not appear in the radial part of a free spherical wave due to the scattering potential being zero in the latter case [272]. Such a potential is assumed to be radial, i.e., spherically symmetric around the external nucleus. Only the first orders of  $l$  in Eq. (3.10) have noticeable contributions to the transport cross section, and higher order terms can be safely neglected [273].

Phase shifts at the Fermi level are calculated from a DFT atomic scattering potential considering frequently LDA for the exchange and correlation part. This is valid for most atoms embedded in a FEG. It is equally true that atoms with not completely filled valence orbitals (i.e., open-shelled) inside low-density regions of a FEG experience spin polarization effects, so that whether the DFT scattering potential determination of such atoms is done with LDA or LSDA, some differences appear in the local electronic friction on these atoms. Such spin-mediated corrections to LDA are very small and therefore often neglected for the usual atoms considered in surface femtochemistry. In the case of C atoms there is a sizable effect on the local friction at low densities, whereas for O atoms the friction coefficients calculated with either LDA and LSDA are basically equal [274]. In this Thesis we have indistinctively employed both approaches, the LDA values in the molecular dynamics with electronic friction (MDEF) simulations of Chapters 5 to 7 and LSDA values in the ab initio molecular dynamics with electronic friction (AIMDEF) simulations of Chapter 8.

It is clear that  $\mathbf{F}_S(\mathbf{v}_i)$  can be interpreted as a friction force due to the substrate electronic subsystem on each atom  $i$ ,  $\mathbf{F}_{S,i}(\mathbf{v}_i) = -\eta_{e,i}(R_i)\mathbf{v}_i$ , with a position-dependent

electronic friction coefficient as follows [271, 275, 276]:

$$\eta_{e,i}(\mathbf{R}_i) = \frac{4\pi n_{FEG}(\mathbf{R}_i)}{k_F} \sum_{l=0}^{\infty} (l+1)^2 \sin(\delta_l(k_F) - \delta_{l+1}(k_F)). \quad (3.11)$$

If adsorbed or projectile molecules are involved, correlation effects between their constituent atoms are neglected, which is achieved by treating them as independent atoms. This additional simplification is called independent atom approximation (IAA) [51].

On the basis of the original MDEF proposal of Tully's group as in Eq. (3.7) [270], it has become clear that LDFA provides a powerful enhancement to that approach. Adsorbate dynamical description in a MDEF model with LDFA can be further refined in order to provide a more accurate description of femtosecond laser-induced phenomenology. This is achieved by incorporating to the random force of (3.7) a dependence with the instantaneous electronic temperature  $\mathcal{R}_e \propto T_e(t)$ . The random force is now calculated at each time step according to the  $T_e(t)$  provided by the 2TM for the system under study (Section 3.2.1) [66]. In this MDEF framework, on each  $i$ -th adsorbate the following Langevin equations hold,

$$M_i \frac{d^2 \mathbf{R}_i}{dt^2} = -\nabla_{\mathbf{R}_i} V(\{\mathbf{R}_m\}) - \eta_{e,i}(\mathbf{R}_i) \frac{d\mathbf{R}_i}{dt} + \mathcal{R}_{e,i}[T_e(t), \eta_{e,i}(\mathbf{R}_i)], \quad (3.12)$$

where the effect of hot electrons on the adsorbed species comes from the electronic friction term of Eq. (3.11). As before, both electronic friction and random forces are related through the fluctuation-dissipation theorem, and  $\mathcal{R}_{e,i}$  is modeled by a Gaussian white noise with variance,

$$\text{Var}\{\mathcal{R}_{e,i}[T_e(t), \eta_{e,i}(\mathbf{R}_i)]\} = \frac{2k_B T_e(t) \eta_{e,i}(\mathbf{R}_i)}{\Delta t}. \quad (3.13)$$

### 3.2.2.3 Contribution of phononic excitations

It remains to be clarified how surface phonons affect the adsorbates in MDEF. In the context of simple six-dimensional PESs for single diatomic adsorbates, a preliminary proposal suggested modeling the effects of surface temperature on the adsorbates with the generalized Langevin oscillator (GLO) thermostat [53, 54, 55, 56]. In this respect, adsorbates undergo Langevin dynamics and experience thermal fluctuation and friction forces due to the coupling to the lattice atoms, which are assumed to move synchronously. This method was employed to study the photoinduced desorption of O<sub>2</sub>/Ag(110) [45, 46] and CO/Ru(0001) [47, 48]. However,

this approach carries an important limitation with, as distortion of the surface at the atomic level is not adequately covered. Such effects can noticeably affect the outcome of chemical reactions undergone by adsorbates, as found, for instance, in the dissociation of  $N_2$  on W(110) [277, 278] at 800 K and, therefore, are expected to be particularly relevant at the high temperatures reached by the surface after laser excitation. As a result, describing each surface atom movement independently from its slab neighbors becomes necessary to provide a more accurate dynamical description of the system.

An alternative strategy requires the surface to be at thermal equilibrium. This is achieved with thermalization of the surface to some initial temperature prior to laser excitation, i.e., at  $t = 0$ , from which a set of initial velocities for the substrate atoms is determined. Then, part of the slab is coupled to a thermostat that keeps its temperature at a constant, nonfluctuating value for each time. Controlling the temperature of the involved substrate layer(s) so that it follows accurately a 2TM provides the energy transfer channel to adsorbates due to the substrate lattice, which also contributes to chemical processes such as their desorption [62]. Among different thermostats one can choose according to their features (see, e.g., Ref. [279] for some examples), a true canonical ensemble can be reproduced coupling at least part of the surface slab to the Nosé-Hoover (NH) thermostat, first proposed by Nosé [280] and later reformulated in a simpler way by himself and Hoover separately [281, 282]. Ensuring the canonicity of the atomic system implies that the surface layers coupled to the NH thermostat have a well-defined, nonfluctuating temperature at each time, given by the 2TM.

The idea is to extend the subsystem of the mentioned surface layers to an additional, artificial degree of freedom: the thermal reservoir coupled to them. The thermostat is then represented by a fictitious dynamical variable  $s > 0$  acting as a time-scaling quantity, which stretches the ordinary time scale  $t$  into a fictitious one  $t_s$  as  $dt_s = s dt$ . There is also a fictitious velocity  $\dot{s} = ds/dt$ , as well as a fictitious reservoir "mass"  $Q > 0$ , with units  $[Q] = [E] \times [t]^2$ . Positions of the surface atoms are the same for real and fictitious times, but remaining time-dependent quantities such as velocity get modified in terms of  $s$  for the thermostat. From a Lagrangian or Hamiltonian approach, and in NH formulation, one can arrive, for a subsystem of  $N_j$  surface atoms coupled to the thermostat, at the following dynamical equations [279]:

$$M_j \frac{d^2 \mathbf{R}_j}{dt^2} = -\nabla_{\mathbf{R}_j} V(\{\mathbf{R}_m\}) - M_j \frac{d\mathbf{R}_j}{dt} \xi \left[ T_l(t), \frac{d\mathbf{R}_j}{dt} \right], \quad (3.14)$$

$$\frac{d\xi}{dt} = \frac{1}{Q} \left( \sum_j M_j \left| \frac{d\mathbf{R}_j}{dt} \right|^2 - 3N_j k_B T_l(t) \right). \quad (3.15)$$

Here, each atom  $j$  has a mass  $M_j$  and is placed at  $\mathbf{R}_j$ , and  $\xi = sp_s/Q$  is the thermodynamic friction coefficient of the NH thermostat, proportional to the artificial mass, the time-stretching parameter and the fictitious momentum  $p_s = Q dr_s/dt_s$ . In Nosé formulation, time evolution of  $s$  is described with a second order equation analogous to a harmonic oscillator [279]. As a consequence of this, nearly periodic fluctuations in the kinetic temperature of the thermostat-coupled surface atom  $\langle T \rangle = (3N_j k_B)^{-1} \left\langle \sum_j M_j \left| \frac{d\mathbf{R}_j}{dt} \right|^2 \right\rangle$  occur around the thermostat temperature, equal to the macroscopic surface temperature  $T_l(t)$  computed with 2TM. The size of the thermal fluctuations depends on how small or large is  $Q$ ; its positivity implies that the atomic ensemble considered is canonical, but some care needs to be taken when choosing its value. So, too small values of  $Q$  (strong coupling) originate too ample high-frequency temperature oscillations, whereas for large  $Q$  values (weak coupling) a canonical distribution for the system is attained only after very long simulation times. In the limit case  $Q \rightarrow \infty$  one recovers a microcanonical ensemble. A reasonable choice to fix  $Q$  is to choose a value such that the temperature oscillation frequency is approximately the same as the characteristic resonance frequency of surface atomic species (see Ref. [279] for more details).

If we look at the right hand side of Eq. (3.15), action of the thermostat on the surface layers can be easily identified according to the sign of  $d\xi/dt$ . If  $\langle T \rangle < T_l(t)$ , that is, the average kinetic temperature of the thermostat-coupled atoms is below the thermostat temperature, then  $(d\xi/dt) < 0$  and the rightmost force term of Eq. (3.14) becomes bigger with time, so heat is extracted from the NH thermal bath and plunged into the surface atoms. This raises the average temperature of the latter. Reversely, when the topmost layers surface atoms become hotter than the thermostat,  $\langle T \rangle > T_l(t)$ , so  $(d\xi/dt) > 0$  and its force contribution to Eq. (3.14) decreases with  $\xi$ , thus heat being removed from the surface atoms into the reservoir and atoms becoming colder.

Both Eqs. (3.14) and (3.15) are then solved for each time step of the dynamics simulation. This can be done in the stretched time scale in uneven time intervals  $\Delta t_s$  following original Nosé approach [281], or in a simpler, equally sized, even time interval  $\Delta t$  formulation as done above following Nosé and Hoover simplification [280, 282].

At this stage, the MDEF surface representation is completed by introducing a transition region consisting of one or more layers between the hotter, thermostat-coupled upper layers and the unheated inner bulk. These intermediate  $N_k$  lattice

atoms are described just adiabatically so that they evolve according to classical Newton equations of motion:

$$M_k \frac{d^2 \mathbf{R}_k}{dt^2} = -\nabla_{\mathbf{R}_k} V(\{\mathbf{R}_m\}), \quad (3.16)$$

for each atom  $k$  of mass  $m_k$  and position vector  $\mathbf{R}_k$ . The innermost layers are kept frozen all the time, hence modeling a thermal gradient towards the inner bulk.

### 3.2.2.4 Calculation of adiabatic forces: ab initio molecular dynamics with electronic friction

As we have seen, nonfrozen atoms experience, in all cases, adiabatic forces. If they are evaluated on-the-fly at each integration time step, one talks about AIMDEF [57]. Ab initio force calculation is carried out within DFT using the Hellmann-Feynman theorem [283, 284]. According to this theorem, the energy derivatives with respect to a given parameter are equal to the expected value of the derivative of the Hamiltonian with respect to that parameter. In other words, at each  $t$  adiabatic forces acting on atom  $i$  are computed from electronic Hamiltonian  $H_e$  (recall Section 2.2) as follows:

$$\begin{aligned} \mathbf{F}_{ad,i}(t) &= -\nabla_{\mathbf{R}_i} V(\{\mathbf{R}_m\}) \\ &= -\langle \varphi(\{\mathbf{R}_m\}, \{\mathbf{r}_j(t)\}) | \nabla_{\mathbf{R}_i} H_e(\{\mathbf{R}_m\}, \{\mathbf{r}_j(t)\}) | \varphi(\{\mathbf{R}_m\}, \{\mathbf{r}_j(t)\}) \rangle. \end{aligned} \quad (3.17)$$

As a reminder,  $|\varphi(\{\mathbf{R}_m\}, \{\mathbf{r}_j(t)\})\rangle$  is the electronic wavefunction obtained at a given time by solving the KS equations. This wavefunction depends on a set of occupied KS orbitals (Eq. (2.63)). The system electrons are located in the set of positions  $\{\mathbf{r}_j\}$  and the atomic nuclei positions  $\{\mathbf{R}_i\}$  enter as time-independent parameters.

Now, the notion of AIMDEF can be further enhanced according to which kind of energy transfer mechanisms to the adsorbate are incorporated in the simulations. Three possible methodological scenarios can be contemplated. If the phononic energy input is suppressed by imposing all surface atoms to remain frozen, we can talk of  $T_e$  – AIMDEF. Next, leaving aside the electronic contribution by setting the friction coefficients on the adsorbates equal to zero and thus accounting solely the lattice-driven energy input through a thermostat happens in  $T_1$ –AIMDEF. Finally, in  $(T_e, T_1)$  – AIMDEF both nonadiabatic effect of laser-heated metal electrons through the Langevin equation (3.12) and the lattice contribution of the atoms coupled to a thermostat to the adsorbate excitation are considered. The allowance of both energy channels into the adsorbates, or the hindrance of one, is highly valuable

for determining how significant is the contribution of each energy channel to the femtochemical processes on surfaces [31, 63].

In this respect, the next pertinent question is how to evaluate the surface electronic density  $n_{sur}(\mathbf{R})$  in order to determine the electronic friction (recall that in LDFA,  $n_{sur}(\mathbf{R}) = n_{FEG}(\mathbf{R})$ ). In AIMDEF, bare surface electronic density was originally approached to the self-consistent DFT calculation of the electronic density produced by the bulk of frozen surface atoms at each position,  $n_{sur}(\mathbf{R}) = n_{sur}^{FS}(\mathbf{R})$ , with the superscript FS standing for frozen surface [57]. This approximation works properly in the case where surface atoms move negligibly with respect to their respective equilibrium positions or remain at them directly during dynamics [57, 58]. In this case, neither remarkable surface profile deformation nor a subsequent large electronic charge redistribution on the surface arises. Such a frozen surface scenario does not happen in general. Instead, surface atoms do not remain close enough to their equilibrium positions during whole dynamics and therefore non-negligible electronic charge redistribution effects can happen, so  $n_{sur}^{FS}(\mathbf{R})$  is no more time-constant, i.e.,  $n_{sur}(\mathbf{R}) \rightarrow n_{sur}(\mathbf{R}, t)$ . For this usual scenario, two valid approaches for evaluating time-dependent surface electronic density have been formulated in the AIMDEF context [60]:

- **Superposing density:** Within AIMDEF, the first proposed simpler improvement to evaluate the electronic density of moving surface atoms is additive on the basis of a superposition principle [60]. More precisely, we start from the ground-state electronic density each individual atom of the substrate  $j$  would create at a given  $t$  and  $\mathbf{R}_i$  if being isolated from the rest of lattice atoms at some position  $\mathbf{R}_j$ . Total density contribution of the atomic sum  $n_{sur}^{AS}(\mathbf{R}_i, t)$  then comes from superposing all individual densities created by the  $N_s$  surface atoms, i.e.,

$$n_{sur}^{AS}(\mathbf{R}_i, t) = \sum_{j=1}^{N_s} n_j^{\text{atom}}(\mathbf{R}_i, t). \quad (3.18)$$

This definition better characterizes the evolution of the electronic charge density for moving lattice atoms interacting with single adsorbate or projectile atoms. However, such method comes with a limitation. The method does not consider the charge redistribution that occurs when surface atoms form bonds between each other. When atoms bond together, electrons may be transferred or rearranged, leading to changes in the electron density around each of the bonded surface atoms. Plain superposition of surface atom densities just misses this charge redistribution effect.

- **Hirshfeld partitioning:** An alternative approach that overcomes the latter limitation [59, 60, 61], thus being used for the systems considered in this Thesis. Among the different available schemes for decomposition of molecules into their constituent atomic subsystems by the electronic density (e.g., the proposals of Politzer [285] and Bader [286, 287]), this way of calculating the density takes as a basis the Hirshfeld partitioning scheme [288]. The key idea is to subtract from the DFT self-consistent calculation of the density of the adsorbate-surface system  $n^{SCF}(\mathbf{R}_i, t)$  the contribution solely due to the electronic density around the adsorbate atoms at each time. Hence, electronic density computed in the dynamics becomes:

$$n_{sur}^H(\mathbf{R}_i, t) = n^{SCF}(\mathbf{R}_i, t) \left[ 1 - \sum_{n=1}^{N_a} w_n(\mathbf{R}_i, t) \right], \quad (3.19)$$

$$w_n(\mathbf{R}_i, t) = \frac{n_n^{\text{atom}}(\mathbf{R}_i, t)}{\sum_{m=1}^N n_m^{\text{atom}}(\mathbf{R}_i, t)}. \quad (3.20)$$

Here,  $N$  is the total number of atoms in the system, while  $N_a$  is the number of adsorbate atoms. Moreover, Hirshfeld weighting factor  $w_n(\mathbf{R}_i, t)$  ponderates the contribution of the  $n$ -th adsorbed or projectile atom-associated electronic density with respect to the total superposition of electronic densities of all system atoms, running  $n$  along each of the gas-phase adsorbate atoms. The index  $m$  goes along all the atoms in the system.

The three proposals for evaluating the surface bare electron density are studied comparatively in Ref. [60]. For the systems this work focuses on, involving CO and/or O adsorbed in Pd(111), there are non-negligible displacements of Pd atoms during femtosecond laser-driven dynamical processes and charge redistributes inside the lattice and also between adsorbate and substrate. For the latter, the influence of adsorbed species can even produce local distortions in the atomic arrangement of the topmost slab layers [60], as it happens in fact for Pd(111). Together, these factors motivate the use of the Hirshfeld approach in the AIMDEF calculations performed in Chapter 8.

To close this subsection, let us remark something about the computational evaluation of the AIMDEF dynamics equations and key parameters. In them, atomic positions and velocities have to be obtained as well, which is done by solving classical Newton equations of motion numerically by integration algorithms. Different integrators have been proposed, such as the Runge-Kutta [289, 290] and Verlet [291] algorithms. In this Thesis, a variation of the Verlet algorithm has been used, which is

the Beeman algorithm [292]. Instead of explicitly determining atomic positions and implicitly computing their velocities, Beeman integrator allows explicit evaluation of both quantities (recall that friction forces are proportional to atomic velocities and therefore their determination is also crucial). In its standard formulation, at a given time  $t$  the positions and velocities of the time  $t + \Delta t$ , with  $\Delta t$  being a given time step, are calculated as follows:

$$\mathbf{r}(t + \Delta t) = \mathbf{r}(t) + \mathbf{v}(t) \Delta t + \left( \frac{2}{3} \mathbf{a}(t) - \frac{1}{6} \mathbf{a}(t - \Delta t) \right) \Delta t^2 + \mathcal{O}(\Delta t^4), \quad (3.21)$$

$$\mathbf{v}(t + \Delta t) = \mathbf{v}(t) + \left( \frac{1}{3} \mathbf{a}(t + \Delta t) + \frac{5}{6} \mathbf{a}(t) - \frac{1}{6} \mathbf{a}(t - \Delta t) \right) \Delta t + \mathcal{O}(\Delta t^3). \quad (3.22)$$

being  $\mathbf{a}$  the acceleration of the atom. Beeman approach reaches an overall precision of  $\mathcal{O}(\Delta t^3)$ , which is one order of magnitude larger than the one achieved for both positions and velocities with Verlet ( $\mathcal{O}(\Delta t^2)$ ). Therefore, the Beeman algorithm is more computationally costly, but also more accurate than its Verlet counterpart. In the simulations of this work, a time step of  $\Delta t = 1$  fs has been considered.

### 3.2.2.5 PES-mediated molecular dynamics with electronic friction

Considering all its ingredients, the AIMDEF methodology provides an accurate characterization of femtosecond laser-induced desorption on adsorbate-covered substrates. However, this comes at the expense of long computation times and large computational resource requirements. As an example, simulating a dynamic of 4 ps on CO/Pd(111) takes of the order of one week to complete. These hardships can be drastically reduced if an accurate PES is available for the system, as the evaluation of adiabatic forces simplifies greatly. As the PES-mediated evaluation of adiabatic forces is not performed *ab initio* as in Section 3.2.2.4, in this case we just talk about MDEF. Regarding the adiabatic forces, as system PES is now known, Eq. (3.17) is replaced by the more straightforward expression,

$$\mathbf{F}_{ad,i}^{\text{PES}} = -\nabla_{\mathbf{R}_i} V^{\text{PES}}(\{\mathbf{R}_m\}), \quad (3.23)$$

which saves a considerable amount of computational time.

As for AIMDEF, according to which energy channel contribution/s, electron- or phonon-mediated, one wants to incorporate to dynamical simulations, one can classify the MDEF methodology into different subcategories [87, 88]. Thus, in  $T_e$ -MDEF only energy transfer due to the hot electronic subsystem is considered, whereas in  $T_1$ -MDEF electronic friction is neglected and adsorbates gain energy

only from phononic subsystem excitations. Finally, in  $(T_e, T_1)$ -MDEF both the electronic and phononic energy inputs on the adsorbed species are considered.

Direct fitting of a PES using neural networks (NNs) also brings a change in how the electronic density is determined. In the AIMDEF procedure, evaluation of  $n(\mathbf{R}_i)$  is performed on-the-fly in the same way as the Hellmann-Feynman adiabatic forces. Here, in contrast, forces are simply derived from the precalculated PES, so that the electronic density still needs to be obtained somehow in order to determine the friction coefficients. As data of AIMDEF electronic densities are available for a large amount of atomic configurations of the system at different times, this information can be interpolated to get an accurate, additive-like electronic density strictly due to the surface atoms, as in Eq. (3.18) [87]. To this end, an appropriate function or a combination of functions may be searched by trial-test. Afterwards, the electronic friction coefficients can be evaluated accordingly. This approach becomes a key aspect of the  $(T_e, T_1)$  – MDEF methodology and will be described more thoroughly in Section 5.3.

Now we have to deal with one of the central questions in this Thesis work: how one can generate a PES using NN-like approaches and check its accuracy describing photoinduced dynamics of the adsorbate-substrate system under study. To get to this point, it is necessary first to understand aspects such as what a PES is or which methods are being utilized to produce accurate PESs in chemical physics. The following chapter is devoted to clarify the latter aspects more thoroughly.

# 4

## Machine learning and surface science

---

As we have seen in the previous chapter, AIMDEF provides us with powerful tools to theoretically describe accurately photoinduced chemistry on gas-decorated surfaces. This includes particularly photodesorption from metal surfaces, such as the case of the CO desorption from Pd(111) studied in this Thesis. However, this comes with the downside of a large computational expense. For example, a 3.5 ps dynamics (hereafter also called as trajectory) elapses approximately 7 days when computed with 24 cores of a cluster node. This means that no statistically significant AIMDEF data can be produced in reasonable times: e.g., a sample of 100 dynamics requires some months in the cluster used during this Thesis. In Section 3.2.2.5 it has been explained how this bottleneck can be solved, replacing AIMDEF scheme with another valid methodology where a dynamic of 3.5 ps can be determined in a few minutes. This can be achieved with a working PES that gives the potential energy of the adsorbate-substrate photoexcited complex at each time according to previously calculated AIMDEF data, so that the latter step is unavoidable in principle. In order to determine such a PES, NN-based methods are considered; a deeper insight on this topic of increasing interest will be the main goal of this chapter.

### 4.1 Neural networks: general features and training process

NNs are clearly among the most popular advances in computation nowadays, as well as a cornerstone of what is known as machine learning (ML). Quite simply, according to their definition, NNs are groups of highly interconnected nodes called neurons or perceptrons, which form a structure that processes some input information to give an output. Artificial NNs are called that because they mimic the interconnection of neurons in the brain and the transmission of information occurring inside it. Here is a daily life example: let us suppose that someone is looking at a soccer ball. The process of figuring out that the object we are watching is a ball is not as straightforward as one may naively think. Some input information enters our brain through different sensory channels, e.g., its shape or colors through our eyes or its texture and material through our touch. Now this information is processed

by a given arrangement of neurons in the brain –the neural network– until the object with the mentioned features is determined to be a soccer ball as the output of this cognitive process. Such kind of processes can be replicated mathematically, arranging a number of nodes or neurons in different layers that are interconnected and allow transmission of numerical values between them. Once a neuron receives some output, certain mathematical operations are applied on its value and the final output is sent to neurons on the next layer until a desired output is achieved at the end of the process. This includes the generation of NN-based PESs, as we will see shortly, as some function of pure mathematical origin, as no physical first principles are involved in its construction, but just a fit of parameters.

Among other kinds of structures, the simpler ones or feed-forward NNs have a linear, single-oriented arrangement. They start with an input layer and move rightward until they reach some output layer. During this process, they traverse one or multiple intermediate layers. Each of them is composed by some not necessarily equal number of neurons that have no physical meaning, but instead give the NN more or less flexibility to fit the input-output mathematical link to a more or less complicated functional form. Each NN structure of nodes and layers, also called the NN architecture, globally describes it. For example, given a NN with 10 input nodes, two hidden layers of 15 and 40 nodes in that order, and a single output node would form a 10-15-40-1 NN or simply a 15-40 NN if we omit the input and output nodes. NN architecture has to be explored carefully according to the amount of degrees of freedom or dimensionality that one wants to fit, as choosing not enough hidden nodes or layers can result in the NN not being able to describe in detail features such as the corrugation of a PES.

Now, the way each neuron works is very interesting. Mathematically, a given target neuron  $x_i^k$  labeled with a number  $i$  and belonging to a layer  $k$  receives input information of the  $j$  neurons of previous layer  $k - 1$  in a nested way as follows [68, 293]:

$$x_i^k(\{x_j^{k-1}\}) = f_i^k \left( b_i^k + \sum_j w_{j,i}^{k-1,k} x_j^{k-1} \right). \quad (4.1)$$

More precisely,  $x_i^k$  receives a linear combination of the previous layer neurons multiplied by some numerical coefficient or weights  $w_{j,i}^{k-1,k}$ . This sum of values or incoming signals is afterwards shifted by addition of a bias value  $b_i^k$  that is nonzero and constant for all layers  $k$ . This constant is provided by a bias node connected to all neurons of the system, hidden or output, except the ones in the input layer. A mathematical transfer function  $f_i^k$ , referred to as the activation function, is subsequently applied to this linear combination. The activation function can modify

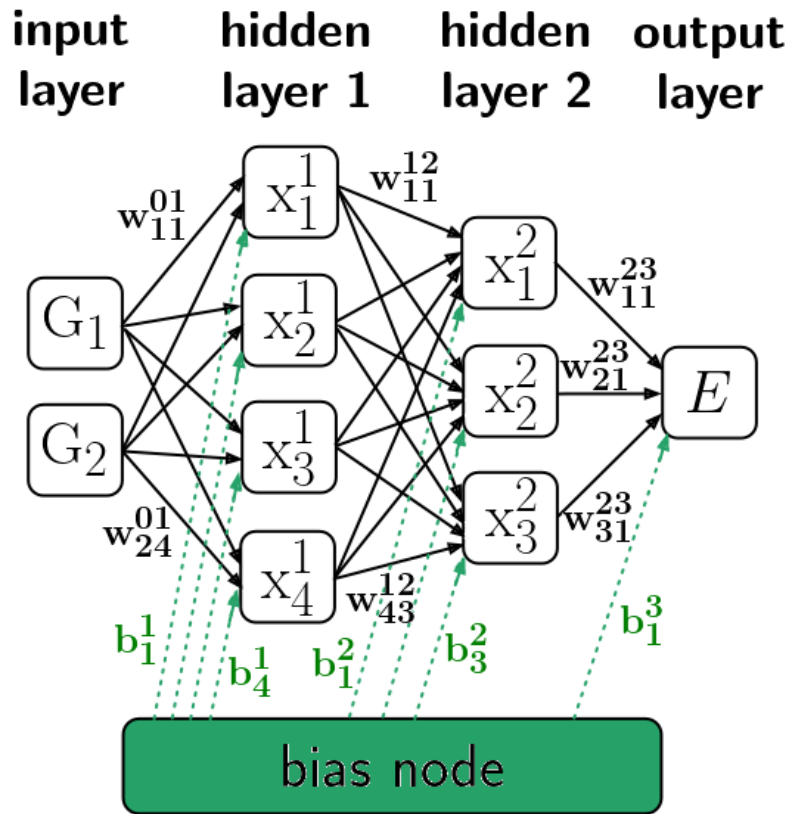


**Figure 4.1:** Example of a feed-forward NN with two hidden layers of 4 and 3 nodes, respectively. Such NN has a 2-4-3-1 architecture, or, if one regards only the hidden layers, a 4-3 one. Input layer contains two functions  $G_1$  and  $G_2$  and, after the input is processed by all  $x_i^k$  nodes, some energy  $E$  is yielded as an output. Some of the weights  $w_{j,i}^{k-1,k}$ , represented by black arrows, are pictured as an example. Here, superscript  $k$  relates to the layer number, and subscripts  $j$  and  $i$  denote the number of nodes providing some input value and receiving it, respectively. This includes the bias weights  $b_i^k$  pictured with green dashed arrows, which are fed into each non-inputting node by the bias node, also pictured in green. Bias node adds a value of 1 to each node.

the incoming numerical information by enhancing, reducing or even suppressing it (again, making use of the analogy with biological neurons, artificial ones *fire* or not) [69]. It can be of different types, from a simple linear function to more elaborate combinations of nonlinear functions, making it possible to obtain complex arbitrary expressions of the NN function. Hidden layers typically use activation functions presenting some nonlinear region and saturating for very large positive and negative input values [68], so the NN becomes capable of performing nonlinear functional fits [70, 294]. Instead, for output layer, a linear activation function is the usual choice to avoid restrictions in the output values brought by the nonlinear functions. Some typical examples of activation functions are as follows (Fig. 4.2):

$$\begin{aligned}
 f_{i,(1)}^k &= x && \text{linear function} \\
 f_{i,(2)}^k &= \frac{1}{1+e^{-x}} && \text{logistic function} \\
 f_{i,(3)}^k &= \tanh x = \frac{1-e^{-2x}}{1+e^{-2x}} && \text{hyperbolic tangent} \\
 f_{i,(4)}^k &= a \tanh bx + cx && \text{tanh + linear twist, with a, b, c} \equiv \text{constants.}
 \end{aligned}
 \tag{4.2}$$

At this point, we may better understand the importance of adding a constant bias to the sum of input signals. Addition of a nonzero bias shifts the activation function, so that it is not always forced to become zero if the incoming sum of neuron signals equals zero. This provides the target neuron with an additional degree of freedom to fit the incoming data more flexibly. To better understand this, suppose that we want to fit a set of input data points on the  $xy$  plane, among which the origin (0,0) is not included, to a linear function. If no bias was applied, the fitted line would always pass through the origin, hence becoming inaccurate.

Furthermore, Eq. (4.1) in vector form becomes,

$$\mathbf{x}^k(\mathbf{x}^{k-1}) = f^k(\mathbf{W}^k \mathbf{x}^{k-1}),
 \tag{4.3}$$

where  $\mathbf{W}^k$  is the weight matrix containing all individual weights. Fitting the set of different weights according to the input and output data leads to the construction of a mathematical function that gives the expected output for some input information. This function is something totally arbitrary, whose form is unknown to us apart from the weights. Interestingly, full knowledge of this functional form is not needed, as the only relevant thing is the input and output parts. Therefore, the NN works as a black box in this context.

Now comes the key question of how these coefficients can be determined in an appropriate way. At the beginning, the set of weights is initialized either randomly or in a directed manner [68]. Then, some input data  $\{\mathbf{x}_0\}$  is chosen in a way de-

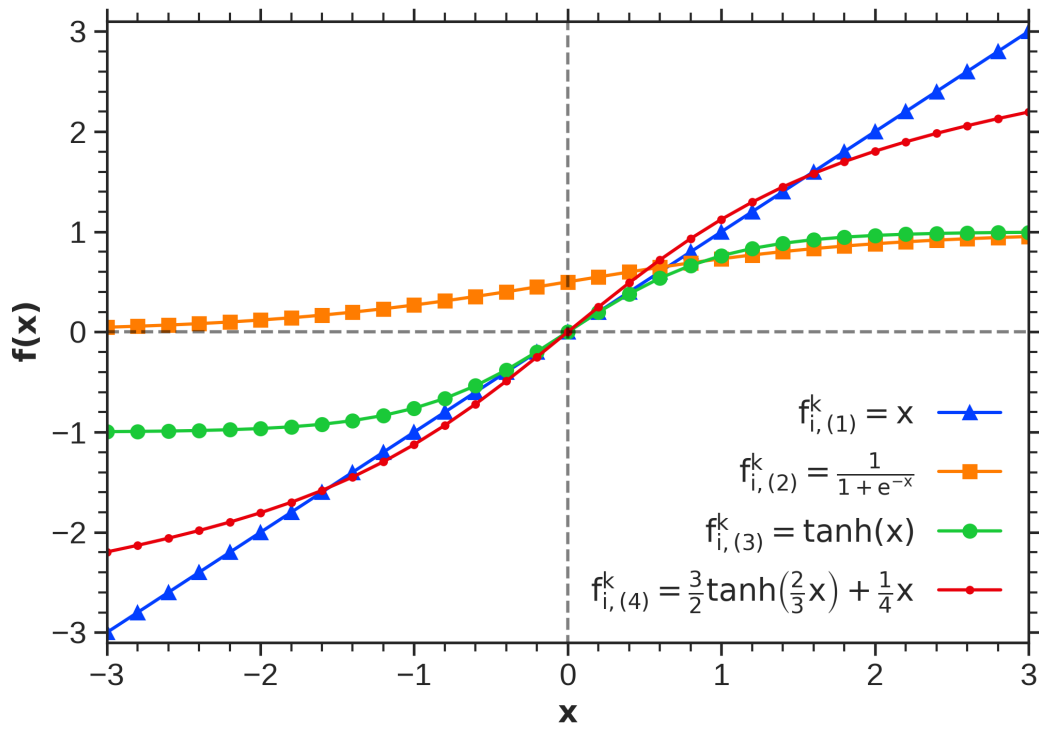


**Figure 4.2:** Examples of commonly used activation functions of Eq. (4.2) in the range  $x \in [-3, 3]$ . In this case,  $f_{i,(4)}^k$  has the parameters  $a = 3/2$ ,  $b = 2/3$  and  $c = 1/4$ .

pendent on the main system features that one wants to describe through a NN. If their actual outputs  $\{y_0\}$  are known beforehand, they can be incorporated into the NN training, which falls under the category of supervised training, whereas their absence in the process leads to non-supervised training scenarios. Particularly for NN PES generation, supervised trainings are the rule. After this, weight optimization begins. This involves an iterative process in which input parameters are passed through the NN function to generate an output, which is then compared to the expected output parameters. One iteration or, as called in the literature, one epoch involves the full set strictly devoted to the NN iterative process or NN training. During training, a minimization is performed on a quantity proportional to a function of the differences between the prediction and the expected output values across the entire training set of input parameters, commonly referred to as the error function  $e(\mathbf{y}_{NN} - \mathbf{y}_0)$ . Such magnitude is, known as cost function  $\Gamma$ , has the following general expression:

$$\Gamma = \frac{1}{N_{\text{conf}}} \gamma_y \sum_{j=1}^{N_{\text{conf}}} e(\mathbf{y}_{NN} - \mathbf{y}_0). \quad (4.4)$$

Here  $N_{\text{conf}}$  is the amount of configurations or data points involved in the NN training, understanding each configuration as containing some specific, scalar or vector-form input and/or output information.  $\gamma_y$  is a scalar parameter that weighs the output data  $y$  according to its nature. To clarify its role, let us take the example of PES training yielding a set of output energies  $\{E\}$  and forces on moving atoms  $\{\mathbf{F}\}$ . In this case,  $\gamma_E = 1$  whereas for forces it would be  $\gamma_F = a/N_{\text{for}}$ , where  $N_{\text{for}}$  is the total amount of force coordinates in the system considering the three spatial directions (i.e., three times the output force vectors available) and  $a$  is a constant balancing the error contributions of energies and forces in  $\Gamma$  [68].

Training process continues until  $\Gamma$  reaches a value below some prefixed threshold close to zero [293]. This happens gradually, as a result of an iterative process during which all weights (also the biases) are corrected or updated after each epoch by adding to each of them some factor proportional to the gradient of the cost function with respect to the weights  $\nabla\Gamma$ . One talks about a backward error propagation procedure, because weight update relies on the output errors  $e(\mathbf{y}_{NN} - \mathbf{y}_0)$  being propagated through the NN layer by layer towards the input layer, as the mentioned derivatives of  $\Gamma$  are computed with the chain rule. Backward propagation of errors can be performed with algorithms such as gradient descent [295, 296], conjugate gradient method [297], Broyden-Fletcher-Goldfarb-Shanno (BFGS) method [298, 299, 300, 301] or its limited-memory variant [302], or Levenberg-Marquardt (LM)

algorithm [303, 304]. In the end, the result of the iterative process is a mathematical NN function that can be used to predict accurate outputs for input data not used during training.

A relevant remark is that the evolution with respect to the iteration of a given  $\Gamma$  used for some NN training can be difficult to interpret. In this case, quality of the fitted NN function can be tracked with other cost functions easier to interpret. Particularizing again for NN PES training, it is usual to consider some cost functions called mean absolute error (MAE) and root mean square error (RMSE) for both energies or forces. Here, a configuration or data point is referred to a particular arrangement of atoms in the system, each of them characterized by its position  $\mathbf{r}_i = (x_i, y_i, z_i)$ , as well as by a DFT-computed potential energy value  $E$  of the full atomic arrangement and a force vector on each  $i$ -th atom  $\mathbf{F}_i = (F_{x,i}, F_{y,i}, F_{z,i})$  due to the potential created by the other system atoms. Considering atomic positions as inputs and energy and forces as outputs, each configuration  $j$  characterized by its set of atomic coordinates at a fixed time  $\sigma_j \equiv \{\mathbf{r}_{i,j}\}$  has an individual error contribution to both energy MAE and RMSE. Summing up to the  $N_{\text{conf}}$  configurations of a given set and dividing by the amount of configurations involved yields the final expressions for both MAE and RMSE parameters:

$$\Delta E_{\text{MAE}} = \frac{1}{N_{\text{conf}}} \sum_{j=1}^{N_{\text{conf}}} |E_j^{\text{NN}}(\sigma_j) - E_j^{\text{DFT}}(\sigma_j)|, \quad (4.5)$$

$$\Delta E_{\text{RMSE}} = \sqrt{\frac{1}{N_{\text{conf}}} \sum_{j=1}^{N_{\text{conf}}} \left( E_j^{\text{NN}}(\sigma_j) - E_j^{\text{DFT}}(\sigma_j) \right)^2}, \quad (4.6)$$

and analogous expressions can be formulated straightforwardly for each of the single force coordinates. In addition, dividing each energy value by the number of atoms  $N_{\text{atom}}$  one can determine the MAE and RMSE error values per atom. Whether they are expressed per atom or not, such kind of cost functions act as "easily interpretable" proxies of the quality of the fitted NN function.

An additional crucial step during the training process is the one shown in Fig. 4.3. The NN function is validated on-the-fly against some additional input information not used for training in order to ensure the correctness of the training process. The extra input set is of much smaller size than the one devoted for training (e.g., around 10 % of the train+test set sums). It enters into the so-called test or validation process, in which no weights are updated, but outputs are predicted simply with the NN function at each iteration from test input data. As for the training process,  $\Gamma$  and/or some easier-to-interpret error parameter –RMSE, MAE– are evaluated

after each iteration for the test data points. If the training process improves the functional fit, this is also reflected in the test error parameter values. But after some iteration, test set errors begin to grow and diverge from the still decreasing training ones. At this point, the NN is able to reproduce not only the training data points but also its random noise and statistical errors. This phenomenon of overfitting implies that the functional fit describes the training set in too much detail, losing, at the same time, its ability to accurately predict features of data not present in the training set, giving rise to large prediction errors in the latter case (see the black insets in Fig. 4.3). To avoid such a scenario, one common-use solution is to abort the training right before overfitting appears and keep the weights in that last epoch (early stopping procedure).

Afterwards, the NN function can be used to predict data points not present in the training set. This stage reveals regions of the configurational space (i.e., the space to which all available data points belong) not properly described by the fit. To improve the quality of the fit, an additional training can be performed, either incorporating more points of the poorly covered region of the configurational space or adding certain points calculated with first principle methods, e.g., DFT to obtain those configurations or points for a NN PES generation. The latter situation also includes the extrapolation of the PES dynamics to situations not covered in the ab initio calculations, e.g., when considering longer time scales or different amounts of atoms or arrangements of the system. The iteration of this training process allows the quality of the NN fit and its ability to describe progressively larger regions of the configurational space. As a result, one obtains a NN fitting function that, in particular for us, is a PES capable of accurately describing the femtochemistry of adsorbed gas molecules on a metal surface much faster than with first-principle methods like DFT. The different steps of the training process are summarized in Fig. 4.4. Now, let us dig deeper into the details of NN PESs production.

## 4.2 Methods for constructing neural network potential energy surfaces

As we have stated in the previous section, NN PESs –which are purely physically motivated potentials because of the DFT data they are trained from– offer a faster way to evaluate energies and specially forces (following (3.23)) than on-the-fly. The latter methods allow to explore small gas-solid systems, but their range of applicability is severely limited by the computational cost regarding the dynamics time interval and the complexity of the multiatomic system. As an example of the main system treated in this Thesis, 100 AIMDEF trajectories or dynamical

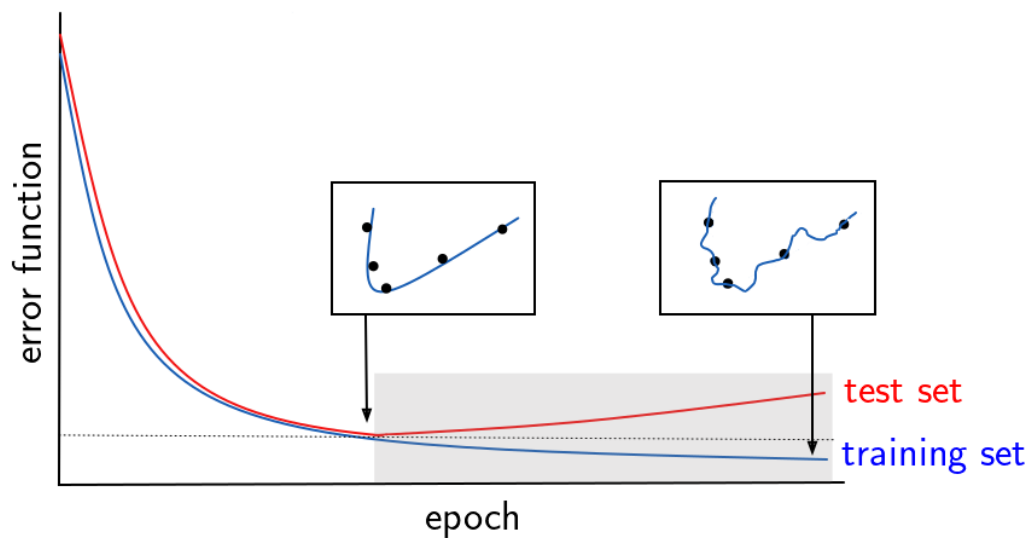


**Figure 4.3:** Schematics of the overfitting problem. In initial iterations or epochs, the NN function is trained according to some input data, and at the same time is validated against some test data missing from the training set. Weight update after each epoch leads to a decrease in the error functions for both train (blue) and test (red) sets, which also implies a better predictive ability of the NN function curve (showed in blue in the insets) to fit known data points (black dots in the insets), as shown in the left inset. After some given iteration, weight update fits training input data points with increasing accuracy as shown in the right inset in the black dots, thus its related error still decreases. However, test set description starts to become increasingly poorer, as shown for the NN function in the right inset, and its related error begins to increase. As a result, the NN function is said to be overfitted, being such region pictured in grey in the figure. Consequently, optimal NN training lasts as many epochs as required for error decrement, but are stopped prior to overfitting with the help of some early stopping mechanism.

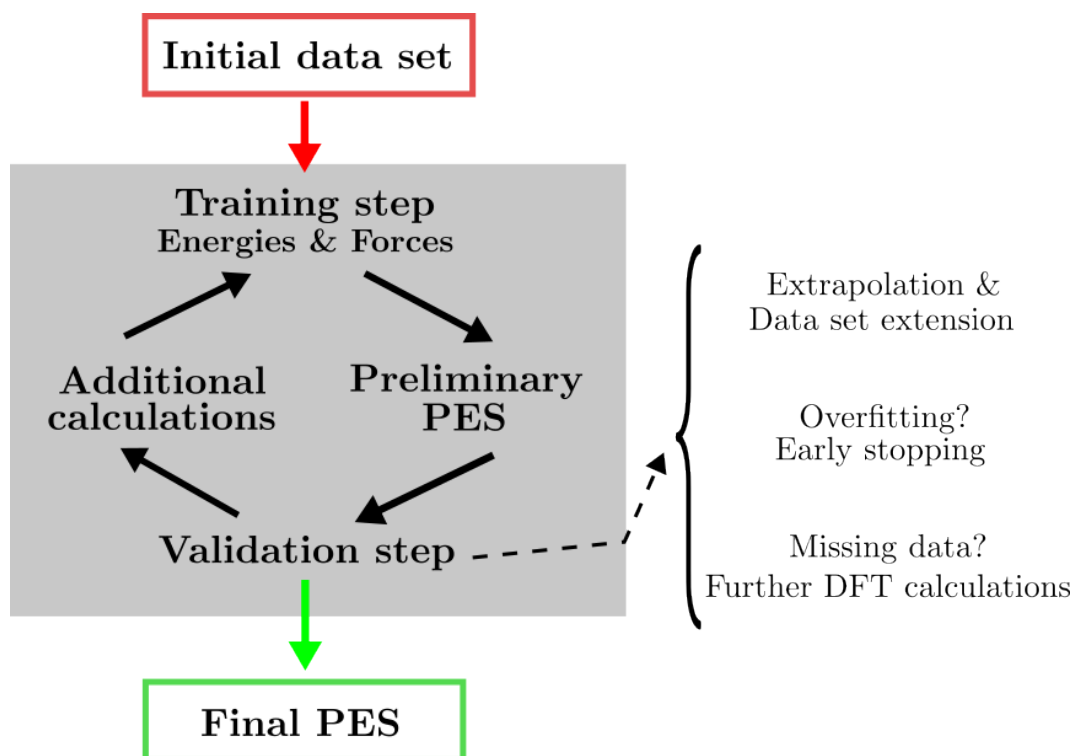


**Figure 4.4:** Flowchart of the full NN training process. It begins with a set of initial configurations of atomic positions, energies and forces that is used as the input of a NN with some architecture. Then, a PES function is trained in a NN with some architecture, where the errors or differences in PES-predicted energies and atomic forces with respect to the input reference values are minimized during a number of iterations. The output PES is made to undergo a validation process consisting of different steps. First, NN training has to be stopped early enough to prevent overfitting. In addition, in order to validate its quality, the NN PES is used to predict energies and forces of some set of configurations not present among the training data, and those configurations that have larger errors in predicted energy and force values can be incorporated to the training step. Not only this, but also poorly described regions of the configuration space may be encountered during this process, this motivating the calculation of some selected data points to further enhance the training set. Afterwards, additional training and validation cycles can be performed on the PES until getting a final NN PES robust and accurate enough.

computations of the 4 ps time range after femtosecond laser peak incidence on the Pd(111) surface decorated with CO required around 3 months to complete with the computational settings available to us. Instead, NN PESs allow a dramatic decrease of the costs, as completion of one trajectory on the same time interval and computational conditions required approximately 10 s of computational time. Replacing an electronic structure-based calculation with the evaluation of some available NN function clearly paves the way for more complex dynamics simulations over longer time scales, with modified initial conditions, and significantly larger dynamics statistics, leading to much smaller statistical errors.

Development of ML-inspired PESs began during the 1990s [67, 68], although science on NN appeared decades earlier, when studying how signals are processed in the nervous system of biological organisms. In this context, the first mathematical description of an artificial neuron or perceptron was suggested in 1943 [305], while its first computational realization of neural network formulation was due to Rosenblatt in 1958, by building a simple structure after connecting artificial neurons arranged in two layers, input and output [306]. Such NN could not reproduce certain logical functions, which motivated the addition of hidden layers in a work in 1969 to overcome this problem [307]. The first reports on NN usage to produce PESs had to wait until the 1990s. In this respect, in 1992 a NN approach was proposed to link ground- and excited-state vibrational spectral information of a polyethylene molecule with some parameters of an anharmonic PES [69]. But the first actual NN PESs were reported in 1995 by Doren's group to describe the adsorption of CO on a Ni(111) substrate and the adsorption and the recombinative desorption of H<sub>2</sub> on Si(100) [70]. For the first system, two input parameters were initially considered (a coordinate  $x$  for the position of the CO center of mass along the line connecting two adsorption sites, and an angle  $\theta$  of the molecular axis with the surface normal), and later the center of mass  $z$  coordinate above the surface was incorporated. In the second one, they chose as inputs the positions of two H and two Si atoms relevant in the recombinative reaction pathway located on the topmost layer of a 2×1 cell, thus the input layer containing 12 nodes. For both systems PESs were calculated with simple feed-forward NNs of a single hidden layer. They were able to identify some key aspects of the NN PES training such as the speed up in dynamics description they offer, the need for a comprehensive enough input data set, and the PES ability to predict configurations close to the training set ones more accurately.

First-generation PESs were trained mainly with feed-forward NNs profiting from the simplicity and flexibility provided by such logical structures. Feed-forward PESs have simple functional expressions due to the NN structure, so that the analytical calculation of their first derivatives becomes affordable and, with this, the evaluation of forces and error gradients for error function minimization. Moreover, hidden

layers of variable node amount can be easily incorporated to the NN structure, and so the complexity of the functional form of the fit is easy to tune, such feed-forward architectures being very flexible in this respect. In addition, no knowledge about the chemistry of the system is needed (e.g., about the nature of the chemical bonds involved).

However, some major drawbacks arise regarding these primitive PESs. The main one is that such kind of NN PESs lacks transferability to other systems due to two reasons. First, taking plain atomic coordinates and/or angles as NN input parameters implies that the computed feed-forward PES cannot work properly for the same chemical system having different amounts of atoms, as the number of input nodes would change forcibly. Secondly, using atomic coordinates as input does not preserve in general the three symmetries a well-constructed PES requires: invariances under rotations, translations, and permutations of atoms. To illustrate this point, for example, positioning of a given adsorbate atom in the same kind of adsorption site would require different NN trainings depending on the coordinates of such adsorbed atom, although such situations are equivalent. Moreover, exchange of two atoms of the same species would lead to a modification of the NN to use due to the absence of invariance under permutations, thus giving different output energies for equal configurations. This would hold only in very simple concrete systems, e.g., certain frozen surfaces with the same adsorbed species. Additionally, the more complicated the NN architecture, the higher the computational cost becomes to determine the NN PES. Several strategies were suggested to overcome such challenges without managing to solve all the drawbacks (see Ref. [68] for a list of proposals). For instance, to achieve permutational invariance, symmetrization of input coordinates for molecules [308] and gas-solid systems [309], as well as symmetrization of the NN structure, have been proposed. However, symmetrized quantities become increasingly complex and computationally challenging to handle as the number of atoms grows. Another choice could be to use internal coordinates as NN inputs, which would work for some low-dimensional systems but would imply a large number of input coordinates for higher-dimensional ones, while violating permutational symmetry, as the ordering of the input vector of internal coordinates would modify the total energy [68, 310].

As a result, feed forward NN PESs with spatial coordinates as inputs work properly for simple, low-dimensional systems, understanding simplicity as the existence of a small number of degrees of freedom in the form of atoms allowed to move and thus under the effect of PES force fields. Such kind of systems are small molecules and small molecules interacting on frozen metal substrates (see, e.g., Ref. [67] or Ref. [68] for references on such studies). As a result, although the PESs determined for different low-dimensional chemical systems seemed promising, a

paradigm change was definitely required to make the NN pathway truly work for a vast majority of systems containing large amounts of degrees of freedom. Such a change arrived in 2007 –with the seminal work of Behler and Parrinello– supported by three key points [71]:

- Most of the internal system interactions are supposed to occur between a given atom and its local chemical environment rather than at a global configurational level. The interatomic interactions that the central atom of a given cutoff sphere experiences with atoms outside that sphere are safely neglected due to their smallness.
- The required invariances (rotational, translational, and permutational) are ensured by the introduction of some atom-centered symmetry functions as NN inputs.
- Active learning is considered in order to extend the configurational space and thus improve the PES predictive performance, a crucial step for systems of many degrees of freedom.

Such is the high-dimensional neural network potential (HDNNP) framework, or more precisely, the "second generation" HDNNPs following Ref. [68]. Let us explore their features in more detail. Here, a local environment centered at each atom is defined, which contributes to the total energy of the system. Contribution of each atom depends on the size of the atomic environment, which is considered to be a sphere of cutoff radius  $r_c$ , or cutoff sphere. Atoms inside the cutoff sphere interact non-negligibly with the atom at its center and thus contribute to the local environment energy; atoms outside the sphere are assumed to have negligible interactions with the central atom of the order of 1 meV/atom and their contributions do not enter in the environmental energy. As only nearest neighbors affect the energy contribution of each environment, each atom-centered cutoff sphere contributes to the total energy with a short-range kind of energy [68]. Let us assume that there are  $N_{\text{elem}}$  atomic elements in the system, with  $N_{\text{atom}}^i$  atoms of each element  $i$ . With this partitioning, total short-range-like energy of the system  $E_s$  becomes as follows:

$$E_s = \sum_{i=1}^{N_{\text{elem}}} \sum_{j=1}^{N_{\text{atom}}^i} E_j^i. \quad (4.7)$$

The value of  $r_c$  is defined prior to the NN training. The values of  $r_c$  in the range [6,10] Å suffice to describe all main forces on the center atom in each environment for several systems, including the long-range electrostatic and dispersion

forces (although the NN PES does not discern the physical nature of each force, but yields total forces on each atom) [68]. NN PESs obtained become thus very accurate, although the smallness of the prediction errors can be comparable to some physical magnitudes in certain systems [311]. Such errors can be further reduced as needed by adding more information of the configurational space to training with later specific DFT calculations, which is part of the aforementioned active learning procedure. Also, one can hint that Eq. (4.7) does not change whenever the ordering of each of the atomic terms changes, thus ensuring the preservation of the permutational invariance.

The next ingredient in this model involves replacing the raw position and/or angular coordinates of the atoms as input parameters for NN that do not preserve the system invariance under translations and rotations in general. Instead, the NN input is a set of invariant coordinates obtained after transforming the atomic positions and angles of atoms inside the cutoff sphere  $\mathbf{R}_j^i \equiv \{\mathbf{r}_j^i\}$  (notice the change of notation with respect to Chapters 2 and 3 adopted here for convenience) into a set of arrays containing invariance-preserving coordinate values (one array per atom in the local environment),  $\mathbf{G}_j^i \equiv \{\mathbf{g}_j^i(\{\mathbf{r}_j^i\})\}$ . Such invariant coordinate values are the output of certain suitable functional descriptors. The order in which atomic coordinates enter such functions does not alter the output, so permutational symmetry is then conserved. Afterwards NN training is performed on the set of invariant coordinate arrays  $\mathbf{G}_j^i$  for the atom  $j$  of element  $i$  on a NN of prefixed architecture and the atomic contribution  $E_j^i$  to the sum in Eq. (4.7) is determined. Mathematically,

$$E_j^i = \text{NN}^i(\mathbf{G}_j^i), \quad i \in [1, N_{\text{elem}}], j \in [1, N_{\text{atom}}^i], \quad (4.8)$$

where  $\text{NN}^i$  is the NN function for each element  $i$ . The reason why  $\text{NN}^i$  is equal for all atoms of the same element is to ensure the chemical equivalence of all atoms of the same element, as well as the transferability of this NN to systems with the same elements but distinct amounts of them. As each atomic environment undergoes a NN calculation for its energetic contribution, graphically this means that we are describing the system with as many low-dimensional NNs as non-frozen atoms available in the training, which motivates the adoption of the HDNNP terminology for such kind of PESs. Figure 4.5 shows a schematic example of how  $E_s$  is determined within the HDNNP framework for a system of three elements a, b, and c. As an additional remark, since these "second generation" HDNNPs rely on an atomwise

sum of NN-computed energies, these HDNNPs are also often referred to in the literature as atomistic NN potentials.

Preserving the required invariances implies that the NN input arrays  $\mathbf{G}_j^i$ , though being strictly numerical, actually carry some physical meaning about the local atom environment with them, and their modifications are linked to physical variations in the atomic environment. To illustrate this point, for example, equivalent atomic environments can be obtained if a gas-solid system is rotated from some starting position around a given axis; this will modify the atomic coordinates, which enter the NN of a given atom, but still the same output atomic energy has to be regained. In this way, equal environments must correspond to the same energy value, whereas different energies imply different local configurations around the atom under consideration. Moreover, since inside the cutoff spheres for different atoms there are also diverse amounts of neighbor atoms, the amount of descriptors used must be independent of the quantity of atoms in a cutoff sphere [71]. As a further requisite, as one wants to determine forces or first derivatives of the PES, functional descriptors need to be differentiable for the whole domain of the radial coordinate and to go smoothly to zero at the cutoff sphere limit in its value and first derivative in order to avoid discontinuities. When possible, the smooth decay requirement can be extended to higher-order derivatives [310].

Among the different functional descriptors, the atom-centered symmetry functions (ACSFs) first proposed in 2007 [71] are actually a predominant choice in the HDNNP generation science [68]. In order to construct them, the first crucial step is to mathematically define the cutoff sphere. For that, a cutoff function  $f_c(r_{ij})$  is defined, which acts on  $r_{ij}$ , the norm of the vector that links the positions of the central atom  $i$  and some neighbor inside the cutoff sphere  $j$  of radius  $r_c$ . The first proposed, and perhaps more popular form of cutoff function contains a decaying cosine (Fig. 4.6) [71]:

$$f_c(r_{ij}) = \begin{cases} 0.5 \left[ \cos \left( \pi \frac{r_{ij}}{r_c} \right) + 1 \right] & , r_{ij} < r_c \\ 0 & , r_{ij} \geq r_c \end{cases} . \quad (4.9)$$

Such  $f_c$  is derivable at first order, but presents a discontinuity at  $r_{ij} = 0$  for its second derivative. The latter does not become problematic with a large enough value choice for  $r_c$  [310]. Other variants of  $f_c$  do not produce discontinuities in the second derivative (using some hyperbolic tangent) or even in no higher-order derivatives (with an exponential) [310, 312]. Whatever form is taken, any descriptor contains a product of one or more symmetry functions times one or more cutoff

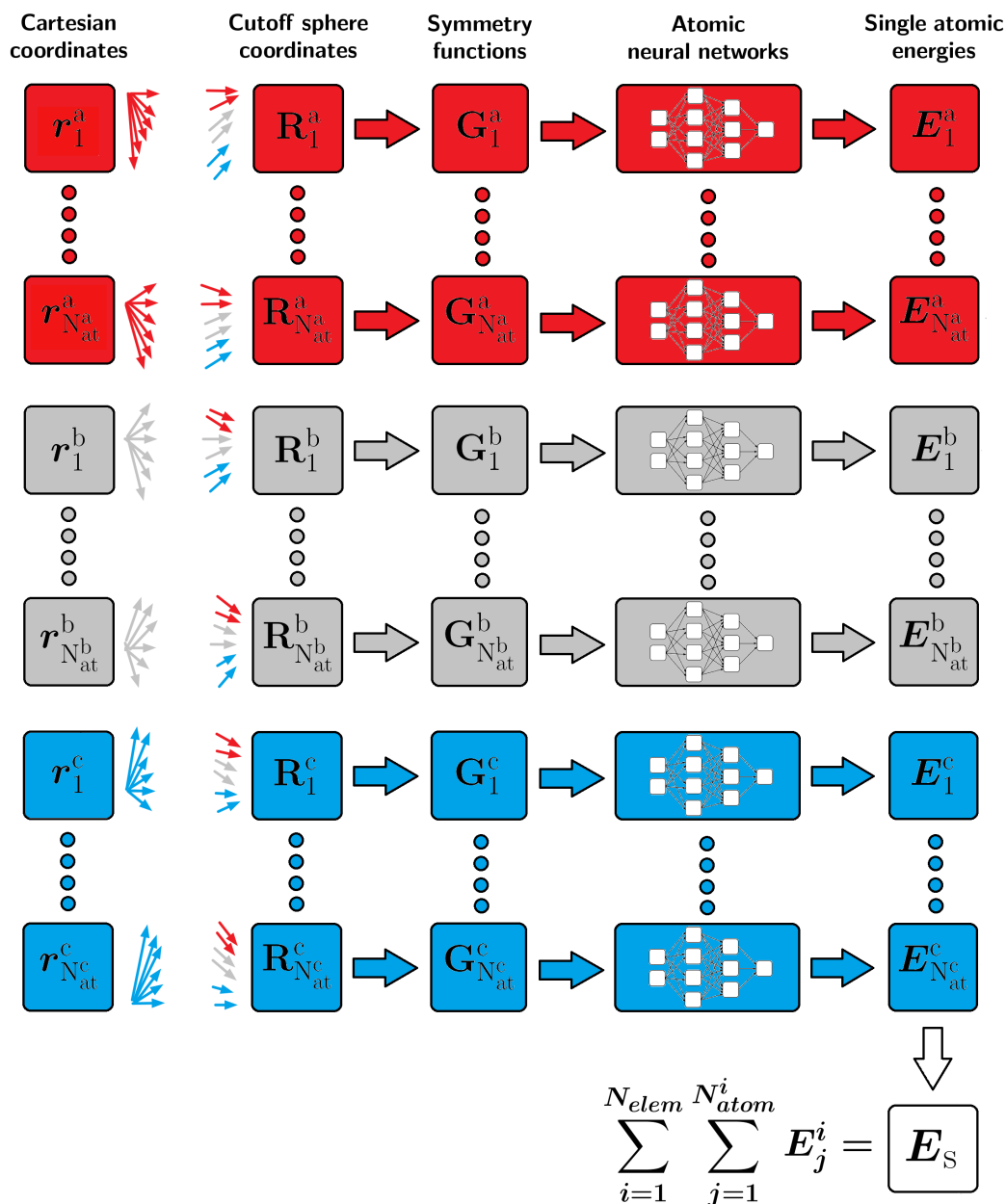


**Figure 4.5:** General schema of a "second generation" HDNNP model (also called atomistic NN model) for a system of three atomic species  $j = a$  (red),  $b$  (grey) and  $c$  (blue). Given a set of atomic positions  $\mathbf{r}_j^i$ , where  $i$  refers to the specific atom of element  $j$  considered, a cutoff sphere can be defined around each of them, characterized by a set of positions  $\mathbf{R}_j^i \equiv \{\mathbf{r}_j^i\}$  corresponding to the central atom position  $\mathbf{r}_j^i$  and the position vectors of its neighbors. Participation of central and neighbor atoms is represented with the multiple out- and ingoing colored arrows between the two first columns. Cutoff sphere coordinates are then transformed into sets of symmetry functions fulfilling the required invariances,  $\mathbf{G}_j^i \equiv \{\mathbf{g}_j^i(\{\mathbf{r}_j^i\})\}$ . Each of these sets of functions enter a NN as input and this yields some energy  $E_j^i$  for the given local atomic environment. In the end, total energy of the atomic configuration  $E_s$  is a sum of the individual environmental energies of the atom-centered cutoff spheres, subscript  $s$  standing for short-range to further address the local feature of each  $E_j^i$ .

functions, so that they are strictly nonzero inside each atom environment and go to zero at the cutoff boundary.

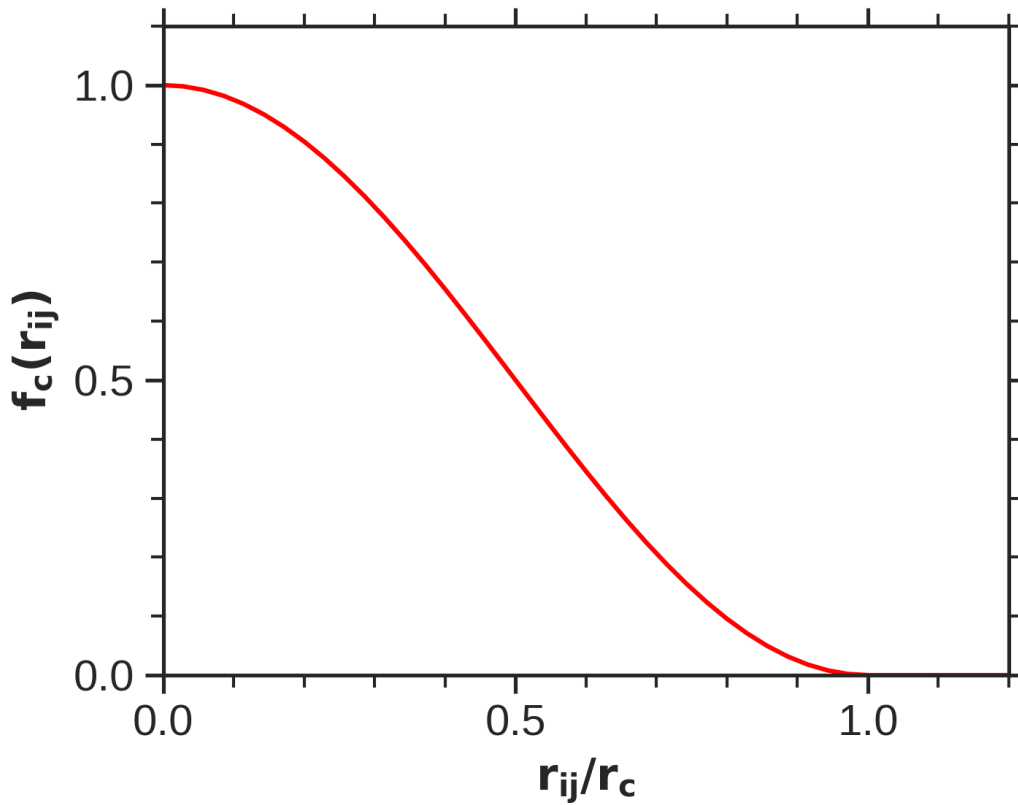


**Figure 4.6:** Plot of the cutoff function  $f_c(r_{ij})$  defined in Eq. (4.9) in terms of  $r_{ij}/r_c$ .

The next step consists of properly defining the ACSFs. There are of two types: radial, involving two-body summands, and angular, proportional to three-body terms. Starting with the radial ones, the first straightforward choice is to take a sum of cutoff functions,

$$G_{i,1}^{\text{rad}} = \sum_{\substack{j \neq i \\ j \in V_c}} f_c(r_{ij}), \quad (4.10)$$

where  $V_c$  is the volume of the cutoff sphere and  $N_{\text{at}}$  is the total number of atoms in the system. Apart from them, more elaborated radial symmetry functions can be

considered:

$$G_{i,2}^{\text{rad}} = \sum_{\substack{N_{\text{at}} \in V_c \\ j \neq i}} e^{-\eta(r_{ij}-r_s)^2} f_c(r_{ij}). \quad (4.11)$$

Here,  $\eta$  defines the width of the Gaussians, whereas  $r_s$  is the radial coordinate of the Gaussian center, being  $0 \leq r_s \leq r_c$ . Tuning  $\eta$ , one changes the spatial extension explored inside the cutoff sphere by the  $G_{i,2}^{\text{rad}}$ 's: for increasing positive values of  $\eta$ , the Gaussians become narrower and vice versa (Fig. 4.7, upper part). Notice that, in fact, (4.10) is the particular case of (4.11) with  $\eta = 0$ . Adjusting  $r_s$  allows to map different spherical shells around center atom  $i$  inside the atomic environment (Fig. 4.7, lower part). In all cases, the maximum height of the Gaussians cannot exceed  $f_c(r_{ij})$  at a given distance. Other radial functions rely on cosine sums,

$$G_{i,3}^{\text{rad}} = \sum_{\substack{N_{\text{at}} \in V_c \\ j \neq i}} \cos(\kappa r_{ij}) f_c(r_{ij}), \quad (4.12)$$

where  $\kappa$  is an adjustable period linked to a length scale. The sum of terms as given in Eq. (4.12) allows to describe the different radius regions of the cutoff sphere. However, they are advised to be used in combination with other radial functions  $G_{i,1}^{\text{rad}}$  or  $G_{i,2}^{\text{rad}}$  due to the appearance of negative values of  $G_{i,3}^{\text{rad}}$  that can cancel positive summands in Eq. (4.12) [310].

To this picture, angular symmetry functions need to be incorporated so that atoms of equal  $r_{ij}$  but different positions in the cutoff sphere can be correctly distinguished. Such are three body terms that characterize the relevant angles. To this end, two kind of angular ACSFs are defined:

$$G_{i,4}^{\text{ang}} = 2^{1-\zeta} \sum_{i,j \neq i, k \neq i}^{N_{\text{at}} \in V_c} (1 + \lambda \cos \theta_{ijk})^\zeta e^{-\eta(r_{ij}^2 + r_{ik}^2 + r_{jk}^2)} f_c(r_{ij}) f_c(r_{ik}) f_c(r_{jk}), \quad (4.13)$$

$$G_{i,5}^{\text{ang}} = 2^{1-\zeta} \sum_{i,j \neq i, k \neq i}^{N_{\text{at}} \in V_c} (1 + \lambda \cos \theta_{ijk})^\zeta e^{-\eta(r_{ij}^2 + r_{ik}^2)} f_c(r_{ij}) f_c(r_{ik}). \quad (4.14)$$

Here,  $\theta_{ijk}$  is the angle subtended by the vectors originating from center atom  $i$ ,  $\mathbf{r}_{ij}$  and  $\mathbf{r}_{ik}$ , and arises from their scalar product.  $\lambda = 1$  or  $-1$  can invert the shape of the cosine function by shifting their maxima at angles  $\theta_{ijk} = 0$  or  $\pi$ , respectively, and it is included so that for the equivalent angles  $\theta_{ijk}$  and  $2\pi - \theta_{ijk}$  the same values of  $G_{i,4}^{\text{ang}}$  and  $G_{i,5}^{\text{ang}}$  are obtained.  $\zeta$  is the angular resolution parameter that sets the width of the cosine sums of Eqs. (4.13) and (4.14) (the strictly angular parts of  $G_{i,4}^{\text{ang}}$

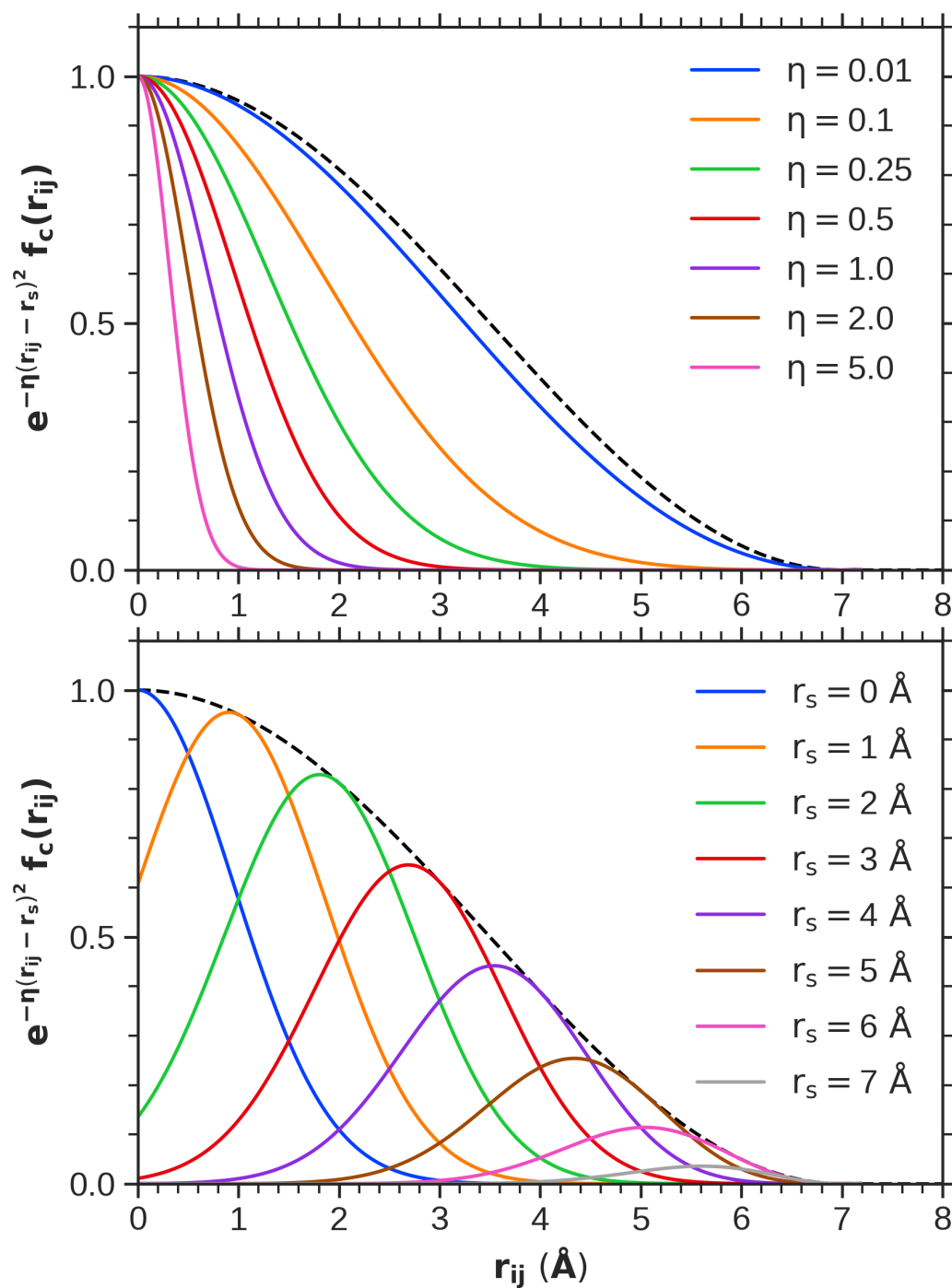


**Figure 4.7:**  $\eta$  (upper graph) and  $r_s$ -dependencies (lower graph) of radial functions  $e^{-\eta(r_{ij}-r_s)^2} f_c(r_{ij})$  in terms of interatomic distance  $r_{ij}$ . For all functions plotted,  $r_c = 7$  Å. For upper graph,  $r_s = 0$  Å, whereas for the lower one  $\eta = 0.5$ . Cutoff function  $f_c$  is pictured in dashed black lines in both graphs.

and  $G_{i,5}^{\text{ang}}$ ); the larger  $\zeta$ , the smaller the range of angles probed by the angular ACSFs. The sums are normalized by the factor  $2^{1-\zeta}$  so that the angular symmetry function values are balanced regardless of the  $\zeta$  considered [68]. However, such operation is not required because the range of values the symmetry functions can take are normalized prior to training, thus avoiding too large, positive, or negative input symmetry function values to heavily influence the node outputs in the first NN layer compared to the smaller symmetry function values [310, 313].  $\eta$  plays the same role as for radial ACSFs, delimiting spherical slices of the atom environment; for complex environmental settings, symmetry functions with different  $\eta$ 's can be utilized. Figure 4.8 shows some examples of the angular functions depending on the values of  $\zeta$  and  $\lambda$  considered.

Furthermore, the cutoff functions included in the product of  $G_{i,4}^{\text{ang}}$  force the three interatomic distances involved to be smaller than  $r_c$ , including the distance between the atoms  $j$  and  $k$ ,  $r_{jk}$ . This condition is less restrictive for  $G_{i,5}^{\text{ang}}$ , as  $r_{jk}$  does not enter the latter functions, allowing the description of atom triplets  $ijk$  with  $r_c \leq r_{jk} \leq 2r_c$ . For this last reason  $G_{i,5}^{\text{ang}}$  often reach larger values than  $G_{i,4}^{\text{ang}}$ . Alternative radial ACSFs have been proposed in other works [314, 315]. In addition, element-specific information can be incorporated in the ACSFs, as suggested and tried elsewhere [316, 317, 318].

Combinations of radial and angular ACSFs with different parameters are chosen to probe different regions of the atomic environments, and their output values are subsequently processed by the NN. Setup of parameters can be performed either unbiased –selecting some given amount of descriptors, taking equidistant values of, e.g.,  $r_s$  or  $\eta$ , selecting some "promising" values of  $r_c$  or  $\zeta$ ...– or following some educated guesses from the features of the system [68]. An unbiased approach is advised at the beginning of the HDNNP production, and it can evolve to a more directed methodology as one gains information about, e.g., the system configurational setup, PES predictions or holes in the configurational space. Considering that the system contains  $N_{\text{elem}}$  elements, an orientative amount of symmetry functions  $N_{\text{sym}}$  can be considered in the early training stages [68],

$$N_{\text{sym}} = N_{\text{sym,rad}} + N_{\text{sym,ang}} = N_{\text{elem}} + \frac{(N_{\text{elem}} + 1) N_{\text{elem}}}{2}, \quad (4.15)$$

and can be increased for later retraining processes according to the system one studies. In fact, Eq. (4.15) gives a hint of how computationally demanding HDNNP generation can become for a system with a large number of species. This downside could be mitigated by reducing the cutoff radius, and consequently, the cutoff sphere size. However, this adjustment might compromise the accuracy of the PES

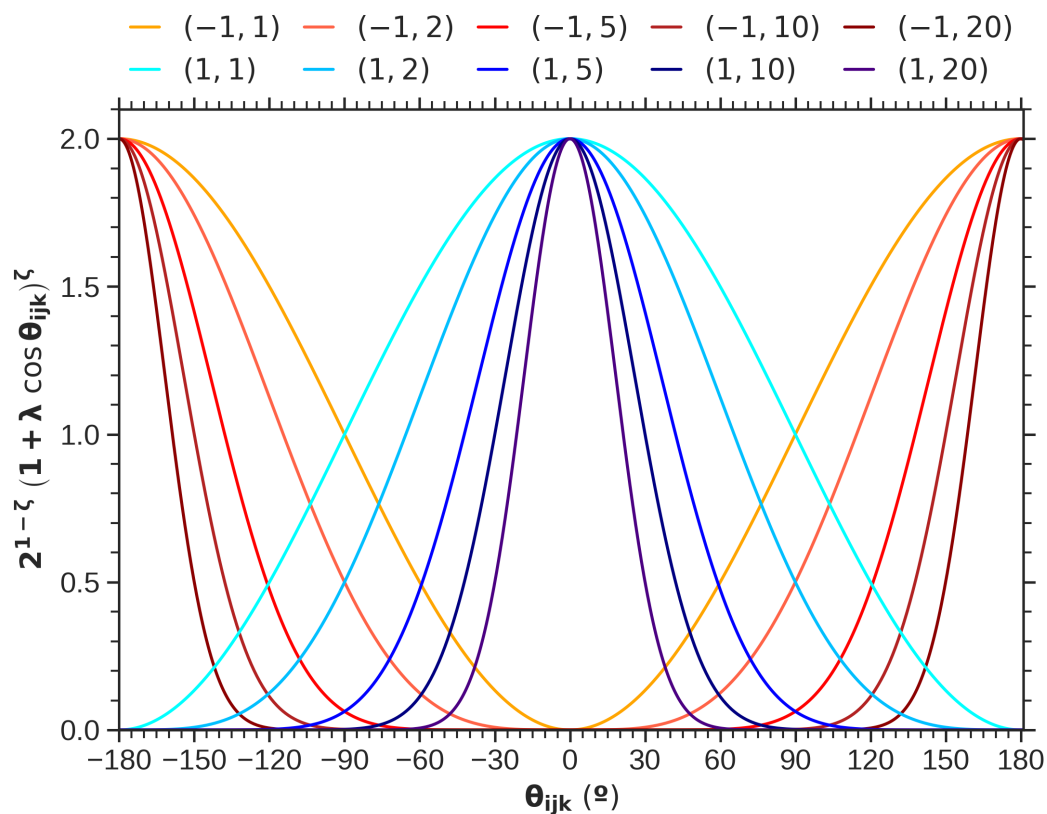


**Figure 4.8:**  $\zeta$  and  $\lambda$  dependencies of the angular functions  $2^{1-\zeta} (1 + \lambda \cos \theta_{ijk})^\zeta$  with the angles  $\theta_{ijk}$  subtended between the central atom  $i$  of a cutoff sphere and two neighbor atoms  $j$  and  $k$ . Each curve corresponds to a certain choice of parameters  $(\lambda, \zeta)$ , so that reddish curves share  $\lambda = -1$ , whereas bluish ones have  $\lambda = 1$ . Selected values for  $\zeta$  exponent are 1, 2, 5, 10 and 20.

in predicting energies and forces. Anyway, it is almost needless to say that research on the ACSF topic remains an ongoing task as deduced from recent proposals for its improvement (see, e.g., Ref. [319]).

Even though the main part of the short- and particularly long-range forces is typically accounted for by the cutoff sphere approximation, there are cases where interactions with ranges longer than  $r_c$  –specifically electrostatic and/or dispersion interactions– are significant enough to be included in the training process [68, 313]. This motivated an evolution of the HDNNPs to a *third generation* in which not only energies, but also local charge distributions inside the atomic environments are fitted with another family of NNs also taking symmetry function values as inputs [320, 321]. As fitting local charge distributions in a PES does not properly describe neither long-range transfer of charge, nor global charge distribution modifications brought to the global system being in a different ionization state, a further evolution of this latter framework was proposed years later, to give the *fourth-generation* HDNNPs [322]. Such recent refinements of the original HDNNP framework exceed the purpose of this Thesis, but the reader is advised to check, e.g., Ref. [68] and the corresponding references therein for a deeper insight.

Another way to improve the HDNNPs is to consider alternative input descriptors from ACSFs suitable enough to generate improved PESs while also ensuring symmetry conservations. Several alternative suggestions have been done in this respect (see Ref. [68] for some examples). In principle, there does not exist a family of descriptors above the others, but descriptors are simply a tool whose success is measured through the quality of the PESs they serve to fit. With the increasing availability of diverse descriptors, the number of possible combinations of them as PES input has also grown. Among them, local density-like descriptors have proven to be valuable inputs regarding HDNNP production, as checked for the PESs produced in this Thesis. Now let us focus on the particular approach we have considered for NN PES generation of CO/Pd(111): the embedded atom neural network (EANN) framework.

### 4.3 Embedded atom neural network (EANN) approach

The NN framework considered in this Thesis is the EANN one, first proposed by Bin Jiang’s group in 2019 [323]. It takes as inspiration the embedded atom model (EAM), valid for metallic systems, which is built on the basis of quasiautom theory [324] –also called effective medium theory [325]–, a theory devoted to the description of, e.g., impurities, fractures, or dislocations in metal systems. Consider an impurity

atom  $i$  located at position  $\mathbf{r}_i$  within a host composed of metallic atoms that generate an electron gas. In the absence of the impurity, both the potential and the energy of the system are functionals of the electron density of the system without impurity, as the HK theorem told us (Section 2.3.1). The presence of an impurity atom introduces an atomic potential that is added to the potential of the host, which remains being a functional of the *pure* system electron density. As the impurity potential only depends on the charge and position of the impurity atomic nucleus, the potential of the host with the impurity is a functional of the pure system electron density. Consequently, the energy of the full system, and in particular of the impurity, is a functional of the density  $n^{\text{host}}$  that the pure electron distribution of the metal would create at  $\mathbf{r}_i$  [324]. This key corollary of the quasiatom theory is expressed mathematically for the impurity energy as follows:

$$E_i^{\text{quas}} = \mathcal{F}[\rho^{\text{host}}(\mathbf{r})]. \quad (4.16)$$

In this case,  $\mathcal{F}$  is a functional of some generally unknown, likely complicated shape, which is also independent of the host atomic species present in the metal. As both the energy of the impurity and the one of the full system depend on the electron density before adding the impurity, this corollary is not exactly to be compared to the HK theorem, which relates the energy and electron density of a system in the same "stage".

Now, the next challenge consists of hinting the form of  $\mathcal{F}$ . A first step is to take approximations, such as assuming that the impurity energy is dependent on its surrounding environment [326] or equivalently that at the position of the impurity  $\mathbf{r}_i$  the electron density is locally uniform [324]. The latter is called the uniform-density approximation and can be seen as a local approximation or the lowest-order contribution in a perturbative expansion of the density. To guide the next steps, a set of DFT calculations performed for all atomic species in the first three rows of the Periodic Table is considered [327]. Each of these atoms was considered as a single impurity inside a HEG in order to determine its energy as a function of the HEG electron density. Some common features could be observed for the graph of each atom, namely a linear behavior between both quantities at high densities and either vanishing or concave up (i.e., with an energy minimum) profiles for densities approaching to zero. Energy minima appear for chemically active elements and are not present for the rare gases investigated. Linear energy ranges correspond to the chemically inactive regimes of each atomic species and can be represented by pairwise potential terms between the atom  $i$  and its closest neighbors. However, low-density, nonlinear regimes, especially for active impurity

atoms, are ill behaved under description with pair potentials, but are instead better characterized by quasiatom energy terms [328].

Taking into account these aspects, EAM was proposed [328, 329]. Based on the quasiatom approach, each atom can be considered as an impurity for the remaining atoms of a system of  $N$  atoms. Aforementioned locality approximation is also used here, i.e., each atom  $i$  feels a local uniform electron density at its position  $\mathbf{r}_i$ . The total energy of such a system in the EAM framework is as follows:

$$E^{\text{EAM,tot}} = \sum_{i=1}^N \left[ F_i(\rho_i^{\text{host}}(\mathbf{r}_i)) + \frac{1}{2} \sum_{j \neq i} \phi_{ij}(\mathbf{r}_{ij}) \right]. \quad (4.17)$$

Here  $F_i$  is the so-called embedding energy function, which is defined as the energy variation that an impurity atom experiences inside a uniform electron gas with respect to its value outside the gas. This embedding energy describes the nonlinear energy dependence of atom  $i$  with the total host electron density created by the whole system at  $\mathbf{r}_i$ ,  $\rho_i^{\text{host}}(\mathbf{r}_i)$ . Finally,  $\phi_{ij}$  is the short-range pair potential term that accounts for the linear dependence between energy and electron density on atom  $i$ , which is proportional to the interatomic distances to the other nearby atoms  $\mathbf{r}_{ij} = \mathbf{r}_i - \mathbf{r}_j$  within some cutoff sphere. An additional approximation can be made by decomposing  $\rho_i^{\text{host}}(\mathbf{r}_i)$  into a superposition of the local electron density contributions generated by each of the surrounding atoms  $j \neq i$  near  $\mathbf{r}_i$ ,

$$\rho_i^{\text{host}}(\mathbf{r}_i) = \sum_{j \neq i} \rho_j^{\text{atom}}(\mathbf{r}_{ij}), \quad (4.18)$$

so that, substituting Eq. (4.18) in Eq. (4.17), the latter equation becomes simply a function of the interatomic distances between the atom  $i$  and the rest of atoms in its vicinity  $j$ . All of this simplifies the problem of determining each impurity energy and, therefore, the total energy, but the question of how to obtain the embedding functions remains. Although semiempirical expressions have been suggested in accordance with experimental properties [328] or electron gas calculations [273], the exact expressions of  $F_i$  are unknown, which affects the accuracy of theoretical calculations. This fact also limits the applicability of EAM to metallic systems.

To improve and generalize the EAM framework to nonmetal systems as well, one has to explore more appropriate forms of the functions  $F_i$  and  $\rho_j^{\text{atom}}$ . To this end, an evolution of EAM, known as the EANN model, was proposed [330]. The first step consists of looking for a set of functions that can describe atomic environments around each atom optimally enough to improve the expression of the electronic density due to each atom. Original EANN considers the Gaussian-type orbital

(GTO) functions centered at each atom [331],

$$\varphi_{l_x l_y l_z}^{\alpha, r_s}(\mathbf{r}) = x^{l_x} y^{l_y} z^{l_z} \exp(-\alpha|r - r_s|^2), \quad (4.19)$$

By squaring the GTOs, the embedded local atomic densities  $\rho^i$  are generated, analogous to how the electron density is obtained by squaring the wavefunction. For each embedded atom  $i$  an embedding density vector  $\rho_i$  can be defined, being each of its components the local electron density due to each of the nearby atoms  $j$  at the position of the atom  $i$ . For atom  $i$  one has,

$$\rho_{L, \alpha, r_s}^i = \sum_{l_x, l_y, l_z}^{l_x + l_y + l_z = L} \frac{L!}{l_x! l_y! l_z!} \left( \sum_{j=1}^{n_{\text{at}}} f_c(r_{ij}) c_j \varphi_{l_x l_y l_z}^{\alpha, r_s}(r_{ij}) \right)^2. \quad (4.20)$$

Here  $c_j$  are element- and orbital-dependent weights [317] for the atoms  $j$  in the environment of atom  $i$  and whose values are adjusted during the NN training;  $r_{ij} = |\mathbf{r}_i - \mathbf{r}_j|$ , and  $n_{\text{at}}$  is the total number of atoms that are at a distance  $r_{ij} < r_c$  from atom  $i$ , i.e., inside a cutoff sphere centered at  $\mathbf{r}_i$  and with a cutoff radius  $r_c$ . Each weight  $c_j$  can be seen as the expansion coefficient of each atom  $j$  in the orbital  $\varphi_{l_x l_y l_z}^{\alpha, r_s}$ . The effect of the cutoff sphere is incorporated through the cutoff function  $f_c$  as defined in Eq. (4.9) [71].

It is interesting to notice that (4.20) can be expressed using the multinomial theorem as [332]:

$$\rho_{L, \alpha, r_s}^i = \sum_{j, k \neq i} c_j f(r_{ij}) c_k f(r_{ik}) r_{ij}^L r_{ik}^L (\cos \theta_{ijk})^L, \quad (4.21)$$

where  $f(r_{ij}) = \exp(-\alpha(|r_{ij} - r_s|)^2)$ . The equality of (4.20) and (4.21) has some crucial implications. It is clear that the embedded density expressed in (4.20) implicitly includes the two-body terms  $r_{ij}$  and  $r_{ik}$  ( $L = 0$ ), and the three-body contribution  $\cos \theta_{ijk}$  for  $L > 0$ , even though it depends only on the Cartesian coordinates of the neighbors of atom  $i$ . This leads to a computational ease in terms of cost, as the sums over the two- and three-body information are avoided. Such circumstance is particularly important when computing the system forces as first derivatives of the EANN PES. In addition, (4.21) shows that the  $\rho^i$  densities preserve the symmetries to translations, rotations and permutations of equivalent atoms, so that the PESs generated with them are universal instead of specific of the particular setting of atoms and their positions. Full EANN schema is represented in Fig. 4.9.

The total energy  $E$  of a system composed of  $N_{\text{at}}$  atoms is then evaluated with

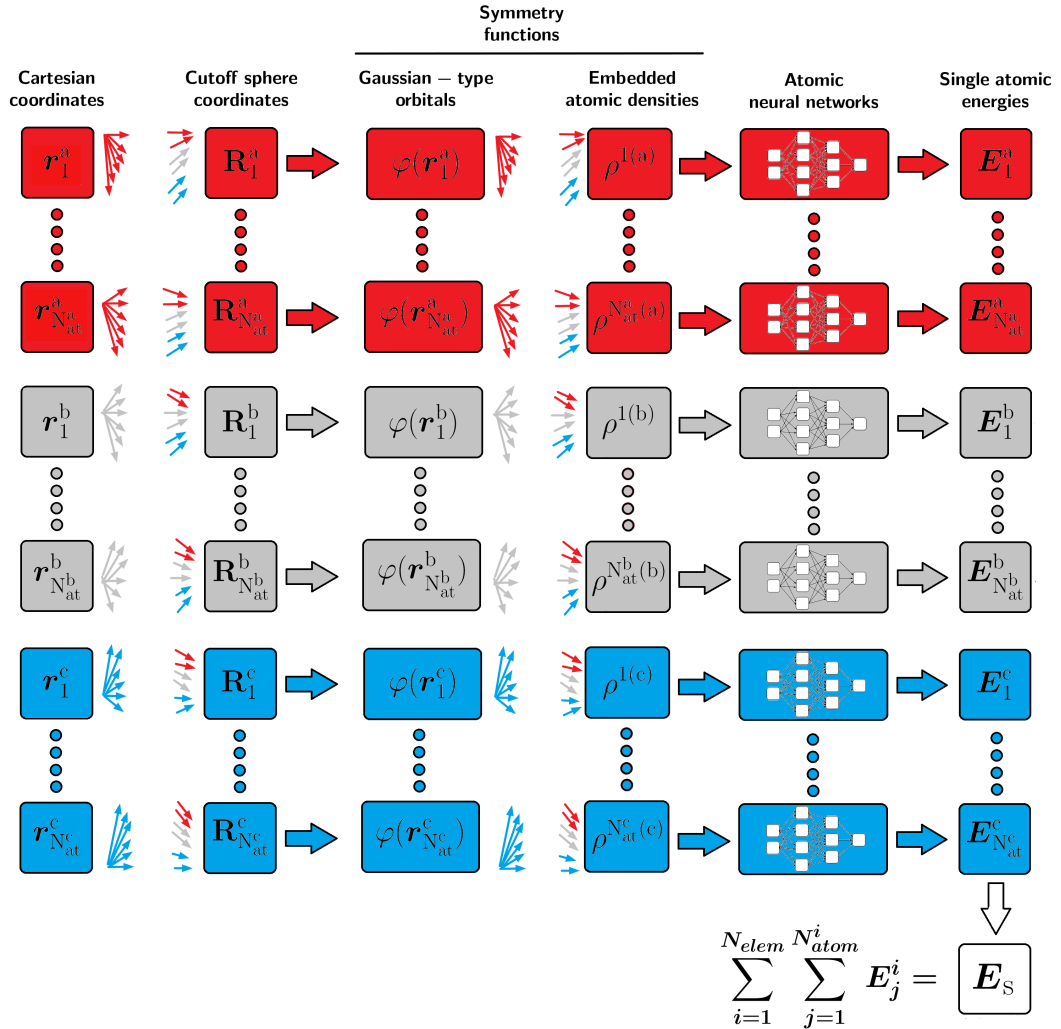


**Figure 4.9:** Schema of the EANN framework for the same system of three atomic species  $j = a$  (red),  $b$  (grey) and  $c$  (blue) considered in Fig. 4.5 (see its description). One starts from a given set of atomic positions  $\mathbf{R}_j^i \equiv \{\mathbf{r}_j^i\}$  inside a cutoff sphere around the  $i$ -th atom of element  $j$ ,  $\mathbf{r}_j^i$ . Then, one determines the set of GTOs centered at  $\mathbf{r}_j^i$ ,  $\varphi_{l_x l_y l_z}^{\alpha, r_s}(\mathbf{r}_j^i) \equiv \varphi(\mathbf{r}_j^i)$ . Depending on their proximity to each of the system atoms  $i$ , the GTOs linked to each centering atom feed or not –therefore the multiple colored arrows between the third and fourth column of the graph– the embedding atomic densities  $\rho_{L, \alpha, r_s}^i \equiv \rho^i$ , which preserve the required spacial and permutational invariances. The latter are processed into NNs as corresponds for a HDNNP schema and yield the individual energies  $E_j^i$ , and their sum equals to the short-range energy  $E_s \equiv E$  of Eq. (4.22).

NN-trained functions following the atomistic representation, i.e., in the same spirit as the HDNNP framework [71] (Section 4.2). This means  $E$  is the sum of the energy contributions provided by each atom of the system,  $E_i(\{\mathbf{r}_i\})$ , as follows:

$$E = \sum_{i=1}^{N_{\text{at}}} E_i(\{\mathbf{r}_i\}) = \sum_{i=1}^{N_{\text{at}}} \text{NN}_i(\boldsymbol{\rho}^i). \quad (4.22)$$

Here  $\text{NN}_i$  is the atomic neural network function of embedded atom  $i$ , which has some specific form for each atom species in the system. It is a function of  $\boldsymbol{\rho}^i$ , an input set that contains the embedded densities coming from atoms inside the cutoff sphere of the  $i$ -th atom. These EANN functions replace the aforementioned embedding energy functions  $F_i$  of the EAM model and also contain the repulsive short-range electrostatic potential terms between the atom  $i$  and each atom  $j$  in its vicinity,  $\phi_{ij}(r_{ij})$ . As EANN functions do not require any other simplification because of their pure mathematical nature, the EANN framework naturally extends EAM to cover metal and nonmetal systems with greater accuracy.

The EANN methodology takes into account not only the positions, but also the energies and forces determined with AIMDEF for each configuration considered in the training process. In order to improve the NN calculation of energies and forces, both physical quantities enter the mean-squared cost function  $S(\mathbf{w})$ . The latter is minimized in the backward error propagation done after each EANN training iteration:

$$S(\mathbf{w}) = \frac{1}{N_{\text{conf}}} \sum_{i=1}^{N_{\text{conf}}} \left[ \eta_E \left( E_i^{\text{EANN}} - E_i^{\text{AIMDEF}} \right)^2 + \eta_F \sum_{j=1}^{N_{\text{moving}}} \sum_{\tau=1}^3 \left( F_{j\tau,i}^{\text{EANN}} - F_{j\tau,i}^{\text{AIMDEF}} \right)^2 \right]. \quad (4.23)$$

In this expression,  $\mathbf{w}$  is the set of NN weight parameters, which contains AIMDEF energies  $E_i^{\text{AIMDEF}}$  and forces  $F_{j\tau,i}^{\text{AIMDEF}}$  of the training set configurations and their EANN counterparts,  $E_i^{\text{EANN}}$  and  $F_{j\tau,i}^{\text{EANN}}$ , respectively, being  $\tau$  the index signalling the spacial component of the force (x, y or z). Next,  $N_{\text{conf}}$  is the total number of configurations that are used for training and  $N_{\text{moving}}$  is the number of atoms allowed to move at the beginning of AIMDEF dynamics (i.e. non frozen), which therefore experience the effect of system's internal forces. Finally,  $\eta_E$  and  $\eta_F$  are parameters weighing the energy or the force contribution in the  $S(\mathbf{w})$  minimization (recall Eq. (4.4) and its explanation).

Let us conclude with some final remarks on EANN and its evolution. It is interesting to mention that the EANN model has also been used to predict the tensorial properties of many body systems such as the electronic friction tensor [333] or the

dipole momenta or polarizability tensor [334]. Furthermore, based on the original EANN model, some recent proposals have been made to improve its features. One of them introduces a different type of orbital proportional to a piecewise function that defines shells with outer and inner radii,  $r_{\text{out}}$  and  $r_{\text{in}}$ , respectively. This modification leads to a faster version of the EANN, known as the piecewise embedded atom neural network (PEANN) model [335].

However, a limitation of the EANN model is that, in certain atomic systems, different environments can share identical sets of interatomic distances and angles, which can incorrectly result in identical EANN-predicted values for physical quantities, such as their energies (see, for instance, the example of  $\text{CH}_4$  discussed in Ref. [336] for clarification). To overcome this problem, the  $c_j$  coefficients of Eq. (4.20) can be made environmentally dependent on the cutoff sphere centered at each atom  $j$  entering the sum as a neighbor of atom  $i$ , in the same spirit as the embedded densities. Assuming that the procedure is carried out for  $T > 0$  iterations, if we focus on Eq. (4.20), each of the  $c_j$  coefficients at some iteration  $T$  carries the embedding density information of the cutoff sphere centered at  $j$ -th atom in the iteration  $T - 1$ ,  $\rho_j^{T-1}$ , and this process repeats recursively until reaching the original environmental settings  $T$  iterations before. Environmental information is transmitted between some atom  $j$  and its neighbors and spreads iteration after iteration reaching farther atoms. In fact, since the calculation of each  $c_j^T$  is performed recursively using the  $c_j$ 's from earlier iterations, this motivates the naming of this evolution of EANN as recursive embedded atom neural network (REANN) [336, 337].

In any case, neither PEANN nor REANN are included in the calculations of this work and are mentioned here solely to illustrate the evolution of the EANN model. This decision is justified by the accurate results already provided by the PESs trained with the original EANN framework for characterizing the photodesorption of CO on Pd(111). A more detailed explanation and discussion of this topic are presented in the following chapters of this work.

Part II

Research results



# 5

## 0.75 ML CO/Pd(111) potential energy surface

As discussed in Chapter 4, NN-generated multidimensional PESs are emerging as a computationally faster, versatile, and accurate alternative to traditional ab initio methods for studying gas-surface processes. In particular, HDNNP-based approaches have become particularly promising, enabling the accurate modeling of complex interactions and energy exchange between surfaces and molecules of variable sizes. This explains the steadily increasing number of studies that are appearing in different areas, such as solid-liquid water surfaces [72, 73, 74] and gas-solid interfaces [75, 76, 77, 78, 79, 80, 81, 82, 83, 84, 85, 86, 338]. However, modeling femtosecond laser-induced reactions with NN PESs can be more demanding than other gas-surface processes. Reasons for this are the need to account for multiple adsorbates and, hence, more surface atoms, a possible time-changing adsorbate coverage caused by the desorption events, and a large surface temperature variability. Therefore, multiple degrees of freedom and a large configurational space have to be accurately described by the PES. The results in this chapter and in Chapter 7 will show that the EANN method [323, 339, 340] can successfully account for this complex task.

In this chapter, we study the photoinduced desorption dynamics of CO from Pd(111) at a specific coverage of 0.75 ML, employing an EANN PES that is obtained using data extracted from existing  $(T_e, T_1)$  – AIMDEF simulations of the same process [31]. The outline of the chapter is as follows. The first section provides relevant details of the  $(T_e, T_1)$  – AIMDEF simulations. Section 5.2 is devoted to the construction of the 0.75 ML CO/Pd(111) EANN PES. This process involves choosing suitable input data for EANN training (Section 5.2.1), optimizing EANN-specific parameters for our system (Section 5.2.2), and a static evaluation to determine the more accurate PES trained and its accuracy predicting the CO/Pd(111) energies and forces (Section 5.2.3). In Section 5.3 we detail the numerical fitting procedure that is used to calculate the surface electronic density, which is needed to calculate within the LDFA the friction coefficients on the adsorbate species, as accurately as in  $(T_e, T_1)$  – AIMDEF. Subsequently, Section 5.4 discusses the molecular dynamics simulations performed using the precalculated PES. The results of these calculations reproduce accurately the 0.75 ML CO/Pd(111) photodesorption results obtained from the aforementioned  $(T_e, T_1)$  – AIMDEF simulations [31] and even permit us to learn more about this chemical pathway in its early stages. Finally, Section 5.5

summarizes the principal conclusions and potential implications drawn from this research.

## 5.1 Description of the system in the reference ( $T_e, T_1$ ) – AIMDEF simulations

In the ( $T_e, T_1$ ) – AIMDEF study performed in Ref. [31], the adiabatic forces were calculated with DFT and the vdW-DF exchange-correlation functional proposed by Dion *et al.* [172], using version 5.4 of Vienna Ab initio Simulation Package (VASP) [341, 342] and the AIMDEF module developed in our group [57, 58, 59, 60, 61, 62, 66]. The 0.75 ML CO/Pd(111) system was described using a periodic supercell composed by six CO adsorbates placed pairwise on the top, hexagonal close packed (hcp), and face-centered cubic (fcc) adsorption sites on a ( $4 \times 2$ ) four-layer slab containing eight Pd atoms per layer, as shown in Figure 5.1. Periodic boundary conditions in all spatial directions were considered for the system. This means that dimensions of the working supercell had to be defined with particular care in the  $z$  direction, as some vacuum size above the adsorbate-substrate complex had to be left to avoid fictitious iterations of desorbing CO with the upper periodic slab. Calculation of the Pd bulk lattice constant yielded a value  $a = 4.0 \text{ \AA}$ , which corresponds to an initial interlayer spacing of  $2.31 \text{ \AA}$  along the [111] direction. Although after relaxing the two topmost Pd layers, the bulk interlayer spacing was slightly modified between the two topmost layers ( $2.33 \text{ \AA}$ ) and between the second and third topmost ones ( $2.30 \text{ \AA}$ ), the average interlayer spacing in the 4-layer slab remains to be of  $2.31 \text{ \AA}$ . Therefore, an empty space equivalent to 8 layers was set on the upper part of the supercell. All this considered, the supercell had dimensions  $s(\mathbf{a}_1, \mathbf{a}_2, \mathbf{a}_3)$ , with a dimensionless scale factor  $s = 2.83$  and the lattice vectors of the supercell, in  $\text{\AA}$  and in Cartesian coordinates, being:  $\mathbf{a}_1 = (4, 0, 0)$ ,  $\mathbf{a}_2 = (1, 1.7321, 0)$ , and  $\mathbf{a}_3 = (0, 0, 9.7980)$ .

The electronic friction coefficient describing the coupling of adsorbates to the laser-excited hot electrons were calculated with LDFA, using the Hirshfeld partitioning scheme to calculate the surface electronic density at the position of each atom conforming the adsorbates (see Section 3.2.2.4). Furthermore, the hot Pd(111) surface created by the laser-excited electrons was described by coupling the two topmost Pd layers to a Nosé-Hoover thermostat (Eqs. (3.14) and (3.15)), while Pd atoms in the third topmost layer followed adiabatic dynamics (Eq. (3.16)) to recreate a thermal gradient that decreases with the surface depth. Lastly, the bottom surface layer was kept frozen.

The ( $T_e, T_1$ ) – AIMDEF simulations were performed following the experimental

conditions of Ref. [30]. Specifically, the system, which is initially thermalized at 90 K, is irradiated with a laser pulse of  $\text{sech}^2$  profile, wavelength  $\lambda = 780$  nm and FWHM of 100 fs. Because of the high computational cost, only the experimental absorbed laser fluence  $F = 13.0$  mJ/cm<sup>2</sup> was considered. Using a time step of 1 fs, sets of 100 trajectories lasting 3.5–4.0 ps were generated for each type of dynamics simulation, namely: (i)  $(T_e, T_l)$  – AIMDEF that accounts for both hot electrons and hot phonons in the adsorbate dynamics, (ii)  $T_e$  – AIMDEF that only incorporates hot electron effects by keeping all Pd atoms frozen, and (iii)  $T_l$  – AIMDEF that only includes hot phonon effects by neglecting the friction and random forces in the adsorbate dynamics. In all cases the incident laser peak reaches the adsorbate-substrate complex at  $t = 410$  fs. In the present chapter, only data from  $(T_e, T_l)$  – AIMDEF are used to generate the EANN PES.

## 5.2 Construction of a 0.75 ML CO/Pd(111) EANN PES: computational details

### 5.2.1 Input data selection

When it comes to generating a EANN PES, it is beneficial to initiate the process by examining specific characteristics of the system under investigation. This approach helps to streamline the training process, ensuring that the selected input data is truly representative of the entire system. In the case of the 0.75 ML CO/Pd(111) adsorbate-substrate system, we consider the potential energy  $E_0^{\text{DFT},j}$  of each configuration  $j$  explored during each of the 100  $(T_e, T_l)$  – AIMDEF trajectories. Unless otherwise stated, each configuration  $j$  will be hereafter characterized by the atomic positions  $\{\mathbf{r}_i^j\}$  and forces  $\{\mathbf{F}_i^{\text{DFT},j}\}$  on each atom  $i$  and the corresponding system potential energy  $E_0^{\text{DFT},j}$ . Additionally, we categorize the trajectories based on the number of CO desorption events (0, 1, and 2). Other previous works considered, e.g., the force distribution [83] and the distance of the gas molecule from the surface [77] as characteristic quantities. In our case, categorizing the available trajectories in terms of the desorption events will assure us to provide the EANN PES meaningful information about how the system atoms interact with each other at variable coverages. Subsequent analysis of the system potential energy  $\{E_0^{\text{DFT},j}\}$  for each subset, as well as for the entire combined data set, will serve as a reference to check the representativeness of the data chosen for training.

Now, let us proceed by selecting the input data for EANN training. The complete data set comprises 352 505 configurations. Forces for the bottom-layer Pd atoms,

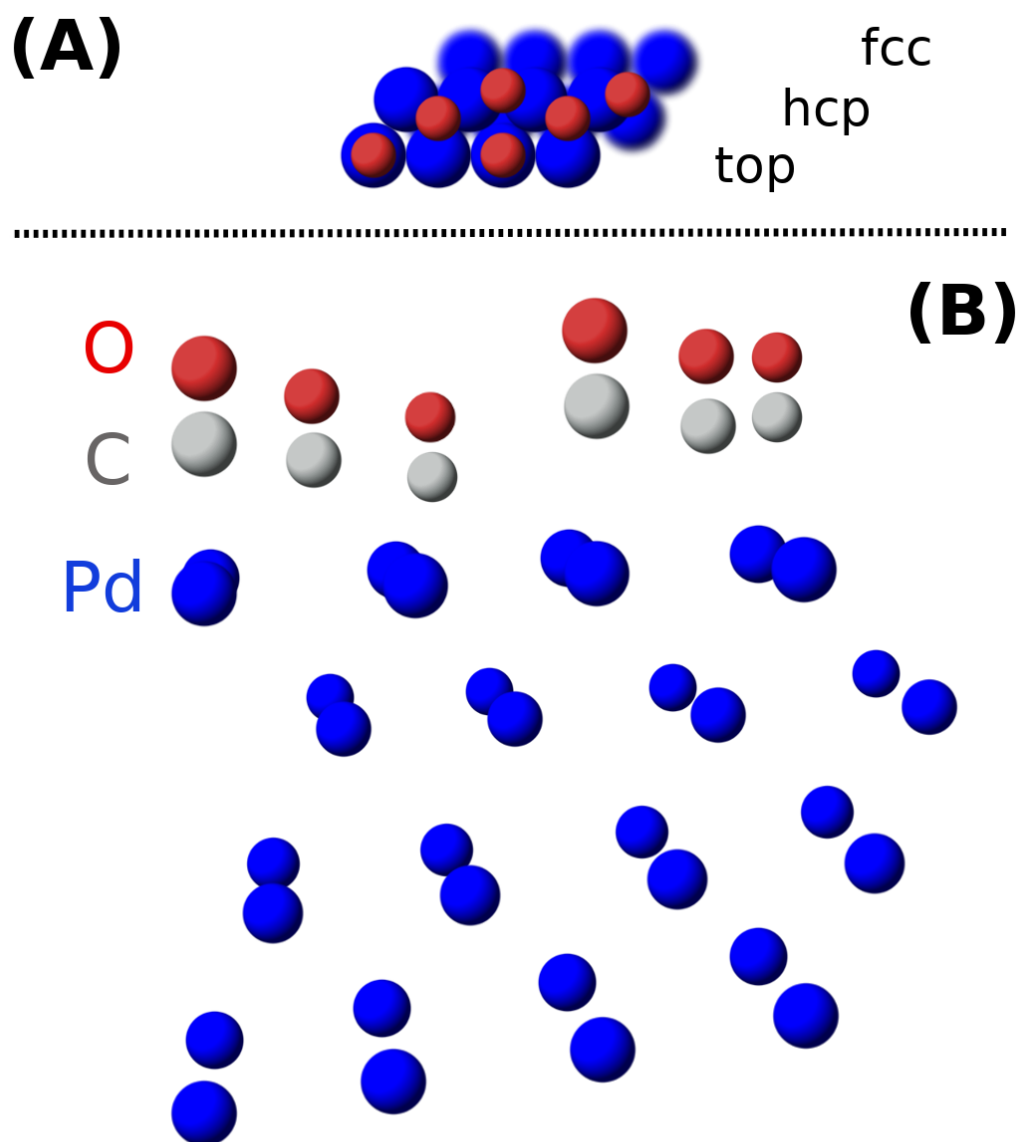


**Figure 5.1:** Schematic illustration of our 0.75 ML CO/Pd(111)  $4 \times 2$  simulation cell, composed by O (red) and C atoms (grey) forming CO adsorbates, and a 4-layer slab of Pd atoms (blue). (A) Orthogonal top view, highlighting the CO top, hcp, and fcc adsorption sites, as well as, the topmost (blue) and second topmost (blurred blue) surface layers. (B) Perspective view. In  $(T_e, T_1)$  – AIMDEF and  $(T_e, T_1)$  – MDEF, each adsorbate dynamics is modeled with a Langevin equation. Regarding the surface, Pd atoms in the two topmost Pd layers are coupled to the Nosé-Hoover thermostat, Pd atoms in the third layer undergo adiabatic evolution and Pd atoms in the bottom layer remain frozen throughout the simulation [31, 87].

which were kept fixed in the simulations, are not considered. As trajectories yielding different number of CO desorbing events conceivably provide information on the interaction at variable coverages, we choose to construct an initial data set with 4500, 6000, and 4500 configurations that are randomly selected from the set of trajectories with zero, one, and two desorption events, respectively. After plotting the  $E_0^{\text{DFT},j}$  histograms associated with the input data set of 15 000 configurations (Fig. 5.2, bottom) and comparing them to the full  $(T_e, T_1)$  – AIMDEF data set (Fig. 5.2, top), one can observe that the configuration selection method accurately reproduces the behavior of the entire system, both within each desorption event category and across the combined data set. Note that the range of the system potential energy in the whole data set is as large as  $\approx 12$  eV.

Regarding the specifics of the training process, a subset of 13 500 configurations, which constitutes 90% of the data set, is randomly chosen during each run of the EANN code for each single PES, so that different EANN PESs can be generated in the same run. The remaining 10% of each run is reserved for testing each PES, hence, this partitioning serves the purpose of assessing convergence of the PESs and preventing them from overfitting. Optimization of the element- and orbital-dependent weights  $c_j$  involved in the embedded atomic densities  $\rho_{L,\alpha,r_s}^i$  (Eq. (4.20)) forming the EANN input layer is carried out with an efficient hybrid extreme machine learning and Levenberg-Marquardt (EML-LM) algorithm [330]. Training process entails the minimization of the cost function  $S(\mathbf{w})$ , defined in Eq. (4.23), which is constructed from both energies and atomic forces. Therefore, some values for the energy and force weights,  $\eta_E$  and  $\eta_F$ , respectively, must be given prior to the PES generation. It has to be remarked that  $\eta_F$  has to incorporate some normalization of the three spatial coordinates and of the number of force vectors (one per moving atom in the calculation). This is reflected in the summation terms of the force contribution to  $S(\mathbf{w})$  in Eq. (4.23). Actually, the force weight is provided in the EANN program through a parameter  $W_F$ , which is related to  $\eta_F$  as follows [343]:

$$\eta_F = \sqrt{\frac{W_F}{3 N_{\text{moving}}}}, \quad (5.1)$$

so that for  $N_{\text{moving}} = 36$ ,  $\eta_F \approx 0.096 \sqrt{W_F}$ . Once both weights are set, minimization of  $S(\mathbf{w})$  leads to EANN convergence if the cost function between consecutive iterations hits some cutoff value  $\Delta S_c$  we can prefix. More precisely, EANN training finishes when, at some iteration  $t$ ,  $S_t(\mathbf{w}) - S_{t-1}(\mathbf{w}) < \Delta S_c$  for both train and test data sets. Moreover, we consider as overfitting criterion to have six consecutive iterations with  $S_t(\mathbf{w})(t) > S_{t-1}(\mathbf{w})$  for the test set. In that case, the cost function

value is taken as the value obtained in the last epoch previous to these six epochs that serve to identify EANN overfitting. It is noteworthy, as discussed in Ref. [323], that the EANN PESs usually converge within few iterations. This will also be a common feature in all the EANN PESs constructed in this Thesis. Taking advantage of the aforementioned random separation into training and validation subsets, we train five distinct PES from which we will select the most accurate one.

## 5.2.2 EANN parameter optimization

Next, let us turn our attention to the selection of the EANN input parameters, already detailed in Chapter 4. These parameters have to be chosen properly to maximize accuracy while minimizing computational calculation times. They are the following ones:

- NN architecture
- Total angular momentum  $L$ , for which  $l = 0, 1, \dots, L$
- Number of GTOs,  $N_\varphi$
- Energy and force weights,  $\eta_E$  and  $\eta_F$  (in Eq. (4.23)), the latter one through  $W_F$  as defined in Eq. (5.1)
- Cost function cutoff for PES training convergence,  $\Delta S_c$
- Cutoff radius  $r_c$

The selection is performed in two stages. First, we aim to determine an appropriate NN architecture tailored to our system, using a specific and well-motivated set of values for the remaining parameters (i.e.,  $L$ ,  $N_\varphi$ ,  $W_F$ ,  $\Delta S_c$ , and  $r_c$ ). Next, these latter parameters will be adjusted for the chosen architecture, if necessary. All these tests are performed with the input data set of 15 000 configurations that is described in the previous section.

Our strategy being clear, we begin assigning values to all EANN parameters except for the architecture. In EANN training it is convenient to set either  $\eta_E$  or  $\eta_F$  equal to 1 and tune the other weight depending on how much we want the energy and force contributions to influence  $S(\mathbf{w})$ . For simplicity we choose  $\eta_E = 1$  and  $\eta_F \approx 0.096$  (i.e.,  $W_F = 1$ ) so that energy and forces contribute approximately equally to the cost function minimization. As above mentioned, each input configuration  $j$  only contains information on the 36 moving atoms (i.e., 12 atoms contained in the six CO adsorbates and 24 Pd atoms forming the three topmost moving layers of

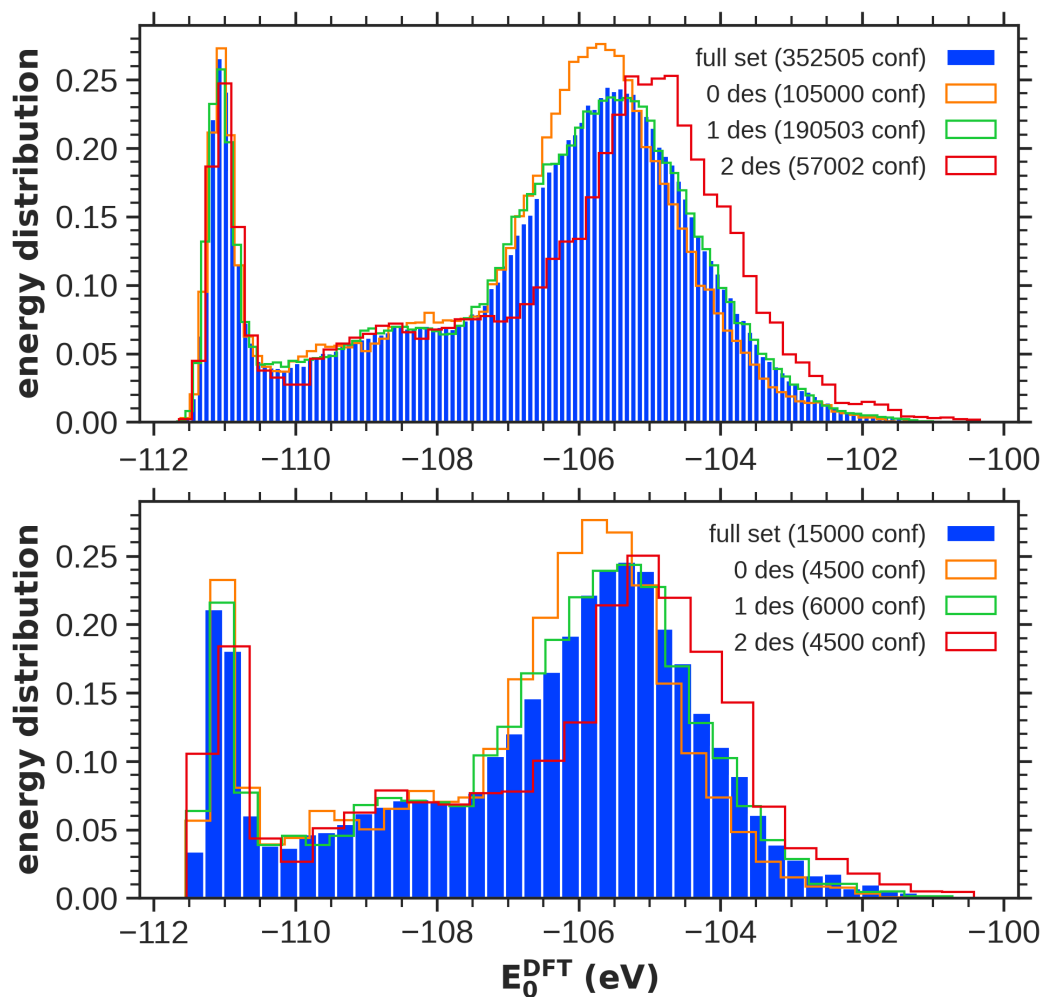


**Figure 5.2:** Normalized histograms of potential energies  $E_0^{\text{DFT}}$  obtained from  $(T_e, T_1) - \text{AIMDEF}$  (filled blue bars) [31]. Superimposed empty bars distinguish energy distributions from trajectories with zero (yellow), one (green) or two CO desorption events. (Top) Full  $(T_e, T_1) - \text{AIMDEF}$  data set histograms (352 505 configurations). (Bottom) Distributions for the 15 000 configurations accounted first for the EANN parameter optimization and afterwards for the first EANN PES training.

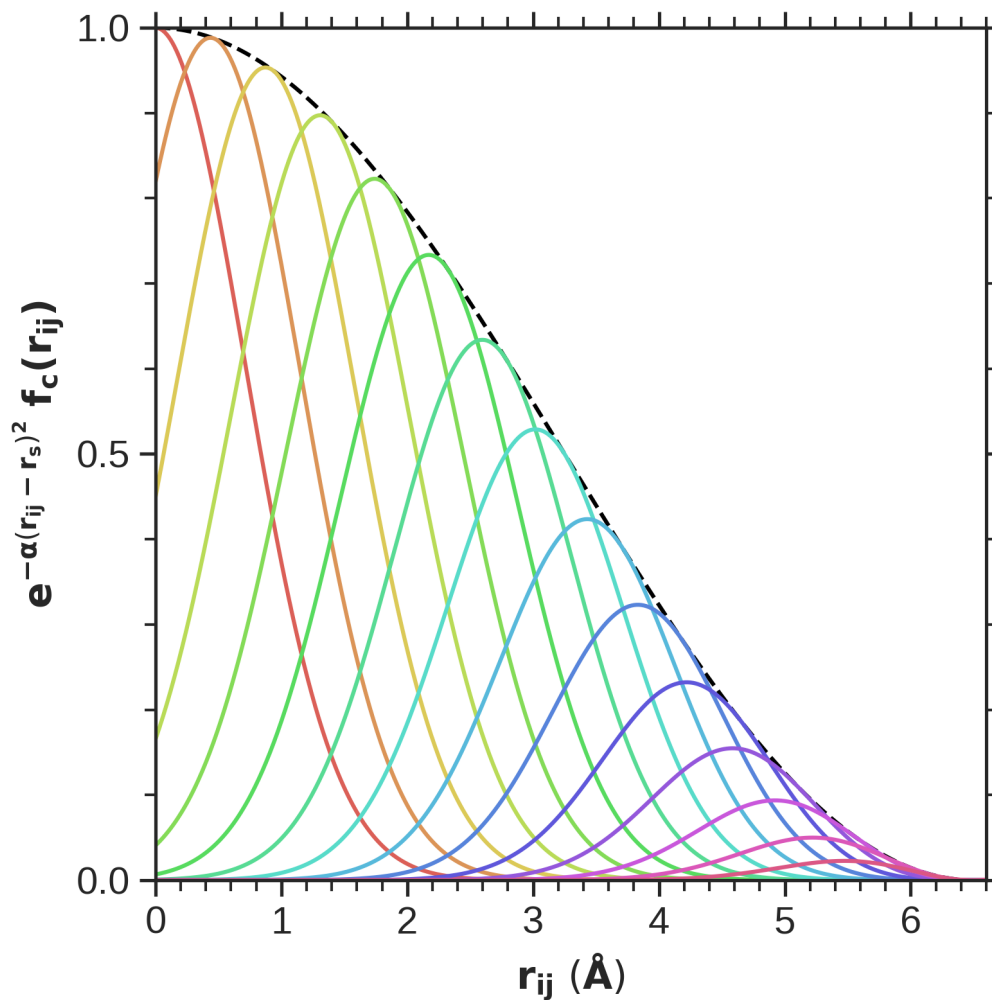
the surface). Therefore, 36 atomic force vectors per configuration enter the cost function evaluation in each EANN training iteration. Based on our experience, the remaining EANN parameters are chosen as follows:  $L = 3$  corresponding to the allowed orbital angular momentum values  $l = 0, 1, 2, 3$  (or, in spectroscopic notation, the possible atom orbitals  $s, p, d, f$ , respectively);  $N_\varphi = 15$  GTOs;  $\Delta S_c = 10^{-2}$ ; and  $r_c = 6.5 \text{ \AA}$ . As  $N_\varphi = 15$ , this also means that there are 15 different values of the GTO center  $r_s$  (Eq. (4.19)) starting from  $r_s = 0$ . As highlighted in Ref. [323], achieving a high spatial resolution relies on ensuring robust overlap among neighboring GTOs. To this end, we establish an evenly spaced grid of  $r_s$  values within the interval  $[0, r_c]$  for simplicity. With 15 GTOs and the  $r_c$  we have chosen, this grid results in 14 equidistant intervals, each with  $\Delta r_s \simeq 0.4643 \text{ \AA}$ . The recommended relationship between  $\Delta r_s$  and the GTOs width  $\alpha$  is  $\Delta r_s = \sqrt{\beta/\alpha}$ , where  $\beta = 0.2$  is an empirical constant [323]. The latter leads to  $\alpha \simeq 0.93 \text{ \AA}^{-2}$  in our training context. Figure 5.3 depicts the exponential part of the GTOs corresponding to these settings, multiplied by the cutoff function  $f_c$  as defined in Eq. (4.9). Besides, we choose to have the same amount of GTOs for each value of  $l$ , this meaning that each PES of the tests has 60 embedded atomic densities  $\rho_{L,\alpha,r_s}^i$  (Eq. (4.20)) in the EANN input layer.

Table 5.1 presents the results obtained from these initial assessments. For each NN architecture, we consider the following key quantities:

- The average computation time per iteration  $\bar{t}_{\text{comp}}$
- The mean number of iterations required during the EANN PES training,  $\bar{N}_{\text{iter}}$ , and its standard deviation  $\sigma_{N_{\text{iter}}}$
- The average of the minimum cost function values for both the training and test data sets, denoted as  $\bar{S}^{\text{train}}(\mathbf{w})$  and  $\bar{S}^{\text{test}}(\mathbf{w})$ , respectively

As we want to obtain accurate PESs, our main criterion is the minimization of the cost functions. Additionally, we note that the mean number of iterations encompasses the initial six iterations that may involve overfitting when it arises, after which the corresponding PES training is finished in the EANN code. However, for those cases the provided cost function values correspond to the final iteration just before overfitting starts.

The results in Table 5.1 show that an improvement in accuracy (i.e., a reduction in  $\bar{S}(\mathbf{w})$ ) may come at the cost of longer computational times for each iteration. Therefore, some compromise between computational cost and accuracy has to be reached. Regarding the accuracy, it is reasonable to exclude architectures simpler than 60-60, either containing two or three hidden layers. Compared to 60-60, the more complex architectures 70-70, 60-80, 80-80, 60-60-60, and 70-70-70 yield only



**Figure 5.3:** Representation of the exponential part of the GTOs,  $\exp[-\alpha(r_{ij} - r_s)^2]$  (Eq. (4.19)), multiplied by the cutoff function  $f_c(r_{ij})$  (Eq. (4.9)), for 15 GTOs with equal separation intervals between consecutive orbitals of  $\Delta r_s = 0.4643 \text{ \AA}$ , equal widths  $\alpha \approx 0.93 \text{ \AA}^{-2}$  and  $r_c = 6.5 \text{ \AA}$ . First GTO is centered at  $r_s = 0 \text{ \AA}$  and last one is centered at  $r_s = r_c = 6.5 \text{ \AA}$ .

marginal reductions in the cost function minima. In this subset, the smallest mean iteration time is for 70-70 with 31.31 minutes, even though it is quite similar to that for 60-60 (32.40 min); for 60-80, 80-80, 60-60-60, and 70-70-70, the mean iteration time is clearly longer than for 60-60 and 70-70. Regarding the number of iterations, 60-60 has the lowest average value among the more complex architectures. Altogether, this analysis indicates that the 60-60 architecture provides the best overall performance in terms of accuracy and computational time, thus being chosen for PES training hereinafter.

CO/Pd(111) EANN PES, architecture tests				
NN architecture	$\bar{t}_{\text{comp}}$ (min/iter.)	$\bar{N}_{\text{iter}} \pm \sigma_{N_{\text{iter}}}$ (iteration)	$\bar{S}^{\text{train}}(\mathbf{w})$	$\bar{S}^{\text{test}}(\mathbf{w})$
10-10	4.12	90.2 $\pm$ 114.8	115.76	5122.80
20-20	5.44	24.8 $\pm$ 27.1	91.22	6844.00
30-30	6.67	122.0 $\pm$ 214.5	68.85	221.98
40-40	14.37	11.6 $\pm$ 4.7	67.64	164.32
40-40-40	31.44	14.7 $\pm$ 8.5	69.48	197.67
50-50	20.61	14 $\pm$ 10.1	62.13	147.19
50-50-50	40.59	7 $\pm$ 0	60.65	200.88
60-60	32.40	38.4 $\pm$ 7.5	5.1380	6.0188
60-80	43.12	39.0 $\pm$ 0.7	4.8860	5.8566
60-60-60	77.02	37.0 $\pm$ 6.6	4.7520	5.8410
70-70	31.31	42.2 $\pm$ 6.1	4.8160	5.7426
70-70-70	118.72	42.3 $\pm$ 5.9	4.5740	5.6460
80-80	66.81	40.2 $\pm$ 1.3	4.6568	5.6772

**Table 5.1:** Results of the tests for EANN PES training regarding the selection of an optimal NN architecture. For each set of architectures, five PES have been generated. Four parameters have been evaluated: the computational time elapsed per iteration  $\bar{t}_{\text{comp}}$ , the average amount of training steps  $\bar{N}_{\text{iter}}$  with its standard deviation  $\sigma_{N_{\text{iter}}}$ , and the average cost function values for both train and test/validation sets,  $\bar{S}^{\text{train}}(\mathbf{w})$  and  $\bar{S}^{\text{test}}(\mathbf{w})$ , respectively. For all tests, the following set of EANN parameters is chosen:  $\eta_E = 1$ ,  $\eta_F \approx 0.096$  ( $W_F = 1$ ),  $L = 3$  ( $l = 0, 1, 2, 3$ ),  $N_\varphi = 15$  GTOs,  $\Delta S_c = 10^{-2}$  and  $r_c = 6.5 \text{ \AA}$  (see text for the values of other EANN quantities related to this choice).

Next, we fix the 60-60 architecture and search for optimum values of the remaining EANN parameters aligned with the features of our system. As before, five

PESs are generated for each trial set of parameters ( $L$ ,  $N_\varphi$ ,  $W_F$ ,  $\Delta S_c$ , and  $r_c$ ). Results are collected in Table 5.2 together with those obtained previously for the 60-60 architecture with  $L = 3$ ,  $N_\varphi = 15$ ,  $W_F = 1$ ,  $\Delta S_c = 10^{-2}$  and  $r_c = 6.5 \text{ \AA}$ , which will be considered as the benchmark against which the performance of the new trial sets will be evaluated. In general, modifications to  $L$ ,  $N_\varphi$ ,  $W_F$ , and  $\Delta S_c$  result in less accurate PESs than the reference data, in particular, when increasing  $L$ ,  $N_\varphi$  or  $W_F$  with respect to benchmark values. However, we observe some notable exceptions. Perhaps the more remarkable one comes from setting  $W_F = 0.1$  ( $\eta_F = 0.030$ ), for which  $\bar{S}(\mathbf{w})$  for both train and test sets decreases significantly compared to the reference. However, this setting results in approximately a third of the force weight used in reference data, while the same weight in energy is preserved in both cases. The risk that the energy term could influence more strongly  $\bar{S}(\mathbf{w})$  than the force ones can compromise the accuracy in the dynamical description of the  $(T_e, T_1)$  – AIMDEF forces. Such an imbalance could potentially degrade the dynamical characterization more so than a marginally less precise energy fit. In essence, a higher precision in energy estimation might be achieved at the cost of force accuracy when compared to our reference parameters. This remark is supported by comparison of the average energy and force RMSE values for each parameter choice. We get  $\overline{\text{RMSE}}_E^{\text{train}} = 0.149$  and  $0.438$  meV/moving-atom for  $W_F = 0.1$  and reference parameters in training set, respectively, while for test data set  $\overline{\text{RMSE}}_E^{\text{test}} = 0.890$  and  $0.897$  meV/moving-atom, in the same order. However, RMSE results for all force components altogether indicate the opposite trend. We obtain average RMSEs for the training set equal to  $\overline{\text{RMSE}}_F^{\text{train}} = 58.536$  and  $51.018$  meV/Å for  $W_F = 0.1$  and reference parameters, respectively, while for test set the respective results are  $\overline{\text{RMSE}}_F^{\text{test}} = 60.544$  and  $53.629$  meV/Å. Hence, error minimization of EANN training where energy and force data enter with the same proportional weights seems to be the most advantageous choice, particularly looking forward to performing accurate dynamics with the PES.

Regarding the choice of  $N_\varphi$ , the cost function values are slightly smaller when taking  $N_\varphi = 13$  instead of 15. However, this is accompanied by minor changes in the number of iterations and a slight increase in the time per iteration. Therefore, setting  $N_\varphi = 15$  seems to offer a more balanced trade-off between computational efficiency and accuracy. A similar argument serves to reject the use of the cutoff value,  $\Delta S_c = 10^{-4}$ .

Another parameter that shows margin for model improvement is the cutoff radius  $r_c$ , which defines the size of atomic environments. In fact, for  $r_c = 7.5 \text{ \AA}$  we see slightly improved cost function averages than for  $r_c = 6.5 \text{ \AA}$ , and also shorter iteration times, likely due to a larger variety of atomic environments been

captured while maintaining the spatial overlap of the set of 15 GTOs. However, the mean number of iterations for  $r_c = 6.5 \text{ \AA}$  is somewhat lower, which may seem counterintuitive when considering other cutoff radii. This observation could be related to the limited sample size of five PES trained per parameter set, so a larger sample might offer a clearer trend relative to  $r_c$ . Nevertheless, this specific remark falls apart from the focus of this preliminary study. Even though a more optimal choice of  $r_c$  in terms of accuracy can be found, these do not result in substantial differences in the cost functions. All in all, we conclude that the initial set of EANN parameters shown in the first line of Table 5.2, performs consistently well across the four quantities of interest. Therefore, we proceed with these parameters and continue the EANN PES training until reaching an optimal accuracy, as detailed in the next section.

### 5.2.3 PES quality assessment: static approach

Once the previous tests have been completed, let us summarize our choice of EANN parameters to proceed with the 0.75 ML CO/Pd(111) PES training. A set of five PESs is trained using a 60-60 architecture,  $\eta_E = 1$  and  $\eta_F \approx 0.096$  (i.e.,  $W_F = 1$ ),  $L = 3$  ( $l = 0, 1, 2, 3$ ),  $N_\varphi = 15$  (being the same amount for each  $l$ ),  $\Delta S_c = 10^{-2}$ , and  $r_c = 6.5 \text{ \AA}$ . The GTO centers  $r_s$  are uniformly distributed within the range  $[0, r_c]$  by intervals  $\Delta r_s = 0.46 \text{ \AA}$  being the first GTO center at  $r_s = 0$  and the width of the 15 GTOs,  $\alpha = 0.93 \text{ \AA}^{-2}$ . Our choice implies an EANN input layer of 60 embedded atomic densities  $\rho_{L,\alpha,r_s}^i$ .

Convergence of the five PESs generated with these parameters using as input data the 15 000 configurations described in Section 5.2.1 was already done in the previous section. It took between 27 and 48 iterations, thus further proving the efficiency of the EANN training as mentioned earlier [323]. No overfitting was observed in any of these training cycles. Cost function values lie between 4.976 and 5.473 for the training configurations and between 5.850 and 6.276 for the validation ones (test set). The corresponding mean values were already given in Table 5.2. The energy RMSEs vary from 0.393 to 0.528 meV/moving-atom for the training set and between 0.821 and 0.964 meV/moving-atom for the test one.

Due to the already indicated extreme conditions involved in the photoinduced desorption of our system –high surface temperatures, highly excited adsorbates, and varying surface coverage–, it is key to evaluate how accurately our PESs can predict not only energies, but, critically, atomic forces. To this end, we build a new data set containing 87 382 configurations not present in the EANN training process. Configurations for this predict data set are also chosen from the subsets of trajectories with none, one, and two CO desorption events as done for the

CO/Pd(111) 60-60 PES, $\eta_E = 1$ , EANN parameter tests								
L	$N_\phi$	$W_F$	$\Delta S_c$	$r_c$ (Å)	$\bar{t}_{\text{comp}}$ (min/it.)	$\bar{N}_{\text{iter}} \pm \sigma_{N_{\text{iter}}}$ (iteration)	$\bar{S}^{\text{train}}(\mathbf{w})$	$\bar{S}^{\text{test}}(\mathbf{w})$
3	15	1	$10^{-2}$	6.5	32.40	$38.4 \pm 7.5$	5.1380	6.1740
2	15	1	$10^{-2}$	6.5	29.39	$52.5 \pm 8.3$	5.9880	6.9565
4	15	1	$10^{-2}$	6.5	103.09	$23.2 \pm 8.3$	42.19	201.70
3	13	1	$10^{-2}$	6.5	38.99	$41.5 \pm 0.7$	5.0750	5.9455
3	17	1	$10^{-2}$	6.5	45.97	$15.7 \pm 14.2$	57.69	114.00
3	15	0.1	$10^{-2}$	6.5	30.55	$44.3 \pm 2.1$	1.8620	3.6040
3	15	10	$10^{-2}$	6.5	18.79	$59.8 \pm 4.4$	14.39	15.58
3	15	100	$10^{-2}$	6.5	27.15	$55.7 \pm 24.3$	44.97	47.86
3	15	1	$10^{-1}$	6.5	37.27	$21.7 \pm 1.2$	5.2590	6.0377
3	15	1	$10^{-4}$	6.5	49.02	$117.5 \pm 0.7$	4.7375	5.6870
3	15	1	$10^{-2}$	4.0	44.18	$49.2 \pm 2.6$	6.9866	8.2256
3	15	1	$10^{-2}$	5.5	33.75	$47.2 \pm 8.9$	5.2718	6.1268
3	15	1	$10^{-2}$	7.5	21.76	$45.4 \pm 4.6$	4.9594	5.8336

**Table 5.2:** Results of the tests for different values of the EANN parameters fixing 60-60 architecture and  $\eta_E = 1$ . For each test, five PES have been generated. Evaluated quantities are the maximum angular momentum  $L$  –for which admissible angular momenta values are  $l = 0, 1, \dots, L$ –, the number of GTOs  $N_\phi$ , the factor  $W_F$  (see Eq. (5.1)) related to the force weight prefactor  $\eta_F$  in the cost function  $S(\mathbf{w})$  (Eq. (4.23)) and the cutoff radius of the embedded atom environments  $r_c$ . Reference values we try changes on are  $L = 3$ ,  $N_\phi = 15$ ,  $W_F = 1$ ,  $\Delta S_c = 10^{-2}$  and  $r_c = 6.5$  Å. Four parameters have been evaluated: the computational time elapsed per iteration  $\bar{t}_{\text{comp}}$ , the average amount of training steps  $\bar{N}_{\text{iter}}$  with its standard deviation  $\sigma_{N_{\text{iter}}}$ , and the average cost function values for both train and test/validation sets,  $\bar{S}^{\text{train}}(\mathbf{w})$  and  $\bar{S}^{\text{test}}(\mathbf{w})$ , respectively. Number of moving atoms for 0.75 ML CO/Pd(111) is  $N_{\text{moving}} = 36$ .

initial input data set of 15 000 configurations (see Section 5.2.1). The results of our evaluation demonstrate the accuracy of the obtained PESs, showcasing remarkably low RMSE values in energy, ranging from 0.865 to 0.948 meV per moving atom. Furthermore, all RMSEs in the Cartesian components of the forces take values between 0.05 and 0.06 eV/Å. However, it is noteworthy that in some cases, the maximum errors in the forces are relatively large, varying between 1.039 and 5.839 eV/Å, depending on the specific coordinate and the trained EANN PES considered. This justifies our attempt to improve the quality of our PESs by increasing the initial training set of 15 000 data points.

The procedure for selecting new configurations to be added to the training data set is as follows. For each trained PES we calculate the absolute error in each force component of each of the 36 moving atoms,  $|\Delta F_\gamma|_i = |F_\gamma^{\text{EANN}} - F_\gamma^{\text{DFT}}|_i$  and identify the 10 largest values for each component  $\gamma = x, y, z$  and moving atom  $i$ . Among the five trained PES, we choose the one displaying small maximum errors for the three force components. Such selection is performed by comparing the force coordinate error histograms among the trained PESs and by examining the larger maximum errors each of them shows for each component. The  $|\Delta F_\gamma|$  distributions for the selected PES are shown in Fig. 5.4 (black histograms). The corresponding energy and force error values are given in Table 5.3 (first PES column). It is useful to determine the mean absolute error for such distributions, hereafter referred to as maximum error set mean absolute error (MESMAE),

$$\overline{|\Delta F_\gamma|} = \frac{1}{N_{\text{me},\gamma}} \frac{1}{N_{\text{moving}}} \sum_{i=1}^{N_{\text{me},\gamma}} \sum_{j=1}^{N_{\text{moving}}} |\Delta F_{j,\gamma}|_i = \frac{1}{N_{\text{me},\gamma}} \frac{1}{N_{\text{moving}}} \sum_{i=1}^{N_{\text{me},\gamma}} \sum_{j=1}^{N_{\text{moving}}} \left| F_{j,\gamma}^{\text{EANN}} - F_{j,\gamma}^{\text{DFT}} \right|_i, \quad (5.2)$$

where  $\gamma = x, y, z$ ;  $N_{\text{moving}}$  is the number of moving atoms in the system and  $N_{\text{me},\gamma}$  is the amount of maximum errors taken for each atom and force component, which we have chosen to be equal to 10 for all components. In total, the nominal 1080 force errors are provided by 883 configurations in this case (as errors in different force coordinates and different atoms can stem from the same configuration), which are next incorporated into our training data set. Subsequently, five new EANN PESs are trained from scratch under the same optimal conditions of architecture and parameter choice used in the initial training. Now 14 383 configurations randomly chosen for each PES shape the training set, while the remaining 1500 ones remain for validation. As a result, we obtain five new PESs, which take between 40 and 47 iterations for convergence. Average cost function values are slightly smaller than for first trained PESs, i.e.,  $\bar{S}^{\text{train}}(\mathbf{w}) = 5.1588$  and  $\bar{S}^{\text{test}}(\mathbf{w}) = 5.9092$ , thus hinting at certain accuracy improvement of the new set of PESs. This becomes more apparent

looking at the energy RMSEs, ranging between 0.410 and 0.461 meV/moving-atom (train) and between 0.811 and 0.869 meV/moving-atom (test). Subsequently, we repeat the prediction process as described before.

Recall that the 883 configurations that were added in this second training are not excluded from the original predict set of 87 382 configurations. Some of these may not be among the training configurational set for a given PES, thus potentially contributing to the maximum force and/or energy errors set and increasing RMSEs. Nevertheless, such contribution would be negligible, as the 883 configurations constitute only the 1.01% of the predict set, and the configurational space for training is representative of full  $(T_e, T_1)$  – AIMDEF and detailed enough to yield already small errors in energies and forces prediction. Aforementioned comparative determination of the more accurate PES among a bunch of candidates does the rest to avoid such risk.

Our new candidate PESs demonstrate impressive quality in both energies and forces as indicated in Table 5.3, first column under final PES category. We need to ensure as much accuracy as possible in atomic forces, as this is crucial for faithful system dynamics representation and proper physical behavior characterization. Therefore, following the comparative procedure already mentioned, we choose as our final PES that with the smallest maximum errors in atomic forces. It converged in 40 iterations and has an energy RMSEs per moving atom of 0.412 meV for training and 0.869 meV for validation set. PES-predicted energies for the predict data set align closely with  $(T_e, T_1)$  – AIMDEF data, as depicted in Fig. 5.5, left panel. Although the maximum error in energies is of 8.274 meV/moving-atom, the small energy RMSE of 0.852 meV reflects the minor discrepancies between EANN and AIMDEF for most of the data points, as becomes evident in the distribution of the energy error shown in the right panel of Fig. 5.5.

When we assess the accuracy of atomic force predictions, RMSE values persist within the range of 0.05 to 0.06 eV/Å as for the first five PESs, so no significant improvement is obtained in this regard. However, a closer look at maximum force errors and MESMAEs documented in Table 5.3 reveals an enhancement in predictive accuracy for all coordinates, specially regarding the maximum error in  $|\Delta F_z|$ . Compared to our PES selected from the first PES group, the maximum error reduction is twofold in  $|\Delta F_x|$  and  $|\Delta F_y|$ , and fourfold in  $|\Delta F_z|$ . When it comes to MESMAE values, improvements are more modest due to the already high accuracy reached in our previous and final PES selection, although a slightly bigger enhancement is noticeable in  $\overline{|\Delta F_z|}$ . A broader inspection reveals clear distinctions when comparing the maximum force error distributions of our final PES (red bars in Fig. 5.4) against our initial training choice (black bars). Overall, our final PES is

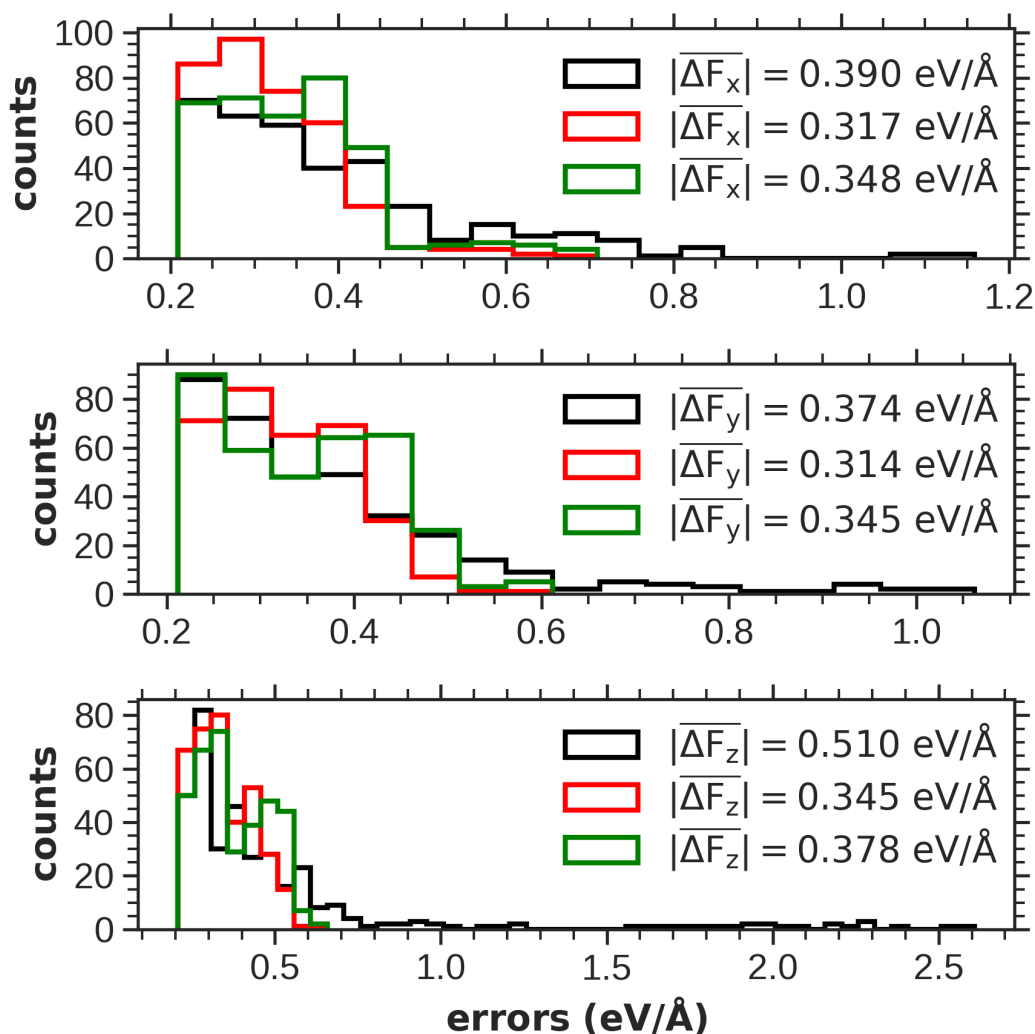


**Figure 5.4:** Cartesian coordinate-wise histograms depicting, for each of the 36 moving atoms of the 0.75 ML CO/Pd(111) system, the 10 maximum force errors  $|\Delta F_\gamma| = |F_\gamma^{\text{DFT}} - F_\gamma^{\text{EANN}}|$ , with  $\gamma = x, y, z$ . Black (red) histogram bars correspond to errors for the predict set in the EANN PES having the smaller maximum force errors of the first (final) training. Green histogram bars correspond to the whole  $(T_e, T_1)$  – AIMDEF data set of 352 505 configurations and were obtained with the final EANN PES. For each error distribution, MESMAEs,  $|\overline{\Delta F_\gamma}|$ , are given as well.

**0.75 ML CO/Pd(111), (T<sub>e</sub>,T<sub>l</sub>)-AIMDEF,  
PES energy and force errors**

		First PES	Final PES	
Predict configurations		87 382	87 382	352 505
$E/N_{\text{moving}}$ (meV)	Max. error	12.614	8.274	8.318
	RMSE	0.943	0.852	0.842
$F_x$ (eV/Å)	Max. error	1.134	0.665	0.676
	MESMAE	0.390	0.374	0.348
	RMSE	0.0527	0.0512	0.0511
$F_y$ (eV/Å)	Max. error	1.039	0.578	0.581
	MESMAE	0.374	0.314	0.345
	RMSE	0.0509	0.0496	0.0495
$F_z$ (eV/Å)	Max. error	2.563	0.624	0.628
	MESMAE	0.510	0.345	0.378
	RMSE	0.0580	0.0558	0.0555

**Table 5.3:** Maximum absolute-valued errors and RMSEs per moving atom in energies and forces, and maximum errors set mean absolute errors (MESMAEs) of all moving atoms in forces predicted by the first and final PESs (see text) for 0.75 ML CO/Pd(111) (T<sub>e</sub>, T<sub>l</sub>) – AIMDEF configurations selected from Ref. [31]. First and second data columns corresponds to the energy and force errors linked to PES predictions on a set of 87 382 configurations following the (T<sub>e</sub>, T<sub>l</sub>) – AIMDEF representativeness criteria as described in Section 5.2.1. Last column shows the energy and force errors after predicting energies and atomic forces on all 352 505 (T<sub>e</sub>, T<sub>l</sub>) – AIMDEF available data points. In all cases  $N_{\text{moving}} = 36$ .

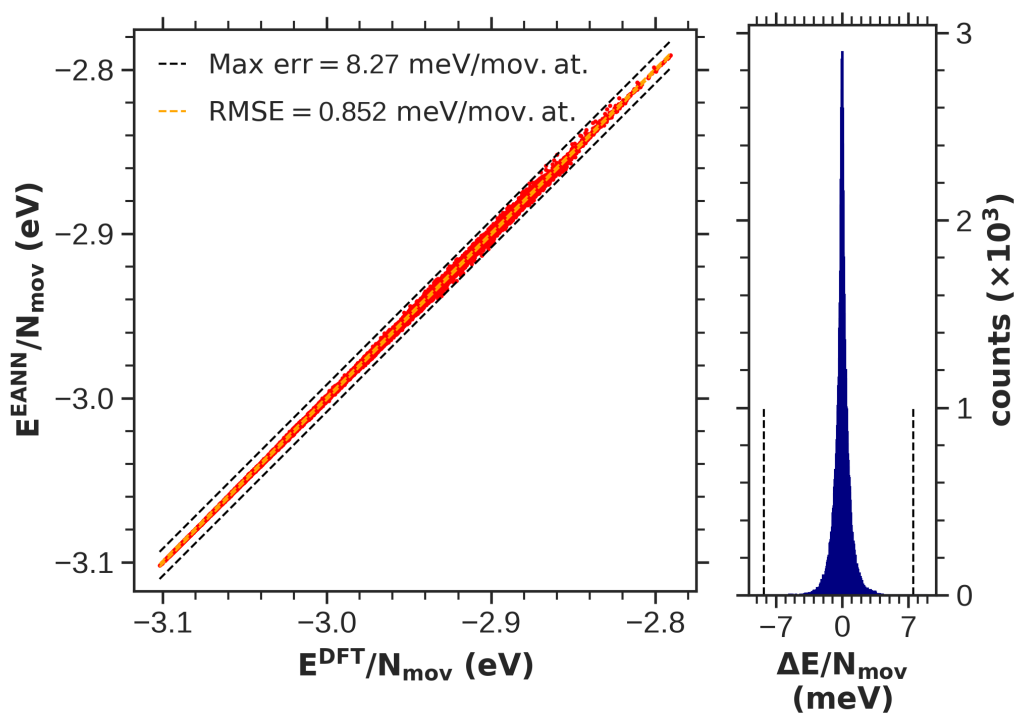


**Figure 5.5:** Left: Comparison of the potential energies per moving atom computed as determined by the (final) EANN PES against their corresponding DFT values, for a set of 87 382 configurations absent from the training data. Right: Error distribution for the energy per moving atom,  $\Delta E/N_{\text{moving}} = (E^{\text{DFT}} - E^{\text{EANN}})/N_{\text{moving}}$ , for the same ensemble of predict configurations.

accurate in forces as well, as we can see in the force convergence examples pictured in Figs. 5.6 and 5.7 for one fcc C and one hcp O atom, respectively.

Taking a step further, we examine the accuracy of our PES in predicting the energies and forces of all 352 505 configurations comprising the  $(T_e, T_l)$  – AIMDEF set (Table 5.3, last column under final PES category). As shown in this table, the maximum errors in energy and forces increase very subtly compared to the previous predict set of 87 382 configurations, thus highlighting the degree of accuracy achieved for our final PES. The slight increments and decrements in MESMAE values, which depend on the coordinate explored, reinforce this remark. Finally, all RMSEs experience marginal diminutions, caused by the larger data set we are predicting on, the representativeness of  $(T_e, T_l)$  – AIMDEF present in training configurational choice and the accuracy of our EANN PES. Maximum error histogram depicted in Fig. 5.4 in empty green bars is quite similar to the predict set of 87 382 configurations (red bars), further demonstrating our confidence in the accuracy shown by this final PES.

### 5.3 Determination of friction: numerical fit

Once we have our 0.75 ML CO/Pd(111) EANN PES, whose accuracy in predicting energies and forces has been assessed for  $(T_e, T_l)$  – AIMDEF data, it is time to perform  $(T_e, T_l)$  – MDEF with it. Thus, adiabatic forces of Eq. (3.23) can be evaluated straightforwardly, hence avoiding the more lengthy step of Hellmann-Feynman theorem usage (Eq. (3.17)). But  $(T_e, T_l)$  – MDEF still misses a crucial ingredient: we have not established the methodology for modeling the surface electron density that is necessary to calculate within LDFA the electronic friction coefficients for each adsorbate (and specifically, for each atom forming an adsorbate –IAA–). Let us first discuss how friction coefficients can be determined in an efficient way; then we will be ready for proper  $(T_e, T_l)$  – MDEF calculations.

For an efficient application of the EANN PES in  $(T_e, T_l)$  – MDEF, it is crucial to calculate the friction coefficients with a speed that matches or surpasses the computation of the potential energy. We propose a numerical fit of the surface electron density values  $\{n(\mathbf{r}_C), n(\mathbf{r}_O)\}$ , which were calculated and saved for each position of each C and O atom in the  $(T_e, T_l)$  – AIMDEF simulations, for checkup purposes. Interpolation of the surface electron density or the friction coefficients is feasible with NNs as referenced in the literature [344], and has been applied to more complex objects such as the electronic friction tensor [333, 345, 346]. Nevertheless, our method (useful within the LDFA context) favors a simpler, yet precise, approach,

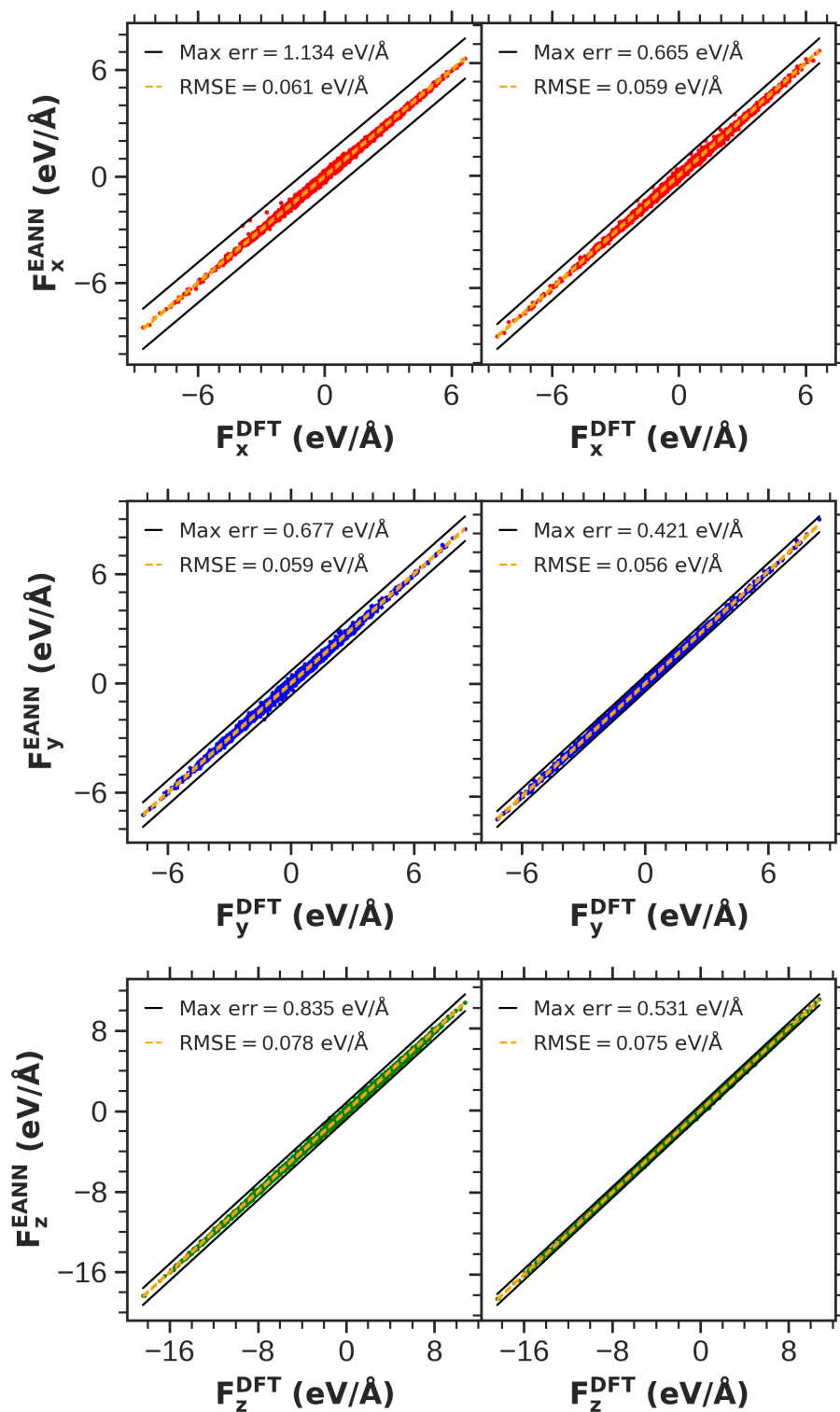


**Figure 5.6:** Cartesian component-wise comparison of the forces acting on a fcc carbon atom within the 0.75 ML CO/Pd(111) system [31],  $F_{\beta}^{\text{EANN}}$  versus  $F_{\beta}^{\text{DFT}}$ ,  $\beta = x$  (red),  $y$  (blue) and  $z$  (green). Left column EANN forces come from the initially trained PES, while the right panels correspond to the final PES. Maximum error and RMSE for each plot are also presented.

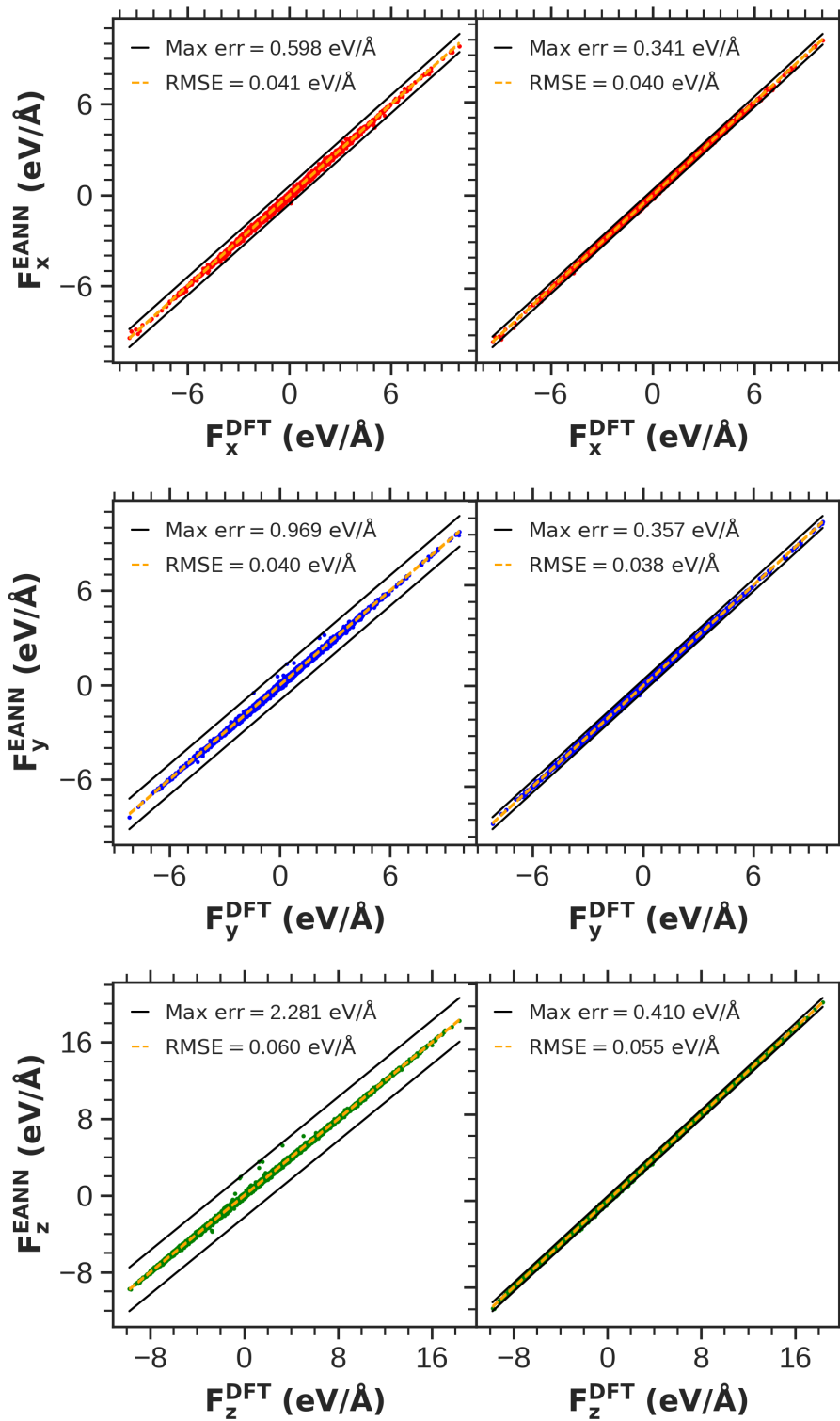
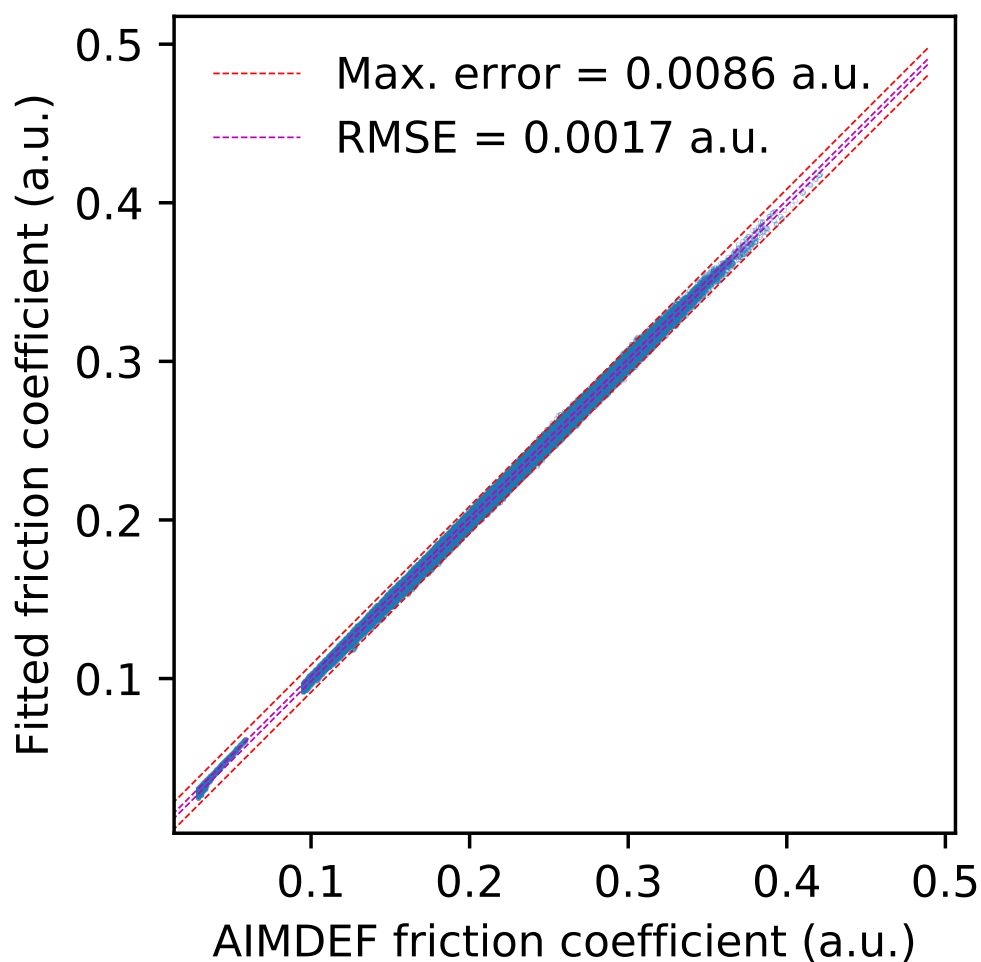


Figure 5.7: Same as Fig. 5.6 for an hcp O atom.

which we demonstrate to be both faster and more stable compared to the NN-based ones.



**Figure 5.8:** Comparison of the LDFA friction coefficients calculated with the fitted electronic density function  $n(\mathbf{r})$  (Eqs. (5.3) and (5.4)) against the data set of friction coefficients from  $(T_e, T_1)$  – AIMDEF [31]. Coefficients are given in atomic units (a.u.). (Taken from Ref. [87])

In this point, let us explore in more detail some ideas already mentioned in Section 3.2.2.5 [87]. The surface electron density at a certain position  $\mathbf{r}$  from the surface is written as a sum of the electronic densities contributed by individual Pd

atoms at this position:

$$n(\mathbf{r}) = \sum_{\text{Pd}} n(|\mathbf{r} - \mathbf{r}_{\text{Pd}}|). \quad (5.3)$$

Next, we postulate that  $n(|\mathbf{r} - \mathbf{r}_{\text{Pd}}|)$  can be effectively modeled by a superposition of two exponentially decaying functions,

$$n(|\mathbf{r} - \mathbf{r}_{\text{Pd}}|) = a \exp(-b|\mathbf{r} - \mathbf{r}_{\text{Pd}}|) + c \exp(-d|\mathbf{r} - \mathbf{r}_{\text{Pd}}|), \quad (5.4)$$

that depends on four parameters numerically fitted to the whole set of densities  $\{n(\mathbf{r}_{\text{C}}), n(\mathbf{r}_{\text{O}})\}$  that were stored during the  $(T_e, T_1)$  – AIMDEF simulations. Their values are  $a = 3.15975$  a.u. (atomic units),  $b = 4.25214 \text{ \AA}^{-1}$ ,  $c = 0.29080$  a.u., and  $d = 2.52252 \text{ \AA}^{-1}$ . Alternative functions, such as Gaussian ones and their combinations with exponential functions, were also examined; however, the dual exponential model yielded optimal results with minimal complexity and parameter count. Equations (5.3) and (5.4) constitute the density generator function (DGF) of our system.

Upon establishing how to calculate the surface electron density  $n(\mathbf{r})$ , the friction coefficients on C and O atoms  $\eta(\mathbf{r})$  are calculated via the LDFA [51, 52], as also done in  $(T_e, T_1)$  – AIMDEF. Specifically, the LDFA friction coefficients at a certain position  $\mathbf{r}$  in terms of the surface electron density at that position are given by the following (fitted) expression:

$$\eta(\mathbf{r}) = \sum_{i=1}^2 A_i r_s(\mathbf{r})^{B_i} \exp(C_i r_s(\mathbf{r})), \quad (5.5)$$

where  $r_s(\mathbf{r}) = [3/(4\pi n(\mathbf{r}))]^{1/3}$  is the mean electron radius and the parameters  $(A_i, B_i, C_i)$  are atom specific. In particular,  $(A_1=22.654, B_1=2.004, C_1=-3.134, A_2=2.497, B_2=-2.061, C_2=0.0793)$  for C and  $(A_1=1.36513, B_1=-1.8284, C_1=-0.0820301, A_2=50.342, B_2=0.490785, C_2=-2.70429)$  for O.

In Fig. 5.8, the friction coefficients obtained with the surface electron density calculated with Eq. (5.3) are compared to their  $(T_e, T_1)$  – AIMDEF counterparts. The results demonstrate a maximum error of 0.0086 a.u. and a  $\text{RMSE}_{\eta(\mathbf{r})} = 0.0017$  a.u. Such discrepancies are notably minimal, particularly when compared to the larger errors typically encountered in alternative embedding density calculations [60]. Therefore, the proposed method to calculate  $n(\mathbf{r})$  (and hence  $\eta(\mathbf{r})$ ) can be safely incorporated to the  $(T_e, T_1)$  – MDEF framework to accurately and quickly evaluate the friction and stochastic forces in Eq. (3.12).

## 5.4 $(T_e, T_l)$ – MDEF on 0.75 ML CO/Pd(111): dynamical quality tests

Up to this point, we have demonstrated that both our optimally trained EANN PES and our density generator function accurately reproduce the 0.75 ML CO/Pd(111)  $(T_e, T_l)$  – AIMDEF data. Despite this being a reasonable quality check, it is not sufficient to prove that using both functions in  $(T_e, T_l)$  – MDEF simulations will reproduce the  $(T_e, T_l)$  – AIMDEF results. This is due to two possible undesirable situations [313]. Firstly,  $(T_e, T_l)$  – MDEF trajectories may sample regions of the configurational space that, in spite of being close to the EANN PES training set and the DGF data set, can be inaccurately described by the optimized parameters. Secondly, these trajectories might enter regions of the configurational space different from the  $(T_e, T_l)$  – AIMDEF data set, where extrapolation of the EANN PES and the DGF function could produce odd or even unphysical dynamics results. Moreover, due to the large amount of DOFs in our system, up to 108, the likelihood of encountering these issues increases.

In order to rule out these sources of error and further address the precision of our EANN PES and DGF, we perform  $(T_e, T_l)$  – MDEF simulations of the ultrafast photoinduced CO desorption in the 0.75 ML CO/Pd(111) system for exactly the same experimental conditions simulated with  $(T_e, T_l)$  – AIMDEF [31] (see Section 5.1). This includes using the same simulation cell, same desorption criteria (CO CM height greater than 6 Å and positive CO CM momentum along the  $z$ -axis), and the same time-dependent electronic and lattice temperatures that were used in Ref. [31] to describe the laser-induced excitations. In particular, we perform two sets of dynamics calculations independent of each other:

- **$(T_e, T_l)$  – MDEF-1:** The first set contains the same 100 initial configurations of Ref. [31]. This allows  $(T_e, T_l)$  – AIMDEF and  $(T_e, T_l)$  – MDEF trajectories to be compared step by step, thus allowing for the detection of possible major discrepancies in the potential energy and electronic friction values that could lead to strong deviations of  $(T_e, T_l)$  – MDEF from the  $(T_e, T_l)$  – AIMDEF results.
- **$(T_e, T_l)$  – MDEF-2:** This second set consists on 2000 configurations randomly chosen from a set of 10 000 structures obtained after leaving the initial 100  $(T_e, T_l)$  – AIMDEF configurations evolve over 1 ps at a constant temperature  $T_0 = 90$  K. This broader set serves to evaluate how well  $(T_e, T_l)$  – MDEF

trajectories behave when they commence from data points not contained in the training data sets.

We observe that the (T<sub>e</sub>, T<sub>l</sub>) – MDEF-1 trajectories closely follow their (T<sub>e</sub>, T<sub>l</sub>) – AIMDEF counterparts, especially during the early stage of dynamics. As an example, we compare in Fig. 5.9 the time evolution of the friction coefficient experienced by each C atom between a typical (T<sub>e</sub>, T<sub>l</sub>) – MDEF-1 trajectory and its corresponding (T<sub>e</sub>, T<sub>l</sub>) – AIMDEF trajectory. For all adsorption sites, the correlation of friction coefficients during the first 400–500 fs is striking, and for some C atoms it is almost perfect. After 500 fs, the friction coefficients start to diverge as trajectories start to follow different pathways due to cumulative differences in the dynamics. This behavior is shared among all (T<sub>e</sub>, T<sub>l</sub>) – MDEF-1 simulations and reflects that the quality of our fitted EANN PES and DGF is good enough to keep (T<sub>e</sub>, T<sub>l</sub>) – MDEF trajectories close to their (T<sub>e</sub>, T<sub>l</sub>) – AIMDEF analogues in a very detailed way for several hundred femtoseconds. This is a remarkable quality achievement as the agreement was attained despite the possible dynamical instability, the stochastic nature of the Langevin equations of motion, and the different integration time step used in the simulations ( $\Delta t = 0.2$  fs in MDEF,  $\Delta t = 1$  fs in AIMDEF) for an amount of time in which the electronic temperature of the 2TM changes from 90 K ( $t = 0$  fs) to 5500 K ( $t = 500$  fs).

Next let us analyze the CO desorption probability, which is calculated as follows:

$$P_{\text{CO,des}}(t) = \frac{N^{\text{CO,des}}(t)}{N^{\text{CO,tot}}} = \frac{N^{\text{CO,des}}(t)}{n_0^{\text{CO,cell}} N_{\text{traj}}}, \quad (5.6)$$

being  $N^{\text{CO,des}}(t)$  the cumulative sum of CO molecules desorbed from the surface within the simulated trajectories at a given time and  $N^{\text{CO,tot}}$  the total initial amount of CO molecules in the full ensemble of simulations. The latter is calculated as the product of the initial number of CO molecules in a single simulation supercell,  $n_0^{\text{CO,cell}}$  (for our 0.75 ML ( $4 \times 2$ ) cell,  $n_0^{\text{CO,cell}} = 6$ ) and the total number of trajectories  $N_{\text{traj}}$ . Moreover, a site-dependent version of  $P_{\text{CO,des}}(t)$  can be defined,

$$P_{\text{CO,site,des}}(t) = \frac{N^{\text{CO,site,des}}(t)}{n_0^{\text{CO,site}} N_{\text{traj}}}, \quad (5.7)$$

where  $N^{\text{CO,des}}(t)$  and  $n_0^{\text{CO,cell}}$  of Eq. (5.6) are replaced by the cumulative amount of CO adsorbates desorbed from a specific initial adsorption site,  $N^{\text{CO,site,des}}(t)$ , and the number of CO molecules initially adsorbed on that site in a single cell,  $n_0^{\text{CO,site}}$ , respectively. For our system,  $n_0^{\text{CO,site}} = 2$ , while site  $\equiv$  top,hcp,fcc. Furthermore,

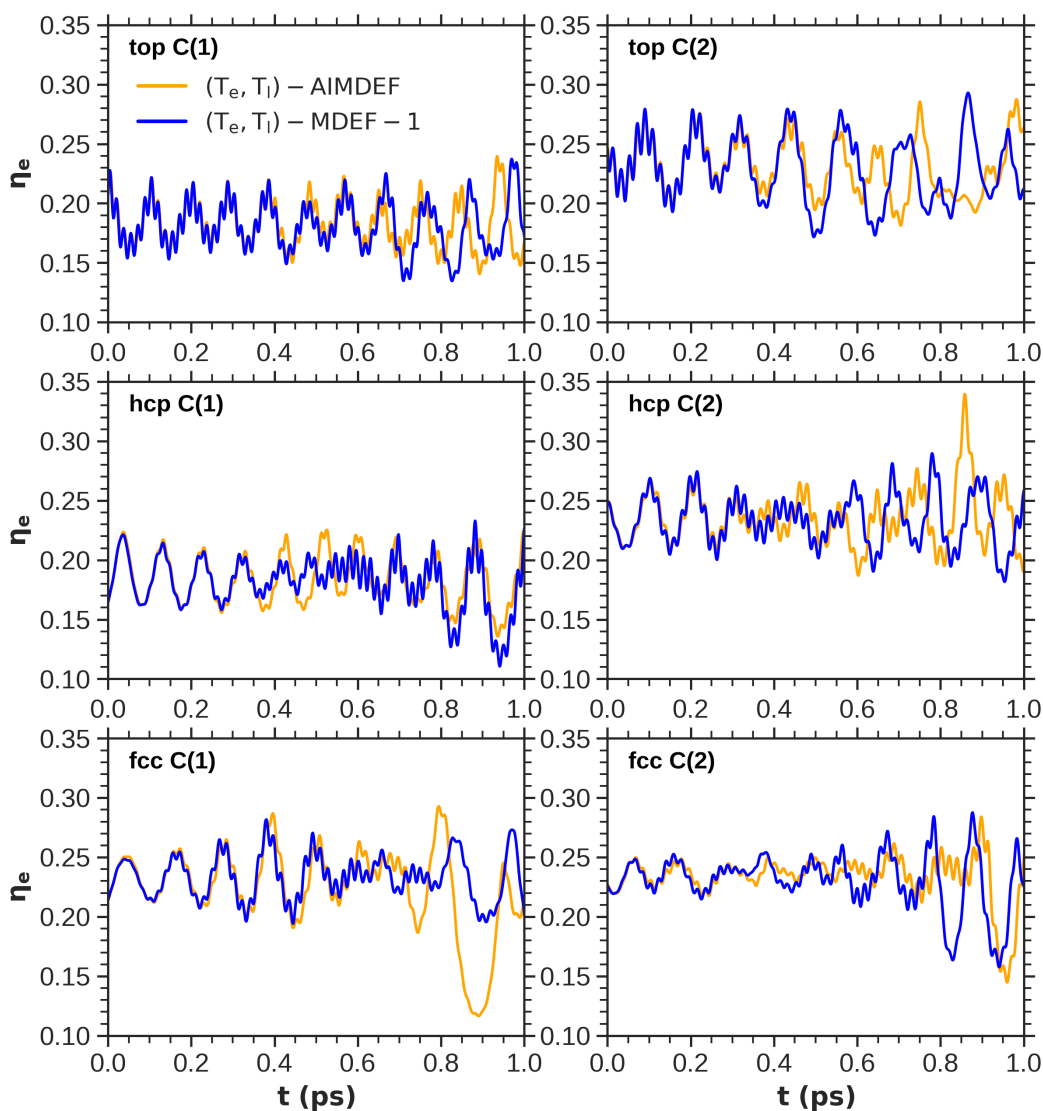


**Figure 5.9:** Time evolution of the friction coefficients  $\eta_e$  for C atoms along a representative trajectory. Orange lines depict the  $(T_e, T_i)$  - AIMDEF results for a specific trajectory of Ref. [31]. Blue lines represent the results obtained from  $(T_e, T_i)$  - MDEF-1 –i.e., performing molecular dynamics with our final EANN PES and the density generation function–, for a trajectory initiated under identical  $(T_e, T_i)$  - AIMDEF conditions. Each graph shows the results for a different C atom in the simulation model, whose initial positions are labeled in the figures and correspond to the top (upper row), fcc (middle), and hcp sites (lower).

these definitions imply that the desorption events follow a binomial distribution (desorbed or not desorbed) with 6  $N_{\text{traj}}$  independent events and  $P_{\text{CO,des}}(t)$  as the success probability. In order to obtain a detailed statistical picture, we want to determine the standard deviation associated with each desorption probability with some confidence level. Due to their advantages in maximizing accuracy of the uncertainty interval, particularly when dealing with small sample sizes and probabilities very close to 0 or 1, from here on Wilson score intervals with a confidence level  $z = 99\%$  [347] will be used. Let us note that, for this study on CO photodesorption at early times, we have considered as desorbed those molecules whose CM  $z$  position,  $z_{\text{cm,CO}}$ , verifies that  $z_{\text{cm,CO}} \geq \bar{z}_{\text{surf}} + 6 \text{ \AA}$  at any given time, being  $\bar{z}_{\text{surf}}$  the CM of the first layer Pd atoms, and with its velocity on  $z$  coordinate  $v_{z,\text{cm,CO}} > 0$ .

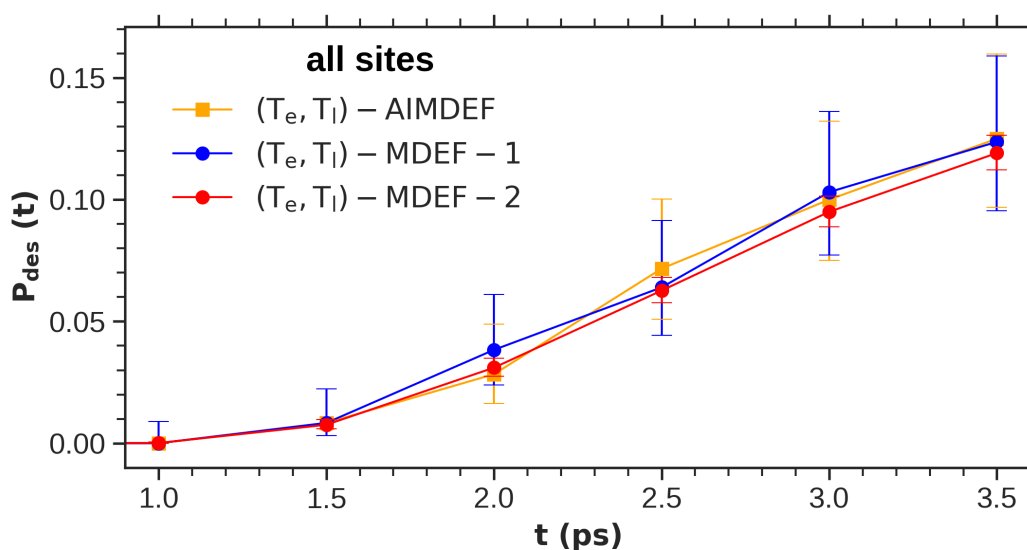


**Figure 5.10:** Total CO desorption probabilities in the interval [1.0, 3.5] ps for the three ensembles of dynamics calculations considered in this work:  $(T_e, T_l)$  – AIMDEF (orange),  $(T_e, T_l)$  – MDEF-1 (blue) and  $(T_e, T_l)$  – MDEF-2 (red). Here,  $(T_e, T_l)$  – AIMDEF results are extracted from the simulations performed in Ref. [31]. Both  $(T_e, T_l)$  – MDEF-1 and  $(T_e, T_l)$  – MDEF-2 stand for results obtained from simulations performed with our best trained EANN PES using, respectively, the same 100 initial conditions than in  $(T_e, T_l)$  – AIMDEF, and 2000 random initial conditions. Standard deviations are depicted for multiples of 500 fs to give an idea of the uncertainty intervals while maintaining the clarity of the exact curves.

Figure 5.10 shows the total CO desorption probability over time, while Figure 5.11 depicts this probability decomposed by the initial adsorption sites. Three sets of data

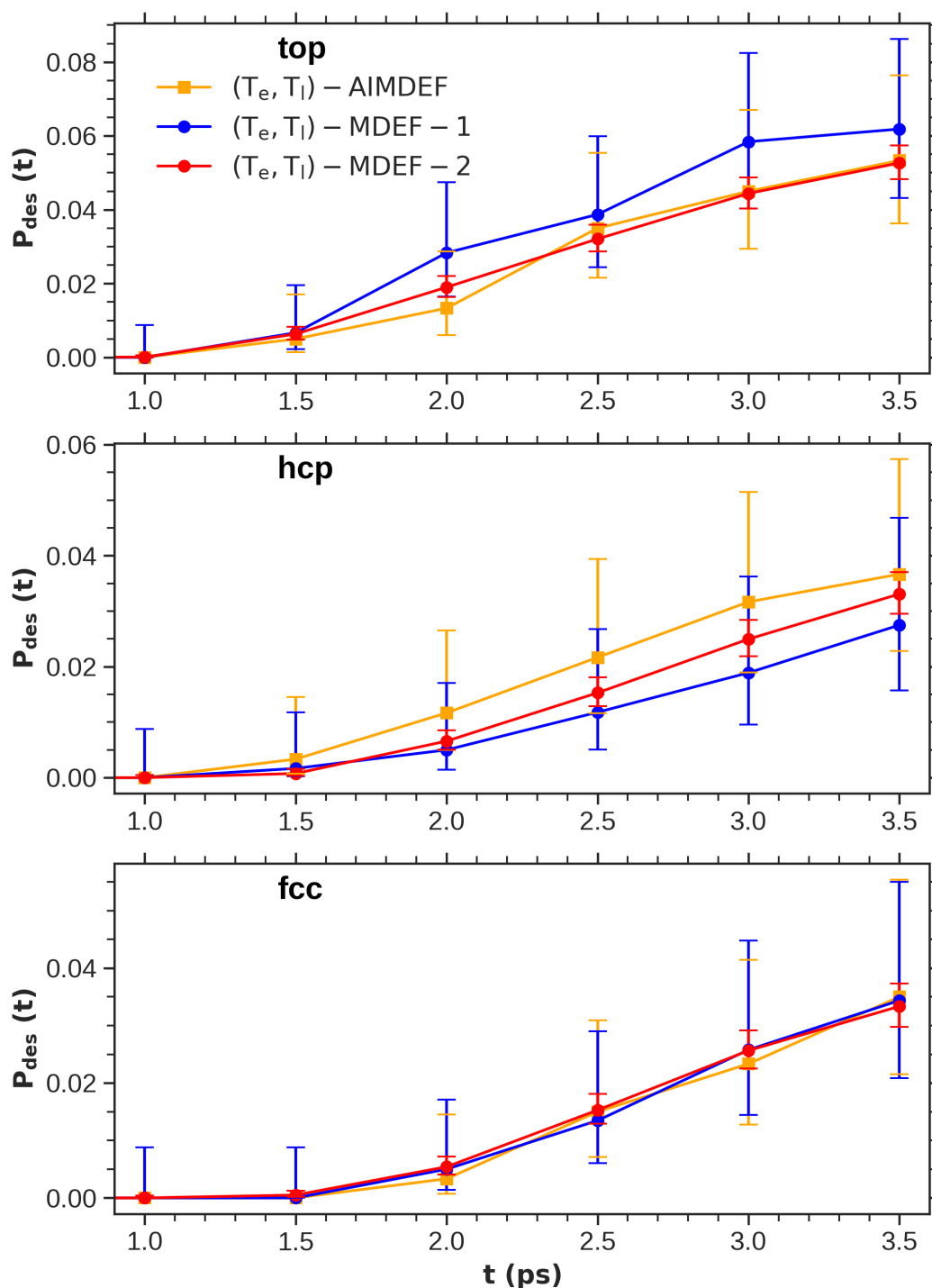


**Figure 5.11:** Site-specific CO desorption probabilities in the interval [1.0, 3.5] ps for the three ensembles of dynamics calculations considered in this work: ( $T_e, T_l$ ) – AIMDEF (orange), ( $T_e, T_l$ ) – MDEF-1 (blue) and ( $T_e, T_l$ ) – MDEF-2 (red). Here, ( $T_e, T_l$ ) – AIMDEF results are extracted from the simulations performed in Ref. [31]. Both ( $T_e, T_l$ ) – MDEF-1 and ( $T_e, T_l$ ) – MDEF-2 stand for results obtained from simulations performed with our best trained EANN PES using, respectively, the same 100 initial conditions than in ( $T_e, T_l$ ) – AIMDEF, and 2000 random initial conditions. Standard deviations are depicted for multiples of 500 fs to give an idea of the uncertainty intervals while maintaining the clarity of the exact curves. Here, desorption probabilities correspond to CO initially adsorbed at top (upper), hcp (middle) and fcc (lower panel) sites.

are shown in each panel for both figures, namely (T<sub>e</sub>, T<sub>l</sub>)–MDEF-1 (blue), (T<sub>e</sub>, T<sub>l</sub>)–MDEF-2 (red), and (T<sub>e</sub>, T<sub>l</sub>) – AIMDEF (orange). Since no desorption event occurs during the first ps of the dynamics, the desorption probabilities are shown in the interval 1.0 to 3.5 ps –the latter time coinciding with the (T<sub>e</sub>, T<sub>l</sub>)–AIMDEF final time. For the sake of clarity, the Wilson score intervals are plotted only for multiples of 500 fs in all cases. Desorption probabilities for both (T<sub>e</sub>, T<sub>l</sub>) – MDEF-1 and (T<sub>e</sub>, T<sub>l</sub>) – MDEF-2 are in close agreement with (T<sub>e</sub>, T<sub>l</sub>) – AIMDEF, particularly, for the total and the fcc site-specific CO desorption probabilities. Regarding the site-resolved desorption probabilities, (T<sub>e</sub>, T<sub>l</sub>) – MDEF-1 diverges a bit more from (T<sub>e</sub>, T<sub>l</sub>) – AIMDEF than (T<sub>e</sub>, T<sub>l</sub>) – MDEF-2, as (T<sub>e</sub>, T<sub>l</sub>) – MDEF-1 shows a higher desorption probability for top-site CO, while it underestimates the hcp-site CO desorption. Nevertheless, (T<sub>e</sub>, T<sub>l</sub>) – AIMDEF results are contained in almost all specific data points depicted for (T<sub>e</sub>, T<sub>l</sub>) – MDEF-1, and their respective standard deviation intervals for a 99% confidence level overlap in all cases. Therefore, discrepancies arise simply from the statistical variability inherent in the 100-trajectory ensembles of each method, and (T<sub>e</sub>, T<sub>l</sub>) – MDEF-1 is anyway consistent compared to the (T<sub>e</sub>, T<sub>l</sub>) – AIMDEF reference. Furthermore, the (T<sub>e</sub>, T<sub>l</sub>) – MDEF-2 probabilities match closer (T<sub>e</sub>, T<sub>l</sub>) – AIMDEF ones overall, with only some underestimation of hcp-CO desorption more subtle than for (T<sub>e</sub>, T<sub>l</sub>) – MDEF-1. Despite originating from a distinct set of initial configurations, this concordance endorses the reliability of our EANN PES and DGF in accurately characterizing the dynamic energy barriers faced by CO molecules during laser-induced desorption, comparable to the original (T<sub>e</sub>, T<sub>l</sub>) – AIMDEF findings. And, importantly, the improved statistics of (T<sub>e</sub>, T<sub>l</sub>) – MDEF-2 over the original (T<sub>e</sub>, T<sub>l</sub>) – AIMDEF simulations allows us to describe the different desorption properties with higher precision.

Taking advantage of the enhanced statistics provided by (T<sub>e</sub>, T<sub>l</sub>) – MDEF-2, a more precise determination of the desorption process timeline is enabled. Recalling that the laser pulse peak arrives at  $t = 410$  fs in our simulations, the first desorption events are recorded 0.6 ps later. Such occurrences involve predominantly top-site CO, with CO desorption from hcp and fcc sites requiring approximately an additional 500 fs to commence.

Having demonstrated the accuracy of our methodology to reproduce the (T<sub>e</sub>, T<sub>l</sub>)–AIMDEF trajectories for the first few hundred femtoseconds and the final result in terms of CO desorption probabilities, we now focus on the time evolution of the kinetic energy of CO molecules, which is more sensitive to the subtle details of the paths followed on the PES. The left panel of Fig. 5.12 shows, in full thick lines, the time evolution of the mean translational ( $\langle E_{\text{kin}}^{\text{trans}} \rangle$ ) and mean rovibrational ( $\langle E_{\text{kin}}^{\text{rovibr}} \rangle$ ) kinetic energy of adsorbed CO molecules averaged over trajectories.

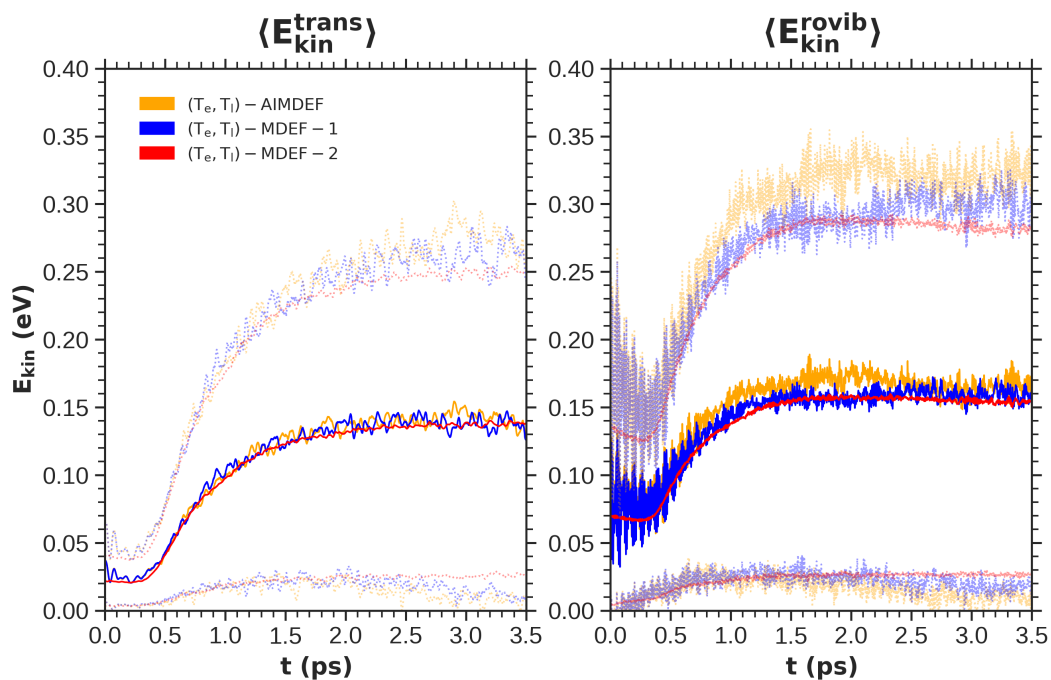


**Figure 5.12:** Mean center of mass translational kinetic energy,  $\langle E_{kin}^{trans} \rangle$ , (left panel, full thick lines) and mean rovibrational kinetic energy,  $\langle E_{kin}^{rovibr} \rangle$ , (right panel, full thick lines) of adsorbed CO molecules as a function of time. Corresponding dotted thin curves above and below each  $\langle E_{kin}^{trans(rovibr)} \rangle$  curve show the mean values plus and minus associated standard deviations, respectively. For both panels,  $(T_e, T_1) - \text{AIMDEF}$  stands for results extracted from Ref. [31] calculations,  $(T_e, T_1) - \text{MDEF-1}$  stands for dynamics results obtained from our best trained EANN PES using the same 100  $(T_e, T_1) - \text{AIMDEF}$  initial conditions, and  $(T_e, T_1) - \text{MDEF-2}$  stands for dynamics results obtained with the same EANN PES using 2000 random initial conditions.

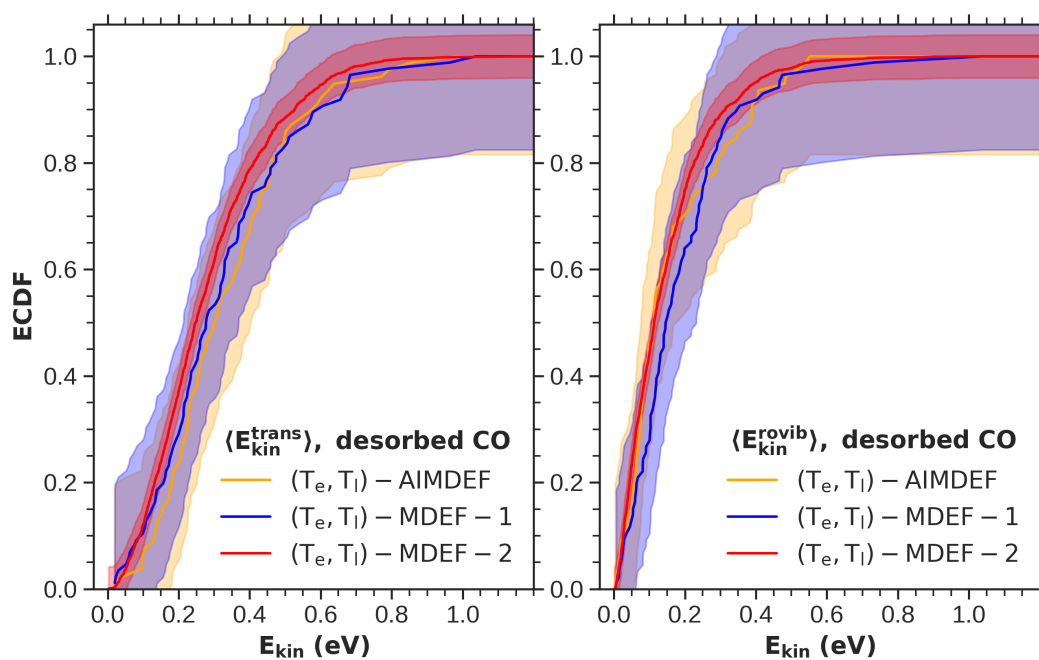


**Figure 5.13:** Empirical cumulative distribution functions (ECDFs) of desorbed CO for the center of mass translational kinetic energy (left panel) and rovibrational kinetic energy (right panel). Shaded areas mark 99% Dvoretzky-Kiefer-Wolfowitz confidence intervals [348]. For both panels,  $(T_e, T_l)$  – AIMDEF stands for results extracted from Ref. [31] calculations,  $(T_e, T_l)$  – MDEF-1 stands for dynamics results obtained from our best trained EANN PES using the same 100  $(T_e, T_l)$  – AIMDEF initial conditions, and  $(T_e, T_l)$  – MDEF-2 stands for dynamics results obtained with the same EANN PES using 2000 random initial conditions.

Let us clarify that  $\langle E_{\text{kin}}^{\text{trans}} \rangle$  refers to the kinetic energy of the CO CM, whereas  $\langle E_{\text{kin}}^{\text{rovibr}} \rangle$  is calculated as the mean of C and O total kinetic energy minus  $E_{\text{kin}}^{\text{trans}}$ , i.e.,  $\langle E_{\text{kin}}^{\text{rovibr}} \rangle = \langle E_{\text{kin}}(\text{CO}) - E_{\text{kin}}^{\text{trans}} \rangle$ . Examining  $\langle E_{\text{kin}}^{\text{trans}} \rangle$ , we observe that the results from both  $(T_e, T_1)$ -MDEF-1 (in blue) and  $(T_e, T_1)$ -MDEF-2 (in red) align closely with the  $(T_e, T_1)$ -AIMDEF values (in orange). This similarity indicates that our EANN PES effectively reproduces the mean translational kinetic energies. Following the same color code as in the left panel of Fig. 5.12, rovibrational energies for both  $(T_e, T_1)$ -MDEF-1 and  $(T_e, T_1)$ -MDEF-2 also reflect analogous behaviors with respect to the  $(T_e, T_1)$ -AIMDEF  $\langle E_{\text{kin}}^{\text{rovibr}} \rangle$  results. Together with the mean kinetic energies, the instantaneous energy distributions of the adsorbed species constitute an additional and even more stringent test to assess the accuracy of our PES. To this end, we can compare the kinetic energy standard deviations for each data set and for each kinetic contribution  $\Delta E_{\text{kin}}^{\text{trans(rovibr)}}$ . For the sake of clarity, in Fig. 5.12 two additional sets of thin dotted curves represent the values  $\langle E_{\text{kin}}^{\text{trans(rovibr)}} \rangle \pm \Delta E_{\text{kin}}^{\text{trans(rovibr)}}$  in order to delimit the standard deviation regions linked to each distribution average. The figure demonstrates a notable consistency between  $(T_e, T_1)$ -AIMDEF instantaneous standard deviations and their  $(T_e, T_1)$ -MDEF-1 and  $(T_e, T_1)$ -MDEF-2 counterparts, thereby underscoring the accuracy of our EANN PES.

As for adsorbed CO species, a similar check can be performed for the kinetic energy of the desorbed molecules. Notice that, in our current analysis, a molecule is considered as desorbed if its CM height from the surface plane is greater than 6.0 Å and the  $z$ -component of its CM momentum is positive at the end of the simulation (3500 fs). Fig. 5.13 displays the empirical cumulative distribution functions (ECDFs) for both kinetic terms in solid lines. Let us briefly recall that a cumulative distribution function  $\text{CDF}(x)$  represents the probability of some random variable  $X$  to take on values equal to or smaller than a given value  $x$ ,  $\text{CDF}(x) = P(X \leq x)$ . Furthermore,  $\text{CDF}(x)$  does not decrease along its domain, hence only increasing or remaining constant as  $x$  grows, and takes values within the interval  $[0, 1]$ . In this case, we are evaluating the cumulative distribution function for the kinetic energy values we have calculated for all desorbed CO molecules at each time step they were desorbed at, for all trajectories of each ensemble. Along with the ECDFs, we plot their related Dvoretzky-Kiefer-Wolfowitz confidence intervals [348] for a confidence level of 99% (shaded colors). Latter ones represent the ranges where the exact ECDF for a given kinetic energy distribution can be found with a 99% probability. As for Fig. 5.12, translational and rovibrational mean kinetic energies are represented in the left and right panels, respectively, under the same colors assigned for each dynamics set. Firstly, one can notice that both mean kinetic energy contributions of the desorbed molecules (solid lines) for  $(T_e, T_1)$ -MDEF-1

and (T<sub>e</sub>, T<sub>l</sub>) – MDEF-2 fall within the confidence intervals of (T<sub>e</sub>, T<sub>l</sub>) – AIMDEF, thus (T<sub>e</sub>, T<sub>l</sub>) – MDEF curves matching (T<sub>e</sub>, T<sub>l</sub>) – AIMDEF trends substantially. Such a conclusion is supported by the proximity of all exact kinetic energy distribution trends and by the overlapping of their respective confidence intervals. In particular for (T<sub>e</sub>, T<sub>l</sub>) – MDEF-2, its larger sample size leads to significantly narrower confidence intervals, therefore reflecting a closer approximation to the exact distribution. These findings further corroborate the consistency of the rovibrational and translational behaviors of the CO molecules described in Ref. [31], both when they are adsorbed on the surface and after desorption has taken place.

Taking advantage of the improved statistics provided by (T<sub>e</sub>, T<sub>l</sub>) – MDEF-2, we can now reliably determine the final rovibrational state of the desorbed CO molecules ( $\nu, j$ ), an analysis that cannot be performed in (T<sub>e</sub>, T<sub>l</sub>) – AIMDEF due to the poor statistics. Following the quasiclassical action-angle variable approach [349], the vibrational state number  $\nu$  is defined as the closest integer value that satisfies the condition,

$$\nu = \frac{\alpha_\nu}{h} - \frac{1}{2}, \quad (5.8)$$

with  $h$  being the Planck constant and  $\alpha_\nu$  the vibrational action, defined as follows,

$$\alpha_\nu = \oint d\mathbf{r} \mathbf{p} = \oint dr p_r = \frac{1}{\pi} \int_{r_{\text{in}}}^{r_{\text{out}}} dr \sqrt{2\mu \left( E_{\text{CO}} - V(r) - \frac{L_{\text{cl}}^2}{2\mu r^2} \right)}, \quad (5.9)$$

where  $\mathbf{p} = p_r \hat{r}$  is the desorbed CO vibrational momentum,  $\mu$  is its reduced mass,  $r_{\text{out}}$  and  $r_{\text{in}}$  are the outer and inner turning points of the CO vibrational motion,  $E_{\text{CO}}$  is its total internal energy,  $V(r)$  is the CO vibrational potential in vacuum (here provided by our PES) and  $L_{\text{cl}}$  is the classical total angular momentum. Furthermore, the rotational quantum number  $j$  is computed from the classical angular momentum  $L_{\text{cl}}$  as the closest integer that verifies

$$j = \frac{1}{2} \left( \sqrt{1 + 4 \frac{L_{\text{cl}}^2}{\hbar^2}} \right), \quad (5.10)$$

where  $\hbar$  is the reduced Planck constant.

The vibrational profile of the desorbed CO is plotted in Fig. 5.14, whereas its probability distribution of rotational quantum numbers is depicted in Fig. 5.15. As shown in Fig. 5.14, most of the desorbed molecules (83.3%) are in the vibrational ground state  $\nu = 0$ . There is a significantly smaller probability for  $\nu = 1$ , and even smaller probabilities for  $\nu = 2$  and  $\nu = 3$ . The rotational state distribution is

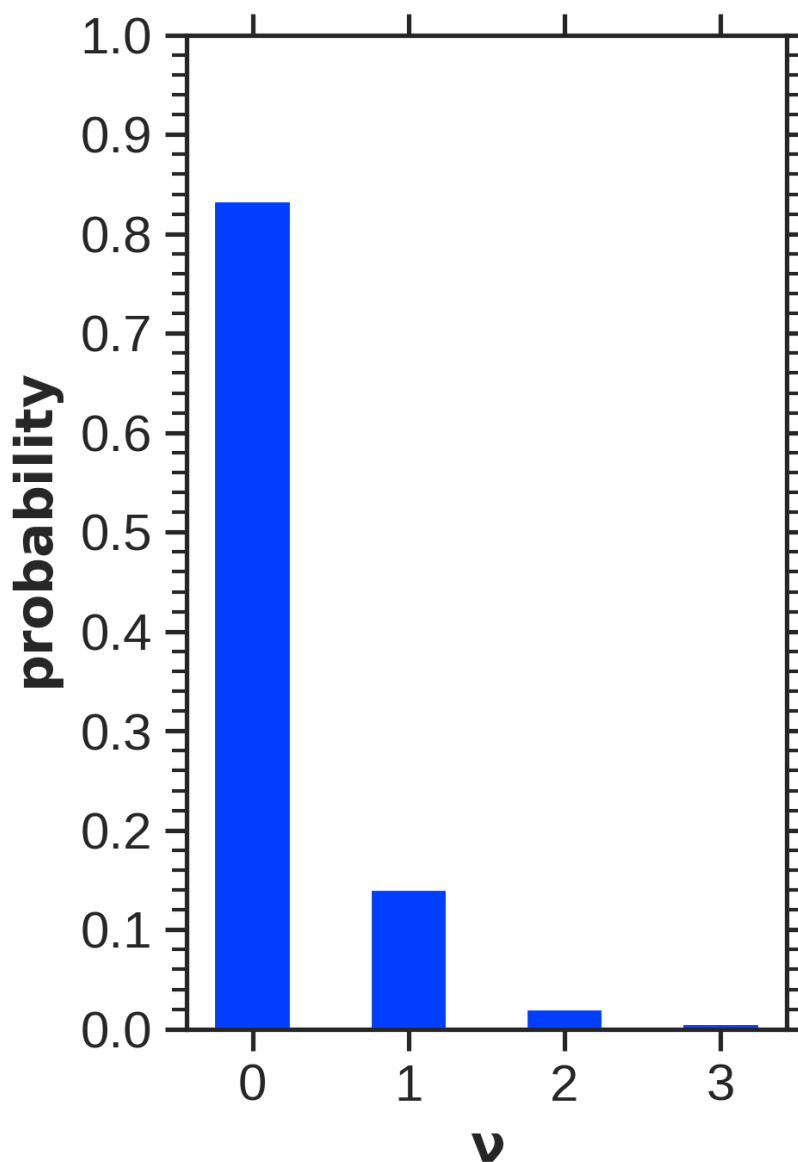


**Figure 5.14:** Probability distribution of the vibrational quantum number  $\nu$  of desorbed CO in the  $(T_e, T_1)$  – MDEF-2 data set, determined from Eq. (5.8) after the quasiclassical approach of Ref. [349]. All CO molecules considered in this distribution have rotational states  $j \geq 0$ .

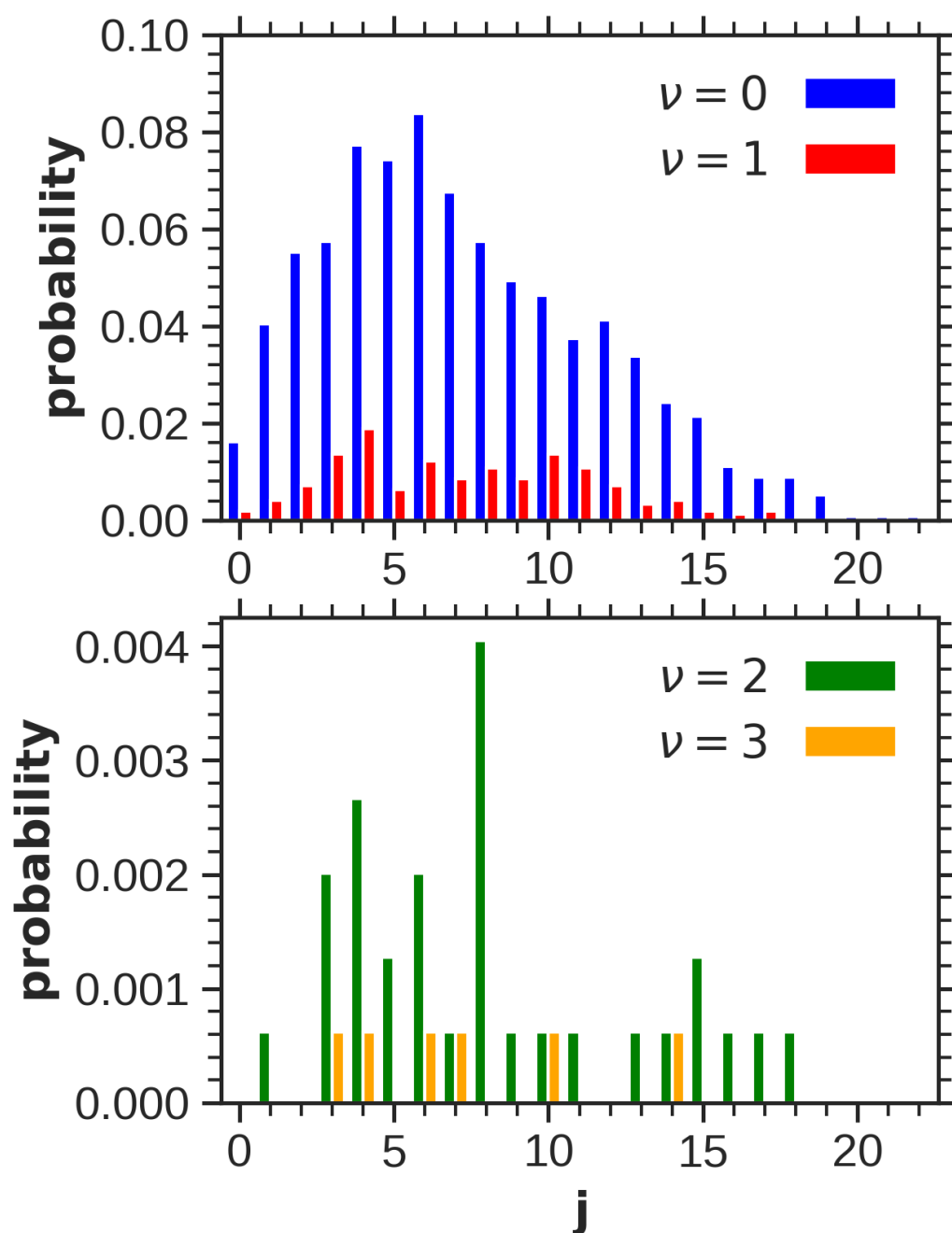


**Figure 5.15:** Probability distributions of the rotational quantum number  $j$  for each of the vibrational states observed among the desorbed CO in (T<sub>e</sub>, T<sub>1</sub>) – MDEF-2 set,  $\nu = 0, 1$  (blue and red bars of top panel, respectively) and  $\nu = 2, 3$  (green and orange bars of bottom panel, respectively). Rotational states were determined from Eq. (5.10) following the quasiclassical approach of Ref. [349].

analyzed in Fig. 5.15 for each vibrational state. For the vibrational ground state, the histogram shows a wide range of populated rotational states, with a distribution that peaks at low values ( $j = 4-7$ ) and progressively decreases within the range  $j \lesssim 20$ . For  $\nu > 0$  more limited conclusions can be drawn due to the poorer statistics, specially for  $\nu = 3$ . Nevertheless, we observe that for  $\nu = 1$  and  $\nu = 2$  rotational state distributions also peak at lower  $j$  values ( $j < 10$ ) and their tails lie below  $j = 20$ . Overall, we conclude that desorption predominantly leaves CO molecules in the vibrational ground state and rotationally excited ( $j \leq 20$ ).

## 5.5 Conclusions

The research presented in this chapter builds upon the theoretical framework outlined in previous chapters, focusing on the femtosecond laser-induced desorption of CO from Pd(111) surfaces. This is a complex phenomenon, where the coupling of electronic and phononic subsystems plays a crucial role, influencing adsorbate dynamics and potentially leading to enhancement of desorption yields [31]. Our approach has focused on simulating these dynamics using molecular dynamics with electronic friction and thermostat [( $T_e, T_l$ ) – MDEF], which rely on recently developed ML techniques [87].

A central aspect in the ( $T_e, T_l$ ) – MDEF simulations discussed in this chapter was the construction of a multidimensional PES. Using the embedded atom neural network (EANN) framework, we have performed such a process to describe the photoinduced desorption of 0.75 ML CO from Pd(111). Such a PES needs to account for some challenges linked to the complexity of our system: multiple adsorbates and moving surface atoms –this leading to 108 degrees of freedom in our simulation cell–, time-varying adsorbate coverages, and large surface temperature variability (90–1000 K). For this, a correct description of the configurational space visited by the adsorbate-substrate complex is required. Therefore, we have conducted a detailed survey of the whole ( $T_e, T_l$ ) – AIMDEF data of Ref. [31] according to its distribution of potential energies and the different number of desorption events occurring in the same trajectory. This has resulted in a set of 15 000 configurations ensuring a balanced representation of dynamics trajectories according to the number of CO desorption events (none, one, or two) following the ratio 3:4:3, respectively. Using these ( $T_e, T_l$ ) – AIMDEF data points, we have optimized our choice of EANN model parameters following the criteria of accuracy, required computational time per iteration, and number of iterations for error convergence. Quality of our first set of candidate PESs trained has been validated against almost 87 382 ( $T_e, T_l$ ) – AIMDEF data points absent from the training phase. From these preliminary checks and to

improve the quality of our final PES, the size of the training set has been increased to nearly 16 000 configurations, among which the PES showing the smaller maximum force errors has been selected for  $(T_e, T_l)$  – MDEF. The results are remarkably accurate, with RMSEs as small as 0.85 meV per moving atom for the potential energy and as  $\sim 0.05$  eV/Å for forces.

To describe the coupling of the laser-induced hot electrons with the adsorbates in  $(T_e, T_l)$  – MDEF, we have fitted the available  $(T_e, T_l)$  – AIMDEF surface density data to a density generator function (DGF). The latter will allow us to determine the friction coefficient on each adsorbate within the local density friction approximation as also done in  $(T_e, T_l)$  – AIMDEF. With subsequent  $(T_e, T_l)$  – MDEF simulations,  $(T_e, T_l)$  – AIMDEF results have been reproduced with notable precision across different quantities. This replication was not only based on the original 100  $(T_e, T_l)$  – AIMDEF initial data points, but was also extended to an additional ensemble of 2000 new trajectories, thereby reproducing  $(T_e, T_l)$  – AIMDEF calculations with a smaller statistical uncertainty. Such results support the strength of our  $(T_e, T_l)$  – MDEF methodology and, particularly, the efficacy of our EANN PES covering the aforementioned complexity of our system under ultrafast photodesorption conditions. Furthermore, the extensive statistical data set afforded by  $(T_e, T_l)$  – MDEF has provided us with new information on the initial stages of desorption and the rovibrational states of the desorbed CO molecules.

As a result,  $(T_e, T_l)$  – MDEF with a EANN PES has opened a promising way to simulate CO/Pd(111) femtosecond laser-induced desorption under varied initial conditions. This allows us to overcome the main shortcoming of  $(T_e, T_l)$  – AIMDEF, namely the large computational demands, which severely limit the amount of statistics and dynamical scenarios that are approachable in reasonable times. With  $(T_e, T_l)$  – MDEF one can reproduce  $(T_e, T_l)$  – AIMDEF results orders of magnitude faster (from one week to a few seconds for the same computational and dynamics settings) and produce larger statistical sets in reasonable times. This opens the way to investigate beyond  $(T_e, T_l)$  – AIMDEF limits; let us give some examples.  $(T_e, T_l)$  – MDEF capabilities allow us to extend the dynamics times beyond 3.5 or 4.0 ps, allowing to observe saturation of desorption probabilities, or make it possible to expand the simulation cell size to mitigate finite-size effects. The response of CO/Pd(111) under distinct incident laser fluences or adsorbate coverages becomes also feasible from a theoretical standpoint, among other several experiments. In this respect, the calculations we have performed hitherto are detailed in Chapters 6 and 7. To conclude with, it is also important to remark that our findings support the EANN framework to be used in the development of precise EANN PESs for other complex gas-solid interfaces.



# 6

## Isotopic effect search on 0.75 ML CO/Pd(111)

---

In the last chapter, we have developed our MDEF methodology with a EANN PES trained from the  $(T_e, T_l)$  – AIMDEF data on the femtosecond laser-induced photodesorption of 0.75 ML CO adsorbed on Pd(111) [31]. Making use of that PES and our numerically fitted DGF function, some sets of  $(T_e, T_l)$  – MDEF simulations have been performed. Benchmark  $(T_e, T_l)$  – AIMDEF results are mimicked with remarkable precision, and even some insights about the first 3.5 ps of desorption photochemistry have been gained [87]. At this point we are ready to overcome AIMDEF limitations safely and study other properties of interest in the femtosecond laser-induced desorption on CO-covered Pd(111), as, for example, understanding how different CO isotopologues behave when desorbing from Pd(111).

The search for isotope effects has been used as an additional tool to disentangle if electronic or phononic excitations dominate ultrafast photoinduced desorption, their presence being interpreted as a fingerprint of electron-mediated interactions [32, 36, 90, 91, 92]. In this context, experiments have been conducted in various adsorbate-surface complexes. To list some examples, notable isotope effects have been observed in the recombinative desorption of CO<sub>2</sub> in O+CO/Ru(0001) [36, 90], the recombinative desorption of different H<sub>2</sub> isotopologues in (H,D)/Ru(0001) [37] and the recombinative desorption of O<sub>2</sub> from O-decorated Pd(111) [91]. Nevertheless, systems without an isotope effect have been reported as well, as, e.g., the CO desorption from Ru(0001) [92].

Actually, the AIMDEF methodology already demonstrated its effectiveness in describing the isotope effect of photoinduced H<sub>2</sub>, HD, and D<sub>2</sub> desorption from Ru(0001) [66]. In this system, because of the small mass of H and the low to medium lattice temperatures, only coupling to the electronic system was considered, thus omitting the lattice energy input into the adsorbates. For heavier adsorbates, inclusion of the phononic channel becomes necessary. However, up to now, due to AIMDEF aforementioned limitations no AIMDEF-based approach for studying different adsorbate isotopes accounting for both excitation channels has been feasible in a reasonable time frame. Instead, once we have an EANN PES able to accurately predict atomic energies and forces, as shown in the previous chapter and corresponding publication [87], we can then look for any isotope effect in realistic times using PES-mediated MDEF. Therefore, in this chapter photoinduced CO

desorption processes on Pd(111) has been simulated from a theoretical viewpoint for two different CO isotopologues, the light  $^{12}\text{C}^{16}\text{O}$  and the heavy  $^{13}\text{C}^{18}\text{O}$  [88].

Contents of this chapter are arranged in the following way. First, the main theoretical details and relevant quantities involved in this study and not introduced in previous chapters are covered in Section 6.1. Next, MDEF results and findings for both CO isotopologues are presented in Section 6.2. Finally, a summary of the key results and future implications of our research is provided in Section 6.3.

## 6.1 Theoretical background

Our starting point is the same system thoroughly detailed in Section 5.1 of Chapter 5, a Pd(111) surface covered by 0.75 ML CO that is simulated with a  $(4 \times 2)$  supercell. To investigate potential isotope effects in the 0.75 ML CO/Pd(111) system, we consider two different adlayers, each formed by a different CO isotopologue:  $^{12}\text{C}^{16}\text{O}$  and  $^{13}\text{C}^{18}\text{O}$ . The atomic masses of these isotopologues are  $m(^{12}\text{C}) = 12.011$  a.u.,  $m(^{13}\text{C}) = 13.000$  a.u.,  $m(^{16}\text{O}) = 15.999$  a.u., and  $m(^{18}\text{O}) = 17.999$  a.u. Regarding the Pd atoms, the same isotope  $^{106}\text{Pd}$  is taken for both CO variants, with an atomic mass  $m(^{106}\text{Pd}) = 106.421$  a.u. for each surface atom. As done in our study presented in Chapter 5, a laser pulse of  $\text{sech}^2$  profile, wavelength  $\lambda = 780$  nm and FWHM of 100 fs will irradiate each of the CO/Pd(111) systems under study. In both cases, incident laser peak reaches the adsorbate-substrate complex at  $t = 410$  fs and its total fluence is  $F = 13.0$  mJ/cm<sup>2</sup>. Therefore, the corresponding electronic and lattice temperatures  $T_e(t)$  and  $T_l(t)$  calculated with 2TM are the same as in  $(T_e, T_l)$  – AIMDEF [31] and in the  $(T_e, T_l)$  – MDEF simulations discussed in Chapter 5 and in Ref. [87]. Energies and forces will be described by the EANN PES derived in the previous chapter.

For each CO isotopologue we perform 2000  $(T_e, T_l)$  – MDEF calculations with an integration time step of 0.2 fs. These initial atomic configurations are randomly chosen from an ensemble of 10 000 configurations generated by thermalizing the 100  $(T_e, T_l)$  – AIMDEF starting data points [31] at  $T_0 = 90$  K for 1 ps and using a time step of 1.0 fs. Besides  $(T_e, T_l)$  – MDEF, we aim to determine the contribution of both hot electrons and hot phonons in the photoinduced desorption of each CO isotopologue. To this end, starting from the same set of 2000 initial conditions used in  $(T_e, T_l)$  – MDEF, we additionally perform  $T_l$  – MDEF simulations (see Section 3.2.2.5), in which only the effect of the hot surface lattice is included in the adsorbate dynamics.

In this study, we take advantage of MDEF capabilities by significantly extending the duration of our dynamic simulations to 50 ps, thus surpassing the  $(T_e, T_l)$  –

AIMDEF final time by a factor of 12. Such an extension, while beneficial for a comprehensive analysis, raises the possibility of PES extrapolation errors. As mentioned in Section 5.4, our new trajectories may venture into configurations beyond the confidence zone of the trained EANN PES, as it was trained with  $(T_e, T_1)$  – AIMDEF data of the first 4 ps of photoinduced desorption. A rigorous check was performed in Ref. [88] comparing how different are all the 2000 data points explored every 100 fs from all their  $(T_e, T_1)$  – AIMDEF counterparts, which showed no remarkable differences between  $(T_e, T_1)$  – MDEF and  $(T_e, T_1)$  – AIMDEF visited configurational spaces. Such check supports the safe applicability of our EANN PES in the range [0, 50] ps with no need of further retraining it with more configurations.

Now, let us define some relevant quantities to describe the statistics of the  $(T_e, T_1)$  – MDEF and  $T_1$  – MDEF ensembles. Some of them were already defined in Chapter 5, namely, the CO desorption probability  $P_{\text{CO,des}}(t)$  (Eq. (5.6)) and the semiclassical vibrational quantum number  $\nu$  (Eq. (5.8)) [349]. In this chapter two additional quantities will be studied, the coverage occupation  $\xi(t)$  and the desorption rate  $R(t)$ . The first one is defined as,

$$\xi(t) = \frac{n_0^{\text{CO,cell}} - n^{\text{CO,des}}(t)}{n_0^{\text{Pd}}}, \quad (6.1)$$

where  $n^{\text{CO,des}}(t) = N^{\text{CO,des}}(t)/N_{\text{traj}}$  is the cumulative number of desorbed CO at instant  $t$  ( $N^{\text{CO,des}}(t)$ ) averaged over all the trajectories ( $N_{\text{traj}}$ ). In our case,  $N_{\text{traj}} = 2000$  in both  $(T_e, T_1)$  – MDEF and  $T_1$  – MDEF. It also involves the initial number of CO molecules in our 0.75 ML ( $4 \times 2$ ) simulation cell,  $n_0^{\text{CO,cell}} = 6$  – as defined in Section 5.4, Eq. (5.6)–, and the amount of Pd atoms in the topmost surface layer,  $n_0^{\text{Pd}} = 8$ .

Using Eq. (5.6), the usual text-book definition of desorption rate  $R(t) = -d\xi(t)/dt$  (see, e.g., Ref. [350]) is expressed as:

$$R(t) = \xi_0 \frac{dP_{\text{CO,des}}(t)}{dt}, \quad (6.2)$$

where  $\xi_0 \equiv \xi(0) = n_0^{\text{CO,cell}}/n_0^{\text{Pd}} = 0.75$ , as it is obvious for our adsorbate-substrate complex. Once these quantities have been defined, let us discuss the results from the  $(T_e, T_1)$  – MDEF and  $T_1$  – MDEF simulations.

## 6.2 MDEF results for both CO isotopologues

To begin with, let us analyze the time evolution of  $P_{\text{CO,des}}(t)$  during the first 4 ps for both the light and heavy CO adlayers. As observed in Fig. 6.1, there are minor differences in the time evolution of  $P_{\text{CO,des}}(t)$  between both isotopologues when considering either  $(T_e, T_1)$  – MDEF trajectories (full lines) or  $T_1$  – MDEF (dashed lines). Red and blue full lines correspond to the  $(T_e, T_1)$  – MDEF evolutions for the light  $^{12}\text{C}^{16}\text{O}$  and heavier isotopologue  $^{13}\text{C}^{18}\text{O}$ , respectively, while purple and orange dashed lines show the respective  $T_1$  – MDEF results for  $^{12}\text{C}^{16}\text{O}$  and  $^{13}\text{C}^{18}\text{O}$ . Surrounding each curve, there are shaded regions representing statistical uncertainty intervals, which were calculated as 99% confidence Wilson score intervals (see Section 5.4) [347]. On a closer look, although these differences are small, the desorption probability of  $^{12}\text{C}^{16}\text{O}$  at a given instant is always higher than for  $^{13}\text{C}^{18}\text{O}$  in the whole 4 ps interval. The difference becomes more apparent at  $t \gtrsim 1.75$  ps for  $(T_e, T_1)$  – MDEF and at  $t \gtrsim 3.25$  ps for  $T_1$  – MDEF. This result is consistent with the overall larger acceleration experienced by the lighter CO due to the mass dependency in the equations of motion (Eq. (3.12)). As a result,  $^{12}\text{C}^{16}\text{O}$  molecules are able to achieve kinetic energies  $E_{\text{kin}}$  larger than the desorption barrier in shorter average times than  $^{13}\text{C}^{18}\text{O}$  molecules. Notably, when the interaction of adsorbates with the hot electrons is ruled out in  $T_1$  – MDEF, the differences in  $P_{\text{CO,des}}(t)$  for each CO isotopologue diminish, as expected from the theoretical prediction that isotope effects do not appear in scenarios where phonon-mediated desorption is the primary mechanism. Therefore, we can conclude that within the initial 4 ps of dynamics, the slightly larger differences between both CO isotopologues in the  $(T_e, T_1)$  – MDEF desorption probabilities arise mainly from their interactions with laser-excited electrons, rather than from the coupling to the surface DOFs.

However, at this point, no conclusive remark on the potential existence of an isotope effect for CO/Pd(111) can be made yet because the  $P_{\text{CO,des}}(t)$  results in Fig. 6.1 represent a very early stage of photodesorption dynamics process. As all  $P_{\text{CO,des}}(t)$  graphs seem to keep growing for  $t > 4$  ps, it is desirable to extend our  $(T_e, T_1)$  – MDEF simulations beyond 4 ps. The idea is to either reach or, at least, closely approach the saturation point of all desorption probabilities, to see whether the apparent isotope effect observed for  $(T_e, T_1)$  – MDEF persists or not. Figure 6.2 shows the corresponding  $P_{\text{CO,des}}(t)$  curves extended until 50 ps, instant at which all the curves are basically saturated. As observed in the figure, the desorption probabilities of both isotopologues saturate to similar values, which are  $P_{\text{CO,sat}} \approx 0.35$  for  $(T_e, T_1)$  – MDEF (solid lines) and  $\approx 0.34$  for  $T_1$  – MDEF (dashed lines). This means that the little differences observed in  $(T_e, T_1)$  – MDEF during the initial time interval  $[0, 4]$  ps, not only do not increase but become negligible at

longer times. Furthermore, the fact that  $P_{\text{CO,sat}}$  for  $T_1$  – MDEF is only 1% smaller than for  $(T_e, T_1)$  – MDEF supports the phonon-mediated desorption mechanism dominating over the electron-mediated one after the initial stages of the dynamics. The reason can be the very high lattice temperatures  $T_l(t)$  reached for the absorbed laser fluence  $F = 130 \text{ J/m}^2$  that varies from  $\approx 1200$  to 700 K in the interval 4–50 ps. Therefore, even if during the first stages of the dynamics the electron-mediated desorption mechanism is important, as reflected in the high difference in desorption probability found between  $(T_e, T_1)$  – MDEF and  $T_1$  – MDEF in Fig. 6.1 and the subtle isotope effect, at later times the lattice temperature is high enough to dominate the desorption process regardless of whether the interaction with the electronic bath is present or not.

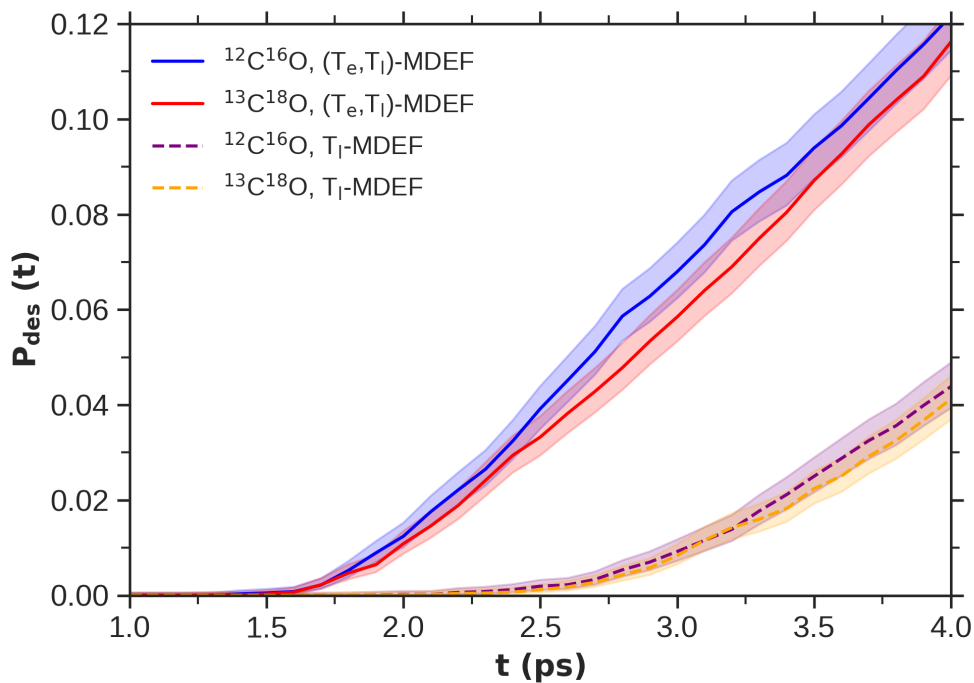


**Figure 6.1:** Time evolution of  $^{12}\text{C}^{16}\text{O}$   $(T_e, T_1)$  – MDEF (full blue) and  $T_1$  – MDEF (dashed purple), and  $^{13}\text{C}^{18}\text{O}$   $(T_e, T_1)$  – MDEF (full red) and  $T_1$  – MDEF (dashed orange) desorption probabilities in the interval [1, 4] ps. Shaded areas correspond to Wilson score intervals of 99% confidence level [347].

Further insights into the desorption dynamics can be achieved by studying the time evolution of the desorption rate  $R(t)$ , which was defined in Eq. (6.2). The

results for the two types of simulations and for the light and heavy CO adlayers are shown in Fig. 6.2 (bottom panel). Raw noisy data (translucent lines) have been interpolated with spline polynomials of fifth order to obtain smooth functions for  $(T_e, T_1)$  – MDEF (solid lines)  $^{12}\text{C}^{16}\text{O}$  (blue) and  $^{13}\text{C}^{18}\text{O}$  (red) as well as for  $T_1$  – MDEF (dashed lines)  $^{12}\text{C}^{16}\text{O}$  (purple) and  $^{13}\text{C}^{18}\text{O}$  (orange). We can notice that the time interval considered allows us to fully appreciate the characteristic functional form of each  $R(t)$ . Maximum values for  $(T_e, T_1)$  – MDEF and  $T_1$  – MDEF are reached at approximately 3 and 5 ps, respectively. In agreement with the previous analysis of CO desorption probabilities, for each type of dynamics, the desorption rates for both isotopologues are nearly identical. Regarding the differences between  $(T_e, T_1)$  – MDEF and  $T_1$  – MDEF, it is apparent that the  $(T_e, T_1)$  – MDEF desorption rate reaches higher values in a shorter amount of time, exhibiting a narrower profile than in the case of  $T_1$  – MDEF rate. This difference reinforces our conclusion that despite the absence of any relevant isotope effect in the desorption of CO molecules, interaction with substrate electrons is still important for the description of the desorption dynamics during the first 15 ps, as one can check in the inset graph drawn for the first 10 ps interval.

To further clarify the relevance of the interactions of each CO isotopologue with the hot electronic subsystem, let us study their distribution of quasiclassical vibrational states according to Eq. (5.8). Figure 6.3 shows the normalized distribution of desorbed molecules in the vibrational ground state ( $\nu = 0$ ) and in vibrationally excited states ( $\nu > 0$ ). Blue and red bars represent  $^{12}\text{C}^{16}\text{O}$  and  $^{13}\text{C}^{18}\text{O}$   $(T_e, T_1)$  – MDEF simulations, respectively (upper panels), whereas purple and orange bars depict their respective  $T_1$  – MDEF counterparts (lower panels). Error bars indicate the standard deviation of  $\nu$  as for a binomial distribution. When examining the complete sets of desorbed CO molecules (left panels), for both isotopologue species their related  $(T_e, T_1)$  – MDEF sets reach almost the same probabilities for zero and positive  $\nu_f$  values. In the case of  $T_1$  – MDEF, all desorbed CO isotopologues remain in the vibrational ground state, their distributions being then identical. These results suggest that phonons do not efficiently couple to molecular vibrational motion, whereas hot electrons do. Quantitatively, in the case of  $(T_e, T_1)$  – MDEF, we observe that 5% of the desorbed CO for both the light and heavy isotopologues ends in vibrational excited states, so this vibrational excitation is not only subtle among all species that desorb, but also appears to be isotopologue-independent.

Nevertheless, it is interesting to focus on molecules in the higher translational kinetic energy tail ( $E_{\text{kin}}^{\text{trans}} \geq 0.67$  eV (Fig. 6.3, right panels). This situation would correspond to adsorbates at temperatures  $T \geq 5200$  K. For this subset of dynamics,  $T_1$  – MDEF results do not vary from overall desorption ensemble data, so no isotopic effect is found in this dynamical situation. On the contrary, under  $(T_e, T_1)$  – MDEF

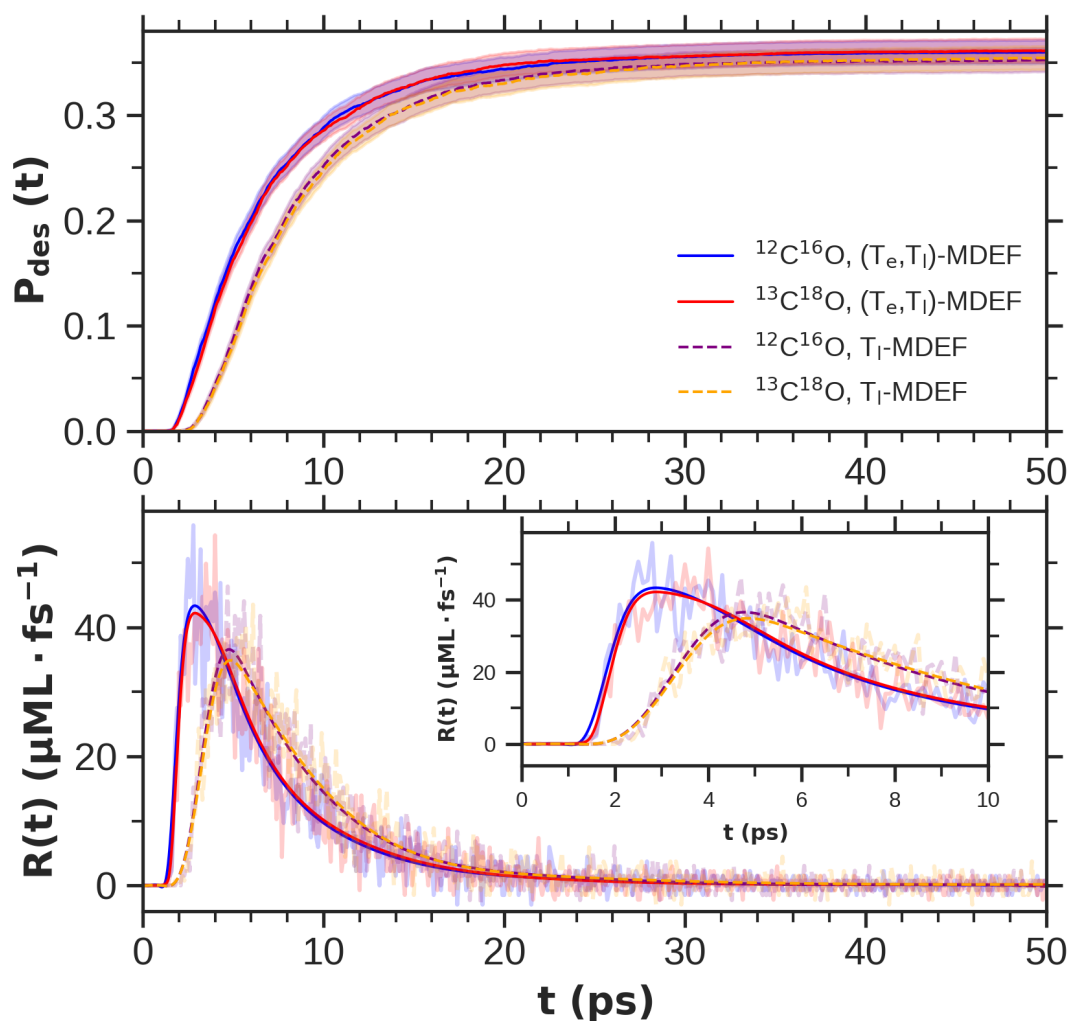


**Figure 6.2:** (Top) Time evolution of the desorption probability along the time interval  $[0, 50]$  ps.  $(T_e, T_1)$  – MDEF (solid lines) data sets for  $^{12}\text{C}^{16}\text{O}$  (blue) and  $^{13}\text{C}^{18}\text{O}$  (red) and  $T_1$  – MDEF ones (dashed lines) for  $^{12}\text{C}^{16}\text{O}$  (purple) and  $^{13}\text{C}^{18}\text{O}$  (orange) are depicted. Shaded areas show the uncertainty intervals for 99% confidence level according to Wilson score intervals framework [347]. (Bottom) Corresponding desorption rate obtained during 50 ps. Raw noisy desorption rates (translucent lines) were obtained from desorption probabilities by numerical differentiation. Smooth desorption rates (thick lines) were obtained after applying a fifth order noise-reduction spline interpolation over raw desorption probabilities. Desorption rates during the first 10 ps are depicted in the inset.

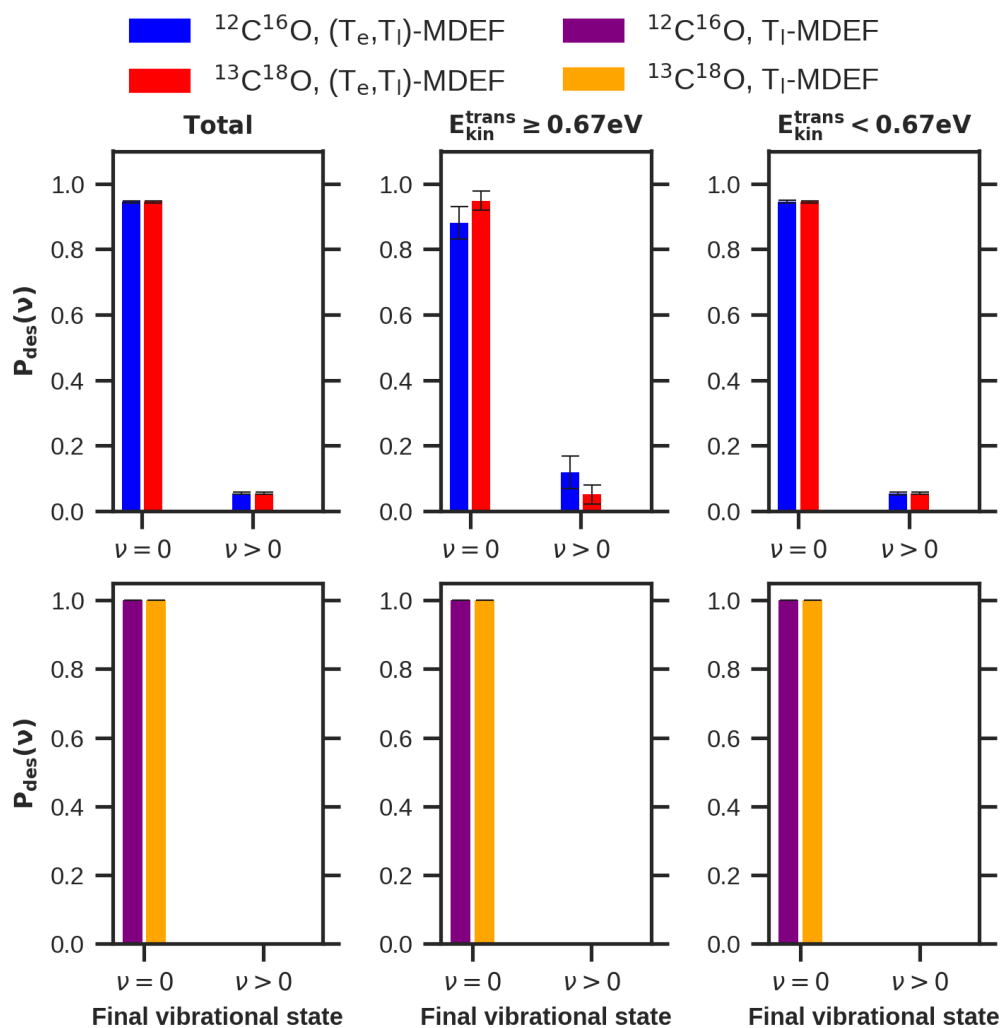


**Figure 6.3:** Quasi-classical vibrational state distribution of  $^{12}\text{C}^{16}\text{O}$  and  $^{13}\text{C}^{18}\text{O}$ . Upper graph row corresponds to  $(T_e, T_i)$  – MDEF  $^{12}\text{C}^{16}\text{O}$  (blue) and  $^{13}\text{C}^{18}\text{O}$  (red) while bottom ones stand for  $T_i$  – MDEF  $^{12}\text{C}^{16}\text{O}$  (purple) and  $^{13}\text{C}^{18}\text{O}$  (orange) data sets. For each smaller graph, a distinction between molecules in their vibrational ground state ( $v = 0$ ) or after undergoing vibrational excitation ( $v > 0$ ) is made. Error bars reflect the standard deviation as for binomial distributions. Left column of panels display vibrational state probabilities with respect to total amounts of desorbed CO species. Right column shows results for the CO molecules that desorbed with the larger translational kinetic energies,  $E_{\text{kin}}^{\text{trans}} \geq 0.67\text{eV}$  –or, alternatively,  $T \geq 5200\text{K}$ – (see text).

conditions there is a small but observable isotope effect that must hence be caused by the laser-induced hot electrons. As observed in the figure, the probability of vibrational excitation for  $^{12}\text{C}^{16}\text{O}$  is 6% higher than that for  $^{13}\text{C}^{18}\text{O}$ . We have to stress the subtlety of this effect, as it is experienced by only around 1% of the total number of CO molecules that desorb in the  $(T_e, T_l)$  – AIMDEF simulations.

## 6.3 Conclusions

In this chapter, we have explored the dynamics of photoinduced desorption of two CO isotopologues, namely light  $^{12}\text{C}^{16}\text{O}$  and heavy  $^{13}\text{C}^{18}\text{O}$ , from a Pd(111) surface at 0.75 ML coverage in the high laser fluence regime. Using the EANN PES described in Chapter 6, which was shown to reproduce with remarkable fidelity previous  $(T_e, T_l)$  – AIMDEF simulations [31], photodesorption dynamics for both adlayers, each conformed by a different CO isotopologue, have been performed computationally. Sets of 2000 trajectories along a longer-than-AIMDEF time interval [0.0, 50.0] ps have been calculated for each isotopologue using two different types of simulations,  $(T_e, T_l)$  – MDEF and  $T_l$  – MDEF. In the former, adsorbates were allowed to interact with both femtosecond laser pulse-excited electrons and phonons, whereas in the latter, only the interaction with the hot surface lattice was included. The comparative analysis of the results obtained with both types of simulations permits us to identify the role of the laser-excited electrons in the adsorbate dynamics. Furthermore, in order to look for potential isotope effects, we have evaluated CO desorption probabilities, desorption rates, and quasiclassical vibrational states of the desorbed species.

Our comprehensive analysis points out the absence of isotope effects in the desorption probabilities for the 0.75 ML CO/Pd(111). It is true that minor differences between  $^{12}\text{C}^{16}\text{O}$  and  $^{13}\text{C}^{18}\text{O}$  desorption probabilities appear at early times of  $(T_e, T_l)$  – MDEF, more precisely in the interval [0, 4] ps. However, they become negligible over extended times (up to 50 ps), when lattice-mediated desorption mechanism dominates over its electronic counterpart. The prevalence of interactions between adsorbates and excited phonons also leads to both  $(T_e, T_l)$  – MDEF and  $T_l$  – MDEF desorption probabilities for each CO isotopologue saturating at constant and almost identical values. However, the electronic interactions may play some relevant role at early desorption times, as desorption rate peaks for  $(T_e, T_l)$  – MDEF are sharper and occur earlier than for  $T_l$  – MDEF. Focusing on this point, when examining the vibrational excitation of desorbed molecules, we observe that such excitations are minimal and predominantly originated by the hot electronic subsystem. Only for desorbed molecules in the high translational kinetic

energy tail ( $E_{\text{kin}}^{\text{trans}} > 0.67$  eV), a little isotope effect has been detected, favoring the vibrational excitation of light  $^{12}\text{C}^{16}\text{O}$  over the heavy  $^{13}\text{C}^{18}\text{O}$  by 6%. However, it is necessary to remark that these excited molecules represent a mere 1% of the total desorption yield.

Our findings show that the CO photodesorption process from a highly covered CO/Pd(111) surface at high laser fluence,  $130 \text{ J/m}^2$ , is dominated by a phonon-mediated mechanism and that the complete photodesorption process takes several tens of picoseconds to finalize. These results extend our understanding of photodesorption dynamics beyond previous experimental observations made at lower fluences ( $50$  to  $80 \text{ J/m}^2$ ) for the same system [30]. Interestingly, in that reference a further phenomenological three temperature model analysis of two-pulse correlation (2PC) results suggested that CO femtosecond laser pulse-induced desorption is primarily driven by an electron-mediated energy transfer to adsorbates for CO coverages ranging from  $0.24$  ML to  $0.75$  ML, which contrasts with our molecular dynamics simulations at higher fluence. This leads us to study how different incident laser fluences could affect desorption, as well as to simulate 2PC on CO/Pd(111), in order to explore in deeper detail whether hot electrons or phonons rule over desorption. Looking at our results in this chapter, MDEF appears to be the way to go to respond to those questions in reasonable time from a theoretical point of view and overcoming former AIMDEF limitations.

# 7

## Multicoverage studies on CO/Pd(111) with MDEF

In the previous Chapter 5 we have developed in detail the MDEF methodology with a EANN PES, and verified that some previous  $(T_e, T_1)$  – AIMDEF results for 0.75 ML CO/Pd(111) [31] were closely reproduced [87]. Not only that, but  $(T_e, T_1)$  – MDEF calculations anticipated some preliminary new details about early stages of ultrafast photodesorption dynamics. Continuing with this newly opened pathway, we searched for a potential isotope effect in that adsorbate-substrate system, as detailed in Chapter 6, but no remarkable isotope-conditioned variation was found in general [88]. Overall, we have seen that MDEF approach works to go beyond AIMDEF from a theoretical point of view. Now we are interested in unveiling the CO/Pd(111) desorption dynamical mechanism in more depth by investigating its dependence with the initial CO coverage decorating the surface, the incoming laser fluence, and the delay time between the arrival of a pump and a probe pulse as in the 2PC experiments. Having as a reference some previous experiments and their corresponding results [30], we want to gain a deeper insight on the aforementioned three issues using MDEF. During this chapter we are reporting and discussing our current comprehensive findings on femtosecond laser-induced desorption of CO from Pd(111), part of which have been recently published [89].

This set, our first goal is to advance towards an improved EANN PES description of CO/Pd(111) photodesorption. As a preliminary step, in Section 7.1 we analyze how our 0.75 ML EANN PES predicts energies, adiabatic forces or adsorption site-specific minimum energy paths for a different coverage from the one it was trained on, namely 0.33 ML. To this end, previous  $(T_e, T_1)$  – AIMDEF data for this latter adlayer is considered [31]. This procedure is complemented with the training of a new EANN PES on 0.33 ML  $(T_e, T_1)$  – AIMDEF data and its application to 0.75 ML adlayer characterization. With the lessons learned from this process, in Section 7.2 we tackle the construction of a multicoverage EANN PES incorporating previous 0.33 and 0.75 ML  $(T_e, T_1)$  – AIMDEF and  $T_e$  – AIMDEF configurations [31]. Its robustness is verified across different tests, not only limited to aforementioned low and high coverages, but also involving 0.60 ML CO coverage. The startling accuracy of our newly trained PES across different quantities validates its usage for the more advanced MDEF research we want to do with it. First, different calculations are run for single pulse excitation scenario taking an extensive duration of 100 ps, as detailed in Section 7.3. Next, we investigate the CO photodesorption dependence

with incident laser fluence, with size of simulation cell and with coverage for a single fluence, and compare it with previous experimental results [30]. Moreover, we advance in our understanding on the relative role played by hot electrons and phonons in desorption mechanism, as well as in the CO behavior during desorption and how it can be either direct or preceded by some residence time in a physisorption well. Afterwards, in Section 7.4 we simulate 2PC experiments with  $(T_e, T_1)$  – MDEF and compute the desorption yield dependence on the relative delay between pump and probe, and compare it with the experimental work of Ref. [30]. To end the chapter, our procedures, main findings and concluding remarks are summarized in Section 7.5.

## 7.1 Preliminary studies on multicoverage PESs

Hitherto we have trained an EANN PES for 0.75 ML CO/Pd(111) system [87]. As a preliminary approach, we can investigate how accurate are the predictions of our PES on a different coverage that was not included in the training data set. One straightforward choice is the 0.33 ML coverage, as it was previously examined using the AIMDEF approach [31]. To broaden our analysis, we have also trained a new EANN PES using 0.33 ML  $3 \times 3$   $(T_e, T_1)$  – AIMDEF data (light green region of Fig. 7.1, top panel), and we have evaluated its proficiency in predicting energies and forces on 0.75 ML  $4 \times 2$  data points (light red region of Fig. 7.1, bottom panel).

Let us provide an overview of the 0.33 ML  $3 \times 3$  supercell considered in AIMDEF (Fig. 7.1, top panel). It is composed of three CO molecules adsorbed at fcc sites on a 4-layer Pd surface with 9 atoms per layer. Dynamical description of adsorbates and each Pd layer is the same as for the 0.75 ML system (see Section 5.1), resulting in a supercell with  $N_{\text{moving}} = 33$  moving atoms or 99 DOFs. The dimensions of the supercell are represented by  $s(\mathbf{a}_1, \mathbf{a}_2, \mathbf{a}_3)$ , with  $s = 8.49$  and the lattice vectors, in Å and in Cartesian coordinates, are  $\mathbf{a}_1 = (1, 0, 0)$ ,  $\mathbf{a}_2 = (0.5, 0.866, 0)$  and  $\mathbf{a}_3 = (0, 0, 3.266)$ . As for 0.75 ML coverage, we conducted a thorough analysis of the configurational space in terms of the potential energies with varying numbers of CO desorption events (see Section 5.2.1). This yields a training data set of 12 750 configurations for trajectories without desorption and 2250 for those with a single CO desorption early in the dynamics. Notably, in this case, no trajectories with two CO desorption processes were present in the AIMDEF simulations. Furthermore, we kept the same EANN-specific parameters as for the 0.75 ML PES, detailed in Section 5.2.2 [323]. As done for 0.75 ML (Chapter 5), we begin training an initial set of five PESs with 15 000 data points (13 500 for training and 1500 for validation). For the one with smaller maximum force errors, we report its energy and maximum

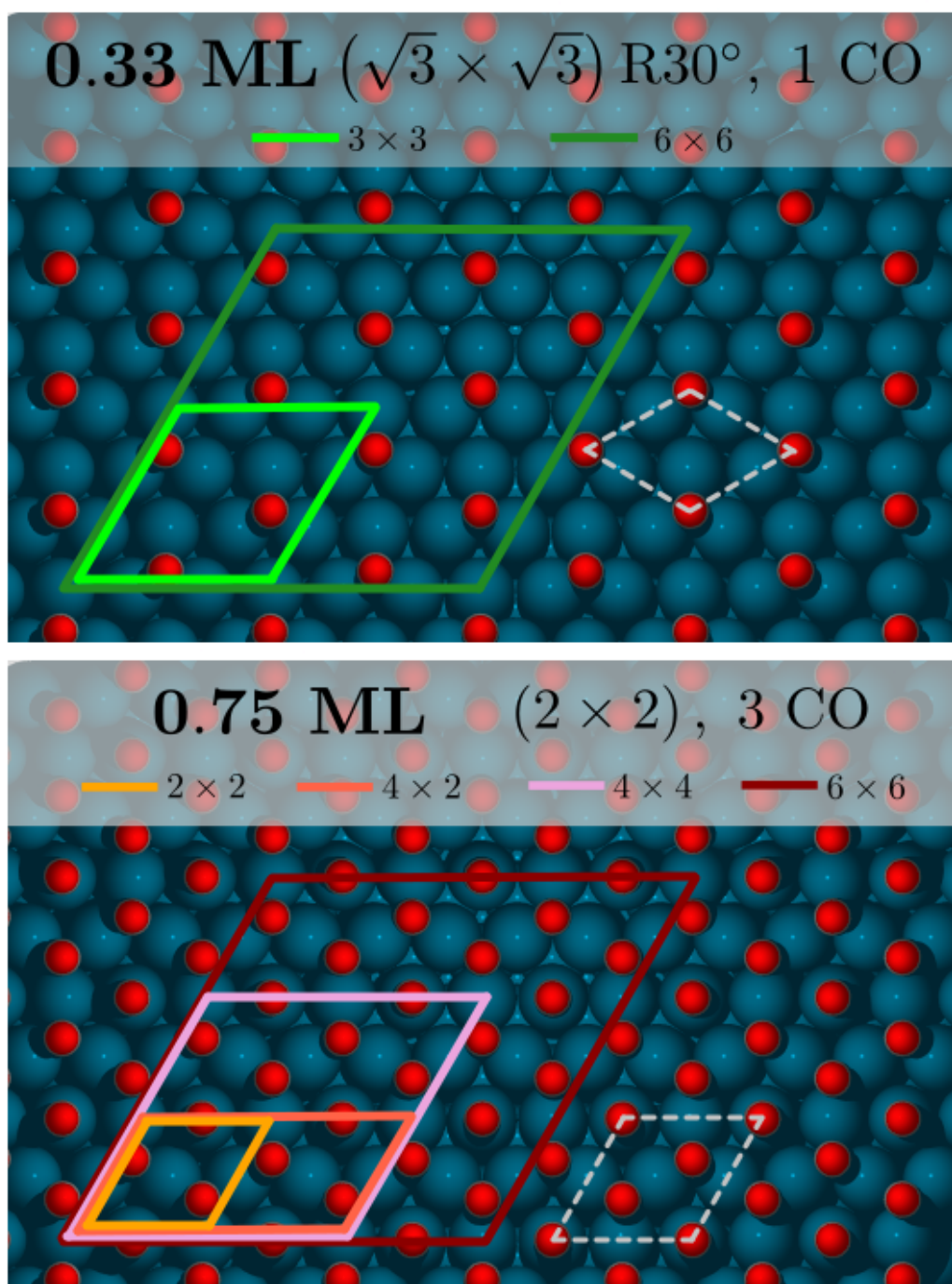


**Figure 7.1:** Top view of minimum energy configurations obtained with the multicoverage EANN PES for 0.33 ML (top) and 0.75 ML (bottom panel). The supercells considered in our  $(T_e, T_1)$  – MDEF simulations are represented in solid lines. Grey dashed lines show the smallest pattern that is repeated within supercells.

force errors and RMSEs, together with force MESMAEs in Table 7.1, left error data column. Then, those configurations yielding larger force errors per atom and coordinate for our first batch PES choice are incorporated into the previous training set, adding up to 15 882 data points (14 382 for training and 1500 for validation). The errors for our final PES are presented in the right error data column of Table 7.1. This allows us to confirm the enhanced accuracy of the final 0.33 ML PES relative to our first choice, as we observed for 0.75 ML PES in Table 5.3.

We aim to assess how accurately each PES describes a coverage different from the one on which it was trained. A straightforward test involves examining the minimum energy desorption paths for each adsorption site and coverage as modeled by each potential. These paths are determined using DFT by stimulating the desorption of a single CO molecule under equilibrium conditions. This consists of driving the molecule away from the surface along the normal and studying how its interaction with the remaining CO/Pd(111) system changes with distance. These minimum energy path configurations were not included in the training sets for any of the PESs. Desorption minimal potential energy curves for each PES are shown in Figs. 7.2 and 7.3 in solid lines and compared to DFT+vdW-DF reference calculations of Ref. [31]. From these comparisons, we derive several insights. For the 0.33 ML CO/Pd(111) coverage, the 0.33 ML PES accurately predicts the size of the desorption barrier, although an oscillatory pattern is observed as the molecule approaches the desorption energy. However, for the 0.75 ML coverage, the potential energy curves diverge significantly from the DFT+vdW-DF reference results. Nevertheless, when examining our 0.75 ML PES predictions, we find that the match between the data sets improves. For 0.75 ML coverage, the top site minimum energy path closely resembles that of DFT+vdW-DF in terms of shape and well depth, while the fcc and especially hcp sites, although not diverging much in shape from the reference, are predicted to be deeper by our PES. The ordering of the desorption energies is correct, with the top site being the lowest, and the hcp and fcc sites being closer to each other than the DFT+vdW-DF-calculated values. Interestingly, the 0.33 ML potential energy curve predicted by the 0.75 ML PES closely matches the reference curve shape, despite predicting a larger desorption energy.

The superior predictive accuracy of the 0.75 ML PES for both 0.75 and 0.33 ML coverage scenarios, compared to its 0.33 ML counterpart, can be attributed to the more comprehensive atomic environmental data on which the former PES was trained. This set involved not only adsorbed and desorbing CO molecules from a wider range of sites, but also captured the dynamics of one or even two CO molecules desorbing within the first 3.5 ps of dynamics. This diversity in the training data allowed the 0.75 ML PES to explore a broader array of atomic environments,

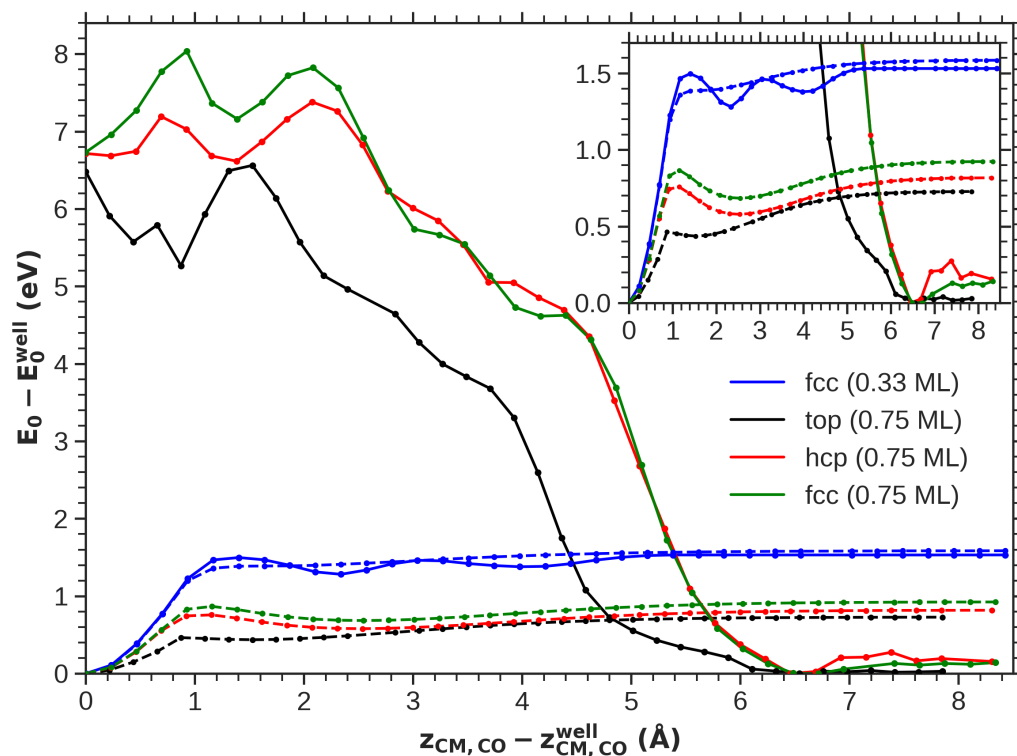


**Figure 7.2:** Potential energy  $E_0$  in terms of the CO CM height  $z_{\text{cm,CO}}$  for one CO species desorbing along its site-specific minimum energy path from a 0.33 ML CO/Pd(111) adsorption site –fcc, in blue– and the three possible adsorption sites in 0.75 ML, namely top (black), hcp (red) and fcc (green). Solid lines represent the 0.33 ML EANN PES energy calculations while dashed lines stand for the energies obtained with DFT+vdW-DF of Ref. [31]. For both sets of plots, solid dots correspond to the data points used. In each curve, the energy and the height are referred to the values obtained at the bottom of the corresponding well,  $E_0^{\text{well}}$  and  $z_{\text{cm,CO}}^{\text{well}}$  respectively. A close-up of the plot in the range [0.0, 1.7] eV is also depicted in the inset for a clearer comparison between the 0.33 ML potential energy curves.

enabling it to more accurately characterize the configurational space for its own coverage level and simpler coverages such as the 0.33 ML one. By *simpler*, we refer to the narrower variety of atomic environments explored in 0.33 ML coverage, or to fewer things happening inside the atom-centered cutoff spheres, from an interatomic perspective. This explains the poor description of 0.75 ML coverage by the 0.33 ML PES.

In conclusion, the effectiveness of an EANN PES is intrinsically linked to the diversity and complexity of the atomic environments encountered during its training. Our analysis reveals that a PES trained with 0.75 ML coverage data offers a more comprehensive and accurate representation of various coverage scenarios than its 0.33 ML counterpart. This superior performance is attributable to its extensive exploration of the configurational space during the training process. Nevertheless, when applied to 0.33 ML, our 0.75 ML PES energy predictions differ from DFT values, thus predicting a clearly deeper potential well. In contrast to our previous observations of the negligible difference in well depths between EANN and DFT for 0.75 ML hcp and fcc sites, this energy discrepancy is significant and merits consideration in the training of multicoverage PESs. To solve this, and using the wealth of AIMDEF data available for both 0.33 and 0.75 ML cases, we propose the development of a new EANN PES that incorporates data points from both coverages. This approach is expected to produce a more robust and universally applicable PES, ensuring more accurate simulations across a range of adsorbate coverages. The subsequent section will detail our methodology to construct and validate this enhanced multicoverage CO/Pd(111) PES.

## 7.2 Multicoverage EANN PES training and quality assessment

To develop a multicoverage EANN PES for CO/Pd(111), we first select the training data for both 0.33 and 0.75 ML coverages. AIMDEF available data configurations involve surface lattice distortion ( $(T_e, T_1)$  – AIMDEF) as well as scenarios with frozen surface conditions ( $T_e$  – AIMDEF). This results in four distinct data sets among which we prepare sets of configurations following the criteria of Section 5.2.1 to train the multicoverage PES. However, note that our different adsorbate coverages do not share the same energy minimum values. Before we have indicated how many atoms contain our supercells for both coverage scenarios: 3 C, 3 O and 36 Pd atoms for 0.33 ML, and 6 C, 6 O and 32 Pd 0.75 ML, the Pd species arranged as 4-layered slabs in both cases. Naively, one might initially think to equalize the energy baselines by simple addition or subtraction of the energy contribution of each individual

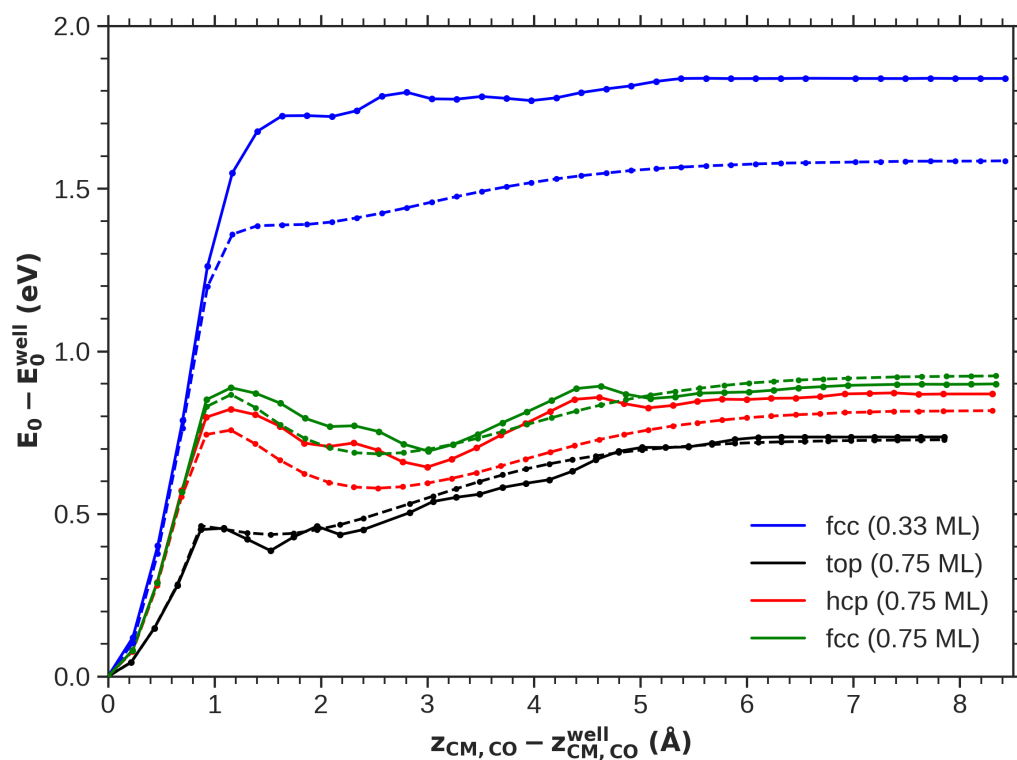


**Figure 7.3:** Potential energy  $E_0$  in terms of the CO CM height  $z_{\text{cm,CO}}$  for one CO species desorbing along its site-specific minimum energy path from a 0.33 ML CO/Pd(111) adsorption site -fcc, in blue- and the three possible adsorption sites in 0.75 ML, namely top (black), hcp (red) and fcc (green). Solid lines represent the 0.75 ML EANN PES energy calculations while dashed lines stand for the energies obtained with DFT+vdW-DF of Ref. [31]. For both sets of plots, solid dots correspond to the data points used. In each curve, the energy and the height are referred to the values obtained at the bottom of the corresponding well,  $E_0^{\text{well}}$  and  $z_{\text{cm,CO}}^{\text{well}}$  respectively.

**0.33 ML CO/Pd(111), (T<sub>e</sub>,T<sub>l</sub>)-AIMDEF,  
PES energy and force errors**

		<b>First PES</b>	<b>Final PES</b>
Predict configurations		116 927	116 927
$E/N_{\text{moving}}$ (meV)	Max. error	10.448	7.147
	RMSE	0.847	0.797
$F_x$ (eV/Å)	Max. error	0.755	0.496
	MESMAE	0.315	0.279
	RMSE	0.0480	0.0470
$F_y$ (eV/Å)	Max. error	0.907	0.626
	MESMAE	0.312	0.282
	RMSE	0.0479	0.0469
$F_z$ (eV/Å)	Max. error	0.700	0.680
	MESMAE	0.322	0.291
	RMSE	0.0486	0.0472

**Table 7.1:** Maximum absolute-valued errors and RMSEs in energies per moving atom and forces, and maximum errors set mean absolute errors (MESMAEs) of all moving atoms in forces predicted by the first and final PESs (see text) for 0.33 ML CO/Pd(111) (T<sub>e</sub>, T<sub>l</sub>) – AIMDEF configurations selected from Ref. [31]. Both error data columns correspond to the energy and force errors linked to PES predictions on a set of 116 927 configurations following the (T<sub>e</sub>, T<sub>l</sub>) – AIMDEF representativeness criteria as described in Section 5.2.1. Here,  $N_{\text{moving}} = 33$ .

atom in vacuum times the difference in atoms for each species. Nevertheless, this approach misses additional contributions to the total energy linked to the atomic arrangements, so a straightforward comparison based solely on atom count becomes insufficient to address the disparity between coverages. To align these minimum energies, we use the retrained 0.75 ML CO/Pd(111) PES to evaluate the energies of the 350 000 available 0.33 ML ( $T_e, T_1$ ) – AIMDEF configurations (Fig. 7.4). Then a linear fit with the slope  $m = 1$  is applied to the predicted energies, thus producing an offset energy of  $b = -22.04651$  eV. Such is subsequently added to the 0.33 ML AIMDEF energies in order to match the energy minima of both coverages.

Once the energy mismatch between the two coverages is solved, we train an initial batch of PESs containing two hidden layers of 60 nodes per layer, having as input 60 embedded density descriptors per atom element (15 Gaussian-type orbitals (GTOs) for allowed angular momentum values of  $L = 0 - 3$ ). The remaining EANN-model parameters on GTO geometry, cutoff radius, and energy and force weights for the cost function are chosen as in Section 5.2.2. The first training data set comprises 34 283 configurations, with 90 % of them derived from the ( $T_e, T_1$ ) – AIMDEF data (the 15 883 of the previous retrained 0.75 ML CO/Pd(111) PES plus the 15 000 starting configurations for 0.33ML coverage). The remaining 10 % of the training configurations are obtained from  $T_e$  – AIMDEF and include 1700 configurations for each coverage. We begin by constructing five PESs, each of them trained with a random selection of 90% of the 34 283 configurations, while the remaining 10% is used to check that the PES has not been overfitted. All PESs achieve convergence with less than 45 iterations and yields for the energy RMSEs values of 0.55–0.65 meV and 0.84–0.92 meV per moving atom for the training and validation data sets, respectively. Notably, as each coverage contributes approximately equally to the total training set, the error values for the energy per moving atom have been obtained by dividing the total energy error values by 34.5 –the average of moving atoms for both coverages (33 for 0.33 ML and 36 for 0.75 ML).

These starting PESs are validated afterwards against four predict sets of 140 766 (0.33 ML  $T_e$  – AIMDEF), 116 297 (0.33 ML ( $T_e, T_1$ ) – AIMDEF), 140 692 (0.75 ML  $T_e$  – AIMDEF) and 87 382 configurations (0.75 ML ( $T_e, T_1$ ) – AIMDEF) not present among the training inputs. Validations are performed separately for each data set due to the differences in the amounts of moving and total atoms in each ensemble. We study the 10 absolute-valued maximum force errors for each moving atom and component,  $|\Delta F_\gamma|_{\max}$ ,  $\gamma = x, y, z$ , as we did in Section 5.2.3, and choose the PES with the overall lower error values. By predict set, maximum force errors correspond to 945 (0.33 ML  $T_e$  – AIMDEF), 863 (0.33 ML ( $T_e, T_1$ ) – AIMDEF), 877 (0.75 ML  $T_e$  – AIMDEF) and 1004 data points (0.75 ML ( $T_e, T_1$ ) – AIMDEF). These configurations are subsequently added into the initial training set, increasing it to 37 972 data

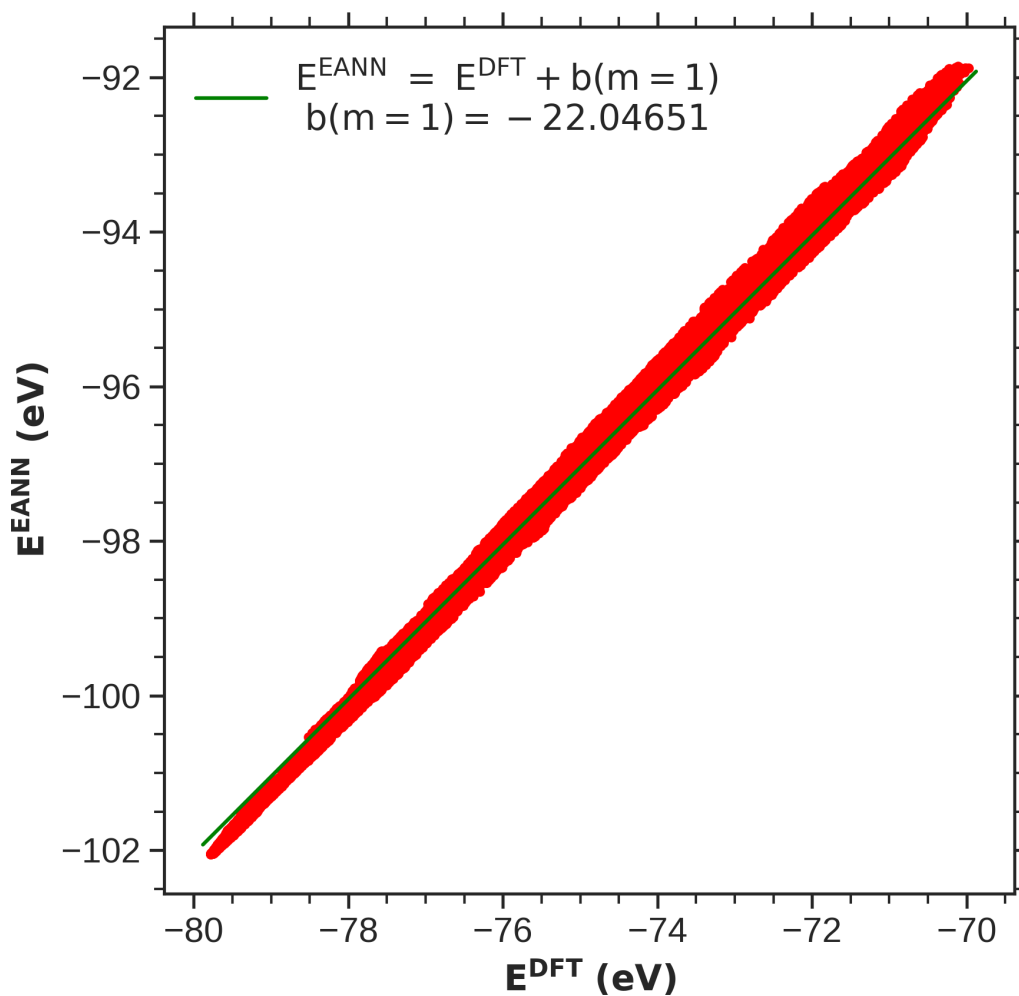


**Figure 7.4:** Linear fit of the energies of the configurations in the 0.33 ML CO/Pd(111) surface predicted by the 0.75 ML CO/Pd(111) PES of Ref. [87] versus their  $(T_e, T_1)$  – AIMDEF counterparts taken from Ref. [31]. The slope of the fitting line has been fixed as  $m = 1$  and only the value of the y-intercept "b" has been fitted.

points. Using the latter ones as input, five new PESs are retrained not from scratch, but using the EANN weights from the previously selected multicoverage PES as initial parameters that are updated during training. All second batch PESs achieve convergence within seven iterations before showing overfitting. This remarks the degree of accuracy already achieved for our first batch PES choice. Following a comparative analysis of the retrained PESs, we select the one with lower maximum force errors for the four predict subsets overall. This meticulous process ensures the refinement and validation of an accurate and reliable PES for multicoverage simulations.

**Multicoverage CO/Pd(111) PES energy and force errors**

		$T_e$ -AIMDEF		$(T_e, T_1)$ -AIMDEF	
		0.33 ML	0.75 ML	0.33 ML	0.75 ML
Predict configurations		140 766	140 692	116 927	87 382
$E/N_{\text{moving}}$ (meV)	Max.err.	1.407	2.441	6.093	9.311
	RMSE	0.210	0.312	1.014	0.954
$F_x$ (eV/Å)	Max.err.	0.1735	0.2331	0.9800	0.5073
	MESMAE	0.0867	0.1212	0.2980	0.3103
	RMSE	0.0146	0.0167	0.0488	0.0536
$F_y$ (eV/Å)	Max.err.	0.1617	0.3138	0.5683	0.5045
	MESMAE	0.0865	0.1194	0.2835	0.3136
	RMSE	0.0144	0.0161	0.0488	0.0519
$F_z$ (eV/Å)	Max.err.	0.3067	0.3492	0.6356	0.5938
	MESMAE	0.1109	0.1752	0.2938	0.3444
	RMSE	0.0187	0.0230	0.0498	0.0589

**Table 7.2:** Maximum absolute-valued errors and RMSEs in the energies per moving atom and in the atomic forces, and MESMAEs for all moving atoms in forces predicted by the final multicoverage EANN PES on predict AIMDEF data points. Two distinctions are made, the first one between the type of dynamics simulations, namely  $T_e$  – AIMDEF and  $(T_e, T_1)$  – AIMDEF, and the subsequent second one among the two CO coverages we have AIMDEF data for, 0.33 ML and 0.75 ML. The number of AIMDEF configurations of each predict subset are given explicitly. Total number of moving atoms  $N_{\text{moving}}$  is 33 for 0.33 ML and 36 for 0.75 ML.

Our final multicoverage PES demonstrates its robustness when calculating the energies and atomic forces of the 485 137 predict set data points distributed into the aforementioned four categories ( $T_e$  – AIMDEF and  $(T_e, T_1)$  – AIMDEF for 0.33 ML

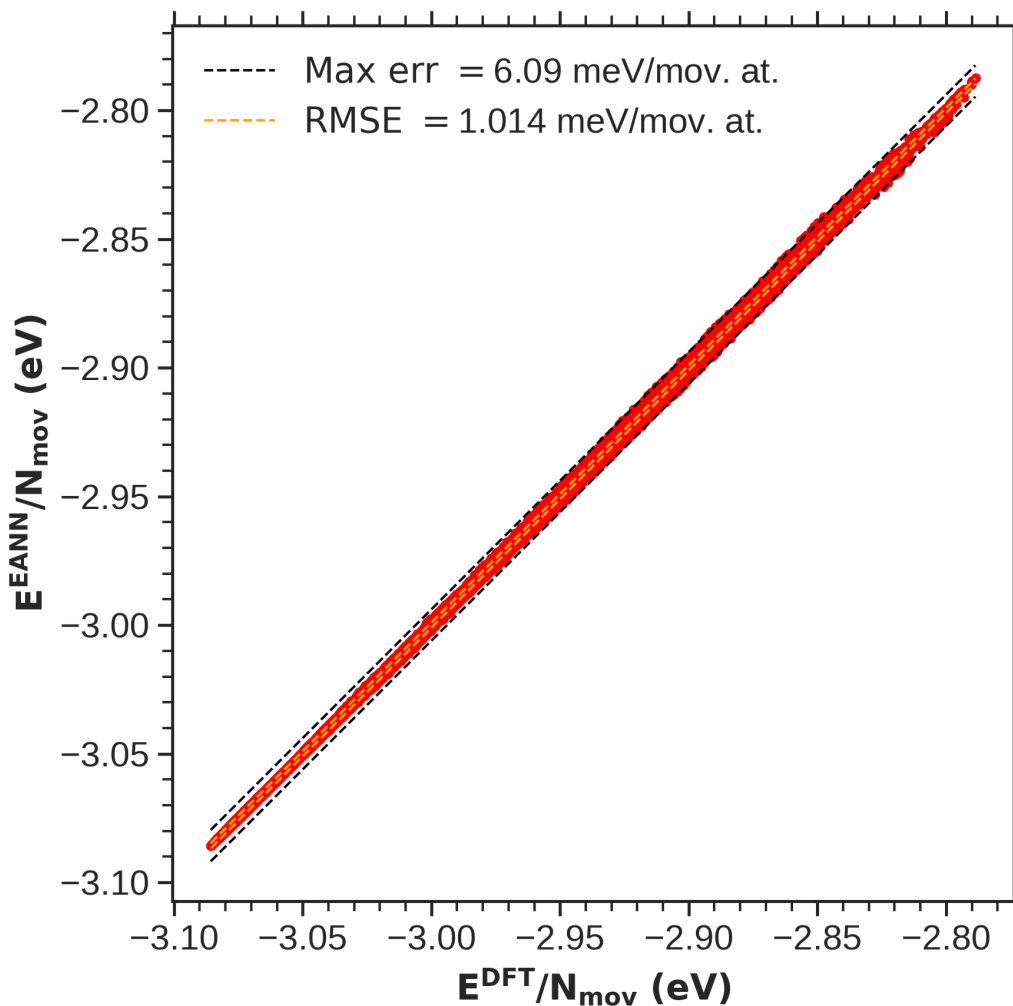


**Figure 7.5:** Comparison of the potential energies per moving atom,  $E^{\text{EANN}}/N_{\text{mov}}$ , computed as determined by the multicoverage EANN PES against their corresponding DFT values,  $E^{\text{DFT}}/N_{\text{mov}}$ , for a set of 116 927 0.33 ML ( $T_e, T_1$ ) – AIMDEF configurations missing from the training data.

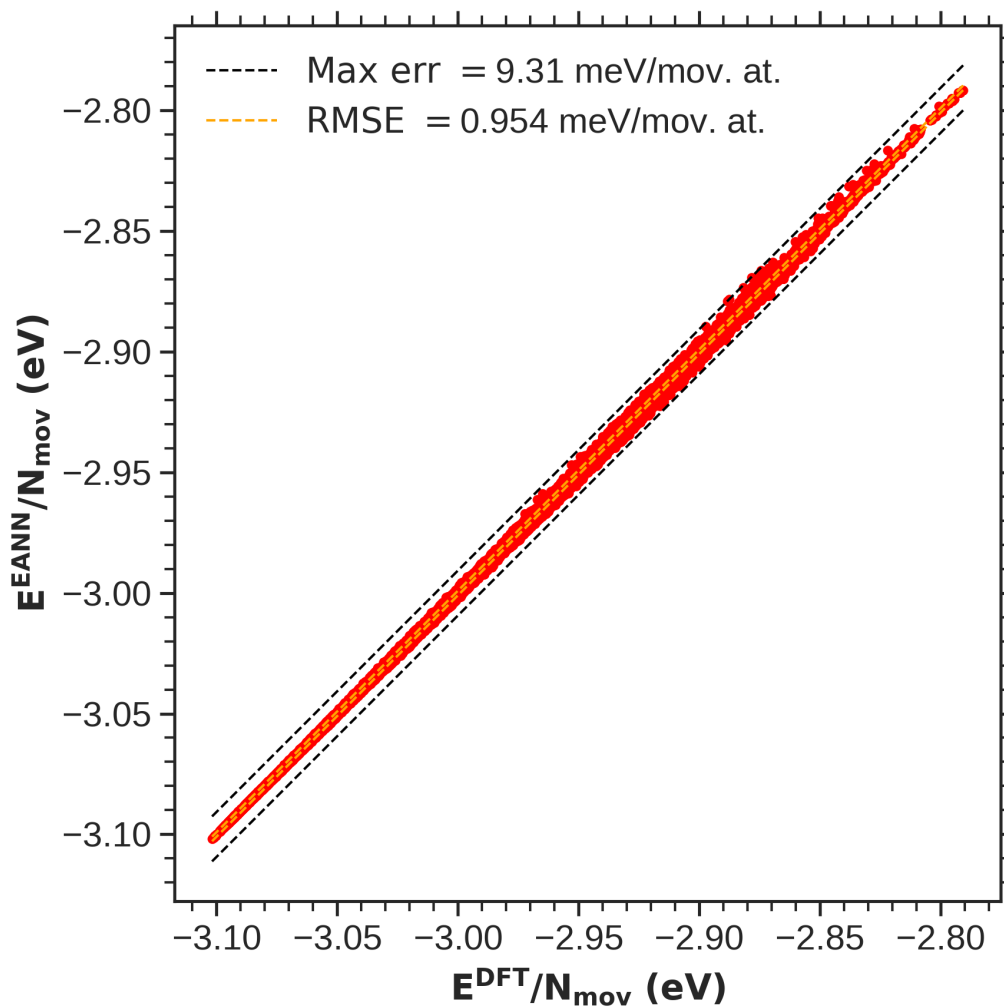


**Figure 7.6:** Comparison of the potential energies per moving atom,  $E^{\text{EANN}}/N_{\text{mov}}$ , computed as determined by the multicoverage EANN PES against their corresponding DFT values  $E^{\text{DFT}}/N_{\text{mov}}$ , for a set of 87 382 0.75 ML ( $T_e, T_1$ ) – AIMDEF configurations missing from the training data.

and 0.75 ML). This can be confirmed with the maximum and RMSE values in energies and forces and in the atomic force MESMAEs collected in Table 7.2. Let us remark that, while energy errors and force RMSEs were calculated considering all configurations of each subset, the maximum errors and MESMAEs in forces were determined based on the top 10 larger errors per moving atom and spatial coordinate. Comparing the central column of Table 5.3 with 0.75 ML ( $T_e, T_l$ ) – AIMDEF column of Table 7.2 we notice close error values overall, with subtly larger errors in energies and in atomic force RMSEs but marginally smaller maximum errors and MESMAEs of forces. A similar trend is observed for 0.33 ML ( $T_e, T_l$ ) – AIMDEF (Table 7.1), as the error magnitudes from the multicoverage PES fluctuate slightly compared to the 0.33 ML PES predictions. Moreover, as only adsorbates are allowed to move for  $T_e$  – AIMDEF,  $T_e$  – AIMDEF errors for each coverage are a few times smaller than their ( $T_e, T_l$ ) – AIMDEF counterparts. This reason led to undergo energy and force predictions for each predict subset in the initial PES batch separately, ensuring  $T_e$  – AIMDEF errors to be not masked by the larger errors from ( $T_e, T_l$ ) – AIMDEF. Following such an approach, configurations with the most significant maximum force errors could be identified for each dynamical situation and coverage. This predictive quality of this multicoverage EANN PES can be further assured if we plot, e.g., the EANN energies against the DFT ones for 0.33 and 0.75 ML ( $T_e, T_l$ ) – AIMDEF predict configurations (Figs. 7.5 and 7.6, respectively).

It is particularly interesting to study the CO desorption minimum energy pathways provided by this enhanced PES. In this respect, Fig. 7.7 presents a comparison between the multicoverage EANN PES predictions and the DFT-vdW-DF reference data. Taking into account both Figures 7.2 and 7.3, it is evident that there is a significant improvement in capturing the minimum energy paths accurately. For the four adsorption sites across both investigated coverages, the desorption energies are approximately correctly predicted by the PES, particularly for 0.75 ML top and hcp sites. Moreover, the potential energy curves align closely with the reference calculations for the four CO desorption possibilities, despite some slightly oscillating pattern for 0.33 ML minimum energy path that was observed for 0.33 ML PES prediction as well (Fig. 7.2). Notably, this alignment is achieved without incorporating data points for desorption under equilibrium conditions in the training set for either coverage. Also, the appearance of physisorption wells for 0.75 ML hcp and fcc adsorption sites for both compared data sets may also be pointed out, despite chemisorption being the CO adsorption mechanism on the Pd surface in each of the sites considered. In this respect, CO chemisorption was also reported in Ru(0001) [94], whereas in Au(111) physisorption was found to be CO adsorption mechanism [84].

Another test we can undergo involves predicting the desorption energies for

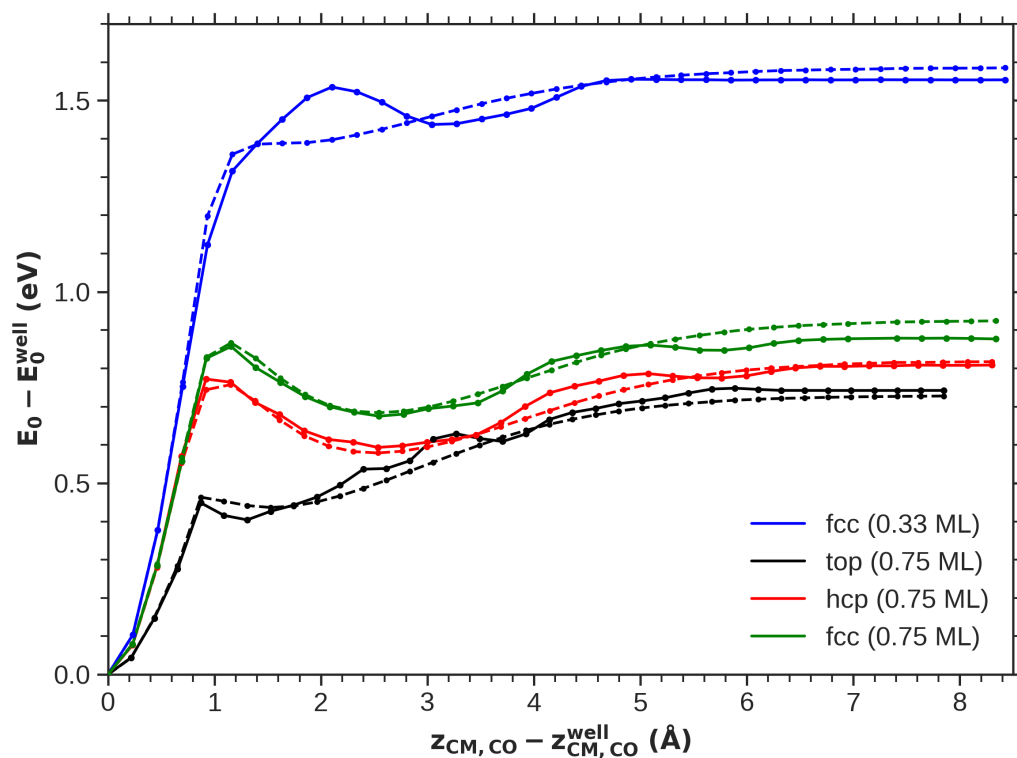


**Figure 7.7:** Potential energy  $E_0$  against the CO CM height  $z_{\text{cm,CO}}$  for one CO species desorbing along its site-specific minimum energy path from a 0.33 ML CO/Pd(111) adsorption site –fcc, in blue– and the three possible adsorption sites in 0.75 ML, namely top (black), hcp (red) and fcc (green). Solid lines represent the multicoverage EANN PES energy calculations while dashed lines stand for the energies obtained with DFT+vdW-DF of Ref. [31]. In all cases, solid dots correspond to the data points used. In each curve, the energy and the height are referred to the values obtained at the bottom of the corresponding well,  $E_0^{\text{well}}$  and  $z_{\text{cm,CO}}^{\text{well}}$  respectively.

<b>Site-specific desorption energies</b>				
<b>Coverage (ML)</b>	<b>Desorption site</b>			
	<b>top</b>	<b>bridge</b>	<b>hcp</b>	<b>fcc</b>
<b>0.33</b>	—	—	—	1.55 / 1.58
<b>0.60</b>	—	0.85 / 0.95	—	0.78 / 0.87
<b>0.75</b>	0.75 / 0.74	—	0.81 / 0.83	0.88 / 0.94

**Table 7.3:** Comparison of site-specific desorption energies, in eV, calculated with the CO/Pd(111) multicoverage EANN PES and with DFT+vdW-DF, shown with the format  $E_{\text{des}}^{\text{EANN}}/E_{\text{des}}^{\text{DFT}}$ . Such energies are defined as the ones required to desorb one CO from Pd(111) for 0.33 ML, 0.60 ML, and 0.75 ML adlayers. Previously estimated experimental desorption energies for 0.24 ML, 0.64 ML, and 0.75 ML (top site) were equal to 1.38, 0.78, and 0.50 eV, respectively, as reported elsewhere [30].

#### Test on random 0.60 ML CO/Pd(111) configurations

<b>F (J/m<sup>2</sup>)</b>		<b>85.0</b>	<b>95.0</b>	<b>115.0</b>
<b>Number of configurations</b>		114	120	1 212
$E/N_{\text{moving}}$ (meV)	Max. error	4.804	5.532	3.524
	RMSE	1.048	1.540	1.612
$F_x$ (eV/Å)	Max. error	0.3321	0.3537	0.3195
	MESMAE	0.1475	0.1328	0.1084
	RMSE	0.0480	0.0521	0.0525
$F_y$ (eV/Å)	Max. error	0.3129	0.3822	0.3434
	MESMAE	0.1486	0.1343	0.1066
	RMSE	0.0478	0.0528	0.0523
$F_z$ (eV/Å)	Max. error	0.4402	0.4148	0.3459
	MESMAE	0.1877	0.1579	0.1323
	RMSE	0.0671	0.0678	0.0685

**Table 7.4:** Maximum absolute-valued errors and RMSEs in the energies per moving atom and forces, and MESMAEs of all moving atoms in forces predicted by our final multicoverage PES on three sets of  $(5 \times 2\sqrt{3})\text{rect}$  0.60 ML CO/Pd(111)  $(T_e, T_1)$  – AIMDEF configurations randomly chosen from previous  $(T_e, T_1)$  – MDEF calculations. For all sets,  $N_{\text{moving}}=84$ .

each adsorption site,  $E_{\text{des}}^{\text{EANN}}$ , and compare those to previous DFT-vdW-DF results,  $E_{\text{des}}^{\text{DFT}}$  [31]. Desorption energies are calculated by comparing the energy of a given CO desorbed along the minimum energy path, i.e., normal with respect to the surface, with the minimum energy configuration corresponding to a previously relaxed adsorbate-substrate complex. Alternatively stated, the CO desorption energy for a given site is, by definition, the one needed to desorb one CO adsorbed at such site on the surface. Table 7.3 collects these results for comparison in the format  $E_{\text{des}}^{\text{EANN}}/E_{\text{des}}^{\text{DFT}}$ . As we can check, our multicoverage PES predicts desorption energies very close to the DFT-vdW-DF benchmark values for all sites of both 0.33 and 0.75 ML adlayers, the differences among values being of between  $\sim 0.01$  to 0.06 eV. For 0.75 ML, it also orders the site-specific desorption energies correctly. As for minimum energy paths, specific configurations with a CO desorbed perpendicularly to its adsorption site were missing from the multicoverage PES training set, hence this being another quality test our PES succeeds at. To end with, note in passing that the latter calculations accurately describe the arrangements of CO adsorbed to Pd(111), even though the experimental adsorption energy was overestimated by about 0.2 eV, as discussed in detail in Ref. [31]. For further reference, a previous experimental estimation of desorption energies yielded the values of 1.38 and 0.50 eV for 0.24 ML and top site of 0.75 ML, respectively [30].

At this point, let us get a first impression of our PES predictive capabilities beyond the data incorporated into its training. The fact that interaction energies are learned additively from atomic environments in EANN enables our multicoverage PES to flexibly model intermediate coverages between 0.33 and 0.75 ML, as discussed elsewhere [339]. To see this, we can evaluate the energies and forces of randomly chosen 0.60 ML configurations previously computed with  $(T_e, T_l)$  – MDEF and compare them to their corresponding DFT values. Here, we consider a supercell of dimensions  $(5 \times 2\sqrt{3})$  rect containing 12 CO adsorbates and a 4-layer slab of 20 Pd atoms per layer, with  $N_{\text{moving}}=84$  moving atoms (Fig. 7.9, top panel). To do this test in under a broader variety of conditions, we consider three different incoming laser pulse fluences, namely 85, 95 and 115 J/m<sup>2</sup>, and perform the tests on sets of 114, 120 and 1212 configurations, respectively. As seen in Table 7.4, for each set, maximum error, MESMAEs and RMSEs for energies and atomic forces are very similar to the 0.33 and 0.75 ML calculations, thus underscoring the transferability of our multicoverage PES. This is also verified after determining the desorption energies for both adsorption sites present in a  $c(5 \times \sqrt{3})$  rect 0.60 ML cell, where one and two CO adsorb at fcc and bridge sites in equilibrium, respectively. Comparison of desorption energies (Table 7.3) shows differences of  $\sim 0.09$  and 0.1 eV for fcc and bridge, respectively, its relative ordering being correctly captured as well. Following

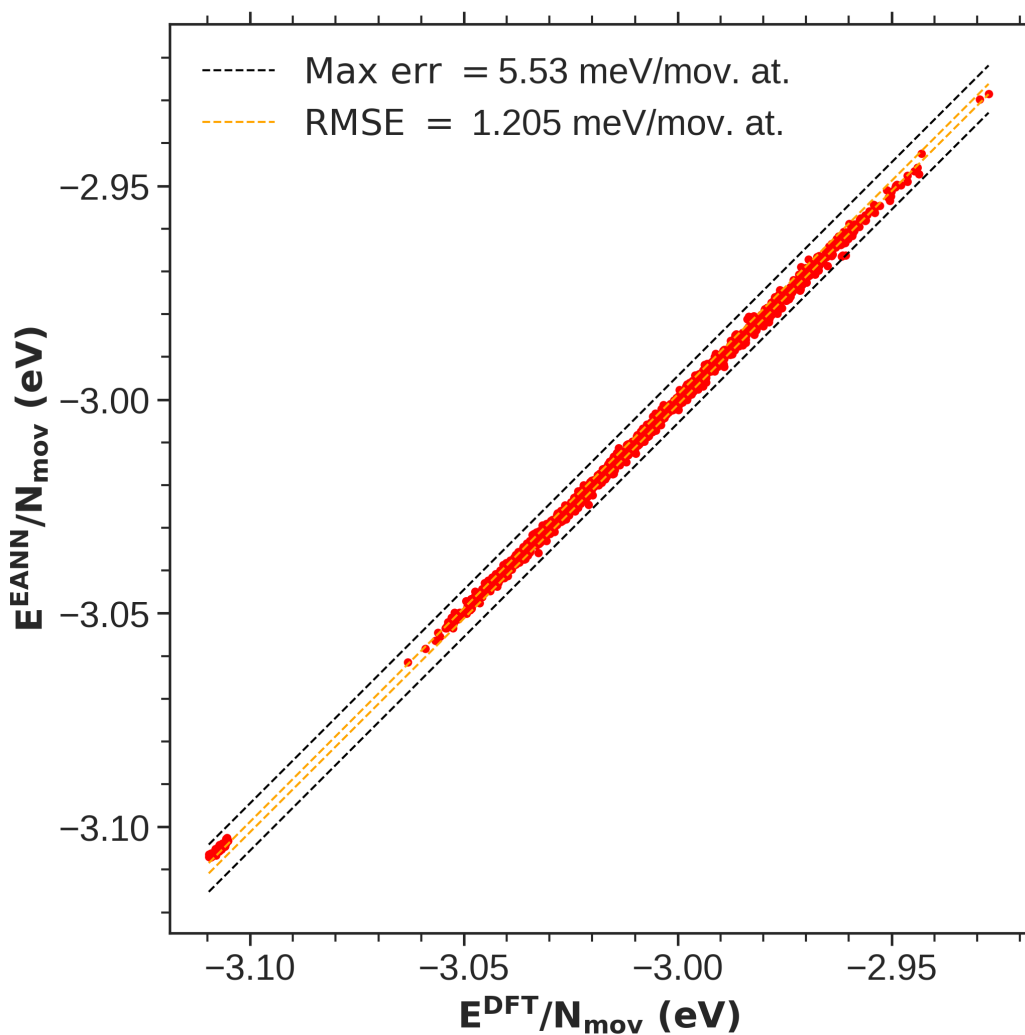


**Figure 7.8:** Comparison of the potential energies per moving atom,  $E^{\text{EANN}}/N_{\text{mov}}$ , computed as determined by the multicoverage EANN PES against their corresponding DFT values  $E^{\text{DFT}}/N_{\text{mov}}$ , for a set of 1446 0.60 ML ( $T_e, T_1$ ) – AIMDEF configurations. Among the latter ensemble, 114, 120, and 1212 data points have been obtained under incident laser fluences of 85, 95, and 115  $\text{J}/\text{m}^2$ , respectively.

the aforementioned remark about  $E_{\text{des}}$  overestimation by DFT+vdW-DF contrasted to experiments, the closer experimental desorption energy available for reference is equal to 0.78 eV for 0.64 ML adlayer [30]. Equally impressively, the predicted energies per moving atom by our PES for the 1446 data points for 0.60 ML (Fig. 7.8) differ from their respective DFT values as little as those energies coming from 0.33 or 0.75 ML configurations (Figures 7.5 and 7.6, respectively).

Overall, with the 0.75 ML and 0.33 ML PESs as previous references, our multicoverage PES seems to behave astonishingly solidly regarding the available AIMDEF data, and even beyond it as seen for 0.60 ML tests. Now we are confident enough to deal with more comprehensive studies about how femtosecond laser-induced desorption of CO from Pd(111) changes under distinct conditions. More precisely, let us analyze its dependence with incident laser fluence, under different CO coverages and in terms of the delay between a pump and a probe pulse in the case of 2PC dynamics.

### 7.3 Coverage dependence of the desorption of CO from Pd(111) induced by a single femtosecond laser pulse

Now that we have a properly working multicoverage EANN PES to perform MDEF on CO/Pd(111), we may proceed with more complex studies on its femtosecond laser-induced desorption dynamics. In fact, we want to analyze how such process varies in this adsorbate-substrate complex with respect to the CO coverage. CO/Pd(111) is a suitable candidate for such a study, as CO can take no less than 17 different stable adlayer arrangements as found using low-energy electron diffraction [17], thus remarking its complexity from a structural perspective. According to the latter work, CO adsorbs on Pd only at three-fold hollow sites for coverages equal to or below 0.33 ML, at both bridge and three-fold hollow sites for 0.50 ML, at a mixture of mainly bridge or close-to-bridge sites in the interval [0.50,0.67] ML, also involving top and three-fold hollow sites above 0.60 ML, and the mixture of top and three-fold hollow sites near saturation at 0.75 ML. Linked to this structural complexity, another later experimental work pointed out how sharply CO desorption varies with the Pd(111) coverage [30]. As reported there, single pulse experiments at different fluences in DIMET regime showed that desorption yield can change up to two orders of magnitude as the initial CO coverage increases from 0.33 ML to 0.75 ML. Furthermore, their 2PC experiments also reveal how distinct the role played by electrons and lattice phonons is in terms of the coverage. Such

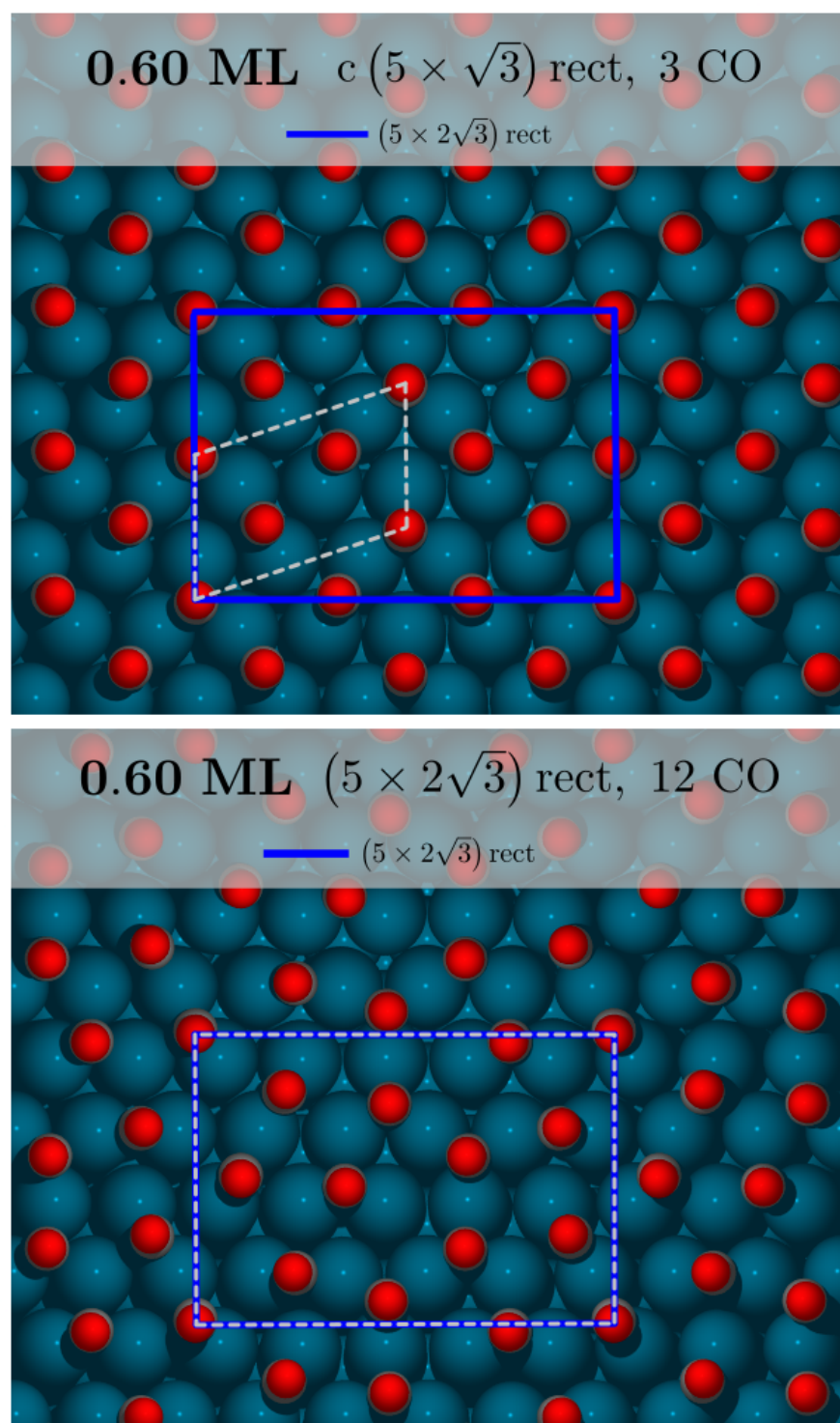


**Figure 7.9:** Top view of minimum energy configurations obtained with the multicoverage EANN PES for 0.60 ML of CO coverage. Top structure corresponds to a local minimum higher in energy than the bottom structure. The supercells used in our  $(T_e, T_i)$  – MDEF simulations are represented in solid lines. Grey dashed lines indicate the smallest pattern that is repeated within supercells.

observation comes not only from the variability in 2PC desorption yield widths for the different adlayers, but also because the results are consistent either with a weak hot electrons-adsorbate or a strong phonons-adsorbate coupling. The latter aspect will be covered more thoroughly in Section 7.4. Further analysis with an empirical friction three temperature model of CO desorption from substrates such as Cu(100) [351] or Ru(001) [92] rules out a significant impact of phonons on the resulting 2PC desorption yields, despite of the large lattice temperature predictions by the model [32]. Previously, MDEF was unable to study questions such as the effect of adlayer structure on laser-initiated DIMET or the relative role played by hot electrons and phonons on this chemical process. However, our  $(T_e, T_l)$  – MDEF methodology with the multicoverage PES opens the way to such theoretical analysis, which we have done for CO/Pd(111) with an unprecedented level of depth [89].

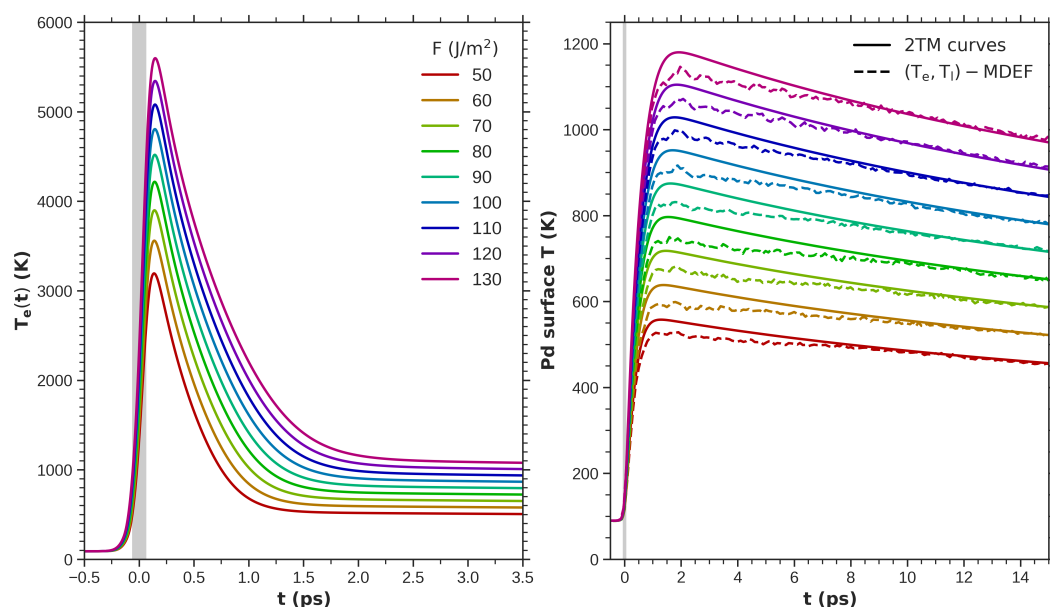


**Figure 7.10:** Time evolution of the electronic temperature,  $T_e$ , (left panel) and the lattice temperature for the three topmost Pd surface layers,  $T_l$ , (right panel), as determined with 2TM (solid lines) for different pulse laser fluences. Dashed lines show the mean temperature of the three topmost mobile Pd layers in  $(T_e, T_l)$  – MDEF calculations. The incoming laser pulse is assumed to reach its peak intensity at time zero, and its FWHM is represented as the gray shaded region.

As we explained in Chapter 3, one of the particular features of DIMET regime is the superlinear dependence of the yield on the laser fluence. To explore how

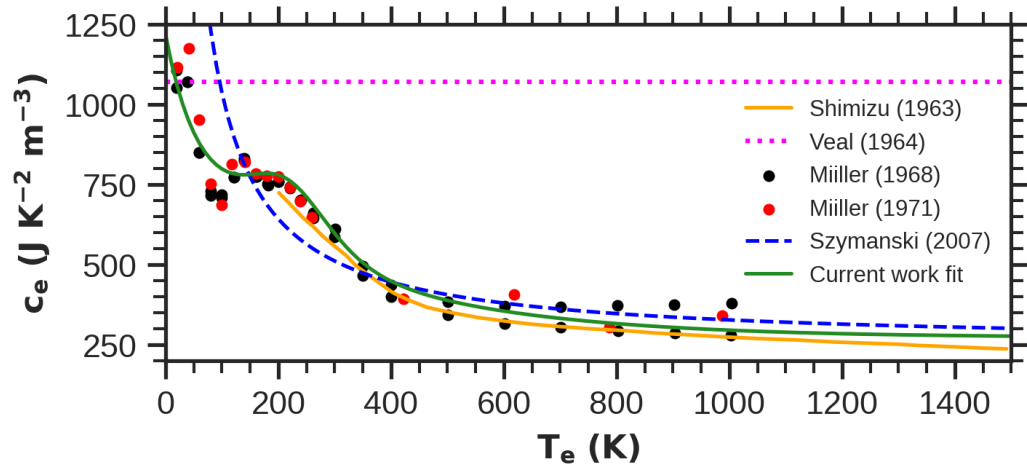


**Figure 7.11:** Electronic heat capacity coefficient  $c_e$  in palladium as a function of the electronic temperature. The  $c_e(T_e)$  considered in our calculations is shown as the solid green line. This result is obtained from a fit to previous experimental data of Shimizu *et al.* (1963) [352] (orange line), Miiller *et al.* (1968) [353] (black dots), and Miiller *et al.* (1971) [354] (red dots). For reference, a previous fit of  $c_e(T_e)$  due to Szymanski *et al.* (2007) [38] is also depicted with a dashed blue line.  $c_e(0)$  has been derived from the heat capacity low temperature measurements in Veal *et al.* (1964) [355] (dotted pink line).

**Fitting parameters for Pd  $c_e(T_e)$**

Parameter	Value	Units
$a_0$	273	$\text{J K}^{-2} \text{m}^{-3}$
$a_1$	2 702	$\text{J K}^{-2} \text{m}^{-3}$
$a_2$	214	$\text{J K}^{-2} \text{m}^{-3}$
$a_3$	98 180	$\text{J K}^{-2} \text{m}^{-3}$
$T_1$	-96	K
$T_2$	213	K
$T_3$	-2 085	K
$\sigma_1$	50	K
$\sigma_2$	103	K
$\sigma_3$	634	K

**Table 7.5:** Fitting parameters used for Pd  $c_e(T_e)$  (Eq. (7.4)) according to previous experimental data of Refs. [352, 353, 354].

DIMET works across different CO/Pd(111) coverages, we perform  $(T_e, T_l)$  – MDEF calculations on 0.33, 0.60, and 0.75 ML coverages. We use the same initial conditions of the experiments reported in Ref. [30], in order to subsequently contrast our calculations with those experimental results. As a result, each laser pulse we employ has a FWHM of 130 fs, wavelength of 780 nm and  $\text{sech}^2$  profile, and their fluences vary along three distinct ranges. Specifically, we take multiple-of-five fluences between the intervals [100,130], [85,115] and [50,80] J/m<sup>2</sup> for 0.33, 0.60 and 0.75 ML, respectively. Time evolution of the surface electronic and phonon bath temperatures according to 2TM (Section 3.2.1) for these incoming pulses along the range of fluences [50,130] J/m<sup>2</sup> is plotted in Fig. 7.10. In this respect, the macroscopic thermal coefficients  $\kappa_e(T_e, T_l)$  and  $C_l(T_l)$ , the electron-phonon coupling constant  $g$  and the laser source term  $S(z, t)$  are taken as defined in Ref. [356]. Electron heat capacity is written as a function of  $T_e$  as  $C_e = c_e(T_e) T_e$ . Here, the proportionality factor  $c_e(T_e)$  has been fitted for Pd according to previous experimental results [352, 353, 354] to the equation,

$$c_e(T_e) = a_0 + a_1 \exp\left(-\frac{T_e - T_1}{\sigma_1}\right) + a_2 \cosh^{-2}\left(\frac{T_e - T_2}{\sigma_2}\right) + a_3 \cosh^{-2}\left(\frac{T_e - T_3}{\sigma_3}\right) \quad (7.1)$$

with the fitting constants  $a_i$ ,  $T_i$ , and  $\sigma_i$  parameterized as shown in Table 7.5. Our fit is contrasted with the aforementioned experimental results and other previous fits in Fig. 7.11.

Regarding the dynamical description of the system atoms, adsorbates are attached to a Langevin thermostat (Eq. (3.12)), as done for previous AIMDEF and MDEF works on CO/Pd(111) [31, 87, 88]. In this respect, friction coefficients for C and O atoms are obtained using LDFA, where electronic densities created by Pd atoms on the surface are evaluated on-the-fly from the DGF according to Eq. (5.4) [87]. Noteworthy, there is a key distinction in the form in which substrate atoms are described dynamically in the following simulations. In previous  $(T_e, T_l)$  – AIMDEF or  $T_l$  – AIMDEF calculations, the two topmost layer substrate atoms were coupled to a NH thermostat, according to Eqs. (3.14) and (3.15). Third topmost layer atoms were modeled with adiabatic dynamics (Eq. (3.16)) and bottom layer ones were taken to be frozen. While for the current calculations the bottom layer atoms are kept motionless, surface atoms of the three topmost Pd layers are instead described with Langevin equation,

$$M_i \frac{d^2 \mathbf{R}_i}{dt^2} = -\nabla_{\mathbf{R}_i} V(\{\mathbf{R}_m\}) - \eta_i^{\text{Pd}}(\mathbf{R}_i) \frac{d\mathbf{R}_i}{dt} + \mathcal{R}_{e,i}[T_e(t), \eta_i^{\text{Pd}}(\mathbf{R}_i)], \quad (7.2)$$

so neither NH thermostat nor the exact  $T_l(t)$  are involved in the moving Pd dynam-

ical treatment. Here, each Pd friction coefficient  $\eta_i^{\text{Pd}}$  is calculated after assuming it to be linearly proportional to the electronic density surrounding each Pd atom, i.e.,  $\eta_i^{\text{Pd}} \propto \rho(\mathbf{R}_i)$ . From Eq. (5.4), one can obtain that:

$$\eta_i^{\text{Pd}}(R) = \left(\frac{R_0}{R}\right)^3 \eta^{\text{Pd}}(R_0), \quad (7.3)$$

where  $R$  represents the Wigner-Seitz radius corresponding to the electronic density  $\rho(\mathbf{R}_i)$  at Pd atom  $i$ , and  $R_0$  is a predefined Wigner-Seitz radius at which  $\eta^{\text{Pd}}(R_0)$  is determined. We fix  $\eta^{\text{Pd}}(R_0)$  according to the electron-phonon coupling constant  $g$  of 2TM. These two quantities fulfill the following relationship as discussed in Ref. [357]:

$$\eta^{\text{Pd}}(R_0) \approx \frac{m_{\text{Pd}}}{3k_{\text{B}}d_{\text{Pd}}}g = 1.6223 \text{ a.u.}, \quad (7.4)$$

being  $m_{\text{Pd}}$  and  $d_{\text{Pd}}$  the Pd atomic mass and density, respectively. We consider the latter quantity to be 4 atoms per  $64 \text{ \AA}^3$ . As the constant  $g$  is a property of the bulk,  $R_0$  can be taken as the Wigner-Seitz radius corresponding to the embedding electronic density of a Pd atom in the bulk. Based on our DFT bulk calculations, we set  $R_0 = 4.38 \text{ a.u.}$ . To verify the validity of these approximations on friction, it is essential to check whether this Langevin thermostat, coupled to the moving Pd surface atoms, accurately provides the desired surface temperature, as with NH thermostat in earlier studies. To this end, we may compare the  $T_l(t)$  curves in the right panel of Fig. 7.10 observed in our  $(T_e, T_l)$  – MDEF trajectories (dashed lines) with the theoretical 2TM calculations (solid lines). As we can observe, our dynamics results align very well with the latter curves, specially from 12 ps after the arrival of the laser pulse maximum on, this supporting our methodology and friction description for substrate Pd atoms.

Prior to perform  $(T_e, T_l)$  – MDEF, we thermalize coverage-specific sets of 100  $(T_e, T_l)$  – MDEF trajectories to  $T_e = T_l = 90 \text{ K}$ , in order to match the initial Pd surface temperature of the experimental work of Ref. [30]. All trajectories of each thermalized ensemble start from the minimum energy configuration corresponding to each CO coverage considered, using randomized atomic initial velocities, and last 50 ps. All configurations sampled before reaching a Boltzmann distribution (from 0 to 15 ps, approximately) were discarded. Then, from the remaining ones, random configurations are chosen as the initial arrangements to do subsequent  $(T_e, T_l)$  – MDEF under femtosecond laser initial excitation. Let us briefly make some remarks about this thermalization stage. First, let us adopt the notation fcc:hcp:bridge:atop to denote the proportion of CO adsorbed at each site in the simulation cell. For both 0.33 and 0.75 ML coverages, and for all configurations

visited during their thermalizations, no CO molecule diffuses along surface, no matter the dimensions of the respective supercells. This implies that the proportions of CO adsorbates in each site remain constant. In other words, the adsorption ratios are constant for the full 50 ps span and, in particular, equal to 1:0:0:0 for 0.33 ML and 1:1:0:1 for 0.75 ML.

Exponents $n$ in $P_{\text{des}} \propto F^n$			
Theory: $(T_e, T_1)$ – MDEF			
Coverage (ML)	0.33	0.60	0.75
$n_{\text{th}}$	$(3 \times 3): 11.6 \pm 1.5$ $(6 \times 6): 12.0 \pm 1.0$	$(5 \times 2\sqrt{3})\text{rect}: 7.1 \pm 0.5$	$(2 \times 2): 7.6 \pm 0.4$ $(4 \times 2): 7.1 \pm 0.3$ $(4 \times 4): 7.0 \pm 0.3$
Experiments (Hong <i>et al.</i> ) [30]			
Coverage (ML)	0.24	0.64	0.75
$n_{\text{exp}}$	$9.3 \pm 0.5$	$10.3 \pm 0.4$	$6.9 \pm 0.3$

**Table 7.6:** Computed  $(T_e, T_1)$  – MDEF theoretical ( $n_{\text{th}}$ ) and experimental [30] ( $n_{\text{exp}}$ ) values of the exponent  $n$  in the power law  $P_{\text{des}} \propto F^n$  for CO/Pd(111) femtosecond laser-induced desorption. Values are provided for various CO coverages. Among theoretical calculations, cross products indicate the dimensions of the particular supercell considered.

On the contrary, at 0.60 ML adlayer, the proportion of CO adsorbed at the different sites changes during thermalization dynamics, even at a goal temperature as low as 90 K, hence showing how mobile CO adsorbates become at this intermediate coverage. Following previous experimental works [17, 30], we set all 0.60 ML trajectories to begin from a  $c(5 \times \sqrt{3})\text{rect}$  structure decorated by three CO molecules that adsorbed at sites 1:0:2:0 after relaxation. Nonetheless, after analyzing the configurations sampled during these thermalization trajectories, our multicoverage PES predicts a more stable, yet more complex structure, namely  $(5 \times 2\sqrt{3})\text{rect}$ -12CO, with site proportions of 2:1:3:0. Figure 7.9 depicts a comparison of both atomic arrangements. Amazingly, DFT calculations support this observation, which is also consistent with a previous report on the broad amount of stable structures observed between 0.50 and 0.60 ML using low energy electron diffraction (LEED) [17]. Let us remind once more that no data from this intermediate coverage was incorporated

to the multicoverage PES training. Altogether, these remarks further support the accuracy and transferability of our multicoverage PES, from which we already gained some insights at the end of Section 7.2.

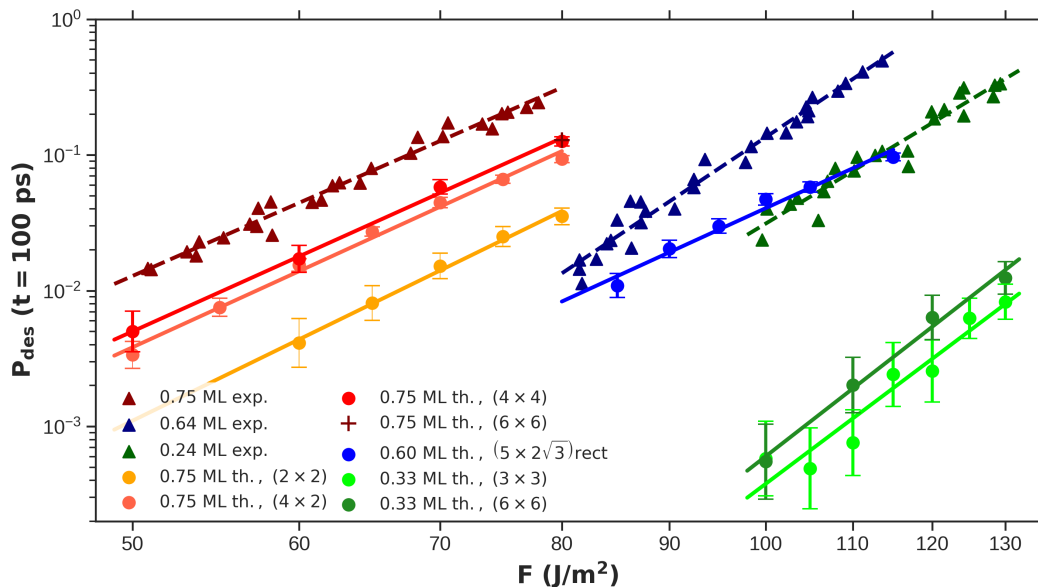


**Figure 7.12:** CO desorption probability against the absorbed fluence for different initial coverages. Reddish, bluish, and greenish full circles stand for  $(T_e, T_1)$  – MDEF theoretical results for 0.75, 0.60, and 0.33 ML coverages, respectively, with varying simulation cell size. Darker red, blue, and green triangles correspond to the experimental results of Ref. [30] for 0.75, 0.64, and 0.24 ML coverages, respectively. Each set of data points has been fitted to a log-linear function (solid lines).

After obtaining for each coverage a set of thermalized configurations, it is time to perform  $(T_e, T_1)$  – MDEF with them along the fluence spans previously indicated. Each trajectory is integrated in time with the Beeman algorithm using a time step of 0.2 fs until reaching a time of 100 ps. Depending on the fluence and coverage, an amount of trajectories between 6750 and 60 000 has been calculated in order to reduce the statistical uncertainty for each data point of Fig. 7.12. This figure shows, in log-log scale, the fluence dependence of the CO desorption probability,  $P_{des}$ , after reaching saturation, and in terms of the laser fluence  $F$  absorbed by the surface. Coverages are distinguished from each other by greenish (0.33 ML, or 0.24 ML for experiment), blueish (0.60 ML, or 0.66 ML for experiment) and reddish colors (0.75 ML). Experimental reference data and  $(T_e, T_1)$  – MDEF data points are displayed with triangles and full circles, respectively. For both sets, log-linear

fits are performed in order to determine the exponent  $n$  characteristic of DIMET mechanism, as  $P_{\text{des}} \propto F^n$ . All  $n$  values are collected in Table 7.6. Furthermore, we have analyzed how  $P_{\text{des}}$  varies with the supercell size for 0.33 and 0.75 ML. In fact, properties of chemical processes may be affected by the size of the simulation cell considered, as reported, e.g., for the energy exchange in the scattering of CO on Au(111) [358], the photoinduced recombinative desorption probability of H<sub>2</sub> on Ru(0001) [359], and the relaxation of hot O atoms after O<sub>2</sub> dissociation on Pd surfaces [360]. In our system, we have also simulated CO photodesorption on 0.33 ML 6×6 and on 0.75 ML 2×2, 4×4 and 6×6 supercells (Fig. 7.1). According to our results,  $P_{\text{des}}$  increases with increasing cell sizes. Particularly for 0.75 ML, we see that for bigger supercells than a 4×4 one this increment starts to become negligible, as hinted from contrasting 6×6 and 4×4 results at 80 J/m<sup>2</sup>. As a result, in the following we are restricting ourselves to the theoretical results of the bigger cell sizes tried for each coverage for discussion purposes. All this said, and despite its influence on desorption probability, cell size does not affect the exponent  $n$  (Table 7.6). For 0.60 ML, instead, (T<sub>e</sub>, T<sub>l</sub>) – MDEF has been done only on a (5 × 2√3)rect supercell.

Now let us discuss in more detail the nonlinear exponent results of Table 7.6. One can see that  $n$  decreases as the coverage increases, being  $n_{\text{th}}(0.33 \text{ ML}) > n_{\text{th}}(0.60 \text{ ML}) \gtrsim n_{\text{th}}(0.75 \text{ ML})$ . In a DIMET process,  $n$  can be interpreted as the effective number of energy jumps that the adsorbate undergoes before escaping its adsorption well and desorbing [47, 361]. At this point, let us look at the desorption energies  $E_d$  for each site and each coverage (Table 7.3). If we compute the average desorption energy for each adlayer  $\bar{E}_d$ , we obtain the following sequence:  $\bar{E}_d(0.33 \text{ ML}) > \bar{E}_d(0.60 \text{ ML}) \gtrsim \bar{E}_d(0.75 \text{ ML})$ . This means that the orderings of both  $n_{\text{th}}$  values and  $\bar{E}_d$  for each adlayer correlate with each other. An analogous, site-specific trend was already determined theoretically for femtosecond laser-induced desorption of O<sub>2</sub> from Ag(110) [45]. Now, if we compare each  $n_{\text{th}}$  with its experimental counterpart [30], we see a reasonably good level of coincidence. For 0.75 ML, the only coverage coincident for both (T<sub>e</sub>, T<sub>l</sub>) – MDEF and experiment, the agreement is impressive between our calculation ( $n_{\text{th}}(0.75 \text{ ML}) = 7.0 \pm 0.3$ ) and the experimental value ( $n_{\text{exp}} = 6.9 \pm 0.3$ ). For both 0.33 and 0.60 ML, our results are compared to the experimental values for 0.24 and 0.66 ML, respectively, yielding in both cases a difference of  $\sim 3$  units between exponents. Such discrepancies make sense given how much  $n$  may vary for slight changes in the CO coverage. Nevertheless, the ordering of  $n_{\text{exp}}$  is nonmonotonic with coverage, i.e.,  $n_{\text{exp}}(0.64 \text{ ML}) \gtrsim n_{\text{exp}}(0.24 \text{ ML}) > n_{\text{exp}}(0.75 \text{ ML})$ . Following Ref. [30], the latter circumstance may be argued to happen due to the presumed high mobility of CO in adlayers below 0.33 ML, this leading to potentially smaller desorption energies than the one for 0.33 ML.

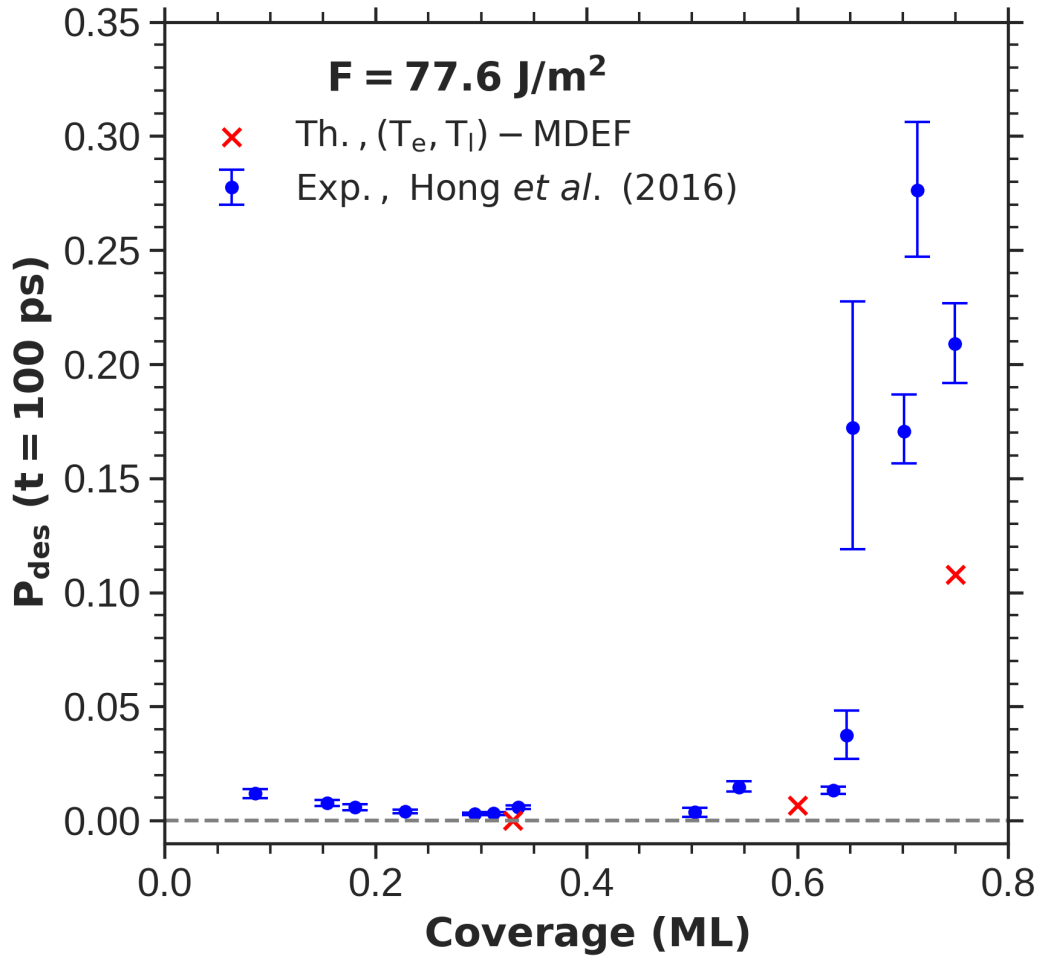


**Figure 7.13:** CO desorption probability as a function of coverage for fixed absorbed fluence 77.6 J/m<sup>2</sup>. Theoretical data points for each adlayer, depicted as red crosses, have been computed from log-linear extrapolation at the required fluence of left graph data fit for the larger supercell size considered. Experimental data points, shown as blue dots with their respective uncertainty intervals, are taken from Ref. [30].

Another conclusion we can draw from Fig. 7.12 is that our theoretical results of  $P_{\text{des}}$  are clearly smaller than their experimental counterparts, namely by factors of  $\sim 32$ ,  $\sim 3.5$ , and  $\sim 2$  for 0.33, 0.60, and 0.75 ML, respectively. Discrepancies for the intermediate- and large-size coverages may be explained by the somewhat overestimated DFT desorption energies compared to experimental measurements [31], yet they can be seen as minor considering the complexity of femtosecond photoinduced CO desorption. Another source of discrepancy may be the differences between low and intermediate coverages handled in  $(T_e, T_1)$  – MDEF and in the experiment. In particular, this may explain the larger underestimation of 0.33 ML desorption probabilities compared to 0.24 ML experimental data. For coverages below 0.33 ML, values of  $P_{\text{des}}$  could increase due to the formation of 0.33 ML stability islands, as a uniform 0.33 ML coverage could not be prepared experimentally. At the island edges, presence of CO adsorbed at bridge sites would then enhance the experimental  $P_{\text{des}}$  due to its lower adsorption energy than at fcc sites, as mentioned earlier [26, 30]. To verify this, such a large 0.33 ML island would need to be simulated, this requiring an accordingly much larger supercell (bigger than 0.33 ML  $6 \times 6$ ) and becoming very expensive computationally, so such simulations have not been tackled.

Furthermore, we can analyze the coverage dependence of CO desorption for a fixed fluence, as experimentally done for a fluence  $F = 77.6 \text{ J/m}^2$  in Ref. [30]. Figure 7.13 depicts the comparison between our  $(T_e, T_1)$  – MDEF calculations for that laser fluence, in red crosses, and the experimental results, shown as blue dots with their respective uncertainty intervals. It should be noted that the theoretical desorption probability values for each coverage have been determined by extrapolating our calculated log-linear functions  $P_{\text{des}}(F)$  (Table 7.6 and Fig. 7.12) to the aforementioned specific fluence. Most of the experimental data points were also obtained by extrapolating to the same fluence [30]. Our calculations align closely with the experimental trend, also reproducing the increase in  $P_{\text{des}}$  with coverage and, particularly, the sharp increase from intermediate ( $\sim 0.50$  ML) to high ( $\sim 0.75$  ML) adlayers. Our previous reasoning on CO desorption energies and their dependence on coverage may also explain this latter trend.

Making use of our multicoverage PES, we can further unravel the relative effect of hot electrons and phonons on CO photodesorption. This can be done with MDEF either after exciting the system with one pulse or studying 2PC (Section 7.4). Focusing on the former, we aim to perform  $T_e$  – MDEF and  $T_1$  – MDEF calculations (see Section 3.2.2.5 for more details) complementary to previous  $(T_e, T_1)$  – MDEF simulations, which start from the same initial configurations and are integrated under the same conditions up to 100 ps. As our multicoverage PES included  $T_e$  – AIMDEF configurations for both 0.33 and 0.75 ML, we choose both adlayers. Among them, we choose some fluences covering the respective intervals previous  $(T_e, T_1)$  –

MDEF calculations are available for, hence we do simulations at fluences 100 and 130 J/m<sup>2</sup> for 0.33 ML and 60, 70, and 80 J/m<sup>2</sup> for 0.75 ML. Figure 7.14 shows the comparison of  $T_e$  – MDEF (dotted lines),  $T_l$  – MDEF (dashed lines) and  $(T_e, T_l)$  – MDEF (full lines) calculations for each combination of coverage and laser fluence considered, along the full integration time. For all combinations, it can be seen that  $P_{\text{des}}(t)$  for  $(T_e, T_l)$  – MDEF is larger throughout the entire integration time than for  $T_e$  – MDEF and  $T_l$  – MDEF separately. Consequently, when adsorbates are excited by both electronic and phononic mechanisms cooperatively, more CO desorption occurs than if either one or the other operates individually. Not only this, but this synergy also triggers the desorption process at earlier times than for  $T_e$  – MDEF and  $T_l$  – MDEF in all cases, as seen along the interval [0,20] ps (Fig. 7.15). Hence, the combined effect of both excitation channels leads to a faster and more substantial photodesorption of CO on Pd, in agreement with the findings of an earlier AIMDEF work [31]. Not only that, but this synergistic view holds for longer time ranges than those reachable by  $(T_e, T_l)$  – AIMDEF, i.e., as long as 100 ps after laser irradiation.

Now let us compare  $T_e$  – MDEF and  $T_l$  – MDEF results. For each combination of adlayer and fluence, we can see in Fig. 7.15 how CO desorption begins earlier for  $T_e$  – MDEF than for  $T_l$  – MDEF. This is consistent with 2TM, since laser absorption by the surface leads to electron heating to very high temperatures in the first instance, as verified earlier in Fig. 7.10. At later times,  $P_{\text{des}}(t)$  becomes very similar for  $T_e$  – MDEF and  $T_l$  – MDEF for 0.75 ML at  $F = 60$  J/m<sup>2</sup> (Fig. 7.14). However, with this sole exception, some picoseconds after the desorption starts, the phonon-only desorption probability becomes larger than the electron-only one in the other cases considered. The crossing happens within the first 15 ps, and arises earlier the higher the incident laser fluence is. Furthermore, we can see that the phonon contribution becomes increasingly important as the fluence increases. Note in passing that 2TM peak lattice temperatures for  $F = 60, 70, 80, 100,$  and  $130$  J/m<sup>2</sup> are equal to 638, 718, 797, 952, and 1180 K, respectively (Fig. 7.10). The Pd surface is able to heat so sharply due to its large electron-phonon energy exchange coupling constant of  $g = 8.95 \times 10^{17}$  W K<sup>-1</sup>m<sup>-3</sup> [356]. Therefore, hot electrons drive the CO desorption process during the first picoseconds after the surface interacts with the laser, while at later times subsequently heated phonons become the dominant desorption mechanism in a nonnegligible way due to the high transient temperatures they reach.

Furthermore, and in contrast to previous kinetic models,  $(T_e, T_l)$  – MDEF allows us to elucidate additional details about how CO desorbs. First, we can observe that CO molecules diffuse uniformly along the entire Pd surface while they are desorbing, also supporting a previous remark obtained with  $(T_e, T_l)$  – AIMDEF [31].

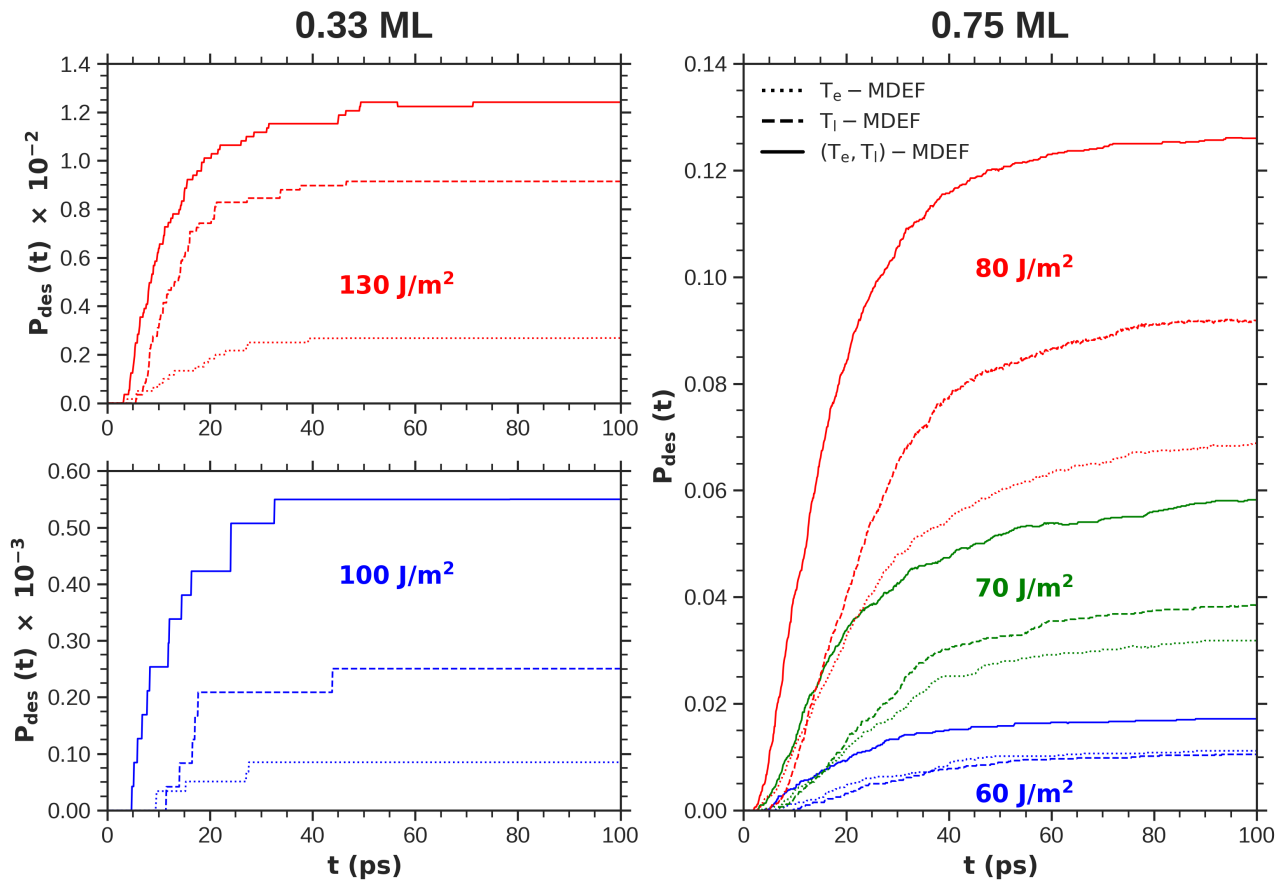


**Figure 7.14:** Time evolution of the average CO desorption probability  $P_{des}(t)$  along the full dynamics integration time of 100 ps.  $(T_e, T_l)$  - MDEF,  $T_e$  - MDEF and  $T_l$  - MDEF results are depicted in full, dotted, and dashed lines, respectively. Left: MDEF results obtained for the 0.33 ML adlayer and fluences 100 J/m<sup>2</sup> (blue, bottom left), and 130 J/m<sup>2</sup> (red, top left). Right: MDEF results obtained for the 0.75 ML adlayer and fluences 60 J/m<sup>2</sup> (blue), 70 J/m<sup>2</sup> (green), and 80 J/m<sup>2</sup> (red).

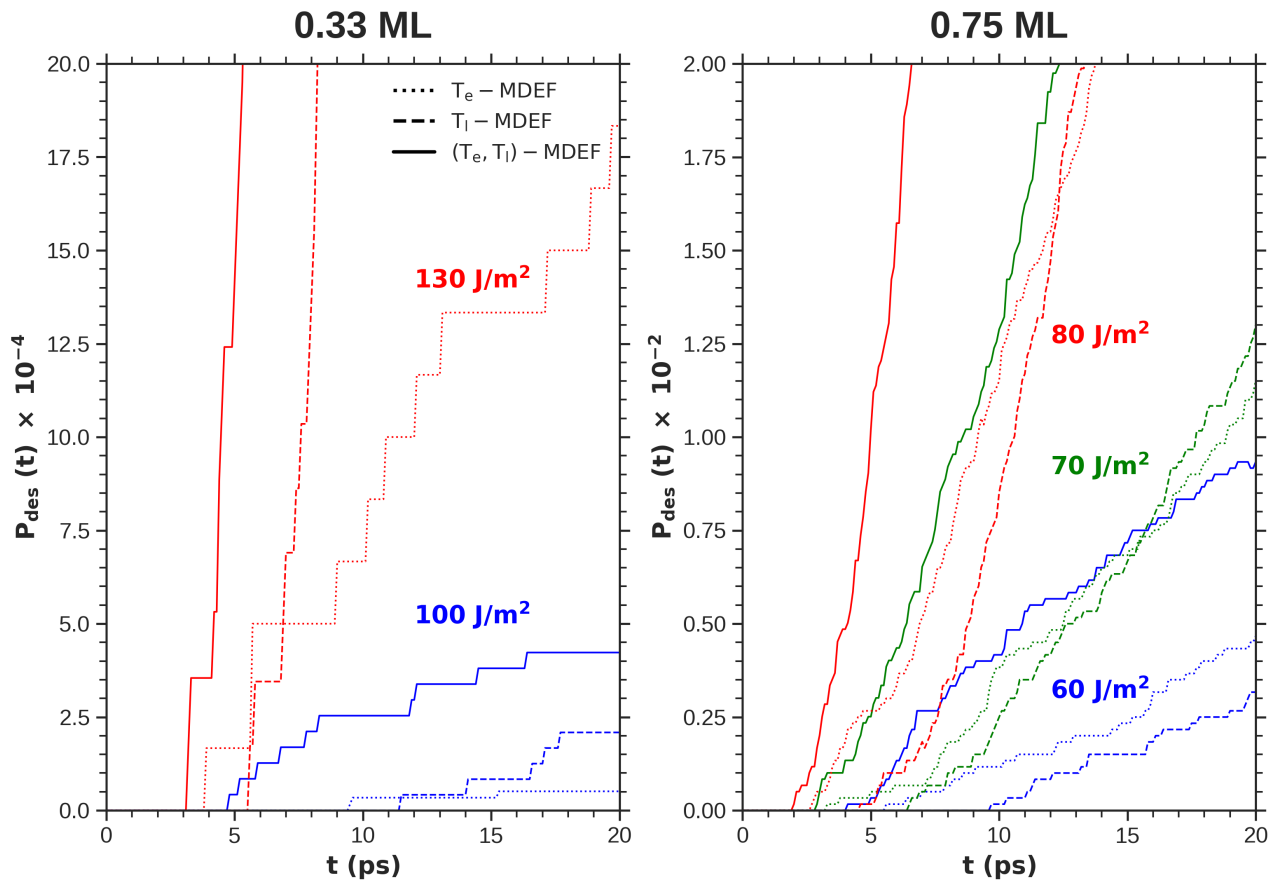


**Figure 7.15:** Close-up of the time evolution of the average CO desorption probability  $P_{des}(t)$  (Fig. 7.14) along the early stage of photodesorption process ranging the initial 20 ps.  $(T_e, T_l) - MDEF$ ,  $T_e - MDEF$  and  $T_l - MDEF$  results are plotted in full, dotted, and dashed lines, respectively. Left: MDEF results for the 0.33 ML adlayer and fluences  $100 \text{ J/m}^2$  (blue), and  $130 \text{ J/m}^2$  (red). Right: MDEF results obtained for the 0.75 ML adlayer and fluences  $60 \text{ J/m}^2$  (blue),  $70 \text{ J/m}^2$  (green), and  $80 \text{ J/m}^2$  (red).

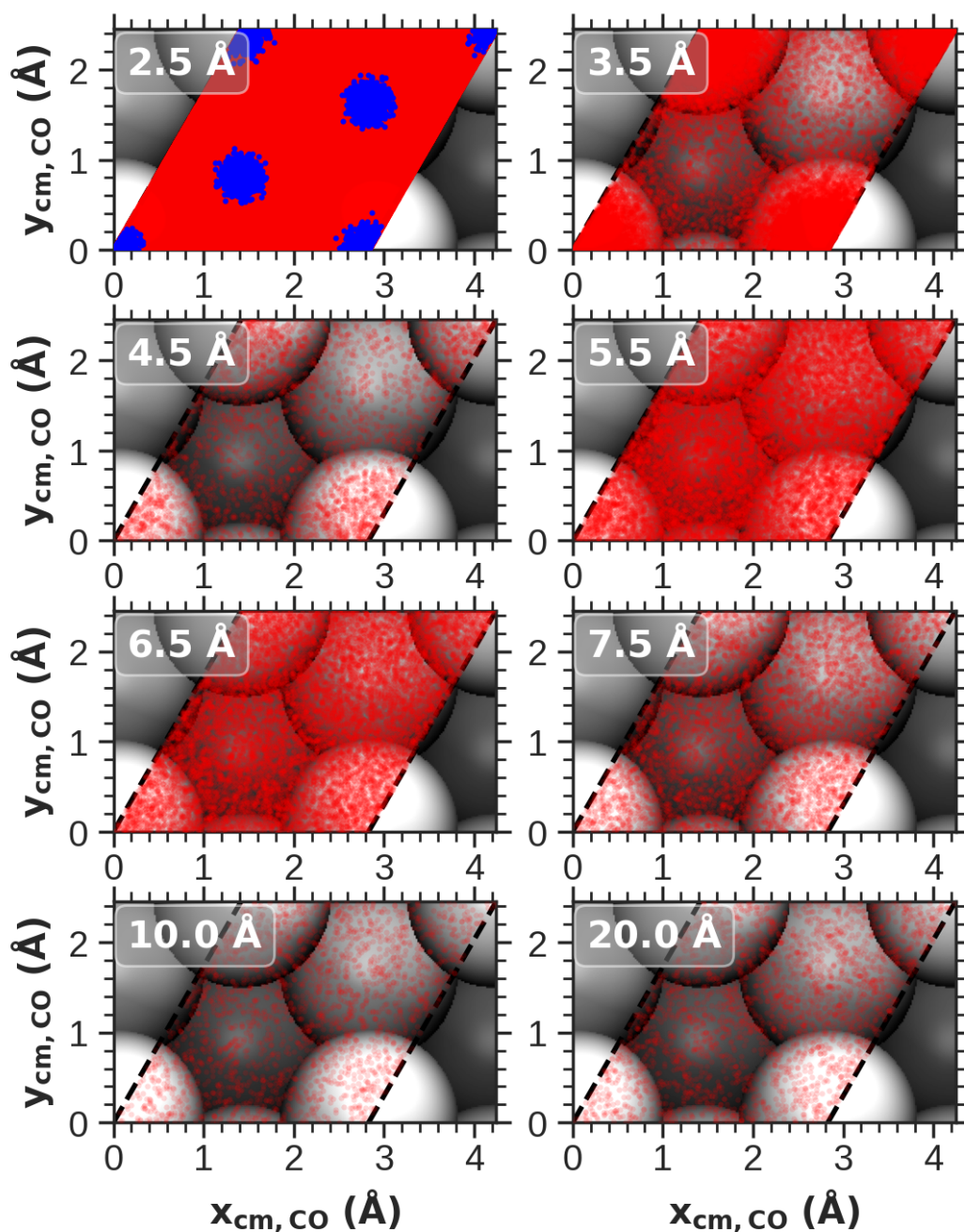


**Figure 7.16:** Distribution of the CO CM coordinates for the CO/Pd(111) system over the Pd surface for all dynamics times and different ranges of heights, centered at the values  $z_{\text{cen}}$  written in the top left part of each subplot, and measured from the Pd topmost layer. For each panel, CO positions are contained within the intervals  $[z_{\text{cen}} - 0.5, z_{\text{cen}} + 0.5]$  Å. Current results correspond to an incident laser fluence  $F = 80 \text{ J/m}^2$  and an adlayer of 0.75 ML.

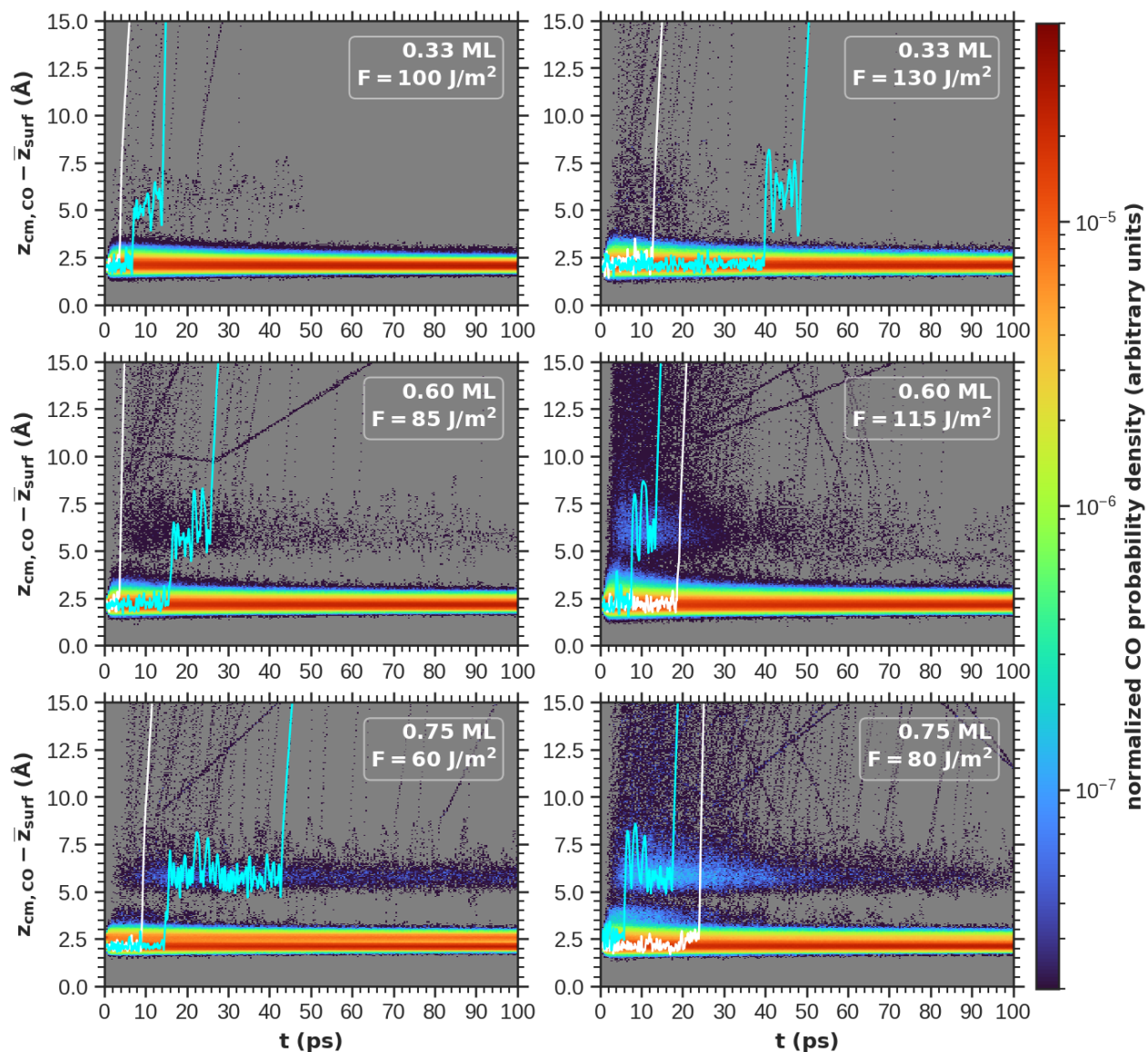


**Figure 7.17:** Probability density map of CO CM height,  $z_{\text{cm,CO}}$ , computed from the topmost Pd layer,  $\bar{z}_{\text{surf}}$ , as a function of time. From top to bottom, results are shown in increasing coverage order: 0.33 ML (top), 0.60 ML (middle), and 0.75 ML (bottom). From left to right, results are sorted in increasing incident laser fluence, which varies between coverages:  $100 \text{ J/m}^2$  (top left),  $130 \text{ J/m}^2$  (top right),  $85 \text{ J/m}^2$  (middle left),  $115 \text{ J/m}^2$  (middle right),  $60 \text{ J/m}^2$  (bottom left), and  $80 \text{ J/m}^2$  (bottom right). White and cyan full lines mark examples of direct CO desorption and desorption after transient trapping, respectively.

An example of this is shown in Fig. 7.16 for 0.75 ML adlayer and  $F=80 \text{ J/m}^2$ . Here, the CM  $x$  and  $y$  coordinates of all CO molecules present in all the simulated trajectories,  $x_{\text{cm,CO}}$  and  $y_{\text{cm,CO}}$ , have been plotted for all simulation times after laser irradiation and different heights  $(z_{\text{cm,CO}} - \bar{z}_{\text{surf}}) \pm \delta z_{\text{cm,CO}}$ . In the latter expression, the CO heights are taken with respect to the average of the surface topmost Pd atom  $z$  coordinates,  $\bar{z}_{\text{surf}}$ . As represented in particular at a distance  $2.5 \pm 0.5 \text{ \AA}$ , CO positions  $(x_{\text{cm,CO}}, y_{\text{cm,CO}})$  are initially well found at the top, hcp and fcc points (blue dots) and after excitation they spread uniformly along the  $xy$  plane and fill the entire region of study (red points). This highlights how mobile CO becomes in this photoexcitation context. Interestingly, Fig. 7.16 also shows how part of the excited CO becomes trapped in the physisorption wells. This has been further analyzed in Fig. 7.17 for 0.33, 0.60 and 0.75 ML at the smaller and larger fluence of the interval for each adlayer. Here we show the normalized probability distributions for finding CO CMs at any height  $z_{\text{cm,CO}} - \bar{z}_{\text{surf}}$ . From the graph, we see that CO may desorb either directly or after remaining trapped for several picoseconds before completing desorption, as indicated for some arbitrary CO desorbates in white and cyan lines, respectively. For all combinations of adlayer and fluence, the trapping region is located at distances  $(z_{\text{cm,CO}} - \bar{z}_{\text{surf}}) \in [5.0, 7.5] \text{ \AA}$ , or, equivalently, at a distance of  $(z_{\text{cm,CO}} - \bar{z}_{\text{cm,CO,ads}}) \in [2.5, 5.0] \text{ \AA}$  from the plane formed by the mean CM positions of CO adsorbates in the adlayer,  $\bar{z}_{\text{cm,CO,ads}}$ . Another aspect is that such a trapping mechanism is more preponderant the larger the coverage is, this hinting at the possibility that CO-CO van der Waals interactions may be causing such phenomenology.

Additionally, we can study the distribution of angles subtended by the desorbing CO molecules with respect to the axis normal to the surface for different coverage and fluence combinations. For each coverage, we consider the lowest and highest fluences for which we have performed  $(T_e, T_1) - \text{MDEF}$  simulations. The results have been represented in Fig. 7.18. The rather broad distributions obtained for the molecules that follow direct desorption (green bars) remark the complexity of the desorption process that does not follow the minimum energy paths in which the CO simply desorbs along the surface normal. Equally, transiently trapped molecules are characterized by broader polar angle distributions (red bars), as expected. Notice that for each individual plot, the joint distributions of both direct and transiently trapped desorbed CO are represented in blue bars.

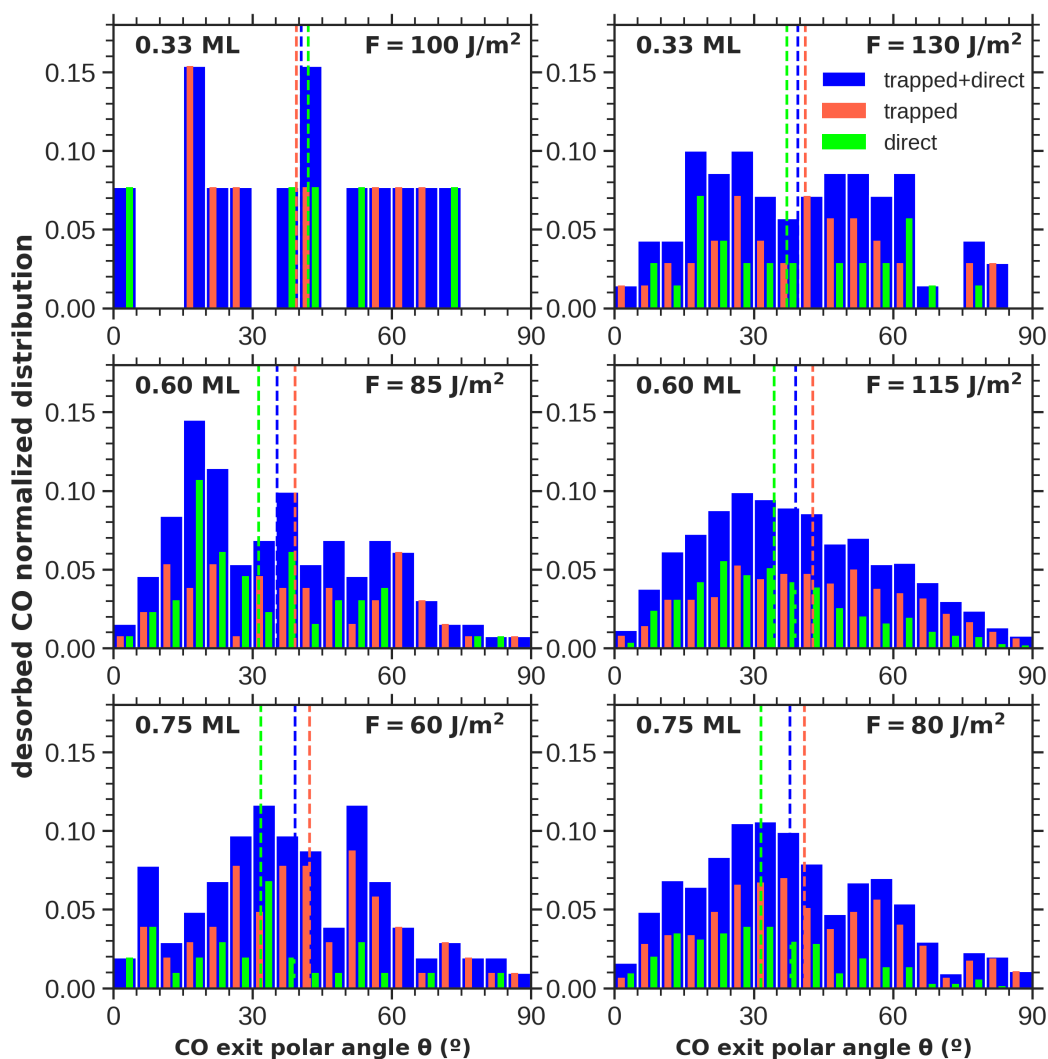


**Figure 7.18:** Polar angle distributions of the desorbing CO calculated for the combination of coverage and laser fluence indicated on top of each plot (blue histograms). For each graph, the angular distribution of the molecules that desorb directly (green) and after being transiently trapped in the physisorption region (red) are depicted separately. Dashed lines mark the mean polar angle for each distribution, where the same color code is utilized.

## 7.4 Simulations of two-pulse correlation experiments of CO desorption from Pd(111) at different coverages

Now, let us turn our attention to the 2PC experiments on adsorbate-decorated surfaces. Although some remarks on femtosecond laser pump-probe spectroscopy were previously given in Section 3.1, let us briefly recall its basics. This experimental technique consists of irradiating an adsorbate-substrate complex with two short laser pulses. The first one, the pump pulse, is used to excite the system and to initiate its dynamical processes that one wants to study. Some time after excitation, a second pulse or probe also irradiates the system to measure how its dynamical properties vary over time. This experimental technique has been used to analyze different adsorbate/surface systems such as NO/Pd(111) [34], CO/Ru(0001) [36], CO/Ru(001) [92], H/Ru(0001) and D/Ru(0001) [37], O<sub>2</sub>/Pd(111) [38] or CO/Pd(111) [30].

In 2PC experiments, both laser pulses have fixed fluences and energies. The time delay between both pulses is then tuned and the yield of the reaction undergone by the adsorbed species is then determined in terms of different delay times [32]. Using this technique, one is able to resolve short time scales of dynamics from an experimental side, so that particularly subpicosecond time ranges may be explored explicitly and hence photoinduced surface reactions such as desorption can be tracked. The time resolution reached depends on the duration of the laser pulses. As a result, 2PC experiments can also clarify how the transfer of energy from the surface to the adsorbed species occurs and, in particular, which subsystem (electronic or phononic) dominates the reaction mechanism. This latter circumstance is reflected in the shape of the 2PC desorption probability curve as a function of the time delay. More precisely, the process is considered to be electron-driven if the 2PC desorption probability curve exhibits a narrow peak centered on zero delay, with FWHMs of the order of  $\sim 1$  ps or less. The reason is that such narrow peaks indicate an energy transfer from the substrate to the adsorbates faster than the electron-phonon thermalization time scale after laser action, and only electrons can react in subpicosecond time scales to the pulses. In other words, hot electrons couple to the adsorbates and induce the subsequent chemical process on the adsorbed species before transferring their energy gains to the lattice. The combined action of both pulses significantly increases the electronic temperature. On the contrary, wider 2PC desorption probability profiles have an ambiguous meaning [30, 32]. FWHMs longer than a few picoseconds, and therefore longer than the electron-phonon thermal equilibration time, may hint at a phonon-driven process with a

strong phonon-adsorbate coupling. Consequently, phonons require long time scales to collect energy from hot electrons and to couple to adsorbate DOFs. However, these wider FWHMs may also be compatible with electron-dominated reactions, in scenarios of weak coupling of electrons to adsorbates and no phonon-driven energy input into the DOFs of the adsorbates. Therefore, in the latter case, further information is needed in order to clarify the reaction-driving mechanism. This further information can be gained from the examination of other experimental characteristics or from theoretical modeling.

It is interesting to note one particular fact of the 2PC desorption probability curve versus the time delay for scenarios where hot phonons are observed to contribute to the excitation of the adsorbate. In these situations, the 2PC desorption probability curve presents a dip around zero delay [92]. It is a consequence of the 2TM linked to the competition between thermal diffusion of hot electrons and electron-phonon coupling [32]. To clarify this point, recall the heat diffusion equation for the electronic bath in 2TM, Eq. (3.1). As we discussed in Section 3.2.1, electrons diffuse heat towards the bulk proportionally to the electronic thermal conductivity  $\kappa_e$ ,  $\nabla_z[\kappa_e(T_e)\nabla_z T_e]$ , and to the lattice through the electron-phonon coupling constant as  $-g(T_e - T_l)$ . For delays close to or equal to zero, the second pulse increases  $T_e$  before the hot electrons have thermally equilibrated with the lattice. Due to the nonlinear behavior with  $T_e$  of the diffusion term, heat diffusion into the bulk dominates over electron-phonon coupling at high  $T_e$ . Consequently, the energy transfer to the surface lattice atoms is briefly reduced, this being reflected in a reduction of  $T_{ph}$  when  $T_e$  peaks, which has as a consequence the aforementioned dip in the desorption probability curve at zero delay.

Now, let us focus on the results obtained in 2PC experiments on the desorption of CO from Pd(111) as reported in Ref. [30]. Fluences of incident pulses were chosen differently for each coverage in order to obtain similar desorption probabilities for delay zero for the three investigated coverages (0.24, 0.64 and 0.75 ML). Furthermore, in the three cases the stronger, p-polarized pulse was chosen to have a fluence 2.4 times higher than the weaker, s-polarized one. Time delays were considered positive when the strong pulse arrived later than the weak pulse and negative otherwise. 2PC desorption probability curves showed different half widths at half maximum (HWHMs) depending on the coverage. Regarding the numerical values, only the HWHM at negative delays for 0.24 ML (1.1 ps) may be consistent with electron-dominated desorption. In contrast, the remaining HWHMs for 0.24, 0.64 and 0.75 ML take values between 6.7 and 25.5 ps. Therefore, experiments do not clarify whether the electrons or phonons dominate the process.

On this basis, let us recall that single pulse ( $T_e, T_l$ ) – AIMDEF simulations in CO/Pd(111) support the collective effect of both hot electrons and phonons on

desorption [31]. Unfortunately, AIMDEF-based simulation of 2PC experiments was practically unaffordable due to the previously referred high computational expenses. However, now we are able to simulate 2PC in the  $(T_e, T_1)$  – MDEF framework. Calculations have been performed for both 0.33 and 0.75 ML coverages. For both coverages, simulations have been run for positive and negative time delays with absolute values equal to 0.0, 0.1, 0.3, 0.6, 1.0, 5.0 and 20.0 ps. The features of the laser pulse are the same as used for the aforementioned experiments [30]: for 0.33 ML, fluences for the strong and weak laser pulses are equal to 93 and 38 J/m<sup>2</sup>, respectively, while for 0.75 ML they are 51 and 21 J/m<sup>2</sup>. Consequently, at zero delay the total laser fluences are 131 and 72 J/m<sup>2</sup> for 0.33 and 0.75 ML, respectively. For each coverage, both pulses have equal wavelengths (780 nm), FWHMs of 130 fs and a sech<sup>2</sup> profile. For each time delay value, 2500 trajectories have been generated. For each of them, atomic positions and forces have been computed every 0.2 fs for a time span of 200 ps after excitation of the first laser pulse in order to obtain CO desorption probabilities converged with respect to time. In this way, large enough statistics are obtained for each time delay value. Besides, we need to be aware that some regions of the configurational space of CO/Pd(111) may be more poorly described by our PES, this leading to physically inconsistent results, such as reaching potential energy values  $E_0$  smaller than the equilibrium values at initial times. Such circumstances may become more likely to be found when we perform dynamics in conditions very different from those involved in the  $(T_e, T_1)$  – AIMDEF configurations used for training. For 0.75 ML, these odd-behaving trajectories were less than 0.25 % of the generated trajectories for each time delay value, while for 0.33 ML they were a 6.88 % in the worst case.

**Half widths at half maximum for different coverages**

	Coverage (ML)	$F^{\text{sum}}$ (J/m <sup>2</sup> )	$F^{\text{strong}}$ (J/m <sup>2</sup> )	$F^{\text{weak}}$ (J/m <sup>2</sup> )	HWHM <sup>-</sup> (ps)	HWHM <sup>+</sup> (ps)
<b>Exp</b>	0.24	131	93	38	1.1	10.4
<b>Th</b>	0.33				15.9	22.1
<b>Exp</b>	0.75	72	51	21	6.7	17.0
<b>Th</b>					14.7	35.6

**Table 7.7:** Fluences of the strong laser pulse,  $F^{\text{strong}}$ , weak laser pulse,  $F^{\text{weak}}$ , their sum,  $F^{\text{sum}}$ , and the half width at half maximum for negative (HWHM<sup>-</sup>) and positive (HWHM<sup>+</sup>) time delays obtained in the 2PC measurements of CO desorption from Pd(111) by Hong *et al.* [30] and in our  $(T_e, T_1)$  – MDEF simulations (Fig. 7.19)

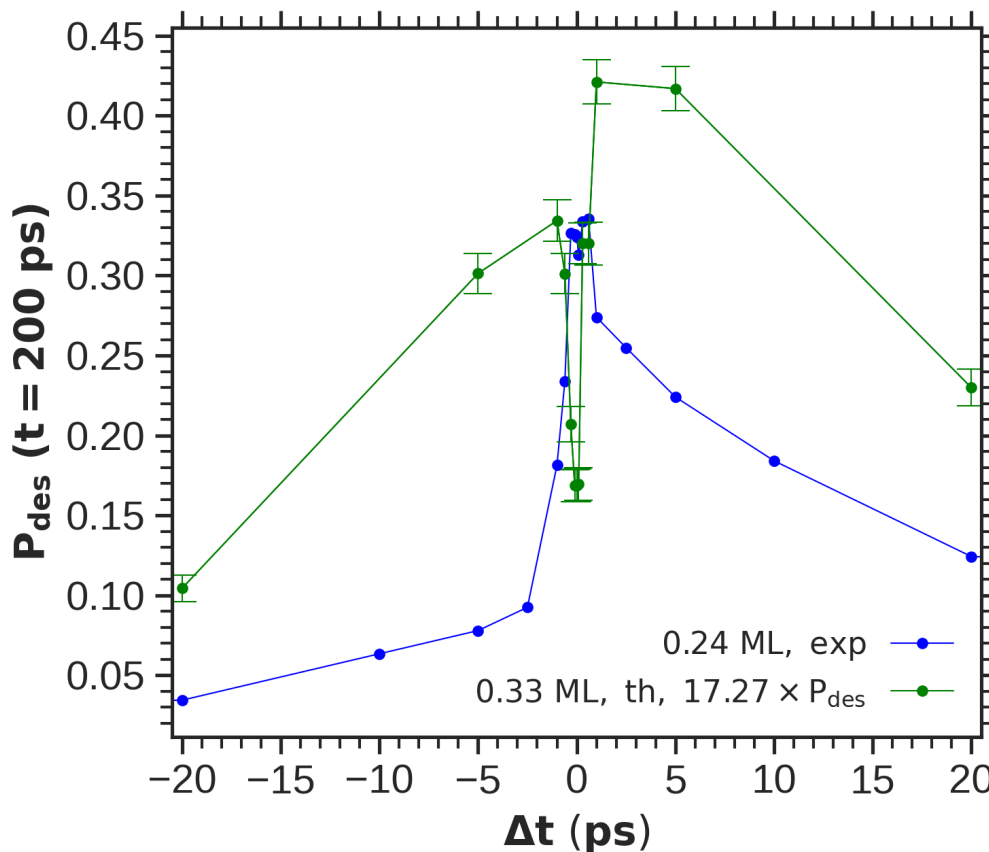


**Figure 7.19:** Two-pulse correlation measurements [30] (blue) and the results of  $(T_e, T_1)$  – MDEF simulations with the corresponding Wilson error bars (green) of the CO desorption probability against the time delay between the two pulses. The initial coverage is 0.24 ML in the experiments and 0.33 ML in the theoretical calculations. The theoretical probabilities are multiplied by 17.27, the average of the ratio  $P_{\text{des}}^{\text{exp}}(\Delta t)/P_{\text{des}}^{(T_e, T_1) - \text{MDEF}}(\Delta t)$ .

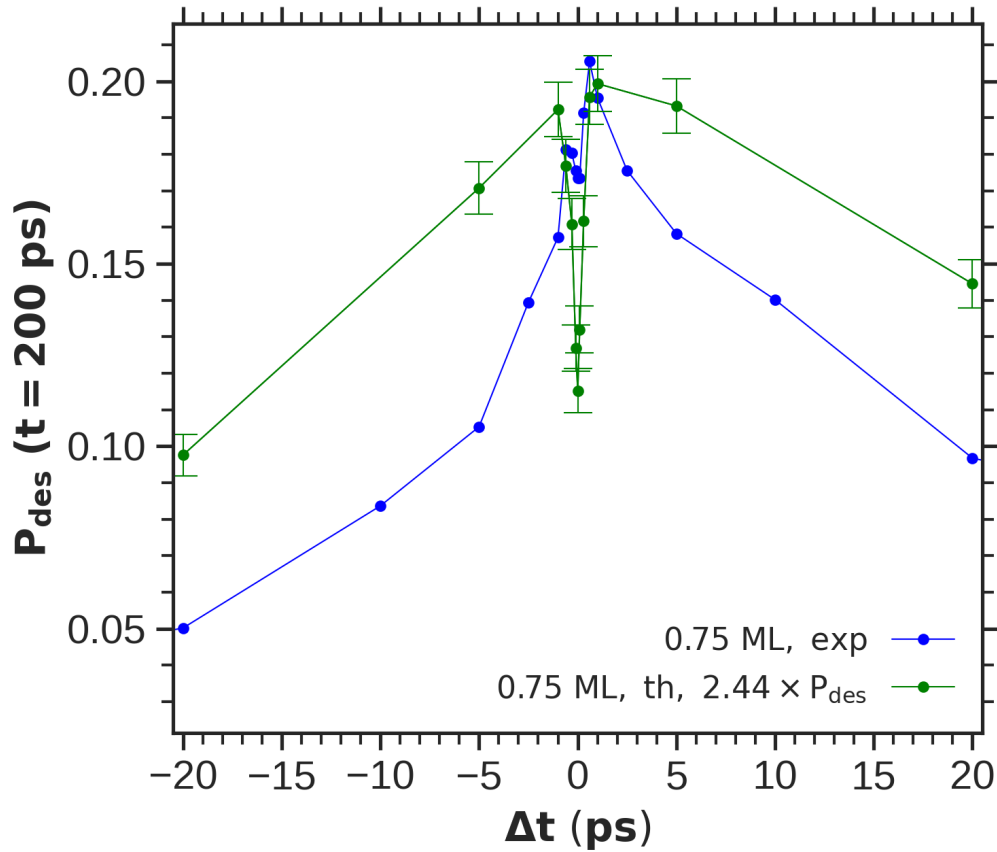


**Figure 7.20:** Two-pulse correlation measurements [30] (blue) and the results of  $(T_e, T_i)$  – MDEF simulations with the corresponding Wilson error bars (green) of the CO desorption probability against the time delay between the two pulses. The initial coverage is 0.75 ML. The theoretical probabilities are multiplied by 2.44, the average of the ratio  $P_{des}^{exp}(\Delta t)/P_{des}^{(T_e, T_i) - MDEF}(\Delta t)$ .

The desorption probability curves as a function of the time delay obtained from the  $(T_e, T_l)$  – MDEF simulations are depicted in green in Figs. 7.19 and 7.20 for 0.33 and 0.75 ML CO/Pd(111), respectively. In order to compare the results with the experiments on the same scale, we have multiplied the theoretical curves by the average of the ratio  $P_{\text{des}}^{\text{exp}}(\Delta t)/P_{\text{des}}^{(T_e, T_l) - \text{MDEF}}(\Delta t)$ . The values of these ratios are 2.44 and 17.27 for 0.75 and 0.33 ML coverages, respectively. As it was stated previously in Section 7.3, in the case of the high coverage, the quantitative difference between the theoretical and experimental desorption probabilities must be linked to the overestimation of the theoretical desorption energy. The much larger scaling factor required for the low coverage was also explained in Section 7.3. Namely, the experimental coverage (0.24 ML) is different from the theoretical one (0.33 ML), and at this coverage the desorption probability increases due to the presence at the surface of CO adsorbates, located at the edges of 0.33 ML islands, with a much lower desorption energy. From these curves, one can calculate the HWHM values for the  $(T_e, T_l)$  – MDEF simulations. The corresponding results are collected in Table 7.7. As a first remark, for both coverages, the theoretical HWHMs for both negative and positive delays,  $\text{HWHM}^-$ , and  $\text{HWHM}^+$ , have values larger than  $\sim 1$  ps, therefore being inconsistent with an scenario dominated by electronic excitations. According to our previous discussion, they agree either with a weak electron-adsorbate coupling in the absence of phonon coupling or with a strong phonon-adsorbate coupling along with electron-adsorbate coupling. Note that these results are consistent with those obtained in Section 7.3 in the case of a single pulse excitation. In that case, we found that both electronic and phononic excitations contribute efficiently to the CO desorption probability, but that in the majority of cases, when considered individually, the contribution of phononic excitations was more important, particularly for large laser fluences (see Figs. 7.14 and 7.15, and the accompanying discussion).

Moreover, we may obtain information from the maximum electronic and phononic temperatures reached in the  $(T_e, T_l)$  – MDEF simulations. With this aim, in Figs. 7.21 and 7.22 we plot the maximum electronic and phononic temperatures reached at each given time delay according to the 2TM model for 0.33 and 0.75 ML, respectively. For comparison, in these figures the desorption probability curves are also plotted. Interestingly, for both coverages the theoretical 2PC desorption probabilities present a higher resemblance to the maximum  $T_l$  curve than to the maximum  $T_e$  one, which constitutes an additional indication of the dominant role played by phononic excitations. Finally, it is worth mentioning that, as expected, both the calculated desorption probabilities and the maximum  $T_l$  values exhibit a dip in the

region around zero delay, which, as discussed above, is a characteristic of the 2TM model.

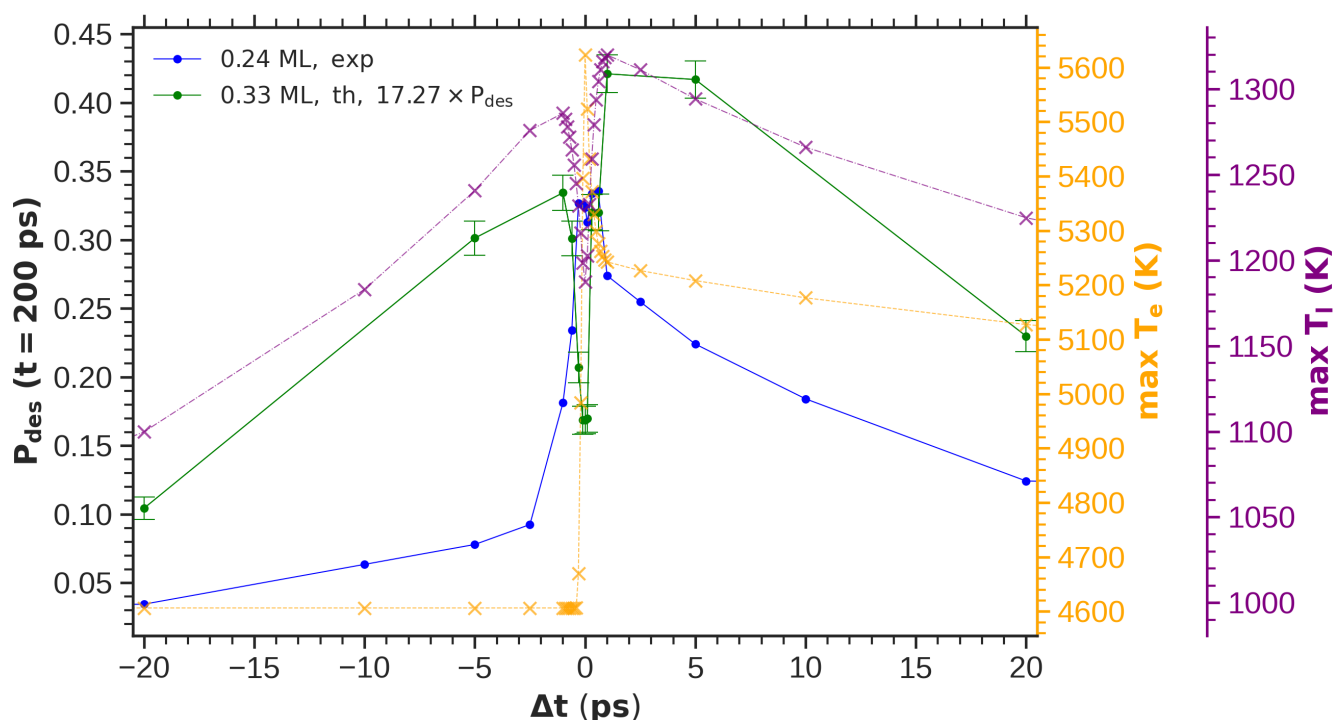


**Figure 7.21:** (Left y axis) Two-pulse correlation measurements [30] (blue) and the results of  $(T_e, T_l)$  – MDEF simulations with the corresponding Wilson error bars (green) of the CO desorption probability against the time delay between the two pulses. The theoretical probabilities are multiplied by 17.27, the average of the ratio  $P_{\text{des}}^{\text{exp}}(\Delta t)/P_{\text{des}}^{(T_e, T_l) - \text{MDEF}}(\Delta t)$ . (Right y axis) Maximum  $T_e$  (orange) and maximum  $T_l$  (violet) as obtained from the 2TM as a function of the time delay. The initial coverage is 0.24 ML in the experiments and 0.33 ML in the theoretical calculations.

At this point, let us compare our results with the experimental measurements of 2PC yield. Although the theoretical HWHMs are consistently wider than the experimental ones, semiquantitative agreement can be invoked in all cases except for the value of  $\text{HWHM}^-$  at low coverage. With this notable exception, both the measured and calculated HWHMs are consistent with a phonon-dominated scenario, with the theoretical HWHMs around a factor two larger than the experimental ones. Moreover, the large asymmetry of the experimental curves is qualitatively reproduced. More precisely, in agreement with the measurements,

the theoretical  $\text{HWHM}^+$ s are wider than the  $\text{HWHM}^-$ s. As noted above, the main shortcoming of the theoretical results constitutes their inability to reproduce an electron-dominated scenario ( $\text{HWHM}^-$  around 1.1 ps) at low coverage and negative delay (when the strong pulse arrives before the weak pulse). As in previous cases, this disagreement may be related to the different adsorption characteristics of the experimental (0.24 ML) and theoretical coverages (0.33 ML) discussed above.

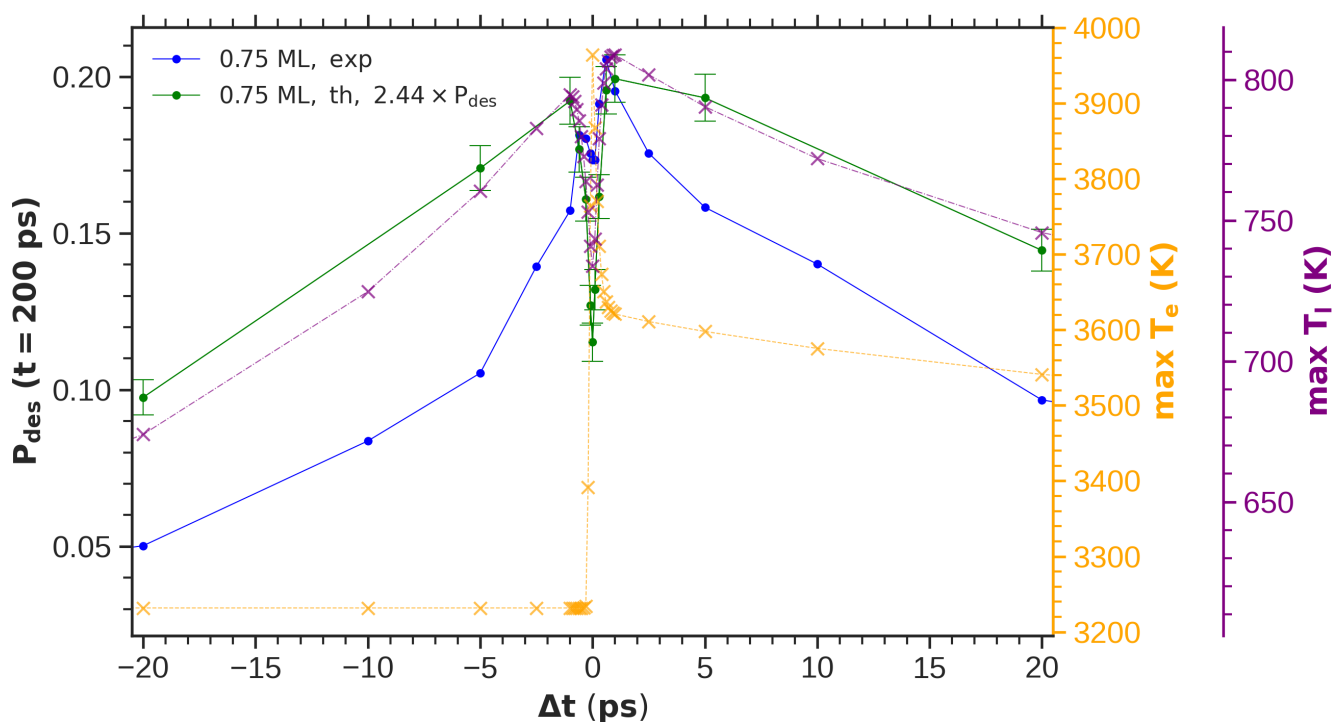


**Figure 7.22:** (Left y axis) Two-pulse correlation measurements [30] (blue) and the results of  $(T_e, T_l)$  – MDEF simulations with the corresponding Wilson error bars (green) of the CO desorption probability against the time delay between the two pulses. The theoretical probabilities are multiplied by 2.44, the average of the ratio  $P_{\text{des}}^{\text{exp}}(\Delta t)/P_{\text{des}}^{(T_e, T_l) - \text{MDEF}}(\Delta t)$ . (Right y axis) Maximum  $T_e$  (orange) and maximum  $T_l$  (violet) as obtained from the 2TM as a function of the time delay. The initial coverage is 0.75 ML.

Finally, it is worth mentioning the apparent differences obtained between theory and experiments in the region of small time delays  $< \sim |1|$  ps. More precisely, we observe that the theory overestimates the dips at around zero delay of the experimental desorption probability curves. Similar disagreements between theory and experiment have also been reported in the photoinduced CO desorption from

Ru(0001) [92] and in the recombinative desorption of H and D from Ru(0001) [37]. As discussed above, the theoretical dips are a characteristic of the 2TM. In this respect, it should be stated that although 2TM successfully describes the behavior of a photoexcited surface, it is still an approximate model that may miss some subtle effects.

## 7.5 Conclusions

In this chapter, we have made a more comprehensive usage of the capabilities of  $(T_e, T_1)$  – MDEF methodology in order to theoretically study the femtosecond laser-induced desorption of CO from a Pd(111) surface with an unprecedented level of depth. As a preliminary step, we have investigated the performance of our preliminary 0.75 ML CO/Pd(111) EANN PES when describing a coverage different from that handled in its training set, namely 0.33 ML. For this, we have predicted the minimum energy paths for desorption from the adsorption sites of both 0.33 and 0.75 ML adlayers and we have compared them to those obtained with  $(T_e, T_1)$  – AIMDEF. In addition, the same test has been run in both coverages after training a new CO/Pd(111) EANN PES using previously obtained 0.33 ML  $(T_e, T_1)$  – AIMDEF configurations [31]. Our analysis has demonstrated that the 0.75 ML EANN PES describes the desorption energy curves on both 0.33 and 0.75 ML adlayers more accurately than its 0.33 ML counterpart. This occurs because 0.75 ML training set encompasses a wider variety of atomic environments and desorption events, thus providing a superior predictive ability for simpler environments and reaction dynamics such as those 0.33 ML. From these preliminary tests, we have concluded that incorporating information about both adlayers to a new EANN PES can allow us to perform reliable MDEF calculations across coverage scenarios beyond 0.33 and 0.75 ML.

After these tests, we have subsequently trained a multicoverage EANN PES using 37 972 configurations corresponding to  $(T_e, T_1)$  – AIMDEF and  $T_e$  – AIMDEF trajectories for both 0.33 and 0.75 ML. Here, the energies of the 0.33 ML training data points have been subtracted by some offset value previously determined by 0.75 ML EANN PES when predicting energies of 0.33 ML configurations. Next, we have verified the outstanding quality of this multicoverage PES. Its quality has been evaluated against 485 767 data points missing from its training set and taken from 0.33 and 0.75 ML  $T_e$  – AIMDEF and  $(T_e, T_1)$  – AIMDEF trajectories. Both energies and adiabatic forces on moving atoms are predicted by this PES with remarkable accuracy, at a level comparable to the previous single coverage EANN PESs or even better. Next, it provides both site-dependent desorption energies and

minimum energy paths for desorption very close to DFT+vdW-DF results, although no minimum energy path configurations were provided during its training. More strikingly, it has successfully yielded very accurate predictions of an intermediate, 0.60 ML coverage absent from its training knowledge. In this respect, it can predict energies and forces of 1446 configurations randomly chosen across three different single pulse fluences with a similar level of accuracy as for the other two coverages, as well as its site-dependent desorption energies. But, more surprisingly, it has been able to predict the DFT equilibrium structure for this coverage. Hence, our multi-coverage EANN PES has demonstrated its transferability by effectively handling coverages not explored during its training, thereby validating its robustness for studies involving, for instance, different coverages, laser fluences or pump-probe delays for 2PC experiments.

Our next natural step has involved conducting sets of between 6750 and 60 000 MDEF simulations to investigate single laser pulse photoinduced CO desorption on Pd(111) over an integration time of 100 ps after the pulse reaches the surface. More precisely, we have studied the fluence dependence of the desorption yield for the three adlayers. We have fitted our results to compute the nonlinear exponents characterizing DIMET regime, and our values compare well with previous experimental results on 0.24, 0.64 and 0.75 ML [30]. Our results capture the strong dependence between desorption probability and adlayer coverage, including the particularly remarkable increase in the desorption probability when going from intermediate to high CO coverages. Such a trend is consistent with the decrease in the average of the site-specific desorption energies for each coverage as the latter increases. Besides, the effect of the supercell size on the desorption yield is investigated, revealing a progressive convergence of the yield to a maximum value at a given fluence as the simulation cell size increases. Complementarily, we have gained further insights into the role of surface electronic and phononic subsystems in CO photodesorption. To this end, we have calculated  $T_e$  – MDEF and  $T_l$  – MDEF trajectories where only hot electrons or phonons, respectively, were allowed to couple the CO adsorbates for different combinations of fluence and adlayer. Our calculations demonstrate that the synergy of both electronic and phononic channels leads to larger desorption yields than each of them by separate along at least 100 ps after laser irradiation, thus extending the scope of this conclusion reported in a previous  $(T_e, T_l)$  – AIMDEF work [31]. Also, comparing each of the two channels, the electronic one dominates during the initial picoseconds after laser irradiation, this shifting to a phonon-mediated predominance afterwards that becomes more pronounced the larger the laser fluence is. Next, we have tried to unveil additional details on CO dynamical features after laser irradiation for all coverages and different fluences by analyzing the CO CM positions at different

distances from the topmost surface layer. During photodesorption, we have seen how mobile the molecules become along the surface, and how the majority of desorbed ones complete this process directly, while another fraction remains trapped in physisorption wells for some picoseconds before completing this reaction. Trapping may be influenced by CO-CO attractive van der Waals forces, as the fraction of CO desorbed after residing in the physisorption well grows for higher coverages. For both fractions of CO desorbates, we have checked how their desorption polar angle distributions are very wide instead of peaking along some preferred vertical directions, this further underlining the complexity of the chemical process they undergo.

Finally, we have simulated 2PC experiments on the CO/Pd(111) system by generating  $(T_e, T_l)$  – MDEF trajectories for a fixed combination of adlayer coverage (0.33 and 0.75 ML) and laser fluences, and different pump-probe time delay values, following the settings of previous experiments [30]. Then, we have calculated the dependence of the CO desorption probability on this relative time delay. The scale of the calculated HWHMs –of tens of picoseconds– is consistent with our previous findings on both electrons and phonons driving the CO desorption process. That order of magnitude, together with the shape of the 2PC yield, clearly aligns with our remarks about the importance of the lattice-driven excitations. Comparison with experiments shows semiquantitative agreement for both low and high coverages except at low coverage and negative delay (strong laser pulse arriving before the weak laser pulse). In this case, the experiments suggest an electronically driven process, whereas the simulations are consistent with a phonon-driven process. The discrepancy may be related to the different coverage in experiments and theory (0.24 vs 0.33 ML). We have also observed that for time delays of  $\pm 1$  ps or less, the theoretically obtained dip in the desorption probability curve is much smaller in the experiments, which could be due to limitations of the 2TM.

Overall, we have conducted a theoretical study on the femtosecond laser-induced desorption of CO from Pd(111) at a degree of comprehensiveness previously unavailable by precedent theoretical models, particularly  $(T_e, T_l)$  – AIMDEF among them. We have explored the intricacies of this chemical process by making use of the multicoverage EANN PES possibilities, hence demonstrating the performance of our  $(T_e, T_l)$  – MDEF methodology for CO/Pd(111) adsorbate-substrate complex. From our results follows the future application of  $(T_e, T_l)$  – MDEF not only to study CO photodesorption on Pd(111) varying other parameters of the process, but also to generalize its usage to investigate a number of chemical processes on other distinct adsorbate-substrate complexes. Following this goal, we may subsequently work on another system involving the same three atomic species as CO/Pd(111) for simplicity, in order to make use of the element-specific fittings we have used for,

e.g., atomic friction calculation. Moreover, this would open the path to comparison with the results detailed along this chapter. Hence, let us turn our attention to a somewhat different adsorbate-substrate complex, namely, O and CO coadsorbed on Pd(111) or O+2CO/Pd(111).

# 8

## Photoinduced desorption on O+2CO/Pd(111) stud- ied with $(T_e, T_l)$ -AIMDEF

---

In this chapter we perform  $(T_e, T_l)$  – AIMDEF simulations to study the CO desorption and CO oxidation induced in the O+2CO/Pd(111) system by femtosecond laser pulses. Additional simulations that only include the effect of the laser-excited electrons will allow us to determine the role of electrons and phonons in both processes, CO desorption and CO oxidation (i.e., the recombinative formation and desorption of CO<sub>2</sub>). The results of CO desorption will also be compared to those obtained in the 0.75 ML CO/Pd(111) system.

### 8.1 The O+2CO/Pd(111) system: computational settings

#### 8.1.1 Relaxation

The Pd(111) surface is considered to be covered with a mixed adlayer of 0.50 ML CO and 0.25 ML O. Following Ref. [362], adsorption sites on Pd are going to be the same as for CO/Pd(111) with 0.75 ML, that is, top, hcp, and fcc positions. As a first step, we start by optimizing the structure of the O+2CO/Pd(111) surface and confirming that in the mixed adlayer the O atoms occupy fcc sites, as suggested in Ref. [362].

In order to facilitate the comparison of the photodesorption simulations between the mixed O+2CO adlayer and the CO saturated adlayer, all DFT calculations and AIMDEF simulations are performed using the same computational settings that were used for 0.75 ML CO/Pd(111) [31]. In particular, we use VASP [341, 342] (versions 5.4 and 6.3) and the vdW-DF exchange-correlation functional proposed by Dion *et al.* [172]. The electron-core interaction is treated with the projector augmented-wave (PAW) method [363] implemented in VASP [364]. The PAW potentials for C, O, and Pd have four, six, and ten valence electrons, respectively. Electron wave functions are expanded in a plane-wave basis set with an energy cut-off of 400 eV. Integration in the Brillouin zone is done with a  $\Gamma$ -centered  $3 \times 6 \times 1$  Monkhorst-Pack grid of special  $\mathbf{k}$ -points [365, 366]. Fractional occupancies are determined through the Methfessel and Paxton broadening scheme of first order using a width of 0.1 eV [367]. The energy criterion for total energy self-consistency

is  $10^{-6}$  eV. The covered Pd(111) surface is described by a 4 layer-slab of Pd atoms and the overlayer that contains four CO molecules and two O atoms in the *large* ( $4 \times 2$ ) surface cell. The latter is selected to better describe the interadsorbate interactions, including out-of-phase movements of equivalent adsorbates. The overlayer is separated along the  $z$ -axis from the bottom of the periodic Pd-slab by about 8 layers of vacuum. The specific dimensions of the supercell in Cartesian coordinates and in Å are:  $\mathbf{a}_1 = (11.32, 0, 0)$ ,  $\mathbf{a}_2 = (2.83, 4.90, 0)$  and  $\mathbf{a}_3 = (0, 0, 27.73)$ .

Using these computational settings, the O+2CO/Pd(111) surface is relaxed until the forces on each atom of the overlayer and the two topmost Pd layers are smaller than  $10^{-2}$  eV/Å (the two Pd bottom layers are not relaxed to leave part of the surface as a rigid bulk). Table 8.1 summarizes the results of the relaxation for the following three possible adsorption site choices for O and CO: (i) O on top and CO on fcc and hcp, (ii) O on hcp and CO on top and fcc, and (iii) O on fcc and CO on hcp and top. In agreement with Ref. [362] the equilibrium configuration corresponds to O adsorbed on a fcc site, while CO molecules equally occupy top and hcp sites. This equilibrium configuration is pictured in Fig. 8.1.

<b>O+2CO/Pd(111), relaxation energies</b>	
<b>O and CO adsorption sites</b>	<b>Relaxation energy <math>E_0^{\text{ads-surf}}</math> (eV)</b>
O (top)+CO (fcc,hcp)	-92.199
O (hcp)+CO (top,fcc)	-93.814
O (fcc)+CO (hcp,top)	-94.113

**Table 8.1:** Energy of the optimized 0.75 ML O+2CO/Pd(111) surface calculated with VASP for different adsorption site arrangements of CO and O. Note that the energy that VASP provides is the system cohesive energy with respect to spherical non spin-polarized atoms. The minimum energy arrangement corresponds to placing the O atoms at fcc sites.

### 8.1.2 Thermalization

As in the case of the  $(T_e, T_l)$  – AIMDEFsimulations for 0.75 ML CO/Pd(111), the system is considered to be at  $T_0 = 90$  K before being irradiated with a femtosecond laser pulse with characteristics similar to those of Chapters 5 to 7.

Thermalization of the O+2CO/Pd(111) surface is done with our modified version of VASP that allows us running a canonical molecular dynamics simulation in which only the three topmost Pd layers are coupled to the NH thermostat, while

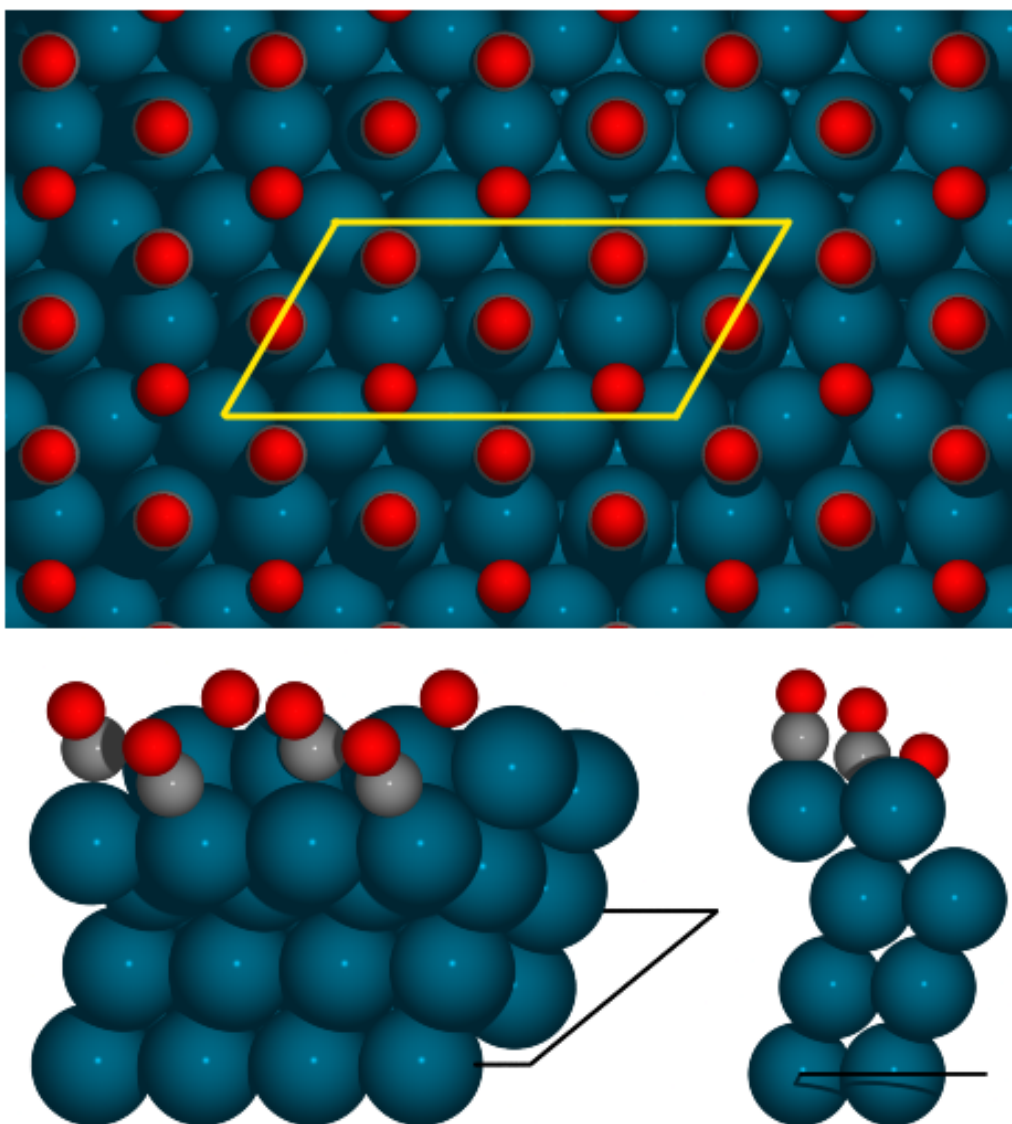


**Figure 8.1:** Top, perspective, and side views of the optimized O+2CO/Pd(111) surface. The 4×2 surface cell is depicted by the yellow parallelogram.

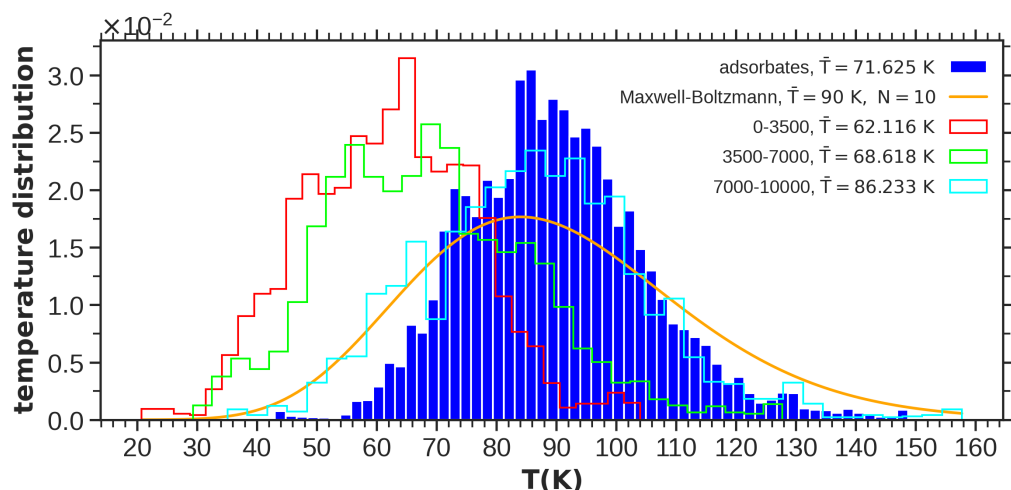


**Figure 8.2:** Normalized adsorbates temperature distributions for the configurations explored during thermalization. Histograms are plotted for the total configurational set (solid blue bars) and for selected subsets (empty bars) corresponding to time intervals [0,3.5] ps (red), [3.5,7.0] ps (green) and [7.0,10.0] ps (cyan). All histograms adjust approximately in shape to the theoretical Maxwell-Boltzmann distribution for  $T_0 = 90$  K and  $N_{\text{at}} = 10$  atoms (orange, solid line), but the nominal temperature is only reached during the last 3 ps.

adsorbates move following the adiabatic forces and the bottom Pd layer remains frozen (see Section 3.2.2.3 for more details). Thermostat mass is chosen to be  $Q \approx 664.05$  eV/s<sup>2</sup> [31]. A single thermalization trajectory is calculated that lasts 10 ps and uses a time integration step  $dt = 1$  fs. During this long simulation time, adsorbates, which are not connected to thermostats, will heat and approach the target temperature by exchanging energy with the surface layers coupled to the thermostat.

The quality of the thermalization run is confirmed by analyzing the distribution of the instantaneous temperature  $T_i(t)$  for each subset of atoms  $i$  in the system, which is defined from their corresponding total kinetic energy as

$$E_{K,i}(t) = \frac{3}{2} N_i k_B T_i(t), \quad (8.1)$$

where  $k_B$  is the Boltzmann constant,  $E_{K,i}(t)$  is the sum of the kinetic energies of all atoms in the subset  $i$  at instant  $t$ , and  $N_i$  is the number of atoms in the corresponding subset. Figures 8.2 and 8.3 show the instantaneous temperature distribution obtained for the adsorbates and nonfrozen surface Pd atoms, respectively. As adsorbates temperature is far from  $T_0 = 90$  K in the initial stage of the

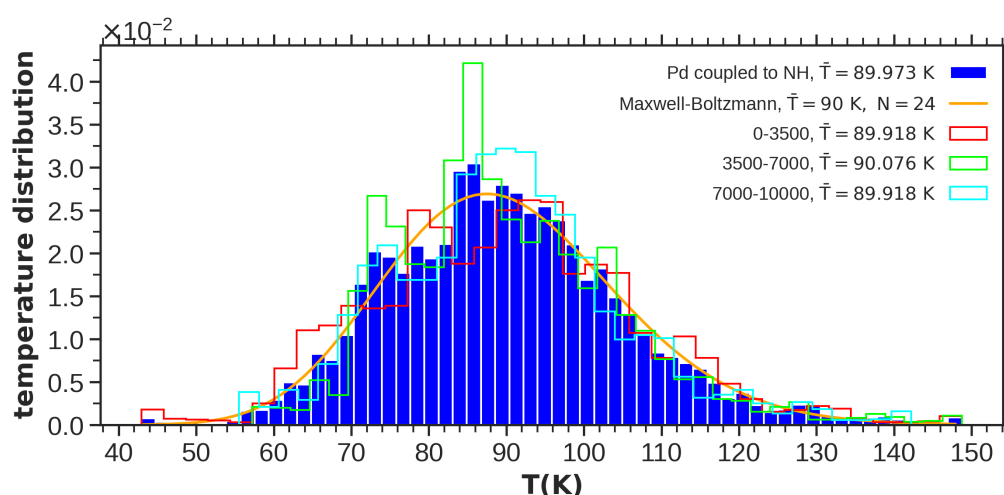


**Figure 8.3:** Normalized temperature distributions for the configurations explored during thermalization by the Pd atoms connected to the thermostat. Histograms are plotted for the total configurational set (solid blue bars) and for selected subsets (empty bars) corresponding to the time intervals [0,3.5] ps (red), [3.5,7.0] ps (green) and [7.0,10.0] ps (cyan). All histograms follow rather well the shape of the theoretical Maxwell-Boltzmann distribution for  $T_0 = 90$  K with  $N_{\text{at}} = 24$  atoms (orange, solid lines).

thermalization, discarding configurations from this initial time interval allows us to select a subset of configurations whose temperatures are closer to  $T_0$  than if the whole configurational set in [0.0,10.0] ps is taken. To this end, we have divided the 10 000 configurations into three subsets, the first two of 3500 and the remaining one of 3000 corresponding to the last 3 ps of thermalization. Figure 8.2 shows that the distribution of the adsorbates temperature in the last 3 ps is clearly closer to the theoretical Maxwell-Boltzmann distribution for  $T_0 = 90$  K than the distributions obtained for the previous intervals [0.0,3.5] ps and [3.5,7.0] ps. For surface Pd atoms (Fig. 8.3), the temperature distributions calculated for each time interval nicely follow the theoretical distribution, but the agreement is even better for the interval accounting for the last 3 ps. Consequently, the initial conditions for the AIMDEF simulations (i.e., initial positions and velocities of all the moving atoms) are selected from the instantaneous configurations proven during the last 3 ps of the thermalization run. In particular, a set of 100 configurations is randomly selected from a total of 3000 configurations.

## 8.2 $(T_e, T_l)$ – AIMDEF and $T_e$ – AIMDEF on O+2CO/Pd(111)

Photoinduced reactions on O+2CO/Pd(111) are simulated with  $(T_e, T_l)$  – AIMDEF for two absorbed laser fluences,  $F = 72$  and  $130 \text{ J/m}^2$ , assuming the same laser pulse employed in previous chapters, i.e., a pulse of sech shape centered at  $t = 0.4 \text{ ps}$ , wavelength equal to  $780 \text{ nm}$ , and FWHM equal to  $100 \text{ fs}$  that follows the settings of the experimental pulse used in Camillone’s group to study photoinduced reactions on  $\text{O}_2/\text{Pd}(111)$  [38, 356] and  $\text{CO}/\text{Pd}(111)$  [30], for instance. Its effect on the Pd surface is modeled with the time-dependent electronic  $T_e(t)$  and lattice  $T_l(t)$  temperatures shown in Fig.3.4 that were calculated with 2TM for a Pd substrate and the laser pulse described above. As detailed in Section 3.2.2.2, in the  $(T_e, T_l)$  – AIMDEF simulations, the effect of the laser-excited electrons in each adsorbate is described through a Langevin equation of motion, using in our case the LDFA and the Hirshfeld partitioning scheme to calculate at each integration step the corresponding electronic friction coefficient. In addition, the effect of the excited lattice is described by coupling the Pd surface atoms to a NH thermostat that follows the lattice temperature  $T_l(t)$ . In particular, the two topmost Pd layers were coupled to the thermostat, while the third one was left to evolve adiabatically and the bottom layer remained fixed. To investigate the role of electrons and phonons on the photoinduced reactions, we also carry out  $T_e$  – AIMDEF simulations that only include the effect of the hot electrons. This is done by solving the Langevin equation of motion for the adsorbates, while the surface atoms are kept fixed during the whole dynamics simulation.

All  $T_e$  – AIMDEF and  $(T_e, T_l)$  – AIMDEF simulations were performed using our modified version of VASP [31] using a time integration step of  $1 \text{ fs}$  and a final propagation time  $t_f = 4 \text{ ps}$  in each trajectory. The initial conditions for  $(T_e, T_l)$  – AIMDEF are the aforementioned 100 random configurations chosen after thermalizing the system to  $90 \text{ K}$ , while for  $T_e$  – AIMDEF each trajectory (100 in total) starts with the minimum energy configuration obtained after relaxation of O+2CO/Pd(111) with O atoms at fcc sites.

Inspection of the adsorbates heights along all the trajectories allows us to determine that at the end of our simulations the adsorbates may have remained adsorbed on the surface or have experienced one of the three following processes, namely, CO desorption, CO trapping, and  $\text{CO}_2$  desorption. A molecule is classified as desorbed if its CM height  $z_{\text{cm,CO}}$ , measured from the topmost Pd layer, is greater than  $9.0 \text{ \AA}$ . A molecule is considered trapped if its CM height verifies  $4.5 \text{ \AA} \leq z_{\text{cm,CO}}$  but without having reached at a later instant the distance that defines desorption.

As in previous chapters, the desorption probability of molecule  $A$  ( $A$  stands for CO or CO<sub>2</sub> in our case) at a certain instant  $t$  is evaluated as,

$$P_{A,\text{des}}(t) = \frac{N^{A,\text{des}}(t)}{N^{\text{CO,tot}}}, \quad (8.2)$$

where  $N^{A,\text{des}}(t)$  is the cumulative sum of  $A$  molecules desorbed up to instant  $t$  and  $N^{\text{CO,tot}}$  is the total number of CO molecules in the simulations (i.e.,  $N^{\text{CO,tot}} = n_0^{\text{CO,cell}} N_{\text{traj}}$ , with  $n_0^{\text{CO,cell}} = 4$  for O+2CO/Pd(111) and  $N_{\text{traj}}$  being the total number of trajectories in each type of simulation). As final desorption probabilities we take the values at the end of the simulations, i.e.,  $P_{A,\text{des}}(t_f)$ .

In our analysis, we are also interested in studying the dependence of the desorption probability on the adsorption site (top and hcp). Thus, we calculate the fraction of molecules desorbed from each specific site at  $t$  as,

$$\chi_{\text{CO,des}}^{\text{site}}(t) = \frac{N^{\text{CO,site}}(t)}{N^{\text{CO,des}}(t)}, \quad (8.3)$$

where  $N^{\text{CO,site}}(t)$  is the total amount of CO desorbed up to  $t$  from a given adsorption site.

### 8.2.1 Insights into adsorbate dynamics

In this Section, we analyze the adsorbate displacements and their dependence on the laser fluence. Figure 8.4 shows the adsorbate height as a function of time obtained in each set of simulations. Comparing the (T<sub>e</sub>, T<sub>l</sub>) – AIMDEF results at laser-absorbed fluences  $F = 72$  and  $130 \text{ J/m}^2$ , it is clear that all adsorbates become more excited, i.e., they experience larger displacements, at the largest laser fluence as expected. At both fluences, the kind of processes that occur are: (i) CO desorption, which starts at  $t \gtrsim 1.5$  (2.5) ps for  $F = 130$  (72)  $\text{J/m}^2$ , (ii) CO trapping, which refers to those molecules that momentarily leave the surface but without desorbing because they are attracted backwards to the surface at a later instant, (iii) absorption of part of the fcc O atoms, which dive inside the surface at heights lower than  $z_{\text{surf}}$ , and (iv) CO oxidation, i.e., recombination of one CO with one O atom to desorb as CO<sub>2</sub>. Interestingly, there is one single CO oxidation event at each laser fluence, but recombination starts at  $t \gtrsim 1.6$  ps for the largest fluence and more than 2 ps later for the smallest. Nonetheless, it is important to remark that the statistics of our (T<sub>e</sub>, T<sub>l</sub>) – AIMDEF simulations are very limited, making it difficult to draw general conclusions about this process. Except for CO oxidation, the other three

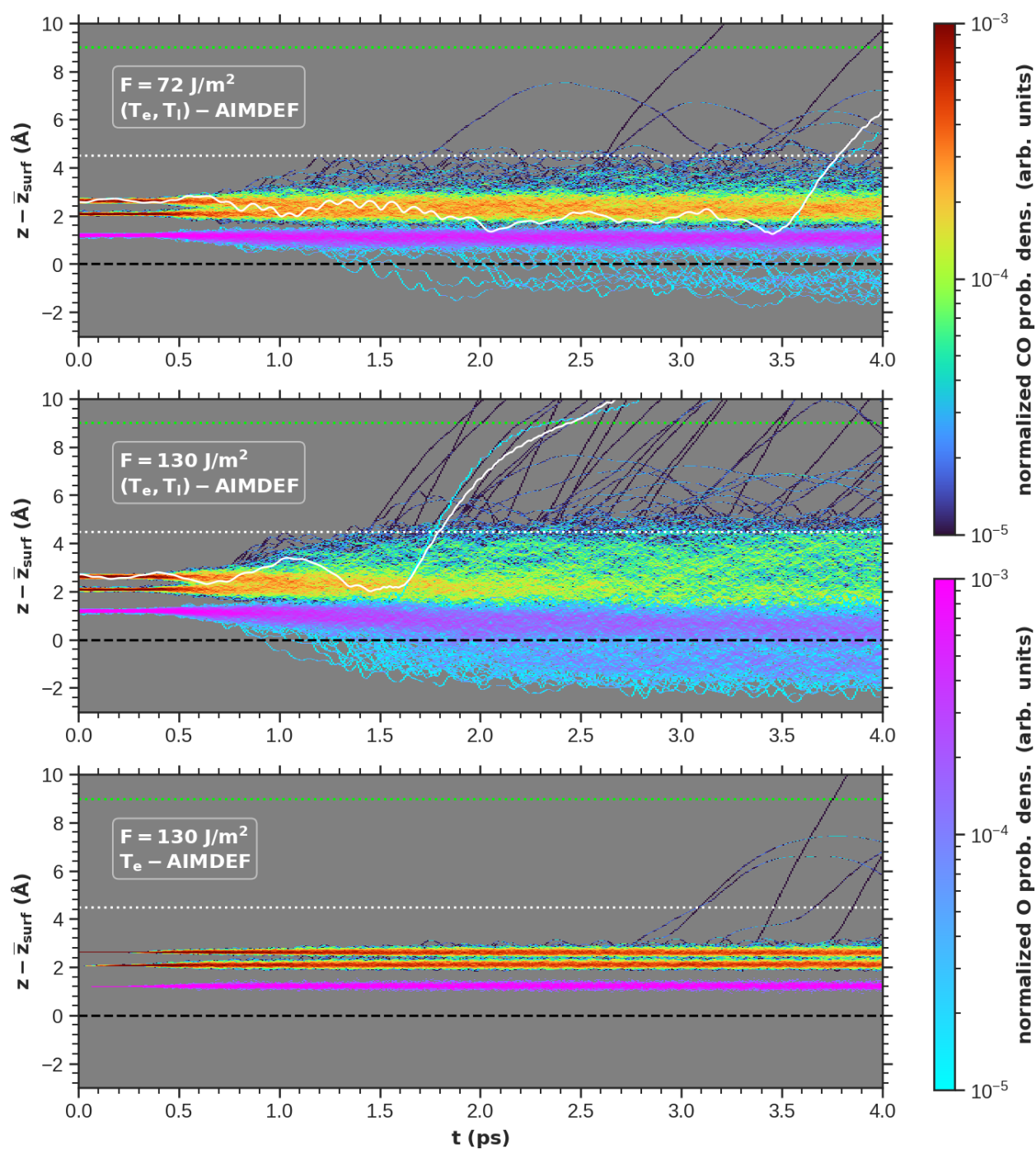


**Figure 8.4:** Probability density map of CO CM heights  $z_{\text{cm,CO}}$  and O heights  $z_{\text{O}}$  respect to the topmost Pd layer  $\bar{z}_{\text{surf}}$  (dashed black line) as a function of time. Different panels correspond to results obtained in  $(T_e, T_l)$  - AIMDEF with  $F = 72 \text{ J/m}^2$  (top),  $(T_e, T_l)$  - AIMDEF with  $F = 130 \text{ J/m}^2$  (middle), and  $T_e$  - AIMDEF with  $F = 130 \text{ J/m}^2$  (bottom). CO heights are shown in colors from dark blue to dark red, while the color palette for O ranges from cyan to pink. White full lines correspond to those CO molecules that undergo recombinitive oxidation with one fcc O atom. Trapping region is considered to be between the dotted white and light green lines, while CO surpassing the dotted green line is counted as desorbed.

processes are clearly more abundant when the system is irradiated with a laser fluence  $F = 130 \text{ J/m}^2$ .

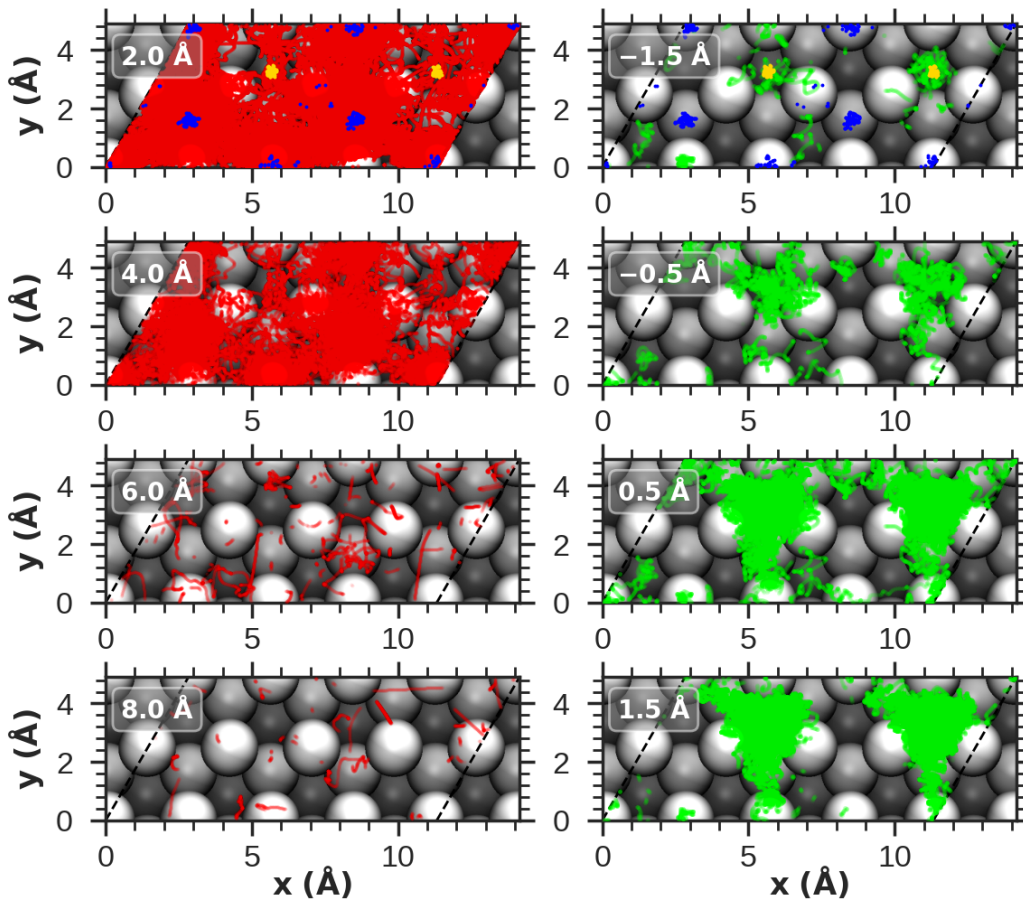


**Figure 8.5:** Density plots of the  $(x, y)$  coordinates of the CO CM (left column) and O adsorbates (right column) when reaching the height  $z_0 \pm \Delta z$  at any instant along the trajectory in the  $(T_e, T_l) - \text{AIMDEF}$  simulations at  $F = 72 \text{ J/m}^2$ . The  $z_0$  value is written in the top left part of each subplot, with  $\Delta z = 1$  and  $0.5 \text{ Å}$  for CO and O, respectively. For reference, topmost subplots in each column show initial CO and O positions as blue and yellow dots, respectively.

The importance of the electron-excited phonons in the  $\text{O}+2\text{CO}/\text{Pd}(111)$  system becomes evident when comparing the previous results to those obtained in the  $T_e - \text{AIMDEF}$  simulations for  $F = 130 \text{ J/m}^2$ . Except for the few CO that desorb, the height of the rest of adsorbates hardly varies in more than  $0.5 \text{ Å}$ . There is a reduction of CO trapping and complete absence of CO oxidation. Neither do we

observe O absorption, but this process is already forbidden in the  $T_e$  – AIMDEF simulations because the surface atoms are fixed and therefore it is not possible to determine the contribution of hot electrons and phonons in this case.

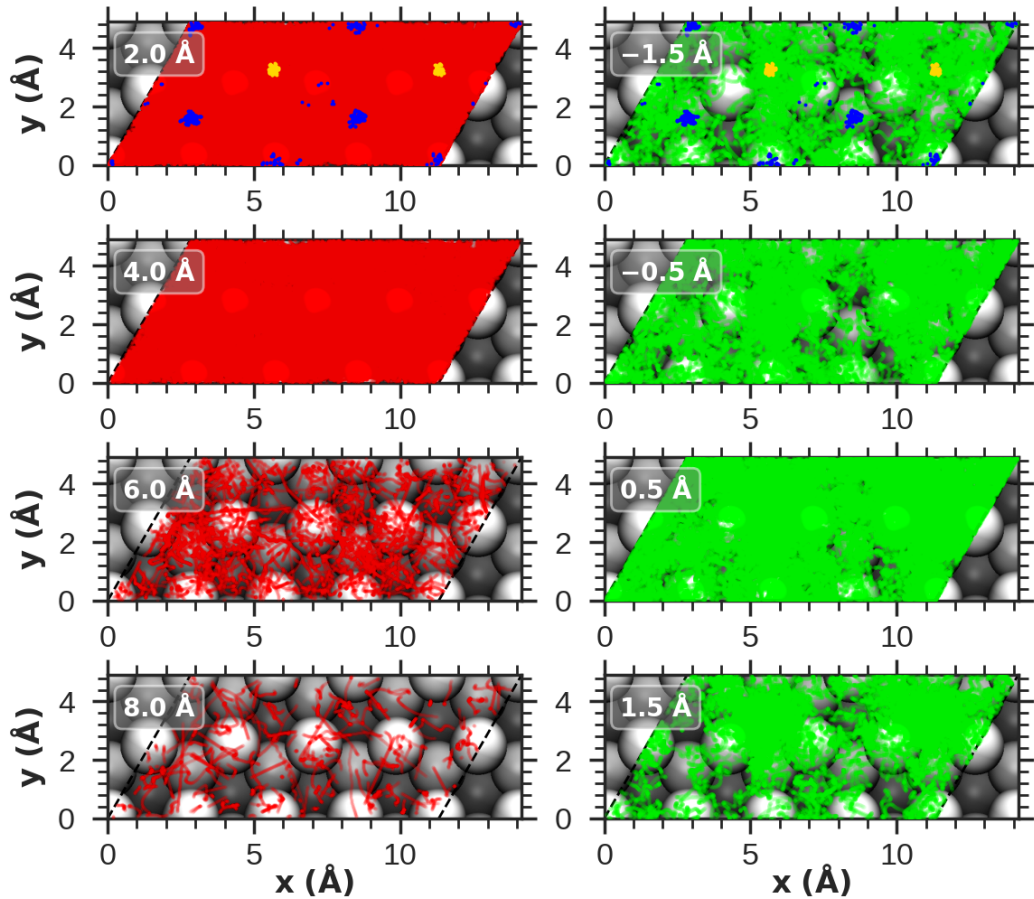


**Figure 8.6:** Same as Fig. 8.5 but for  $(T_e, T_l)$  – AIMDEF simulations at  $F = 130 \text{ J/m}^2$ .

Additionally, it is meaningful to investigate the adsorbate displacements over the surface plane. Figures 8.5 and 8.6 show the results obtained with  $(T_e, T_l)$  – AIMDEF for  $F = 72 \text{ J/m}^2$  and  $F = 130 \text{ J/m}^2$ , respectively. In each figure, initial CM positions  $(x_{\text{cm,CO}}, y_{\text{cm,CO}})$  of CO and  $(x_{\text{O}}, y_{\text{O}})$  of O are shown for reference purposes as blue and yellow dots, respectively. For the two considered laser fluences, adsorbed CO and O gain enough energy to diffuse beyond their adsorption sites. In particular, CO is less bound to the surface than O and can move over the whole  $xy$  plane, as clearly seen in the plots at  $z_0 = 2.0$  and  $4.0 \text{ Å}$  in both figures. At the high fluence,

also the O adsorbates move all over the surface (see plot at  $z_0 = 0.5 \text{ \AA}$  in Fig. 8.6) and even inside the surface in the case of the absorbed O (see plot at  $z_0 = -0.5 \text{ \AA}$  in the same figure). At low fluence, the O movement is localized within the interatomic space close to the fcc adsorption sites, as seen in Fig. 8.5.

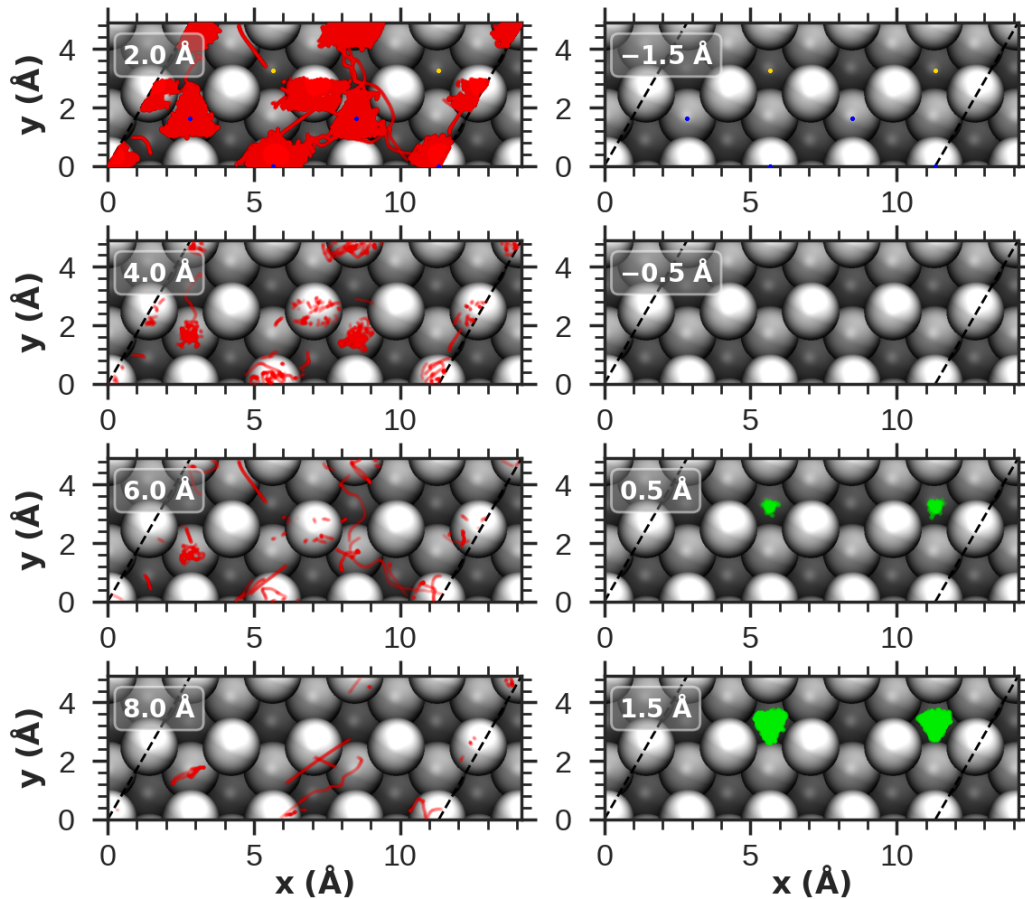


**Figure 8.7:** Same as Fig. 8.5 but for  $T_e - \text{AIMDEF}$  simulations at  $F = 130 \text{ J/m}^2$ .

The results shown in Fig. 8.7 for the  $T_e - \text{AIMDEF}$  simulations remark that the adsorbate mobility on the surface is highly reduced when only the effect of the laser-excited electrons is included. Specifically, there is some subtle CO diffusion that can be identified in the plot at  $z_0 = 2.0 \text{ \AA}$ , but the O adsorbates remain mainly localized around their initial adsorption sites.

## 8.2.2 CO desorption and oxidation probabilities on O+2CO/Pd(111)

O+2CO/Pd(111) total probabilities				
(I) Desorbed CO				
	$T_e$ – AIMDEF	$(T_e, T_l)$ -AIMDEF		
	O+2CO/Pd(111)	O+2CO/Pd(111)	130 J/m <sup>2</sup>	0.75ML CO/Pd(111)
$F$ (J/m <sup>2</sup> )	130	72	130	130
$N^{\text{CO, tot}}$	400	400	400	396
$P_{\text{CO, des}}(t)$ (%)	0.25	0.50	5.00	9.56
$P_{\text{CO}_2, \text{ des}}(t)$ (%)	0.00	0.25	0.25	–
$r_{\text{CO, CO}_2}(t)$	–	2.0	20.0	–

(II) Trapped CO				
	$T_e$ – AIMDEF	$(T_e, T_l)$ -AIMDEF		
	O+2CO/Pd(111)	O+2CO/Pd(111)	130 J/m <sup>2</sup>	0.75ML CO/Pd(111)
$F$ (J/m <sup>2</sup> )	130	72	130	130
$P_{\text{CO}}(t)$ (%)	0.50	1.00	1.50	4.56

**Table 8.2:** Total probabilities at  $t = 4.0$  ps obtained for O+2CO/Pd(111) with different AIMDEF simulations and absorbed laser fluence.  $N^{\text{CO, tot}}$  is the total number of initially adsorbed CO in each simulation type;  $P_{\text{CO, des}}(t)$  and  $P_{\text{CO}_2, \text{ des}}(t)$  are the CO and CO<sub>2</sub> desorption probabilities, respectively;  $r_{\text{CO, CO}_2}(t)$  is the branching ratio between CO desorption and oxidation; and  $P_{\text{CO}}(t)$  is the CO trapping probability. For comparison, the  $(T_e, T_l)$ -AIMDEF results for 0.75 ML CO/Pd(111) and a laser fluence of 130 J/m<sup>2</sup> are written as well.

The CO desorption, oxidation, and trapping probabilities obtained at the end of the simulations (4 ps) for O+2CO/Pd(111) are summarized in Table 8.2. CO desorption increases by a factor 10 when increasing the fluence from 72 to 130 J/m<sup>2</sup>, while CO trapping is rather similar (1.0 and 1.5%, respectively). As mentioned in the previous section, the CO oxidation probabilities are surprisingly the same at both fluences. Note, however, that the statistics are insufficient to extract any meaningful conclusion in this respect. Let us remark that oxidation probabilities measured at zero delay (total fluence  $F \approx 180$  J/m<sup>2</sup>) in 2PC experiments performed by Camillone and co-workers in a mixed overlayer of similar characteristics are larger than the ones obtained here [362]. Therefore, further theoretical simulations,

including the construction of a  $\text{O}+2\text{CO}/\text{Pd}(111)$  NN PES will be new directions to develop in the future.

Considering that the surface total coverage is 0.75 ML it is interesting to compare the CO desorption probabilities between the present mixed overlayer of 0.25 ML O + 0.50 ML CO and a pure CO overlayer of the same total coverage (0.75 ML CO), which was already studied in previous chapters with NN PESs and in Ref. [31] with  $(T_e, T_l) - \text{AIMDEF}$ . Nonetheless, in making this comparison the results in Table 8.2 correspond to new  $(T_e, T_l) - \text{AIMDEF}$  simulations performed for  $\text{CO}/\text{Pd}(111)$  with a coverage of 0.75 ML, a laser fluence  $F = 130 \text{ J/m}^2$ , and the same computational settings that were used for the  $\text{O}+2\text{CO}$  overlayer (see Section 8.1). The main difference respect to the  $(T_e, T_l) - \text{AIMDEF}$  simulations by Alducin et al. is that the zero point energy is not included in the new simulations discussed in this chapter. As done for  $\text{O}+2\text{CO}/\text{Pd}(111)$  and in order to make a meaningful comparison between the two overlayers, we did a first inspection of the CO CM heights  $z_{\text{cm},\text{CO}}$  to establish the desorption and trapping criteria. In particular, a molecule is considered desorbed if it reaches a height  $z_{\text{cm}} > 9.5 \text{ \AA}$  with positive velocity along the surface normal and trapped if at any instant gets further than  $5.0 \text{ \AA}$  but without desorbing at a later time. As shown in Table 8.2, CO desorption (per adsorbed CO) is more probable in 0.75 ML  $\text{CO}/\text{Pd}(111)$  by about a factor 2. And there is also more trapping (4.5% against 1.5% in the  $\text{O}+2\text{CO}$  overlayer). These results are not easily explained in terms of the desorption energies calculated for the equilibrium conditions, since, in general, desorption from the mixed overlayer seems energetically favored (see Table 8.4). We will discuss this point again in Section 8.2.2.1, when analyzing the site-resolved desorption probabilities.

Regarding the role of hot electrons and phonons in the CO photodesorption on  $\text{O}+2\text{CO}/\text{Pd}(111)$ , we see that for  $T_e - \text{AIMDEF}$  at fluence  $F = 130 \text{ J/m}^2$  there is clearly less CO desorption than for  $(T_e, T_l) - \text{AIMDEF}$  at the same fluence. As shown in Table 8.2, the CO desorption probability is only 0.25% when neglecting the effect of the hot lattice, a much smaller value than the 5% obtained in  $(T_e, T_l) - \text{AIMDEF}$  simulations that include both excitation mechanisms (electrons and phonons). Note also that even for  $(T_e, T_l) - \text{AIMDEF}$  with  $F = 72 \text{ J/m}^2$  more CO desorption is observed compared to that obtained in  $T_e - \text{AIMDEF}$  at  $F = 130 \text{ J/m}^2$ . All these comparisons suggest that the hot phonons created by the laser-excited electrons are very important in this system, similarly to what is observed and discussed for  $\text{CO}/\text{Pd}(111)$  in Chapter 7.

Concerning the photooxidation process, we neither observe CO oxidation in  $T_e - \text{AIMDEF}$ , whereas there is a single event in  $(T_e, T_l) - \text{AIMDEF}$ . Still, the statistics for this process is very poor in all the simulations and, as already argued,

insufficient to extract meaningful conclusions about the importance of electrons and phonons for this specific reaction.

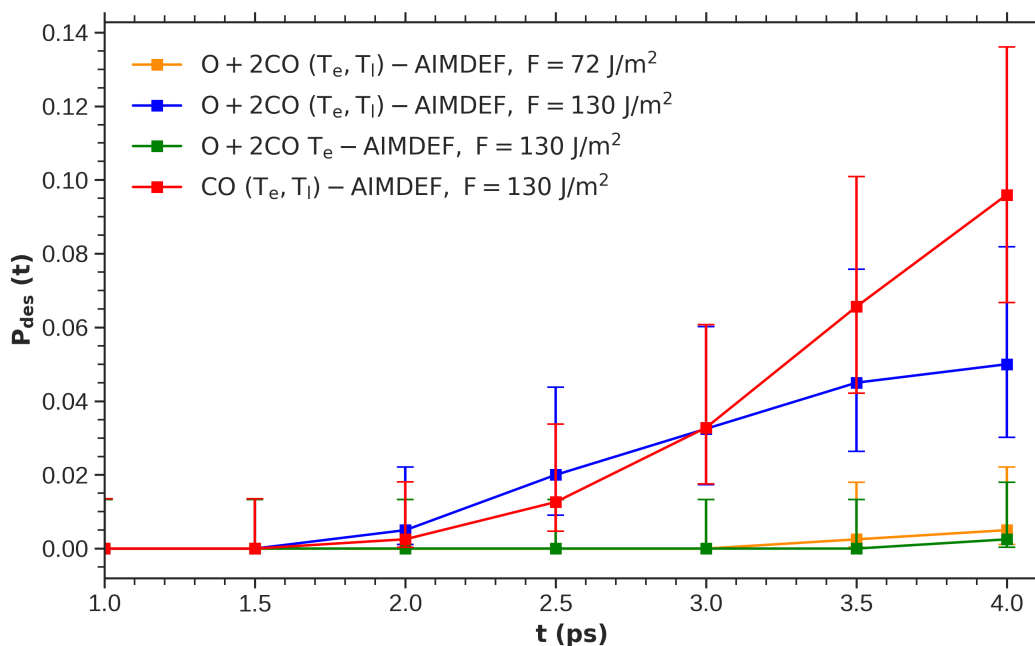


**Figure 8.8:** Time evolution of the CO desorption probability  $P_{\text{des}}(t)$  from the O+2CO/Pd(111) surface as obtained in the  $(T_e, T_l)$  - AIMDEF simulations for  $F = 70 \text{ J/m}^2$  (orange) and  $F = 130 \text{ J/m}^2$  (blue). Results for  $T_e$  - AIMDEF and  $F = 130 \text{ J/m}^2$  are plotted in green. For comparison, also the desorption probability from 0.75 ML CO/Pd(111) calculated with  $(T_e, T_l)$  - AIMDEF for  $F = 130 \text{ J/m}^2$  is shown in red. Data points with their respective Wilson score intervals [347] are plotted every 500 fs.

Additional information on the desorption dynamics can be extracted by analyzing the time evolution of the CO desorption probability  $P_{\text{des,CO}}(t)$ . These results are shown in Fig. 8.8 for the different simulations performed in O+2CO/Pd(111) and also for the  $(T_e, T_l)$  - AIMDEF simulations in 0.75 ML CO/Pd(111). For simplicity, only data points every 500 fs with their Wilson uncertainty intervals [347] are represented. It is convenient to remark that the oxidation probability is not shown because there is only a single CO<sub>2</sub> desorption event within the simulation time of 4 ps for each laser fluence. As already anticipated when analyzing the time evolution of the CO CM heights  $z_{\text{cm,CO}}(t)$ , the first desorption events in O+2CO/Pd(111) start to occur at about 1.5 ps after irradiating the surface for the high laser fluence and at about 3.5 ps for the low laser fluence. It also takes about 1.5 ps to observe CO desorption in the 0.75 ML CO overlayer at high laser fluence. However, the

evolution of CO desorption seems different between both overlayers. While in 0.75 ML CO, desorption is still increasing at the end of the simulation time (as actually confirmed with the (T<sub>e</sub>, T<sub>l</sub>) – MDEF simulations in Chapter 5),  $P_{\text{des,CO}}(t)$  seems to start a kind of saturation in the interval 3.5 to 4.0 ps. However, it will be necessary to continue the dynamics for a few more ps to confirm that this is the case.

### 8.2.2.1 Reaction probabilities by sites

O+2CO/Pd(111), probabilities by sites							
(I) Desorbed CO							
(T <sub>e</sub> ,T <sub>l</sub> )-AIMDEF							
O+2CO/Pd(111)							
0.75ML CO/Pd(111)							
F (J/m <sup>2</sup> )	72		130		130		
Site	top	hcp	top	hcp	top	hcp	fcc
N <sup>CO,site</sup>	2+1*	0	14+1*	6	18	11	9
$\chi_{\text{CO,des}}^{\text{site}}(t)$ (%)	100.00	0.00	70.00	30.00	47.37	28.95	23.68

(II) Trapped CO							
(T <sub>e</sub> ,T <sub>l</sub> )-AIMDEF							
O+2CO/Pd(111)							
0.75ML CO/Pd(111)							
F (J/m <sup>2</sup> )	72		130		130		
Site	top	hcp	top	hcp	top	hcp	fcc
N <sup>CO,site</sup>	12	6	20	38	10	5	3
$\chi_{\text{CO,des}}^{\text{site}}(t)$ (%)	66.67	33.33	34.48	65.51	55.56	27.78	16.67

**Table 8.3:** Adsorption site-resolved probabilities at  $t = 4.0$  ps obtained for O+2CO/Pd(111) with different AIMDEF simulations and absorbed laser fluence.  $N^{\text{CO,site}}$  is the total number of desorbed CO that were initially at this specific site, superscript \* indicates how much CO desorbed after recombining with an fcc O atom and forming CO<sub>2</sub>, but this has not been accounted for calculation of the desorption probability fraction per site  $\chi_{\text{CO,des}}^{\text{site}}$  due to the different chemical process they undergo. For comparison also the (T<sub>e</sub>, T<sub>l</sub>) – AIMDEF results for 0.75 ML CO/Pd(111) and a laser fluence of 130 J/m<sup>2</sup> are also written. Results are provided for desorbed (I) and trapped CO (II).

The contribution of each adsorption site to the total CO desorption probability is given in Table 8.3 for both the O+2CO and 0.75 ML CO adlayers. In this analysis,

we focused on the results from the (T<sub>e</sub>, T<sub>1</sub>) – AIMDEF simulations that include both the effect of electrons and phonons. Notice that in the tables, an asterisk is written next to CO molecules that come from a given adsorption site to indicate that these molecules undergo recombination and desorb as CO<sub>2</sub>. For  $F = 130 \text{ J/m}^2$ , CO desorption in the mixed adlayer is clearly dominated by molecules initially adsorbed at the top site. This is also true for the low fluence but in this case the statistics is limited and the results obtained have to be interpreted with more caution. At first sight, the fact of top-dominated CO desorption is surprising because desorption from this site would require about 100 meV more than desorption from hcp (see Table 8.4). However, the desorption energies do not provide information of the possible existence of additional energy barriers between the adsorbed and desorbed state that would make desorption from hcp energetically less favorable. The larger number of trapped molecules from hcp sites than from top sites that is obtained for  $F = 130 \text{ J/m}^2$  would agree with this idea, but not for  $F = 72 \text{ J/m}^2$ . Neither the analysis of the kinetic energy gained by each type of adsorbate helps much to understand the results obtained. As seen in Fig. 8.9, the molecules in hcp sites gain initially (during the first 1–1.5 ps) a bit more kinetic energy than those adsorbed at top, among other reasons because the coupling with the hot electrons is slightly stronger in the former than in the latter site. The same behavior is observed in Fig. 8.10, where the total energy is separated into translational and rovibrational contributions. In view of all these observations, we have to conclude that the desorption dynamics in the highly excited system is not well explained by the energetics calculated at the equilibrium configurations. Something along this line is found, for instance, in the photoinduced oxidation of CO on Ru(0001) covered with 0.25 ML O+ 0.375 ML CO [65]. Desorption from the 0.75 ML CO/Pd(111) surface can in contrast be easily interpreted in terms of the CO desorption energies, with the contribution from top, hcp, and fcc following the order from less to more bound.

---

**Site-specific desorption energies**

---

System	Desorption site		
	top	hcp	fcc
<b>O+2CO/Pd(111)</b>	0.78	0.67	–
<b>0.75 ML CO/Pd(111)</b>	0.74	0.83	0.94

**Table 8.4:** Site-specific desorption energy  $E_{\text{des}}^{\text{DFT}}$  for desorbing one CO from O+2CO/Pd(111) and 0.75 ML CO/Pd(111), calculated with DFT+vdW-DF using the computational settings described in Section 8.1. All energies are in eV.

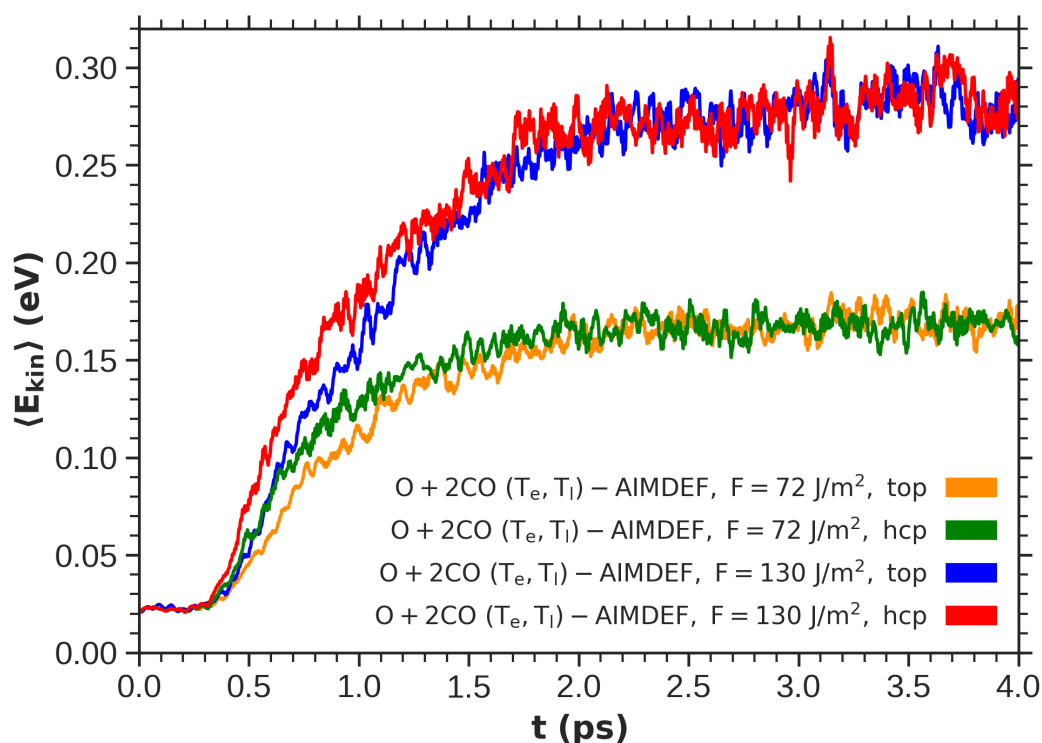


**Figure 8.9:** Site-resolved average kinetic energy  $\langle E_{kin} \rangle$  of the CO molecules that remain adsorbed on O+2CO/Pd(111) as obtained in the  $(T_e, T_l)$  – AIMDEF simulations for the two different laser fluences.

## 8.3 Conclusions

In the present chapter we have discussed the femtosecond laser-induced desorption and oxidation dynamics of CO on Pd(111) covered with 0.25 ML O + 0.50 ML CO. As a first step, a  $4 \times 2$  cell of this system has been relaxed, showing that in the most stable configuration the O atoms adsorb at fcc sites and the CO molecules are equally distributed in top and hcp sites. Next, the system has been thermalized at  $T_0 = 90$  K. Afterwards, AIMDEF simulations have been performed on the O+2CO-coadsorbed Pd(111) in order to study the chemical processes undergone by the adsorbates after being irradiated with a femtosecond laser pulse. Different conditions regarding the absorbed laser fluence (72 and 130 J/m<sup>2</sup>) and the kind of AIMDEF simulations –i.e.,  $T_e$  – AIMDEF, which include only the effect of the laser-excited electrons,

and  $(T_e, T_l)$  – AIMDEF, which include both the effect of the excited electrons and phonons– have been probed.

The analysis of the adsorbates dynamics along the surface normal ( $z$  axis) allows us to identify the following processes: CO desorption, CO trapping, CO<sub>2</sub> desorption, and absorption of O adatoms below the Pd topmost layer. Analysis of their movement on the  $xy$  plane at different  $z$  heights from the surface remarks the high degree of mobility they gain because of their coupling to the excited hot electrons and phonons. CO can move along the entire surface, while the absorbing O tends to displace all over the region centered at the fcc site and limited by the three nearest bridge sites, but with enough excitation energy it can explore the entire surface as well. The reduced adsorbate mobility observed in  $T_e$  – AIMDEF compared to that in  $(T_e, T_l)$  – AIMDEF shows the importance that both electrons and phonons have in this system.

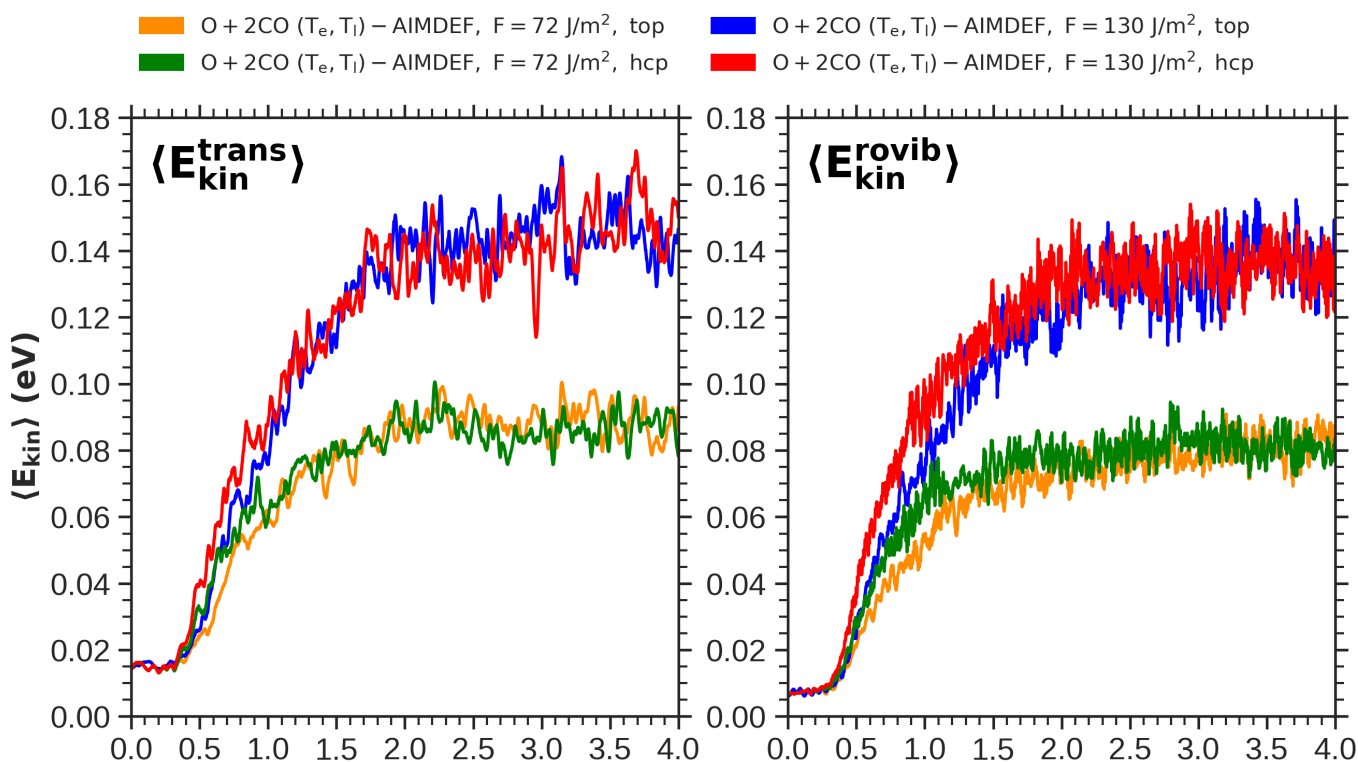


**Figure 8.10:** Site-resolved average translational and rovibrational kinetic energies,  $\langle E_{kin}^{trans} \rangle$  and  $\langle E_{kin}^{rovib} \rangle$  of the CO molecules that remain adsorbed on O+2CO/Pd(111) as obtained in the  $(T_e, T_l)$  – AIMDEF simulations for the two different laser fluences.

The CO desorption probability evaluated at the end of the simulations (4 ps) shows a strong dependence on the laser fluence, as also observed for CO/Pd(111) in previous chapters and expected for the DIMET regime appearing at intense laser fluence. Interestingly, most of the desorbed CO, including the single CO<sub>2</sub> desorption occurring at each fluence, are molecules that were initially at top sites, which are characterized by a higher desorption energy than those adsorbed on hcp sites. Furthermore, analysis of the adsorbate kinetic energies evidences that the latter molecules initially gain slightly more energy than those at top. Altogether, these results showing more desorption from top sites remark that the laser-induced dynamics in this system cannot be interpreted in terms of the energetics under equilibrium conditions.

This study has provided limited understanding of how photodesorption in O+2CO/Pd (111) works due to the shortcomings of the AIMDEF simulations. In general, all results clearly lack sufficient statistics to draw deeper and broader conclusions. Furthermore, the time interval of a few ps we can probe with AIMDEF might be insufficient to capture desorption and oxidation events that could be occurring at a later time. Motivated by the previous success of NN PES-based dynamical approach on CO/Pd(111) [87, 88, 89], a more thorough analysis with NN PES-mediated MDEF seems to be the way forward. This would provide better statistics and allow us to explore broader time intervals and many different initial conditions in reasonable computational times. Consequently, we would be able to study not only CO desorption and oxidation in this system in more detail, but also to understand why most molecules desorb from top sites and why there is more desorption in the 0.75 ML CO adlayer, in which the molecules are in principle less bound.



# 9

## Conclusions & Outlook

---

The aim in the present Thesis has been to get a more profound understanding of the femtosecond laser-induced chemistry of different adsorbates (CO alone and CO mixed with O atoms) on a Pd(111) metal surface from a theoretical perspective. Both systems have different applications, but the main ones are related to heterogeneous catalysis. Understanding the dynamics in the CO/Pd(111) adsorbate-substrate complex has been the focus of several previous works. Most of them come from the experimental side, involving infrared and X-ray spectroscopy, scanning tunneling microscopy (STM), and LEED, among other techniques [17, 18, 19, 20, 21, 23, 24, 25, 26, 30]. This system also received attention from various previous computational studies [27, 28, 29]. More recently, another computational work offered a comprehensive theoretical view of the photodesorption process on this system [31]. The strong coverage dependence of CO desorption previously reported [30] was reproduced and explained in terms of the reduction of desorption barriers with increased coverage. Also, a synergy between hot electrons and phonons in desorption mechanism, a relevant interadsorbate energy exchange for high CO coverages and a high dependence of desorption probabilities with the adsorption site were found. To obtain those results, the authors calculated a few hundreds of trajectories with their newly proposed  $(T_e, T_l)$  – AIMDEF framework, which involves electron- and phonon-mediated excitation on adsorbates through time-dependent electron and lattice temperatures calculated with 2TM. The  $(T_e, T_l)$  – AIMDEF model allows to include both excitation channels in the adsorbates while incorporating all relevant DOFs of the system under study. However, this model comes with an expensive computational cost, as a limited statistics of no more than a few hundreds of trajectories can be obtained in realistic times, under a fixed set of initial conditions, and for simulation times no longer than a few picoseconds. These limitations have motivated the search for some alternative methodology that, preserving the accuracy and flexibility of  $(T_e, T_l)$  – AIMDEF, allows to surpass these limitations.

It is in this context that the  $(T_e, T_l)$  – MDEF framework (i.e., MDEF with both electronic and phononic time-dependent temperatures  $T_e(t)$  and  $T_l(t)$ , respectively) has been developed, being this work the first one covered in this Thesis [87]. Two key ingredients are required for this framework. The main one is to replace the evaluation of the adiabatic forces "on the fly" after determining the instantaneous ground state PES for each time done in AIMDEF. This has been replaced by a

plain derivation of forces from a precalculated NN PES, trained within the EANN model [83] using previous  $(T_e, T_1)$  – AIMDEF data [31]. We have explained the process of construction of such a PES, from the random selection of the set of atomic configurations in such a way that ensures the representativeness of the total ensemble to the fitting of EANN-specific parameters to reach a compromise between accuracy and time required to train the PES. Its accuracy has been verified by calculating the energies and forces of configurations not used to train the PES, these predictions being very close to the  $(T_e, T_1)$  – AIMDEF-calculated values. Next, we have simplified the way the electronic density created by the surface atoms at each point is calculated using a numerically fitted DGF. This simplifies the determination of the friction coefficients for each adsorbate atom, thereby speeding up the process of computing nonadiabatic electronic friction forces on the adsorbates. Subsequently,  $(T_e, T_1)$  – MDEF has been used to replicate  $(T_e, T_1)$  – AIMDEF results. Such has been achieved with two ensembles, one of 100 trajectories starting from the same initial data points used in  $(T_e, T_1)$  – AIMDEF, and the second one of 2000 trajectories that yields very similar results to  $(T_e, T_1)$  – AIMDEF but with smaller statistical uncertainty. Quantities such as the CO desorption probability and the kinetic energy of the adsorbed CO have been reproduced with remarkable closeness with these new ensembles. Moreover, new insights have been gained from the larger  $(T_e, T_1)$  – MDEF set regarding the initial stages of photodesorption and the rovibrational state distribution of CO desorbates.

As each trajectory requires some seconds or minutes instead of some days, depending on the simulated time interval, this work has opened the pathway to explore CO photodesorption for larger computation times, with more statistical reliability, and under different initial conditions. As a first application of the efficient  $(T_e, T_1)$  – MDEF method, we have investigated the potential existence of an isotopic effect in the femtosecond laser-induced desorption of 0.75 ML CO from the Pd(111) surface [88]. To this end, we have carried out  $(T_e, T_1)$  – MDEF simulations using two CO isotopologues, the light  $^{12}\text{C}^{16}\text{O}$  and the heavier  $^{13}\text{C}^{18}\text{O}$ . Using ensembles of 2000  $(T_e, T_1)$  – MDEF and  $T_1$  – MDEF (i.e., MDEF with only phononic excitations) simulations, this study has extended the analysis of desorption dynamics over 50 ps. This analysis has revealed that CO photodesorption from a Pd(111) surface at high laser fluence is governed by the phonon-mediated mechanism, challenging previous experimental results that suggested electron-mediated desorption at lower fluences. After analyzing CO desorption probabilities and rates, as well as desorbed CO vibrational states, no isotope effect has been found. Nevertheless, slight vibrational excitation differences have been noted between isotopologues at higher translational energies, though they represent a small fraction of the total desorption events.

These findings have further emphasized the potential of the MDEF approach for exploring more complex desorption scenarios in subsequent researches, such as varying laser fluences and two-pulse correlation studies. Our next goal has been to perform a more comprehensive multicoverage study of photodesorption on CO/Pd(111). Before tackling this challenge, it was important to gain knowledge of what happened when our 0.75 ML PES was used for a different coverage. Making use of previous  $(T_e, T_1)$  – AIMDEF calculations [31], we have explored how our PES predicts energies and atomic forces for more than 100 000 data points corresponding to 0.33 ML. Conversely, we have trained another PES using information of this latter coverage, and explored its predictions on 0.33 and 0.75 ML data points, as well as the minimum energy path descriptions of both PESs on both adlayers. As we have learned, 0.75 ML PES provides a more accurate description of 0.33 ML data due to the larger variety of atomic environments explored than on the converse case, although the energies predicted on the low coverage data points differ from  $(T_e, T_1)$  – AIMDEF by some consistent value. After fitting this offset and adding it to the set of 0.33 ML configurations used for training, we have trained a multicoverage EANN PES using  $(T_e, T_1)$  – AIMDEF and  $T_e$  – AIMDEF data coming from both coverages. Its robustness has been checked with accurate energy predictions on almost 500 000 data points of 0.33 and 0.75 ML adlayers in both types of MDEF simulations. Moreover, it has also yielded accurate predictions on more than 1000 configurations for 0.60 ML, a coverage missing from multicoverage PES training. Afterwards, using several sets of thousands of trajectories, we have investigated the nonlinear dependence of desorption probability on laser fluence and coverage –for a fixed fluence value–, and the relative contributions of hot electrons and phonons in the desorption mechanism. Our results show that as CO coverage increases, the desorption probability becomes more significant, in agreement with DIMET mechanism, and allow to determine the nonlinear exponents ruling the relationship between desorption probability and fluence. Moreover, we have observed that the desorption process is primarily driven by phonons, particularly at higher fluences, although the larger desorption probabilities arise due to the cooperation of both electrons and phonons in exciting CO adsorbates. The simulations have also provided insights into how mobile CO becomes along the surface  $xy$  plane and the  $z$  axis orthogonal to it, this allowing to see that CO desorbs either directly or after residing some time trapped in the physisorption region. The influence of different adsorption sites on desorption trajectories has been observed as well. Finally, 2PC experiments have been simulated, revealing a strong phonon-mediated desorption mechanism and some discrepancies with experimental data, especially at lower CO coverages, possibly due to differences in coverage and adsorption characteristics. The study has underscored the effectiveness of the multicoverage

EANN PES in advancing the understanding of photoinduced surface reactions and it has highlighted the need for further refinement in theoretical models to fully capture the complexities of these processes.

Ultimately, we have considered a 0.75 ML mixed coverage containing 0.25 ML O and 0.50 ML CO adsorbed on Pd(111). On this complex, we have simulated femtosecond induced desorption. Preliminary settings have involved relaxing the system in order to locate the more stable adsorption site for O atoms, the fcc one resulting to be it, and thermalizing the system in order to select an ensemble of 100 configurations (each configuration includes the positions and velocities of all atoms in the system) that subsequently have served us as our simulation initial conditions. Afterwards, we have performed  $(T_e, T_1)$  – AIMDEF simulations for two laser fluences (72 and 130 J/m<sup>2</sup>) and  $T_e$  – AIMDEF simulations for the highest fluence. Additionally and for comparative purposes, one set of calculations has also been performed for CO/Pd(111) at the latter laser fluence. From the sets of dynamics on both O+2CO/Pd(111) and CO/Pd(111), properties such as the adsorbates position distribution along the surface  $xy$  plane and the  $z$  axis, the time evolution of desorption probability, the total reaction probabilities at the end of the simulations (4.0 ps), and the kinetic energy distribution of adsorbed species have been analyzed. It has been seen that CO and O adsorbates in O+2CO/Pd(111) exhibit different behavior regarding their mobility, as CO can either desorb directly or become trapped in the physisorption region, while O atoms may penetrate into the surface topmost layer and destabilize it due to its movement across. On the  $xy$  plane, CO and O tend to visit regions close to their adsorption sites, but when enough energy is provided to them, they can explore the full  $xy$  plane. Using the  $z$  height distribution, some criteria for each system have been defined in order to identify which CO are trapped and which other one has desorbed, and this has been used to calculate CO desorption probabilities and time evolution of desorption probabilities. Our study has shown that desorption probabilities are higher at increased fluences, as well as the adsorbates kinetic energy and mobility. In the  $(T_e, T_1)$  – AIMDEF simulations at both fluences not only CO desorption, but also CO recombinative oxidation with fcc O atoms have been obtained. Such process happens very unlikely against desorption for larger fluence, but could be not as infrequent for lower fluence. Also, site-specific desorption probabilities show that more desorption occurs for top than for hcp CO in O+2CO/Pd(111). This result is surprising because CO adsorption on top sites is characterized by a higher desorption energy than CO adsorbed on hcp sites. The additional analysis of the adsorbate kinetic energies evidences that the latter molecules gain initially slightly more energy than those at top. Altogether, these results showing more desorption from top sites than from hcp sites remark that the laser-induced dynamics in the

O+2CO/Pd(111) system cannot be interpreted in terms of the energetics under equilibrium conditions. Compared to CO/Pd(111), less CO desorption probability has been obtained in the mixed O and CO adlayer. Finally, it is important to remark that as these results have been obtained from sets of 100 trajectories and for a time span of 4 ps, they contain the aforementioned statistics and time limitations characteristic of AIMDEF.

To close with, let us briefly discuss potential future insights on the research topics here covered. For instance, more studies with our multicoverage EANN PES could be performed for CO/Pd(111), exploring in greater depth the coverage dependence of the desorption probability and the relative role of electron- and phonon-mediated excitation mechanisms for additional adlayers, such as 0.60 ML. Furthermore, investigations could focus on the fluence dependence and CO mobility using  $T_e$  – MDEF or  $T_1$  – MDEF simulations, as well as on performing 2PC simulations for a wider range of adlayers. Regarding O+2CO/Pd(111), perhaps the more straightforward step is to train a suitable EANN PES in order to do a deeper study on this system for longer simulation times and under more diverse conditions, such as those investigated for CO/Pd(111) in our multicoverage study [89] and already mentioned in this Section. In addition, the choice to make more detailed comparisons between both O+2CO and CO-coadsorbed Pd(111) complexes would be open. And finally, following the promising and robust results ( $T_e, T_1$ ) – MDEF methodology has provided for CO/Pd(111), its application to other adsorbate-substrate complexes becomes straightforward. A very recent example on this aspect is a ( $T_e, T_1$ ) – MDEF work on 2O+CO/Ru(0001) with a suitable EANN PES [95]. In summary, highly promising opportunities for advancing the understanding of femtosecond laser-induced chemical processes in gas-metal systems are clearly emerging for the near future. Opportunities to which, it is hoped, the work presented in this Thesis has made a humble contribution.



# List of Figures

---

- 2.1 Flowchart of the self-consistent evaluation of the KS equations for a given system. To begin with, some trial  $n_s(\mathbf{r})$  is guessed. It is then used for evaluating the KS potential (Eq. (2.71)), taking into account some exchange-correlation potential  $v_{xc}(\mathbf{r})$ . For this KS potential, the Schrödinger equations for the ground-state KS wavefunctions are solved (Eq. (2.72)). As a result, one gets a new set of KS orbitals and, consequently, some new electronic density (Eq. (2.73)) and associated total energy. At the end of each iteration  $t$ , either the total energies of the system or the electronic densities are compared with their counterparts at iteration  $t-1$ . If the differences  $\sum_i |\epsilon_i^t - \epsilon_i^{t-1}| \geq \Delta\epsilon_c$  or  $|n_s^t - n_s^{t-1}| \geq \Delta n_c$ , being  $\Delta\epsilon_c$  and  $\Delta n_c$  some cutoff values for the energy and density, respectively, the iterative process undergoes a new iteration. The cutoffs are chosen to be small enough to ensure that the minimum energy of the system, or equivalently the ground-state density has been reached (recall the variational principle of Eq. (2.55)). Only when the difference in energies or densities lies below its corresponding cutoff, this self-consistent process is finished, yielding approximately the ground-state electronic density  $n_0(\mathbf{r})$  and energy of the system  $\epsilon_0$ . . . . . 35

- 2.2 Jacob's Ladder of exchange-correlation functionals in DFT. The ladder starts from Hartree-Fock approximation floor or "Hartree hell", the least precise way of representing exchange and correlation. The higher the considered approximation is in the ladder, the more precisely quantum chemical properties are predicted, with a larger computational expense in time and resources. The ideal peak of the ladder represents discrepancies between the DFT computed and the actual energy density of the many body system below 1 kcal/mol. Moving towards the higher steps implies going from the local density approximation, showed in green, to semilocal approaches exploring first or second derivatives of the density at some point  $n(\mathbf{r})$  (blue) and afterwards to functionals describing nonlocal or long-range effects, depicted in red. Central columns indicate the name of each family of exchange-correlation functionals (left) and the key functions handled by each family (right). Van der Waals approximations (step 3.5) did not exist before Jacob's Ladder diagram was first published in Ref. [133]; a discussion regarding its placement in the diagram is given in Ref. [134]. . . . . 41
- 3.1 Representation of the MGR model showing the energy versus the adsorbate-surface distance  $r$ . Starting from the adsorbate-substrate complex in the ground state A+S, photoexcitation heats the electrons of the surface, and after them colliding the adsorbate the latter is driven through a Franck-Condon excitation into an excited state A\*+S. There, excited adsorbate remains for some time in the excited PES until relaxing back to the ground state with some kinetic energy gain, leading to it separating some  $r$  from the substrate. Two possible situations can arise depending of if time before quenching falls below or reaches some critical value  $t_c^{\text{rel}}$ . For relaxation times as  $t_{\text{el},1}^{\text{rel}} < t_c^{\text{rel}}$  the adsorbate gains not enough energy to surpass the potential well  $E_b$ , so that with an energy gain  $E_1 < E_b$  it loses the kinetic energy gained after excitation and gets recaptures by the substrate. On the contrary, if it remains longer of, at least, as long as some critical time,  $t_{\text{el},2}^{\text{rel}} \geq t_c^{\text{rel}}$ , it gains enough kinetic energy to surpass the potential barrier after quenching back to ground state,  $E_2 \geq E_b$ , and becomes able to desorb. . . . . 58

- 3.2 Surface photodesorption mechanism as described by Antoniewicz. Considering once more the energy dependence of the adsorbate with its distance to the substrate  $r$ , and starting again from the adsorbate-substrate system on ground state as in MGR proposal, some photoexcited surface electrons are captured by the adsorbate orbitals, bringing the adsorbate into a negative ionic state PES  $A^- + S$  through a Franck-Condon process. Anionic atom or molecule then approaches the surface before relaxing back to the ground-state PES after some relaxation time  $t_{el}^{rel}$ . While approaching the surface and quenching back to it, the adsorbate has an energy gain  $E$  which, if it equals or surpasses the energy barrier of the ground PES ( $E \geq E_b$ ), allows the adsorbed species to desorb. . . . 59
- 3.3 Electronic density of states for a metal substrate that is excited with a femtosecond laser pulse. (a) Right after the laser pulse reaches the substrate ( $\Delta t = 0$ ), electrons (black dots) are excited from lower energy states below the Fermi level  $E_F$  to higher energy states, creating a nonequilibrium distribution of electrons (orange area) that deviates from the original, Fermi-Dirac one, part of which is shown in red. This hot electron distribution cannot be characterized by an electronic temperature  $T_e$ . (b) Subsequent relaxation process of the electron distribution due to electrons redistributing their energy by scattering with other electrons and the adsorbates, if present. This leads to the distribution thermalizing to a Fermi-Dirac one with a tail of higher energy states above  $E_F$ , depicted in orange, with a well defined  $T_e$ . Meanwhile, the system seeks to return to thermal equilibrium, and the electronic density of states evolves towards regaining the Fermi-Dirac equilibrium distribution (shaded region). . . . . 63
- 3.4 Time evolution of the electronic temperature  $T_e$  (solid curves) and lattice temperature  $T_l$  (dashed curves) calculated with 2TM for incident femtosecond pulses of sech shape centered at  $t = 0.41$  ps, FWHM equal to 100 fs, wavelength  $\lambda = 780$  nm, and surface absorbed fluences,  $F = 72$  J/m<sup>2</sup> (red curves) and  $= 130$  J/m<sup>2</sup> (blue curves). 67

- 3.5 Schematic summary of the femtosecond laser-mediated photodesorption process on metal surfaces. It starts after a femtosecond laser pulse reaches an adsorbate-decorated (grey and red atoms) metal surface (blue atoms). As a result metal electrons become very hot, reaching temperatures of even thousands of K, and part of them produce several electron-hole pairs and occupy valence energy levels. Hot electrons gradually lose energy by colliding between them or the adsorbate, thus producing a hot Fermi-Dirac distribution of some  $T_e$ . When they return to the conduction band they keep losing energy by collision, not only by colliding with other electrons, but also with energy metal atoms, leading to a coupling between electronic subsystem and the metallic lattice ruled by a coupling constant  $g$ . Electron energy input leads the surface phonons to heat, thus their collective lattice temperature  $T_l$  rises, but not as high as for electronic subsystem due to the smaller heat conductivity of the metal lattice. Both electronic and phononic subsystems plunge energy into the adsorbates, which then become hotter –their temperature  $T_{ads}$  consequently increasing–, and if their kinetic energy grows enough they desorb from the surface. . . . . 69
- 4.1 Example of a feed-forward NN with two hidden layers of 4 and 3 nodes, respectively. Such NN has a 2-4-3-1 architecture, or, if one regards only the hidden layers, a 4-3 one. Input layer contains two functions  $G_1$  and  $G_2$  and, after the input is processed by all  $x_i^k$  nodes, some energy  $E$  is yielded as an output. Some of the weights  $w_{j,i}^{k-1,k}$ , represented by black arrows, are pictured as an example. Here, superscript  $k$  relates to the layer number, and subscripts  $j$  and  $i$  denote the number of nodes providing some input value and receiving it, respectively. This includes the bias weights  $b_i^k$  pictured with green dashed arrows, which are fed into each non-inputting node by the bias node, also pictured in green. Bias node adds a value of 1 to each node. . . . . 83
- 4.2 Examples of commonly used activation functions of Eq. (4.2) in the range  $x \in [-3, 3]$ . In this case,  $f_{i,(4)}^k$  has the parameters  $a = 3/2$ ,  $b = 2/3$  and  $c = 1/4$ . . . . . 85

- 4.3 Schematics of the overfitting problem. In initial iterations or epochs, the NN function is trained according to some input data, and at the same time is validated against some test data missing from the training set. Weight update after each epoch leads to a decrease in the error functions for both train (blue) and test (red) sets, which also implies a better predictive ability of the NN function curve (showed in blue in the insets) to fit known data points (black dots in the insets), as shown in the left inset. After some given iteration, weight update fits training input data points with increasing accuracy as shown in the right inset in the black dots, thus its related error still decreases. However, test set description starts to become increasingly poorer, as shown for the NN function in the right inset, and its related error begins to increase. As a result, the NN function is said to be overfitted, being such region pictured in grey in the figure. Consequently, optimal NN training lasts as many epochs as required for error decrement, but are stopped prior to overfitting with the help of some early stopping mechanism. . . . . 89
- 4.4 Flowchart of the full NN training process. It begins with a set of initial configurations of atomic positions, energies and forces that is used as the input of a NN with some architecture. Then, a PES function is trained in a NN with some architecture, where the errors or differences in PES-predicted energies and atomic forces with respect to the input reference values are minimized during a number of iterations. The output PES is made to undergo a validation process consisting of different steps. First, NN training has to be stopped early enough to prevent overfitting. In addition, in order to validate its quality, the NN PES is used to predict energies and forces of some set of configurations not present among the training data, and those configurations that have larger errors in predicted energy and force values can be incorporated to the training step. Not only this, but also poorly described regions of the configuration space may be encountered during this process, this motivating the calculation of some selected data points to further enhance the training set. Afterwards, additional training and validation cycles can be performed on the PES until getting a final NN PES robust and accurate enough. . . . . 90

- 4.5 General schema of a "second generation" HDNNP model (also called atomistic NN model) for a system of three atomic species  $j = a$  (red),  $b$  (grey) and  $c$  (blue). Given a set of atomic positions  $\mathbf{r}_j^i$ , where  $i$  refers to the specific atom of element  $j$  considered, a cutoff sphere can be defined around each of them, characterized by a set of positions  $\mathbf{R}_j^i \equiv \{\mathbf{r}_j^i\}$  corresponding to the central atom position  $\mathbf{r}_j^i$  and the position vectors of its neighbors. Participation of central and neighbor atoms is represented with the multiple out- and ingoing colored arrows between the two first columns. Cutoff sphere coordinates are then transformed into sets of symmetry functions fulfilling the required invariances,  $\mathbf{G}_j^i \equiv \{\mathbf{g}_j^i(\{\mathbf{r}_j^i\})\}$ . Each of these sets of functions enter a NN as input and this yields some energy  $E_j^i$  for the given local atomic environment. In the end, total energy of the atomic configuration  $E_s$  is a sum of the individual environmental energies of the atom-centered cutoff spheres, subscript  $s$  standing for short-range to further address the local feature of each  $E_j^i$ . . . . . 96
- 4.6 Plot of the cutoff function  $f_c(r_{ij})$  defined in Eq. (4.9) in terms of  $r_{ij}/r_c$ . 97
- 4.7  $\eta$  (upper graph) and  $r_s$ -dependencies (lower graph) of radial functions  $e^{-\eta(r_{ij}-r_s)^2} f_c(r_{ij})$  in terms of interatomic distance  $r_{ij}$ . For all functions plotted,  $r_c = 7 \text{ \AA}$ . For upper graph,  $r_s = 0 \text{ \AA}$ , whereas for the lower one  $\eta = 0.5$ . Cutoff function  $f_c$  is pictured in dashed black lines in both graphs. . . . . 99
- 4.8  $\zeta$  and  $\lambda$  dependencies of the angular functions  $2^{1-\zeta} (1 + \lambda \cos \theta_{ijk})^\zeta$  with the angles  $\theta_{ijk}$  subtended between the central atom  $i$  of a cutoff sphere and two neighbor atoms  $j$  and  $k$ . Each curve corresponds to a certain choice of parameters  $(\lambda, \zeta)$ , so that reddish curves share  $\lambda = -1$ , whereas bluish ones have  $\lambda = 1$ . Selected values for  $\zeta$  exponent are 1, 2, 5, 10 and 20. . . . . 101

- 4.9 Schema of the EANN framework for the same system of three atomic species  $j = a$  (red),  $b$  (grey) and  $c$  (blue) considered in Fig. 4.5 (see its description). One starts from a given set of atomic positions  $\mathbf{R}_j^i \equiv \{\mathbf{r}_j^i\}$  inside a cutoff sphere around the  $i$ -th atom of element  $j$ ,  $\mathbf{r}_j^i$ . Then, one determines the set of GTOs centered at  $\mathbf{r}_j^i$ ,  $\varphi_{l_x l_y l_z}^{\alpha, r_s}(\mathbf{r}_j^i) \equiv \varphi(\mathbf{r}_j^i)$ . Depending on their proximity to each of the system atoms  $i$ , the GTOs linked to each centering atom feed or not –therefore the multiple colored arrows between the third and fourth column of the graph– the embedding atomic densities  $\rho_{L, \alpha, r_s}^i \equiv \rho^i$ , which preserve the required spacial and permutational invariances. The latter are processed into NNs as corresponds for a HDNNP schema and yield the individual energies  $E_j^i$ , and their sum equals to the short-range energy  $E_s \equiv E$  of Eq. (4.22). . . . . 106
- 5.1 Schematic illustration of our 0.75 ML CO/Pd(111)  $4 \times 2$  simulation cell, composed by O (red) and C atoms (grey) forming CO adsorbates, and a 4-layer slab of Pd atoms (blue). (A) Orthogonal top view, highlighting the CO top, hcp, and fcc adsorption sites, as well as, the topmost (blue) and second topmost (blurred blue) surface layers. (B) Perspective view. In  $(T_e, T_1) - \text{AIMDEF}$  and  $(T_e, T_1) - \text{MDEF}$ , each adsorbate dynamics is modeled with a Langevin equation. Regarding the surface, Pd atoms in the two topmost Pd layers are coupled to the Nosé-Hoover thermostat, Pd atoms in the third layer undergo adiabatic evolution and Pd atoms in the bottom layer remain frozen throughout the simulation [31, 87]. . . . . 114
- 5.2 Normalized histograms of potential energies  $E_0^{\text{DFT}}$  obtained from  $(T_e, T_1) - \text{AIMDEF}$  (filled blue bars) [31]. Superimposed empty bars distinguish energy distributions from trajectories with zero (yellow), one (green) or two CO desorption events. (Top) Full  $(T_e, T_1) - \text{AIMDEF}$  data set histograms (352 505 configurations). (Bottom) Distributions for the 15 000 configurations accounted first for the EANN parameter optimization and afterwards for the first EANN PES training. . . . . 117

5.3	Representation of the exponential part of the GTOs, $\exp \left[ -\alpha (r_{ij} - r_s)^2 \right]$ (Eq. (4.19)), multiplied by the cutoff function $f_c (r_{ij})$ (Eq. (4.9)), for 15 GTOs with equal separation intervals between consecutive orbitals of $\Delta r_s = 0.4643 \text{ \AA}$ , equal widths $\alpha \simeq 0.93 \text{ \AA}^{-2}$ and $r_c = 6.5 \text{ \AA}$ . First GTO is centered at $r_s = 0 \text{ \AA}$ and last one is centered at $r_s = r_c = 6.5 \text{ \AA}$ . . . . .	119
5.4	Cartesian coordinate-wise histograms depicting, for each of the 36 moving atoms of the 0.75 ML CO/Pd(111) system, the 10 maximum force errors $ \Delta F_\gamma  = \left  F_\gamma^{\text{DFT}} - F_\gamma^{\text{EANN}} \right $ , with $\gamma = x, y, z$ . Black (red) histogram bars correspond to errors for the predict set in the EANN PES having the smaller maximum force errors of the first (final) training. Green histogram bars correspond to the whole $(T_e, T_1) - \text{AIMDEF}$ data set of 352 505 configurations and were obtained with the final EANN PES. For each error distribution, MESMAEs, $\overline{ \Delta F_\gamma }$ , are given as well. . . . .	126
5.5	Left: Comparison of the potential energies per moving atom computed as determined by the (final) EANN PES against their corresponding DFT values, for a set of 87 382 configurations absent from the training data. Right: Error distribution for the energy per moving atom, $\Delta E/N_{\text{moving}} = (E^{\text{DFT}} - E^{\text{EANN}})/N_{\text{moving}}$ , for the same ensemble of predict configurations. . . . .	128
5.6	Cartesian component-wise comparison of the forces acting on a fcc carbon atom within the 0.75 ML CO/Pd(111) system [31], $F_\beta^{\text{EANN}}$ versus $F_\beta^{\text{DFT}}$ , $\beta = x$ (red), $y$ (blue) and $z$ (green). Left column EANN forces come from the initially trained PES, while the right panels correspond to the final PES. Maximum error and RMSE for each plot are also presented. . . . .	130
5.7	Same as Fig. 5.6 for an hcp O atom. . . . .	131
5.8	Comparison of the LDFA friction coefficients calculated with the fitted electronic density function $n(\mathbf{r})$ (Eqs. (5.3) and (5.4)) against the data set of friction coefficients from $(T_e, T_1) - \text{AIMDEF}$ [31]. Coefficients are given in atomic units (a.u.). (Taken from Ref. [87])	132

- 5.9 Time evolution of the friction coefficients  $\eta_e$  for C atoms along a representative trajectory. Orange lines depict the  $(T_e, T_l)$  – AIMDEF results for a specific trajectory of Ref. [31]. Blue lines represent the results obtained from  $(T_e, T_l)$  – MDEF-1 –i.e., performing molecular dynamics with our final EANN PES and the density generation function–, for a trajectory initiated under identical  $(T_e, T_l)$  – AIMDEF conditions. Each graph shows the results for a different C atom in the simulation model, whose initial positions are labeled in the figures and correspond to the top (upper row), fcc (middle), and hcp sites (lower). . . . . 136
- 5.10 Total CO desorption probabilities in the interval [1.0, 3.5] ps for the three ensembles of dynamics calculations considered in this work:  $(T_e, T_l)$  – AIMDEF (orange),  $(T_e, T_l)$  – MDEF-1 (blue) and  $(T_e, T_l)$  – MDEF-2 (red). Here,  $(T_e, T_l)$  – AIMDEF results are extracted from the simulations performed in Ref. [31]. Both  $(T_e, T_l)$  – MDEF-1 and  $(T_e, T_l)$  – MDEF-2 stand for results obtained from simulations performed with our best trained EANN PES using, respectively, the same 100 initial conditions than in  $(T_e, T_l)$  – AIMDEF, and 2000 random initial conditions. Standard deviations are depicted for multiples of 500 fs to give an idea of the uncertainty intervals while maintaining the clarity of the exact curves. . . . . 137
- 5.11 Site-specific CO desorption probabilities in the interval [1.0, 3.5] ps for the three ensembles of dynamics calculations considered in this work:  $(T_e, T_l)$  – AIMDEF (orange),  $(T_e, T_l)$  – MDEF-1 (blue) and  $(T_e, T_l)$  – MDEF-2 (red). Here,  $(T_e, T_l)$  – AIMDEF results are extracted from the simulations performed in Ref. [31]. Both  $(T_e, T_l)$  – MDEF-1 and  $(T_e, T_l)$  – MDEF-2 stand for results obtained from simulations performed with our best trained EANN PES using, respectively, the same 100 initial conditions than in  $(T_e, T_l)$  – AIMDEF, and 2000 random initial conditions. Standard deviations are depicted for multiples of 500 fs to give an idea of the uncertainty intervals while maintaining the clarity of the exact curves. Here, desorption probabilities correspond to CO initially adsorbed at top (upper), hcp (middle) and fcc (lower panel) sites. . . . . 138

- 5.12 Mean center of mass translational kinetic energy,  $\langle E_{\text{kin}}^{\text{trans}} \rangle$ , (left panel, full thick lines) and mean rovibrational kinetic energy,  $\langle E_{\text{kin}}^{\text{rovibr}} \rangle$ , (right panel, full thick lines) of adsorbed CO molecules as a function of time. Corresponding dotted thin curves above and below each  $\langle E_{\text{kin}}^{\text{trans(rovibr)}} \rangle$  curve show the mean values plus and minus associated standard deviations, respectively. For both panels,  $(T_e, T_1)$  – AIMDEF stands for results extracted from Ref. [31] calculations,  $(T_e, T_1)$  – MDEF-1 stands for dynamics results obtained from our best trained EANN PES using the same 100  $(T_e, T_1)$  – AIMDEF initial conditions, and  $(T_e, T_1)$  – MDEF-2 stands for dynamics results obtained with the same EANN PES using 2000 random initial conditions. . . . . 140
- 5.13 Empirical cumulative distribution functions (ECDFs) of desorbed CO for the center of mass translational kinetic energy (left panel) and rovibrational kinetic energy (right panel). Shaded areas mark 99% Dvoretzky-Kiefer-Wolfowitz confidence intervals [348]. For both panels,  $(T_e, T_1)$  – AIMDEF stands for results extracted from Ref. [31] calculations,  $(T_e, T_1)$  – MDEF-1 stands for dynamics results obtained from our best trained EANN PES using the same 100  $(T_e, T_1)$  – AIMDEF initial conditions, and  $(T_e, T_1)$  – MDEF-2 stands for dynamics results obtained with the same EANN PES using 2000 random initial conditions. . . . . 141
- 5.14 Probability distribution of the vibrational quantum number  $\nu$  of desorbed CO in the  $(T_e, T_1)$  – MDEF-2 data set, determined from Eq. (5.8) after the quasiclassical approach of Ref. [349]. All CO molecules considered in this distribution have rotational states  $j \geq 0$ . 144
- 5.15 Probability distributions of the rotational quantum number  $j$  for each of the vibrational states observed among the desorbed CO in  $(T_e, T_1)$  – MDEF-2 set,  $\nu = 0, 1$  (blue and red bars of top panel, respectively) and  $\nu = 2, 3$  (green and orange bars of bottom panel, respectively). Rotational states were determined from Eq. (5.10) following the quasiclassical approach of Ref. [349]. . . . . 145
- 6.1 Time evolution of  $^{12}\text{C}^{16}\text{O}$   $(T_e, T_1)$  – MDEF (full blue) and  $T_1$  – MDEF (dashed purple), and  $^{13}\text{C}^{18}\text{O}$   $(T_e, T_1)$  – MDEF (full red) and  $T_1$  – MDEF (dashed orange) desorption probabilities in the interval [1, 4] ps. Shaded areas correspond to Wilson score intervals of 99% confidence level [347]. . . . . 153

- 6.2 (Top) Time evolution of the desorption probability along the time interval  $[0, 50]$  ps.  $(T_e, T_1)$  – MDEF (solid lines) data sets for  $^{12}\text{C}^{16}\text{O}$  (blue) and  $^{13}\text{C}^{18}\text{O}$  (red) and  $T_1$  – MDEF ones (dashed lines) for  $^{12}\text{C}^{16}\text{O}$  (purple) and  $^{13}\text{C}^{18}\text{O}$  (orange) are depicted. Shaded areas show the uncertainty intervals for 99% confidence level according to Wilson score intervals framework [347]. (Bottom) Corresponding desorption rate obtained during 50 ps. Raw noisy desorption rates (translucent lines) were obtained from desorption probabilities by numerical differentiation. Smooth desorption rates (thick lines) were obtained after applying a fifth order noise-reduction spline interpolation over raw desorption probabilities. Desorption rates during the first 10 ps are depicted in the inset. . . . . 155
- 6.3 Quasiclassical vibrational state distribution of  $^{12}\text{C}^{16}\text{O}$  and  $^{13}\text{C}^{18}\text{O}$ . Upper graph row corresponds to  $(T_e, T_1)$  – MDEF  $^{12}\text{C}^{16}\text{O}$  (blue) and  $^{13}\text{C}^{18}\text{O}$  (red) while bottom ones stand for  $T_1$ –MDEF  $^{12}\text{C}^{16}\text{O}$  (purple) and  $^{13}\text{C}^{18}\text{O}$  (orange) data sets. For each smaller graph, a distinction between molecules in their vibrational ground state ( $v = 0$ ) or after undergoing vibrational excitation ( $v > 0$ ) is made. Error bars reflect the standard deviation as for binomial distributions. Left column of panels display vibrational state probabilities with respect to total amounts of desorbed CO species. Right column shows results for the CO molecules that desorbed with the larger translational kinetic energies,  $E_{\text{kin}}^{\text{trans}} \geq 0.67$  eV –or, alternatively,  $T \geq 5200$  K– (see text). 156
- 7.1 Top view of minimum energy configurations obtained with the multicoverage EANN PES for 0.33 ML (top) and 0.75 ML (bottom panel). The supercells considered in our  $(T_e, T_1)$ –MDEF simulations are represented in solid lines. Grey dashed lines show the smallest pattern that is repeated within supercells. . . . . 161

7.2	Potential energy $E_0$ in terms of the CO CM height $z_{\text{cm,CO}}$ for one CO species desorbing along its site-specific minimum energy path from a 0.33 ML CO/Pd(111) adsorption site –fcc, in blue– and the three possible adsorption sites in 0.75 ML, namely top (black), hcp (red) and fcc (green). Solid lines represent the 0.33 ML EANN PES energy calculations while dashed lines stand for the energies obtained with DFT+vdW-DF of Ref. [31]. For both sets of plots, solid dots correspond to the data points used. In each curve, the energy and the height are referred to the values obtained at the bottom of the corresponding well, $E_0^{\text{well}}$ and $z_{\text{cm,CO}}^{\text{well}}$ respectively. A close-up of the plot in the range [0.0, 1.7] eV is also depicted in the inset for a clearer comparison between the 0.33 ML potential energy curves.	163
7.3	Potential energy $E_0$ in terms of the CO CM height $z_{\text{cm,CO}}$ for one CO species desorbing along its site-specific minimum energy path from a 0.33 ML CO/Pd(111) adsorption site –fcc, in blue– and the three possible adsorption sites in 0.75 ML, namely top (black), hcp (red) and fcc (green). Solid lines represent the 0.75 ML EANN PES energy calculations while dashed lines stand for the energies obtained with DFT+vdW-DF of Ref. [31]. For both sets of plots, solid dots correspond to the data points used. In each curve, the energy and the height are referred to the values obtained at the bottom of the corresponding well, $E_0^{\text{well}}$ and $z_{\text{cm,CO}}^{\text{well}}$ respectively. . . . .	165
7.4	Linear fit of the energies of the configurations in the 0.33 ML CO/Pd(111) surface predicted by the 0.75 ML CO/Pd(111) PES of Ref. [87] versus their $(T_e, T_l)$ – AIMDEF counterparts taken from Ref. [31]. The slope of the fitting line has been fixed as $m = 1$ and only the value of the y-intercept "b" has been fitted. . . . .	168
7.5	Comparison of the potential energies per moving atom, $E^{\text{EANN}}/N_{\text{mov}}$ , computed as determined by the multicoverage EANN PES against their corresponding DFT values, $E^{\text{DFT}}/N_{\text{mov}}$ , for a set of 116 927 0.33 ML $(T_e, T_l)$ – AIMDEF configurations missing from the training data. . . . .	170
7.6	Comparison of the potential energies per moving atom, $E^{\text{EANN}}/N_{\text{mov}}$ , computed as determined by the multicoverage EANN PES against their corresponding DFT values $E^{\text{DFT}}/N_{\text{mov}}$ , for a set of 87 382 0.75 ML $(T_e, T_l)$ – AIMDEF configurations missing from the training data. . . . .	171

- 7.7 Potential energy  $E_0$  against the CO CM height  $z_{\text{cm,CO}}$  for one CO species desorbing along its site-specific minimum energy path from a 0.33 ML CO/Pd(111) adsorption site –fcc, in blue– and the three possible adsorption sites in 0.75 ML, namely top (black), hcp (red) and fcc (green). Solid lines represent the multicoverage EANN PES energy calculations while dashed lines stand for the energies obtained with DFT+vdW-DF of Ref. [31]. In all cases, solid dots correspond to the data points used. In each curve, the energy and the height are referred to the values obtained at the bottom of the corresponding well,  $E_0^{\text{well}}$  and  $z_{\text{cm,CO}}^{\text{well}}$  respectively. . . . . 173
- 7.8 Comparison of the potential energies per moving atom,  $E^{\text{EANN}}/N_{\text{mov}}$ , computed as determined by the multicoverage EANN PES against their corresponding DFT values  $E^{\text{DFT}}/N_{\text{mov}}$ , for a set of 1446 0.60 ML ( $T_e, T_l$ ) – AIMDEF configurations. Among the latter ensemble, 114, 120, and 1212 data points have been obtained under incident laser fluences of 85, 95, and 115 J/m<sup>2</sup>, respectively. . . . . 176
- 7.9 Top view of minimum energy configurations obtained with the multicoverage EANN PES for 0.60 ML of CO coverage. Top structure corresponds to a local minimum higher in energy than the bottom structure. The supercells used in our ( $T_e, T_l$ ) – MDEF simulations are represented in solid lines. Grey dashed lines indicate the smallest pattern that is repeated within supercells. . . . . 178
- 7.10 Time evolution of the electronic temperature,  $T_e$ , (left panel) and the lattice temperature for the three topmost Pd surface layers,  $T_l$ , (right panel), as determined with 2TM (solid lines) for different pulse laser fluences. Dashed lines show the mean temperature of the three topmost mobile Pd layers in ( $T_e, T_l$ ) – MDEF calculations. The incoming laser pulse is assumed to reach its peak intensity at time zero, and its FWHM is represented as the gray shaded region. 179
- 7.11 Electronic heat capacity coefficient  $c_e$  in palladium as a function of the electronic temperature. The  $c_e(T_e)$  considered in our calculations is shown as the solid green line. This result is obtained from a fit to previous experimental data of Shimizu *et al.* (1963) [352] (orange line), Müller *et al.* (1968) [353] (black dots), and Müller *et al.* (1971) [354] (red dots). For reference, a previous fit of  $c_e(T_e)$  due to Szymanski *et al.* (2007) [38] is also depicted with a dashed blue line.  $c_e(0)$  has been derived from the heat capacity low temperature measurements in Veal *et al.* (1964) [355] (dotted pink line). . . . . 180

7.12 CO desorption probability against the absorbed fluence for different initial coverages. Reddish, bluish, and greenish full circles stand for  $(T_e, T_1)$  – MDEF theoretical results for 0.75, 0.60, and 0.33 ML coverages, respectively, with varying simulation cell size. Darker red, blue, and green triangles correspond to the experimental results of Ref. [30] for 0.75, 0.64, and 0.24 ML coverages, respectively. Each set of data points has been fitted to a log-linear function (solid lines). 184

7.13 CO desorption probability as a function of coverage for fixed absorbed fluence  $77.6 \text{ J/m}^2$ . Theoretical data points for each adlayer, depicted as red crosses, have been computed from log-linear extrapolation at the required fluence of left graph data fit for the larger supercell size considered. Experimental data points, shown as blue dots with their respective uncertainty intervals, are taken from Ref. [30]. . . . . 186

7.14 Time evolution of the average CO desorption probability  $P_{\text{des}}(t)$  along the full dynamics integration time of 100 ps.  $(T_e, T_1)$  – MDEF,  $T_e$  – MDEF and  $T_1$  – MDEF results are depicted in full, dotted, and dashed lines, respectively. Left: MDEF results obtained for the 0.33 ML adlayer and fluences  $100 \text{ J/m}^2$  (blue, bottom left), and  $130 \text{ J/m}^2$  (red, top left). Right: MDEF results obtained for the 0.75 ML adlayer and fluences  $60 \text{ J/m}^2$  (blue),  $70 \text{ J/m}^2$  (green), and  $80 \text{ J/m}^2$  (red). . . . . 189

7.15 Close-up of the time evolution of the average CO desorption probability  $P_{\text{des}}(t)$  (Fig. 7.14) along the early stage of photodesorption process ranging the initial 20 ps.  $(T_e, T_1)$  – MDEF,  $T_e$  – MDEF and  $T_1$  – MDEF results are plotted in full, dotted, and dashed lines, respectively. Left: MDEF results for the 0.33 ML adlayer and fluences  $100 \text{ J/m}^2$  (blue), and  $130 \text{ J/m}^2$  (red). Right: MDEF results obtained for the 0.75 ML adlayer and fluences  $60 \text{ J/m}^2$  (blue),  $70 \text{ J/m}^2$  (green), and  $80 \text{ J/m}^2$  (red). . . . . 190

7.16 Distribution of the CO CM coordinates for the CO/Pd(111) system over the Pd surface for all dynamics times and different ranges of heights, centered at the values  $z_{\text{cen}}$  written in the top left part of each subplot, and measured from the Pd topmost layer. For each panel, CO positions are contained within the intervals  $[z_{\text{cen}} - 0.5, z_{\text{cen}} + 0.5) \text{ \AA}$ . Current results correspond to an incident laser fluence  $F = 80 \text{ J/m}^2$  and an adlayer of 0.75 ML. . . . . 191

- 7.17 Probability density map of CO CM height,  $z_{\text{cm,CO}}$ , computed from the topmost Pd layer,  $\bar{z}_{\text{surf}}$ , as a function of time. From top to bottom, results are shown in increasing coverage order: 0.33 ML (top), 0.60 ML (middle), and 0.75 ML (bottom). From left to right, results are sorted in increasing incident laser fluence, which varies between coverages: 100 J/m<sup>2</sup> (top left), 130 J/m<sup>2</sup> (top right), 85 J/m<sup>2</sup> (middle left), 115 J/m<sup>2</sup> (middle right), 60 J/m<sup>2</sup> (bottom left), and 80 J/m<sup>2</sup> (bottom right). White and cyan full lines mark examples of direct CO desorption and desorption after transient trapping, respectively. . . . . 192
- 7.18 Polar angle distributions of the desorbing CO calculated for the combination of coverage and laser fluence indicated on top of each plot (blue histograms). For each graph, the angular distribution of the molecules that desorb directly (green) and after being transiently trapped in the physisorption region (red) are depicted separately. Dashed lines mark the mean polar angle for each distribution, where the same color code is utilized. . . . . 194
- 7.19 Two-pulse correlation measurements [30] (blue) and the results of  $(T_e, T_1) - \text{MDEF}$  simulations with the corresponding Wilson error bars (green) of the CO desorption probability against the time delay between the two pulses. The initial coverage is 0.24 ML in the experiments and 0.33 ML in the theoretical calculations. The theoretical probabilities are multiplied by 17.27, the average of the ratio  $P_{\text{des}}^{\text{exp}}(\Delta t)/P_{\text{des}}^{(T_e, T_1) - \text{MDEF}}(\Delta t)$ . . . . . 198
- 7.20 Two-pulse correlation measurements [30] (blue) and the results of  $(T_e, T_1) - \text{MDEF}$  simulations with the corresponding Wilson error bars (green) of the CO desorption probability against the time delay between the two pulses. The initial coverage is 0.75 ML. The theoretical probabilities are multiplied by 2.44, the average of the ratio  $P_{\text{des}}^{\text{exp}}(\Delta t)/P_{\text{des}}^{(T_e, T_1) - \text{MDEF}}(\Delta t)$ . . . . . 199

7.21 (Left y axis) Two-pulse correlation measurements [30] (blue) and the results of  $(T_e, T_l) - \text{MDEF}$  simulations with the corresponding Wilson error bars (green) of the CO desorption probability against the time delay between the two pulses. The theoretical probabilities are multiplied by 17.27, the average of the ratio  $P_{\text{des}}^{\text{exp}}(\Delta t)/P_{\text{des}}^{(T_e, T_l) - \text{MDEF}}(\Delta t)$ . (Right y axis) Maximum  $T_e$  (orange) and maximum  $T_l$  (violet) as obtained from the 2TM as a function of the time delay. The initial coverage is 0.24 ML in the experiments and 0.33 ML in the theoretical calculations. . . . . 201

7.22 (Left y axis) Two-pulse correlation measurements [30] (blue) and the results of  $(T_e, T_l) - \text{MDEF}$  simulations with the corresponding Wilson error bars (green) of the CO desorption probability against the time delay between the two pulses. The theoretical probabilities are multiplied by 2.44, the average of the ratio  $P_{\text{des}}^{\text{exp}}(\Delta t)/P_{\text{des}}^{(T_e, T_l) - \text{MDEF}}(\Delta t)$ . (Right y axis) Maximum  $T_e$  (orange) and maximum  $T_l$  (violet) as obtained from the 2TM as a function of the time delay. The initial coverage is 0.75 ML. . . . . 202

8.1 Top, perspective, and side views of the optimized O+2CO/Pd(111) surface. The  $4 \times 2$  surface cell is depicted by the yellow parallelogram. 209

8.2 Normalized adsorbates temperature distributions for the configurations explored during thermalization. Histograms are plotted for the total configurational set (solid blue bars) and for selected subsets (empty bars) corresponding to time intervals [0,3.5] ps (red), [3.5,7.0] ps (green) and [7.0,10.0] ps (cyan). All histograms adjust approximately in shape to the theoretical Maxwell-Boltzmann distribution for  $T_0 = 90$  K and  $N_{\text{at}} = 10$  atoms (orange, solid line), but the nominal temperature is only reached during the last 3 ps. . . . 210

8.3 Normalized temperature distributions for the configurations explored during thermalization by the Pd atoms connected to the thermostat. Histograms are plotted for the total configurational set (solid blue bars) and for selected subsets (empty bars) corresponding to the time intervals [0,3.5] ps (red), [3.5,7.0] ps (green) and [7.0,10.0] ps (cyan). All histograms follow rather well the shape of the theoretical Maxwell-Boltzmann distribution for  $T_0 = 90$  K with  $N_{\text{at}} = 24$  atoms (orange, solid lines). . . . . 211

8.4	Probability density map of CO CM heights $z_{\text{cm,CO}}$ and O heights $z_{\text{O}}$ respect to the topmost Pd layer $\bar{z}_{\text{surf}}$ (dashed black line) as a function of time. Different panels correspond to results obtained in $(T_e, T_l)$ – AIMDEF with $F = 72 \text{ J/m}^2$ (top), $(T_e, T_l)$ – AIMDEF with $F = 130 \text{ J/m}^2$ (middle), and $T_e$ – AIMDEF with $F = 130 \text{ J/m}^2$ (bottom). CO heights are shown in colors from dark blue to dark red, while the color palette for O ranges from cyan to pink. White full lines correspond to those CO molecules that undergo recombinative oxidation with one fcc O atom. Trapping region is considered to be between the dotted white and light green lines, while CO surpassing the dotted green line is counted as desorbed. . . . .	214
8.5	Density plots of the $(x, y)$ coordinates of the CO CM (left column) and O adsorbates (right column) when reaching the height $z_0 \pm \Delta z$ at any instant along the trajectory in the $(T_e, T_l)$ – AIMDEF simulations at $F = 72 \text{ J/m}^2$ . The $z_0$ value is written in the top left part of each subplot, with $\Delta z = 1$ and $0.5 \text{ \AA}$ for CO and O, respectively. For reference, topmost subplots in each column show initial CO and O positions as blue and yellow dots, respectively. . . . .	215
8.6	Same as Fig. 8.5 but for $(T_e, T_l)$ – AIMDEF simulations at $F = 130 \text{ J/m}^2$ .	216
8.7	Same as Fig. 8.5 but for $T_e$ – AIMDEF simulations at $F = 130 \text{ J/m}^2$ .	217
8.8	Time evolution of the CO desorption probability $P_{\text{des}}(t)$ from the O+2CO/Pd(111) surface as obtained in the $(T_e, T_l)$ – AIMDEF simulations for $F = 70 \text{ J/m}^2$ (orange) and $F = 130 \text{ J/m}^2$ (blue). Results for $T_e$ – AIMDEF and $F = 130 \text{ J/m}^2$ are plotted in green. For comparison, also the desorption probability from 0.75 ML CO/Pd(111) calculated with $(T_e, T_l)$ – AIMDEF for $F = 130 \text{ J/m}^2$ is shown in red. Data points with their respective Wilson score intervals [347] are plotted every 500 fs. . . . .	220
8.9	Site-resolved average kinetic energy $\langle E_{\text{kin}} \rangle$ of the CO molecules that remain adsorbed on O+2CO/Pd(111) as obtained in the $(T_e, T_l)$ – AIMDEF simulations for the two different laser fluences. . . . .	223
8.10	Site-resolved average translational and rovibrational kinetic energies, $\langle E_{\text{kin}}^{\text{trans}} \rangle$ and $\langle E_{\text{kin}}^{\text{rovib}} \rangle$ of the CO molecules that remain adsorbed on O+2CO/Pd(111) as obtained in the $(T_e, T_l)$ – AIMDEF simulations for the two different laser fluences. . . . .	224



# List of Tables

---

- 5.1 Results of the tests for EANN PES training regarding the selection of an optimal NN architecture. For each set of architectures, five PES have been generated. Four parameters have been evaluated: the computational time elapsed per iteration  $\bar{t}_{\text{comp}}$ , the average amount of training steps  $\bar{N}_{\text{iter}}$  with its standard deviation  $\sigma_{N_{\text{iter}}}$ , and the average cost function values for both train and test/validation sets,  $\bar{S}^{\text{train}}(\mathbf{w})$  and  $\bar{S}^{\text{test}}(\mathbf{w})$ , respectively. For all tests, the following set of EANN parameters is chosen:  $\eta_E = 1$ ,  $\eta_F \approx 0.096$  ( $W_F = 1$ ),  $L = 3$  ( $l = 0, 1, 2, 3$ ),  $N_\varphi = 15$  GTOs,  $\Delta S_c = 10^{-2}$  and  $r_c = 6.5 \text{ \AA}$  (see text for the values of other EANN quantities related to this choice). 120
- 5.2 Results of the tests for different values of the EANN parameters fixing 60-60 architecture and  $\eta_E = 1$ . For each test, five PES have been generated. Evaluated quantities are the maximum angular momentum  $L$  –for which admissible angular momenta values are  $l = 0, 1, \dots, L-$ , the number of GTOs  $N_\varphi$ , the factor  $W_F$  (see Eq. (5.1)) related to the force weight prefactor  $\eta_F$  in the cost function  $S(\mathbf{w})$  (Eq. (4.23)) and the cutoff radius of the embedded atom environments  $r_c$ . Reference values we try changes on are  $L = 3$ ,  $N_\varphi = 15$ ,  $W_F = 1$ ,  $\Delta S_c = 10^{-2}$  and  $r_c = 6.5 \text{ \AA}$ . Four parameters have been evaluated: the computational time elapsed per iteration  $\bar{t}_{\text{comp}}$ , the average amount of training steps  $\bar{N}_{\text{iter}}$  with its standard deviation  $\sigma_{N_{\text{iter}}}$ , and the average cost function values for both train and test/validation sets,  $\bar{S}^{\text{train}}(\mathbf{w})$  and  $\bar{S}^{\text{test}}(\mathbf{w})$ , respectively. Number of moving atoms for 0.75 ML CO/Pd(111) is  $N_{\text{moving}} = 36$ . . . . . 123

- 5.3 Maximum absolute-valued errors and RMSEs per moving atom in energies and forces, and maximum errors set mean absolute errors (MESMAEs) of all moving atoms in forces predicted by the first and final PESs (see text) for 0.75 ML CO/Pd(111) ( $T_e$ ,  $T_l$ ) – AIMDEF configurations selected from Ref. [31]. First and second data columns corresponds to the energy and force errors linked to PES predictions on a set of 87 382 configurations following the ( $T_e$ ,  $T_l$ ) – AIMDEF representativeness criteria as described in Section 5.2.1. Last column shows the energy and force errors after predicting energies and atomic forces on all 352 505 ( $T_e$ ,  $T_l$ ) – AIMDEF available data points. In all cases  $N_{\text{moving}} = 36$ . . . . . 127
- 7.1 Maximum absolute-valued errors and RMSEs in energies per moving atom and forces, and maximum errors set mean absolute errors (MESMAEs) of all moving atoms in forces predicted by the first and final PESs (see text) for 0.33 ML CO/Pd(111) ( $T_e$ ,  $T_l$ ) – AIMDEF configurations selected from Ref. [31]. Both error data columns correspond to the energy and force errors linked to PES predictions on a set of 116 927 configurations following the ( $T_e$ ,  $T_l$ ) – AIMDEF representativeness criteria as described in Section 5.2.1. Here,  $N_{\text{moving}} = 33$ . 166
- 7.2 Maximum absolute-valued errors and RMSEs in the energies per moving atom and in the atomic forces, and MESMAEs for all moving atoms in forces predicted by the final multicoverage EANN PES on predict AIMDEF data points. Two distinctions are made, the first one between the type of dynamics simulations, namely  $T_e$  – AIMDEF and ( $T_e$ ,  $T_l$ ) – AIMDEF, and the subsequent second one among the two CO coverages we have AIMDEF data for, 0.33 ML and 0.75 ML. The number of AIMDEF configurations of each predict subset are given explicitly. Total number of moving atoms  $N_{\text{moving}}$  is 33 for 0.33 ML and 36 for 0.75 ML. . . . . 169
- 7.3 Comparison of site-specific desorption energies, in eV, calculated with the CO/Pd(111) multicoverage EANN PES and with DFT+vdW-DF, shown with the format  $E_{\text{des}}^{\text{EANN}}/E_{\text{des}}^{\text{DFT}}$ . Such energies are defined as the ones required to desorb one CO from Pd(111) for 0.33 ML, 0.60 ML, and 0.75 ML adlayers. Previously estimated experimental desorption energies for 0.24 ML, 0.64 ML, and 0.75 ML (top site) were equal to 1.38, 0.78, and 0.50 eV, respectively, as reported elsewhere [30]. 174

7.4	Maximum absolute-valued errors and RMSEs in the energies per moving atom and forces, and MESMAEs of all moving atoms in forces predicted by our final multicoverage PES on three sets of $(5 \times 2\sqrt{3})_{\text{rect}}$ 0.60 ML CO/Pd(111) $(T_e, T_1)$ – AIMDEF configurations randomly chosen from previous $(T_e, T_1)$ – MDEF calculations. For all sets, $N_{\text{moving}} = 84$ . . . . .	174
7.5	Fitting parameters used for Pd $c_e(T_e)$ (Eq. (7.4)) according to previous experimental data of Refs. [352, 353, 354]. . . . .	180
7.6	Computed $(T_e, T_1)$ – MDEF theoretical ( $n_{\text{th}}$ ) and experimental [30] ( $n_{\text{exp}}$ ) values of the exponent $n$ in the power law $P_{\text{des}} \propto F^n$ for CO/Pd(111) femtosecond laser-induced desorption. Values are provided for various CO coverages. Among theoretical calculations, cross products indicate the dimensions of the particular supercell considered. . . . .	183
7.7	Fluences of the strong laser pulse, $F^{\text{strong}}$ , weak laser pulse, $F^{\text{weak}}$ , their sum, $F^{\text{sum}}$ , and the half width at half maximum for negative (HWHM <sup>-</sup> ) and positive (HWHM <sup>+</sup> ) time delays obtained in the 2PC measurements of CO desorption from Pd(111) by Hong <i>et al.</i> [30] and in our $(T_e, T_1)$ – MDEF simulations (Fig. 7.19) . . . . .	197
8.1	Energy of the optimized 0.75 ML O+2CO/Pd(111) surface calculated with VASP for different adsorption site arrangements of CO and O. Note that the energy that VASP provides is the system cohesive energy with respect to spherical non spin-polarized atoms. The minimum energy arrangement corresponds to placing the O atoms at fcc sites. . . . .	208
8.2	Total probabilities at $t = 4.0$ ps obtained for O+2CO/Pd(111) with different AIMDEF simulations and absorbed laser fluence. $N^{\text{CO,tot}}$ is the total number of initially adsorbed CO in each simulation type; $P_{\text{CO,des}}(\mathbf{t})$ and $P_{\text{CO}_2,\text{des}}(\mathbf{t})$ are the CO and CO <sub>2</sub> desorption probabilities, respectively; $r_{\text{CO,CO}_2}(\mathbf{t})$ is the branching ratio between CO desorption and oxidation; and $P_{\text{CO}}(\mathbf{t})$ is the CO trapping probability. For comparison, the $(T_e, T_1)$ – AIMDEF results for 0.75 ML CO/Pd(111) and a laser fluence of 130 J/m <sup>2</sup> are written as well. . . . .	218

8.3	Adsorption site-resolved probabilities at $t = 4.0$ ps obtained for O+2CO/Pd(111) with different AIMDEF simulations and absorbed laser fluence. $N^{\text{CO,site}}$ is the total number of desorbed CO that were initially at this specific site, superscript * indicates how much CO desorbed after recombining with an fcc O atom and forming CO <sub>2</sub> , but this has not been accounted for calculation of the desorption probability fraction per site $\chi_{\text{CO,des}}^{\text{site}}$ due to the different chemical process they undergo. For comparison also the (T <sub>e</sub> , T <sub>l</sub> ) – AIMDEF results for 0.75 ML CO/Pd(111) and a laser fluence of 130 J/m <sup>2</sup> are also written. Results are provided for desorbed (I) and trapped CO (II).	221
8.4	Site-specific desorption energy $E_{\text{des}}^{\text{DFT}}$ for desorbing one CO from O+2CO/Pd(111) and 0.75 ML CO/Pd(111), calculated with DFT+vdW-DF using the computational settings described in Section 8.1. All energies are in eV. . . . .	222

# Bibliography

---

- [1] **CRC Handbook of Chemistry and Physics: A Ready-Reference of Chemical and Physical Data**. 85th. CRC Press LLC, Boca Raton (2004). ISBN: 0-8493-0485-7 (see page 1).
- [2] B. D. Adams and A. Chen. **The role of palladium in a hydrogen economy**. *Mater. Today* **14**, 6, 282–289 (2011). DOI: [10.1016/S1369-7021\(11\)70143-2](https://doi.org/10.1016/S1369-7021(11)70143-2) (see page 1).
- [3] W.-J. Shen, M. Okumura, Y. Matsumura, and M. Haruta. **The influence of the support on the activity and selectivity of Pd in CO hydrogenation**. *Appl. Catal. A-Gen.* **213**, 2, 225–232 (2001). DOI: [10.1016/S0926-860X\(01\)00465-3](https://doi.org/10.1016/S0926-860X(01)00465-3) (see page 1).
- [4] G. Rothenberg. **Heterogeneous Catalysis**, 127–187. In: *Catalysis*. Ed. by G. Rothenberg. John Wiley & Sons, Ltd, Chichester, UK (2008). ISBN: 9783527621866. DOI: [10.1002/9783527621866.ch4](https://doi.org/10.1002/9783527621866.ch4) (see pages 1, 55).
- [5] D. Rainer, S. Vesecky, M. Koranne, W. Oh, and D. Goodman. **The CO+NO Reaction over Pd: A Combined Study Using Single-Crystal, Planar-Model-Supported, and High-Surface-Area Pd/Al<sub>2</sub>O<sub>3</sub>Catalysts**. *J. Catal.* **167**, 1, 234–241 (1997). DOI: [10.1006/jcat.1997.1571](https://doi.org/10.1006/jcat.1997.1571) (see page 1).
- [6] Y. Zheng, Q. Qiao, J. Wang, X. Li, and J. Jian. **Gas sensing behavior of palladium oxide for carbon monoxide at low working temperature**. *Sens. Actuators B Chem.* **212**, 256–263 (2015). DOI: [10.1016/j.snb.2015.02.035](https://doi.org/10.1016/j.snb.2015.02.035) (see page 1).
- [7] Y. Zhou, Z. Wang, and C. Liu. **Perspective on CO oxidation over Pd-based catalysts**. *Catal. Sci. Technol.* **5**, 69–81 (2015). DOI: [10.1039/C4CY00983E](https://doi.org/10.1039/C4CY00983E) (see page 1).
- [8] G. I. Golodets. **Chapter X: The Oxidation of Carbon Monoxide**, 280–311. In: *Heterogeneous Catalytic Reactions Involving Molecular Oxygen*. Vol. 15. Studies in Surface Science and Catalysis. Elsevier, Amsterdam (1983). DOI: [10.1016/S0167-2991\(08\)64835-1](https://doi.org/10.1016/S0167-2991(08)64835-1) (see page 1).
- [9] X. Xie, Y. Li, Z.-Q. Liu, M. Haruta, and W. Shen. **Low-temperature oxidation of CO catalysed by Co<sub>3</sub>O<sub>4</sub> nanorods**. *Nature* **458**, 7239, 746–749 (2009). DOI: [10.1038/nature07877](https://doi.org/10.1038/nature07877) (see page 1).

- [10] C. V. S. Almeida, F. Colmati, E. G. Ciapina, K. I. B. Eguiluz, and G. R. Salazar-Banda. **Nanowires of Pd and Pd alloys for fuel cell applications: A review of the current state-of-the-art.** *J. Electroanal. Chem.* **955**, 118073 (2024). DOI: 10.1016/j.jelechem.2024.118073 (see page 1).
- [11] X. Chen, L. P. Granda-Marulanda, I. T. McCrum, and M. T. M. Koper. **How palladium inhibits CO poisoning during electrocatalytic formic acid oxidation and carbon dioxide reduction.** *Nat. Commun.* **13**, 1, 38 (2022). DOI: 10.1038/s41467-021-27793-5 (see page 1).
- [12] C. Torborg and M. Beller. **Recent Applications of Palladium-Catalyzed Coupling Reactions in the Pharmaceutical, Agrochemical, and Fine Chemical Industries.** *Adv. Synth. Catal.* **351**, 18, 3027–3043 (2009). DOI: 10.1002/adsc.200900587 (see page 1).
- [13] A. Kolmakov, D. O. Klenov, Y. Lilach, S. Stemmer, and M. Moskovits. **Enhanced Gas Sensing by Individual SnO<sub>2</sub> Nanowires and Nanobelts Functionalized with Pd Catalyst Particles.** *Nano Lett.* **5**, 4, 667–673 (2005). DOI: 10.1021/nl050082v (see page 1).
- [14] N. Barsan, D. Koziej, and U. Weimar. **Metal oxide-based gas sensor research: How to?** *Sens. Actuators B Chem.* **121**, 1, 18–35 (2007). DOI: 10.1016/j.snb.2006.09.047 (see page 1).
- [15] Y. Lee, H. Huang, O. Tan, and M. Tse. **Semiconductor gas sensor based on Pd-doped SnO<sub>2</sub> nanorod thin films.** *Sens. Actuators B Chem.* **132**, 1, 239–242 (2008). DOI: 10.1016/j.snb.2008.01.028 (see page 1).
- [16] P. Saalfrank. **Quantum Dynamical Approach to Ultrafast Molecular Desorption from Surfaces.** *Chem. Rev.* **106**, 10, 4116–4159 (2006). DOI: 10.1021/cr0501691 (see pages 2, 3, 55, 60, 66).
- [17] M. Tüshaus, W. Berndt, H. Conrad, A. M. Bradshaw, and B. Persson. **Understanding the Structure of High Coverage CO Adlayers.** *Appl. Phys. A* **51**, 2, 91–98 (1990). DOI: 10.1007/BF00324270 (see pages 2, 177, 183, 227).
- [18] H. Conrad, G. Ertl, and J. Küppers. **Interactions between oxygen and carbon monoxide on a Pd(111) surface.** *Surf. Sci.* **76**, 2, 323–342 (1978). DOI: 10.1016/0039-6028(78)90101-2 (see pages 2, 227).
- [19] H. Ohtani, M. V. Hove, and G. Somorjai. **Leed intensity analysis of the surface structures of Pd(111) and of CO adsorbed on Pd(111) in a ( $\sqrt{3} \times \sqrt{3}$ )R30° arrangement.** *Surf. Sci.* **187**, 2, 372–386 (1987). DOI: 10.1016/S0039-6028(87)80063-8 (see pages 2, 227).
- [20] F. M. Hoffmann. **Infrared reflection-absorption spectroscopy of adsorbed molecules.** *Surf. Sci. Rep.* **3**, 2, 107–192 (1983). DOI: 10.1016/0167-5729(83)90001-8 (see pages 2, 227).

- [21] W. Kuhn, J. Szanyi, and D. Goodman. **CO adsorption on Pd(111): the effects of temperature and pressure.** *Surf. Sci.* **274**, 3, L611–L618 (1992). DOI: 10.1016/0039-6028(92)90834-S (see pages 2, 227).
- [22] J. Butorac, E. L. Wilson, H. H. Fielding, W. A. Brown, and R. S. Minns. **A RAIRS, TPD and femtosecond laser-induced desorption study of CO, NO and coadsorbed CO + NO on Pd(111).** *RSC Adv.* **6**, 66346–66359 (2016). DOI: 10.1039/C6RA13722A (see page 2).
- [23] M. Morkel, G. Rupprechter, and H.-J. Freund. **Ultrahigh vacuum and high-pressure coadsorption of CO and H<sub>2</sub> on Pd(111): A combined SFG, TDS, and LEED study.** *J. Chem. Phys.* **119**, 20, 10853–10866 (2003). DOI: 10.1063/1.1619942 (see pages 2, 227).
- [24] T. Gießel, O. Schaff, C. Hirschmugl, V. Fernandez, K.-M. Schindler, A. Theobald, S. Bao, R. Lindsay, W. Berndt, A. Bradshaw, C. Baddeley, A. Lee, R. Lambert, and D. Woodruff. **A photoelectron diffraction study of ordered structures in the chemisorption system Pd111-CO.** *Surf. Sci.* **406**, 1, 90–102 (1998). DOI: 10.1016/S0039-6028(98)00098-3 (see pages 2, 227).
- [25] S. Surnev, M. Sock, M. Ramsey, F. Netzer, M. Wiklund, M. Borg, and J. Andersen. **CO adsorption on Pd(111): a high-resolution core level photoemission and electron energy loss spectroscopy study.** *Surf. Sci.* **470**, 1, 171–185 (2000). DOI: 10.1016/S0039-6028(00)00853-0 (see pages 2, 227).
- [26] M. Rose, T. Mitsui, J. Dunphy, A. Borg, D. Ogletree, M. Salmeron, and P. Sautet. **Ordered structures of CO on Pd(111) studied by STM.** *Surf. Sci.* **512**, 1, 48–60 (2002). DOI: 10.1016/S0039-6028(02)01560-1 (see pages 2, 187, 227).
- [27] D. Loffreda, D. Simon, and P. Sautet. **Dependence of stretching frequency on surface coverage and adsorbate–adsorbate interactions: a density-functional theory approach of CO on Pd (111).** *Surf. Sci.* **425**, 1, 68–80 (1999). DOI: 10.1016/S0039-6028(99)00186-7 (see pages 2, 227).
- [28] J. Zhang, Z. Wang, and Z. X. Wang. **Adsorption of carbon monoxide on Pd low-index surfaces and (110) reconstructed surface.** *Surf. Interface Anal.* **43**, 7, 1038–1045 (2011). DOI: 10.1002/sia.3687 (see pages 2, 227).
- [29] C. Fan and W.-D. Xiao. **Origin of site preference of CO and NO adsorption on Pd(111) at different coverages: A density functional theory study.** *Comput. Theor. Chem.* **1004**, 22–30 (2013). DOI: 10.1016/j.comptc.2012.10.027 (see pages 2, 227).

- [30] S.-Y. Hong, P. Xu, N. R. Camillone, M. G. White, and N. Camillone III. **Adlayer structure dependent ultrafast desorption dynamics in carbon monoxide adsorbed on Pd (111)**. *J. Chem. Phys.* **145**, 1, 014704 (2016). DOI: [10.1063/1.4954408](https://doi.org/10.1063/1.4954408) (see pages 2, 3, 6, 7, 61, 113, 158–160, 174, 175, 177, 181–187, 195–199, 201, 202, 204, 205, 212, 227, 247, 248, 252, 253).
- [31] M. Alducin, N. Camillone, S.-Y. Hong, and J. I. Juaristi. **Electrons and Phonons Cooperate in the Laser-Induced Desorption of CO from Pd(111)**. *Phys. Rev. Lett.* **123**, 246802 (2019). DOI: [10.1103/PhysRevLett.123.246802](https://doi.org/10.1103/PhysRevLett.123.246802) (see pages 2, 5, 7, 8, 77, 111, 112, 114, 117, 127, 130, 132, 134, 136–138, 140, 141, 143, 146, 149, 150, 157, 159, 160, 162, 163, 165, 166, 168, 173, 175, 181, 187, 188, 197, 203, 204, 207, 210, 212, 219, 227–229).
- [32] C. Frischkorn and M. Wolf. **Femtochemistry at Metal Surfaces: Nonadiabatic Reaction Dynamics**. *Chem. Rev.* **106**, 10, 4207–4233 (2006). DOI: [10.1021/cr050161r](https://doi.org/10.1021/cr050161r) (see pages 2, 3, 54, 55, 61, 62, 65, 66, 149, 179, 195, 196).
- [33] H. Guo, P. Saalfrank, and T. Seideman. **Theory of photoinduced surface reactions of admolecules**. *Prog. Surf. Sci.* **62**, 7, 239–303 (1999). DOI: [10.1016/S0079-6816\(99\)00013-1](https://doi.org/10.1016/S0079-6816(99)00013-1) (see pages 2, 3).
- [34] F. Budde, T. F. Heinz, M. M. T. Loy, J. A. Misewich, F. de Rougemont, and H. Zacharias. **Femtosecond time-resolved measurement of desorption**. *Phys. Rev. Lett.* **66**, 3024–3027 (1991). DOI: [10.1103/PhysRevLett.66.3024](https://doi.org/10.1103/PhysRevLett.66.3024) (see pages 3, 7, 56, 61, 62, 195).
- [35] J. A. Misewich, T. F. Heinz, and D. M. Newns. **Desorption induced by multiple electronic transitions**. *Phys. Rev. Lett.* **68**, 3737–3740 (1992). DOI: [10.1103/PhysRevLett.68.3737](https://doi.org/10.1103/PhysRevLett.68.3737) (see pages 3, 56, 60).
- [36] M. Bonn, S. Funk, C. Hess, D. N. Denzler, C. Stampfl, M. Scheffler, M. Wolf, and G. Ertl. **Phonon- Versus Electron-Mediated Desorption and Oxidation of CO on Ru(0001)**. *Science* **285**, 5430, 1042–1045 (1999). DOI: [10.1126/science.285.5430.1042](https://doi.org/10.1126/science.285.5430.1042) (see pages 3, 6, 7, 149, 195).
- [37] D. N. Denzler, C. Frischkorn, C. Hess, M. Wolf, and G. Ertl. **Electronic Excitation and Dynamic Promotion of a Surface Reaction**. *Phys. Rev. Lett.* **91**, 226102 (2003). DOI: [10.1103/PhysRevLett.91.226102](https://doi.org/10.1103/PhysRevLett.91.226102) (see pages 3, 5–7, 149, 195, 203).
- [38] P. Szymanski, A. L. Harris, and N. Camillone. **Adsorption-state-dependent subpicosecond photoinduced desorption dynamics**. *J. Chem. Phys.* **126**, 21, 214709 (2007). DOI: [10.1063/1.2735594](https://doi.org/10.1063/1.2735594) (see pages 3, 7, 180, 195, 212).
- [39] C. Springer, M. Head-Gordon, and J. C. Tully. **Simulations of Femtosecond Laser-Induced Desorption of CO from Cu(100)**. *Surf. Sci.* **320**, L57–L62 (1994) (see pages 3, 62).

- [40] C. Springer and M. Head-Gordon. **Simulations of the Femtosecond Laser-Induced Desorption of CO from Cu(100) at 0.5 ML Coverage.** *Chem. Phys.* **205**, 73–89 (1996) (see pages 3, 62).
- [41] A. C. Luntz, M. Persson, S. Wagner, C. Frischkorn, and M. Wolf. **Femtosecond Laser Induced Associative Desorption of H<sub>2</sub> from Ru(0001): Comparison of “First Principles” Theory with Experiment.** *J. Chem. Phys.* **124**, 244702 (2006) (see page 3).
- [42] T. Vazhappilly, T. Klamroth, P. Saalfrank, and R. Hernandez. **Femtosecond-Laser Desorption of H-2 (D-2) from Ru(0001): Quantum and Classical Approaches.** *J. Phys. Chem. C* **113**, 18, 7790–7801 (2009). DOI: 10.1021/jp810709k (see page 3).
- [43] G. Fuchsel, T. Klamroth, J. C. Tremblay, and P. Saalfrank. **Stochastic Approach to Laser-Induced Ultrafast Dynamics: The Desorption of H<sub>2</sub>/D<sub>2</sub> from Ru(0001).** *Phys. Chem. Chem. Phys.* **12**, 14082–14094 (2010). DOI: 10.1039/C0CP00895H (see page 3).
- [44] G. Fuchsel, T. Klamroth, S. Monturet, and P. Saalfrank. **Dissipative Dynamics within the Electronic Friction Approach: The Femtosecond Laser Desorption of H<sub>2</sub>/D<sub>2</sub> from Ru(0001).** *Phys. Chem. Chem. Phys.* **13**, 8659 (2011). DOI: 10.1039/c0cp02086a (see page 3).
- [45] I. Lončarić, M. Alducin, P. Saalfrank, and J. I. Juaristi. **Femtosecond-laser-driven molecular dynamics on surfaces: Photodesorption of molecular oxygen from Ag(110).** *Phys. Rev. B* **93**, 014301 (2016). DOI: 10.1103/PhysRevB.93.014301 (see pages 3, 4, 8, 73, 185).
- [46] I. Lončarić, M. Alducin, P. Saalfrank, and J. I. Juaristi. **Femtosecond Laser Pulse Induced Desorption: a Molecular Dynamics Simulation.** *Nucl. Instrum. Methods B* **382**, 114–118 (2016). DOI: 10.1016/j.nimb.2016.02.051 (see pages 3, 4, 8, 73).
- [47] R. Scholz, G. Floß, P. Saalfrank, G. Fuchsel, I. Lončarić, and J. I. Juaristi. **Femtosecond-Laser Induced Dynamics of CO on Ru(0001): Deep Insights from a Hot-Electron Friction Model Including Surface Motion.** *Phys. Rev. B* **94**, 16, 165447 (2016). DOI: 10.1103/PhysRevB.94.165447 (see pages 3, 4, 8, 73, 185).
- [48] I. Lončarić, G. Fuchsel, J. I. Juaristi, and P. Saalfrank. **Strong Anisotropic Interaction Controls Unusual Sticking and Scattering of CO at Ru(0001).** *Phys. Rev. Lett.* **119**, 146101 (2017). DOI: 10.1103/PhysRevLett.119.146101 (see pages 3, 4, 73).

- [49] R. Scholz, S. Lindner, I. Lončarić, J. C. Tremblay, J. I. Juaristi, M. Alducin, and P. Saalfrank. **Vibrational Response and Motion of Carbon Monoxide on Cu(100) Driven by Femtosecond Laser Pulses: Molecular Dynamics with Electronic Friction**. *Phys. Rev. B* **100**, 24, 245431 (2019). DOI: [10.1103/physrevb.100.245431](https://doi.org/10.1103/physrevb.100.245431) (see pages 3, 8).
- [50] S. I. Anisimov, B. L. Kapeliovich, and T. L. Perel'man. **Electron emission from metal surfaces exposed to ultrashort laser pulses**. *Zhurnal Eksperimentalnoi i Teoreticheskoi Fiziki* **39**, 2, 776–781 (1974). URL: <https://ui.adsabs.harvard.edu/abs/1974ZhETF..66..776A> (see pages 3, 8, 61, 64, 65).
- [51] J. I. Juaristi, M. Alducin, R. D. Muiño, H. F. Busnengo, and A. Salin. **Role of Electron-Hole Pair Excitations in the Dissociative Adsorption of Diatomic Molecules on Metal Surfaces**. *Phys. Rev. Lett.* **100**, 116102 (2008). DOI: [10.1103/PhysRevLett.100.116102](https://doi.org/10.1103/PhysRevLett.100.116102) (see pages 4, 8, 71, 73, 133).
- [52] M. Alducin, R. Díez Muiño, and J. Juaristi. **Non-adiabatic effects in elementary reaction processes at metal surfaces**. *Prog. Surf. Sci.* **92**, 4, 317–340 (2017). DOI: [10.1016/j.progsurf.2017.09.002](https://doi.org/10.1016/j.progsurf.2017.09.002) (see pages 4, 8, 71, 133).
- [53] S. A. Adelman and J. D. Doll. **Generalized Langevin equation approach for atom/solid-surface scattering: General formulation for classical scattering off harmonic solids**. *J. Chem. Phys.* **64**, 6, 2375–2388 (1976). DOI: [10.1063/1.432526](https://doi.org/10.1063/1.432526) (see pages 4, 73).
- [54] J. C. Tully. **Dynamics of gas–surface interactions: 3D generalized Langevin model applied to fcc and bcc surfaces**. *J. Chem. Phys.* **73**, 4, 1975–1985 (1980). DOI: [10.1063/1.440287](https://doi.org/10.1063/1.440287) (see pages 4, 73).
- [55] H. F. Busnengo, W. Dong, and A. Salin. **Trapping, Molecular Adsorption, and Precursors for Nonactivated Chemisorption**. *Phys. Rev. Lett.* **93**, 236103 (2004). DOI: [10.1103/PhysRevLett.93.236103](https://doi.org/10.1103/PhysRevLett.93.236103) (see pages 4, 73).
- [56] H. F. Busnengo, M. A. Di Césare, W. Dong, and A. Salin. **Surface temperature effects in dynamic trapping mediated adsorption of light molecules on metal surfaces: H<sub>2</sub> on Pd(111) and Pd(110)**. *Phys. Rev. B* **72**, 125411 (2005). DOI: [10.1103/PhysRevB.72.125411](https://doi.org/10.1103/PhysRevB.72.125411) (see pages 4, 73).
- [57] M. Blanco-Rey, J. I. Juaristi, R. Díez Muiño, H. F. Busnengo, G. J. Kroes, and M. Alducin. **Electronic Friction Dominates Hydrogen Hot-Atom Relaxation on Pd(100)**. *Phys. Rev. Lett.* **112**, 103203 (2014). DOI: [10.1103/PhysRevLett.112.103203](https://doi.org/10.1103/PhysRevLett.112.103203) (see pages 4, 8, 76, 77, 112).
- [58] P. Saalfrank, J. I. Juaristi, M. Alducin, M. Blanco-Rey, and R. D. Muiño. **Vibrational lifetimes of hydrogen on lead films: An ab initio molecular dynamics with electronic friction (AIMDEF) study**. *J. Chem. Phys.* **141**, 23, 234702 (2014). DOI: [10.1063/1.4903309](https://doi.org/10.1063/1.4903309) (see pages 4, 8, 77, 112).

- [59] D. Novko, M. Blanco-Rey, J. I. Juaristi, and M. Alducin. **Ab Initio Molecular Dynamics with Simultaneous Electron and Phonon Excitations: Application To The Relaxation of Hot Atoms and Molecules On Metal Surfaces.** *Phys. Rev. B* **92**, 201411 (2015). DOI: [10.1103/PhysRevB.92.201411](https://doi.org/10.1103/PhysRevB.92.201411) (see pages 4, 8, 78, 112).
- [60] D. Novko, M. Blanco-Rey, M. Alducin, and J. I. Juaristi. **Surface electron density models for accurate ab initio molecular dynamics with electronic friction.** *Phys. Rev. B* **93**, 245435 (2016). DOI: [10.1103/PhysRevB.93.245435](https://doi.org/10.1103/PhysRevB.93.245435) (see pages 4, 8, 77, 78, 112, 133).
- [61] D. Novko, M. Blanco-Rey, J. I. Juaristi, and M. Alducin. **Energy Loss in Gas-Surface Dynamics: Electron-Hole Pair and Phonon Excitation Upon Adsorbate Relaxation.** *Nucl. Instrum. Methods B* **382**, 26–31 (2016). DOI: [10.1016/j.nimb.2016.02.031](https://doi.org/10.1016/j.nimb.2016.02.031) (see pages 4, 8, 78, 112).
- [62] D. Novko, I. Lončarić, M. Blanco-Rey, J. I. Juaristi, and M. Alducin. **Energy loss and surface temperature effects in ab initio molecular dynamics simulations: N adsorption on Ag(111) as a case study.** *Phys. Rev. B* **96**, 085437 (2017). DOI: [10.1103/PhysRevB.96.085437](https://doi.org/10.1103/PhysRevB.96.085437) (see pages 4, 8, 74, 112).
- [63] A. Tetenoire, C. Ehlert, J. I. Juaristi, P. Saalfrank, and M. Alducin. **Why Ultrafast Photoinduced CO Desorption Dominates over Oxidation on Ru(0001).** *J. Phys. Chem. Lett.* **13**, 36, 8516–8521 (2022). DOI: [10.1021/acs.jpcclett.2c02327](https://doi.org/10.1021/acs.jpcclett.2c02327) (see pages 5, 7, 77).
- [64] A. Tetenoire, J. I. Juaristi, and M. Alducin. **Disentangling the Role of Electrons and Phonons in the Photoinduced CO Desorption and CO Oxidation on (O,CO)-Ru(0001).** *Front. Chem.* **11**, 1235176 (2023). DOI: [10.3389/fchem.2023.1235176](https://doi.org/10.3389/fchem.2023.1235176) (see pages 5, 7).
- [65] A. Tetenoire, J. I. Juaristi, and M. Alducin. **Photoinduced CO Desorption Dominates over Oxidation on Different O + CO Covered Ru(0001) Surfaces.** *J. Phys. Chem. C* **127**, 21, 10087–10096 (2023). DOI: [10.1021/acs.jpcc.3c01192](https://doi.org/10.1021/acs.jpcc.3c01192) (see pages 5, 7, 222).
- [66] J. I. Juaristi, M. Alducin, and P. Saalfrank. **Femtosecond laser induced desorption of H<sub>2</sub>, D<sub>2</sub>, and HD from Ru(0001): Dynamical promotion and suppression studied with ab initio molecular dynamics with electronic friction.** *Phys. Rev. B* **95**, 125439 (2017). DOI: [10.1103/PhysRevB.95.125439](https://doi.org/10.1103/PhysRevB.95.125439) (see pages 5, 8, 73, 112, 149).
- [67] C. M. Handley and P. L. A. Popelier. **Potential Energy Surfaces Fitted by Artificial Neural Networks.** *J. Phys. Chem. A* **114**, 10, 3371–3383 (2010). DOI: [10.1021/jp9105585](https://doi.org/10.1021/jp9105585) (see pages 5, 91, 92).

- [68] J. Behler. **Four Generations of High-Dimensional Neural Network Potentials**. *Chem. Rev.* **121**, 16, 10037–10072 (2021). DOI: [10.1021/acs.chemrev.0c00868](https://doi.org/10.1021/acs.chemrev.0c00868) (see pages 5, 82, 84, 86, 91–95, 100, 102).
- [69] B. G. Sumpter and D. W. Noid. **Potential energy surfaces for macromolecules. A neural network technique**. *Chem. Phys. Lett.* **192**, 5, 455–462 (1992). DOI: [10.1016/0009-2614\(92\)85498-Y](https://doi.org/10.1016/0009-2614(92)85498-Y) (see pages 5, 84, 91).
- [70] T. B. Blank, S. D. Brown, A. W. Calhoun, and D. J. Doren. **Neural network models of potential energy surfaces**. *J. Chem. Phys.* **103**, 10, 4129–4137 (1995). DOI: [10.1063/1.469597](https://doi.org/10.1063/1.469597) (see pages 5, 84, 91).
- [71] J. Behler and M. Parrinello. **Generalized neural-network representation of high-dimensional potential-energy surfaces**. *Phys. Rev. Lett.* **98**, 14, 1–4 (2007). DOI: [10.1103/PhysRevLett.98.146401](https://doi.org/10.1103/PhysRevLett.98.146401) (see pages 5, 93, 95, 105, 107).
- [72] V. Quaranta, M. Hellström, and J. Behler. **Proton-Transfer Mechanisms at the Water-ZnO Interface: The Role of Presolvation**. *J. Phys. Chem. Lett.* **8**, 7, 1476–1483 (2017). DOI: [10.1021/acs.jpcclett.7b00358](https://doi.org/10.1021/acs.jpcclett.7b00358) (see pages 6, 111).
- [73] M. Hellström, V. Quaranta, and J. Behler. **One-dimensional vs. two-dimensional proton transport processes at solid-liquid zinc-oxide-water interfaces**. *Chem. Sci.* **10**, 1232–1243 (2019). DOI: [10.1039/C8SC03033B](https://doi.org/10.1039/C8SC03033B) (see pages 6, 111).
- [74] H. Ghorbanfekr, J. Behler, and F. M. Peeters. **Insights into Water Permeation through hBN Nanocapillaries by Ab Initio Machine Learning Molecular Dynamics Simulations**. *J. Phys. Chem. Lett.* **11**, 17, 7363–7370 (2020). DOI: [10.1021/acs.jpcclett.0c01739](https://doi.org/10.1021/acs.jpcclett.0c01739) (see pages 6, 111).
- [75] B. Jiang and H. Guo. **Dynamics of Water Dissociative Chemisorption on Ni(111): Effects of Impact Sites and Incident Angles**. *Phys. Rev. Lett.* **114**, 166101 (2015). DOI: [10.1103/PhysRevLett.114.166101](https://doi.org/10.1103/PhysRevLett.114.166101) (see pages 6, 111).
- [76] X. Shen, J. Chen, Z. Zhang, K. Shao, and D. H. Zhang. **Methane dissociation on Ni(111): A fifteen-dimensional potential energy surface using neural network method**. *J. Chem. Phys.* **143**, 14, 144701 (2015). DOI: [10.1063/1.4932226](https://doi.org/10.1063/1.4932226) (see pages 6, 111).
- [77] B. Kolb, X. Luo, X. Zhou, B. Jiang, and H. Guo. **High-Dimensional Atomistic Neural Network Potentials for Molecule-Surface Interactions: HCl Scattering from Au(111)**. *J. Phys. Chem. Lett.* **8**, 3, 666–672 (2017). DOI: [10.1021/acs.jpcclett.6b02994](https://doi.org/10.1021/acs.jpcclett.6b02994) (see pages 6, 111, 113).
- [78] K. Shakouri, J. Behler, J. Meyer, and G.-J. Kroes. **Accurate Neural Network Description of Surface Phonons in Reactive Gas–Surface Dynamics: N<sub>2</sub> + Ru(0001)**. *J. Phys. Chem. Lett.* **8**, 10, 2131–2136 (2017). DOI: [10.1021/acs.jpcclett.7b00784](https://doi.org/10.1021/acs.jpcclett.7b00784) (see pages 6, 111).

- [79] Q. Liu, X. Zhou, L. Zhou, Y. Zhang, X. Luo, H. Guo, and B. Jiang. **Constructing High-Dimensional Neural Network Potential Energy Surfaces for Gas-Surface Scattering and Reactions.** *J. Phys. Chem. C* **122**, 3, 1761–1769 (2018). DOI: [10.1021/acs.jpcc.7b12064](https://doi.org/10.1021/acs.jpcc.7b12064) (see pages 6, 111).
- [80] J. Chen, X. Zhou, Y. Zhang, and B. Jiang. **Vibrational control of selective bond cleavage in dissociative chemisorption of methanol on Cu(111).** *Nat. Commun.* **9**, 1, 4039 (2018). DOI: [10.1038/s41467-018-06478-6](https://doi.org/10.1038/s41467-018-06478-6) (see pages 6, 111).
- [81] K. Shakouri, J. Behler, J. Meyer, and G.-J. Kroes. **Analysis of Energy Dissipation Channels in a Benchmark System of Activated Dissociation: N<sub>2</sub> on Ru(0001).** *J. Phys. Chem. C* **122**, 41, 23470–23480 (2018). DOI: [10.1021/acs.jpcc.8b06729](https://doi.org/10.1021/acs.jpcc.8b06729) (see pages 6, 111).
- [82] N. Gerrits, K. Shakouri, J. Behler, and G.-J. Kroes. **Accurate Probabilities for Highly Activated Reaction of Polyatomic Molecules on Surfaces Using a High-Dimensional Neural Network Potential: CHD<sub>3</sub> + Cu(111).** *J. Phys. Chem. Lett.* **10**, 8, 1763–1768 (2019). DOI: [10.1021/acs.jpcllett.9b00560](https://doi.org/10.1021/acs.jpcllett.9b00560) (see pages 6, 111).
- [83] Y. Zhang, X. Zhou, and B. Jiang. **Bridging the Gap between Direct Dynamics and Globally Accurate Reactive Potential Energy Surfaces Using Neural Networks.** *J. Phys. Chem. Lett.* **10**, 6, 1185–1191 (2019). DOI: [10.1021/acs.jpcllett.9b00085](https://doi.org/10.1021/acs.jpcllett.9b00085) (see pages 6, 111, 113, 228).
- [84] M. Huang, X. Zhou, Y. Zhang, L. Zhou, M. Alducin, B. Jiang, and H. Guo. **Adiabatic and nonadiabatic energy dissipation during scattering of vibrationally excited CO from Au(111).** *Phys. Rev. B* **100**, 201407 (2019). DOI: [10.1103/PhysRevB.100.201407](https://doi.org/10.1103/PhysRevB.100.201407) (see pages 6, 111, 172).
- [85] B. Jiang, J. Li, and H. Guo. **High-Fidelity Potential Energy Surfaces for Gas-Phase and Gas-Surface Scattering Processes from Machine Learning.** *J. Phys. Chem. Lett.* **11**, 13, 5120–5131 (2020). DOI: [10.1021/acs.jpcllett.0c00989](https://doi.org/10.1021/acs.jpcllett.0c00989) (see pages 6, 111).
- [86] A. Rivero Santamaría, M. Ramos, M. Alducin, H. F. Busnengo, R. Díez Muiño, and J. I. Juaristi. **High-Dimensional Atomistic Neural Network Potential to Study the Alignment-Resolved O<sub>2</sub> Scattering from Highly Oriented Pyrolytic Graphite.** *J. Phys. Chem. A* **125**, 12, 2588–2600 (2021). DOI: [10.1021/acs.jpca.1c00835](https://doi.org/10.1021/acs.jpca.1c00835) (see pages 6, 111).
- [87] A. Serrano Jiménez, A. P. S. Muzas, Y. Zhang, J. O. Ovčar, B. Jiang, I. Lončarić, J. I. Juaristi, and M. Alducin. **Photoinduced Desorption Dynamics of CO from Pd(111): A Neural Network Approach.** *J. Chem. Theory Comput.* **17**, 8, 4648–4659 (2021). DOI: [10.1021/acs.jctc.1c00347](https://doi.org/10.1021/acs.jctc.1c00347) (see pages 6, 79, 80, 114, 132, 146, 149, 150, 159, 160, 168, 181, 225, 227).

- [88] A. P. S. Muzas, **A. Serrano Jiménez**, J. Ovčar, I. Lončarić, M. Alducin, and J. I. Juaristi. **Absence of isotope effects in the photo-induced desorption of CO from saturated Pd(111) at high laser fluence.** *Chem. Phys.* **558**, 111518 (2022). DOI: [10.1016/j.chemphys.2022.111518](https://doi.org/10.1016/j.chemphys.2022.111518) (see pages 6, 79, 150, 151, 159, 181, 225, 228).
- [89] A. P. S. Muzas, **A. Serrano Jiménez**, Y. Zhang, B. Jiang, J. I. Juaristi, and M. Alducin. **Multicoverage Study of Femtosecond Laser-Induced Desorption of CO from Pd(111).** *J. Phys. Chem. Lett.* **15**, 9, 2587–2594 (2024). DOI: [10.1021/acs.jpcclett.4c00026](https://doi.org/10.1021/acs.jpcclett.4c00026) (see pages 6, 7, 159, 179, 225, 231).
- [90] C. Hess, S. Funk, M. Bonn, D. Denzler, M. Wolf, and G. Ertl. **Femtosecond dynamics of chemical reactions at surfaces.** *Appl. Phys. A* **71**, 477–483 (2000). DOI: [10.1007/s003390000703](https://doi.org/10.1007/s003390000703) (see pages 6, 149).
- [91] D. P. Quinn and T. F. Heinz. **Observation of an isotope effect in femtosecond laser-induced desorption of O<sub>2</sub>/Pd(111).** *J. Vac. Sci. Technol. A* **21**, 4, 1312–1316 (2003). DOI: [10.1116/1.1580486](https://doi.org/10.1116/1.1580486) (see pages 6, 149).
- [92] S. Funk, M. Bonn, D. N. Denzler, C. Hess, M. Wolf, and G. Ertl. **Desorption of CO from Ru(001) induced by near-infrared femtosecond laser pulses.** *J. Chem. Phys.* **112**, 22, 9888–9897 (2000). DOI: [10.1063/1.481626](https://doi.org/10.1063/1.481626) (see pages 6, 7, 149, 179, 195, 196, 203).
- [93] A. Weiner. **Ultrafast Time-Resolved Spectroscopy**, 422–506. In: *Ultrafast Optics*. Ed. by G. Boreman and A. Weiner. John Wiley & Sons, Ltd (2009). ISBN: 9780470473467. DOI: <https://doi.org/10.1002/9780470473467.ch9> (see pages 6, 54).
- [94] A. Tetenoire, J. I. Juaristi, and M. Alducin. **Insights into the Coadsorption and Reactivity of O and CO on Ru(0001) and Their Coverage Dependence.** *J. Phys. Chem. C* **125**, 23, 12614–12627 (2021). DOI: [10.1021/acs.jpcc.1c01618](https://doi.org/10.1021/acs.jpcc.1c01618) (see pages 7, 172).
- [95] I. Žugeč, A. Tetenoire, A. S. Muzas, Y. Zhang, B. Jiang, M. Alducin, and J. I. Juaristi. **Understanding the Photoinduced Desorption and Oxidation of CO on Ru(0001) Using a Neural Network Potential Energy Surface.** *JACS Au* **4**, 5, 1997–2004 (2024). DOI: [10.1021/jacsau.4c00197](https://doi.org/10.1021/jacsau.4c00197) (see pages 7, 231).
- [96] M. Born and V. Fock. **Beweis des Adiabatenatzes.** *Z. Phys.* **51**, 3, 165–180 (1928). DOI: [10.1007/BF01343193](https://doi.org/10.1007/BF01343193) (see pages 7, 13, 16).
- [97] M. Born and R. Oppenheimer. **Zur Quantentheorie der Molekeln.** *Ann. Phys.* **389**, 20, 457–484 (1927). DOI: [10.1002/andp.19273892002](https://doi.org/10.1002/andp.19273892002) (see pages 7, 18).
- [98] D. Menzel and R. Gomer. **Desorption from Metal Surfaces by Low-Energy Electrons.** *J. Chem. Phys.* **41**, 11, 3311–3328 (1964). DOI: [10.1063/1.1725730](https://doi.org/10.1063/1.1725730) (see pages 8, 56).

- [99] P. R. Antoniewicz. **Model for electron- and photon-stimulated desorption.** *Phys. Rev. B* **21**, 3811–3815 (1980). DOI: [10.1103/PhysRevB.21.3811](https://doi.org/10.1103/PhysRevB.21.3811) (see pages 8, 57).
- [100] L. I. Schiff. **Quantum Mechanics.** McGraw-Hill, New York (1968). ISBN: 978-0070856431 (see pages 13, 14).
- [101] T. Kato. **On the Adiabatic Theorem of Quantum Mechanics.** *J. Phys. Soc. Japan* **5**, 6, 435–439 (1950). DOI: [10.1143/JPSJ.5.435](https://doi.org/10.1143/JPSJ.5.435) (see pages 13, 16).
- [102] J. E. Avron and A. Elgart. **Adiabatic Theorem without a Gap Condition.** *Commun. Math. Phys.* **203**, 2, 445–463 (1999). DOI: [10.1007/s002200050620](https://doi.org/10.1007/s002200050620) (see page 13).
- [103] V. V. Dodonov, A. B. Klimov, and D. E. Nikonov. **Quantum particle in a box with moving walls.** *J. Math. Phys.* **34**, 8, 3391–3404 (1993). DOI: [10.1063/1.530083](https://doi.org/10.1063/1.530083) (see page 14).
- [104] J. J. Sakurai and J. Napolitano. **Modern quantum mechanics; 3rd ed.** Cambridge University Press, Cambridge (2020). ISBN: 978-1108473224. DOI: [10.1017/9781108587280](https://doi.org/10.1017/9781108587280) (see page 16).
- [105] M. V. Berry. **Quantal phase factors accompanying adiabatic changes.** *Proc. R. Soc. Lond. A* **392**, 1, 45–57 (1984). DOI: [10.1098/rspa.1984.0023](https://doi.org/10.1098/rspa.1984.0023) (see page 17).
- [106] S. Pancharatnam. **Generalized theory of interference, and its applications.** *Proc. Indian Acad. Sci. A* **44**, 5, 247–262 (1956). DOI: [10.1007/BF03046050](https://doi.org/10.1007/BF03046050) (see page 17).
- [107] H. C. Longuet-Higgins, U. Öpik, M. H. L. Pryce, and R. A. Sack. **Studies of the Jahn-Teller effect .II. The dynamical problem.** *Proc. R. Soc. Lond. A* **244**, 1236, 1–16 (1958). DOI: [10.1098/rspa.1958.0022](https://doi.org/10.1098/rspa.1958.0022) (see page 17).
- [108] F. Wilczek and A. D. Shapere. **Geometric Phases in Physics.** Advanced series in mathematical physics. World Scientific, Singapore (1989). ISBN: 978-9971505998. DOI: [10.1142/0613](https://doi.org/10.1142/0613) (see page 17).
- [109] Y. Aharonov and D. Bohm. **Significance of Electromagnetic Potentials in the Quantum Theory.** *Phys. Rev.* **115**, 485–491 (1959). DOI: [10.1103/PhysRev.115.485](https://doi.org/10.1103/PhysRev.115.485) (see page 17).
- [110] J. W. Zwanziger, M. Koenig, and A. Pines. **Berry’s Phase.** *Annu. Rev. Phys. Chem.* **41**, 1, 601–646 (1990). DOI: [10.1146/annurev.pc.41.100190.003125](https://doi.org/10.1146/annurev.pc.41.100190.003125) (see page 17).
- [111] M. V. Berry. **Anticipations of the Geometric Phase.** *Phys. Today* **43**, 12, 34–40 (1990). DOI: [10.1063/1.881219](https://doi.org/10.1063/1.881219) (see page 17).
- [112] B. R. Holstein. **The adiabatic theorem and Berry’s phase.** *Am. J. Phys.* **57**, 12, 1079–1084 (1989). DOI: [10.1119/1.15793](https://doi.org/10.1119/1.15793) (see page 17).

- [113] B. Bransden and C. Joachain. **Physics of Atoms and Molecules**. 2nd ed. Pearson Education Limited, Harlow (2003). ISBN: 978-0-582-35692-4 (see pages 19, 20, 72).
- [114] H. Shull and G. G. Hall. **Atomic Units**. *Nature* **184**, 4698, 1559–1560 (1959). DOI: 10.1038/1841559a0 (see page 19).
- [115] M. Verdaguer and V. Robert. **8.04 - Fundamentals, Principles, and Concepts of Molecular Magnetism and Spintronics**, 131–189. In: *Comprehensive Inorganic Chemistry II*. Ed. by J. Reedijk and K. Poeppelmeier. 2nd ed. Elsevier, Amsterdam (2013). ISBN: 978-0-08-096529-1. DOI: 10.1016/B978-0-08-097774-4.00819-6 (see page 20).
- [116] A. Salin. **A course on Density Functional Theory and its application to Surface Physics**. Course notes. 2003 (see pages 24, 37, 42).
- [117] P. Hohenberg and W. Kohn. **Inhomogeneous Electron Gas**. *Phys. Rev.* **136**, B864–B871 (1964). DOI: 10.1103/PhysRev.136.B864 (see pages 27, 44).
- [118] R. G. Parr, R. A. Donnelly, M. Levy, and W. E. Palke. **Electronegativity: The density functional viewpoint**. *J. Chem. Phys.* **68**, 8, 3801–3807 (1978). DOI: 10.1063/1.436185 (see page 30).
- [119] D. W. Smith. **N-Representability Problem for Fermion Density Matrices. I. The Second-Order Density Matrix with  $N = 3$** . *J. Chem. Phys.* **43**, 10, S258–S264 (1965). DOI: 10.1063/1.1701504 (see page 30).
- [120] E. Engel and R. M. Dreizler. **Density Functional Theory – An advanced course**. Springer, Berlin (2011). ISBN: 978-3-642-14089-1. DOI: 10.1007/978-3-642-14090-7 (see pages 30, 34, 37, 38, 44–46).
- [121] E. Matito. **Time dependent Density Functional Theory: review of Density Functional Theory**. Course notes. 2022 (see pages 30, 31, 43, 45, 48).
- [122] M. Levy. **Universal variational functionals of electron densities, first-order density matrices, and natural spin-orbitals and solution of the v-representability problem**. *Proc. Natl. Acad. Sci. U.S.A.* **76**, 12, 6062–6065 (1979). DOI: 10.1073/pnas.76.12.6062 (see page 30).
- [123] E. H. Lieb. **Density functionals for coulomb systems**. *Int. J. Quantum Chem.* **24**, 3, 243–277 (1983). DOI: 10.1002/qua.560240302 (see page 30).
- [124] L. Delle Site. **Levy-Lieb constrained-search formulation as a minimization of the correlation functional**. *J. Phys. A Math. Theor.* **40** (2007). DOI: 10.1088/1751-8113/40/11/013 (see page 31).
- [125] C. A. Ullrich. **Time-Dependent Density-Functional Theory: Concepts and Applications**. Oxford Graduate Texts. OUP Oxford (2012). ISBN: 978-0-19-956302-9. DOI: 10.1093/acprof:oso/9780199563029.001.0001 (see pages 31, 34, 38).

- [126] W. Kohn and L. J. Sham. **Self-Consistent Equations Including Exchange and Correlation Effects**. *Phys. Rev.* **140**, A1133–A1138 (1965). DOI: [10.1103/PhysRev.140.A1133](https://doi.org/10.1103/PhysRev.140.A1133) (see pages 31, 40).
- [127] A. Szabo and N. S. Ostlund. **Modern Quantum Chemistry: Introduction to Advanced Electronic Structure Theory**. Dover Publications, New York (1996). ISBN: 978-0486691862 (see page 32).
- [128] E. J. Baerends, O. V. Gritsenko, and R. van Meer. **The Kohn–Sham gap, the fundamental gap and the optical gap: the physical meaning of occupied and virtual Kohn–Sham orbital energies**. *Phys. Chem. Chem. Phys.* **15**, 16408–16425 (2013). DOI: [10.1039/C3CP52547C](https://doi.org/10.1039/C3CP52547C) (see page 37).
- [129] C. A. Ullrich and Z.-h. Yang. **A Brief Compendium of Time - Dependent Density Functional Theory**. *Brazilian J. Phys.* **44**, 1, 154–188 (2014). DOI: [10.1007/s13538-013-0141-2](https://doi.org/10.1007/s13538-013-0141-2) (see page 37).
- [130] P. A. M. Dirac. **Note on Exchange Phenomena in the Thomas Atom**. *Math. Proc. Cambridge Philos. Soc.* **26**, 3 (1930). DOI: [10.1017/S0305004100016108](https://doi.org/10.1017/S0305004100016108) (see page 38).
- [131] V. Sahni, J. Gruenebaum, and J. P. Perdew. **Study of the density-gradient expansion for the exchange energy**. *Phys. Rev. B* **26**, 4371–4377 (1982). DOI: [10.1103/PhysRevB.26.4371](https://doi.org/10.1103/PhysRevB.26.4371) (see page 38).
- [132] D. C. Langreth and M. J. Mehl. **Beyond the local-density approximation in calculations of ground-state electronic properties**. *Phys. Rev. B* **28**, 1809–1834 (1983). DOI: [10.1103/PhysRevB.28.1809](https://doi.org/10.1103/PhysRevB.28.1809) (see page 38).
- [133] J. P. Perdew and K. Schmidt. **Jacob’s ladder of density functional approximations for the exchange-correlation energy**. *AIP Conf. Proc.* **577**, 1, 1–20 (2001). DOI: [10.1063/1.1390175](https://doi.org/10.1063/1.1390175) (see pages 40, 41, 48).
- [134] J. Wellendorff, K. T. Lundgaard, A. Møgelhøj, V. Petzold, D. D. Landis, J. K. Nørskov, T. Bligaard, and K. W. Jacobsen. **Density functionals for surface science: Exchange-correlation model development with Bayesian error estimation**. *Phys. Rev. B* **85**, 235149 (2012). DOI: [10.1103/PhysRevB.85.235149](https://doi.org/10.1103/PhysRevB.85.235149) (see pages 41, 51).
- [135] E. Wigner. **On the Interaction of Electrons in Metals**. *Phys. Rev.* **46**, 1002–1011 (1934). DOI: [10.1103/PhysRev.46.1002](https://doi.org/10.1103/PhysRev.46.1002) (see page 42).
- [136] D. M. Ceperley and B. J. Alder. **Ground State of the Electron Gas by a Stochastic Method**. *Phys. Rev. Lett.* **45**, 566–569 (1980). DOI: [10.1103/PhysRevLett.45.566](https://doi.org/10.1103/PhysRevLett.45.566) (see page 42).
- [137] R. G. Parr and W. Yang. **Density-Functional Theory of Atoms and Molecules**. Oxford University Press, New York (1989). ISBN: 978-0195357738 (see page 42).

- [138] S. H. Vosko, L. Wilk, and M. Nusair. **Accurate spin-dependent electron liquid correlation energies for local spin density calculations: a critical analysis.** *Can. J. Phys.* **58**, 8, 1200–1211 (1980). DOI: [10.1139/p80-159](https://doi.org/10.1139/p80-159) (see pages 42, 43).
- [139] J. P. Perdew and A. Zunger. **Self-interaction correction to density - functional approximations for many-electron systems.** *Phys. Rev. B* **23**, 5048–5079 (1981). DOI: [10.1103/PhysRevB.23.5048](https://doi.org/10.1103/PhysRevB.23.5048) (see page 42).
- [140] J. P. Perdew and Y. Wang. **Accurate and simple analytic representation of the electron-gas correlation energy.** *Phys. Rev. B* **45**, 13244–13249 (1992). DOI: [10.1103/PhysRevB.45.13244](https://doi.org/10.1103/PhysRevB.45.13244) (see page 43).
- [141] Q.-C. Inc. URL: <https://manual.q-chem.com/5.2/Ch5.S3.SS3.html> (see pages 43, 45, 46).
- [142] J. P. Perdew, K. Burke, and M. Ernzerhof. **Generalized Gradient Approximation Made Simple.** *Phys. Rev. Lett.* **77**, 3865–3868 (1996). DOI: [10.1103/PhysRevLett.77.3865](https://doi.org/10.1103/PhysRevLett.77.3865) (see pages 45, 50).
- [143] J. P. Perdew, K. Burke, and M. Ernzerhof. **Generalized Gradient Approximation Made Simple [Phys. Rev. Lett. 77, 3865 (1996)].** *Phys. Rev. Lett.* **78**, 1396–1396 (1997). DOI: [10.1103/PhysRevLett.78.1396](https://doi.org/10.1103/PhysRevLett.78.1396) (see pages 45, 50).
- [144] J. P. Perdew, J. A. Chevary, S. H. Vosko, K. A. Jackson, M. R. Pederson, D. J. Singh, and C. Fiolhais. **Atoms, molecules, solids, and surfaces: Applications of the generalized gradient approximation for exchange and correlation.** *Phys. Rev. B* **46**, 6671–6687 (1992). DOI: [10.1103/PhysRevB.46.6671](https://doi.org/10.1103/PhysRevB.46.6671) (see page 45).
- [145] A. D. Becke. **Density-functional exchange-energy approximation with correct asymptotic behavior.** *Phys. Rev. A* **38**, 3098–3100 (1988). DOI: [10.1103/PhysRevA.38.3098](https://doi.org/10.1103/PhysRevA.38.3098) (see pages 45, 47).
- [146] M. A. Marques, M. J. Oliveira, and T. Burnus. **Libxc: A library of exchange and correlation functionals for density functional theory.** *Comput. Phys. Commun.* **183**, 10, 2272–2281 (2012). DOI: [10.1016/j.cpc.2012.05.007](https://doi.org/10.1016/j.cpc.2012.05.007) (see page 45).
- [147] A. C. Cancio, D. Stewart, and A. Kuna. **Visualization and analysis of the Kohn-Sham kinetic energy density and its orbital-free description in molecules.** *J. Chem. Phys.* **144**, 8, 084107 (2016). DOI: [10.1063/1.4942016](https://doi.org/10.1063/1.4942016) (see page 46).
- [148] J. P. Perdew, S. Kurth, A. š. Zupan, and P. Blaha. **Accurate Density Functional with Correct Formal Properties: A Step Beyond the Generalized Gradient Approximation.** *Phys. Rev. Lett.* **82**, 2544–2547 (1999). DOI: [10.1103/PhysRevLett.82.2544](https://doi.org/10.1103/PhysRevLett.82.2544) (see page 46).

- [149] J. Tao, J. P. Perdew, V. N. Staroverov, and G. E. Scuseria. **Climbing the Density Functional Ladder: Nonempirical Meta-Generalized Gradient Approximation Designed for Molecules and Solids**. *Phys. Rev. Lett.* **91**, 146401 (2003). DOI: [10.1103/PhysRevLett.91.146401](https://doi.org/10.1103/PhysRevLett.91.146401) (see page 46).
- [150] A. D. Becke. **A new mixing of Hartree-Fock and local density-functional theories**. *J. Chem. Phys.* **98**, 2, 1372–1377 (1993). DOI: [10.1063/1.464304](https://doi.org/10.1063/1.464304) (see page 47).
- [151] E. Geraniotis, Y.-W. Chang, and W.-B. Yang. **Optimal strategies for admitting voice and data traffic in networks of LEO satellites using CDMA**. *AIP Conf. Proc.* **325**, 1, 57–62 (1995). DOI: [10.1063/1.47293](https://doi.org/10.1063/1.47293) (see page 47).
- [152] J. Heyd, G. E. Scuseria, and M. Ernzerhof. **Hybrid functionals based on a screened Coulomb potential**. *J. Chem. Phys.* **118**, 18, 8207–8215 (2003). DOI: [10.1063/1.1564060](https://doi.org/10.1063/1.1564060) (see page 47).
- [153] J. Heyd, G. E. Scuseria, and M. Ernzerhof. **Erratum: “Hybrid functionals based on a screened Coulomb potential” [J. Chem. Phys. 118, 8207 (2003)]**. *J. Chem. Phys.* **124**, 21, 219906 (2006). DOI: [10.1063/1.2204597](https://doi.org/10.1063/1.2204597) (see page 47).
- [154] A. D. Becke. **Density-functional thermochemistry. III. The role of exact exchange**. *J. Chem. Phys.* **98**, 7, 5648–5652 (1993). DOI: [10.1063/1.464913](https://doi.org/10.1063/1.464913) (see page 47).
- [155] P. J. Stephens, F. J. Devlin, C. F. Chabalowski, and M. J. Frisch. **Ab Initio Calculation of Vibrational Absorption and Circular Dichroism Spectra Using Density Functional Force Fields**. *J. Phys. Chem.* **98**, 45, 11623–11627 (1994). DOI: [10.1021/j100096a001](https://doi.org/10.1021/j100096a001) (see page 47).
- [156] C. Lee, W. Yang, and R. G. Parr. **Development of the Colle-Salvetti correlation-energy formula into a functional of the electron density**. *Phys. Rev. B* **37**, 785–789 (1988). DOI: [10.1103/PhysRevB.37.785](https://doi.org/10.1103/PhysRevB.37.785) (see page 47).
- [157] J. P. Perdew, M. Ernzerhof, and K. Burke. **Rationale for mixing exact exchange with density functional approximations**. *J. Chem. Phys.* **105**, 22, 9982–9985 (1996). DOI: [10.1063/1.472933](https://doi.org/10.1063/1.472933) (see page 47).
- [158] C. D. Sherrill. **Introduction to Density Functional Theory**. URL: <http://vergil.chemistry.gatech.edu/notes/DFT-intro.pdf> (see page 48).
- [159] R. Peverati and D. G. Truhlar. **Quest for a universal density functional: the accuracy of density functionals across a broad spectrum of databases in chemistry and physics**. *Philos. Trans. Royal Soc. A* **372**, 2011, 20120476 (2014). DOI: [10.1098/rsta.2012.0476](https://doi.org/10.1098/rsta.2012.0476) (see page 48).
- [160] Y. Andersson and H. Rydberg. **Dispersion Coefficients for van der Waals Complexes, Including C60–C60**. *Phys. Scr.* **60**, 3, 211 (1999). DOI: [10.1238/Physica.Regular.060a00211](https://doi.org/10.1238/Physica.Regular.060a00211) (see page 48).

- [161] A. D. Buckingham, P. W. Fowler, and J. M. Hutson. **Theoretical studies of van der Waals molecules and intermolecular forces**. *Chem. Rev.* **88**, 6, 963–988 (1988). DOI: [10.1021/cr00088a008](https://doi.org/10.1021/cr00088a008) (see page 48).
- [162] G. Chalasinski and M. M. Szczesniak. **Origins of Structure and Energetics of van der Waals Clusters from ab Initio Calculations**. *Chem. Rev.* **94**, 7, 1723–1765 (1994). DOI: [10.1021/cr00031a001](https://doi.org/10.1021/cr00031a001) (see page 48).
- [163] H. Margenau and N. R. Kestner. **Theory of Intermolecular Forces**. Pergamon Press, Oxford (1969). ISBN: 978-1483119281 (see page 49).
- [164] R. Keil and L. Mayer. **12.12 - Mineral Matrices and Organic Matter**, 337–359. In: *Treatise on Geochemistry*. Ed. by H. D. Holland and K. K. Turekian. 2nd ed. Elsevier, Oxford (2014). ISBN: 978-0-08-098300-4. DOI: [10.1016/B978-0-08-095975-7.01024-X](https://doi.org/10.1016/B978-0-08-095975-7.01024-X) (see page 49).
- [165] Q. Xu and X. Zhao. **Electrostatic interactions versus van der Waals interactions in the self-assembly of dispersed nanodiamonds**. *J. Mater. Chem.* **22**, 16416–16421 (2012). DOI: [10.1039/C2JM32918B](https://doi.org/10.1039/C2JM32918B) (see page 49).
- [166] S. Grimme. **Semiempirical GGA-type density functional constructed with a long-range dispersion correction**. *J. Comput. Chem.* **27**, 15, 1787–1799 (2006). DOI: [10.1002/jcc.20495](https://doi.org/10.1002/jcc.20495) (see page 49).
- [167] A. Tkatchenko and M. Scheffler. **Accurate Molecular Van Der Waals Interactions from Ground-State Electron Density and Free-Atom Reference Data**. *Phys. Rev. Lett.* **102**, 073005 (2009). DOI: [10.1103/PhysRevLett.102.073005](https://doi.org/10.1103/PhysRevLett.102.073005) (see page 49).
- [168] C. D. Sherrill. **Frontiers in electronic structure theory**. *J. Chem. Phys.* **132**, 11, 110902 (2010). DOI: [10.1063/1.3369628](https://doi.org/10.1063/1.3369628) (see page 49).
- [169] Y. Andersson, D. C. Langreth, and B. I. Lundqvist. **van der Waals Interactions in Density-Functional Theory**. *Phys. Rev. Lett.* **76**, 102–105 (1996). DOI: [10.1103/PhysRevLett.76.102](https://doi.org/10.1103/PhysRevLett.76.102) (see page 49).
- [170] J. F. Dobson and B. P. Dinte. **Constraint Satisfaction in Local and Gradient Susceptibility Approximations: Application to a van der Waals Density Functional**. *Phys. Rev. Lett.* **76**, 1780–1783 (1996). DOI: [10.1103/PhysRevLett.76.1780](https://doi.org/10.1103/PhysRevLett.76.1780) (see page 49).
- [171] W. Kohn, Y. Meir, and D. E. Makarov. **van der Waals Energies in Density Functional Theory**. *Phys. Rev. Lett.* **80**, 4153–4156 (1998). DOI: [10.1103/PhysRevLett.80.4153](https://doi.org/10.1103/PhysRevLett.80.4153) (see page 49).
- [172] M. Dion, H. Rydberg, E. Schröder, D. C. Langreth, and B. I. Lundqvist. **Van der Waals Density Functional for General Geometries**. *Phys. Rev. Lett.* **92**, 246401 (2004). DOI: [10.1103/PhysRevLett.92.246401](https://doi.org/10.1103/PhysRevLett.92.246401) (see pages 49, 50, 112, 207).

- [173] D. C. Langreth, B. I. Lundqvist, S. D. Chakarova-Käck, V. R. Cooper, M. Dion, P. Hyldgaard, A. Kelkkanen, J. Kleis, L. Kong, S. Li, P. G. Moses, E. Murray, A. Puzder, H. Rydberg, E. Schröder, and T. Thonhauser. **A density functional for sparse matter**. *J. Phys.: Condens. Matter* **21**, 8, 084203 (2009). DOI: [10.1088/0953-8984/21/8/084203](https://doi.org/10.1088/0953-8984/21/8/084203) (see pages 49–51).
- [174] Y. Zhang and W. Yang. **Comment on “Generalized Gradient Approximation Made Simple”**. *Phys. Rev. Lett.* **80**, 890–890 (1998). DOI: [10.1103/PhysRevLett.80.890](https://doi.org/10.1103/PhysRevLett.80.890) (see page 50).
- [175] J. Klimeš, D. R. Bowler, and A. Michaelides. **Chemical accuracy for the van der Waals density functional**. *J. Phys.: Condens. Matter* **22**, 2, 022201 (2009). DOI: [10.1088/0953-8984/22/2/022201](https://doi.org/10.1088/0953-8984/22/2/022201) (see page 50).
- [176] T. Thonhauser, A. Puzder, and D. C. Langreth. **Interaction energies of mono-substituted benzene dimers via nonlocal density functional theory**. *J. Chem. Phys.* **124**, 16, 164106 (2006). DOI: [10.1063/1.2189230](https://doi.org/10.1063/1.2189230) (see page 50).
- [177] T. Thonhauser, V. R. Cooper, S. Li, A. Puzder, P. Hyldgaard, and D. C. Langreth. **Van der Waals density functional: Self-consistent potential and the nature of the van der Waals bond**. *Phys. Rev. B* **76**, 125112 (2007). DOI: [10.1103/PhysRevB.76.125112](https://doi.org/10.1103/PhysRevB.76.125112) (see page 51).
- [178] J. P. Perdew and W. Yue. **Accurate and simple density functional for the electronic exchange energy: Generalized gradient approximation**. *Phys. Rev. B* **33**, 8800–8802 (1986). DOI: [10.1103/PhysRevB.33.8800](https://doi.org/10.1103/PhysRevB.33.8800) (see page 51).
- [179] K. Lee, É. D. Murray, L. Kong, B. I. Lundqvist, and D. C. Langreth. **Higher-accuracy van der Waals density functional**. *Phys. Rev. B* **82**, 081101 (2010). DOI: [10.1103/PhysRevB.82.081101](https://doi.org/10.1103/PhysRevB.82.081101) (see page 51).
- [180] I. Hamada. **van der Waals density functional made accurate**. *Phys. Rev. B* **89**, 121103 (2014). DOI: [10.1103/PhysRevB.89.121103](https://doi.org/10.1103/PhysRevB.89.121103) (see page 51).
- [181] D. Chakraborty, K. Berland, and T. Thonhauser. **Next-Generation Nonlocal van der Waals Density Functional**. *J. Chem. Theory Comput.* **16**, 9, 5893–5911 (2020). DOI: [10.1021/acs.jctc.0c00471](https://doi.org/10.1021/acs.jctc.0c00471) (see page 51).
- [182] G. Román-Pérez and J. M. Soler. **Efficient Implementation of a van der Waals Density Functional: Application to Double-Wall Carbon Nanotubes**. *Phys. Rev. Lett.* **103**, 096102 (2009). DOI: [10.1103/PhysRevLett.103.096102](https://doi.org/10.1103/PhysRevLett.103.096102) (see page 51).
- [183] J. Jensen. URL: <https://molecularmodelingbasics.blogspot.com/2013/03/dft-d-dft-d2-and-dft-d3-density.html> (see page 51).
- [184] B. G. Janesko. **Rung 3.5 density functionals**. *J. Chem. Phys.* **133**, 10, 104103 (2010). DOI: [10.1063/1.3475563](https://doi.org/10.1063/1.3475563) (see page 51).

- [185] B. G. Janesko and A. Aguero. **Nonspherical model density matrices for Rung 3.5 density functionals**. *J. Chem. Phys.* **136**, 2, 024111 (2012). DOI: [10.1063/1.3675681](https://doi.org/10.1063/1.3675681) (see page 51).
- [186] M. G. Evans and M. Polanyi. **Some applications of the transition state method to the calculation of reaction velocities, especially in solution**. *Trans. Faraday Soc.* **31**, 875–894 (1935). DOI: [10.1039/TF9353100875](https://doi.org/10.1039/TF9353100875) (see page 53).
- [187] H. Eyring. **The Activated Complex in Chemical Reactions**. *J. Chem. Phys.* **3**, 2, 107–115 (1935). DOI: [10.1063/1.1749604](https://doi.org/10.1063/1.1749604) (see page 53).
- [188] J. O. Hirschfelder. **The Energy of the Triatomic Hydrogen Molecule and Ion, V**. *J. Chem. Phys.* **6**, 12, 795–806 (1938). DOI: [10.1063/1.1750173](https://doi.org/10.1063/1.1750173) (see page 53).
- [189] A. H. Zewail. **Femtochemistry: Atomic-Scale Dynamics of the Chemical Bond**. *J. Phys. Chem. A* **104**, 24, 5660–5694 (2000). DOI: [10.1021/jp001460h](https://doi.org/10.1021/jp001460h) (see page 53).
- [190] C. V. Shank, R. L. Fork, R. Yen, R. H. Stolen, and W. J. Tomlinson. **Compression of femtosecond optical pulses**. *Appl. Phys. Lett.* **40**, 9, 761–763 (1982). DOI: [10.1063/1.93276](https://doi.org/10.1063/1.93276) (see page 53).
- [191] J. G. Fujimoto, A. M. Weiner, and E. P. Ippen. **Generation and measurement of optical pulses as short as 16 fs**. *Appl. Phys. Lett.* **44**, 9, 832–834 (1984). DOI: [10.1063/1.94957](https://doi.org/10.1063/1.94957) (see page 53).
- [192] J.-M. Halbout and D. Grischkowsky. **12-fs ultrashort optical pulse compression at a high repetition rate**. *Appl. Phys. Lett.* **45**, 12, 1281–1283 (1984). DOI: [10.1063/1.95112](https://doi.org/10.1063/1.95112) (see page 53).
- [193] W. H. Knox, R. L. Fork, M. C. Downer, R. H. Stolen, C. V. Shank, and J. A. Valdmanis. **Optical pulse compression to 8 fs at a 5-kHz repetition rate**. *Appl. Phys. Lett.* **46**, 12, 1120–1121 (1985). DOI: [10.1063/1.95728](https://doi.org/10.1063/1.95728) (see page 53).
- [194] C. V. Shank. **Investigation of Ultrafast Phenomena in the Femtosecond Time Domain**. *Science* **233**, 4770, 1276–1280 (1986). DOI: [10.1126/science.233.4770.1276](https://doi.org/10.1126/science.233.4770.1276) (see page 53).
- [195] D. E. Spence, P. N. Kean, and W. Sibbett. **60-fsec pulse generation from a self-mode-locked Ti:sapphire laser**. *Opt. Lett.* **16**, 1, 42–44 (1991). DOI: [10.1364/OL.16.000042](https://doi.org/10.1364/OL.16.000042) (see page 53).
- [196] T. Brabec and F. Krausz. **Intense few-cycle laser fields: Frontiers of nonlinear optics**. *Rev. Mod. Phys.* **72**, 545–591 (2000). DOI: [10.1103/RevModPhys.72.545](https://doi.org/10.1103/RevModPhys.72.545) (see page 53).
- [197] Y. Silberberg. **Physics at the attosecond frontier**. *Nature* **414**, 6863, 494–495 (2001). DOI: [10.1038/35107171](https://doi.org/10.1038/35107171) (see page 53).

- [198] N. F. Scherer, J. L. Knee, D. D. Smith, and A. H. Zewail. **Femtosecond Photofragment Spectroscopy: The Reaction  $\text{ICN} \rightarrow \text{CN} + \text{I}$** . *J. Phys. Chem.* **89**, 24, 5141–5143 (1985). DOI: [10.1021/j100270a001](https://doi.org/10.1021/j100270a001) (see page 53).
- [199] M. Dantus, M. J. Rosker, and A. H. Zewail. **Real-time femtosecond probing of “transition states” in chemical reactions**. *J. Chem. Phys.* **87**, 4, 2395–2397 (1987). DOI: [10.1063/1.453122](https://doi.org/10.1063/1.453122) (see page 53).
- [200] T. S. Rose, M. J. Rosker, and A. H. Zewail. **Femtosecond real-time observation of wave packet oscillations (resonance) in dissociation reactions**. *J. Chem. Phys.* **88**, 10, 6672–6673 (1988). DOI: [10.1063/1.454408](https://doi.org/10.1063/1.454408) (see page 53).
- [201] M. Karplus, R. N. Porter, and R. D. Sharma. **Exchange Reactions with Activation Energy. I. Simple Barrier Potential for (H, H<sub>2</sub>)**. *J. Chem. Phys.* **43**, 9, 3259–3287 (1965). DOI: [10.1063/1.1697301](https://doi.org/10.1063/1.1697301) (see page 53).
- [202] P. Brumer and M. Karplus. **Collision complex dynamics in alkali halide exchange reactions**. *Faraday Discuss. Chem. Soc.* **55**, 80–92 (1973). DOI: [10.1039/DC9735500080](https://doi.org/10.1039/DC9735500080) (see page 53).
- [203] A. Zewail and R. Bernstein. **9 - Real-Time Laser Femtochemistry: Viewing the Transition from Reagents to Products**, 223–279. In: *The Chemical Bond*. Ed. by A. Zewail. Academic Press, San Diego (1992). ISBN: 978-0-12-779620-8. DOI: [10.1016/B978-0-08-092669-8.50014-X](https://doi.org/10.1016/B978-0-08-092669-8.50014-X) (see page 53).
- [204] A. H. Zewail. **Laser Femtochemistry**. *Science* **242**, 4886, 1645–1653 (1988). DOI: [10.1126/science.242.4886.1645](https://doi.org/10.1126/science.242.4886.1645) (see page 54).
- [205] G. A. Worth and L. S. Cederbaum. **Beyond Born-Oppenheimer: Molecular Dynamics Through a Conical Intersection**. *Annu. Rev. Phys. Chem.* **55**, 1, 127–158 (2004). DOI: [10.1146/annurev.physchem.55.091602.094335](https://doi.org/10.1146/annurev.physchem.55.091602.094335) (see page 54).
- [206] A. M. Wodtke, J. C. Tully, and D. J. Auerbach. **Electronically non-adiabatic interactions of molecules at metal surfaces: Can we trust the Born-Oppenheimer approximation for surface chemistry?** *Int. Rev. Phys. Chem.* **23**, 4, 513–539 (2004). DOI: [10.1080/01442350500037521](https://doi.org/10.1080/01442350500037521) (see pages 54, 61).
- [207] A. Volpe, C. Gaudiuso, L. Di Venere, F. Licciulli, F. Giordano, and A. Ancona. **Direct Femtosecond Laser Fabrication of Superhydrophobic Aluminum Alloy Surfaces with Anti-icing Properties**. *Coatings* **10**, 6 (2020). DOI: [10.3390/coatings10060587](https://doi.org/10.3390/coatings10060587) (see page 55).
- [208] M. Hassel, K. Svensson, M. Persson, and S. Andersson. **Direct Infrared Photodesorption of Physisorbed H<sub>2</sub>**. *Phys. Rev. Lett.* **80**, 2481–2484 (1998). DOI: [10.1103/PhysRevLett.80.2481](https://doi.org/10.1103/PhysRevLett.80.2481) (see page 55).
- [209] T. Niedermayer, H. Schlichting, D. Menzel, S. H. Payne, and H. J. Kreuzer. **Photo- and Thermodesorption of Helium on Pt(111)**. *Phys. Rev. Lett.* **89**, 126101 (2002). DOI: [10.1103/PhysRevLett.89.126101](https://doi.org/10.1103/PhysRevLett.89.126101) (see page 55).

- [210] T. Vondrak and X.-Y. Zhu. **Dissociation of a Surface Bond by Direct Optical Excitation: H-Si(100)**. *Phys. Rev. Lett.* **82**, 1967–1970 (1999). DOI: [10.1103/PhysRevLett.82.1967](https://doi.org/10.1103/PhysRevLett.82.1967) (see page 55).
- [211] I. Hussla, H. Seki, T. J. Chuang, Z. W. Gortel, H. J. Kreuzer, and P. Piercy. **Infrared-laser-induced photodesorption of NH<sub>3</sub> and ND<sub>3</sub> adsorbed on single-crystal Cu(100) and Ag film**. *Phys. Rev. B* **32**, 3489–3501 (1985). DOI: [10.1103/PhysRevB.32.3489](https://doi.org/10.1103/PhysRevB.32.3489) (see page 55).
- [212] F. M. Zimmermann and W. Ho. **State resolved studies of photochemical dynamics at surfaces**. *Surf. Sci. Rep.* **22**, 4, 127–247 (1995). DOI: [10.1016/0167-5729\(96\)80001-X](https://doi.org/10.1016/0167-5729(96)80001-X) (see page 55).
- [213] S. A. Buntin, L. J. Richter, R. R. Cavanagh, and D. S. King. **Optically Driven Surface Reactions: Evidence for the Role of Hot Electrons**. *Phys. Rev. Lett.* **61**, 1321–1324 (1988). DOI: [10.1103/PhysRevLett.61.1321](https://doi.org/10.1103/PhysRevLett.61.1321) (see page 55).
- [214] S. A. Buntin, L. J. Richter, D. S. King, and R. R. Cavanagh. **State-resolved evidence for hot carrier driven surface reactions: Laser-induced desorption of NO from Pt(111)**. *J. Chem. Phys.* **91**, 10, 6429–6446 (1989). DOI: [10.1063/1.457411](https://doi.org/10.1063/1.457411) (see page 55).
- [215] J. A. Prybyla, T. F. Heinz, J. A. Misewich, M. M. T. Loy, and J. H. Glowina. **Desorption induced by femtosecond laser pulses**. *Phys. Rev. Lett.* **64**, 1537–1540 (1990). DOI: [10.1103/PhysRevLett.64.1537](https://doi.org/10.1103/PhysRevLett.64.1537) (see pages 56, 61).
- [216] J. A. Prybyla, H. W. K. Tom, and G. D. Aumiller. **Femtosecond time-resolved surface reaction: Desorption of Co from Cu(111) in 325 fsec**. *Phys. Rev. Lett.* **68**, 503–506 (1992). DOI: [10.1103/PhysRevLett.68.503](https://doi.org/10.1103/PhysRevLett.68.503) (see pages 56, 62).
- [217] F. Budde, T. Heinz, A. Kalamarides, M. Loy, and J. Misewich. **Vibrational distributions in desorption induced by femtosecond laser pulses: coupling of adsorbate vibration to substrate electronic excitation**. *Surf. Sci.* **283**, 1, 143–457 (1993). DOI: [10.1016/0039-6028\(93\)90973-N](https://doi.org/10.1016/0039-6028(93)90973-N) (see pages 56, 61).
- [218] F.-J. Kao, D. G. Busch, D. Cohen, D. Gomes da Costa, and W. Ho. **Femtosecond laser desorption of molecularly adsorbed oxygen from Pt(111)**. *Phys. Rev. Lett.* **71**, 2094–2097 (1993). DOI: [10.1103/PhysRevLett.71.2094](https://doi.org/10.1103/PhysRevLett.71.2094) (see page 56).
- [219] D. G. Busch and W. Ho. **Direct observation of the crossover from single to multiple excitations in femtosecond surface photochemistry**. *Phys. Rev. Lett.* **77**, 7, 1338–1341 (1996). DOI: [10.1103/PhysRevLett.77.1338](https://doi.org/10.1103/PhysRevLett.77.1338) (see pages 56, 60, 66).
- [220] P. Saalfrank, G. Boendgen, C. Corriol, and T. Nakajima. **Direct and indirect DIET and DIMET from semiconductor and metal surfaces: What can we learn from ‘toy models’?** *Faraday Discuss.* **117**, 65–83 (2000). DOI: [10.1039/B002734K](https://doi.org/10.1039/B002734K) (see pages 56, 60).

- [221] P. A. Redhead. **Interaction of slow electrons with chemisorbed oxygen.** *Can. J. Phys.* **42**, 5, 886–905 (1964). DOI: [10.1139/p64-083](https://doi.org/10.1139/p64-083) (see page 56).
- [222] N. H. March. **Chemical Bonds Outside Metal Surfaces.** Springer New York, New York (1986). ISBN: 978-1-4612-9252-4. DOI: [10.1007/978-1-4613-2117-0](https://doi.org/10.1007/978-1-4613-2117-0) (see page 56).
- [223] J. E. Cunningham, D. Greenlaw, J. L. Erskine, R. P. Layton, and C. P. Flynn. **Coupling of electronically excited physisorbed atoms to metal substrates: Xe on Au and Ti.** *J. Phys. F: Met. Phys.* **7**, 10, L281 (1977). DOI: [10.1088/0305-4608/7/10/001](https://doi.org/10.1088/0305-4608/7/10/001) (see page 57).
- [224] J. E. Cunningham, D. Greenlaw, C. P. Flynn, and J. L. Erskine. **Adsorbate Spectra on Metal and Oxide Surfaces.** *Phys. Rev. Lett.* **42**, 328–331 (1979). DOI: [10.1103/PhysRevLett.42.328](https://doi.org/10.1103/PhysRevLett.42.328) (see page 57).
- [225] P. J. Feibelman and M. L. Knotek. **Reinterpretation of electron-stimulated desorption data from chemisorption systems.** *Phys. Rev. B* **18**, 6531–6539 (1978). DOI: [10.1103/PhysRevB.18.6531](https://doi.org/10.1103/PhysRevB.18.6531) (see page 60).
- [226] H. Nakatsuji, H. Morita, H. Nakai, Y. Murata, and K. Fukutani. **Theoretical study on the photostimulated desorption of CO from a Pt surface.** *J. Chem. Phys.* **104**, 2, 714–726 (1996). DOI: [10.1063/1.470796](https://doi.org/10.1063/1.470796) (see page 60).
- [227] X.-Y. Zhu and J. M. White. **Vibration-mediated uv photodesorption: Ammonia on GaAs.** *Phys. Rev. Lett.* **68**, 3359–3362 (1992). DOI: [10.1103/PhysRevLett.68.3359](https://doi.org/10.1103/PhysRevLett.68.3359) (see page 60).
- [228] J. Misewich, S. Nakabayashi, P. Weigand, M. Wolf, and T. Heinz. **Anomalous branching ratio in the femtosecond surface chemistry of O<sub>2</sub>Pd(111).** *Surf. Sci.* **363**, 1, 204–213 (1996). DOI: [10.1016/0039-6028\(96\)00138-0](https://doi.org/10.1016/0039-6028(96)00138-0) (see page 61).
- [229] J. A. Misewich, T. F. Heinz, P. Weigand, and A. Kalamarides. **Femtosecond Surface Science: The Dynamics of Desorption**, 764–826. In: *Laser Spectroscopy and Photochemistry on Metal Surfaces*. Ed. by H.-L. Dai and W. Ho. World Scientific Publishing Company (1995). DOI: [10.1142/9789814317252\\_0004](https://doi.org/10.1142/9789814317252_0004) (see page 61).
- [230] J. C. Tully. **Nonadiabatic processes in molecular collisions**, 217–267. In: *Dynamics of Molecular Collisions: Part B*. Ed. by W. H. Miller. Vol. 2. Modern Theoretical Chemistry. Springer Science+Business Media, New York (1976). ISBN: 978-1-4757-0644-4. DOI: [10.1007/978-1-4757-0644-4\\_5](https://doi.org/10.1007/978-1-4757-0644-4_5) (see page 61).
- [231] B. Persson and M. Persson. **Vibrational lifetime for CO adsorbed on Cu(100).** *Solid State Commun.* **36**, 2, 175–179 (1980). DOI: [10.1016/0038-1098\(80\)90677-8](https://doi.org/10.1016/0038-1098(80)90677-8) (see page 61).

- [232] T. Greber. **Charge-transfer induced particle emission in gas surface reactions.** *Surf. Sci. Rep.* **28**, 1, 1–64 (1997). DOI: [10.1016/S0167-5729\(97\)00005-8](https://doi.org/10.1016/S0167-5729(97)00005-8) (see page 61).
- [233] L. Diekhöner, L. Hornekær, H. Mortensen, E. Jensen, A. Baurichter, V. V. Petrunin, and A. C. Luntz. **Indirect evidence for strong nonadiabatic coupling in N<sub>2</sub> associative desorption from and dissociative adsorption on Ru(0001).** *J. Chem. Phys.* **117**, 10, 5018–5030 (2002). DOI: [10.1063/1.1498476](https://doi.org/10.1063/1.1498476) (see page 61).
- [234] R. H. M. Groeneveld, R. Sprik, and A. Lagendijk. **Effect of a nonthermal electron distribution on the electron-phonon energy relaxation process in noble metals.** *Phys. Rev. B* **45**, 5079–5082 (1992). DOI: [10.1103/PhysRevB.45.5079](https://doi.org/10.1103/PhysRevB.45.5079) (see page 62).
- [235] R. H. M. Groeneveld, R. Sprik, and A. Lagendijk. **Femtosecond spectroscopy of electron-electron and electron-phonon energy relaxation in Ag and Au.** *Phys. Rev. B* **51**, 11433–11445 (1995). DOI: [10.1103/PhysRevB.51.11433](https://doi.org/10.1103/PhysRevB.51.11433) (see page 62).
- [236] J. Hodak, I. Martini, and G. V. Hartland. **Ultrafast study of electron-phonon coupling in colloidal gold particles.** *Chem. Phys. Lett.* **284**, 1, 135–141 (1998). DOI: [10.1016/S0009-2614\(97\)01369-9](https://doi.org/10.1016/S0009-2614(97)01369-9) (see page 62).
- [237] B. Rethfeld, K. Sokolowski-Tinten, D. von der Linde, and S. I. Anisimov. **Timescales in the response of materials to femtosecond laser excitation.** *Appl. Phys. A* **79**, 4, 767–769 (2004). DOI: [10.1007/s00339-004-2805-9](https://doi.org/10.1007/s00339-004-2805-9) (see page 62).
- [238] J. G. Fujimoto, J. M. Liu, E. P. Ippen, and N. Bloembergen. **Femtosecond Laser Interaction with Metallic Tungsten and Nonequilibrium Electron and Lattice Temperatures.** *Phys. Rev. Lett.* **53**, 1837–1840 (1984). DOI: [10.1103/PhysRevLett.53.1837](https://doi.org/10.1103/PhysRevLett.53.1837) (see page 62).
- [239] W. S. Fann, R. Storz, H. W. K. Tom, and J. Bokor. **Direct measurement of nonequilibrium electron-energy distributions in subpicosecond laser-heated gold films.** *Phys. Rev. Lett.* **68**, 2834–2837 (1992). DOI: [10.1103/PhysRevLett.68.2834](https://doi.org/10.1103/PhysRevLett.68.2834) (see pages 62, 66).
- [240] W. S. Fann, R. Storz, H. W. K. Tom, and J. Bokor. **Electron thermalization in gold.** *Phys. Rev. B* **46**, 13592–13595 (1992). DOI: [10.1103/PhysRevB.46.13592](https://doi.org/10.1103/PhysRevB.46.13592) (see pages 62, 66).
- [241] C.-K. Sun, F. Vallée, L. H. Acioli, E. P. Ippen, and J. G. Fujimoto. **Femtosecond-tunable measurement of electron thermalization in gold.** *Phys. Rev. B* **50**, 15337–15348 (1994). DOI: [10.1103/PhysRevB.50.15337](https://doi.org/10.1103/PhysRevB.50.15337) (see page 62).
- [242] T. Hertel, E. Knoesel, M. Wolf, and G. Ertl. **Ultrafast Electron Dynamics at Cu(111): Response of an Electron Gas to Optical Excitation.** *Phys. Rev. Lett.* **76**, 535–538 (1996). DOI: [10.1103/PhysRevLett.76.535](https://doi.org/10.1103/PhysRevLett.76.535) (see page 62).

- [243] M. Aeschlimann, M. Bauer, S. Pawlik, W. Weber, R. Burgermeister, D. Oberli, and H. C. Siegmann. **Ultrafast Spin-Dependent Electron Dynamics in fcc Co**. *Phys. Rev. Lett.* **79**, 5158–5161 (1997). DOI: [10.1103/PhysRevLett.79.5158](https://doi.org/10.1103/PhysRevLett.79.5158) (see page 62).
- [244] M. Lisowski, P. A. Loukakos, U. Bovensiepen, J. Stähler, C. Gahl, and M. Wolf. **Ultra-fast dynamics of electron thermalization, cooling and transport effects in Ru(001)**. *Appl. Phys. A* **78**, 2, 165–176 (2004). DOI: [10.1007/s00339-003-2301-7](https://doi.org/10.1007/s00339-003-2301-7) (see pages 62, 66).
- [245] G. L. Eesley. **Observation of Nonequilibrium Electron Heating in Copper**. *Phys. Rev. Lett.* **51**, 2140–2143 (1983). DOI: [10.1103/PhysRevLett.51.2140](https://doi.org/10.1103/PhysRevLett.51.2140) (see page 64).
- [246] H. E. Elsayed-Ali, T. B. Norris, M. A. Pessot, and G. A. Mourou. **Time-resolved observation of electron-phonon relaxation in copper**. *Phys. Rev. Lett.* **58**, 1212–1215 (1987). DOI: [10.1103/PhysRevLett.58.1212](https://doi.org/10.1103/PhysRevLett.58.1212) (see page 64).
- [247] S. D. Brorson, J. G. Fujimoto, and E. P. Ippen. **Femtosecond electronic heat-transport dynamics in thin gold films**. *Phys. Rev. Lett.* **59**, 1962–1965 (1987). DOI: [10.1103/PhysRevLett.59.1962](https://doi.org/10.1103/PhysRevLett.59.1962) (see page 64).
- [248] M. Kaganov, I. Lifshitz, and L. Tanatarov. **Relaxation between Electrons and the Crystalline Lattice**. *Sov. Phys.-JETP* **4**, 173–178 (1957). URL: [http://jetp.ras.ru/cgi-bin/dn/e\\_004\\_02\\_0173.pdf](http://jetp.ras.ru/cgi-bin/dn/e_004_02_0173.pdf) (see page 64).
- [249] T. Q. Qiu and C. L. Tien. **Heat Transfer Mechanisms During Short-Pulse Laser Heating of Metals**. *J. Heat Transfer* **115**, 4, 835–841 (1993). DOI: [10.1115/1.2911377](https://doi.org/10.1115/1.2911377) (see pages 64, 65).
- [250] W. J. Scouler. **Temperature-Modulated Reflectance of Gold from 2 to 10 eV**. *Phys. Rev. Lett.* **18**, 445–448 (1967). DOI: [10.1103/PhysRevLett.18.445](https://doi.org/10.1103/PhysRevLett.18.445) (see page 65).
- [251] G. P. Pells and M. Shiga. **The optical properties of copper and gold as a function of temperature**. *J. Phys. C: Solid State Phys.* **2**, 10, 1835 (1969). DOI: [10.1088/0022-3719/2/10/318](https://doi.org/10.1088/0022-3719/2/10/318) (see page 65).
- [252] C. Kittel. **Introduction to Solid State Physics**. John Wiley & Sons, New York (2004). ISBN: 978-0-471-41526-8 (see page 65).
- [253] R. Baierlin. **Thermal Physics**. Cambridge University Press, New York (1999). ISBN: 978-0511840227. DOI: [10.1017/CBO9780511840227](https://doi.org/10.1017/CBO9780511840227) (see page 65).
- [254] L. Jiang and H.-L. Tsai. **Improved Two-Temperature Model and Its Application in Ultrashort Laser Heating of Metal Films**. *J. Heat Transfer* **127**, 10, 1167–1173 (2005). DOI: [10.1115/1.2035113](https://doi.org/10.1115/1.2035113) (see pages 65, 66).

- [255] N. W. Ashcroft and N. D. Mermin. **Solid State Physics**. Saunders College, Philadelphia (1988). ISBN: 978-0030493461 (see page 65).
- [256] E. Majchrzak and J. Poteralska. **Two-temperature microscale heat transfer model. Part I: Determination of electrons parameters**. *Sci. Res. Inst. Math. Comput. Sci.* **9**, 1, 99–108 (2010). URL: [https://amcm.pcz.pl/2010\\_1/art\\_12.pdf](https://amcm.pcz.pl/2010_1/art_12.pdf) (see page 65).
- [257] D. Bejan and G. Raşsev. **Nonequilibrium electron distribution in metals**. *Phys. Rev. B* **55**, 4250–4256 (1997). DOI: [10.1103/PhysRevB.55.4250](https://doi.org/10.1103/PhysRevB.55.4250) (see page 66).
- [258] D. A. Papaconstantopoulos. **Handbook of the Band Structure of Elemental Solids**. Springer Science+Business Media, New York (1986). ISBN: 978-1-4419-8264-3. DOI: [10.1007/978-1-4419-8264-3](https://doi.org/10.1007/978-1-4419-8264-3) (see page 66).
- [259] F.-J. Kao, D. G. Busch, D. Gomes da Costa, and W. Ho. **Femtosecond versus nanosecond surface photochemistry: O<sub>2</sub>+CO on Pt(111) at 80 K**. *Phys. Rev. Lett.* **70**, 4098–4101 (1993). DOI: [10.1103/PhysRevLett.70.4098](https://doi.org/10.1103/PhysRevLett.70.4098) (see page 66).
- [260] S. Deliwala, R. Finlay, J. Goldman, T. Her, W. Mieher, and E. Mazur. **Surface femtochemistry of O<sub>2</sub> and CO on Pt(111)**. *Chem. Phys. Lett.* **242**, 6, 617–622 (1995). DOI: [10.1016/0009-2614\(95\)00791-2](https://doi.org/10.1016/0009-2614(95)00791-2) (see page 66).
- [261] M. Brandbyge, P. Hedegård, T. F. Heinz, J. A. Misewich, and D. M. Newns. **Electronically driven adsorbate excitation mechanism in femtosecond-pulse laser desorption**. *Phys. Rev. B* **52**, 6042–6056 (1995). DOI: [10.1103/PhysRevB.52.6042](https://doi.org/10.1103/PhysRevB.52.6042) (see page 66).
- [262] P. Ehrenfest. **Bemerkung über die angenäherte Gültigkeit der klassischen Mechanik innerhalb der Quantenmechanik**. *Z. Phys.* **45**, 7, 455–457 (1927). DOI: [10.1007/BF01329203](https://doi.org/10.1007/BF01329203) (see page 68).
- [263] D. A. McCormack and G.-J. Kroes. **Accuracy of trajectory methods for activated adsorption of H<sub>2</sub> on Cu(100)**. *Chem. Phys. Lett.* **296**, 5, 515–520 (1998). DOI: [10.1016/S0009-2614\(98\)01103-8](https://doi.org/10.1016/S0009-2614(98)01103-8) (see page 70).
- [264] H. Busnengo, E. Pijper, M. Somers, G. Kroes, A. Salin, R. Olsen, D. Lemoine, and W. Dong. **Six-dimensional quantum and classical dynamics study of H<sub>2</sub>( $\nu=0, J=0$ ) scattering from Pd(111)**. *Chem. Phys. Lett.* **356**, 5, 515–522 (2002). DOI: [10.1016/S0009-2614\(02\)00404-9](https://doi.org/10.1016/S0009-2614(02)00404-9) (see page 70).
- [265] J. C. Tully. **Molecular dynamics with electronic transitions**. *J. Chem. Phys.* **93**, 2, 1061–1071 (1990). DOI: [10.1063/1.459170](https://doi.org/10.1063/1.459170) (see page 70).
- [266] R. Zwanzig. **Time-Correlation Functions and Transport Coefficients in Statistical Mechanics**. *Annu. Rev. Phys. Chem.* **16**, 1, 67–102 (1965). DOI: [10.1146/annurev.pc.16.100165.000435](https://doi.org/10.1146/annurev.pc.16.100165.000435) (see page 70).

- [267] H. Mori. **Transport, Collective Motion, and Brownian Motion\***. *Prog. Theor. Phys.* **33**, 3, 423–455 (1965). DOI: [10.1143/PTP.33.423](https://doi.org/10.1143/PTP.33.423) (see page 70).
- [268] R. Kubo. **The fluctuation-dissipation theorem**. *Rep. Prog. Phys.* **29**, 1, 255 (1966). DOI: [10.1088/0034-4885/29/1/306](https://doi.org/10.1088/0034-4885/29/1/306) (see page 70).
- [269] J. C. Tully, M. Gomez, and M. Head-Gordon. **Electronic and phonon mechanisms of vibrational relaxation: CO on Cu(100)**. *J. Vac. Sci. Technol. A* **11**, 4, 1914–1920 (1993). DOI: [10.1116/1.578522](https://doi.org/10.1116/1.578522) (see page 70).
- [270] M. Head-Gordon and J. C. Tully. **Molecular dynamics with electronic frictions**. *J. Chem. Phys.* **103**, 23, 10137–10145 (1995). DOI: [10.1063/1.469915](https://doi.org/10.1063/1.469915) (see pages 70, 71, 73).
- [271] A. Salin, A. Arnau, P. M. Echenique, and E. Zaremba. **Dynamic nonlinear screening of slow ions in an electron gas**. *Phys. Rev. B* **59**, 2537–2548 (1999). DOI: [10.1103/PhysRevB.59.2537](https://doi.org/10.1103/PhysRevB.59.2537) (see pages 71, 73).
- [272] C. Cohen-Tannoudji, B. Diu, and F. Laloë. **Quantum Mechanics**. 2nd ed. Vol. 2. Wiley-VCH, New York (2020). ISBN: 978-3-527-34554-0 (see page 72).
- [273] M. J. Puska and R. M. Nieminen. **Atoms embedded in an electron gas: Phase shifts and cross sections**. *Phys. Rev. B* **27**, 6121–6128 (1983). DOI: [10.1103/PhysRevB.27.6121](https://doi.org/10.1103/PhysRevB.27.6121) (see pages 72, 104).
- [274] X. Luo, B. Jiang, J. I. Juaristi, M. Alducin, and H. Guo. **Electron-hole pair effects in methane dissociative chemisorption on Ni(111)**. *J. Chem. Phys.* **145**, 4, 044704 (2016). DOI: [10.1063/1.4959288](https://doi.org/10.1063/1.4959288) (see page 72).
- [275] P. Echenique, R. Nieminen, and R. Ritchie. **Density functional calculation of stopping power of an electron gas for slow ions**. *Solid State Commun.* **37**, 10, 779–781 (1981). DOI: [10.1016/0038-1098\(81\)91173-X](https://doi.org/10.1016/0038-1098(81)91173-X) (see page 73).
- [276] P. M. Echenique, R. M. Nieminen, J. C. Ashley, and R. H. Ritchie. **Nonlinear stopping power of an electron gas for slow ions**. *Phys. Rev. A* **33**, 897–904 (1986). DOI: [10.1103/PhysRevA.33.897](https://doi.org/10.1103/PhysRevA.33.897) (see page 73).
- [277] F. Nattino, F. Costanzo, and G.-J. Kroes. **N<sub>2</sub> dissociation on W(110): An ab initio molecular dynamics study on the effect of phonons**. *J. Chem. Phys.* **142**, 10 (2015). DOI: [10.1063/1.4913979](https://doi.org/10.1063/1.4913979) (see page 74).
- [278] F. Nattino, O. Galparsoro, F. Costanzo, R. Díez Muiño, M. Alducin, and G.-J. Kroes. **Modeling surface motion effects in N<sub>2</sub> dissociation on W(110): Ab initio molecular dynamics calculations and generalized Langevin oscillator model**. *J. Chem. Phys.* **144**, 24, 244708 (2016). DOI: [10.1063/1.4954773](https://doi.org/10.1063/1.4954773) (see page 74).

- [279] P. H. Hünenberger. **Thermostat Algorithms for Molecular Dynamics Simulations**, 105–149. In: *Advanced Computer Simulation: Approaches for Soft Matter Sciences I*. Ed. by C. Holm and K. Kremer. Springer Berlin Heidelberg, Berlin, Heidelberg (2005). ISBN: 978-3-540-31558-2. DOI: [10.1007/b99427](https://doi.org/10.1007/b99427) (see pages 74, 75).
- [280] S. Nosé. **A molecular dynamics method for simulations in the canonical ensemble**. *Mol. Phys.* **52**, 2, 255–268 (1984). DOI: [10.1080/00268978400101201](https://doi.org/10.1080/00268978400101201) (see pages 74, 75).
- [281] S. Nosé. **A unified formulation of the constant temperature molecular dynamics methods**. *J. Chem. Phys.* **81**, 1, 511–519 (1984). DOI: [10.1063/1.447334](https://doi.org/10.1063/1.447334) (see pages 74, 75).
- [282] W. G. Hoover. **Canonical dynamics: Equilibrium phase-space distributions**. *Phys. Rev. A* **31**, 1695–1697 (1985). DOI: [10.1103/PhysRevA.31.1695](https://doi.org/10.1103/PhysRevA.31.1695) (see pages 74, 75).
- [283] H. Hellmann. **Einführung in die Quantenchemie**. Franz Deutliche, Leipzig (1937) (see page 76).
- [284] R. P. Feynman. **Forces in Molecules**. *Phys. Rev.* **56**, 340–343 (1939). DOI: [10.1103/PhysRev.56.340](https://doi.org/10.1103/PhysRev.56.340) (see page 76).
- [285] P. Politzer and R. R. Harris. **Electronic density distribution in nitric oxide**. *J. Am. Chem. Soc.* **92**, 7, 1834–1836 (1970). DOI: [10.1021/ja00710a007](https://doi.org/10.1021/ja00710a007) (see page 78).
- [286] R. F. W. Bader and P. M. Beddall. **Virial Field Relationship for Molecular Charge Distributions and the Spatial Partitioning of Molecular Properties**. *J. Chem. Phys.* **56**, 7, 3320–3329 (1972). DOI: [10.1063/1.1677699](https://doi.org/10.1063/1.1677699) (see page 78).
- [287] R. F. W. Bader. **Atoms in Molecules: A Quantum Theory**. Clarendon Press, Oxford (1994). ISBN: 978-0198558651 (see page 78).
- [288] F. L. Hirshfeld. **Bonded-atom fragments for describing molecular charge densities**. *Theoret. Chim. Acta* **44**, 2, 129–138 (1977). DOI: [10.1007/BF00549096](https://doi.org/10.1007/BF00549096) (see page 78).
- [289] C. Runge. **Über die numerische Auflösung von Differentialgleichungen**. *Math. Ann.* **46**, 2, 167–178 (1895). DOI: [10.1007/BF01446807](https://doi.org/10.1007/BF01446807) (see page 78).
- [290] W. Kutta. **Beitrag zur näherungsweise Integration totaler Differentialgleichungen**. *Z. Math. Phys.* **46**, 435–453 (1901) (see page 78).
- [291] L. Verlet. **Computer "Experiments" on Classical Fluids. I. Thermodynamical Properties of Lennard-Jones Molecules**. *Phys. Rev.* **159**, 98–103 (1967). DOI: [10.1103/PhysRev.159.98](https://doi.org/10.1103/PhysRev.159.98) (see page 78).

- [292] D. Beeman. **Some multistep methods for use in molecular dynamics calculations.** *J. Comput. Phys.* **20**, 2, 130–139 (1976). DOI: [10.1016/0021-9991\(76\)90059-0](https://doi.org/10.1016/0021-9991(76)90059-0) (see page 79).
- [293] N. Artrith and A. Urban. **An implementation of artificial neural-network potentials for atomistic materials simulations: Performance for TiO<sub>2</sub>.** *Comput. Mater. Sci.* **114**, 135–150 (2016). DOI: [10.1016/j.commatsci.2015.11.047](https://doi.org/10.1016/j.commatsci.2015.11.047) (see pages 82, 86).
- [294] S. Lorenz, A. Groß, and M. Scheffler. **Representing high - dimensional potential-energy surfaces for reactions at surfaces by neural networks.** *Chem. Phys. Lett.* **395**, 4, 210–215 (2004). DOI: [10.1016/j.cplett.2004.07.076](https://doi.org/10.1016/j.cplett.2004.07.076) (see page 84).
- [295] K. L. Priddy and P. E. Keller. **Artificial Neural Networks: An Introduction.** SPIE Press, Washington (2005). ISBN: 978-0819459879. DOI: [10.1117/3.633187](https://doi.org/10.1117/3.633187) (see page 86).
- [296] Y. A. LeCun, L. Bottou, G. B. Orr, and K.-R. Müller. **Efficient BackProp**, 9–48. In: *Neural Networks: Tricks of the Trade: Second Edition*. Ed. by G. Montavon, G. B. Orr, and K.-R. Müller. Springer Berlin Heidelberg, Berlin, Heidelberg (2012). ISBN: 978-3-642-35289-8. DOI: [10.1007/978-3-642-35289-8\\_3](https://doi.org/10.1007/978-3-642-35289-8_3) (see page 86).
- [297] R. Fletcher and C. M. Reeves. **Function minimization by conjugate gradients.** *Comput. J.* **7**, 2, 149–154 (1964). DOI: [10.1093/comjnl/7.2.149](https://doi.org/10.1093/comjnl/7.2.149) (see page 86).
- [298] C. G. Broyden. **The Convergence of a Class of Double-rank Minimization Algorithms 1. General Considerations.** *IMA J. Appl. Math.* **6**, 1, 76–90 (1970). DOI: [10.1093/imamat/6.1.76](https://doi.org/10.1093/imamat/6.1.76) (see page 86).
- [299] R. Fletcher. **A new approach to variable metric algorithms.** *Comput. J.* **13**, 3, 317–322 (1970). DOI: [10.1093/comjnl/13.3.317](https://doi.org/10.1093/comjnl/13.3.317) (see page 86).
- [300] D. Goldfarb. **A family of variable-metric methods derived by variational means.** *Math. Comp.* **24**, 23–26 (1970). DOI: [10.1090/S0025-5718-1970-0258249-6](https://doi.org/10.1090/S0025-5718-1970-0258249-6) (see page 86).
- [301] D. F. Shanno. **Conditioning of quasi-Newton methods for function minimization.** *Math. Comp.* **24**, 647–656 (1970). DOI: [10.1090/S0025-5718-1970-0274029-X](https://doi.org/10.1090/S0025-5718-1970-0274029-X) (see page 86).
- [302] R. H. Byrd, P. Lu, J. Nocedal, and C. Zhu. **A Limited Memory Algorithm for Bound Constrained Optimization.** *SIAM J. Sci. Comput.* **16**, 5, 1190–1208 (1995). DOI: [10.1137/0916069](https://doi.org/10.1137/0916069) (see page 86).
- [303] K. Levenberg. **A method for the solution of certain non-linear problems in least squares.** *Quart. Appl. Math.* **2**, 164–168 (1944). DOI: [10.1090/qam/10666](https://doi.org/10.1090/qam/10666) (see page 87).

- [304] D. W. Marquardt. **An Algorithm for Least-Squares Estimation of Nonlinear Parameters**. *J. Soc. Indust. Appl. Math.* **11**, 2, 431–441 (1963). DOI: [10.1137/0111030](https://doi.org/10.1137/0111030) (see page 87).
- [305] W. S. McCulloch and W. Pitts. **A logical calculus of the ideas immanent in nervous activity**. *Bull. Math. Biophys.* **5**, 4, 115–133 (1943). DOI: [10.1007/BF02478259](https://doi.org/10.1007/BF02478259) (see page 91).
- [306] F. Rosenblatt. **The perceptron: A probabilistic model for information storage and organization in the brain**. *Psychol. Rev.* **65**, 6, 386–408 (1958). DOI: [10.1037/h0042519](https://doi.org/10.1037/h0042519) (see page 91).
- [307] M. Minsky and S. A. Papert. **Perceptrons: An Introduction to Computational Geometry**. The MIT Press, Cambridge (1969). ISBN: 978-0262343930. DOI: [10.7551/mitpress/11301.001.0001](https://doi.org/10.7551/mitpress/11301.001.0001) (see page 91).
- [308] H. Gassner, M. Probst, A. Lauenstein, and K. Hermansson. **Representation of Intermolecular Potential Functions by Neural Networks**. *J. Phys. Chem. A* **102**, 24, 4596–4605 (1998). DOI: [10.1021/jp972209d](https://doi.org/10.1021/jp972209d) (see page 92).
- [309] J. Behler, S. Lorenz, and K. Reuter. **Representing molecule-surface interactions with symmetry-adapted neural networks**. *J. Chem. Phys.* **127**, 1 (2007). DOI: [10.1063/1.2746232](https://doi.org/10.1063/1.2746232) (see page 92).
- [310] J. Behler. **Atom-centered symmetry functions for constructing high-dimensional neural network potentials**. *J. Chem. Phys.* **134**, 7 (2011). DOI: [10.1063/1.3553717](https://doi.org/10.1063/1.3553717) (see pages 92, 95, 98, 100).
- [311] B. Cheng, E. A. Engel, J. Behler, C. Dellago, and M. Ceriotti. **Ab initio thermodynamics of liquid and solid water**. *Proc. Natl. Acad. Sci. U.S.A.* **116**, 4, 1110–1115 (2019). DOI: [10.1073/pnas.1815117116](https://doi.org/10.1073/pnas.1815117116) (see page 94).
- [312] A. Singraber, J. Behler, and C. Dellago. **Library-Based LAMMPS Implementation of High-Dimensional Neural Network Potentials**. *J. Chem. Theory Comput.* **15**, 3, 1827–1840 (2019). DOI: [10.1021/acs.jctc.8b00770](https://doi.org/10.1021/acs.jctc.8b00770) (see page 95).
- [313] J. Behler. **Constructing high-dimensional neural network potentials: A tutorial review**. *Int. J. Quantum Chem.* **115**, 16, 1032–1050 (2015). DOI: [10.1002/qua.24890](https://doi.org/10.1002/qua.24890) (see pages 100, 102, 134).
- [314] K. V. J. Jose, N. Artrith, and J. Behler. **Construction of high-dimensional neural network potentials using environment-dependent atom pairs**. *J. Chem. Phys.* **136**, 19 (2012). DOI: [10.1063/1.4712397](https://doi.org/10.1063/1.4712397) (see page 100).
- [315] J. S. Smith, O. Isayev, and A. E. Roitberg. **ANI-1: an extensible neural network potential with DFT accuracy at force field computational cost**. *Chem. Sci.* **8**, 3192–3203 (2017). DOI: [10.1039/C6SC05720A](https://doi.org/10.1039/C6SC05720A) (see page 100).

- [316] N. Artrith, A. Urban, and G. Ceder. **Efficient and accurate machine-learning interpolation of atomic energies in compositions with many species.** *Phys. Rev. B* **96**, 014112 (2017). DOI: [10.1103/PhysRevB.96.014112](https://doi.org/10.1103/PhysRevB.96.014112) (see page 100).
- [317] M. Gastegger, L. Schwiedrzik, M. Bittermann, F. Berzsényi, and P. Marquetand. **wACSF—Weighted atom-centered symmetry functions as descriptors in machine learning potentials.** *J. Chem. Phys.* **148**, 24 (2018). DOI: [10.1063/1.5019667](https://doi.org/10.1063/1.5019667) (see pages 100, 105).
- [318] S. Rostami, M. Amsler, and S. A. Ghasemi. **Optimized symmetry functions for machine-learning interatomic potentials of multicomponent systems.** *J. Chem. Phys.* **149**, 12 (2018). DOI: [10.1063/1.5040005](https://doi.org/10.1063/1.5040005) (see page 100).
- [319] S. N. Pozdnyakov, M. J. Willatt, A. P. Bartók, C. Ortner, G. Csányi, and M. Ceriotti. **Incompleteness of Atomic Structure Representations.** *Phys. Rev. Lett.* **125**, 166001 (2020). DOI: [10.1103/PhysRevLett.125.166001](https://doi.org/10.1103/PhysRevLett.125.166001) (see page 102).
- [320] N. Artrith, T. Morawietz, and J. Behler. **High-dimensional neural-network potentials for multicomponent systems: Applications to zinc oxide.** *Phys. Rev. B* **83**, 153101 (2011). DOI: [10.1103/PhysRevB.83.153101](https://doi.org/10.1103/PhysRevB.83.153101) (see page 102).
- [321] T. Morawietz, V. Sharma, and J. Behler. **A neural network potential-energy surface for the water dimer based on environment-dependent atomic energies and charges.** *J. Chem. Phys.* **136**, 6 (2012). DOI: [10.1063/1.3682557](https://doi.org/10.1063/1.3682557) (see page 102).
- [322] T. W. Ko, J. A. Finkler, S. Goedecker, and J. Behler. **A fourth-generation high-dimensional neural network potential with accurate electrostatics including non-local charge transfer.** *Nat. Commun.* **12**, 1, 398 (2021). DOI: [10.1038/s41467-020-20427-2](https://doi.org/10.1038/s41467-020-20427-2) (see page 102).
- [323] Y. Zhang, C. Hu, and B. Jiang. **Embedded Atom Neural Network Potentials: Efficient and Accurate Machine Learning with a Physically Inspired Representation.** *J. Phys. Chem. Lett.* **10**, 17, 4962–4967 (2019). DOI: [10.1021/acs.jpcclett.9b02037](https://doi.org/10.1021/acs.jpcclett.9b02037) (see pages 102, 111, 116, 118, 122, 160).
- [324] M. J. Stott and E. Zaremba. **Quasiatoms: An approach to atoms in nonuniform electronic systems.** *Phys. Rev. B* **22**, 1564–1583 (1980). DOI: [10.1103/PhysRevB.22.1564](https://doi.org/10.1103/PhysRevB.22.1564) (see pages 102, 103).
- [325] J. K. Nørskov and N. D. Lang. **Effective-medium theory of chemical binding: Application to chemisorption.** *Phys. Rev. B* **21**, 2131–2136 (1980). DOI: [10.1103/PhysRevB.21.2131](https://doi.org/10.1103/PhysRevB.21.2131) (see page 102).
- [326] J. K. Nørskov. **Covalent effects in the effective-medium theory of chemical binding: Hydrogen heats of solution in the 3d metals.** *Phys. Rev. B* **26**, 2875–2885 (1982). DOI: [10.1103/PhysRevB.26.2875](https://doi.org/10.1103/PhysRevB.26.2875) (see page 103).

- [327] M. J. Puska, R. M. Nieminen, and M. Manninen. **Atoms embedded in an electron gas: Immersion energies.** *Phys. Rev. B* **24**, 3037–3047 (1981). DOI: [10.1103/PhysRevB.24.3037](https://doi.org/10.1103/PhysRevB.24.3037) (see page 103).
- [328] M. S. Daw and M. I. Baskes. **Embedded-atom method: Derivation and application to impurities, surfaces, and other defects in metals.** *Phys. Rev. B* **29**, 6443–6453 (1984). DOI: [10.1103/PhysRevB.29.6443](https://doi.org/10.1103/PhysRevB.29.6443) (see page 104).
- [329] M. S. Daw and M. I. Baskes. **Semiempirical, Quantum Mechanical Calculation of Hydrogen Embrittlement in Metals.** *Phys. Rev. Lett.* **50**, 1285–1288 (1983). DOI: [10.1103/PhysRevLett.50.1285](https://doi.org/10.1103/PhysRevLett.50.1285) (see page 104).
- [330] Y. Zhang, X. Zhou, and B. Jiang. **Accelerating the Construction of Neural Network Potential Energy Surfaces: A Fast Hybrid Training Algorithm.** *Chin. J. Chem. Phys.* **30**, 6, 727–734 (2017). DOI: [10.1063/1674-0068/30/cjcp1711212](https://doi.org/10.1063/1674-0068/30/cjcp1711212) (see pages 104, 115).
- [331] S. F. Boys. **Electronic Wave Functions. I. A General Method of Calculation for the Stationary States of Any Molecular System.** *Proc. R. Soc. Lond. A* **200**, 1063, 542–554 (1950). DOI: [10.1098/rspa.1950.0036](https://doi.org/10.1098/rspa.1950.0036) (see page 105).
- [332] A. Takahashi, A. Seko, and I. Tanaka. **Conceptual and practical bases for the high accuracy of machine learning interatomic potentials: Application to elemental titanium.** *Phys. Rev. Materials* **1**, 6, 1–7 (2017). DOI: [10.1103/PhysRevMaterials.1.063801](https://doi.org/10.1103/PhysRevMaterials.1.063801) (see page 105).
- [333] Y. Zhang, R. J. Maurer, and B. Jiang. **Symmetry-Adapted High Dimensional Neural Network Representation of Electronic Friction Tensor of Adsorbates on Metals.** *J. Phys. Chem. C* **124**, 1, 186–195 (2020). DOI: [10.1021/acs.jpcc.9b09965](https://doi.org/10.1021/acs.jpcc.9b09965) (see pages 107, 129).
- [334] Y. Zhang, S. Ye, J. Zhang, C. Hu, J. Jiang, and B. Jiang. **Efficient and Accurate Simulations of Vibrational and Electronic Spectra with Symmetry-Preserving Neural Network Models for Tensorial Properties.** *J. Phys. Chem. B* **124**, 33, 7284–7290 (2020). DOI: [10.1021/acs.jpcc.0c06926](https://doi.org/10.1021/acs.jpcc.0c06926) (see page 108).
- [335] Y. Zhang, C. Hu, and B. Jiang. **Accelerating atomistic simulations with piecewise machine-learned ab Initio potentials at a classical force field-like cost.** *Phys. Chem. Chem. Phys.* **23**, 1815–1821 (2021). DOI: [10.1039/D0CP05089J](https://doi.org/10.1039/D0CP05089J) (see page 108).
- [336] Y. Zhang, J. Xia, and B. Jiang. **Physically Motivated Recursively Embedded Atom Neural Networks: Incorporating Local Completeness and Nonlocality.** *Phys. Rev. Lett.* **127**, 156002 (2021). DOI: [10.1103/PhysRevLett.127.156002](https://doi.org/10.1103/PhysRevLett.127.156002) (see page 108).

- [337] Y. Zhang, J. Xia, and B. Jiang. **REANN: A PyTorch-based end-to-end multi-functional deep neural network package for molecular, reactive, and periodic systems.** *J. Chem. Phys.* **156**, 11 (2022). DOI: [10.1063/5.0080766](https://doi.org/10.1063/5.0080766) (see page 108).
- [338] N. Gerrits, J. Geweke, E. W. F. Smeets, J. Voss, A. M. Wodtke, and G.-J. Kroes. **Closing the Gap Between Experiment and Theory: Reactive Scattering of HCl from Au(111).** *J. Phys. Chem. C* **124**, 29, 15944–15960 (2020). DOI: [10.1021/acs.jpcc.0c03756](https://doi.org/10.1021/acs.jpcc.0c03756) (see page 111).
- [339] L. Zhu, Y. Zhang, L. Zhang, X. Zhou, and B. Jiang. **Unified and transferable description of dynamics of H<sub>2</sub> dissociative adsorption on multiple copper surfaces via machine learning.** *Phys. Chem. Chem. Phys.* **22**, 13958–13964 (2020). DOI: [10.1039/D0CP02291H](https://doi.org/10.1039/D0CP02291H) (see pages 111, 175).
- [340] X. Zhou, Y. Zhang, H. Guo, and B. Jiang. **Towards bridging the structure gap in heterogeneous catalysis: the impact of defects in dissociative chemisorption of methane on Ir surfaces.** *Phys. Chem. Chem. Phys.* **23**, 4376–4385 (2021). DOI: [10.1039/D0CP06535H](https://doi.org/10.1039/D0CP06535H) (see page 111).
- [341] G. Kresse and J. Furthmüller. **Efficient iterative schemes for ab initio total-energy calculations using a plane-wave basis set.** *Phys. Rev. B* **54**, 11169–11186 (1996). DOI: [10.1103/PhysRevB.54.11169](https://doi.org/10.1103/PhysRevB.54.11169) (see pages 112, 207).
- [342] G. Kresse and J. Furthmüller. **Efficiency of ab-initio total energy calculations for metals and semiconductors using a plane-wave basis set.** *Comput. Mater. Sci.* **6**, 1, 15–50 (1996). DOI: [10.1016/0927-0256\(96\)00008-0](https://doi.org/10.1016/0927-0256(96)00008-0) (see pages 112, 207).
- [343] Y. Zhang. Personal communication. 2020 (see page 115).
- [344] R. Yin, Y. Zhang, and B. Jiang. **Strong Vibrational Relaxation of NO Scattered from Au(111): Importance of the Adiabatic Potential Energy Surface.** *J. Phys. Chem. Lett.* **10**, 19, 5969–5974 (2019). DOI: [10.1021/acs.jpcclett.9b01806](https://doi.org/10.1021/acs.jpcclett.9b01806) (see page 129).
- [345] P. Spiering and J. Meyer. **Testing Electronic Friction Models: Vibrational De-excitation in Scattering of H<sub>2</sub> and D<sub>2</sub> from Cu(111).** *J. Phys. Chem. Lett.* **9**, 7, 1803–1808 (2018). DOI: [10.1021/acs.jpcclett.7b03182](https://doi.org/10.1021/acs.jpcclett.7b03182) (see page 129).
- [346] P. Spiering, K. Shakouri, J. Behler, G.-J. Kroes, and J. Meyer. **Orbital-Dependent Electronic Friction Significantly Affects the Description of Reactive Scattering of N<sub>2</sub> from Ru(0001).** *J. Phys. Chem. Lett.* **10**, 11, 2957–2962 (2019). DOI: [10.1021/acs.jpcclett.9b00523](https://doi.org/10.1021/acs.jpcclett.9b00523) (see page 129).
- [347] E. B. Wilson. **Probable Inference, the Law of Succession, and Statistical Inference.** *J. Am. Stat. Assoc.* **22**, 158, 209–212 (1927). DOI: [10.1080/01621459.1927.10502953](https://doi.org/10.1080/01621459.1927.10502953) (see pages 137, 152, 153, 155, 220).

- [348] P. Massart. **The tight constant in the Dvoretzky-Kiefer-Wolfowitz inequality**. *Ann. Probab.* **18**, 1269–1283 (1990) (see pages 141, 142).
- [349] G. J. Kroes, E. Pijper, and A. Salin. **Dissociative chemisorption of H<sub>2</sub> on the Cu(110) surface: A quantum and quasiclassical dynamical study**. *J. Chem. Phys.* **127**, 16, 164722 (2007). DOI: [10.1063/1.2798112](https://doi.org/10.1063/1.2798112) (see pages 143–145, 151).
- [350] S. S. Zumdahl, S. A. Zumdahl, and D. J. DeCoste. **Chemistry**. 11th ed. Cengage Learning, Boston (2024). ISBN: 978-0-357-85079-4 (see page 151).
- [351] L. M. Struck, L. J. Richter, S. A. Buntin, R. R. Cavanagh, and J. C. Stephenson. **Femtosecond Laser-Induced Desorption of CO from Cu(100): Comparison of Theory and Experiment**. *Phys. Rev. Lett.* **77**, 22, 4576–4579 (1996). DOI: [10.1103/physrevlett.77.4576](https://doi.org/10.1103/physrevlett.77.4576) (see page 179).
- [352] M. Shimizu, T. Takahashi, and A. Katsuki. **Magnetic Susceptibility and Electronic Specific Heat of Transition Metals and Alloys II. Pd Metal and Pd-Ag and Pd-Rh Alloys**. *J. Phys. Soc. Jpn.* **18**, 2, 240–248 (1963). DOI: [10.1143/jpsj.18.240](https://doi.org/10.1143/jpsj.18.240) (see pages 180, 181).
- [353] A. P. Miiller and B. N. Brockhouse. **Anomalous Behavior of the Lattice Vibrations and the Electronic Specific Heat of Palladium**. *Phys. Rev. Lett.* **20**, 15, 798–801 (1968). DOI: [10.1103/PhysRevLett.20.798](https://doi.org/10.1103/PhysRevLett.20.798) (see pages 180, 181).
- [354] A. P. Miiller and B. N. Brockhouse. **Crystal Dynamics and Electronic Specific Heats of Palladium and Copper**. *Can. J. Phys.* **49**, 6, 704–723 (1971). DOI: [10.1139/p71-087](https://doi.org/10.1139/p71-087) (see pages 180, 181).
- [355] B. W. Veal and J. A. Rayne. **Heat Capacity of Palladium and Dilute Palladium: Iron Alloys from 1.4 to 100°K**. *Phys. Rev.* **135**, 2A, A442–A446 (1964). DOI: [10.1103/physrev.135.a442](https://doi.org/10.1103/physrev.135.a442) (see page 180).
- [356] P. Szymanski, A. Harris, and N. Camillone. **Temperature-dependent electron-mediated coupling in subpicosecond photoinduced desorption**. *Surf. Sci.* **601**, 16, 3335–3349 (2007). DOI: [10.1016/j.susc.2007.06.004](https://doi.org/10.1016/j.susc.2007.06.004) (see pages 181, 188, 212).
- [357] D. M. Duffy and A. M. Rutherford. **Including the Effects of Electronic Stopping and Electron-ion Interactions in Radiation Damage Simulations**. *J. Phys.: Condens. Matter* **19**, 1, 016207 (2006). DOI: [10.1088/0953-8984/19/1/016207](https://doi.org/10.1088/0953-8984/19/1/016207) (see page 182).
- [358] C. Hu, Q. Lin, H. Guo, and B. Jiang. **Influence of Supercell Size on Gas-Surface Scattering: A Case Study of CO Scattering from Au(1 1 1)**. *Chem. Phys.* **554**, 111423 (2022). DOI: [10.1016/j.chemphys.2021.111423](https://doi.org/10.1016/j.chemphys.2021.111423) (see page 185).

- [359] S. Lindner, I. Lončarić, L. Vrček, M. Alducin, J. I. Juaristi, and P. Saalfrank. **Femtosecond Laser-Induced Desorption of Hydrogen Molecules from Ru(0001): A Systematic Study Based on Machine-Learned Potentials.** *J. Phys. Chem. C* **127**, 30, 14756–14764 (2023). DOI: [10.1021/acs.jpcc.3c02941](https://doi.org/10.1021/acs.jpcc.3c02941) (see page 185).
- [360] Q. Lin and B. Jiang. **Modeling Equilibration Dynamics of Hyperthermal Products of Surface Reactions Using Scalable Neural Network Potential with First-Principles Accuracy.** *J. Phys. Chem. Lett.* **14**, 33, 7513–7518 (2023). DOI: [10.1021/acs.jpcclett.3c01708](https://doi.org/10.1021/acs.jpcclett.3c01708) (see page 185).
- [361] M. Nest and P. Saalfrank. **Open-System Density Matrix Description of Femtosecond Laser Desorption of Electronically and Vibrationally Relaxing Adsorbates: Single- and Two-Pulse Scenarios.** *J. Chem. Phys.* **116**, 16, 7189–7199 (2002). DOI: [10.1063/1.1462608](https://doi.org/10.1063/1.1462608) (see page 185).
- [362] P. Szymanski, A. L. Harris, and N. I. Camillone. **Efficient Subpicosecond Photoinduced Surface Chemistry: The Ultrafast Photooxidation of CO on Palladium.** *J. Phys. Chem. C* **112**, 40, 15802–15808 (2008). DOI: [10.1021/jp8044737](https://doi.org/10.1021/jp8044737) (see pages 207, 208, 218).
- [363] P. E. Blöchl. **Projector augmented-wave method.** *Phys. Rev. B* **50**, 17953–17979 (1994). DOI: [10.1103/PhysRevB.50.17953](https://doi.org/10.1103/PhysRevB.50.17953) (see page 207).
- [364] G. Kresse and D. Joubert. **From ultrasoft pseudopotentials to the projector augmented-wave method.** *Phys. Rev. B* **59**, 1758–1775 (1999). DOI: [10.1103/PhysRevB.59.1758](https://doi.org/10.1103/PhysRevB.59.1758) (see page 207).
- [365] H. J. Monkhorst and J. D. Pack. **Special points for Brillouin-zone integrations.** *Phys. Rev. B* **13**, 5188–5192 (1976). DOI: [10.1103/PhysRevB.13.5188](https://doi.org/10.1103/PhysRevB.13.5188) (see page 207).
- [366] J. D. Pack and H. J. Monkhorst. **"Special points for Brillouin-zone integrations"—a reply.** *Phys. Rev. B* **16**, 1748–1749 (1977). DOI: [10.1103/PhysRevB.16.1748](https://doi.org/10.1103/PhysRevB.16.1748) (see page 207).
- [367] M. Methfessel and A. T. Paxton. **High-precision sampling for Brillouin-zone integration in metals.** *Phys. Rev. B* **40**, 3616–3621 (1989). DOI: [10.1103/PhysRevB.40.3616](https://doi.org/10.1103/PhysRevB.40.3616) (see page 207).



In this Thesis, femtosecond laser-induced desorption of CO from Pd(111) at various coverages, as well as photodesorption and photooxidation of CO coadsorbed with oxygen (0.25 ML O + 0.50 ML CO/Pd(111)), are examined. Using ab initio molecular dynamics with electronic friction (AIMDEF) and neural network-based potential energy surfaces (NN PESs), the research addresses the interplay of electronic and phononic excitations. Multiple factors –including coverage, laser fluence, and isotope effects– are investigated.

Simulations underscore the cooperation of electrons and phonons in aforementioned processes, and reveal their relative roles on desorption. Oxygen coadsorption modifies interadsorbate energy exchange, enabling the formation of CO<sub>2</sub>. By incorporating NN PESs, computational efficiency is significantly increased, allowing long-timescale dynamics and more comprehensive statistical analyses. These findings provide a deeper understanding of CO desorption and oxidation on Pd(111), advancing theoretical modeling and potential applications in surface chemistry.



Universidad  
del País Vasco

Euskal Herriko  
Unibertsitatea

